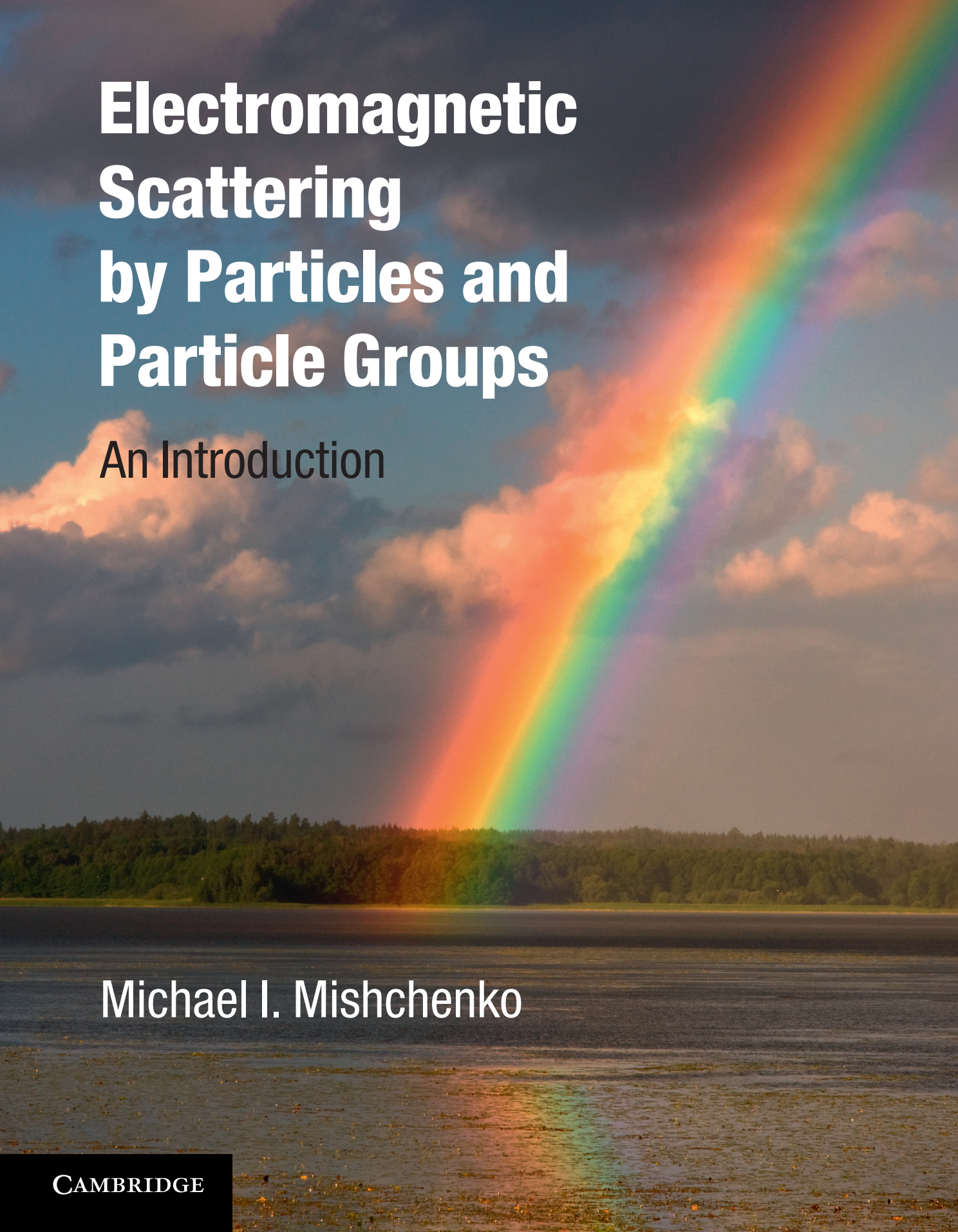

Electromagnetic Scattering by Particles and Particle Groups

An Introduction

Michael I. Mishchenko

CAMBRIDGE

Electromagnetic Scattering by Particles and Particle Groups
An Introduction

The scattering and absorption of light and other electromagnetic radiation by particles and particle groups are central to many science and engineering fields. Unfortunately, the discipline of studying these phenomena has gained the reputation of being very technically complex and incomprehensible. Now, this self-contained and accessible book provides a thorough introduction to the basic physical and mathematical principles of the subject.

For the first time the theories of electromagnetic scattering, radiative transfer, and weak localization are combined into a unified, consistent branch of physical optics based directly on the Maxwell equations. A particular focus is given to key aspects such as time and ensemble averaging at different scales, ergodicity, and the physical nature of measurements afforded by actual photopolarimeters.

Featuring over 120 end-of-chapter exercises, with hints and solutions provided, this clear, one-stop resource is ideal for self-study or classroom use, and will be invaluable to both graduate students and researchers in remote sensing, physical and biomedical optics, optical communications, optical particle characterization, atmospheric physics, and astrophysics.

Michael I. Mishchenko is a Senior Scientist at the NASA Goddard Institute for Space Studies in New York. He has published widely on electromagnetic scattering and remote sensing, including editing three contributory monographs, and is the first author of three books (including *Multiple Scattering of Light by Particles*, with Larry Travis and Andrew Lacis, Cambridge University Press 2006). In other publishing work, he has been Editor-in-Chief of the *Journal of Quantitative Spectroscopy and Radiative Transfer* and served previously as Topical Editor of *Applied Optics*. Dr. Mishchenko is an elected Fellow of four major professional societies and has received many professional awards, including the Henry G. Houghton Award from the American Meteorological Society, two NASA Medals for Exceptional Scientific Achievement, and the Hendrik C. van de Hulst Award from Elsevier.

Electromagnetic Scattering by Particles and Particle Groups

An Introduction

MICHAEL I. MISHCHENKO

NASA Goddard Institute for Space Studies

CAMBRIDGE
UNIVERSITY PRESS

CAMBRIDGE
UNIVERSITY PRESS

University Printing House, Cambridge CB2 8BS, United Kingdom

Published in the United States of America by Cambridge University Press, New York

Cambridge University Press is part of the University of Cambridge.

It furthers the University's mission by disseminating knowledge in the pursuit of education, learning and research at the highest international levels of excellence.

www.cambridge.org
Information on this title: www.cambridge.org/9780521519922

© NASA Goddard Institute for Space Studies 2014

This publication is in copyright. Subject to statutory exception and to the provisions of relevant collective licensing agreements, no reproduction of any part may take place without the written permission of Cambridge University Press.

First published 2014

Printed in the United Kingdom by Clays, St Ives PLC

A catalog record for this publication is available from the British Library

Library of Congress Cataloging in Publication data

ISBN 978-0-521-51992-2 Hardback

Cambridge University Press has no responsibility for the persistence or accuracy of URLs for external or third-party internet websites referred to in this publication, and does not guarantee that any content on such websites is, or will remain, accurate or appropriate.

To Nadia, Andrey, Natasha, and Sergei

Contents

Preface *page* xiii
Acknowledgments xv
Acronyms xvii

1 Introduction 1
1.1 General framework 3
1.2 Electromagnetic scattering 6
1.3 Further remarks 9
1.4 Energy-budget and optical-characterization problems 10
1.5 Electromagnetic spectrum 14

2 The macroscopic Maxwell equations and monochromatic fields 15
2.1 The macroscopic Maxwell equations and constitutive relations 15
2.2 Boundary conditions 17
2.3 Monochromatic fields 19
2.4 Energy budget 21
2.5 Lossless, lossy, and active media 24
Problems 26
Notes and further reading 27

3 Fundamental homogeneous-medium solutions of the macroscopic Maxwell equations 30
3.1 Plane-wave solution 30
3.2 Spherical-wave solution 35
Problems 39

4 Basic theory of frequency-domain electromagnetic scattering by a fixed finite object 41
4.1 Statement of problem 41
4.2 Existence and uniqueness of solution 43

4.3 Volume integral equation 44
4.4 Discussion 47
4.5 Dyadic transition operator 48
Problems 48
Notes and further reading 49

5 Far-field scattering 50
5.1 Scattering in the far zone 50
5.2 Theoretical criteria of the far-field limit 53
5.3 Scattering dyadic and amplitude scattering matrix 56
5.4 Reciprocity 58
5.5 Scale invariance rule 59
Problems 60
Notes 60

6 The Foldy equations 62
6.1 Vector form of the Foldy equations 62
6.2 Neumann expansion of the total field 65
6.3 Far-field Foldy equations 66
6.4 Far-field Neumann expansion of the total field 70
Problems 71
Notes and further reading 71

7 The Stokes parameters 72
7.1 The Stokes parameters of a plane electromagnetic wave 73
7.2 Rotation transformation rule for the Stokes parameters 76
7.3 Ellipsometric content of the Stokes parameters 77
7.4 The Stokes parameters of a spherical electromagnetic wave 82
Problems 83
Notes and further reading 85

8 Poynting–Stokes tensor 87
Problems 88

9 Polychromatic electromagnetic fields 89
9.1 Time-averaged Poynting–Stokes tensor and Poynting vector of a polychromatic field with monochromatic components 89
9.2 Time-averaged Stokes parameters of a parallel polychromatic beam with monochromatic components 91
9.3 Polychromatic field with quasi-monochromatic components 92
9.4 Derivative polarimetric characteristics of a polychromatic beam 96
Problems 98
Further reading 98

10 Polychromatic scattering by fixed and randomly changing objects 99
10.1 Monochromatic scattering by a fixed object 99
10.2 Polychromatic scattering by a fixed object 101
10.3 Stochastic scattering object 103
10.4 Ergodicity 107
Problems 109
Notes and further reading 109

11 Measurement of electromagnetic energy flow 111
11.1 Direction-insensitive detectors 112
11.2 Photoelectric detector as a Poynting-meter 114
11.3 Preisendorfer's radiance-function meter 117
11.4 Well-collimated radiometers 120
11.5 Response of a well-collimated radiometer to polychromatic light 125
11.6 Panoramic radiometers 128
Problems 128
Notes and further reading 129

12 Measurement of the Stokes parameters 131
12.1 Polarizers 131
12.2 Retarders 134
12.3 Measurement of the Stokes parameters 135
Problems 136
Further reading 136

13 Description of far-field scattering in terms of actual optical observables 137
13.1 Electromagnetic response of a well-collimated radiometer 137
13.2 Phase matrix 145
13.3 Extinction matrix 149
13.4 Energy-budget problem 151
13.5 Derivative characteristics of far-field scattering 153
13.6 Polychromatic far-field scattering by a fixed object 156
13.7 Far-field scattering by a stochastic object 157
13.8 Far-field scattering by an ergodic random object 159
13.9 Ensemble averaging 160
Problems 165
Notes and further reading 167

14 Electromagnetic scattering by a small random group of sparsely distributed particles 168
14.1 Single-scattering approximation for a fixed group of particles 169

14.2 Ensemble-averaged Poynting–Stokes tensor of the total field 171
14.3 Energy-budget problem 175
14.4 Response of a remote well-collimated radiometer 176
14.5 First-order-scattering approximation 177
14.6 Analysis of the first-order-scattering approximation 179
Problems 182

15 Statistically isotropic and mirror-symmetric random particles 184
15.1 Symmetries of the Stokes scattering matrix 186
15.2 Statistically isotropic and mirror-symmetric random particle 189
15.3 Phase matrix 190
15.4 Exact forward-scattering direction and extinction matrix 193
15.5 Exact backward scattering 196
15.6 Scattering cross section and asymmetry parameter 198
15.7 Spherically symmetric particle 200
15.8 Effects of morphology and orientation 200
15.9 Normalized scattering and phase matrices 201
15.10 Expansion in Wigner *d*-functions 203
Problems 209

16 Numerical computations and laboratory measurements of electromagnetic scattering 212
16.1 Numerically exact theoretical techniques 213
16.1.1 The Lorenz–Mie theory 213
16.1.2 Separation of variables method 215
16.1.3 Multi-sphere and superposition *T*-matrix methods 215
16.1.4 Finite element method 216
16.1.5 Finite difference time domain method 217
16.1.6 Point-matching method 217
16.1.7 Volume integral equation methods 218
16.1.8 *T*-matrix method 219
16.1.9 Pros and cons of numerically exact computer solvers of the MMEs 224
16.2 Geometrical optics approximation 225
16.3 Controlled laboratory measurements 231
16.3.1 Measurements in the visible and infrared 232
16.3.2 Measurements at microwave frequencies 233
Problem 235
Notes and further reading 235

17 Far-field observables: qualitative and quantitative traits 238
17.1 Deterministic particle 238

17.2 Random spherical particle 247
17.3 Random morphologically complex particle 251
17.4 Optical characterization 266
Problems 269
Further reading 269

18 Electromagnetic scattering by discrete random media: far field 270
18.1 Is there multiple scattering? 271
18.2 Speckle 274
18.3 Dynamic and static scattering 277
18.4 Static scattering by a random particulate volume 277
18.5 Conditions of applicability of the single-scattering approximation 283
Problems 284
Notes and further reading 285

19 Near-field scattering by a sparse discrete random medium: microphysical radiative transfer theory 286
19.1 The Twersky approximation 287
19.2 The Twersky expansion of the coherent field 290
19.3 Coherent field 293
19.4 Transfer equation for the coherent field 298
19.5 Ladder approximation for the dyadic correlation function 299
19.6 Integral equation for the ladder specific coherency dyadic 309
19.7 Integro-differential equation for the diffuse specific coherency dyadic 312
19.8 Radiative transfer equation 314
19.9 Statistically isotropic and mirror-symmetric random particles 318
19.10 Energy-budget problem 318
19.11 Reading of a well-collimated radiometer 319
19.12 External observation point 322
19.13 Summary of assumptions and approximations 324
19.14 Corollaries of the microphysical radiative transfer theory 329
19.15 “Independent” scattering 331
19.16 Gaseous media 332
Problems 333
Notes and further reading 334

20 Radiative transfer in plane-parallel particulate media 338
20.1 The standard problem 339
20.2 Integral equation 342
20.3 Scalar approximation 343

20.4 Directional reflectance and spherical and plane albedos 344
20.5 Polarization as an effect and as a characterization tool 352
Problems 355
Notes and further reading 355

21 Weak localization 357
21.1 Weak localization by a sparse discrete random medium 357
21.2 Weak localization by a plane-parallel discrete random medium 361
21.2.1 Exact backscattering direction 363
21.2.2 Angular dependence of weak localization: Rayleigh scattering 366
Problems 367

22 Epilogue 368
Problems 371

Appendix A Dyads and dyadics 372
Problems 373
Notes and further reading 374
Appendix B Free-space dyadic Green's function 375
Problems 377
Notes and further reading 377
Appendix C Euler rotation angles 378
Appendix D Spherical-wave decomposition of a plane wave in the far zone 380
Appendix E Integration quadrature formulas 382
Appendix F Wigner *d*-functions 385
Further reading 389
Appendix G Stationary phase evaluation of a double integral 390
Appendix H Hints and answers to selected problems 392

References 406
Index 427
Color plates section between pages 222 and 223

Preface

The phenomena of scattering and absorption of light and other electromagnetic radiation by small particles and particle groups are central to a great variety of science and engineering fields. Owing to a large body of research, the discipline of studying these phenomena has recently undergone profound and paradigm-shifting developments. Among the most important advances are the following:

- Dramatic improvements in numerical solvers of the Maxwell equations coupled with the ever-growing computer capability have enabled direct, numerically exact modeling of electromagnetic scattering by particles and particle groups of unprecedented morphological complexity.
- The rigorous physical basis of monochromatic and polychromatic scattering by random particles and random particle groups has been established.
- Owing to the development of a rigorous microphysical approach, the centuries-old disciplines of directional photometry and radiative transfer have become legitimate branches of physical optics.
- Direct computer solutions of the Maxwell equations have confirmed the mesoscopic origin of radiative transfer and weak localization of electromagnetic waves (also known as coherent backscattering) in sparse particulate media.

The main purpose of this textbook is to provide a self-contained and accessible summary of these developments in the framework of a thorough introduction to the fundamental physical and mathematical principles of the subject. Particular attention is paid to key (and often overlooked) aspects, such as time and ensemble averaging at different scales, ergodicity of stochastic scattering objects, and the physical nature of measurements afforded by actual directional photometers and photopolarimeters. Given its subject matter and specific content, it is hoped that this textbook will be useful to graduate students and researchers in terrestrial and planetary remote sensing, physical and biomedical optics, optical communica-

tions, optical particle characterization, atmospheric physics, oceanography, and astrophysics.

Consistent with its overall objective, this textbook features more than 120 end-of-chapter exercises of varying complexity. The simplest ones require the student to complete derivations that are sketched but not detailed in the main text or serve to illustrate certain key concepts and results. Most of these exercises are relatively straightforward, but can sometimes be tedious. Some exercises invite the student to think on issues not specifically covered by the textbook, but nonetheless useful for understanding the main text. A few exercises border on research projects and may have been the subject of recent publications. The more challenging exercises are supplemented by hints or full solutions collected in Appendix H.

Several appendices provide the requisite mathematical background beyond the standard calculus and vector calculus material and help make this textbook a one-stop resource suitable for self-study or classroom use. The reference list is intended to be representative, but not necessarily comprehensive. Preference is given to classical papers, monographs, and state-of-the-art reviews. Most chapters are concluded by notes briefly outlining the history of the subject and helping the reader navigate through more advanced literature.

In many respects this textbook is an outgrowth of the previous monographs by Mishchenko *et al.* (2002, 2006) in which the reader can find further technical details, as well as a plethora of specific examples and applications. Both monographs are available on-line and will hereinafter be referred to as MTL1 and MTL2, respectively.

For consistency, I closely follow the notation adopted in MTL1 and MTL2 and denote vectors using the Times bold font and matrices using the Arial bold font. Unit vectors are denoted by a caret, whereas dyads and dyadics are denoted by the symbol $\leftrightarrow$. The Times italic font is reserved for scalar quantities, important exceptions being the square root of negative one, the differential sign, and the base of natural logarithms, which are denoted by upright Times characters i, d, and e, respectively. Another exception is the relative refractive index, which is denoted by a sloping sans serif m. Simple angular brackets $\langle\cdots\rangle$ are used to denote an average over a time interval much longer than the period of time-harmonic oscillations of a monochromatic electromagnetic field. Double brackets $\langle\langle\cdots\rangle\rangle$ denote an average over a "sufficiently long" time interval T, the actual value of T being defined by the specific context. Averaging over a parameter X other than time is denoted by $\langle\cdots\rangle_X$. All color plates are grouped together into the "Color plates" section and are numbered decimally per chapter as Plate M.N, where N is the plate number in Chapter M.

Acknowledgments

It is a great pleasure to thank the following colleagues for numerous discussions and productive long-term collaborations: Matthew Berg, Anatoli Borovoi, Oleg Bugaenko, Brian Cairns, Barbara Carlson, Jacek Chowdhary, Petr Chýlek, Zhanna Dlugach, Helmut Domke, Oleg Dubovik, James Hansen, Joachim Hovenier, Vsevolod Ivanov, Michael Kahnert, Nikolai Khlebtsov, Nikolai Kiselev, Andrew Lacis, Kuo-Nan Liou, Pavel Litvinov, Li Liu, Daniel Mackowski, M. Pinar Mengüç, Karri Muinonen, Olga Muñoz, Vera Rosenbush, William Rossow, Yuri Shkuratov, Viktor Tishkovets, Larry Travis, Cornelis van der Mee, Gorden Videen, Tõnu Viik, Ping Yang, and Edgard Yanovitskij. Natasha Mishchenko and Nadia Zakharova provided invaluable technical assistance.

My research has been sponsored over the years by many grants from the National Aeronautics and Space Administration (NASA) of the USA, the US Department of Energy, the National Polar-orbiting Operational Environmental Satellite System program of the USA, and the National Academy of Sciences of Ukraine. In particular, I gratefully acknowledge support from the NASA Radiation Sciences Program managed by Hal Maring, the NASA Remote Sensing Theory Program managed by Lucia Tsaoussi, and the NASA Glory Satellite Mission project.

Last but not least, I thank Laura Clark, Jonathan Ratcliffe, and other staff members of Cambridge University Press for their comprehensive assistance and fine cooperation and Jo Tyszka for careful and meticulous copy-editing of the manuscript.

Acronyms

Acronym	Definition	Introduced in
CCD	charge-coupled device	Section 11.1
CPR	circular polarization ratio	Problem 18.4
DDA	discrete dipole approximation	Section 16.1.7
EBCM	extended boundary condition method	Section 16.1.8
FDTDM	finite difference time domain method	Section 16.1.5
FEM	finite element method	Section 16.1.4
FEs	Foldy equations	Foreword to Ch. 6
FFS	far-field scattering	Section 5.2
FIEM	Fredholm integral equation method	Section 16.1.7
FOSA	first-order-scattering approximation	Section 14.5
GOM	geometrical optics method	Section 16.2
GPMM	generalized PMM	Section 16.1.6
ISRP	statistically isotropic and mirror-symmetric random particle	Foreword to Ch. 15
LMT	Lorenz–Mie theory	Section 15.7
LPR	linear polarization ratio	Problem 15.7
ME-GPMM	multiple-expansion GPMM	Section 16.1.6
MMEs	macroscopic Maxwell equations	Foreword to Ch. 1
MOM	method of moments	Section 16.1.7
MSM	multi-sphere method	Section 16.1.3
MTL1	Mishchenko *et al.* (2002)	Preface
MTL2	Mishchenko *et al.* (2006)	Preface
NASA	National Aeronautics and Space Administration	Acknowledgments
PMM	point-matching method	Section 16.1.6
PST	Poynting–Stokes tensor	Foreword to Ch. 7
QED	quantum electrodynamics	Foreword to Ch. 1

RTE	radiative transfer equation	Foreword to Ch. 19
RTT	radiative transfer theory	Foreword to Ch. 1
SSA	single-scattering approximation	Section 14.1
STMM	superposition *T*-matrix method	Section 16.1.3
SVM	separation of variables method	Section 16.1.2
TMM	*T*-matrix method	Section 16.1.8
VIE	volume integral equation	Section 4.3
VIEM	volume integral equation method	Section 16.1.7
VSWF	vector spherical wave function	Section 16.1.1
WCR	well-collimated radiometer	Section 11.2
WL	weak localization	Foreword to Ch. 1

1

Introduction

Electromagnetic scattering by an isolated particle or a multi-particle group is a ubiquitous phenomenon central to a wide variety of science and engineering disciplines. Field–matter interactions described by macroscopic electromagnetics typically occur in a natural way. They can affect accompanying physical and chemical processes as well as the very state of the scattering object and often yield an electromagnetic signal that can be measured and analyzed with the purpose of retrieving useful information about the object. Electromagnetic scattering can also be induced artificially and used as an active means of *in situ* or remote diagnostics of certain physical properties of the particle(s). In order to interpret laboratory, field, and remote-sensing measurements of electromagnetic scattering by various single- and multi-particle objects, one needs a deep understanding of this phenomenon, as well as the ability to predict quantitatively its various manifestations as functions of the physical parameters of the objects.

The diversity of sizes, morphologies, and refractive indices of particles encountered in natural and artificial environments is virtually limitless, as illustrated by Fig. 1.1. This factor complicates accurate quantitative modeling of electromagnetic scattering and absorption, even by solitary particles such as those suspended individually in the trap volume of an electrostatic (as shown in Plate 1.1a) or optical levitator. The task of optical modeling of a large group of sparsely distributed particles such as a cloud (see, e.g., Plates 1.1b and 1.1c) is significantly more involved. However, the problem of utmost complexity is to model the scattering and absorption properties of densely packed disperse media such as various biological and technical suspensions (e.g., Plate 1.1d), as well as natural and artificial particulate surfaces (e.g., Plates 1.1e and 1.1f).

The main purpose of this textbook is to coherently present the theory of electromagnetic scattering by solitary particles and particle groups as a self-consistent and self-contained branch of Maxwell's electromagnetics. We will accept the macroscopic Maxwell equations (MMEs) as axioms valid in a well-defined range of applications and will not use any *ad hoc* phenomenological con-

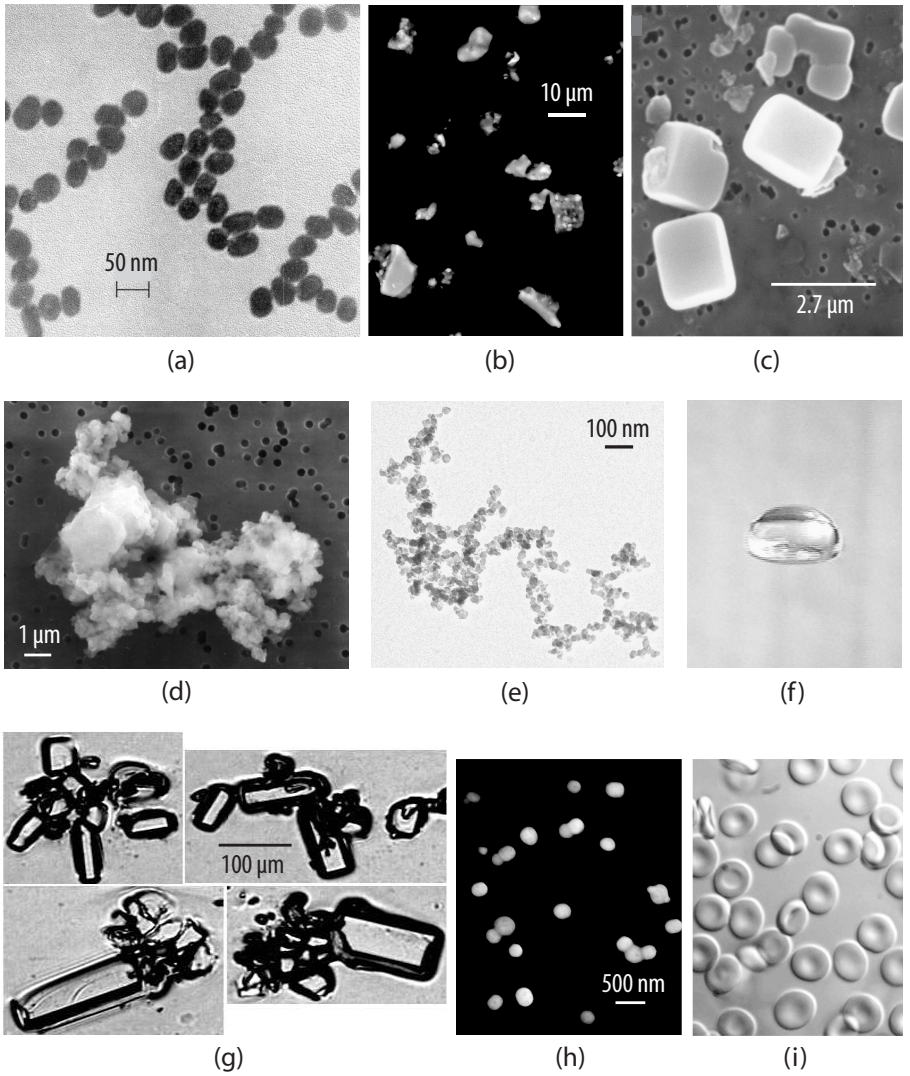

Fig. 1.1. Examples of manmade and natural small particles. **(a)** 40-nm-diameter gold particles (after Khlebtsov *et al.* 1996). **(b)** Sahara-desert soil particles (after Weinzierl *et al.* 2009). **(c)** Dry sea-salt particles (after Chamaillard *et al.* 2003). **(d)** Interplanetary dust particle U2012C11 collected by a NASA U2 aircraft. **(e)** A soot aggregate (after Burr *et al.* 2012). **(f)** A 6-mm-diameter falling raindrop. **(g)** Cirrus cloud crystals (after Arnott *et al.* 1994). **(h)** Submicrometer-sized quasi-spherical ammonium sulphate and dust aerosols (after Weinzierl *et al.* 2009). **(i)** Red blood cells.

cepts and principles not following directly from these equations. This approach is inherently limited in that it ignores specific physical effects described by quantum mechanics and quantum electrodynamics (QED). However, even the inten-

tionally restricted scope of this book will serve to provide accurate quantitative description of many natural and artificially induced electromagnetic scattering effects caused by individual particles and particle groups. Our approach can be called microphysical in that it starts with the MMEs as basic physical laws governing the interaction of electromagnetic radiation with matter and ensures *direct traceability of all derivative results from fundamental physics* not afforded by phenomenological approaches.[1]

There is no doubt that if a specific scattering problem can be addressed by obtaining a direct analytical or numerically exact computer solution[2] of the MMEs, then this would be the preferred course of action. Unfortunately, the range of problems that can be handled analytically is limited. There are several numerically exact techniques for the computer calculation of the electromagnetic field elastically scattered by a finite fixed object composed of one or several particles. These techniques will be reviewed in Chapter 16. However, all of these methodologies have certain practical limitations in terms of the object's morphology and size relative to the wavelength of radiation and cannot be used yet to describe electromagnetic scattering by large multi-particle objects such as atmospheric clouds, particulate surfaces, and particle suspensions. This makes imperative the use of well-characterized approximate solutions that do not require unrealistic computer resources, while being sufficiently accurate for specific applications. One of the objectives of this textbook is to demonstrate that the widely used radiative transfer theory (RTT) as well as the theory of weak localization (WL) of electromagnetic waves in discrete random media are direct asymptotic solutions of the MMEs. Both correspond to the limiting case of a very large number of randomly positioned particles and a very low particle packing density.

1.1 General framework

In contrast to various phenomenological approaches discussed briefly in the following chapters, the microphysical theory of electromagnetic scattering by particles and particle groups pursued in this textbook rests on well-defined assump-

[1] A theory is called phenomenological if it expresses mathematically the results of observed phenomena without paying detailed attention to their fundamental origin and significance. The development of a phenomenological theory is usually based on experience-based heuristic shortcuts lacking rigorous justification. Phenomenological theories are often short-lived and are replaced by fundamental first-principle theories, but some can survive for centuries despite their inherently limited scientific value.

[2] By definition, a numerically exact solution is the outcome of running a direct computer solver of the MMEs that generates numerical results with a guaranteed number of correct decimals. The number of correct decimals may vary depending on the available computer resources and practical accuracy requirements. However, all reported decimals can, in principle, be validated by modifying computer program settings in order to accommodate a more stringent accuracy requirement.

tions intended to formulate the overall problem in strict physical terms. These assumptions are as follows:

1. At each moment in time, the entire scattering object (e.g., a cloud of water droplets or a powder surface) can be represented by a specific spatial configuration of a number $N \geq 1$ of discrete finite particles, as illustrated in Fig. 1.2. The unbounded host medium surrounding the scattering object is homogeneous, isotropic, and nonabsorbing (the general case of an absorbing host medium is discussed by Mishchenko (2007)). Each particle is sufficiently large so that its atomic structure can be ignored and the particle can be characterized by optical constants appropriate to bulk matter. In electromagnetic terms, the presence of a particle means that the optical constants inside the particle volume are different from those of the surrounding host medium. The particles consist of isotropic materials, while their shape and morphology can be arbitrary.

2. Only linear interactions of the electromagnetic field and matter are accounted for. In other words, we will consider only *elastic* electromagnetic scattering. This implies that nonlinear optics effects are excluded by assuming that the optical constants of both the scattering object and the surrounding medium are independent of the electric and magnetic fields. Also excluded are inelastic scattering phenomena, such as Raman and Brillouin scattering and fluorescence, as well as the specific consideration of the small Doppler shift of frequency of the scattered light relative to that of the incident light due to the movement of the particles with respect to the source of illumination. Furthermore, we exclude the phenomenon of thermal emission caused by electron transitions from one energy level to a lower level in macroscopic bodies with absolute temperature different from zero. From the quantum-mechanical standpoint, a macroscopic object is a complex system of molecules with a large number of degrees of freedom. Many different electron transitions produce spectral emission lines so closely spaced that the resulting radiation spectrum becomes effectively continuous and includes

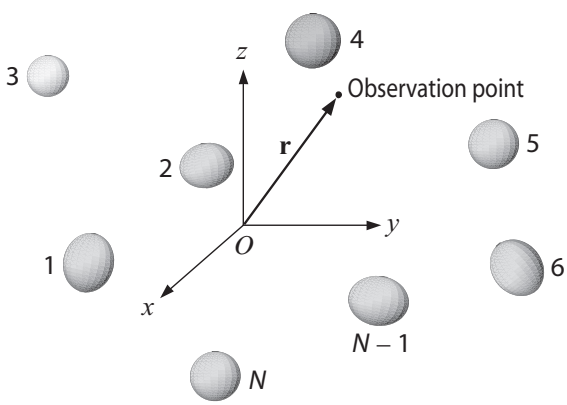

Fig. 1.2. Scattering object in the form of a group of N discrete particles.

emitted energy at all wavelengths. By ignoring thermal emission, we will assume implicitly that the electromagnetic energy at the wavelength in question is much greater than that predicted by the Planck blackbody radiation law. For example, this assumption is usually valid for a short-wave infrared or shorter wavelength in the case of a scattering object at room or lower temperature.

3. Consistent with the restriction of elastic scattering, we will assume that over time intervals much longer than $T_o = 2\pi/\omega$, the time dependence of the electric and magnetic fields everywhere in space is harmonic and described, in the complex-field representation, by the simple complex exponential $\exp(-\mathrm{i}\omega t)$, where ω is the angular frequency, t is time, and $\mathrm{i} = (-1)^{1/2}$. In other words, we will assume that the complex electric and magnetic fields can be factorized as $\widetilde{\boldsymbol{\mathcal{E}}}(\mathbf{r},t) = \exp(-\mathrm{i}\omega t)\mathbf{E}(\mathbf{r})$ and $\widetilde{\boldsymbol{\mathcal{H}}}(\mathbf{r},t) = \exp(-\mathrm{i}\omega t)\mathbf{H}(\mathbf{r})$, respectively, where $\mathbf{r}$ is the position (radius) vector, while the actual real-valued fields are obtained by taking the real part of the respective complex fields: $\boldsymbol{\mathcal{E}}(\mathbf{r},t) = \mathrm{Re}\,\widetilde{\boldsymbol{\mathcal{E}}}(\mathbf{r},t)$ and $\boldsymbol{\mathcal{H}}(\mathbf{r},t) = \mathrm{Re}\,\widetilde{\boldsymbol{\mathcal{H}}}(\mathbf{r},t)$. The amplitudes $\mathbf{E}(\mathbf{r})$ and $\mathbf{H}(\mathbf{r})$ may vary with time implicitly by fluctuating around their respective mean values, but do so much more slowly than the factor $\exp(-\mathrm{i}\omega t)$. Time-independent amplitudes $\mathbf{E}(\mathbf{r})$ and $\mathbf{H}(\mathbf{r})$ correspond to perfectly monochromatic radiation (e.g., a continuous laser beam), whereas the more general case of slowly varying $\mathbf{E}(\mathbf{r})$ and $\mathbf{H}(\mathbf{r})$ represents so-called quasi-monochromatic radiation.

4. In addition, we will assume that if the scattering object varies with time then any *significant* (i.e., modifying the solution of the MMEs) changes in particle positions, morphologies, and/or orientations with respect to the laboratory reference frame occur over time intervals T_v much longer than the period of time-harmonic oscillations of the electromagnetic field T_o.

These assumptions imply that over time intervals long compared to T_o, but short compared to T_v and/or to typical periods T_f of fluctuations of the amplitudes $\mathbf{E}(\mathbf{r})$ and $\mathbf{H}(\mathbf{r})$, all fields can be considered to be perfectly time-harmonic and the object can be considered to be fixed. As a consequence, the instantaneous electromagnetic field everywhere in space can be found by solving the so-called frequency-domain differential MMEs (Stratton 1941; Van Bladel 2007; Rothwell and Cloud 2009) subject to certain boundary conditions. The specific dependence of the optical constants on spatial coordinates and the corresponding boundary conditions at any moment are fully defined by the instantaneous geometrical configuration of the N particles (Fig. 1.2).

Specifically, we will show in Section 4.1 that the frequency-domain monochromatic Maxwell curl equations describing the scattering problem in terms of the time-independent electric and magnetic field amplitudes $\mathbf{E}(\mathbf{r})$ and $\mathbf{H}(\mathbf{r})$ can be written as follows:

$$\left.\begin{aligned} \nabla\times\mathbf{E}(\mathbf{r}) &= \mathrm{i}\omega\mu_0\,\mathbf{H}(\mathbf{r}) \\ \nabla\times\mathbf{H}(\mathbf{r}) &= -\mathrm{i}\omega\epsilon_1\,\mathbf{E}(\mathbf{r}) \end{aligned}\right\} \quad \mathbf{r}\in V_{\mathrm{EXT}}, \tag{1.1}$$

$$\left.\begin{aligned}\nabla\times\mathbf{E}(\mathbf{r}) &= \mathrm{i}\omega\mu_0\,\mathbf{H}(\mathbf{r})\\ \nabla\times\mathbf{H}(\mathbf{r}) &= -\mathrm{i}\omega\varepsilon_2(\mathbf{r},\omega)\,\mathbf{E}(\mathbf{r})\end{aligned}\right\}\quad \mathbf{r}\in V_{\mathrm{INT}}. \tag{1.2}$$

In these equations, V_{INT} is the cumulative "interior" volume occupied by the scattering object; V_{EXT} is the infinite exterior region such that $V_{\mathrm{INT}}\cup V_{\mathrm{EXT}}=\Re^3$, where $\Re^3$ denotes the entire three-dimensional space; the host medium and the scattering object are assumed to be nonmagnetic; μ_0 is the permeability of a vacuum; ϵ_1 is the real-valued electric permittivity of the host medium; and $\varepsilon_2(\mathbf{r},\omega)$ is the (potentially coordinate-dependent) complex permittivity of the scattering object.

Equations (1.1) and (1.2) supplemented by the so-called radiation condition at infinity, as well as by the standard boundary conditions for the electric and magnetic fields defined by the specific spatial distribution of the refractive index have a solution, this solution being unique (Müller 1969). This fundamental fact makes the MMEs a self-sufficient basis of the electromagnetic scattering theory. In other words, the rest of this book will be an outline of analytical and numerical solutions of Eqs. (1.1) and (1.2) (or their integral-equation counterparts) as applied to scattering objects of varying complexity.

1.2 Electromagnetic scattering

In the absence of the scattering object, $\varepsilon_2(\mathbf{r},\omega)\equiv\epsilon_1$. This means that instead of Eqs. (1.1) and (1.2), we have:

$$\left.\begin{aligned}\nabla\times\mathbf{E}(\mathbf{r}) &= \mathrm{i}\omega\mu_0\,\mathbf{H}(\mathbf{r})\\ \nabla\times\mathbf{H}(\mathbf{r}) &= -\mathrm{i}\omega\epsilon_1\,\mathbf{E}(\mathbf{r})\end{aligned}\right\}\quad \mathbf{r}\in\Re^3. \tag{1.3}$$

Obviously, the solution of Eq. (1.3) must differ from that of the system of equations (1.1) and (1.2). It is this *modification* of the electromagnetic field resulting from the presence of the object that is called *electromagnetic scattering*.

We thus see that the specific way to define electromagnetic scattering is to solve the MMEs twice. The first solution, in terms of the respective pair of the electric and magnetic fields $\{\mathbf{E}_1(\mathbf{r}),\mathbf{H}_1(\mathbf{r})\}$, corresponds to the situation with no scattering object (Eq. (1.3)), whereas the second solution, $\{\mathbf{E}_2(\mathbf{r}),\mathbf{H}_2(\mathbf{r})\}$, corresponds to the situation with a scattering object present (Eqs. (1.1) and (1.2)).

The second solution is usually sought in the form

$$\mathbf{E}_2(\mathbf{r}) = \mathbf{E}_1(\mathbf{r}) + \mathbf{E}_3(\mathbf{r}), \tag{1.4}$$

$$\mathbf{H}_2(\mathbf{r}) = \mathbf{H}_1(\mathbf{r}) + \mathbf{H}_3(\mathbf{r}), \tag{1.5}$$

where the vector fields $\mathbf{E}_3(\mathbf{r})$ and $\mathbf{H}_3(\mathbf{r})$ are required to satisfy the radiation condition at infinity by decaying as the inverse distance from the object. The electromagnetic field in the absence of the object is traditionally called the "incident field" (superscript "inc"), whereas the difference between the electromag-

netic field in the presence of the object and the field that would exist in the absence of the object is traditionally called the "scattered field" (superscript "sca"):

$$\mathbf{E}^{\mathrm{sca}}(\mathbf{r}) \equiv \mathbf{E}_3(\mathbf{r}) = \mathbf{E}_2(\mathbf{r}) - \mathbf{E}_1(\mathbf{r}) = \mathbf{E}_2(\mathbf{r}) - \mathbf{E}^{\mathrm{inc}}(\mathbf{r}), \tag{1.6}$$

$$\mathbf{H}^{\mathrm{sca}}(\mathbf{r}) \equiv \mathbf{H}_3(\mathbf{r}) = \mathbf{H}_2(\mathbf{r}) - \mathbf{H}_1(\mathbf{r}) = \mathbf{H}_2(\mathbf{r}) - \mathbf{H}^{\mathrm{inc}}(\mathbf{r}). \tag{1.7}$$

The above discussion makes it clear that although electromagnetic scattering can be said to be a physical *phenomenon* (amounting to the *fact* that the electromagnetic fields computed in the presence and in the absence of an object are different), it is not a solitary physical process. Importantly, Eqs. (1.6) and (1.7) demonstrate again that the electromagnetic field in the presence of the object is intentionally expressed as the sum of the incident and scattered fields:

$$\mathbf{E}(\mathbf{r}) \equiv \mathbf{E}_2(\mathbf{r}) = \mathbf{E}^{\mathrm{inc}}(\mathbf{r}) + \mathbf{E}^{\mathrm{sca}}(\mathbf{r}), \tag{1.8}$$

$$\mathbf{H}(\mathbf{r}) \equiv \mathbf{H}_2(\mathbf{r}) = \mathbf{H}^{\mathrm{inc}}(\mathbf{r}) + \mathbf{H}^{\mathrm{sca}}(\mathbf{r}), \tag{1.9}$$

where $\mathbf{E}^{\mathrm{inc}}(\mathbf{r})$ and $\mathbf{H}^{\mathrm{inc}}(\mathbf{r})$ are obtained by solving the MMEs in the absence of the object. This makes both the incident and the scattered field, as they appear in the solution of Eqs. (1.1) and (1.2) in the form of Eqs. (1.8) and (1.9), purely mathematical entities rather than actual physical fields. The only actual field is the *total* electromagnetic field, either in the presence or in the absence of the object.

This basic point is illustrated in Fig. 1.3. Indeed, a fundamental solution of the MMEs in an infinite nonabsorbing homogeneous space is a time-harmonic plane electromagnetic wave given, in the complex-field representation, by

$$\left.\begin{aligned} \widetilde{\boldsymbol{\mathcal{E}}}^{\mathrm{inc}}(\mathbf{r}, t) &= \mathbf{E}_0^{\mathrm{inc}} \exp(\mathrm{i}\mathbf{k}^{\mathrm{inc}} \cdot \mathbf{r} - \mathrm{i}\omega t) \\ \widetilde{\boldsymbol{\mathcal{H}}}^{\mathrm{inc}}(\mathbf{r}, t) &= \mathbf{H}_0^{\mathrm{inc}} \exp(\mathrm{i}\mathbf{k}^{\mathrm{inc}} \cdot \mathbf{r} - \mathrm{i}\omega t) \end{aligned}\right\} \quad \mathbf{r} \in \Re^3 \tag{1.10}$$

with constant complex amplitudes $\mathbf{E}_0^{\mathrm{inc}}$ and $\mathbf{H}_0^{\mathrm{inc}}$, where $\mathbf{k}^{\mathrm{inc}}$ is a real-valued so-called wave vector. In fact, this solution embodies the concept of a perfectly monochromatic parallel beam of light of infinite lateral extent propagating in the direction of the wave vector. The time-independent part of this solution is visualized in Fig. 1.3a. Placing a spherical particle at the origin of the coordinate system, as shown in Fig. 1.3c, yields a new time-harmonic solution of the MMEs. The time-independent part of this second solution, both inside and outside the particle volume, is visualized in Fig. 1.3b. Subtracting the field visualized in Fig. 1.3a from that depicted in Fig. 1.3b yields the scattered field shown in Fig. 1.3c. It is clear that the fields in Figs. 1.3a and 1.3b are actual physical fields found by solving the MMEs, whereas the field in Fig. 1.3c is a purely mathematical construction.

A fundamental corollary of the above discussion is that, irrespective of the morphological complexity of the scattering object, the latter always remains a single, unified scatterer. Although the human eye may classify a scattering object

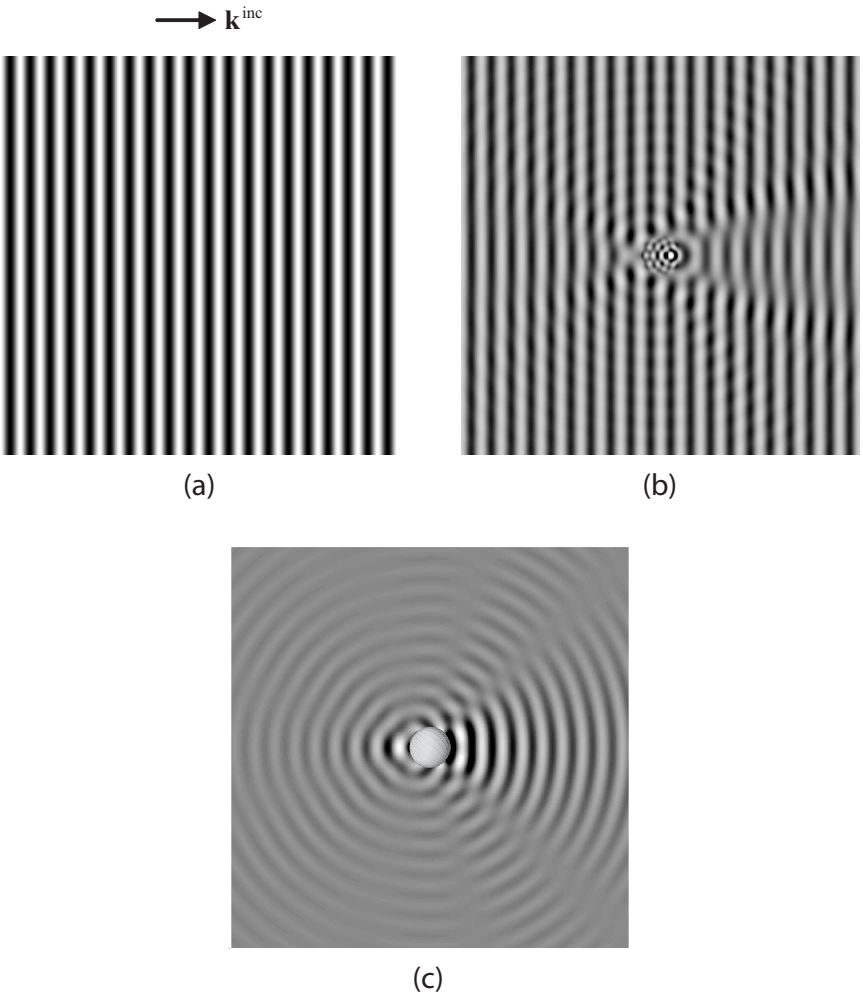

Fig. 1.3. **(a)** The real part of the vertical (i.e., perpendicular to the paper) component of the electric field vector of a plane electromagnetic wave propagating in the direction of the wave vector $\mathbf{k}^{\text{inc}}$. The infinite host medium is homogeneous, isotropic, and nonabsorbing. The wave is fully polarized in the vertical direction so that the horizontal component of the electric field vector is equal to zero. **(b)** The real part of the vertical component of the total electric field in the presence of a small homogeneous spherical particle located in the center of the diagram as to be shown in panel (c). The relative refractive index of the particle is $m = (\varepsilon_2/\epsilon_1)^{1/2} = 2.8$, while its radius a is such that the dimensionless size parameter $k_1 a = \omega(\epsilon_1\mu_0)^{1/2}a$ is equal to 2π. **(c)** The real part of the vertical component of the difference between the fields visualized in panels (b) and (a), respectively. The gray scale is individually adjusted to maximally reveal the specific details in each diagram. (After Mishchenko and Travis (2008); images courtesy of J.-C. Auger.)

(e.g., a cloud of water droplets or ice crystals) as a "collection of discrete particles," the incident field perceives the entire object at any moment in time as one scatterer in the form of a specific instantaneous spatial distribution of the complex permittivity $\varepsilon_2(\mathbf{r}, \omega)$. This means that any of the "multi-particle groups" shown in Plates 1.1b–1.1f is as much a single-scattering object as the solitary particle shown in Plate 1.1a.

This corollary implies that the widely used term "multiple scattering" does not refer to an actual physical phenomenon. We will see in later chapters that it has only a purely mathematical meaning.

1.3 Further remarks

Throughout most of this book, we will consider the incident field in the form of a perfectly monochromatic plane wave given by Eq. (1.10). More generally, the incident field can be a superposition of monochromatic or quasi-monochromatic plane waves. A quasi-monochromatic plane wave is given by

$$\left.\begin{aligned} \widetilde{\mathcal{E}}^{\mathrm{inc}}(\mathbf{r}, t) &= \mathbf{E}_0^{\mathrm{inc}}(t)\exp(\mathrm{i}\mathbf{k}^{\mathrm{inc}} \cdot \mathbf{r} - \mathrm{i}\omega t) \\ \widetilde{\mathcal{H}}^{\mathrm{inc}}(\mathbf{r}, t) &= \mathbf{H}_0^{\mathrm{inc}}(t)\exp(\mathrm{i}\mathbf{k}^{\mathrm{inc}} \cdot \mathbf{r} - \mathrm{i}\omega t) \end{aligned}\right\} \quad \mathbf{r} \in \Re^3, \tag{1.11}$$

where fluctuations in time of the complex amplitudes of the electric and magnetic fields, $\mathbf{E}_0^{\mathrm{inc}}(t)$ and $\mathbf{H}_0^{\mathrm{inc}}(t)$, around their respective mean values are assumed to occur much more slowly than the time-harmonic oscillations of the factor $\exp(-\mathrm{i}\omega t)$. We will not consider in detail other types of incident field such as a focused laser beam of finite lateral extent (e.g., Gouesbet and Gréhan 2011) or an ultra-short pulse. However, as will be discussed in the following chapters, this restriction narrows the scope of the book not nearly as much as it may appear at first glance.

It is worth emphasizing again that macroscopic Maxwell's electromagnetics ignores the discreteness of matter forming the scattering object, operates with continuous sources of fields, and captures only linear field–matter interactions. Therefore, its predictions can fall short in cases where quantum effects are essential. Even so, the quantum theory can often be used to determine the macroscopic electromagnetic properties of bodies consisting of very large numbers of atoms (Akhiezer and Peletminskii 1981; Lukš and Peřinová 2009). It turns out that this approach works well when the external electromagnetic field is sufficiently weak and the particle size exceeds ~50 Å (Huffman 1988). This result is very important since it: (i) implies a rather wide range of applicability of the MMEs and (ii) allows one to clarify the definition of a "macroscopic particle" as the subject of study in this book in terms of the smallest allowable particle size.

We can thus conclude that the use of macroscopic Maxwell's electromagnetics as the point of departure is founded on the well-established fact that this theory follows directly from more fundamental physical theories as a consequence

of well-characterized and verifiable approximations. This fact allows us to adopt the equations of classical macroscopic electromagnetics essentially as basic axioms valid in a wide and well-defined range of practical situations. The reader will see that this approach can be used to develop a mostly self-contained and self-consistent theory in which the need to invoke alternative physical concepts and laws is largely obviated.

1.4 Energy-budget and optical-characterization problems

A clear understanding of the type of field–matter interactions captured by the MMEs helps identify the extent of their applicability to solving specific practical problems. Let us consider, for example, an imaginary liquid-water cloud illuminated by a parallel quasi-monochromatic beam of light with infinite lateral extent, as shown schematically in Fig. 1.4. Suppose that we need to evaluate the energy budget of a macroscopic volume element ΔV bounded by the closed surface ΔS. According to the Poynting theorem discussed specifically in Section 2.4, the net

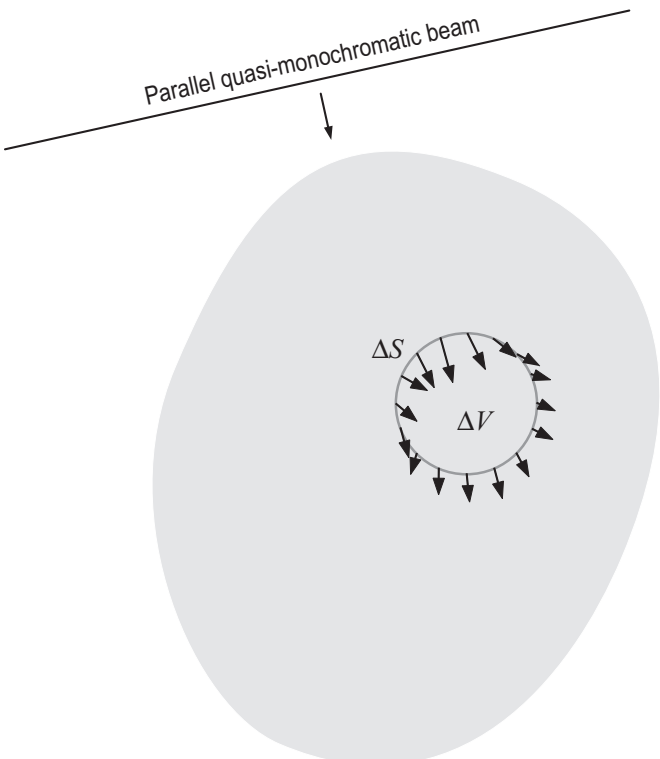

Fig. 1.4. Time-averaged energy budget of a volume element ΔV of a cloud bounded by the closed surface ΔS. The arrows represent the distribution of $\langle\langle \boldsymbol{\mathcal{S}}(\mathbf{r}, t)\rangle\rangle$ over the boundary ΔS.

average rate at which electromagnetic energy enters this volume element is given by the surface integral

$$\langle\langle W_{\Delta S}\rangle\rangle = -\oint_{\Delta S} \mathrm{d}^2\mathbf{r}\,\langle\langle \boldsymbol{\mathcal{S}}(\mathbf{r},t)\rangle\rangle \cdot \hat{\mathbf{n}}(\mathbf{r}) \geq 0, \tag{1.12}$$

where $\boldsymbol{\mathcal{S}}(\mathbf{r},t) = \boldsymbol{\mathcal{E}}(\mathbf{r},t)\times\boldsymbol{\mathcal{H}}(\mathbf{r},t)$ is the Poynting vector of the total electromagnetic field at the point $\mathbf{r}$ at the moment t, $\langle\langle\cdots\rangle\rangle$ denotes averaging over a sufficiently long period of time, and the unit vector $\hat{\mathbf{n}}(\mathbf{r})$ is directed along the local outward normal to the boundary.

The interpretation of the Poynting theorem is straightforward if $\langle\langle W_{\Delta S}\rangle\rangle = 0$; then the incoming energy is balanced by the outgoing energy, which implies that the particulate matter inside ΔV is not affected by the radiation. If, however, $\langle\langle W_{\Delta S}\rangle\rangle > 0$ and ΔV contains no free charges, then the Poynting theorem implies that there is a continuous accumulation of electromagnetic energy inside ΔV, which is, of course, physically unrealistic. This example reveals an inherent weakness of classical macroscopic electromagnetics rooted in its inability to describe nonlinear interactions of the electromagnetic field with matter. The traditional way to circumvent this issue is to postulate that if $\langle\langle W_{\Delta S}\rangle\rangle > 0$ then the excess electromagnetic energy is transformed into other forms of energy (e.g., heat) via physical mechanisms not specifically described by the MMEs.

Despite this intrinsic limitation of classical macroscopic electromagnetics, the measurement or theoretical computation of the integral on the right-hand side of Eq. (1.12) allows one to determine whether the volume element ΔV of the cloud is in a state of energetic balance or imbalance. On a much greater scale, as Plate 1.2 illustrates, the entire Earth's climate and its long-term trend are affected by how accurately the incoming solar energy is balanced by the outgoing electromagnetic radiation. Even a small excess of the incoming over the outgoing energy can cause significant global warming of the climate (Hansen *et al.* 2011).

Other types of relevant practical problems have to do with the fact that there are instruments specifically designed to measure various manifestations of electromagnetic energy flow. The signal measured by these instruments can contain implicit information on the physical properties of the scattering medium. Among typical examples are: remote-sensing instruments flown on satellites around the Earth and measuring various characteristics of the scattered sunlight (Fig. 1.5); ground-based and orbital telescopes combined with appropriate analyzers and detectors of electromagnetic radiation scattered by astronomical objects (Figs. 1.6a and 1.6b); multi-angular and multi-spectral laboratory instruments designed for optical characterization of natural and manmade microscopic particulates having complex morphologies (Fig. 1.6c); and laboratory facilities intended for measurements of electromagnetic scattering by artificial targets at microwave frequencies (Fig. 1.6d).

To deduce useful macro- and microphysical information from such measurements, one needs a clear understanding of the physical nature of the meas-

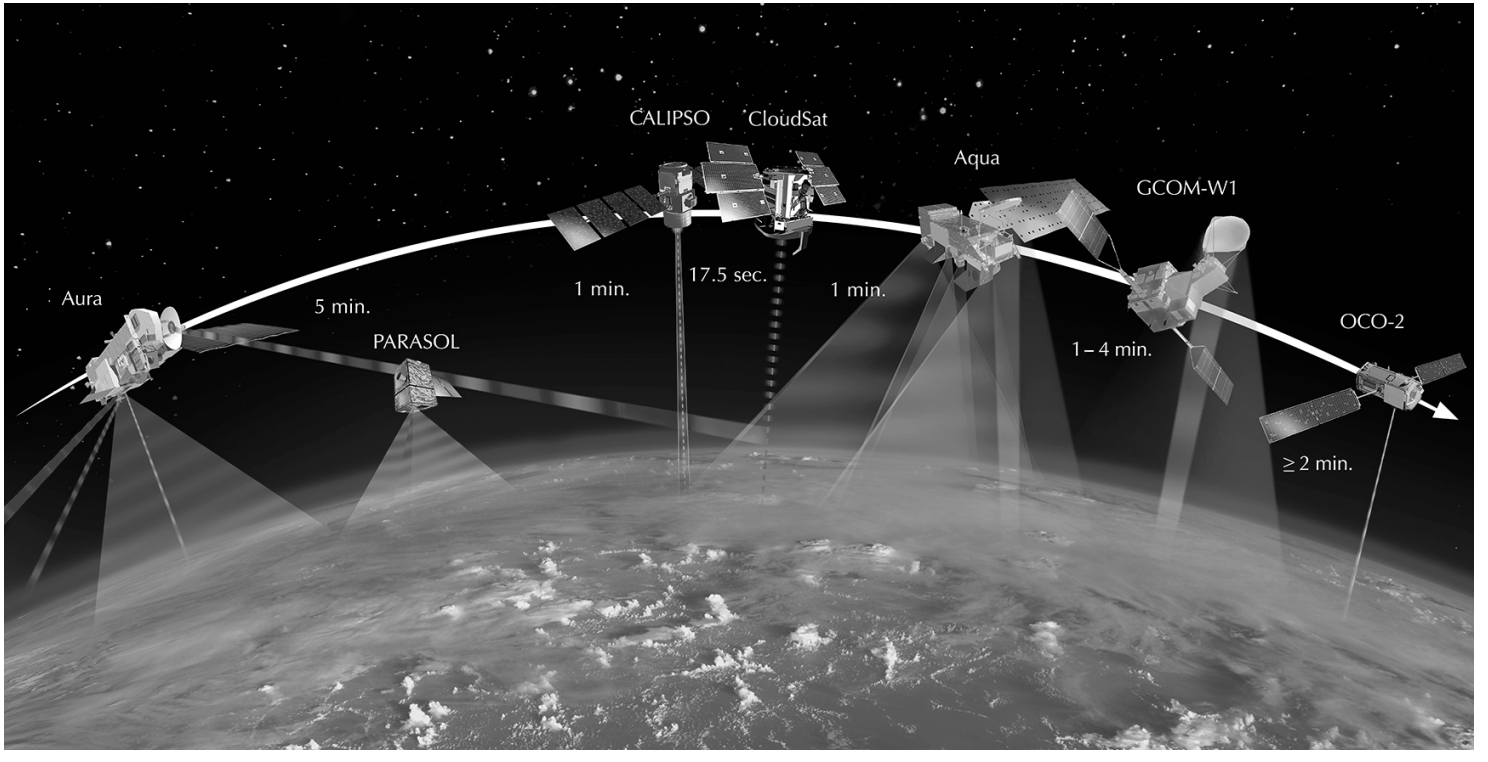

Fig. 1.5. Initially, the so-called Afternoon Constellation (or A-Train) of Earth-orbiting satellites consisted of four NASA missions and a French Centre National d'Etudes Spatiales mission flying in close proximity to one another: Aqua, Aura, the Cloud-Aerosol Lidar and Infrared Pathfinder Satellite Observations (CALIPSO), CloudSat, and the Polarization and Anisotropy of Reflectances for Atmospheric Science coupled with Observations from a Lidar (PARASOL). By 2014 it should include the six missions shown along the white arrow above. PARASOL has by now drifted out of the A-Train completely. This image also shows the amount of time each spacecraft is (or will be) separated along the group's orbit track.

urements. In addition, one needs to address the so-called inverse problem of identifying the physical model of a particulate medium that provides the best fit of theoretical computations of electromagnetic scattering to the measurement data. Needless to say, an integral part of solving the inverse problem is solving the direct problem, i.e., finding an accurate solution of the MMEs for a given particulate model and a specfic type of illumination.

In the final analysis, it is the great practical importance of such energy-budget and optical-characterization problems encountered in many areas of science and technology that provides a major motivation for this book.

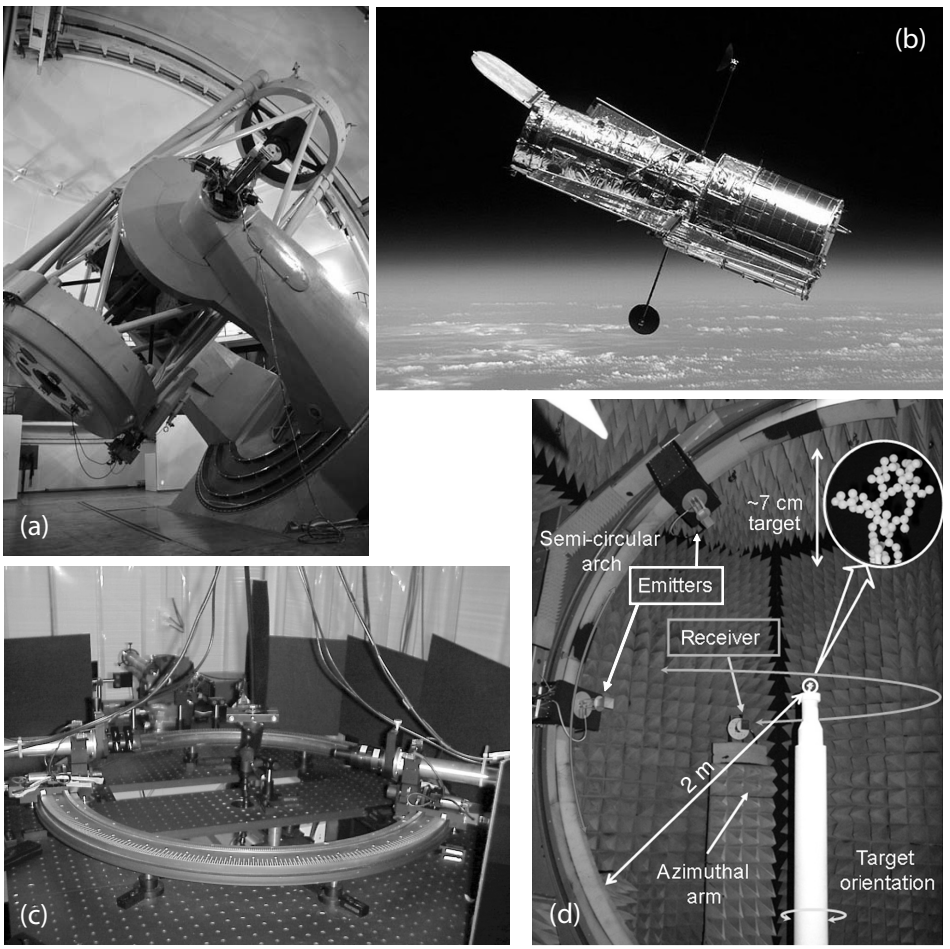

Fig. 1.6. **(a)** 2.6-m reflecting telescope of the Crimean Astrophysical Observatory (Nauchny, Ukraine) used for photopolarimetric observations of Solar System objects (after Mishchenko *et al.* 2011a). **(b)** NASA's Hubble Space Telescope. **(c)** Light scattering setup built at the University of Amsterdam (after Muñoz and Hovenier 2011). **(d)** Microwave scattering facility of the Institut Fresnel, Marseille (after Vaillon *et al.* 2011).

1.5 Electromagnetic spectrum

It is the existence of the solution of the MMEs in the form of Eq. (1.10) that had led Maxwell to conclude that light consists of electromagnetic waves propagating with a velocity $(\epsilon_1 \mu_0)^{-1/2}$. The fact that the speed of light in various homogeneous media agreed well with the corresponding values of $(\epsilon_1 \mu_0)^{-1/2}$ determined from electrostatic and magnetostatic measurements was viewed by Maxwell as a decisive argument in favor of his bold assertion that light was a form of electromagnetic radiation. Although visible light was the only part of the electromagnetic spectrum known to Maxwell, subsequent research has led to the discovery of other parts of the spectrum, which now extends from gamma rays to radio waves (Plate 1.3).

For historical reasons, the term "light scattering by particles" has been ubiquitous in the scientific literature, even though it may often be viewed as being unnecessarily restrictive by implicitly referring to a rather narrow part of the spectrum. In this book the terms "light scattering" and "electromagnetic scattering" are used as synonyms, both referring to all manifestations of elastic scattering of electromagnetic waves in any part of the spectrum, as long as these manifestations can be described accurately by the MMEs.

2

The macroscopic Maxwell equations and monochromatic fields

In accordance with the preceding discussion, the theoretical foundation for describing electromagnetic scattering by particles and particle groups in this book is provided by classical macroscopic electromagnetics. This chapter is intended to summarize basic concepts and equations of electromagnetic theory that will be used extensively in the remainder of the book and introduce the necessary notation.

We start by formulating the primordial set of time-domain MMEs, constitutive relations, and boundary conditions. This is followed by a general analysis of time-harmonic fields and the frequency-domain MMEs. Finally, we discuss energy conservation in the framework of the frequency-domain macroscopic electromagnetics.

2.1 The macroscopic Maxwell equations and constitutive relations

As already mentioned, the basic laws of macroscopic electromagnetics are adopted in this textbook essentially as axioms describing the spatial distribution and temporal behavior of the electromagnetic field and its interaction with matter. A thorough justification of this approach can be found in the textbook by Rothwell and Cloud (2009). The microphysical derivation of the MMEs from more fundamental physical principles and the range of their validity are discussed by de Groot (1969), Robinson (1973), Akhiezer and Peletminskii (1981), Suttorp (1989), and Jackson (1998).

In SI units, the set of four Maxwell equations for the instantaneous macroscopic electromagnetic field at an arbitrary observation point $\mathbf{r}$ is as follows:

$$\nabla \cdot \mathcal{D}(\mathbf{r}, t) = \rho(\mathbf{r}, t), \tag{2.1}$$

$$\nabla \times \mathcal{E}(\mathbf{r},t) = -\frac{\partial \mathcal{B}(\mathbf{r},t)}{\partial t}, \tag{2.2}$$

$$\nabla \cdot \mathcal{B}(\mathbf{r},t) = 0, \tag{2.3}$$

$$\nabla \times \mathcal{H}(\mathbf{r},t) = \mathcal{J}(\mathbf{r},t) + \frac{\partial \mathcal{D}(\mathbf{r},t)}{\partial t}, \tag{2.4}$$

where $\mathcal{E}$ is the electric and $\mathcal{H}$ the magnetic field, $\mathcal{B}$ the magnetic induction, $\mathcal{D}$ the electric displacement, and ρ and $\mathcal{J}$ the macroscopic (free) charge density and current density, respectively. All quantities entering Eqs. (2.1)–(2.4) are real-valued functions of time, t, and spatial coordinates, $\mathbf{r}$. Implicit in the MMEs is the continuity equation

$$\frac{\partial \rho(\mathbf{r},t)}{\partial t} + \nabla \cdot \mathcal{J}(\mathbf{r},t) = 0, \tag{2.5}$$

which is obtained by combining the time derivative of Eq. (2.1) with the divergence of Eq. (2.4) and taking into account the vector identity $\nabla \cdot (\nabla \times \mathbf{a}) = 0$. The vector fields entering Eqs. (2.1)–(2.4) are related by

$$\mathcal{D}(\mathbf{r},t) = \epsilon_0 \mathcal{E}(\mathbf{r},t) + \mathcal{P}(\mathbf{r},t), \tag{2.6}$$

$$\mathcal{H}(\mathbf{r},t) = \frac{1}{\mu_0}\mathcal{B}(\mathbf{r},t) - \mathcal{M}(\mathbf{r},t), \tag{2.7}$$

where $\mathcal{P}$ is the electric polarization (average electric dipole moment per unit volume), $\mathcal{M}$ is the magnetization (average magnetic dipole moment per unit volume), and ϵ_0 and μ_0 are the electric permittivity and the magnetic permeability of a vacuum, respectively.

In many cases Eqs. (2.1)–(2.4), (2.6), and (2.7) are insufficient for a unique determination of the electric and magnetic fields and must be supplemented with a set of additional axioms called constitutive relations:

$$\mathcal{P}(\mathbf{r},t) = \epsilon_0 \chi(\mathbf{r}) \mathcal{E}(\mathbf{r},t), \tag{2.8}$$

$$\mathcal{B}(\mathbf{r},t) = \mu(\mathbf{r}) \mathcal{H}(\mathbf{r},t), \tag{2.9}$$

$$\mathcal{J}(\mathbf{r},t) = \sigma(\mathbf{r}) \mathcal{E}(\mathbf{r},t), \tag{2.10}$$

where χ is the electric susceptibility, μ the magnetic permeability, and σ the conductivity. Equations (2.6) and (2.8) yield

$$\mathcal{D}(\mathbf{r},t) = \epsilon(\mathbf{r}) \mathcal{E}(\mathbf{r},t), \tag{2.11}$$

where

$$\epsilon(\mathbf{r}) = \epsilon_0 [1 + \chi(\mathbf{r})] \tag{2.12}$$

is the electric permittivity. For linear and isotropic media considered in this book, χ, μ, σ, and ϵ are scalars independent of the fields.

The constitutive relations (2.9)–(2.11) connect the field vectors at the same moment of time t and are valid for electromagnetic fields in a vacuum, as well as for electromagnetic fields in macroscopic material media provided that the fields are constant or vary in time rather slowly. For a rapidly varying electromagnetic field in a material medium, the state of the medium depends not only on the current value of the field, but also on the values of the field at all previous times. Therefore, for a linear, time-invariant medium, the constitutive relations (2.9)–(2.11) must be replaced by the following general causal relations that take into account the effect of the prior history on the electromagnetic properties of the medium:

$$\mathcal{D}(\mathbf{r},t) = \int_{-\infty}^{t} \mathrm{d}t' \epsilon(\mathbf{r},t-t')\mathcal{E}(\mathbf{r},t'), \tag{2.13}$$

$$\mathcal{B}(\mathbf{r},t) = \int_{-\infty}^{t} \mathrm{d}t' \mu(\mathbf{r},t-t')\mathcal{H}(\mathbf{r},t'), \tag{2.14}$$

$$\mathcal{J}(\mathbf{r},t) = \int_{-\infty}^{t} \mathrm{d}t' \sigma(\mathbf{r},t-t')\mathcal{E}(\mathbf{r},t'). \tag{2.15}$$

The medium characterized by the constitutive relations (2.13)–(2.15) is called time-dispersive. Again, in the framework of classical macroscopic electromagnetics Eqs. (2.13)–(2.15) are accepted as axioms.

2.2 Boundary conditions

The differential MMEs are strictly valid only for points in whose neighborhood the physical properties of the medium, as characterized by the constitutive parameters χ, μ, and σ, vary continuously. If we restrict ourselves to regions of space without spatial discontinuities then we can find a meaningful solution of the differential MMEs. However, across interfaces separating one medium from another, the constitutive parameters may change abruptly, and one may expect similar discontinuous behavior of the field vectors $\mathcal{E}$, $\mathcal{D}$, $\mathcal{H}$, and $\mathcal{B}$. Solving the MMEs in different adjacent regions with continuous physical properties and then linking the partial solutions to determine the fields throughout all space requires the specification of appropriate boundary conditions at discontinuous interfaces.

Usually such boundary conditions are derived from the integral form of the MMEs. However, this approach relies implicitly on the questionable assumption that while the integral Maxwell equations are derived from the differential Maxwell equations, the former are valid across discontinuous interfaces, even though the latter are not. Therefore, instead of "deriving" the boundary conditions for the field vectors $\mathcal{E}$, $\mathcal{D}$, $\mathcal{H}$, and $\mathcal{B}$, it is more appropriate to adopt them as axioms explicitly supplementing the set of the differential MMEs and constitutive relations (Schelkunoff 1972; Tai 1994; Rothwell and Cloud 2009).

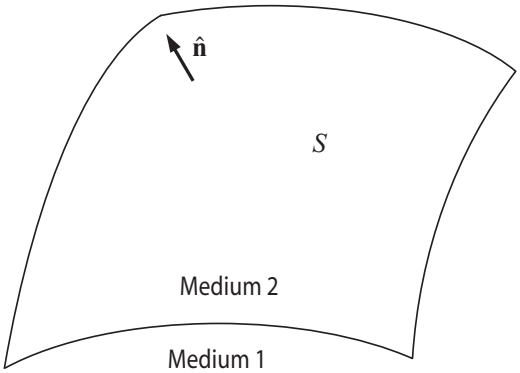

Fig. 2.1. Interface S separates two adjacent media with different constitutive parameters.

Consider two different continuous media separated by an interface S, as shown in Fig. 2.1. Let $\hat{\mathbf{n}}$ be a unit vector along the local normal to the interface, pointing from medium 1 toward medium 2. Then the first boundary condition is as follows:

$$(\mathcal{B}_2 - \mathcal{B}_1) \cdot \hat{\mathbf{n}} = 0, \tag{2.16}$$

which implies that the normal component of the magnetic induction is continuous across the interface. The second boundary condition reads

$$(\mathcal{D}_2 - \mathcal{D}_1) \cdot \hat{\mathbf{n}} = \rho_S, \tag{2.17}$$

where ρ_S is the surface charge density (the charge per unit area) measured in coulombs per square meter. Thus, there is a discontinuity in the normal component of $\mathcal{D}$ if the interface carries an infinitesimally thin layer of surface charge. The third boundary condition,

$$\hat{\mathbf{n}} \times (\mathcal{E}_2 - \mathcal{E}_1) = \mathbf{0}, \tag{2.18}$$

where $\mathbf{0}$ is a zero vector, implies that the tangential component of the electric field vector is continuous across the interface. Finally, the boundary condition for the magnetic field is as follows:

$$\hat{\mathbf{n}} \times (\mathcal{H}_2 - \mathcal{H}_1) = \mathcal{J}_S, \tag{2.19}$$

where $\mathcal{J}_S$ is the surface current density measured in amperes per meter. This condition means that there can be a discontinuity in the tangential component of $\mathcal{H}$ if the interface is capable of carrying a surface current. Media with finite conductivity cannot support surface currents, and so

$$\hat{\mathbf{n}} \times (\mathcal{H}_2 - \mathcal{H}_1) = \mathbf{0} \quad \text{(finite conductivity)}. \tag{2.20}$$

2.3 Monochromatic fields

Let us now make the standard assumption that all fields, charges, and currents are time harmonic (or monochromatic), which means that their time dependence can be fully described by expressing them as sums of terms proportional to either $\cos\omega t$ or $\sin\omega t$, where ω is the angular frequency. It is customary to represent real monochromatic fields as real parts of the respective complex time-harmonic fields (denoted hereinafter by a tilde), e.g.,

$$\begin{aligned}\mathcal{E}(\mathbf{r},t) &= \mathrm{Re}\,\widetilde{\mathcal{E}}(\mathbf{r},t) = \mathrm{Re}[\mathbf{E}(\mathbf{r})\exp(-\mathrm{i}\omega t)] \\ &= \frac{1}{2}[\mathbf{E}(\mathbf{r})\exp(-\mathrm{i}\omega t) + \mathbf{E}^*(\mathbf{r})\exp(\mathrm{i}\omega t)],\end{aligned} \tag{2.21}$$

and analogously for $\mathcal{D}$, $\mathcal{H}$, $\mathcal{B}$, $\mathcal{J}$, ρ, $\mathcal{P}$, and $\mathcal{M}$, where $\mathbf{E}(\mathbf{r})$ is complex, and the asterisk denotes a complex-conjugate value.[1] Equations (2.1)–(2.5) then imply the following frequency-domain MMEs and continuity equation for the time-independent components of the complex fields (Problem 2.3):

$$\nabla\cdot\mathbf{D}(\mathbf{r}) = \rho(\mathbf{r}), \tag{2.22}$$

$$\nabla\times\mathbf{E}(\mathbf{r}) = \mathrm{i}\omega\mathbf{B}(\mathbf{r}), \tag{2.23}$$

$$\nabla\cdot\mathbf{B}(\mathbf{r}) = 0, \tag{2.24}$$

$$\nabla\times\mathbf{H}(\mathbf{r}) = \mathbf{J}(\mathbf{r}) - \mathrm{i}\omega\mathbf{D}(\mathbf{r}), \tag{2.25}$$

$$\nabla\cdot\mathbf{J}(\mathbf{r}) - \mathrm{i}\omega\rho(\mathbf{r}) = 0, \tag{2.26}$$

where we exploit the typographical distinction between the symbols for the real-valued quantities $\mathcal{E}$, $\mathcal{D}$, $\mathcal{H}$, $\mathcal{B}$, $\mathcal{J}$, and ρ and for their complex-valued counterparts $\mathbf{E}$, $\mathbf{D}$, $\mathbf{H}$, $\mathbf{B}$, $\mathbf{J}$, and ρ.

The constitutive relations remain unchanged in the frequency domain if the medium is nondispersive:

$$\mathbf{D}(\mathbf{r}) = \epsilon(\mathbf{r})\mathbf{E}(\mathbf{r}), \tag{2.27}$$

$$\mathbf{B}(\mathbf{r}) = \mu(\mathbf{r})\mathbf{H}(\mathbf{r}), \tag{2.28}$$

$$\mathbf{J}(\mathbf{r}) = \sigma(\mathbf{r})\mathbf{E}(\mathbf{r}). \tag{2.29}$$

For a time-dispersive medium, we can substitute the monochromatic fields of the form (2.21) into Eqs. (2.13)–(2.15) and derive

$$\mathbf{D}(\mathbf{r}) = \epsilon(\mathbf{r},\omega)\mathbf{E}(\mathbf{r}), \tag{2.30}$$

[1] A complex vector is defined as $\mathbf{a} = \mathbf{b} + \mathrm{i}\mathbf{c}$, where $\mathbf{b}$ and $\mathbf{c}$ are regular real vectors. All operations with complex vectors are defined in a way analogous to the definition of operations with complex numbers and real vectors. For example, the complex conjugate $\mathbf{a}^*$ is defined as $\mathbf{b} - \mathrm{i}\mathbf{c}$, the scalar product of two complex vectors $\mathbf{a} = \mathbf{b} + \mathrm{i}\mathbf{c}$ and $\mathbf{d} = \mathbf{e} + \mathrm{i}\mathbf{f}$ with real $\mathbf{b}$, $\mathbf{c}$, $\mathbf{e}$, and $\mathbf{f}$ is defined as $\mathbf{a}\cdot\mathbf{d} = \mathbf{b}\cdot\mathbf{e} - \mathbf{c}\cdot\mathbf{f} + \mathrm{i}(\mathbf{b}\cdot\mathbf{f} + \mathbf{c}\cdot\mathbf{e})$, etc.

$$\mathbf{B}(\mathbf{r}) = \mu(\mathbf{r}, \omega)\mathbf{H}(\mathbf{r}), \tag{2.31}$$

$$\mathbf{J}(\mathbf{r}) = \sigma(\mathbf{r}, \omega)\mathbf{E}(\mathbf{r}), \tag{2.32}$$

where

$$\epsilon(\mathbf{r}, \omega) = \int_0^\infty \mathrm{d}t\, \epsilon(\mathbf{r}, t)\exp(\mathrm{i}\omega t), \tag{2.33}$$

$$\mu(\mathbf{r}, \omega) = \int_0^\infty \mathrm{d}t\, \mu(\mathbf{r}, t)\exp(\mathrm{i}\omega t), \tag{2.34}$$

$$\sigma(\mathbf{r}, \omega) = \int_0^\infty \mathrm{d}t\, \sigma(\mathbf{r}, t)\exp(\mathrm{i}\omega t) \tag{2.35}$$

are complex functions of the angular frequency. Please note that we use sloping Greek letters in Eqs. (2.27)–(2.29) and upright Greek letters in Eqs. (2.30)–(2.32) to differentiate between the frequency-independent and the frequency-dependent constitutive parameters, respectively. Equations (2.22) and (2.25) can be rewritten in the form

$$\nabla \cdot [\varepsilon(\mathbf{r}, \omega)\mathbf{E}(\mathbf{r})] = 0, \tag{2.36}$$

$$\nabla \times \mathbf{H}(\mathbf{r}) = -\mathrm{i}\omega\varepsilon(\mathbf{r}, \omega)\mathbf{E}(\mathbf{r}), \tag{2.37}$$

where

$$\varepsilon(\mathbf{r}, \omega) = \epsilon(\mathbf{r}, \omega) + \mathrm{i}\frac{\sigma(\mathbf{r}, \omega)}{\omega} \tag{2.38}$$

is the so-called complex permittivity. Again note the typographical distinction between the frequency-dependent electric permittivity ϵ (which can, in principle, be complex-valued for a dispersive medium) and the complex permittivity ε. We will discuss later that a direct consequence of a complex-valued ε and/or μ is a nonzero imaginary part of the refractive index (see Eq. (3.15)) as well as absorption of electromagnetic energy via conversion into other forms of energy such as heat.

Neither the scalar nor the vector product of two real vector fields is equal to the real part of the respective product of the corresponding complex vector fields. Instead,

$$\begin{aligned}\mathcal{C}(\mathbf{r}, t) &= \boldsymbol{\mathcal{A}}(\mathbf{r}, t) \cdot \boldsymbol{\mathcal{G}}(\mathbf{r}, t) \\ &= \frac{1}{4}[\mathbf{A}(\mathbf{r})\exp(-\mathrm{i}\omega t) + \mathbf{A}^*(\mathbf{r})\exp(\mathrm{i}\omega t)] \cdot [\mathbf{G}(\mathbf{r})\exp(-\mathrm{i}\omega t) + \mathbf{G}^*(\mathbf{r})\exp(\mathrm{i}\omega t)] \\ &= \frac{1}{2}\mathrm{Re}[\mathbf{A}(\mathbf{r}) \cdot \mathbf{G}^*(\mathbf{r}) + \mathbf{A}(\mathbf{r}) \cdot \mathbf{G}(\mathbf{r})\exp(-2\mathrm{i}\omega t)],\end{aligned} \tag{2.39}$$

and similarly for a vector product. Often, however, ω is so large that traditional optical measuring devices are not capable of following the rapid oscillations of the instantaneous product values, but rather respond to a time average

$$\langle \mathcal{C}(\mathbf{r},t)\rangle = \frac{1}{T}\int_{t-T/2}^{t+T/2} \mathrm{d}t'\,\mathcal{C}(\mathbf{r},t'), \tag{2.40}$$

where T is a time interval long compared with the period of the time-harmonic oscillations: $T \gg T_\mathrm{o} = 2\pi/\omega$. Therefore, Eqs. (2.39) and (2.40) imply that the time average of a product of two real fields is equal to one half of the real part of the respective product of one complex field with the complex conjugate of the other, e.g.,

$$\langle \mathcal{C}(\mathbf{r},t)\rangle = \frac{1}{2}\mathrm{Re}[\mathbf{A}(\mathbf{r})\cdot\mathbf{B}^*(\mathbf{r})]. \tag{2.41}$$

While this is a welcome result, it also means that the frequency-domain formalism becomes less convenient if one needs to trace the detailed temporal evolution of various quadratic combinations of the electric and magnetic field vectors.

Strictly speaking, the frequency-domain formalism introduced in this section describes steady-state electromagnetic fields which, apart from the time-harmonic factor $\exp(-\mathrm{i}\omega t)$, do not change over the entire time interval $t \in (-\infty, +\infty)$. However, the use of time-harmonic fields is not as restrictive as it may appear at first sight. Indeed, many time-varying fields can be expressed in terms of time-harmonic components using the Fourier analysis, e.g.,

$$\boldsymbol{\mathcal{E}}(\mathbf{r},t) = \int_{-\infty}^{\infty} \mathrm{d}\omega\,\mathbf{E}(\mathbf{r},\omega)\exp(-\mathrm{i}\omega t), \tag{2.42}$$

where the frequency spectrum $\mathbf{E}(\mathbf{r},\omega)$ is given by the Fourier transform

$$\mathbf{E}(\mathbf{r},\omega) = \frac{1}{2\pi}\int_{-\infty}^{\infty} \mathrm{d}t\,\boldsymbol{\mathcal{E}}(\mathbf{r},t)\exp(\mathrm{i}\omega t). \tag{2.43}$$

Therefore, if the frequency-domain field $\mathbf{E}(\mathbf{r},\omega)$ is known for any ω, then its time-domain counterpart $\boldsymbol{\mathcal{E}}(\mathbf{r},t)$ can be found by evaluating the integral (2.42). Of course, this procedure can be quite involved, and so a direct numerical solution of the original time-domain MMEs may often be a more efficient approach (Taflove and Hagness 2005; Van Bladel 2007).

More importantly, one can expect the frequency-domain formalism to be applicable to any electromagnetic field that is steady-state over a time interval much longer than the period of time-harmonic oscillations T_o. This practical requirement is met quite often, which explains why the majority of books on electromagnetics and optics are largely based on the frequency-domain MMEs (e.g., Statton 1941; van de Hulst 1957; Born and Wolf 1999; Van Bladel 2007).

2.4 Energy budget

The MMEs and constitutive relations by themselves do not allow one to solve energy-budget and optical-characterization problems, discussed in Section 1.4. In

addition to the abstract concepts of charge and field, the system of axioms of classical electromagnetics must provide a link to other physical quantities, including those directly measurable with suitable instrumentation. This is accomplished in part by using the Lorentz force equation, which postulates that if a differential volume element $\mathrm{d}V$ contains a total charge $\rho(\mathbf{r},t)\,\mathrm{d}V$ moving at a velocity $\mathbf{v}(\mathbf{r},t)$ then the force exerted by the electromagnetic field on that charge is

$$\mathrm{d}\mathbf{F} = \rho(\mathbf{r},t)\boldsymbol{\mathcal{E}}(\mathbf{r},t)\,\mathrm{d}V + \rho(\mathbf{r},t)\,\mathbf{v}(\mathbf{r},t)\times\boldsymbol{\mathcal{B}}(\mathbf{r},t)\,\mathrm{d}V. \tag{2.44}$$

Let us now consider the conservation of energy in a finite volume V by taking into account that, according to Eq. (2.44), the magnetic field does no work, while for the local charge $\rho(\mathbf{r},t)\,\mathrm{d}V$ the rate of doing work by the electric field is $\rho(\mathbf{r},t)\,\mathbf{v}(\mathbf{r},t)\cdot\boldsymbol{\mathcal{E}}(\mathbf{r},t)\,\mathrm{d}V$. Thus the total rate of work done by the electromagnetic field is given by

$$\int_V \mathrm{d}^3\mathbf{r}\,\boldsymbol{\mathcal{J}}(\mathbf{r},t)\cdot\boldsymbol{\mathcal{E}}(\mathbf{r},t) \tag{2.45}$$

and represents the rate of conversion of electromagnetic energy into mechanical energy. This power must be balanced by the corresponding rate of decrease of the electromagnetic field energy within the volume V. Using Eqs. (2.2) and (2.4) and the vector identity

$$\nabla\cdot(\mathbf{a}\times\mathbf{b}) = \mathbf{b}\cdot(\nabla\times\mathbf{a}) - \mathbf{a}\cdot(\nabla\times\mathbf{b}), \tag{2.46}$$

we derive the so-called Poynting theorem:

$$\begin{aligned}\int_V \mathrm{d}^3\mathbf{r}\,\boldsymbol{\mathcal{J}}\cdot\boldsymbol{\mathcal{E}} &= \int_V \mathrm{d}^3\mathbf{r}\,\boldsymbol{\mathcal{E}}\cdot\left(\nabla\times\boldsymbol{\mathcal{H}} - \frac{\partial\boldsymbol{\mathcal{D}}}{\partial t}\right)\\ &= -\int_V \mathrm{d}^3\mathbf{r}\left[\nabla\cdot(\boldsymbol{\mathcal{E}}\times\boldsymbol{\mathcal{H}}) + \boldsymbol{\mathcal{E}}\cdot\frac{\partial\boldsymbol{\mathcal{D}}}{\partial t} + \boldsymbol{\mathcal{H}}\cdot\frac{\partial\boldsymbol{\mathcal{B}}}{\partial t}\right].\end{aligned} \tag{2.47}$$

Let us now discuss consequences of Eq. (2.47) and consider first a medium without dispersion. Using the Gauss theorem,

$$\int_V \mathrm{d}^3\mathbf{r}\,\nabla\cdot\mathbf{A} = \oint_S \mathrm{d}^2\mathbf{r}\,\mathbf{A}\cdot\hat{\mathbf{n}}, \tag{2.48}$$

we obtain

$$\int_V \mathrm{d}^3\mathbf{r}\,\boldsymbol{\mathcal{J}}\cdot\boldsymbol{\mathcal{E}} + \oint_S \mathrm{d}^2\mathbf{r}\,\boldsymbol{\mathcal{S}}\cdot\hat{\mathbf{n}} + \int_V \mathrm{d}^3\mathbf{r}\,\frac{\partial\mathcal{U}}{\partial t} = 0, \tag{2.49}$$

where the closed surface S bounds the volume V, $\hat{\mathbf{n}}$ is a unit vector in the direction of the local outward normal to the surface,

$$\boldsymbol{\mathcal{S}}(\mathbf{r},t) = \boldsymbol{\mathcal{E}}(\mathbf{r},t)\times\boldsymbol{\mathcal{H}}(\mathbf{r},t) \tag{2.50}$$

is the Poynting vector having the dimension of energy/(area × time), and the scalar quantity

$$\mathcal{U}(\mathbf{r},t) = \frac{1}{2}[\boldsymbol{\mathcal{E}}(\mathbf{r},t)\cdot\boldsymbol{\mathcal{D}}(\mathbf{r},t) + \boldsymbol{\mathcal{H}}(\mathbf{r},t)\cdot\boldsymbol{\mathcal{B}}(\mathbf{r},t)], \tag{2.51}$$

traditionally called the electromagnetic energy density, has the dimension of energy/volume. Equation (2.49) manifests the conservation of energy by establishing that the rate of total work done by the fields on the charges within the volume, Eq. (2.45), the rate of change of electromagnetic energy within the volume,

$$\int_V \mathrm{d}^3\mathbf{r}\,\frac{\partial\mathcal{U}}{\partial t}, \tag{2.52}$$

and the electromagnetic energy flowing out through the volume boundary per unit time,

$$\oint_S \mathrm{d}^2\mathbf{r}\,\boldsymbol{\mathcal{S}}\cdot\hat{\mathbf{n}}, \tag{2.53}$$

add up to zero. Since the volume V is arbitrary, Eq. (2.49) can also be written in the form of a differential continuity equation:

$$\frac{\partial\mathcal{U}}{\partial t} + \nabla\cdot\boldsymbol{\mathcal{S}} = -\boldsymbol{\mathcal{J}}\cdot\boldsymbol{\mathcal{E}}. \tag{2.54}$$

One should recognize that, strictly speaking, the Poynting vector does not characterize the direction and rate of the local electromagnetic energy flow. Indeed, adding the curl of any vector field to $\boldsymbol{\mathcal{S}}(\mathbf{r},t)$ yields a vector field $\boldsymbol{\mathcal{S}}'(\mathbf{r},t)$ that also satisfies the Poynting theorem in either integral or differential form. Certain problems are also caused by associating $\mathcal{U}(\mathbf{r},t)$ with the local electromagnetic energy density (Stratton 1941; Rothwell and Cloud 2009). It is important, however, that one does not need to attribute any specific physical meaning to either $\boldsymbol{\mathcal{S}}(\mathbf{r},t)$ or $\mathcal{U}(\mathbf{r},t)$, since in the final analysis only the integrals (2.52) and (2.53) have actual practical significance. Therefore, it is only one's ability to calculate or measure $\boldsymbol{\mathcal{S}}(\mathbf{r},t)$ and $\mathcal{U}(\mathbf{r},t)$ that matters.

Let us now allow the medium to be dispersive. Instead of Eq. (2.45), we consider the integral

$$\frac{1}{2}\int_V \mathrm{d}^3\mathbf{r}\,\mathbf{J}^*(\mathbf{r})\cdot\mathbf{E}(\mathbf{r}) \tag{2.55}$$

whose real part gives the time-averaged rate of work done by the electromagnetic field (cf. Eq. (2.41)). Using Eqs. (2.23), (2.25), and (2.46), we derive

$$\frac{1}{2}\int_V \mathrm{d}^3\mathbf{r}\,\mathbf{J}^*(\mathbf{r})\cdot\mathbf{E}(\mathbf{r}) = \frac{1}{2}\int_V \mathrm{d}^3\mathbf{r}\,\mathbf{E}(\mathbf{r})\cdot[\nabla\times\mathbf{H}^*(\mathbf{r}) - \mathrm{i}\omega\mathbf{D}^*(\mathbf{r})]$$

$$= -\frac{1}{2}\int_V \mathrm{d}^3\mathbf{r}\,\{\nabla\cdot[\mathbf{E}(\mathbf{r})\times\mathbf{H}^*(\mathbf{r})] + \mathrm{i}\omega[\mathbf{E}(\mathbf{r})\cdot\mathbf{D}^*(\mathbf{r}) - \mathbf{B}(\mathbf{r})\cdot\mathbf{H}^*(\mathbf{r})]\}. \quad (2.56)$$

If we now define the complex Poynting vector by

$$\mathbf{S}(\mathbf{r}) = \frac{1}{2}\mathbf{E}(\mathbf{r})\times\mathbf{H}^*(\mathbf{r}), \quad (2.57)$$

denote

$$w_\mathrm{e}(\mathbf{r}) = \frac{1}{4}\mathbf{E}(\mathbf{r})\cdot\mathbf{D}^*(\mathbf{r}), \quad (2.58)$$

$$w_\mathrm{m}(\mathbf{r}) = \frac{1}{4}\mathbf{B}(\mathbf{r})\cdot\mathbf{H}^*(\mathbf{r}), \quad (2.59)$$

and apply the Gauss theorem, then we obtain:

$$\frac{1}{2}\int_V \mathrm{d}^3\mathbf{r}\,\mathbf{J}^*(\mathbf{r})\cdot\mathbf{E}(\mathbf{r}) + \oint_S \mathrm{d}^2\mathbf{r}\,\mathbf{S}(\mathbf{r})\cdot\hat{\mathbf{n}}(\mathbf{r}) + 2\mathrm{i}\omega\int_V \mathrm{d}^3\mathbf{r}[w_\mathrm{e}(\mathbf{r}) - w_\mathrm{m}(\mathbf{r})] = 0. \quad (2.60)$$

Obviously, the real part of Eq. (2.60) manifests the conservation of energy for the corresponding time-averaged quantities. In particular, the time-averaged Poynting vector $\langle\boldsymbol{\mathcal{S}}(\mathbf{r},t)\rangle$ is equal to the real part of the complex Poynting vector:

$$\langle\boldsymbol{\mathcal{S}}(\mathbf{r},t)\rangle = \mathrm{Re}\,\mathbf{S}(\mathbf{r}). \quad (2.61)$$

The net time-averaged rate $\langle W\rangle$ at which the electromagnetic energy crosses the closed surface S is given by

$$\langle W\rangle = -\oint_S \mathrm{d}^2\mathbf{r}\,\langle\boldsymbol{\mathcal{S}}(\mathbf{r},t)\rangle\cdot\hat{\mathbf{n}}(\mathbf{r}). \quad (2.62)$$

The rate is defined such that it is positive if there is a net transfer of electromagnetic energy into the volume V and is negative otherwise.

It is worth emphasizing that, unlike Eq. (2.49), Eq. (2.60) cannot provide the instantaneous solution of an energy-budget problem, but rather describes the energy balance of the volume V averaged over a time interval capturing a sufficiently large number of time-harmonic oscillations of the electromagnetic field. Since typical optical instruments cannot trace these high-frequency oscillations anyway, appropriate use of Eq. (2.60) can be justified in the majority of practical applications.

2.5 Lossless, lossy, and active media

Let us now apply Eq. (2.62) to a small homogeneous volume element ΔV bounded by a closed surface ΔS. The material that fills up the volume element is

classified as *lossless* (or nonabsorbing) if the net time-averaged flow of electromagnetic power entering ΔV, i.e.,

$$\langle W_{\Delta S}\rangle = -\oint_{\Delta S} \mathrm{d}^2\mathbf{r}\,\langle \boldsymbol{\mathcal{S}}(\mathbf{r},t)\rangle \cdot \hat{\mathbf{n}}(\mathbf{r}), \tag{2.63}$$

is zero when there are sources of electromagnetic power external to ΔV, but no sources internal to ΔV. This means that the physical mechanisms within ΔV either do not dissipate the incoming electromagnetic power or that there is a mechanism that creates power[2] to exactly balance the dissipation. If the time-averaged electromagnetic power entering ΔV is positive, then the material dissipates power and is called *lossy* (or absorbing). Finally, if the time-averaged power entering ΔV is negative then power must be created inside ΔV, and the material is *active*.

In summary, the material is classified as follows (Stratton 1941; Rothwell and Cloud 2009):

$$\begin{aligned}
&\langle W_{\Delta S}\rangle = 0, \text{ lossless},\\
&\langle W_{\Delta S}\rangle > 0, \text{ lossy},\\
&\langle W_{\Delta S}\rangle \geq 0, \text{ passive},\\
&\langle W_{\Delta S}\rangle < 0, \text{ active}.
\end{aligned}$$

It can be proven (Problem 2.7) that a passive material is lossless when the permittivity ϵ and permeability μ are real, while the conductivity σ is zero. A passive material is lossy when one or more of the following holds:

- the permittivity has a positive imaginary part;
- the permeability has a positive imaginary part;
- the conductivity has a positive real part.

Finally, the material is active when one or more of the following holds:

- the permittivity has a negative imaginary part;
- the permeability has a negative imaginary part;
- the conductivity has a negative real part.

In the remainder of this book we will deal only with passive materials.

We have already pointed out in Section 1.4 that in the case of a lossy material with zero conductivity, the inequality $W_{\Delta S} > 0$ appears to imply that there is an infinite accumulation of electromagnetic energy inside the volume element ΔV. This paradoxical result demonstrates that classical electromagnetics is not a self-contained physical discipline in terms of accounting for all types of field–

[2] Note that, consistent with the general framework of this book outlined in Section 1.1, the created power is not described as arising from sources such as thermal emission, but is rather defined via appropriate values of the constitutive parameters entering Eqs. (2.30)–(2.32).

matter interactions. The traditional way to circumvent this issue without invoking more fundamental physical laws is to postulate that, instead of being infinitely accumulated, the electromagnetic energy is dissipated via conversion into other forms of energy, such as heat, this energy dissipation possibly being accompanied by re-radiation of electromagnetic energy at other frequencies.

A rigorous and self-consistent way to solve this problem must be based on QED, which provides a complete modern description of the interaction of the electromagnetic field with atomic and molecular matter (Healy 1982; Craig and Thirunamachandran 1984; Cohen-Tannoudji *et al.* 1989, 1992). It is imperative to recognize that, in general, the Hamiltonian describing the field–matter interaction is not controlled by the Poynting vector of the electromagnetic field, but rather is defined in terms of the electric and magnetic field vectors. This factor implies that the physical significance of the Poynting vector is limited. The main reason to calculate or measure this quantity is that it enters the Poynting theorem and thereby helps identify physical systems strongly affected by nonlinear field–matter interactions. In fact, we will see in Chapter 11 that the limited physical content of the (time-averaged) Poynting vector can make the actual measurement of this quantity quite problematic.

Problems

2.1: What are $\epsilon(\mathbf{r}, t-t')$, $\mu(\mathbf{r}, t-t')$, and $\sigma(\mathbf{r}, t-t')$ in Eqs. (2.13)–(2.15) for a nondispersive medium?

2.2: Consider two real time-harmonic vectors $\boldsymbol{\mathcal{E}}_1(\mathbf{r}, t)$ and $\boldsymbol{\mathcal{E}}_2(\mathbf{r}, t)$ represented by complex vectors $\mathbf{E}_1(\mathbf{r})$ and $\mathbf{E}_2(\mathbf{r})$ according to Eq. (2.21). Let $\mathbf{E}_1(\mathbf{r}) = \hat{\mathbf{x}} + \mathrm{i}\hat{\mathbf{y}}$ and $\mathbf{E}_2(\mathbf{r}) = \mathrm{i}\hat{\mathbf{x}} + \hat{\mathbf{y}}$, where $\hat{\mathbf{x}}$ and $\hat{\mathbf{y}}$ are unit vectors in the positive directions of the x- and y-axes, respectively.

(a) Are both $\langle \boldsymbol{\mathcal{E}}_1(\mathbf{r}, t) \cdot \boldsymbol{\mathcal{E}}_2(\mathbf{r}, t) \rangle$ and $\mathbf{E}_1(\mathbf{r}) \cdot \mathbf{E}_2(\mathbf{r})$ zero?

(b) Are both $\langle \boldsymbol{\mathcal{E}}_1(\mathbf{r}, t) \times \boldsymbol{\mathcal{E}}_2(\mathbf{r}, t) \rangle$ and $\mathbf{E}_1(\mathbf{r}) \times \mathbf{E}_2(\mathbf{r})$ zero vectors?

2.3: Derive Eqs. (2.22)–(2.26).

2.4: Express the length of time T over which one must accumulate the signal to make Eq. (2.41) accurate to within $\pm 0.01\%$ in terms of the angular frequency ω. What is T in the visible part of the electromagnetic spectrum ($\omega \sim 2\pi \times 10^{15}\ \mathrm{s}^{-1}$)? What is T at microwave frequencies ($\omega \sim 2\pi \times 10^{10}\ \mathrm{s}^{-1}$)?

2.5: Generalize Eq. (2.41) to the vector and dyadic products of two vectors (see Appendix A for a summary of dyadic algebra).

2.6: Prove that the frequency spectrum satisfies the symmetry relation $\mathbf{E}(\mathbf{r}, -\omega) = [\mathbf{E}(\mathbf{r}, \omega)]^*$.

2.7: Prove the six statements in the middle of Section 2.5.

Notes and further reading

Maxwell's electromagnetics is the first relativistic field theory and one of the supreme intellectual achievements in the history of humankind. Ludwig Boltzmann was so enchanted by the beauty and might of the Maxwell equations that he quoted from Johann Goethe's *Faust*: "War es ein Gott, der diese Zeichen schrieb (?)" ("Was it a God who wrote these signs (?)") (Boltzmann 1893, p. iii). In his magnificent history of mathematical thought from ancient to modern times, Morris Kline wrote: "The most spectacular triumph of the nineteenth century, with an enormous impact on science and technology, was Maxwell's derivation in 1864 of the laws of electromagnetism" (Kline 1972, p. 698). It is therefore profoundly symbolic that Maxwell's equations of electromagnetism have been voted by scientists to be the greatest equations ever (Crease 2004).

For a long time, James Clerk Maxwell (1831–79) had been among the most underappreciated personalities in the history of science. Only recently has it be-

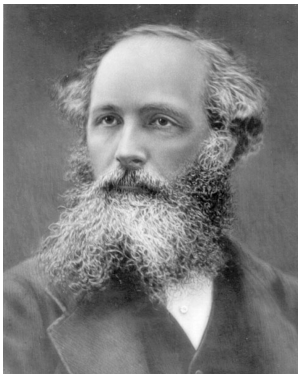

James Clerk Maxwell

Oliver Heaviside

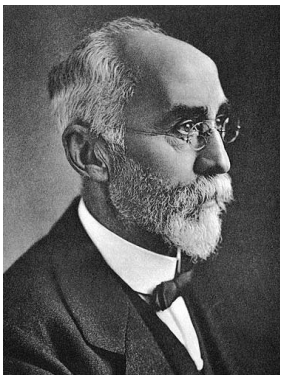

Hendrik Lorentz

John Henry Poynting

Jules Henri Poincaré

come widely recognized that Maxwell's influence on science and technology can be compared only to that of Sir Isaac Newton (1642–1727). The title of a recent biography of Maxwell is thus quite revealing: *The Man Who Changed Everything* (Mahon 2003). More on Maxwell's life and personality can be found in the thoroughly documented earlier biography by Campbell and Garnett (1884) (see also Tolstoy 1981).

By far the best account of the history of classical electromagnetics from the time of Gilbert and Descartes to the relativity theory of Poincaré and Lorentz is that by Whittaker (1987). Although this book may not be easy to find, those who persevere will be rewarded by reading a masterful and meticulously documented recreation of the *actual* sequence of events and publications that shaped the physical science. The book by Hunt (1991) describes how Maxwell's ideas, summarized in his famous *Treatise* (Maxwell 1873), were picked up, organized, and reworked mathematically by his immediate followers, most notably by Oliver Heaviside (1850–1925) (see also Nahin 2002 and Mahon 2009). A "by-product" of Heaviside's work on electromagnetics (Heaviside 1950) was the creation (independently of J. Willard Gibbs) of vector algebra and vector analysis. Jules Henri Poincaré (1854–1912) introduced the overarching principle of relativity (Poincaré 1904) and derived the relativity theory as a direct corollary of the Maxwell equations (Poincaré 1905, 1906).

The famous Poynting theorem quantifying the energy budget of a finite volume element was derived by John Henry Poynting (1852–1914) in 1884 (Poynting 1884) and independently by Heaviside (1885). In 1916, Hendrik Antoon Lorentz (1853–1928) wrote that "Poynting's theorem throws a clear light on many questions. Indeed, its importance can hardly be overstated, and it is now difficult to recall the state of electromagnetic theory of some thirty years ago, when we had to do without this beautiful theorem." Yet Lorentz also warned against too literal an interpretation of the Poynting vector as describing a *current* or *flow* of electromagnetic energy by noting that "in general it will not be possible to trace the paths of parts or elements of energy in the same sense in which we can follow in their course the ultimate particles of which matter is made up. …It might even be questioned whether, in electromagnetic phenomena, the transfer of energy really takes place in the way indicated by Poynting's law" (Lorentz 1916, pp. 25–26).

Lorentz gave the first derivation of the MMEs from classical microscopic electromagnetics (see Lorentz 1916). His work was refined and generalized by de Groot and Suttorp (1972) and Robinson (1973). The complete derivation of the MMEs from QED has turned out to be a much more nontrivial endeavor. It is especially involved if a dielectric medium is lossy, in which case one needs to link the dielectric to a thermal field reservoir. Although recent progress in this direction has been substantial (see, e.g., Huttner and Barnett 1992; Ho and Kumar 1993; Suttorp and Wubs 2004), further research is still required (Lukš and Peřinová 2009).

While there are many good books on Maxwell's macroscopic electromagnetics, those by Stratton (1941), Jackson (1998), Van Bladel (2007), and Rothwell and Cloud (2009) stand out. The recently reissued monograph by Julius Adams Stratton (1901–94) is a classical text which had set the tone for virtually all subsequent textbooks on electromagnetic theory. The comprehensive books by Jackson and Van Bladel are widely accepted benchmarks that have served to educate generations of scientists and engineers. The textbook by Rothwell and Cloud contains a remarkably thorough and systematic outline, which is highly recommended to any thoughtful student of physics.

3

Fundamental homogeneous-medium solutions of the macroscopic Maxwell equations

In this chapter we will discuss two simple, yet fundamental, solutions of the frequency-domain MMEs in an infinite homogeneous medium. The first is a time-harmonic plane-wave solution that underlies the basic optical idea of a perfectly monochromatic parallel beam of light. The second is an asymptotic solution in the form of an outgoing or incoming time-harmonic spherical wave. Both solutions play a key role in the theory of monochromatic and polychromatic electromagnetic scattering by finite objects and in particular by multi-particle groups with widely separated components. As such, they will be frequently used in the following chapters.

3.1 Plane-wave solution

Consider an infinite homogeneous isotropic medium without sources (i.e., assuming that $\rho(\mathbf{r}) \equiv 0$ and $\mathbf{J}(\mathbf{r}) \equiv \mathbf{0}$). Recalling Eqs. (2.23), (2.24), (2.36), and (2.37), it is rather straightforward to demonstrate (see Problem 3.1) that the pair of complex electric and magnetic field vectors given by

$$\widetilde{\mathcal{E}}(\mathbf{r}, t) = \mathbf{E}_0 \exp(\mathrm{i}\mathbf{k} \cdot \mathbf{r} - \mathrm{i}\omega t), \tag{3.1}$$

$$\widetilde{\mathcal{H}}(\mathbf{r}, t) = \mathbf{H}_0 \exp(\mathrm{i}\mathbf{k} \cdot \mathbf{r} - \mathrm{i}\omega t), \tag{3.2}$$

where $\mathbf{E}_0$, $\mathbf{H}_0$, and $\mathbf{k}$ are constant complex vectors, represents a solution of the frequency-domain MMEs, provided that the following conditions are met:

$$\mathbf{k} \cdot \mathbf{E}_0 = 0, \tag{3.3}$$

$$\mathbf{k} \cdot \mathbf{H}_0 = 0, \tag{3.4}$$

$$\mathbf{k} \times \mathbf{E}_0 = \omega\mu\mathbf{H}_0, \tag{3.5}$$

$$\mathbf{k} \times \mathbf{H}_0 = -\omega\varepsilon\mathbf{E}_0. \tag{3.6}$$

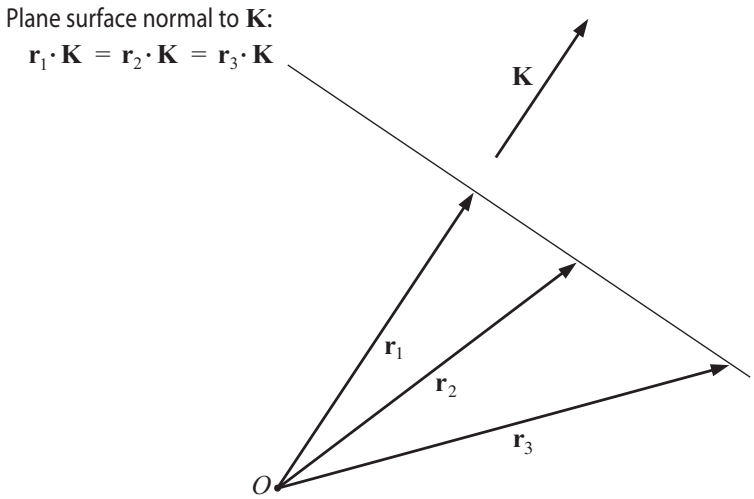

Fig. 3.1. Plane surface normal to a real vector **K**.

The wave vector **k** is usually expressed as

$$\mathbf{k} = \mathbf{k}_\mathrm{R} + \mathrm{i}\mathbf{k}_\mathrm{I}, \tag{3.7}$$

where $\mathbf{k}_\mathrm{R}$ and $\mathbf{k}_\mathrm{I}$ are real vectors, and it is assumed that $\mathbf{k}_\mathrm{R} \neq \mathbf{0}$. Thus

$$\widetilde{\mathcal{E}}(\mathbf{r}, t) = \mathbf{E}_0 \exp(-\mathbf{k}_\mathrm{I} \cdot \mathbf{r}) \exp(\mathrm{i}\mathbf{k}_\mathrm{R} \cdot \mathbf{r} - \mathrm{i}\omega t), \tag{3.8}$$

$$\widetilde{\mathcal{H}}(\mathbf{r}, t) = \mathbf{H}_0 \exp(-\mathbf{k}_\mathrm{I} \cdot \mathbf{r}) \exp(\mathrm{i}\mathbf{k}_\mathrm{R} \cdot \mathbf{r} - \mathrm{i}\omega t), \tag{3.9}$$

where $\mathbf{E}_0 \exp(-\mathbf{k}_\mathrm{I} \cdot \mathbf{r})$ and $\mathbf{H}_0 \exp(-\mathbf{k}_\mathrm{I} \cdot \mathbf{r})$ are the complex amplitudes of the electric and magnetic fields, respectively, while $\phi = \mathbf{k}_\mathrm{R} \cdot \mathbf{r} - \omega t$ is their phase. It is rather straightforward to show (see Problem 3.2) that

$$\mathbf{k} \cdot \mathbf{k} = \omega^2 \varepsilon\mu. \tag{3.10}$$

A plane surface normal to a real vector **K** is described by $\mathbf{r} \cdot \mathbf{K} =$ constant, where **r** is the radius vector drawn from the origin of the reference frame to any point in the plane (see Fig. 3.1). Therefore, the vector $\mathbf{k}_\mathrm{R}$ is normal to the surfaces of constant phase, whereas $\mathbf{k}_\mathrm{I}$ is normal to the surfaces of constant amplitude. Also, the planes corresponding to the instant times t and $t + \Delta t$ are separated by the distance $\Delta s = \omega \Delta t / |\mathbf{k}_\mathrm{R}|$ (see Fig. 3.2), which implies that the surfaces of constant phase propagate in the direction of $\mathbf{k}_\mathrm{R}$ with the phase velocity

$$v = \frac{\omega}{|\mathbf{k}_\mathrm{R}|}. \tag{3.11}$$

Thus Eqs. (3.1) and (3.2) do describe a plane electromagnetic wave. Equations (3.1), (3.2), and (3.5) imply that

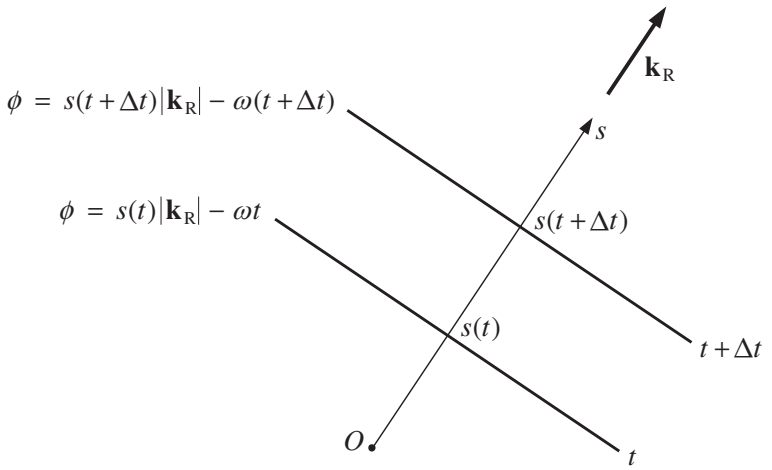

Fig. 3.2. The plane of constant phase ϕ = constant travels a distance Δs over the time interval Δt. The s axis is drawn from the origin of the coordinate system O along the vector $\mathbf{k}_R$.

$$\widetilde{\mathcal{H}}(\mathbf{r}, t) = \frac{1}{\omega\mu}\mathbf{k} \times \widetilde{\mathcal{E}}(\mathbf{r}, t). \tag{3.12}$$

Therefore, a plane electromagnetic wave can always be considered in terms of only the electric (or only the magnetic) field.

The electromagnetic wave is called homogeneous if $\mathbf{k}_R$ and $\mathbf{k}_I$ are parallel (including the case $\mathbf{k}_I = \mathbf{0}$); otherwise it is called inhomogeneous. If $\mathbf{k}_R \| \mathbf{k}_I$ then the complex wave vector can be expressed as $\mathbf{k} = (k_R + \mathrm{i}k_I)\hat{\mathbf{n}}$, where $\hat{\mathbf{n}}$ is a real unit vector in the direction of propagation and both k_R and k_I are real and non-negative.

According to Eqs. (3.3) and (3.4), the plane electromagnetic wave is transverse: both $\mathbf{E}_0$ and $\mathbf{H}_0$ are perpendicular to $\mathbf{k}$. Furthermore, either Eq. (3.5) or (3.6) implies that $\mathbf{E}_0$ and $\mathbf{H}_0$ are mutually perpendicular: $\mathbf{E}_0 \cdot \mathbf{H}_0 = 0$. Since $\mathbf{E}_0$, $\mathbf{H}_0$, and $\mathbf{k}$ are, in general, complex vectors, the physical interpretation of these facts may not be straightforward. It becomes most obvious when both ε, μ, and, owing to Eq. (3.10), $\mathbf{k}$ are real-valued. The reader can easily verify that in this case the real field vectors $\mathcal{E}$ and $\mathcal{H}$ are mutually perpendicular and lie in a plane normal to the direction of wave propagation $\hat{\mathbf{n}}$ (see Fig. 3.3).

In the practically important case of a homogeneous plane wave, Eq. (3.10) implies that

$$k = k_R + \mathrm{i}k_I = \omega\sqrt{\varepsilon\mu} = \frac{\omega m}{c}, \tag{3.13}$$

where k is the wave number,

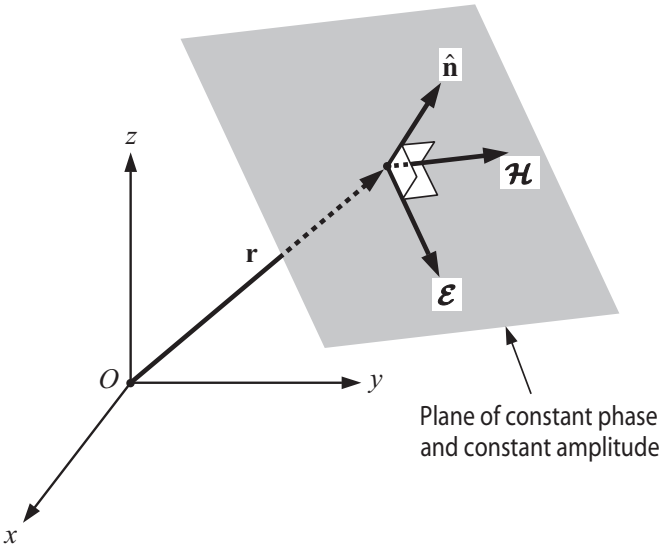

Fig. 3.3. Plane wave propagating in a homogeneous lossless medium.

$$c = \frac{1}{\sqrt{\epsilon_0 \mu_0}} \tag{3.14}$$

is the speed of light in a vacuum, and

$$m = \frac{ck}{\omega} = m_{\mathrm{R}} + \mathrm{i} m_{\mathrm{I}} = \sqrt{\frac{\varepsilon\mu}{\epsilon_0 \mu_0}} = c\sqrt{\varepsilon\mu} \tag{3.15}$$

is the complex refractive index with a nonnegative real part m_{R} and a nonnegative imaginary part m_{I}. Thus, the complex electric field vector of the homogeneous plane wave has the form

$$\widetilde{\mathcal{E}}(\mathbf{r}, t) = \mathbf{E}_0 \exp\left(-\frac{\omega}{c} m_{\mathrm{I}} \hat{\mathbf{n}} \cdot \mathbf{r}\right) \exp\left(\mathrm{i}\frac{\omega}{c} m_{\mathrm{R}} \hat{\mathbf{n}} \cdot \mathbf{r} - \mathrm{i}\omega t\right). \tag{3.16}$$

If the imaginary part of the refractive index is nonzero then it determines the exponential decay of the amplitude of the wave as it propagates through the medium, which is thus absorbing. On the other hand, a medium is nonabsorbing if $\epsilon = \epsilon$, $\mu = \mu$, and $\sigma = 0$, which causes the refractive index $m = m_{\mathrm{R}} = c(\epsilon\mu)^{1/2}$ to be real-valued. The real part of the refractive index determines the phase velocity of the wave:

$$v = \frac{c}{m_{\mathrm{R}}}. \tag{3.17}$$

In a vacuum, $m = m_{\mathrm{R}} = 1$ and $v = c$.

It follows from Eqs. (2.57), (2.61), (3.1), (3.2), (3.12), and the vector identity

$$\mathbf{a}\times(\mathbf{b}\times\mathbf{c}) = \mathbf{b}(\mathbf{a}\cdot\mathbf{c}) - \mathbf{c}(\mathbf{a}\cdot\mathbf{b}) \tag{3.18}$$

that the time-averaged Poynting vector of a plane wave is given by

$$\langle\boldsymbol{\mathcal{S}}(\mathbf{r},t)\rangle = \mathrm{Re}\left(\frac{\mathbf{k}^*[\mathbf{E}(\mathbf{r})\cdot\mathbf{E}^*(\mathbf{r})] - \mathbf{E}^*(\mathbf{r})[\mathbf{k}^*\cdot\mathbf{E}(\mathbf{r})]}{2\omega\mu^*}\right). \tag{3.19}$$

If the wave is homogeneous then $\mathbf{k}\cdot\mathbf{E}(\mathbf{r}) = 0$ and so $\mathbf{k}^*\cdot\mathbf{E}(\mathbf{r}) = 0$. Therefore,

$$\langle\boldsymbol{\mathcal{S}}(\mathbf{r},t)\rangle = \frac{1}{2}\mathrm{Re}\left(\sqrt{\frac{\varepsilon}{\mu}}\right)|\mathbf{E}_0|^2\exp\left(-2\frac{\omega}{c}m_{\mathrm{I}}\hat{\mathbf{n}}\cdot\mathbf{r}\right)\hat{\mathbf{n}}. \tag{3.20}$$

Thus, $\langle\boldsymbol{\mathcal{S}}(\mathbf{r},t)\rangle$ is in the direction of propagation and its absolute value, called the intensity, is attenuated exponentially, provided that the medium is lossy:

$$I(\mathbf{r}) = |\langle\boldsymbol{\mathcal{S}}(\mathbf{r},t)\rangle| = I_0\exp(-\alpha\hat{\mathbf{n}}\cdot\mathbf{r}), \tag{3.21}$$

where I_0 is the intensity at $\mathbf{r}=\mathbf{0}$. The absorption coefficient is given by

$$\alpha = 2\frac{\omega}{c}m_{\mathrm{I}} = \frac{4\pi m_{\mathrm{I}}}{\lambda_0}, \tag{3.22}$$

where

$$\lambda_0 = \frac{2\pi c}{\omega} \tag{3.23}$$

is the free-space wavelength. The intensity has the dimension of monochromatic energy flux, i.e., energy/(area$\times$time), and is sometimes interpreted as the amount of electromagnetic energy crossing a unit surface element normal to $\hat{\mathbf{n}}$ per unit time. As we have discussed in Section 2.4, such an interpretation is, strictly speaking, unnecessary.

Figure 3.4 gives an example of a plane electromagnetic wave propagating along the y axis in a nonabsorbing homogeneous medium and described by the following real electric and magnetic field vectors:

$$\boldsymbol{\mathcal{E}}(\mathbf{r},t) = \mathcal{E}\cos(ky-\omega t-\pi/2)\hat{\mathbf{z}}, \tag{3.24}$$

$$\boldsymbol{\mathcal{H}}(\mathbf{r},t) = \mathcal{H}\cos(ky-\omega t-\pi/2)\hat{\mathbf{x}}, \tag{3.25}$$

where $\mathcal{E}$, $\mathcal{H}$, and k are real and $\hat{\mathbf{x}}$ and $\hat{\mathbf{z}}$ are the unit vectors along the x- and z-axis, respectively. Figure 3.4a shows the electric and magnetic fields as functions of y at the moment $t = 0$, while Fig. 3.4b depicts the fields as functions of time at any point in the plane $y = 0$. The period of the sinusoids in Fig. 3.4a is

$$\lambda = 2\pi/k \tag{3.26}$$

and defines the wavelength of light in the nonabsorbing material medium. The period of the sinusoids in Fig. 3.4b is equal to $2\pi/\omega$.

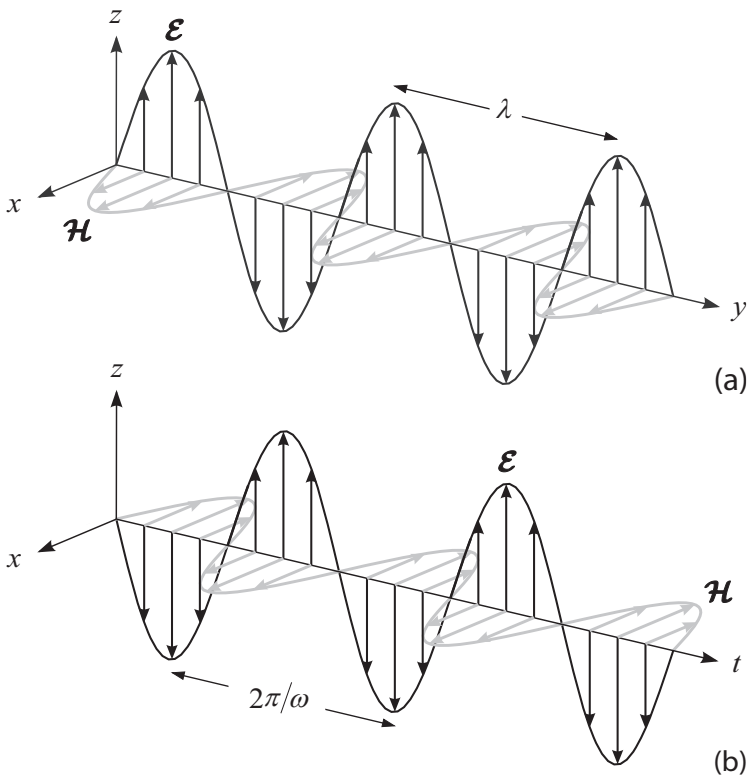

Fig. 3.4. Plane electromagnetic wave described by Eqs. (3.24) and (3.25).

It is straightforward to verify (see Problem 3.3) that a choice of the time dependence $\exp(\mathrm{i}\omega t)$ rather than $\exp(-\mathrm{i}\omega t)$ in the complex representation of time-harmonic fields in Eq. (2.21) would have led to $m = m_{\mathrm{R}} - \mathrm{i}m_{\mathrm{I}}$ with a nonnegative m_{I}. The $\exp(-\mathrm{i}\omega t)$ time-factor convention adopted here has been used in the majority of books on optics and light scattering (e.g., Born and Wolf 1999; Bohren and Huffman 1983; Barber and Hill 1990; MTL-1, MTL-2), electromagnetics (e.g., Stratton 1941; Jackson 1998; Tsang *et al.* 2000; Zangwill 2013), and solid-state physics (e.g., Kittel 1963). However, van de Hulst (1957), Kerker (1969), and Hovenier *et al.* (2004) used the time factor $\exp(\mathrm{i}\omega t)$, which implies a nonpositive imaginary part of the complex refractive index. It does not matter in the final analysis which convention is chosen, because all measurable quantities of practical interest are always real. However, once a choice of the time factor has been made, its consistent use throughout all derivations is imperative.

3.2 Spherical-wave solution

Another fundamental solution of the frequency-domain MMEs representing the outward propagation from a point-like source is a transverse outgoing spherical

wave. To derive this solution, we need to recall Eqs. (2.23), (2.24), (2.31), (2.36), (2.37), (H.1), (H.2), and the following well-known formulas:

$$\nabla \frac{\exp(\pm \mathrm{i}kr)}{r} = \left(\pm \mathrm{i}k - \frac{1}{r}\right)\frac{\exp(\pm \mathrm{i}kr)}{r}\hat{\mathbf{r}}, \tag{3.27}$$

$$\nabla \cdot \mathbf{a} = \frac{\partial a_r}{\partial r} + \frac{2a_r}{r} + \frac{1}{r}\frac{\partial a_\theta}{\partial \theta} + \frac{a_\theta}{r\tan\theta} + \frac{1}{r\sin\theta}\frac{\partial a_\varphi}{\partial \varphi}, \tag{3.28}$$

$$\nabla \times \mathbf{a} = \left(\frac{1}{r}\frac{\partial a_\varphi}{\partial \theta} + \frac{a_\varphi}{r\tan\theta} - \frac{1}{r\sin\theta}\frac{\partial a_\theta}{\partial \varphi}\right)\hat{\mathbf{r}} + \left(\frac{1}{r\sin\theta}\frac{\partial a_r}{\partial \varphi} - \frac{\partial a_\varphi}{\partial r} - \frac{a_\varphi}{r}\right)\hat{\boldsymbol{\theta}} + \left(\frac{\partial a_\theta}{\partial r} + \frac{a_\theta}{r} - \frac{1}{r}\frac{\partial a_r}{\partial \theta}\right)\hat{\boldsymbol{\varphi}}, \tag{3.29}$$

where $\hat{\mathbf{r}} = \mathbf{r}/|\mathbf{r}|$, θ is the polar (zenith) angle, φ is the azimuth angle, and $\hat{\boldsymbol{\theta}}$ and $\hat{\boldsymbol{\varphi}}$ are the corresponding unit vectors in the right-handed spherical coordinate system, as shown in Fig. 3.5 (Arfken and Weber 2005). It is then straightforward to verify that the complex field vectors

$$\tilde{\mathcal{E}}(\mathbf{r}, t) = \frac{\exp(\mathrm{i}kr)}{r}\mathbf{E}_1(\hat{\mathbf{r}})\exp(-\mathrm{i}\omega t), \tag{3.30}$$

$$\tilde{\mathcal{H}}(\mathbf{r}, t) = \frac{\exp(\mathrm{i}kr)}{r}\mathbf{H}_1(\hat{\mathbf{r}})\exp(-\mathrm{i}\omega t) \tag{3.31}$$

form a solution of the MMEs in the limit $kr \to \infty$, provided that the medium is homogeneous and that

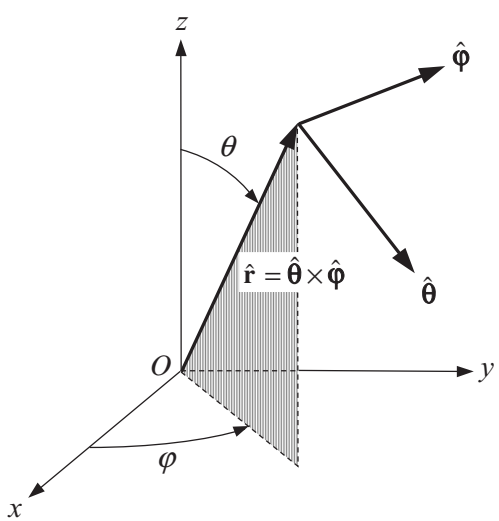

Fig. 3.5. Right-handed spherical coordinate system.

$$\hat{\mathbf{r}} \cdot \mathbf{E}_1(\hat{\mathbf{r}}) = 0, \tag{3.32}$$

$$\hat{\mathbf{r}} \cdot \mathbf{H}_1(\hat{\mathbf{r}}) = 0, \tag{3.33}$$

$$k\hat{\mathbf{r}} \times \mathbf{E}_1(\hat{\mathbf{r}}) = \omega\mu\, \mathbf{H}_1(\hat{\mathbf{r}}), \tag{3.34}$$

$$k\hat{\mathbf{r}} \times \mathbf{H}_1(\hat{\mathbf{r}}) = -\omega\varepsilon\, \mathbf{E}_1(\hat{\mathbf{r}}), \tag{3.35}$$

where the wave number $k = k_{\mathrm{R}} + \mathrm{i}k_{\mathrm{I}} = \omega(\varepsilon\mu)^{1/2} = \omega m/c$ may be complex and the $\mathbf{E}_1(\hat{\mathbf{r}})$ and $\mathbf{H}_1(\hat{\mathbf{r}})$ are independent of the distance r from the origin.

Equations (3.30)–(3.35) describe an *outgoing* transverse time-harmonic spherical wave propagating radially with the phase velocity $v = \omega/k_{\mathrm{R}}$ and having mutually perpendicular complex electric and magnetic field vectors. The wave is homogeneous in that the real and imaginary parts of the local complex wave vector $k\hat{\mathbf{r}}$ are parallel. The surfaces of constant phase coincide with the surfaces of constant amplitude and are spherical. It is obvious that

$$\widetilde{\mathcal{H}}(\mathbf{r}, t) = \frac{k}{\omega\mu}\, \hat{\mathbf{r}} \times \widetilde{\mathcal{E}}(\mathbf{r}, t), \tag{3.36}$$

which allows one to consider the spherical-wave solution in terms of the electric (or the magnetic) field only. The time-averaged Poynting vector of the wave is given by

$$\langle \mathcal{S}(\mathbf{r}, t)\rangle = \frac{1}{2}\mathrm{Re}\left(\sqrt{\frac{\varepsilon}{\mu}}\right)\frac{|\mathbf{E}_1(\hat{\mathbf{r}})|^2}{r^2}\exp\left(-2\frac{\omega}{c}m_{\mathrm{I}}r\right)\hat{\mathbf{r}}, \tag{3.37}$$

where, as before, $m_{\mathrm{I}} = ck_{\mathrm{I}}/\omega$. Thus, the local direction of $\langle \mathcal{S}(\mathbf{r}, t)\rangle$ is away from the origin. The intensity of the spherical wave is defined as the absolute value of the time-averaged Poynting vector,

$$I(\mathbf{r}) = |\langle \mathcal{S}(\mathbf{r}, t)\rangle| = \frac{1}{2}\mathrm{Re}\left(\sqrt{\frac{\varepsilon}{\mu}}\right)\frac{|\mathbf{E}_1(\hat{\mathbf{r}})|^2}{r^2}\exp\left(-2\frac{\omega}{c}m_{\mathrm{I}}r\right), \tag{3.38}$$

and has the dimension of monochromatic energy flux. It is attenuated exponentially by absorption and in addition decreases as the inverse square of the distance from the origin.

In the case of a nonabsorbing medium, the real electric and magnetic field vectors are mutually orthogonal and are normal to the direction of propagation $\hat{\mathbf{r}}$ (Fig. 3.6). The energy conservation law takes the form

$$\begin{aligned}\oint_S \mathrm{d}^2\mathbf{r}\langle \mathcal{S}(\mathbf{r}, t)\rangle \cdot \hat{\mathbf{r}} &= \oint_S \mathrm{d}^2\mathbf{r}\, I(\mathbf{r}) = \frac{1}{2}\sqrt{\frac{\epsilon}{\mu}}\frac{1}{r^2}\oint_S \mathrm{d}^2\mathbf{r}\,|\mathbf{E}_1(\hat{\mathbf{r}})|^2 \\ &= \frac{1}{2}\sqrt{\frac{\epsilon}{\mu}}\int_{4\pi} \mathrm{d}\hat{\mathbf{r}}\,|\mathbf{E}_1(\hat{\mathbf{r}})|^2 = \text{constant},\end{aligned} \tag{3.39}$$

where S is a sphere of radius r and

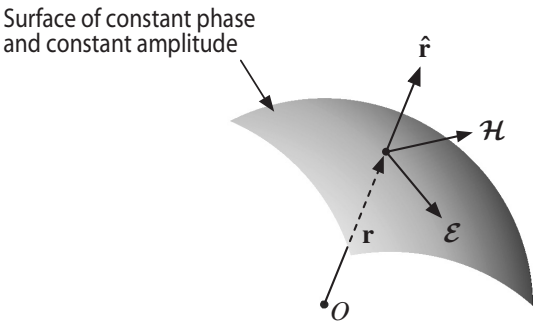

Fig. 3.6. Spherical electromagnetic wave propagating in a homogeneous lossless medium.

$$\mathrm{d}\hat{\mathbf{r}} = \frac{\mathrm{d}S}{r^2} = \sin\theta\,\mathrm{d}\theta\,\mathrm{d}\varphi \tag{3.40}$$

is a differential solid angle element around the direction $\hat{\mathbf{r}}$ (see Fig. 3.7).

The reader is invited to verify by analogy (see Problem 3.7) that the complex electric and magnetic field vectors

$$\widetilde{\mathcal{E}}(\mathbf{r},t) = \frac{\exp(-\mathrm{i}kr)}{r}\mathbf{E}_1(\hat{\mathbf{r}})\exp(-\mathrm{i}\omega t), \tag{3.41}$$

$$\widetilde{\mathcal{H}}(\mathbf{r},t) = \frac{\exp(-\mathrm{i}kr)}{r}\mathbf{H}_1(\hat{\mathbf{r}})\exp(-\mathrm{i}\omega t) \tag{3.42}$$

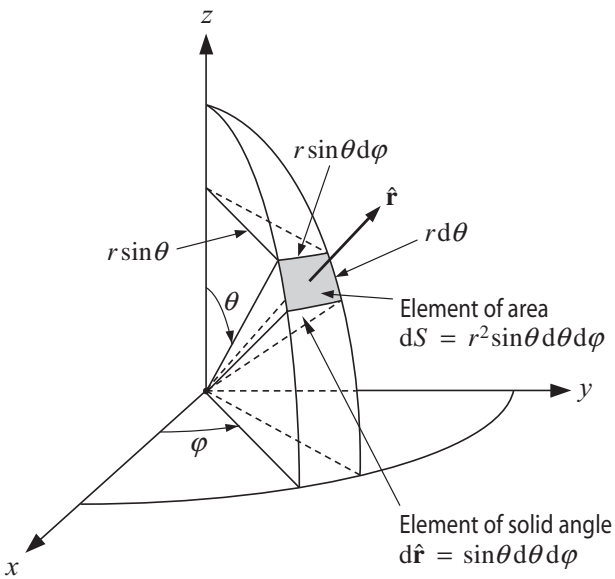

Fig. 3.7. Differential solid angle element in spherical coordinates.

represent yet another solution of the frequency-domain MMEs in the limit $kr \to \infty$, provided that the medium is homogeneous and that

$$\hat{\mathbf{r}} \cdot \mathbf{E}_1(\hat{\mathbf{r}}) = 0, \tag{3.43}$$

$$\hat{\mathbf{r}} \cdot \mathbf{H}_1(\hat{\mathbf{r}}) = 0, \tag{3.44}$$

$$k\hat{\mathbf{r}} \times \mathbf{E}_1(\hat{\mathbf{r}}) = -\omega\mu\,\mathbf{H}_1(\hat{\mathbf{r}}), \tag{3.45}$$

$$k\hat{\mathbf{r}} \times \mathbf{H}_1(\hat{\mathbf{r}}) = \omega\varepsilon\mathbf{E}_1(\hat{\mathbf{r}}). \tag{3.46}$$

These formulas describe an *incoming* transverse spherical wave with mutually perpendicular complex electric and magnetic field vectors. The spherical surfaces of constant phase and constant amplitude propagate radially in the direction of the local unit vector $-\hat{\mathbf{r}}$. The latter also gives the direction of the local Poynting vector.

Problems

3.1: Verify that Eqs. (3.1) and (3.2) satisfy the frequency-domain MMEs for an isotropic homogeneous medium without sources.

3.2: Derive Eq. (3.10).

3.3: Show that the choice of the time dependence $\exp(\mathrm{i}\omega t)$ rather than $\exp(-\mathrm{i}\omega t)$ in the complex representation of time-harmonic fields in Eq. (2.21) results in a relative refractive index $m = m_{\mathrm{R}} - \mathrm{i}m_{\mathrm{I}}$ with a nonnegative m_{I}.

3.4: Derive the following expression for the time-averaged energy density of a time-harmonic electromagnetic field existing in a medium without dispersion:

$$\langle \mathcal{U}(\mathbf{r},t)\rangle = \frac{1}{4}[\epsilon\mathbf{E}(\mathbf{r})\cdot\mathbf{E}^*(\mathbf{r}) + \mu\mathbf{H}(\mathbf{r})\cdot\mathbf{H}^*(\mathbf{r})]. \tag{3.47}$$

3.5: Assume that the host medium is lossless and show that for a plane electromagnetic wave,

$$\langle \mathcal{U}(\mathbf{r},t)\rangle = \frac{1}{2}\epsilon|\mathbf{E}_0|^2. \tag{3.48}$$

3.6: Show that for a plane wave propagating in a lossless medium,

$$I(\mathbf{r}) = v\langle \mathcal{U}(\mathbf{r},t)\rangle, \tag{3.49}$$

where $v = 1\big/\sqrt{\epsilon\mu}$ is the speed of light in the nonabsorbing material medium.

3.7: Demonstrate that Eqs. (3.41)–(3.46) represent a time-harmonic solution of the MMEs in an infinite homogeneous medium in the limit $kr \to \infty$.

3.8: Show that in the case of a lossless medium, the time-averaged energy density of a spherical wave is given by

$$\langle \mathcal{U}(\mathbf{r}, t) \rangle = \frac{1}{2} \epsilon \frac{|\mathbf{E}_1(\hat{\mathbf{r}})|^2}{r^2} \tag{3.50}$$

and its intensity is given by

$$I(\mathbf{r}) = v \langle \mathcal{U}(\mathbf{r}, t) \rangle. \tag{3.51}$$

4

Basic theory of frequency-domain electromagnetic scattering by a fixed finite object

As we have discussed in Chapter 1, the presence of an object with a refractive index different from that of the surrounding host medium changes the electromagnetic field that would otherwise exist in an unbounded homogeneous space. The difference between the total field in the presence of the object and the total field that would exist in the absence of the object can be thought of as the field scattered by the object. In other words, the total electromagnetic field in the presence of the object is mathematically represented as the vector sum of the *incident* and *scattered* fields.

The spatial distribution of the scattered field depends on specific characteristics of the incident field as well as on such properties of the scatterer as its size relative to the wavelength and its morphology, composition, and orientation. Therefore, in practice one usually must solve the scattering problem anew every time some or all of these input parameters change. It is appropriate, however, to consider first the general mathematical description of electromagnetic scattering without making any detailed assumptions about the scattering object, except that it is composed of linear, isotropic, and nonmagnetic materials. Hence the goal of this chapter is to establish a basic theoretical framework underlying specific problems discussed in the following chapters. Consistent with this objective and with the discussion in Section 1.1, we will assume that the scattering object is stationary and will consider only monochromatic fields whose dependence on time is completely described by the time-harmonic factor $\exp(-\mathrm{i}\omega t)$.

4.1 Statement of problem

Consider a fixed finite scattering object embedded in an infinite medium that is assumed to be homogeneous, linear, isotropic, nonmagnetic, and nonabsorbing. The scatterer can be either a single body or a cluster consisting of a finite number

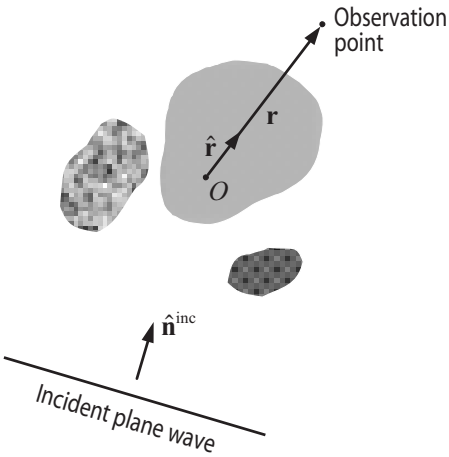

Fig. 4.1. Schematic representation of the standard electromagnetic scattering problem. The unshaded exterior region V_{EXT} is unbounded in all directions, whereas the shaded areas collectively represent the interior region V_{INT}.

N of separated or touching components; it occupies a finite interior region V_{INT} given by

$$V_{\mathrm{INT}} = \bigcup_{i=1}^{N} V_i, \tag{4.1}$$

where V_i is the volume occupied by the ith component (see Fig. 4.1). The object is surrounded by the infinite exterior region V_{EXT} such that $V_{\mathrm{INT}} \cup V_{\mathrm{EXT}} = \Re^3$, where, as before, $\Re^3$ denotes the entire three-dimensional space. The interior region is filled with isotropic, linear, nonmagnetic, and possibly inhomogeneous material. Point O serves as the common origin of all position vectors and as the origin of the laboratory coordinate system.

As a consequence of the assumption of harmonic time dependence, the four MMEs (2.22)–(2.25) are no longer independent. Indeed, Eqs. (2.22) and (2.24) now follow from Eqs. (2.23) and (2.25) (see Problem 4.1). This simplification allows one to consider only the Maxwell curl equations (2.23) and (2.25), which can conveniently be re-written as follows:

$$\left.\begin{aligned} \nabla\times\mathbf{E}(\mathbf{r}) &= \mathrm{i}\omega\mu_0\,\mathbf{H}(\mathbf{r}) \\ \nabla\times\mathbf{H}(\mathbf{r}) &= -\mathrm{i}\omega\epsilon_1\,\mathbf{E}(\mathbf{r}) \end{aligned}\right\} \quad \mathbf{r}\in V_{\mathrm{EXT}}, \tag{4.2}$$

$$\left.\begin{aligned} \nabla\times\mathbf{E}(\mathbf{r}) &= \mathrm{i}\omega\mu_0\,\mathbf{H}(\mathbf{r}) \\ \nabla\times\mathbf{H}(\mathbf{r}) &= -\mathrm{i}\omega\varepsilon_2(\mathbf{r},\omega)\,\mathbf{E}(\mathbf{r}) \end{aligned}\right\} \quad \mathbf{r}\in V_{\mathrm{INT}}, \tag{4.3}$$

where, as before, μ_0 is the permeability of a vacuum; ϵ_1 is the real-valued electric permittivity of the infinite host medium; and $\varepsilon_2(\mathbf{r},\omega)$ is the (potentially co-

ordinate-dependent) complex permittivity of the scattering object. The corresponding boundary conditions now read (cf. Eqs. (2.18) and (2.20)):

$$\left.\begin{aligned}\hat{\mathbf{n}}\times[\mathbf{E}_1(\mathbf{r})-\mathbf{E}_2(\mathbf{r})] &= \mathbf{0}\\ \hat{\mathbf{n}}\times[\mathbf{H}_1(\mathbf{r})-\mathbf{H}_2(\mathbf{r})] &= \mathbf{0}\end{aligned}\right\}\quad \mathbf{r}\in S_{\mathrm{INT}}, \tag{4.4}$$

where the subscripts 1 and 2 correspond to the exterior and interior sides of the boundary S_{INT} of the object, respectively, and $\hat{\mathbf{n}}$ is the local outward normal to S_{INT}. In agreement with Eq. (4.1), S_{INT} is the union of the closed surfaces of the N components of the object:

$$S_{\mathrm{INT}} = \bigcup_{i=1}^{N} S_i. \tag{4.5}$$

Let us assume that the total field $\{\mathbf{E}(\mathbf{r}),\mathbf{H}(\mathbf{r})\}$ everywhere in space can be represented by a vector superposition of a plane-wave "incident field" (superscript "inc") propagating in the direction of the unit vector $\hat{\mathbf{n}}^{\mathrm{inc}}$ and a "scattered field" (superscript "sca"):

$$\begin{aligned}\mathbf{E}(\mathbf{r}) &= \mathbf{E}_0^{\mathrm{inc}}\exp(\mathrm{i}k_1\hat{\mathbf{n}}^{\mathrm{inc}}\cdot\mathbf{r}) + \mathbf{E}^{\mathrm{sca}}(\mathbf{r}),\\ \mathbf{H}(\mathbf{r}) &= \sqrt{\frac{\epsilon_1}{\mu_0}}\,\hat{\mathbf{n}}^{\mathrm{inc}}\times\mathbf{E}_0^{\mathrm{inc}}\exp(\mathrm{i}k_1\hat{\mathbf{n}}^{\mathrm{inc}}\cdot\mathbf{r}) + \mathbf{H}^{\mathrm{sca}}(\mathbf{r}),\end{aligned} \tag{4.6}$$

where $k_1=\omega(\epsilon_1\mu_0)^{1/2}$ is the wave number of the exterior region. Furthermore, we postulate that the scattered field satisfies the following condition at infinity:

$$\lim_{r\to\infty}\left\{\sqrt{\mu_0}\,\mathbf{r}\times\mathbf{H}^{\mathrm{sca}}(\mathbf{r}) + r\sqrt{\epsilon_1}\,\mathbf{E}^{\mathrm{sca}}(\mathbf{r})\right\} = \mathbf{0}, \tag{4.7}$$

where $r=|\mathbf{r}|$ is the distance from the origin to the observation point (Fig. 4.1). The limit (4.7) holds uniformly over all directions $\hat{\mathbf{r}}=\mathbf{r}/|\mathbf{r}|$ and is traditionally called the Silver–Müller radiation condition at infinity (Silver 1949; Müller 1969).

The curl equations (4.2) and (4.3) supplemented by the boundary conditions (4.4) and the asymptotic condition (4.7) constitute the *standard electromagnetic scattering problem* for plane-wave illumination, according to Eq. (4.6).

4.2 Existence and uniqueness of solution

The above formulation of the standard electromagnetic scattering problem would serve little practical purpose if this problem had no solution and/or if the solution was not unique. To the best of the author's knowledge, the existence and the uniqueness of the solution of the standard scattering problem have been proven only in some particular cases (e.g., for a scattering object in the form of a single homogeneous body). However, the thorough analysis by Müller (1969) demon-

strates the fundamental importance of imposing both the boundary conditions and the radiation condition at infinity. We will, therefore, assume that the standard scattering problem, as formulated in the preceding section, does have a solution, this solution being unique. While this general assumption remains to be proven mathematically, it both appears to be quite plausible and is essential for the remainder of this book.

Although the standard scattering problem is formulated for the incident field represented by a plane electromagnetic wave, its actual range of relevance is much wider. Indeed, the MMEs, the boundary conditions, and the radiation condition at infinity are all linear in the electric and magnetic fields. This fundamental property implies that the if $\{\mathbf{E}', \mathbf{H}'\}$ and $\{\mathbf{E}'', \mathbf{H}''\}$ are the solutions of the standard problem corresponding to the incident plane waves $\{(\mathbf{E}^{\text{inc}})', (\mathbf{H}^{\text{inc}})'\}$ and $\{(\mathbf{E}^{\text{inc}})'', (\mathbf{H}^{\text{inc}})''\}$, respectively, then $\{\mathbf{E}' + \mathbf{E}'', \mathbf{H}' + \mathbf{H}''\}$ is the unique solution of the boundary-value scattering problem for the incident field given by $\{(\mathbf{E}^{\text{inc}})' + (\mathbf{E}^{\text{inc}})'', (\mathbf{H}^{\text{inc}})' + (\mathbf{H}^{\text{inc}})''\}$. Therefore, solutions of the standard scattering problem can be used to obtain the solution of a more general scattering problem, as long as the corresponding incident field can be represented as a superposition of plane electromagnetic waves.

4.3 Volume integral equation

Although the standard scattering problem is formulated as a boundary-value problem for the differential frequency-domain MMEs, we will see later that in many cases it is more convenient to deal with an equivalent integral-equation formulation. Hence the objective of this section is to derive the so-called volume integral equation (VIE), which expresses the total electromagnetic field everywhere in space in terms of the incident field and the total field inside the scattering object.

Equations (4.2) and (4.3) imply that if $\mathbf{E}(\mathbf{r})$ is known everywhere in space, then $\mathbf{H}(\mathbf{r})$ can also be found everywhere in space, and vice versa. From these equations, we easily derive the following vector wave equations for $\mathbf{E}(\mathbf{r})$:

$$\nabla \times \nabla \times \mathbf{E}(\mathbf{r}) - k_1^2 \mathbf{E}(\mathbf{r}) = \mathbf{0}, \quad \mathbf{r} \in V_{\text{EXT}}, \tag{4.8}$$

$$\nabla \times \nabla \times \mathbf{E}(\mathbf{r}) - [k_2(\mathbf{r}, \omega)]^2 \mathbf{E}(\mathbf{r}) = \mathbf{0}, \quad \mathbf{r} \in V_{\text{INT}}, \tag{4.9}$$

where $k_2(\mathbf{r}, \omega) = \omega [\varepsilon_2(\mathbf{r}, \omega) \mu_0]^{1/2}$ is the wave number of the interior region. Equations (4.8) and (4.9) can be rewritten as a single inhomogeneous differential equation

$$\nabla \times \nabla \times \mathbf{E}(\mathbf{r}) - k_1^2 \mathbf{E}(\mathbf{r}) = \mathbf{j}(\mathbf{r}), \quad \mathbf{r} \in \Re^3, \tag{4.10}$$

where

$$\mathbf{j}(\mathbf{r}) = k_1^2 [\tilde{m}^2(\mathbf{r}, \omega) - 1] \mathbf{E}(\mathbf{r}), \tag{4.11}$$

$$\tilde{m}(\mathbf{r},\omega) = \begin{cases} 1, & \mathbf{r} \in V_{\mathrm{EXT}}, \\ m(\mathbf{r},\omega) = k_2(\mathbf{r},\omega)/k_1 = m_2(\mathbf{r},\omega)/m_1, & \mathbf{r} \in V_{\mathrm{INT}}, \end{cases} \tag{4.12}$$

and $m(\mathbf{r},\omega)$ is the refractive index of the interior relative to that of the exterior. From this point on, we will omit the argument ω for the sake of brevity, while still remembering that the relative refractive index may be frequency dependent. It follows from Eq. (4.11) that the forcing function $\mathbf{j}(\mathbf{r})$ vanishes everywhere outside the interior region.

Any solution of an inhomogeneous linear differential equation can be divided into two parts: (i) a solution of the respective homogeneous equation with the right-hand side identically equal to zero and (ii) a particular solution of the inhomogeneous equation. The first part satisfies the equation

$$\nabla \times \nabla \times \mathbf{E}^{\mathrm{inc}}(\mathbf{r}) - k_1^2 \mathbf{E}^{\mathrm{inc}}(\mathbf{r}) = \mathbf{0}, \quad \mathbf{r} \in \Re^3 \tag{4.13}$$

and describes the field that would exist in free space in the absence of the scattering object, i.e., the *incident field.* The physically appropriate particular solution of Eq. (4.10) must give the *scattered field* $\mathbf{E}^{\mathrm{sca}}(\mathbf{r})$ corresponding to the forcing function $\mathbf{j}(\mathbf{r})$. Obviously, of all possible particular solutions of Eq. (4.10), we must choose the one that satisfies the boundary conditions (4.4) and the radiation condition (4.7).

To find $\mathbf{E}^{\mathrm{sca}}(\mathbf{r})$, we use the free space dyadic Green's function $\overleftrightarrow{G}(\mathbf{r},\mathbf{r}')$ defined by Eq. (B.1). We scalar post-multiply Eq. (4.10) by $\overleftrightarrow{G}$ and scalar premultiply Eq. (B.9) by $\mathbf{E}^{\mathrm{sca}}$:

$$[\nabla' \times \nabla' \times \mathbf{E}^{\mathrm{sca}}(\mathbf{r}')] \cdot \overleftrightarrow{G}(\mathbf{r}',\mathbf{r}) - k_1^2 \mathbf{E}^{\mathrm{sca}}(\mathbf{r}') \cdot \overleftrightarrow{G}(\mathbf{r}',\mathbf{r}) = \mathbf{j}(\mathbf{r}') \cdot \overleftrightarrow{G}(\mathbf{r}',\mathbf{r}), \tag{4.14}$$

$$\mathbf{E}^{\mathrm{sca}}(\mathbf{r}') \cdot [\nabla' \times \nabla' \times \overleftrightarrow{G}(\mathbf{r}',\mathbf{r})] - k_1^2 \mathbf{E}^{\mathrm{sca}}(\mathbf{r}') \cdot \overleftrightarrow{G}(\mathbf{r}',\mathbf{r}) = \mathbf{E}^{\mathrm{sca}}(\mathbf{r}')\delta(\mathbf{r}'-\mathbf{r}). \tag{4.15}$$

Subtracting Eq. (4.14) from Eq. (4.15) yields

$$\begin{aligned} &[\nabla' \times \nabla' \times \mathbf{E}^{\mathrm{sca}}(\mathbf{r}')] \cdot \overleftrightarrow{G}(\mathbf{r}',\mathbf{r}) - \mathbf{E}^{\mathrm{sca}}(\mathbf{r}') \cdot [\nabla' \times \nabla' \times \overleftrightarrow{G}(\mathbf{r}',\mathbf{r})] \\ &\quad = \mathbf{j}(\mathbf{r}') \cdot \overleftrightarrow{G}(\mathbf{r}',\mathbf{r}) - \mathbf{E}^{\mathrm{sca}}(\mathbf{r}')\delta(\mathbf{r}'-\mathbf{r}). \end{aligned} \tag{4.16}$$

Let us now invoke the dyadic Green's theorem (see Appendix 4 of Van Bladel 2007):

$$\begin{aligned} &\int_V \mathrm{d}^3\mathbf{r}[(\nabla \times \nabla \times \mathbf{a}) \cdot \overleftrightarrow{A} - \mathbf{a} \cdot (\nabla \times \nabla \times \overleftrightarrow{A})] \\ &\quad = \oint_S \mathrm{d}^2\mathbf{r}\{(\hat{\mathbf{n}} \times \mathbf{a}) \cdot (\nabla \times \overleftrightarrow{A}) + [\hat{\mathbf{n}} \times (\nabla \times \mathbf{a})] \cdot \overleftrightarrow{A}\}, \end{aligned} \tag{4.17}$$

where the closed surface S bounds the finite volume V and $\hat{\mathbf{n}}$ is the unit vector along the local outward normal to S. The integration of Eq. (4.16) over the interior region V_{INT} then yields

$$\int_{V_{\rm INT}} \mathrm{d}^3\mathbf{r}'\,\mathbf{j}(\mathbf{r}')\cdot\overleftrightarrow{G}(\mathbf{r}',\mathbf{r}) - \int_{V_{\rm INT}} \mathrm{d}^3\mathbf{r}'\,\mathbf{E}^{\rm sca}(\mathbf{r}')\,\delta(\mathbf{r}'-\mathbf{r})$$
$$= \oint_{S_{\rm INT}} \mathrm{d}^2\mathbf{r}'\{[\hat{\mathbf{n}}'\times\mathbf{E}^{\rm sca}(\mathbf{r}')]\cdot[\nabla'\times\overleftrightarrow{G}(\mathbf{r}',\mathbf{r})] + [\hat{\mathbf{n}}'\times\nabla'\times\mathbf{E}^{\rm sca}(\mathbf{r}')]\cdot\overleftrightarrow{G}(\mathbf{r}',\mathbf{r})\}$$
$$= \oint_{S_{\rm INT}} \mathrm{d}^2\mathbf{r}'\{[\hat{\mathbf{n}}'\times\mathbf{E}^{\rm sca}(\mathbf{r}')]\cdot[\nabla'\times\overleftrightarrow{G}(\mathbf{r}',\mathbf{r})] + \mathrm{i}\omega\mu_0[\hat{\mathbf{n}}'\times\mathbf{H}^{\rm sca}(\mathbf{r}')]\cdot\overleftrightarrow{G}(\mathbf{r}',\mathbf{r})\}. \tag{4.18}$$

To apply Eq. (4.17) to the exterior region $V_{\rm EXT}$, we surround the scattering object by a sphere S_R of radius R and then take the limit $R\to\infty$. We thus have:

$$-\int_{V_{\rm EXT}} \mathrm{d}^3\mathbf{r}'\,\mathbf{E}^{\rm sca}(\mathbf{r}')\,\delta(\mathbf{r}'-\mathbf{r})$$
$$= -\oint_{S_{\rm INT}} \mathrm{d}^2\mathbf{r}'\{[\hat{\mathbf{n}}'\times\mathbf{E}^{\rm sca}(\mathbf{r}')]\cdot[\nabla'\times\overleftrightarrow{G}(\mathbf{r}',\mathbf{r})] + \mathrm{i}\omega\mu_0[\hat{\mathbf{n}}'\times\mathbf{H}^{\rm sca}(\mathbf{r}')]\cdot\overleftrightarrow{G}(\mathbf{r}',\mathbf{r})\}$$
$$+ \lim_{R\to\infty}\oint_{S_R} \mathrm{d}^2\mathbf{r}'\{[\hat{\mathbf{r}}'\times\mathbf{E}^{\rm sca}(\mathbf{r}')]\cdot[\nabla'\times\overleftrightarrow{G}(\mathbf{r}',\mathbf{r})]$$
$$+ \mathrm{i}\omega\mu_0[\hat{\mathbf{r}}'\times\mathbf{H}^{\rm sca}(\mathbf{r}')]\cdot\overleftrightarrow{G}(\mathbf{r}',\mathbf{r})\}, \tag{4.19}$$

where $\hat{\mathbf{r}}'=\mathbf{r}'/r'$, $r'=|\mathbf{r}'|$, and we have taken into account that now the local outward normal to $S_{\rm INT}$ is given by $-\hat{\mathbf{n}}'$ and that the forcing function $\mathbf{j}(\mathbf{r}')$ vanishes in the exterior region. Taking into account the dyadic identity (A.18) and the asymptotic behavior of the free space dyadic Green's function at infinity (cf. Eq. (B.22))

$$\lim_{r'\to\infty}\mathbf{r}'\times[\nabla'\times\overleftrightarrow{G}(\mathbf{r}',\mathbf{r})] = -\lim_{r'\to\infty}\mathrm{i}k_1 r'\overleftrightarrow{G}(\mathbf{r}',\mathbf{r}), \tag{4.20}$$

as well as recalling the limit (B.21) and the radiation condition (4.7), we can conclude that the second integral on the right-hand side of Eq. (4.19) vanishes in the limit $R\to\infty$. Adding Eqs. (4.18) and (4.19) thus yields

$$\mathbf{E}^{\rm sca}(\mathbf{r}) = \int_{V_{\rm INT}} \mathrm{d}^3\mathbf{r}'\,\overleftrightarrow{G}(\mathbf{r},\mathbf{r}')\cdot\mathbf{j}(\mathbf{r}'),\quad \mathbf{r}\in\Re^3, \tag{4.21}$$

where we have taken into account the boundary conditions (4.4), the dyadic identity (A.4), and the symmetry property (B.13).

The final step is to substitute Eq. (4.11) in Eq. (4.21) and recall that

$$\mathbf{E}(\mathbf{r}) = \mathbf{E}^{\rm inc}(\mathbf{r}) + \mathbf{E}^{\rm sca}(\mathbf{r}). \tag{4.22}$$

The result is the following VIE:

$$\mathbf{E}(\mathbf{r}) = \mathbf{E}^{\rm inc}(\mathbf{r}) + k_1^2\int_{V_{\rm INT}} \mathrm{d}^3\mathbf{r}'\,[m^2(\mathbf{r}')-1]\overleftrightarrow{G}(\mathbf{r},\mathbf{r}')\cdot\mathbf{E}(\mathbf{r}'),\quad \mathbf{r}\in\Re^3. \tag{4.23}$$

4.4 Discussion

The VIE (4.23) plays a key role in the theory of electromagnetic scattering by particles and particle groups. It is therefore important to discuss its main conceptual implications.

First, the VIE can be viewed as the very embodiment of the notion of electromagnetic scattering. Indeed, it demonstrates that in the absence of the scattering object, i.e., when $m(\mathbf{r}') \equiv 1$, the total field is identically equal to the incident field. The presence of the object changes the total field, which means that the scattered field can be defined as the difference between the total fields in the presence and in the absence of the object. Importantly, the VIE implies that the incident field is not modified by the presence of the object and, thus, is not transformed into the scattered field. This means that, contrary to the widespread misconception, the cause of scattering is not the incident field, but rather the very presence of an object with a refractive index different from that of the host medium (Mishchenko 2009).

Second, the boundary conditions (4.4) and the radiation condition (4.7) are built into the VIE rather than serve as additional constraints imposed on the physically relevant solution of the differential frequency-domain MMEs. Furthermore, the VIE shows that if the total field in the interior region is known then the total field everywhere in space can be computed by evaluating the integral over the finite volume V_{INT} on the right-hand side of Eq. (4.23). Thus, the open-domain boundary-value problem for the differential MMEs is replaced by the finite-domain integral-equation problem. This often makes the VIE a more convenient and potent tool for solving the electromagnetic scattering problem than the original MMEs.

Third, the existence of the solution of the standard scattering problem implies that if the incident field is a plane electromagnetic wave then the VIE has at least one solution; however, the uniqueness of this solution has not been proven in general. Yet it is known that Fredholm integral equations of the second kind, such as the VIE, have a unique solution under rather generic assumptions (see, e.g., Vladimirov 1971). We will, therefore, assume in what follows that the VIE always has a unique solution.

Fourth, the discussion in Section 4.2 implies that the incident field in Eq. (4.23) may be any solution of Eq. (4.13), as long as it can be expanded in plane electromagnetic waves. This factor makes the range of applicability of the VIE quite broad.

Fifth, one could assume that since the general radiation condition (4.7) is built into the VIE, the latter should imply a rather universal behavior of the scattered field at sufficiently large distances from the scattering object. We will see in the following chapter that the VIE can indeed be used to derive the general so-called far-field limit for the scattered field without making any assumptions about the scattering object, except that it is finite.

4.5 Dyadic transition operator

Since the total field in the interior of the scattering object is not known in general, the first step in using the VIE is to solve it for the total internal field either numerically or analytically. Initially, the internal field can be approximated by the incident field. This is the gist of the so-called Rayleigh–Gans approximation otherwise known as the Rayleigh–Debye or first Born approximation (van de Hulst 1957; Ishimaru 1978). The total field computed in the Rayleigh–Gans approximation can be substituted in the integral on the right-hand side of Eq. (4.23) in order to compute an improved approximation, and this iterative process can be continued until the total field converges within a given numerical accuracy. Although this procedure can be rather involved, it shows that, in the final analysis, the scattered field can be expressed mathematically in terms of the incident field as follows:

$$\mathbf{E}^{\mathrm{sca}}(\mathbf{r}) = \int_{V_{\mathrm{INT}}} \mathrm{d}^3\mathbf{r}'\,\overleftrightarrow{G}(\mathbf{r},\mathbf{r}') \cdot \int_{V_{\mathrm{INT}}} \mathrm{d}^3\mathbf{r}''\,\overleftrightarrow{T}(\mathbf{r}',\mathbf{r}'') \cdot \mathbf{E}^{\mathrm{inc}}(\mathbf{r}''), \quad \mathbf{r} \in \Re^3, \tag{4.24}$$

where $\overleftrightarrow{T}$ is the so-called dyadic transition operator (Tsang *et al.* 1985). Substituting Eq. (4.24) in Eq. (4.23) yields the following integral equation for $\overleftrightarrow{T}$:

$$\begin{aligned}\overleftrightarrow{T}(\mathbf{r},\mathbf{r}') &= k_1^2[m^2(\mathbf{r})-1]\,\delta(\mathbf{r}-\mathbf{r}')\overleftrightarrow{I} \\ &\quad + k_1^2[m^2(\mathbf{r})-1]\int_{V_{\mathrm{INT}}} \mathrm{d}^3\mathbf{r}''\,\overleftrightarrow{G}(\mathbf{r},\mathbf{r}'') \cdot \overleftrightarrow{T}(\mathbf{r}'',\mathbf{r}'), \quad \mathbf{r},\mathbf{r}' \in V_{\mathrm{INT}}.\end{aligned} \tag{4.25}$$

Equations of this type also appear in the quantum theory of scattering and are called Lippmann–Schwinger equations (Newton 1982).

An essential property of $\overleftrightarrow{T}$ is that it is independent of the incident field and is a function of the scattering object only: it is fully defined by the distribution of the relative refractive index throughout the interior volume. We will see later that owing to this fundamental property, the concept of the dyadic transition operator is central to the theory of electromagnetic scattering by multi-particle groups. In particular, it can be used to derive from Eqs. (4.24) and (4.25) the system of so-called Foldy equations serving as a natural precursor to the microphysical theories of radiative transfer and weak localization in particulate media.

Unfortunately, neither the convergence of the iterative procedure leading to Eq. (4.24) nor the existence and uniqueness of solution of Eq. (4.25) have generally been proven. As before, we will accept both as plausible mathematical hypotheses.

Problems

4.1: Derive the frequency-domain Maxwell divergence equations from the frequency-domain Maxwell curl equations.

4.2: It is often stated in the literature that upon scattering, the incident field is transformed into the scattered field. Discuss the correctness of this statement (cf. Mishchenko 2009).

4.3: Verify that the dyadic Green's function has the dimension of inverse length, m^{-1}.

4.4: Verify that the dyadic transition operator has the dimension of m^{-5}.

Notes and further reading

The basic model of electromagnetic scattering outlined in this chapter relies on the assumption that the incident field is the same in the absence and in the presence of the scattering object. It is therefore implied that the object is located sufficiently far from the source of the incident field and thereby does not affect the physical processes responsible for the generation of the incident field.

Furthermore, in the framework of the basic model of electromagnetic scattering the existence of the monochromatic incident field is taken for granted. This allows us to bypass altogether the discussion of specific physical phenomena resulting in the emission of electromagnetic waves, at the expense of making the model of purely monochromatic scattering vulnerable to criticism of being too idealistic in many actual cases. As will be discussed in Chapter 9, a practical way out of this potentially problematic situation is to consider the scattering of a polychromatic electromagnetic field consisting of monochromatic or quasi-monochromatic components.

The dyadic Green's function $\ddot{G}(\mathbf{r}, \mathbf{r}')$ has a singularity at $\mathbf{r} = \mathbf{r}'$, which makes the actual solution of the VIE for the internal field nontrivial. This aspect of the VIE formalism is discussed by Van Bladel (1961) and Lakhtakia and Mulholland (1993) who show that for $\mathbf{r} \in V_{\mathrm{INT}}$ the integrals in Eq. (4.23) should be taken as principal values around the point $\mathbf{r}'$. The same applies, of course, to Eqs. (4.24) and (4.25).

Some derivations of the VIE published in monographs and journal papers, including the original derivation by Saxon (1955b), do not invoke explicitly the boundary conditions (4.4). As such, they are applicable only to "fuzzy" scattering objects without distinct boundaries. This means that the refractive index is assumed to depend on spatial coordinates continuously throughout the entire space rather than being discontinuous across particle surfaces.

5

Far-field scattering

Panels (b) and (c) of Fig. 1.3 show that the structure of the electric field inside the scattering object as well as in its immediate vicinity can be quite complex. Yet there is an obvious simplification as the distance from the object increases, the scattered field eventually becoming a spherical outgoing wave irrespective of the specific nature of the object. This universal behavior of the scattered field in the so-called far zone plays an extremely important role in many applications of electromagnetic scattering and thus deserves an express analysis. In this chapter we will derive general formulas describing the far-field regime and discuss theoretical criteria of their applicability.

5.1 Scattering in the far zone

Let us denote by $\boldsymbol{\rho}' = \mathbf{r} - \mathbf{r}'$ the vector connecting the center of the differential volume element $\mathrm{d}^3\mathbf{r}'$ and an external observation point $\mathbf{r}$ (Fig. 5.1). Let us also assume that

$$k_1 \rho' \gg 1 \text{ for any } \mathbf{r}' \in V_{\mathrm{INT}}, \tag{5.1}$$

where $\rho' = |\boldsymbol{\rho}'|$. Then Eq. (4.23) implies that

$$\mathbf{E}^{\mathrm{sca}}(\mathbf{r}) = \frac{k_1^2}{4\pi} \int_{V_{\mathrm{INT}}} \mathrm{d}^3\mathbf{r}' [m^2(\mathbf{r}') - 1] \frac{\exp(\mathrm{i}k_1 \rho')}{\rho'} (\vec{I} - \hat{\boldsymbol{\rho}}' \otimes \hat{\boldsymbol{\rho}}') \cdot \mathbf{E}(\mathbf{r}'), \quad \mathbf{r} \in V_{\mathrm{EXT}}, \tag{5.2}$$

where $\hat{\boldsymbol{\rho}}' = \boldsymbol{\rho}'/\rho'$ is the unit vector originating at $\mathbf{r}'$ and directed towards the observation point (Problem 5.1).

This formula has two important implications. First, it shows that the scattered field at an external observation point is a vector superposition of partial scattered fields (wavelets) which are created by infinitesimal volume elements constituting the interior of the object. Second, it demonstrates that each wavelet is an outgoing transverse spherical wave (Fig. 5.2). Indeed, the identity dyadic in spherical

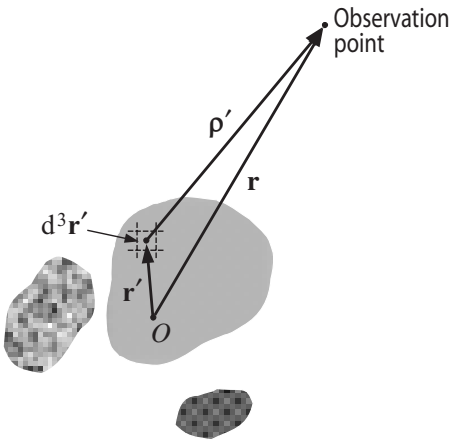

Fig. 5.1. Derivation of Eq. (5.2).

polar coordinates is given by Eq. (A.20), so that the dyadic factor $\vec{I} - \hat{\boldsymbol{\rho}}' \otimes \hat{\boldsymbol{\rho}}'$ in Eq. (5.2) ensures that each wavelet is transverse, i.e., the electric field vector of the wavelet at the observation point is perpendicular to its propagation direction $\hat{\boldsymbol{\rho}}'$:

$$\hat{\boldsymbol{\rho}}' \cdot (\vec{I} - \hat{\boldsymbol{\rho}}' \otimes \hat{\boldsymbol{\rho}}') \cdot \mathbf{E}(\mathbf{r}') = 0. \tag{5.3}$$

Furthermore, the electric field of the wavelet decays inversely with distance ρ' from the center of the infinitesimal volume element.

Let us now assume that the origin of the laboratory coordinate system O is close to the geometrical center of the scattering object (Figs. 5.1 and 5.3) and consider the scattered field in the far zone of the entire object. Specifically, assuming that the distance r from the origin to the observation point is much greater than any linear dimension of the scatterer,

$$r \gg r' \text{ for any } \mathbf{r}' \in V_{\text{INT}}, \tag{5.4}$$

we have

$$\vec{I} - \hat{\boldsymbol{\rho}}' \otimes \hat{\boldsymbol{\rho}}' \approx \vec{I} - \hat{\mathbf{r}} \otimes \hat{\mathbf{r}}, \tag{5.5}$$

$$\rho' = |\mathbf{r} - \mathbf{r}'| = r\sqrt{1 - 2\frac{\hat{\mathbf{r}} \cdot \mathbf{r}'}{r} + \frac{r'^2}{r^2}} \approx r - \hat{\mathbf{r}} \cdot \mathbf{r}' + \frac{r'^2}{2r}, \tag{5.6}$$

where $\hat{\mathbf{r}} = \mathbf{r}/r$ is the unit vector in the direction of $\mathbf{r}$, Fig. 5.3. The last two terms on the right-hand side of Eq. (5.6) can be neglected in computing the slowly varying denominator in the expression on the right-hand side of Eq. (5.2), thereby yielding

$$\frac{1}{\rho'} \approx \frac{1}{r}, \tag{5.7}$$

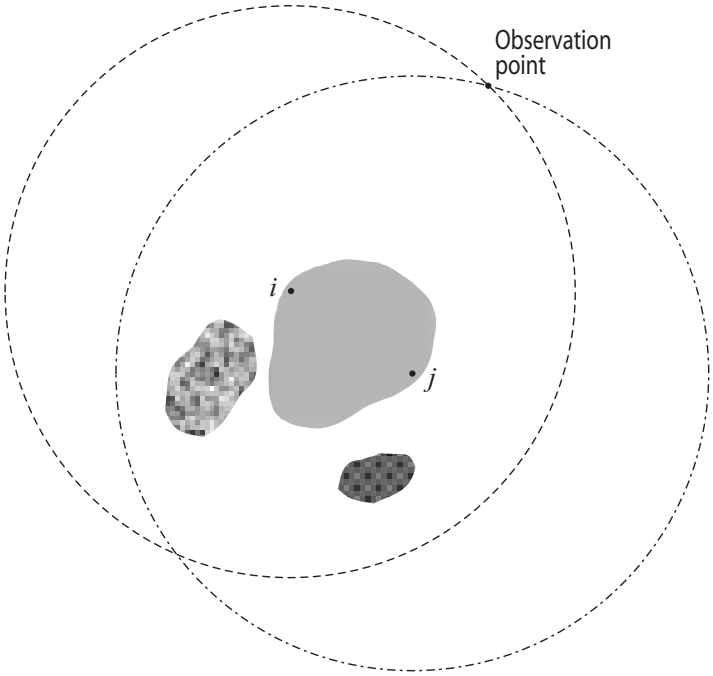

Fig. 5.2. Spherical wavelets generated by infinitesimal volume elements centered at points i (dashed circle) and j (dot-dashed circle).

but not in computing the rapidly oscillating factor $\exp(\mathrm{i}k_1\rho')$. Assuming, however, that

$$\frac{k_1 r'^2}{2r} \ll 1 \text{ for any } \mathbf{r}' \in V_{\mathrm{INT}}, \tag{5.8}$$

we finally derive:

$$\mathbf{E}^{\mathrm{sca}}(\mathbf{r}) \approx \frac{\exp(\mathrm{i}k_1 r)}{r}\frac{k_1^2}{4\pi}(\vec{I} - \hat{\mathbf{r}} \otimes \hat{\mathbf{r}}) \cdot \int_{V_{\mathrm{INT}}} \mathrm{d}^3\mathbf{r}'[m^2(\mathbf{r}') - 1]\mathbf{E}(\mathbf{r}')\exp(-\mathrm{i}k_1\hat{\mathbf{r}} \cdot \mathbf{r}'). \tag{5.9}$$

This remarkable formula is the main result of the *far-field limit* and demonstrates that the scattered electric field at a large distance from the object behaves as a single outgoing transverse spherical wave centered at O and propagating in the direction of the radial unit vector $\hat{\mathbf{r}}$. Indeed, the scattered field decays inversely with distance r from the origin and

$$\hat{\mathbf{r}} \cdot \mathbf{E}^{\mathrm{sca}}(\mathbf{r}) = 0. \tag{5.10}$$

Thus, only the θ- and φ-components of the electric vector of the scattered field are nonzero.

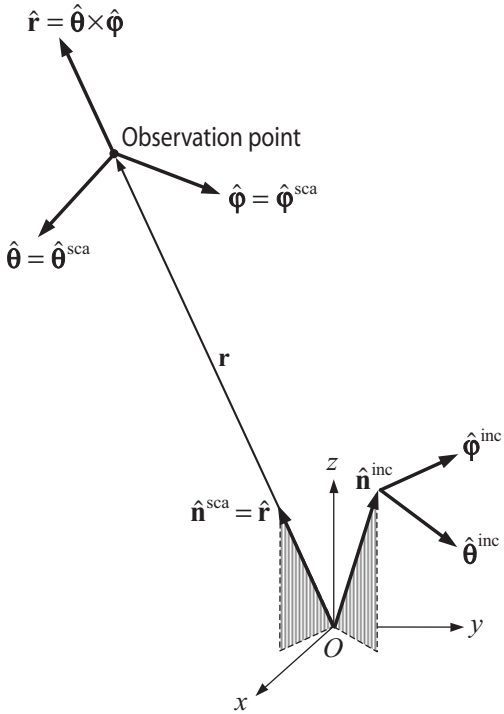

Fig. 5.3. Scattering in the far zone of the entire object.

Equation (5.9) can be rewritten in the form

$$\mathbf{E}^{\text{sca}}(\mathbf{r}) = \frac{\exp(\mathrm{i}k_1 r)}{r}\,\mathbf{E}_1^{\text{sca}}(\hat{\mathbf{r}}), \quad \hat{\mathbf{r}} \cdot \mathbf{E}_1^{\text{sca}}(\hat{\mathbf{r}}) = 0, \tag{5.11}$$

where the vector $\mathbf{E}_1^{\text{sca}}(\hat{\mathbf{r}})$ is independent of r and describes the angular distribution of the scattered field in the far zone.

5.2 Theoretical criteria of the far-field limit

Let a be the radius of the smallest circumscribing sphere of the scattering object centered at O. Then the criteria (5.1), (5.4), and (5.8) of the far-field limit can be summarized as follows:

$$k_1(r - a) \gg 1, \tag{5.12}$$

$$r \gg a \quad \text{or} \quad k_1 r \gg k_1 a, \tag{5.13}$$

$$r \gg \frac{k_1 a^2}{2} \quad \text{or} \quad k_1 r \gg \frac{k_1^2 a^2}{2}. \tag{5.14}$$

The inequality (5.13) means that the distance from any point inside the object to the external observation point must be much greater than the wavelength. This

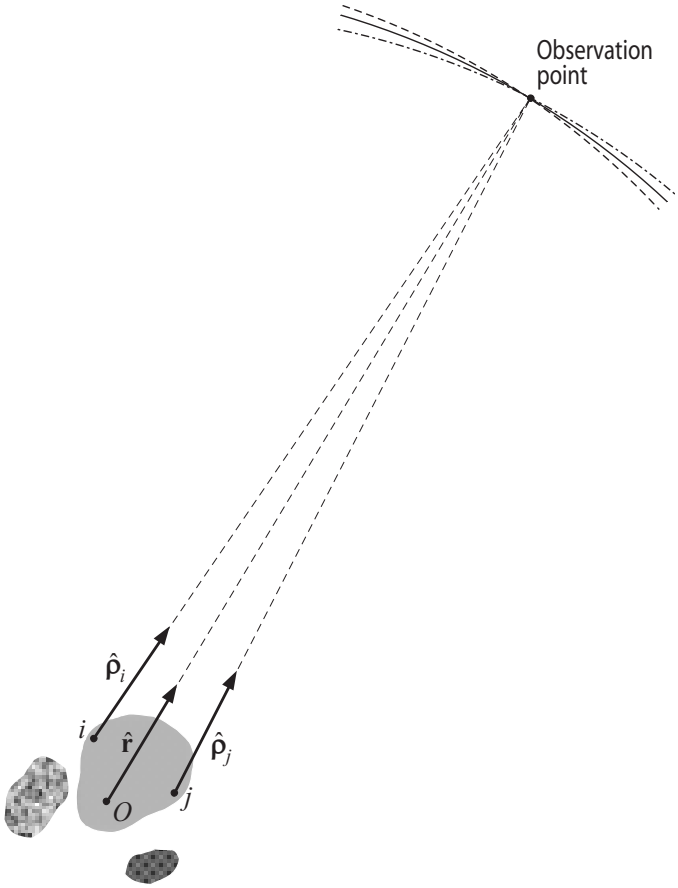

Fig. 5.4. The individual spherical wavefronts generated by infinitesimal volume elements centered at points i (dashed curve) and j (dot-dashed curve) nearly merge with increasing distance of the observation point from the scattering object and become locally indistinguishable from the cumulative spherical wavefront centered at the common origin (solid curve). The respective propagation directions at the observation point also become progressively close and eventually coincide.

requirement ensures that at the remote observation point, the partial field scattered by any differential volume element develops into an outgoing spherical wavelet.

The inequality (5.13) requires that the external observation point be located at a distance from the object much greater than the object's size. This ensures that when the partial wavelets generated by the elementary volume elements constituting the object arrive at the observation point, they propagate in essentially the same scattering direction, Fig. 5.4, and are equally attenuated by the factor 1/distance:

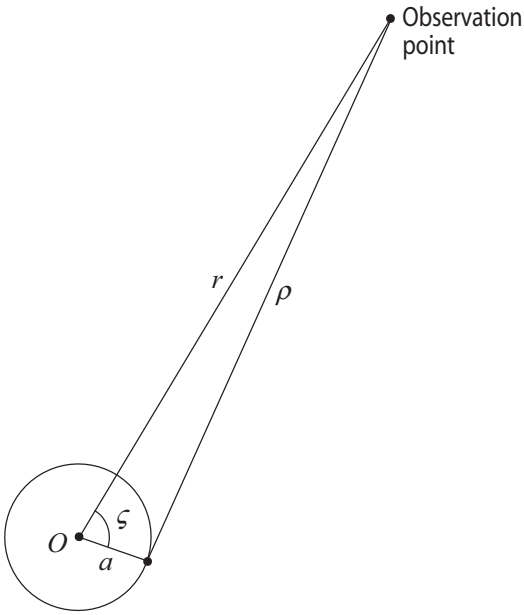

Fig. 5.5. Interpretation of the inequality (5.14).

$$\hat{\boldsymbol{\rho}}' \approx \hat{\mathbf{r}} \quad \text{and} \quad \frac{1}{\rho'} \approx \frac{1}{r} \quad \text{for any } \mathbf{r}' \in V_{\text{INT}}. \tag{5.15}$$

The meaning of the inequality (5.14) is somewhat more subtle, but becomes clear from inspection of Fig. 5.5, in which the observation point is shown relative to the smallest circumscribing sphere of the object. The phase difference between the straight path connecting the observation point and a point on the sphere surface, on one hand, and the path connecting the observation point and the origin, on the other hand, is given by

$$k_1(\rho - r) \approx \frac{k_1 a^2}{2r} - k_1 a \cos\varsigma. \tag{5.16}$$

The second term on the right-hand side of this expression is independent of r (for a fixed scattering direction), whereas the variation of the first term with changing r is significant, unless $k_1 a^2/2r \ll 1$. Therefore, we can interpret the inequality (5.14) as the requirement that the external observation point be so far from the entire scatterer that the phase difference between the paths connecting the observation point and any two points of the scatterer becomes independent of r for any fixed scattering direction. As a consequence, the surfaces of constant phase of the partial wavelets generated by the elementary volume elements constituting the object coincide locally when they reach an observation point situated in the far zone, and the wavelets form a single outgoing spherical wave (compare Figs. 5.2

and 5.4). This implies that the entire scatterer is effectively treated as a point-like body located at the origin of the laboratory coordinate system.

The relative importance of the far-zone criteria (5.12)–(5.14) changes with particle size relative to the wavelength. For particles much smaller than the wavelength $(k_1 a \ll 1)$, the inequality (5.12) is the most restrictive of the three. When $k_1 a$ is of order unity, all three criteria are roughly equivalent. For particles much greater than the wavelength $(k_1 a \gg 1)$, the inequality (5.14) becomes the most demanding and can "move" the far zone much farther from the particle than the other two inequalities.

In view of the inequality (5.13), the inequality (5.12) can be simplified as follows:

$$k_1 r \gg 1. \tag{5.17}$$

Furthermore, all three criteria of far-field scattering (FFS) can be written as the following single inequality:

$$k_1 r \gg \max\left(1, \tfrac{1}{2}x^2\right), \tag{5.18}$$

where $x = k_1 a$ is the dimensionless so-called size parameter of the object.

5.3 Scattering dyadic and amplitude scattering matrix

Assuming that the incident field is a plane electromagnetic wave with the time-independent amplitude given by

$$\mathbf{E}^{\text{inc}}(\mathbf{r}) = \mathbf{E}_0^{\text{inc}} \exp(\mathrm{i}k_1 \hat{\mathbf{n}}^{\text{inc}} \cdot \mathbf{r}) \tag{5.19}$$

and using Eqs. (4.24) and (B.21), we have in the far-field limit:

$$\mathbf{E}^{\text{sca}}(r\hat{\mathbf{n}}^{\text{sca}}) = \frac{\exp(\mathrm{i}k_1 r)}{r} \overleftrightarrow{A}(\hat{\mathbf{n}}^{\text{sca}}, \hat{\mathbf{n}}^{\text{inc}}) \cdot \mathbf{E}_0^{\text{inc}}, \tag{5.20}$$

where $\hat{\mathbf{n}}^{\text{sca}} = \hat{\mathbf{r}}$ (see Fig. 5.3) and $\overleftrightarrow{A}$ is the so-called scattering dyadic. Although $\overleftrightarrow{A}$ depends on the incidence and scattering direction, it is independent of $\mathbf{E}_0^{\text{inc}}$. It follows from Eqs. (5.10) and (5.20) that

$$\hat{\mathbf{n}}^{\text{sca}} \cdot \overleftrightarrow{A}(\hat{\mathbf{n}}^{\text{sca}}, \hat{\mathbf{n}}^{\text{inc}}) = \mathbf{0}. \tag{5.21}$$

However, because the incident field given by Eq. (5.19) is a transverse wave with electric field vector perpendicular to the direction of propagation, the dot product $\overleftrightarrow{A}(\hat{\mathbf{n}}^{\text{sca}}, \hat{\mathbf{n}}^{\text{inc}}) \cdot \hat{\mathbf{n}}^{\text{inc}}$ is not defined by Eq. (5.20). To complete the definition, we take this product to be zero:

$$\overleftrightarrow{A}(\hat{\mathbf{n}}^{\text{sca}}, \hat{\mathbf{n}}^{\text{inc}}) \cdot \hat{\mathbf{n}}^{\text{inc}} = \mathbf{0}. \tag{5.22}$$

Therefore, the final expression for the scattering dyadic in terms of the dyadic transition operator is as follows:

$$\overleftrightarrow{A}(\hat{\mathbf{n}}^{\text{sca}}, \hat{\mathbf{n}}^{\text{inc}}) = \frac{1}{4\pi}(\overleftrightarrow{I} - \hat{\mathbf{n}}^{\text{sca}} \otimes \hat{\mathbf{n}}^{\text{sca}}) \cdot \int_{V_{\text{INT}}} \mathrm{d}^3\mathbf{r}' \exp(-\mathrm{i}k_1 \hat{\mathbf{n}}^{\text{sca}} \cdot \mathbf{r}')$$
$$\times \int_{V_{\text{INT}}} \mathrm{d}^3\mathbf{r}'' \overleftrightarrow{T}(\mathbf{r}', \mathbf{r}'') \exp(\mathrm{i}k_1 \hat{\mathbf{n}}^{\text{inc}} \cdot \mathbf{r}'') \cdot (\overleftrightarrow{I} - \hat{\mathbf{n}}^{\text{inc}} \otimes \hat{\mathbf{n}}^{\text{inc}}). \tag{5.23}$$

The reader can easily verify (cf. Problem 4.4) that the elements of the scattering dyadic have the dimension of length.

According to the above definition, the scattering dyadic describes FFS of a plane electromagnetic wave. Although this may appear to suggest that the usefulness of the scattering dyadic is rather limited, its actual range of applicability is much wider. Indeed, it follows from the preceding discussion that the quantity $\overleftrightarrow{A}(\hat{\mathbf{n}}^{\text{sca}}, \hat{\mathbf{n}}^{\text{inc}})$ can be used to compute FFS of any incident field as long as the latter is expandable in elementary plane waves.

Equations (5.21) and (5.22) show that only four out of the nine components of the scattering dyadic are independent in the spherical coordinate system centered at the origin, Fig. 5.3. It is therefore convenient to introduce the 2×2 so-called amplitude scattering matrix $\mathbf{S}$, which expresses the θ- and φ-components of the scattered spherical wave in the θ- and φ-components of the incident plane wave:

$$\mathbf{E}^{\text{sca}}(r\hat{\mathbf{n}}^{\text{sca}}) = \frac{\exp(\mathrm{i}k_1 r)}{r} \mathbf{S}(\hat{\mathbf{n}}^{\text{sca}}, \hat{\mathbf{n}}^{\text{inc}}) \mathbf{E}_0^{\text{inc}}, \tag{5.24}$$

where $\mathbf{E}$ denotes a two-component column formed by the θ- and φ-components of the electric field vector:

$$\mathbf{E} = \begin{bmatrix} E_\theta \\ E_\varphi \end{bmatrix}. \tag{5.25}$$

The elements of the amplitude scattering matrix have the dimension of length and are expressed in terms of the scattering dyadic as follows:

$$S_{11} = \hat{\boldsymbol{\theta}}^{\text{sca}} \cdot \overleftrightarrow{A} \cdot \hat{\boldsymbol{\theta}}^{\text{inc}}, \tag{5.26}$$

$$S_{12} = \hat{\boldsymbol{\theta}}^{\text{sca}} \cdot \overleftrightarrow{A} \cdot \hat{\boldsymbol{\varphi}}^{\text{inc}}, \tag{5.27}$$

$$S_{21} = \hat{\boldsymbol{\varphi}}^{\text{sca}} \cdot \overleftrightarrow{A} \cdot \hat{\boldsymbol{\theta}}^{\text{inc}}, \tag{5.28}$$

$$S_{22} = \hat{\boldsymbol{\varphi}}^{\text{sca}} \cdot \overleftrightarrow{A} \cdot \hat{\boldsymbol{\varphi}}^{\text{inc}}. \tag{5.29}$$

Besides the wave number, the amplitude scattering matrix depends on the directions of incidence and scattering, as well as on the size, morphology, composition, and orientation of the scattering object with respect to the coordinate system. It also depends on the choice of the origin of the coordinate system relative to the object. If known, the amplitude scattering matrix gives the scattered and thus the total field, thereby providing a complete description of the scattering pattern in the far zone.

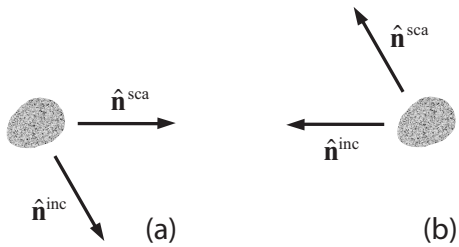

Fig. 5.6. **(a)** Direct scattering configuration. **(b)** Reciprocal scattering configuration.

Equation (5.20) describes FFS in a tensorial form independent of the orientation of the laboratory reference frame. Unlike the scattering dyadic, the elements of the amplitude scattering matrix change if the reference frame is rotated without a shift of its origin. The corresponding rotation transformation rule is derived in Section 2.4 of MTL1, assuming that the rotation is parameterized in terms of the Euler angles discussed in Appendix C.

It should be kept in mind that if a transverse wave propagates along the z-axis then the θ- and φ-components of the electric field vector are determined by the specific choice of the meridional plane. Therefore, the amplitude scattering matrix explicitly depends on φ^{inc} and φ^{sca}, even when $\theta^{\text{inc}} = 0$ or π and/or $\theta^{\text{sca}} = 0$ or π.

5.4 Reciprocity

A fundamental property of the scattering dyadic is the Saxon's reciprocity relation (Saxon 1955a):

$$\overleftrightarrow{A}(-\hat{\mathbf{n}}^{\text{inc}}, -\hat{\mathbf{n}}^{\text{sca}}) = [\overleftrightarrow{A}(\hat{\mathbf{n}}^{\text{sca}}, \hat{\mathbf{n}}^{\text{inc}})]^{\text{T}}, \tag{5.30}$$

where T denotes a transposed dyadic (see Appendix A). It is easy to see that this relation can be interpreted as follows: if the incidence and scattering directions are reversed and interchanged, then the new scattering dyadic is obtained by transposing the original scattering dyadic (Fig. 5.6). The derivation of Eq. (5.30) can be found in Section 2.3 of MTL1 or Section 3.4 of MTL2.

The reciprocity relation for the amplitude scattering matrix follows from Eqs. (5.26)–(5.30):

$$\mathbf{S}(-\hat{\mathbf{n}}^{\text{inc}}, -\hat{\mathbf{n}}^{\text{sca}}) = \begin{bmatrix} S_{11}(\hat{\mathbf{n}}^{\text{sca}}, \hat{\mathbf{n}}^{\text{inc}}) & -S_{21}(\hat{\mathbf{n}}^{\text{sca}}, \hat{\mathbf{n}}^{\text{inc}}) \\ -S_{12}(\hat{\mathbf{n}}^{\text{sca}}, \hat{\mathbf{n}}^{\text{inc}}) & S_{22}(\hat{\mathbf{n}}^{\text{sca}}, \hat{\mathbf{n}}^{\text{inc}}) \end{bmatrix} \tag{5.31}$$

(Problem 5.3). An interesting consequence of reciprocity is the so-called backscattering theorem (van de Hulst 1957), which directly follows from Eq. (5.31), after substituting $\hat{\mathbf{n}}^{\text{inc}} = \hat{\mathbf{n}}$ and $\hat{\mathbf{n}}^{\text{sca}} = -\hat{\mathbf{n}}$:

$$S_{21}(-\hat{\mathbf{n}},\hat{\mathbf{n}}) = -S_{12}(-\hat{\mathbf{n}},\hat{\mathbf{n}}). \tag{5.32}$$

Because of the universal nature of reciprocity, Eqs. (5.30)–(5.32) are important tests in computations or measurements of light scattering by small particles: violation of reciprocity means that the computations or measurements are incorrect or inaccurate. Alternatively, the use of reciprocity can substantially shorten required computer time or reduce the measurement effort because one may calculate or measure light scattering for only half of the scattering geometries and then use Eqs. (5.30) and (5.31) for the reciprocal geometries. Reciprocity also plays a fundamental role in the effect of WL of electromagnetic waves in discrete random media, discussed in Chapter 21.

Equations (5.30) and (5.31) are valid provided that the permeability, permittivity, and conductivity of the scattering object are symmetric tensors. If the scattering object and/or the surrounding medium consist of magneto-optic materials and are placed in a constant magnetic field $\boldsymbol{\mathcal{B}}$, then Eqs. (5.30) and (5.31) must be replaced by

$$\overleftrightarrow{A}(-\hat{\mathbf{n}}^{\rm inc},-\hat{\mathbf{n}}^{\rm sca};-\boldsymbol{\mathcal{B}}) = [\overleftrightarrow{A}(\hat{\mathbf{n}}^{\rm sca},\hat{\mathbf{n}}^{\rm inc};\boldsymbol{\mathcal{B}})]^{\rm T}, \tag{5.33}$$

$$\mathbf{S}(-\hat{\mathbf{n}}^{\rm inc},-\hat{\mathbf{n}}^{\rm sca};-\boldsymbol{\mathcal{B}}) = \begin{bmatrix} S_{11}(\hat{\mathbf{n}}^{\rm sca},\hat{\mathbf{n}}^{\rm inc};\boldsymbol{\mathcal{B}}) & -S_{21}(\hat{\mathbf{n}}^{\rm sca},\hat{\mathbf{n}}^{\rm inc};\boldsymbol{\mathcal{B}}) \\ -S_{12}(\hat{\mathbf{n}}^{\rm sca},\hat{\mathbf{n}}^{\rm inc};\boldsymbol{\mathcal{B}}) & S_{22}(\hat{\mathbf{n}}^{\rm sca},\hat{\mathbf{n}}^{\rm inc};\boldsymbol{\mathcal{B}}) \end{bmatrix} \tag{5.34}$$

(Dolginov *et al.* 1995).

5.5 Scale invariance rule

A fundamental property of frequency-domain electromagnetic scattering is the so-called scale invariance rule (also referred to as the principle of electromagnetic similitude). The general derivation of this rule based on the Lippmann–Schwinger equation (4.25) can be found in Section 3.5 of MTL2. In application to the scattering dyadic and the amplitude scattering matrix, the scale invariance rule implies the following. If one multiplies all linear dimensions of the scattering object by a constant factor f (thereby not changing the shape and morphology of the object and its orientation with respect to the coordinate system) and multiplies the wave number k_1 by a factor $1/f$, then the dimensionless ratios $\overleftrightarrow{A}(\hat{\mathbf{n}}^{\rm sca},\hat{\mathbf{n}}^{\rm inc})/a$ and $\mathbf{S}(\hat{\mathbf{n}}^{\rm sca},\hat{\mathbf{n}}^{\rm inc})/a$ do not change, where a is any linear dimension of the object.

In other words, the dimensionless ratios $\overleftrightarrow{A}(\hat{\mathbf{n}}^{\rm sca},\hat{\mathbf{n}}^{\rm inc})/a$ and $\mathbf{S}(\hat{\mathbf{n}}^{\rm sca},\hat{\mathbf{n}}^{\rm inc})/a$ do not change if the dimensionless product $k_1 a$, traditionally called the size parameter, remains the same. The size parameter can also be expressed in terms of the wavelength in the exterior region $\lambda_1 = 2\pi/k_1$ as $x = 2\pi a/\lambda_1$. This means that multiplying the particle size and the wavelength by the same factor f (see Fig. 5.7) does not change the dimensionless scattering characteristics $\overleftrightarrow{A}(\hat{\mathbf{n}}^{\rm sca},\hat{\mathbf{n}}^{\rm inc})/a$ and $\mathbf{S}(\hat{\mathbf{n}}^{\rm sca},\hat{\mathbf{n}}^{\rm inc})/a$.

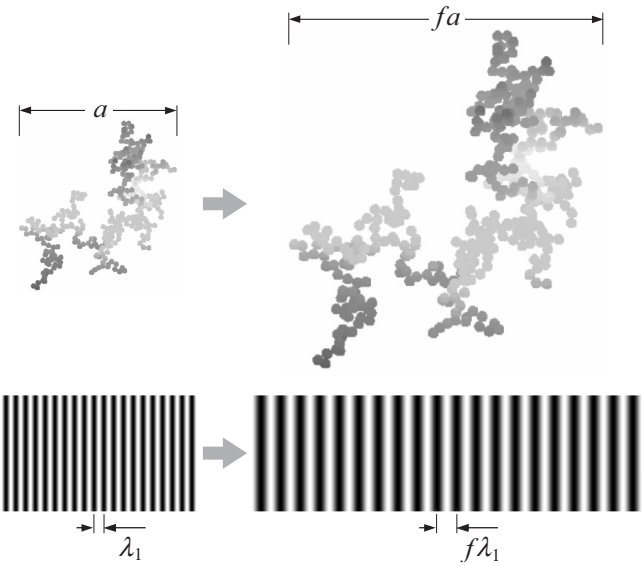

Fig. 5.7. Scale invariance rule.

The scale invariance rule can be very helpful in practice because it makes a single computation or measurement applicable to all couplets {size, wavelength} having the same ratio of size to wavelength, *provided that the relative refractive index also remains the same*. In particular, the scale invariance rule is the basic physical principle of the so-called microwave analog technique. The latter involves measurements of microwave scattering by easy-to-manufacture centimeter-sized objects followed by extrapolation to other wavelengths (e.g., visible or infrared) by keeping the ratio of size to wavelength fixed (Section 16.3.2).

Problems

5.1: Derive Eq. (5.2).

5.2: Discuss the implications of the criteria (5.12)–(5.14) for scattering objects comparable to and greater than the wavelength.

5.3: Derive Eq. (5.31).

5.4: Verify that the backscattering dyadic is symmetric:

$$\overleftrightarrow{A}(-\hat{\mathbf{n}},\hat{\mathbf{n}}) = [\overleftrightarrow{A}(-\hat{\mathbf{n}},\hat{\mathbf{n}})]^{\mathrm{T}}. \tag{5.35}$$

Notes

Until quite recently, the entire discipline of electromagnetic scattering by particles had essentially been limited to the far-field approximation (see, e.g., van de

Hulst 1957; Kerker 1969; Bohren and Huffman 1983). However, rapid advances in nanoscience and nanotechnology have resulted in the emergence of the discipline of near-field scattering (e.g., Novonty and Hecht 2012). Furthermore, the recent derivation of the century-old radiative transfer equation directly from the MMEs has revealed the RTT to be an expressly near-field theory, even though it deals with a group of particles located in the far zones of each other (Chapter 19).

6

The Foldy equations

The formalism described in Chapters 4 and 5 applies equally to a scatterer in the form of a single body and to a fixed multi-particle group. However, when the scattering object is a cluster consisting of touching and/or separated distinct components, then it is often convenient to use a modified formalism in which the total scattered field is explicitly represented as a vector superposition of the partial fields contributed by the cluster components. This approach is based on the system of integral so-called Foldy equations (FEs) which follow directly from the MMEs, automatically incorporate all boundary conditions and the radiation condition at infinity, and rigorously describe the scattered electric field at any point in space. In this chapter, we will derive both the exact form of the FEs and an approximate far-field version. The latter applies to a group of widely separated particles and offers significant simplifications essential for the development of microphysical theories of radiative transfer and WL.

6.1 Vector form of the Foldy equations

Consider electromagnetic scattering by a fixed group of N finite particles collectively occupying the interior region V_{INT}, according to Eq. (4.1). As before, we assume that the particles are imbedded in an infinite, homogeneous, linear, isotropic, and nonabsorbing medium. We begin by re-writing Eq. (4.23) as follows:

$$\mathbf{E}(\mathbf{r}) = \mathbf{E}^{\mathrm{inc}}(\mathbf{r}) + \int_{\Re^3} \mathrm{d}^3\mathbf{r}' U(\mathbf{r}') \overleftrightarrow{G}(\mathbf{r}, \mathbf{r}') \cdot \mathbf{E}(\mathbf{r}'), \quad \mathbf{r} \in \Re^3, \tag{6.1}$$

where the integration is performed over the entire space, the potential function $U(\mathbf{r})$ is given by

$$U(\mathbf{r}) = \sum_{i=1}^{N} U_i(\mathbf{r}), \quad \mathbf{r} \in \Re^3, \tag{6.2}$$

and $U_i(\mathbf{r})$ is the ith-particle potential function. The latter is given by

$$U_i(\mathbf{r}) = \begin{cases} 0, & \mathbf{r} \notin V_i, \\ k_1^2[m_i^2(\mathbf{r}) - 1], & \mathbf{r} \in V_i, \end{cases} \tag{6.3}$$

where

$$m_i(\mathbf{r}) = k_{2i}(\mathbf{r})/k_1 \tag{6.4}$$

is the refractive index of particle i relative to that of the host medium. All position vectors originate at the origin O of an arbitrarily chosen laboratory coordinate system.

We will now show that the solution of Eq. (6.1) everywhere in space can be expressed as follows:

$$\mathbf{E}(\mathbf{r}) = \mathbf{E}^{\text{inc}}(\mathbf{r}) + \sum_{i=1}^{N} \int_{V_i} \mathrm{d}^3\mathbf{r}' \overleftrightarrow{G}(\mathbf{r}, \mathbf{r}') \cdot \int_{V_i} \mathrm{d}^3\mathbf{r}'' \overleftrightarrow{T}_i(\mathbf{r}', \mathbf{r}'') \cdot \mathbf{E}_i(\mathbf{r}''), \quad \mathbf{r} \in \Re^3, \tag{6.5}$$

where the electric field $\mathbf{E}_i(\mathbf{r})$ "exciting" particle i is given by

$$\mathbf{E}_i(\mathbf{r}) = \mathbf{E}^{\text{inc}}(\mathbf{r}) + \sum_{j(\neq i)=1}^{N} \mathbf{E}_{ij}^{\text{exc}}(\mathbf{r}), \tag{6.6}$$

the $\mathbf{E}_{ij}^{\text{exc}}(\mathbf{r})$ are partial exciting fields given by

$$\mathbf{E}_{ij}^{\text{exc}}(\mathbf{r}) = \int_{V_j} \mathrm{d}^3\mathbf{r}' \overleftrightarrow{G}(\mathbf{r}, \mathbf{r}') \cdot \int_{V_j} \mathrm{d}^3\mathbf{r}'' \overleftrightarrow{T}_j(\mathbf{r}', \mathbf{r}'') \cdot \mathbf{E}_j(\mathbf{r}''), \quad \mathbf{r} \in V_i, \tag{6.7}$$

and $\overleftrightarrow{T}_i$ is the ith-particle dyadic transition operator with respect to the laboratory coordinate system and satisfies the following Lippmann–Schwinger equation:

$$\overleftrightarrow{T}_i(\mathbf{r}, \mathbf{r}') = U_i(\mathbf{r})\delta(\mathbf{r} - \mathbf{r}')\overleftrightarrow{I} + U_i(\mathbf{r}) \int_{V_i} \mathrm{d}^3\mathbf{r}'' \overleftrightarrow{G}(\mathbf{r}, \mathbf{r}'') \cdot \overleftrightarrow{T}_i(\mathbf{r}'', \mathbf{r}'), \quad \mathbf{r}, \mathbf{r}' \in V_i. \tag{6.8}$$

We first introduce the ith potential dyadic centered at the origin of the laboratory reference frame,

$$\overleftrightarrow{U}_i(\mathbf{r}, \mathbf{r}') = U_i(\mathbf{r})\delta(\mathbf{r} - \mathbf{r}')\overleftrightarrow{I}, \tag{6.9}$$

and rewrite Eqs. (6.1) and (6.5)–(6.8) in the following compact operator form:

$$E = E^{\text{inc}} + \hat{G}\hat{U}E, \tag{6.10}$$

$$E = E^{\text{inc}} + \sum_{i=1}^{N} \hat{G}\hat{T}_i E_i, \tag{6.11}$$

$$E_i = E^{\text{inc}} + \sum_{j(\neq i)=1}^{N} \hat{G}\hat{T}_j E_j, \tag{6.12}$$

$$\hat{T}_i = \hat{U}_i + \hat{U}_i \hat{G}\hat{T}_i, \tag{6.13}$$

where

$$\hat{U} = \sum_{i=1}^{N} \hat{U}_i \tag{6.14}$$

and

$$\hat{B}E = \int \mathrm{d}^3\mathbf{r}' \vec{B}(\mathbf{r}, \mathbf{r}') \cdot \mathbf{E}(\mathbf{r}'). \tag{6.15}$$

Note that the ordering of operators in Eqs. (6.10)–(6.13) is important and cannot be changed at will. Equations (6.14) and (6.13) yield

$$\begin{aligned} \hat{U}\hat{G}\hat{T}_i &= \hat{U}_i \hat{G}\hat{T}_i + \sum_{j(\neq i)=1}^{N} \hat{U}_j \hat{G}\hat{T}_i \\ &= \hat{T}_i - \hat{U}_i + \sum_{j(\neq i)=1}^{N} \hat{U}_j \hat{G}\hat{T}_i. \end{aligned} \tag{6.16}$$

Let us now evaluate the right-hand side of Eq. (6.10). Substituting sequentially Eqs. (6.11), (6.16), and (6.12) and then again Eq. (6.11) gives

$$\begin{aligned} E^{\mathrm{inc}} + \hat{G}\hat{U}E &= E^{\mathrm{inc}} + \hat{G}\hat{U}\left(E^{\mathrm{inc}} + \sum_{i=1}^{N} \hat{G}\hat{T}_i E_i \right) \\ &= E^{\mathrm{inc}} + \hat{G}\hat{U}E^{\mathrm{inc}} + \hat{G}\sum_{i=1}^{N}\left(\hat{T}_i - \hat{U}_i + \sum_{j(\neq i)=1}^{N} \hat{U}_j \hat{G}\hat{T}_i \right) E_i \\ &= E^{\mathrm{inc}} + \sum_{i=1}^{N} \hat{G}\hat{T}_i E_i + \hat{G}\hat{U}E^{\mathrm{inc}} + \hat{G}\sum_{i=1}^{N} \hat{U}_i \sum_{j(\neq i)=1}^{N} \hat{G}\hat{T}_j E_j \\ &\quad - \hat{G}\sum_{i=1}^{N} \hat{U}_i E_i \\ &= E^{\mathrm{inc}} + \sum_{i=1}^{N} \hat{G}\hat{T}_i E_i + \hat{G}\hat{U}E^{\mathrm{inc}} + \hat{G}\sum_{i=1}^{N} \hat{U}_i \left(\sum_{j(\neq i)=1}^{N} \hat{G}\hat{T}_j E_j - E_i \right) \\ &= E^{\mathrm{inc}} + \sum_{i=1}^{N} \hat{G}\hat{T}_i E_i + \hat{G}\hat{U}E^{\mathrm{inc}} - \hat{G}\sum_{i=1}^{N} \hat{U}_i E^{\mathrm{inc}} \\ &= E. \end{aligned} \tag{6.17}$$

Thus, the substitution of Eqs. (6.11)–(6.13) into the right-hand side of Eq. (6.10) yields the left-hand side, which proves that Eqs. (6.5)–(6.7) indeed give the solution of the VIE (6.1).

Equations (6.5)–(6.7) are a direct consequence of the frequency-domain MMEs and represent the full vector form of the FEs. Importantly, $\vec{T}_i$ is the dy-

adic transition operator of the ith particle in the absence of all the other particles (cf. Eqs. (4.25) and (6.8)).

6.2 Neumann expansion of the total field

The FEs (6.5)–(6.8) are mathematically equivalent to the VIE (4.23) and hardly offer computational advantages. There are three factors, however, which make them important. First, the FEs serve as a precursor to a highly efficient numerically exact technique called the superposition T-matrix method (Litvinov and Ziegler 2008). Second, they allow one to introduce the Neumann expansion of the total field playing a key role in the theories of radiative transfer and WL. Third, as will be demonstrated in the following section, they can be used to incorporate the notion of the single-particle far field in the computation of the near field of a multi-particle group.

The Neumann expansion is based on the fact that $\overleftrightarrow{T}_i$ for each i is an individual property of the ith particle computed as if this particle were alone rather than a member of the group. Indeed, iterating Eq. (6.12) yields

$$E_i = E^{\text{inc}} + \sum_{j(\neq i)=1}^{N} \hat{G}\hat{T}_j E^{\text{inc}} + \sum_{\substack{j(\neq i)=1\\ l(\neq j)=1}}^{N} \hat{G}\hat{T}_j \hat{G}\hat{T}_l E^{\text{inc}} + \sum_{\substack{j(\neq i)=1\\ l(\neq j)=1\\ m(\neq l)=1}}^{N} \hat{G}\hat{T}_j \hat{G}\hat{T}_l \hat{G}\hat{T}_m E^{\text{inc}} + \cdots, \tag{6.18}$$

whereas the substitution of Eq. (6.18) in Eq. (6.11) results in the following expansion, traditionally called in mathematics the Neumann series:

$$E = E^{\text{inc}} + E^{\text{sca}}, \tag{6.19}$$

$$E^{\text{sca}} = \sum_{i=1}^{N} \hat{G}\hat{T}_i E^{\text{inc}} + \sum_{\substack{i=1\\ j(\neq i)=1}}^{N} \hat{G}\hat{T}_i \hat{G}\hat{T}_j E^{\text{inc}} + \sum_{\substack{i=1\\ j(\neq i)=1\\ l(\neq j)=1}}^{N} \hat{G}\hat{T}_i \hat{G}\hat{T}_j \hat{G}\hat{T}_l E^{\text{inc}} + \cdots. \tag{6.20}$$

If one truly wishes to discuss electromagnetic scattering by a multi-particle group in terms of "multiple scattering," it is these latter formulas that can be interpreted, purely mathematically, as an order-of-scattering expansion of the total field. Indeed, the N dyadic transition operators $\hat{T}_i$ $(i = 1, \ldots, N)$ are independent of each other, and each of them is a unique and complete electromagnetic identifier of the corresponding particle. Therefore, the term $\hat{G}\hat{T}_i E^{\text{inc}}$ might be thought of as the partial scattered field at the observation point generated by the ith particle in response to the excitation by the incident field only, $\hat{G}\hat{T}_i \hat{G}\hat{T}_j E^{\text{inc}}$ is the partial field generated by the same particle in response to the excitation caused by the jth particle in response to the excitation by the incident field, etc. This implies that the first term on the right-hand side of Eq. (6.20) might be interpreted as the sum of all single-scattering contributions, the second term as the sum of all double-scattering contributions, etc. The first term on the right-hand side of Eq.

(6.19) represents the zeroth order of scattering, i.e., the incident field.

It is important to recognize, however, that although multiple scattering, as embodied by Eqs. (6.19) and (6.20), can be a useful mathematical abstraction, it is not a real physical phenomenon wherein the incident light is scattered sequentially by one, two, three or more particles before reaching the observation point. For example, the term $\hat{G}\hat{T}_i\hat{G}\hat{T}_j\hat{G}\hat{T}_l E^{\text{inc}}$ on the right-hand side of Eq. (6.20) cannot be interpreted by saying that "the incident wave approaches particle l, gets scattered by particle l towards particle j, approaches particle j, gets scattered by particle j towards particle i, approaches particle i, gets scattered by particle i towards the observation point, and finally arrives at the observation point." Indeed, it follows from Eqs. (6.6) and (6.7) that all mutual excitations $\mathbf{E}_{ij}(\mathbf{r})$ occur simultaneously and are not temporally discrete and ordered events. Furthermore, they are not, in general, electromagnetic waves and do not propagate in a specific direction. We can thus conclude that Eqs. (6.19) and (6.20) are nothing more than a mathematical expansion of the total field in a certain series.

Furthermore, even though we have used in this chapter the "multi-particle group" terminology, the reader can easily verify that our derivation of the FEs applies to any set of N finite, nonoverlapping volume elements with refractive indices different from that of the unbounded host medium. Therefore, the interior region V_{INT} in the FEs can be, for example, a single spheroid subdivided arbitrarily into N nonoverlapping volume elements V_i. Of course, no one would claim that a spheroid is a multiple-scattering object, which demonstrates again that the FEs and their iterative order-of-scattering solution do not describe multiple scattering as a real physical phenomenon.

To the best of the author's knowledge, the convergence of the Neumann expansion (6.19)–(6.20) has not been proven in general. As before, we will assume the convergence as a plausible mathematical hypothesis.

6.3 Far-field Foldy equations

Although the FEs can be solved numerically in order to compute the electric field scattered by a finite cluster consisting of arbitrarily positioned components, the solution becomes increasingly problematic and eventually impracticable with increasing number of cluster components and/or their sizes relative to the wavelength. To make the problem more manageable, we will often assume that:

- the particles forming the group are separated widely enough that each of them is located in the far zones of all the other particles; and
- the observation point is located in the far zone of any constituent particle (but not necessarily in the far zone of the entire group).

Although these assumptions define a rather special type of scattering object, they lead to a drastic simplification of the FEs and will eventually enable us to develop the microphysical theories of radiative transfer and WL.

Indeed, according to Eqs. (4.24), (5.11), and (6.7), the contribution of the jth particle to the field "exciting" the ith particle in Eq. (6.6) can now be represented as a simple outgoing spherical wavelet centered at the origin of particle j:

$$\mathbf{E}_{ij}^{\text{exc}}(\mathbf{r}) \approx G(r_j)\mathbf{E}_{1ij}(\hat{\mathbf{r}}_j) \tag{6.21a}$$

$$\approx \exp(-\mathrm{i}k_1\hat{\mathbf{R}}_{ij}\cdot\mathbf{R}_i)\mathbf{E}_{ij}\exp(\mathrm{i}k_1\hat{\mathbf{R}}_{ij}\cdot\mathbf{r}), \quad \mathbf{r}\in V_i. \tag{6.21b}$$

Here,

$$G(r) = \frac{\exp(\mathrm{i}k_1 r)}{r}, \tag{6.22}$$

$$\mathbf{E}_{ij} = G(R_{ij})\mathbf{E}_{1ij}(\hat{\mathbf{R}}_{ij}), \quad \mathbf{E}_{ij}\cdot\hat{\mathbf{R}}_{ij} = 0, \tag{6.23}$$

$$\hat{\mathbf{r}}_j = \frac{\mathbf{r}_j}{r_j}, \quad \hat{\mathbf{R}}_{ij} = \frac{\mathbf{R}_{ij}}{R_{ij}}, \tag{6.24}$$

$$r_j = |\mathbf{R}_{ij}+\mathbf{r}-\mathbf{R}_i| \approx R_{ij} + \hat{\mathbf{R}}_{ij}\cdot(\mathbf{r}-\mathbf{R}_i) + \frac{|\mathbf{r}-\mathbf{R}_i|^2}{2R_{ij}}, \tag{6.25}$$

and the vectors $\mathbf{r}$, $\mathbf{r}_j$, $\mathbf{R}_i$, $\mathbf{R}_j$, and $\mathbf{R}_{ij}$ are shown in Fig. 6.1a. Note that we use a lower case bold letter to denote a vector ending at an observation point, a capital bold letter to denote a vector ending at a particle origin, and a caret above a vector to denote a unit vector in the corresponding direction.

Obviously, $\mathbf{E}_{ij}$ is the partial exciting field at the origin of the ith particle (i.e., at $\mathbf{r} = \mathbf{R}_i$) generated by the jth particle. Thus, Eqs. (6.6) and (6.21b) show that each particle is excited by the incident field and the superposition of *locally plane* waves with amplitudes $\exp(-\mathrm{i}k_1\hat{\mathbf{R}}_{ij}\cdot\mathbf{R}_i)\mathbf{E}_{ij}$ and propagation directions $\hat{\mathbf{R}}_{ij}$:

$$\mathbf{E}_i(\mathbf{r}) \approx \mathbf{E}_0^{\text{inc}}\exp(\mathrm{i}k_1\hat{\mathbf{s}}\cdot\mathbf{r}) + \sum_{j(\neq i)=1}^{N}\exp(-\mathrm{i}k_1\hat{\mathbf{R}}_{ij}\cdot\mathbf{R}_i)\mathbf{E}_{ij}\exp(\mathrm{i}k_1\hat{\mathbf{R}}_{ij}\cdot\mathbf{r}), \quad \mathbf{r}\in V_i, \tag{6.26}$$

where we have assumed that the incident field is a plane electromagnetic wave given by

$$\mathbf{E}^{\text{inc}}(\mathbf{r}) = \mathbf{E}_0^{\text{inc}}\exp(\mathrm{i}k_1\hat{\mathbf{s}}\cdot\mathbf{r}), \quad \mathbf{E}_0^{\text{inc}}\cdot\hat{\mathbf{s}} = 0. \tag{6.27}$$

According to Eq. (5.20), the outgoing spherical wave contributed by the jth particle in response to a plane-wave excitation of the form $\mathbf{E}_0^{\text{inc}}\exp(\mathrm{i}k_1\hat{\mathbf{s}}\cdot\mathbf{r}_j)$ is given by $G(r_j)\overleftrightarrow{A}_j(\hat{\mathbf{r}}_j,\hat{\mathbf{s}})\cdot\mathbf{E}_0^{\text{inc}}$, where $\mathbf{r}_j$ originates at O_j and $\overleftrightarrow{A}_j(\hat{\mathbf{r}}_j,\hat{\mathbf{s}})$ is the jth particle scattering dyadic centered at O_j. To exploit this fact, we must rewrite Eq. (6.26) for particle j with respect to the jth-particle coordinate system centered at O_j, Fig. 6.1a. Taking into account that $\mathbf{r} = \mathbf{r}_j + \mathbf{R}_j$ yields

$$\mathbf{E}_j(\mathbf{r}) \approx \mathbf{E}^{\text{inc}}(\mathbf{R}_j)\exp(\mathrm{i}k_1\hat{\mathbf{s}}\cdot\mathbf{r}_j) + \sum_{l(\neq j)=1}^{N}\mathbf{E}_{jl}\exp(\mathrm{i}k_1\hat{\mathbf{R}}_{jl}\cdot\mathbf{r}_j), \quad \mathbf{r}\in V_j. \tag{6.28}$$

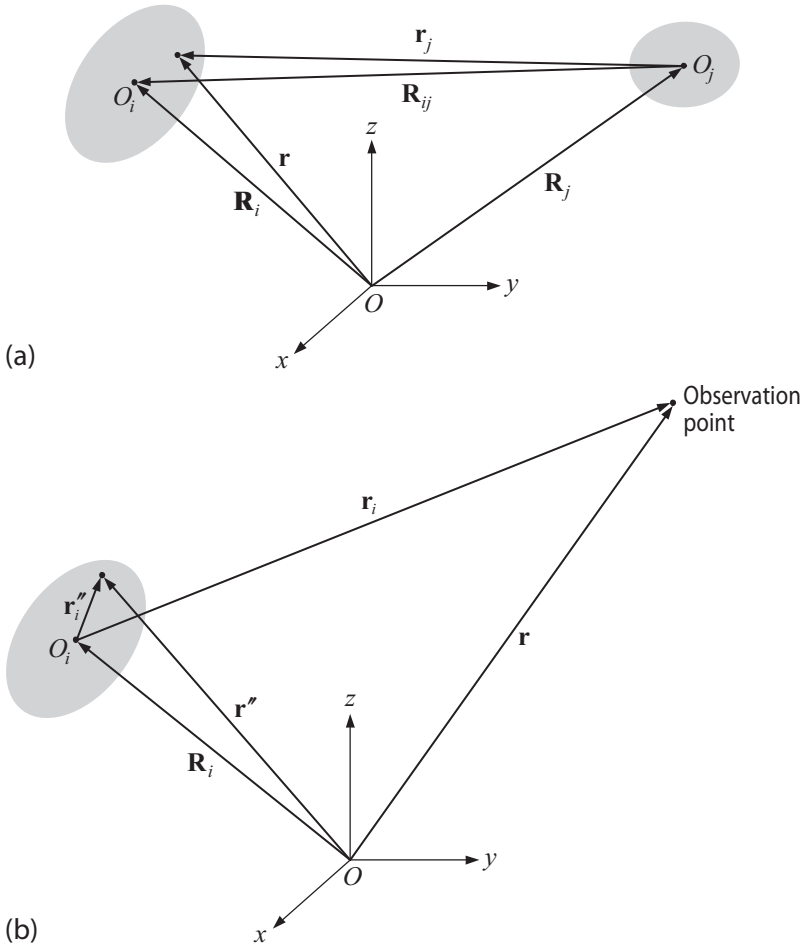

Fig. 6.1. Scattering by widely separated particles. The local origins O_i and O_j are chosen arbitrarily inside particles i and j, respectively.

The electric field at O_i generated in response to this excitation is simply

$$G(R_{ij})\left[\overleftrightarrow{A}_j(\hat{\mathbf{R}}_{ij}, \hat{\mathbf{s}}) \cdot \mathbf{E}^{\text{inc}}(\mathbf{R}_j) + \sum_{l(\neq j)=1}^{N} \overleftrightarrow{A}_j(\hat{\mathbf{R}}_{ij}, \hat{\mathbf{R}}_{jl}) \cdot \mathbf{E}_{jl}\right]. \tag{6.29}$$

Equating Eq. (6.29) with the right-hand side of Eq. (6.21b) evaluated for $\mathbf{r} = \mathbf{R}_i$ finally yields a system of linear algebraic equations for determining the partial exciting fields $\mathbf{E}_{ij}$:

$$\mathbf{E}_{ij} = G(R_{ij})\overleftrightarrow{A}_j(\hat{\mathbf{R}}_{ij}, \hat{\mathbf{s}}) \cdot \mathbf{E}^{\text{inc}}(\mathbf{R}_j) + G(R_{ij}) \sum_{l(\neq j)=1}^{N} \overleftrightarrow{A}_j(\hat{\mathbf{R}}_{ij}, \hat{\mathbf{R}}_{jl}) \cdot \mathbf{E}_{jl}, \tag{6.30}$$

$$i, j = 1, \ldots, N, \quad j \neq i.$$

This system is much simpler than the original system of integral equations (6.6)–(6.7) and can be solved readily on a computer, provided that N is not too large.

After the system (6.30) has been solved, one can find the electric field exciting each particle and the total field. Indeed, Eq. (6.26) gives, for a point $\mathbf{r}'' \in V_i$:

$$\mathbf{E}_i(\mathbf{r}'') \approx \mathbf{E}^{\text{inc}}(\mathbf{R}_i)\exp(\mathrm{i}k_1\hat{\mathbf{s}}\cdot\mathbf{r}_i'') + \sum_{j(\neq i)=1}^{N}\mathbf{E}_{ij}\exp(\mathrm{i}k_1\hat{\mathbf{R}}_{ij}\cdot\mathbf{r}_i'') \tag{6.31}$$

(see Fig. 6.1b), which is a vector superposition of plane waves. Substituting $\mathbf{r}_i'' = \mathbf{0}$ in Eq. (6.31) gives a simple formula for the exciting field at the origin of particle i:

$$\mathbf{E}_i(\mathbf{R}_i) = \mathbf{E}^{\text{inc}}(\mathbf{R}_i) + \sum_{j(\neq i)=1}^{N}\mathbf{E}_{ij}. \tag{6.32}$$

Finally, substituting Eq. (6.31) in Eq. (6.5) and recalling the mathematical form of the far-field response of a particle to a plane-wave excitation, we derive for the total electric field:

$$\mathbf{E}(\mathbf{r}) = \mathbf{E}^{\text{inc}}(\mathbf{r}) + \sum_{i=1}^{N}G(r_i)\overleftrightarrow{A}_i(\hat{\mathbf{r}}_i,\hat{\mathbf{s}})\cdot\mathbf{E}^{\text{inc}}(\mathbf{R}_i) + \sum_{i=1}^{N}G(r_i)\sum_{j(\neq i)=1}^{N}\overleftrightarrow{A}_i(\hat{\mathbf{r}}_i,\hat{\mathbf{R}}_{ij})\cdot\mathbf{E}_{ij}, \tag{6.33}$$

where the observation point $\mathbf{r}$, Fig. 6.1b, is assumed to be in the far zone of any particle forming the group.

Equation (6.33) can also be re-written as follows:

$$\mathbf{E}(\mathbf{r}) = \mathbf{E}^{\text{inc}}(\mathbf{r}) + \mathbf{E}^{\text{sca}}(\mathbf{r}), \tag{6.34}$$

where

$$\mathbf{E}^{\text{sca}}(\mathbf{r}) = \sum_{i=1}^{N}\mathbf{E}_i^{\text{sca}}(\mathbf{r}), \tag{6.35}$$

$$\mathbf{E}_i^{\text{sca}}(\mathbf{r}) = G(r_i)\left[\overleftrightarrow{A}_i(\hat{\mathbf{r}}_i,\hat{\mathbf{s}})\cdot\mathbf{E}^{\text{inc}}(\mathbf{R}_i) + \sum_{j(\neq i)=1}^{N}\overleftrightarrow{A}_i(\hat{\mathbf{r}}_i,\hat{\mathbf{R}}_{ij})\cdot\mathbf{E}_{ij}\right]. \tag{6.36}$$

These formulas show that the total field at any observation point located sufficiently far from any particle in the sparse multi-particle group is the superposition of the incident plane wave and N partial spherical wavelets contributed by the N particles. The observation point is not required to be in the far zone of the entire group. It can be anywhere in space (e.g., between particles i and j in Fig. 6.1a) as long as it is in the far zones of all the particles forming the group.

Even though each component of the scattered field (6.35) is a transverse electromagnetic wave, the scattered field itself is not, in general, a transverse electromagnetic wave. This is not surprising, since Eqs. (6.34) and (6.35) describe the near field of the multi-particle group despite the underlying assumption that the

observation point is located in the far zone of any constituent particle. The scattered field (6.35) becomes a transverse electromagnetic wave only if the observation point is located in the far zone of the entire group, as defined by the criteria (5.12)–(5.14).

6.4 Far-field Neumann expansion of the total field

Let us now rewrite Eqs. (6.33) and (6.30) in a compact symbolic form:

$$\mathbf{E} = \mathbf{E}^{\text{inc}} + \sum_{i=1}^{N} \overleftrightarrow{B}_{ri0} \cdot \mathbf{E}_i^{\text{inc}} + \sum_{i=1}^{N} \sum_{j(\neq i)=1}^{N} \overleftrightarrow{B}_{rij} \cdot \mathbf{E}_{ij}, \tag{6.37}$$

$$\mathbf{E}_{ij} = \overleftrightarrow{B}_{ij0} \cdot \mathbf{E}_j^{\text{inc}} + \sum_{l(\neq j)=1}^{N} \overleftrightarrow{B}_{ijl} \cdot \mathbf{E}_{jl}, \tag{6.38}$$

where

$$\mathbf{E} = \mathbf{E}(\mathbf{r}), \tag{6.39}$$

$$\mathbf{E}^{\text{inc}} = \mathbf{E}^{\text{inc}}(\mathbf{r}), \tag{6.40}$$

$$\mathbf{E}_i^{\text{inc}} = \mathbf{E}^{\text{inc}}(\mathbf{R}_i), \tag{6.41}$$

$$\overleftrightarrow{B}_{ri0} = G(r_i)\overleftrightarrow{A}_i(\hat{\mathbf{r}}_i, \hat{\mathbf{s}}), \tag{6.42}$$

$$\overleftrightarrow{B}_{rij} = G(r_i)\overleftrightarrow{A}_i(\hat{\mathbf{r}}_i, \hat{\mathbf{R}}_{ij}), \tag{6.43}$$

$$\overleftrightarrow{B}_{ij0} = G(R_{ij})\overleftrightarrow{A}_j(\hat{\mathbf{R}}_{ij}, \hat{\mathbf{s}}), \tag{6.44}$$

$$\overleftrightarrow{B}_{ijl} = G(R_{ij})\overleftrightarrow{A}_j(\hat{\mathbf{R}}_{ij}, \hat{\mathbf{R}}_{jl}). \tag{6.45}$$

Iterating Eq. (6.38) yields

$$\mathbf{E}_{ij} = \overleftrightarrow{B}_{ij0} \cdot \mathbf{E}_j^{\text{inc}} + \sum_{l(\neq j)=1}^{N} \overleftrightarrow{B}_{ijl} \cdot \overleftrightarrow{B}_{jl0} \cdot \mathbf{E}_l^{\text{inc}} + \sum_{l(\neq j)=1}^{N} \sum_{m(\neq l)=1}^{N} \overleftrightarrow{B}_{ijl} \cdot \overleftrightarrow{B}_{jlm} \cdot \overleftrightarrow{B}_{lm0} \cdot \mathbf{E}_m^{\text{inc}}$$
$$+ \sum_{l(\neq j)=1}^{N} \sum_{m(\neq l)=1}^{N} \sum_{n(\neq m)=1}^{N} \overleftrightarrow{B}_{ijl} \cdot \overleftrightarrow{B}_{jlm} \cdot \overleftrightarrow{B}_{lmn} \cdot \overleftrightarrow{B}_{mn0} \cdot \mathbf{E}_n^{\text{inc}} + \cdots, \tag{6.46}$$

whereas the substitution of Eq. (6.46) in Eq. (6.37) gives the far-field Neumann expansion of the total electric field:

$$\mathbf{E} = \mathbf{E}^{\text{inc}} + \mathbf{E}^{\text{sca}}, \tag{6.47}$$

where

$$\mathbf{E}^{\text{sca}} = \sum_{i=1}^{N} \overleftrightarrow{B}_{ri0} \cdot \mathbf{E}_i^{\text{inc}} + \sum_{i=1}^{N} \sum_{j(\neq i)=1}^{N} \overleftrightarrow{B}_{rij} \cdot \overleftrightarrow{B}_{ij0} \cdot \mathbf{E}_j^{\text{inc}}$$

$$+\sum_{i=1}^{N}\sum_{j(\neq i)=1}^{N}\sum_{l(\neq j)=1}^{N}\vec{\vec{B}}_{rij}\cdot\vec{\vec{B}}_{ijl}\cdot\vec{\vec{B}}_{jl0}\cdot\mathbf{E}_l^{\text{inc}}$$

$$+\sum_{i=1}^{N}\sum_{j(\neq i)=1}^{N}\sum_{l(\neq j)=1}^{N}\sum_{m(\neq l)=1}^{N}\vec{\vec{B}}_{rij}\cdot\vec{\vec{B}}_{ijl}\cdot\vec{\vec{B}}_{jlm}\cdot\vec{\vec{B}}_{lm0}\cdot\mathbf{E}_m^{\text{inc}}+\cdots. \tag{6.48}$$

The last two formulas represent the starting point in the development of the microphysical theories of radiative transfer and WL.

Problems

6.1: What are the formal conditions of applicability of Eqs. (6.21a) and (6.21b)?

6.2: What are the formal conditions of applicability of Eq. (6.33)?

Notes and further reading

A simplified version of Eqs. (6.5)–(6.7) was proposed phenomenologically by Leslie Foldy (László Földi, 1919–2001) to describe acoustic scattering by a system of isotropically scattering centers (Foldy 1945). Various applications of Foldy's approach were discussed by Lax (1951). A rigorous derivation of the quantum-mechanical version of these equations from the Schrödinger equation was given by Kenneth M. Watson (born in 1921) (see Watson (1953) as well as Section 11.3 of Goldberger and Watson (1964)). The case of electromagnetic scattering by a group of widely separated electrons was considered by Watson (1969). The general electromagnetic FEs in the form of Eqs. (6.5)–(6.7) were derived by Prishivalko *et al.* (1984), using Watson's approach.

The Neumann expansion (also known as the Liouville–Neumann or Liouville–Neumann–Volterra series) was introduced by the French mathematician Joseph Liouville (1809–82) in 1837 and by the German mathematician Carl Gottfried Neumann (1832–1925) 30 years later. The Italian mathematician Vito Volterra (1860–1940) used this expansion in his general theory of integral equations as a technique for solving Fredholm and Volterra integral equations of the second kind. The unknown function is expanded in a power series in terms of so-called iterated kernels. The method is applicable whenever the series converges (see Chapter 3 of Yosida (1960) and Section 16.3 of Arfken and Weber (2005) for further details).

7

The Stokes parameters

Because of the high frequency of time-harmonic oscillations, traditional optical instruments cannot measure the instantaneous electric and magnetic vectors associated with an electromagnetic field. Furthermore, they cannot measure time averages of linear combinations of the electric and magnetic field vectors because accumulating and averaging a signal proportional to $\mathcal{E}(\mathbf{r},t)$ or $\mathcal{H}(\mathbf{r},t)$ over a time interval long compared with the period of time-harmonic oscillations would yield a zero net result:

$$\begin{aligned} \frac{1}{T}\int_{t-T/2}^{t+T/2} \mathrm{d}t' \sin\omega t' &\underset{T\gg 2\pi/\omega}{=} 0, \\ \frac{1}{T}\int_{t-T/2}^{t+T/2} \mathrm{d}t' \cos\omega t' &\underset{T\gg 2\pi/\omega}{=} 0. \end{aligned} \tag{7.1}$$

Therefore, the majority of optical instruments measure quantities that have the dimension of energy flux, are bilinear/quadratic forms in the electric and/or magnetic field vector components, and involve terms proportional to either $\sin^2\omega t$ or $\cos^2\omega t$. In the framework of the frequency-domain formalism, all these quantities are defined in such a way that the time-harmonic factor $\exp(-\mathrm{i}\omega t)$ vanishes upon multiplication by its complex-conjugate value: $\exp(-\mathrm{i}\omega t)[\exp(-\mathrm{i}\omega t)]^* \equiv 1$. This implies that in order to make the theory of electromagnetic scattering applicable to analyses of actual optical observations, the scattering phenomenon must be characterized in terms of appropriately defined derivative quantities that can be measured directly. It is, thus, clear that the concept of an actual *observable* must be central to the discipline of light scattering by particles and particle groups.

We have seen in Section 2.4 that an important vectorial characteristic of the electromagnetic field at a point in space is the Poynting vector (2.50). However, this is not the only quantity that has the dimension of energy flux, which implies that the Poynting vector does not carry all the information about the electromag-

netic field that can potentially be measured with an optical instrument. For example, it is easy to see from Eq. (3.20) that two plane electromagnetic waves with different complex vectors $\mathbf{E}_0'$ and $\mathbf{E}_0''$ can have identical Poynting vectors provided that $|\mathbf{E}_0'| = |\mathbf{E}_0''|$. The measurement of the Poynting vector would not discriminate between these two waves, whereas the measurement of a quadratic form in the electric and/or magnetic field vector components other than $\mathbf{E}_0 \cdot \mathbf{E}_0^*$ could.

We will see in the following chapters that as far as an actual optical measurement is concerned, a more general and useful characteristic of an arbitrary electromagnetic field is the so-called Poynting–Stokes tensor (PST), defined as $\ddot{\mathcal{P}}(\mathbf{r},t) = \boldsymbol{\mathcal{E}}(\mathbf{r},t) \otimes \boldsymbol{\mathcal{H}}(\mathbf{r},t)$. In this chapter, we will discuss an important particular case of the PST formalism which dates back to Sir George Gabriel Stokes. He proposed the use of four real-valued quantities that have the dimension of monochromatic energy flux and fully characterize a *transverse* electromagnetic wave inasmuch as it is subject to practical optical analysis. These quantities, traditionally referred to as the Stokes parameters, form the four-component so-called Stokes column vector and carry information about both the intensity and the polarization state of the wave.

In this chapter we will define the Stokes parameters of a plane or spherical wave propagating in a homogeneous nonabsorbing medium and explain their so-called ellipsometric content.

7.1 The Stokes parameters of a plane electromagnetic wave

To define the Stokes parameters, we use polar spherical coordinates associated with the local right-handed Cartesian coordinate system having its origin at the observation point, as shown in Fig. 7.1. Assuming that the medium is homogeneous and lossless, we specify the direction of propagation of a plane electromagnetic wave by a unit vector $\hat{\mathbf{n}}$ or, equivalently, by a couplet $\{\theta, \varphi\}$, where, as before, $\theta \in [0, \pi]$ is the polar (zenith) angle measured from the positive z-axis and $\varphi \in [0, 2\pi)$ is the azimuth angle measured from the positive x-axis in the clockwise direction when looking in the direction of the positive z-axis. Since the component of the electric field vector along the direction of propagation $\hat{\mathbf{n}}$ is equal to zero, the electric field at the observation point can be expressed as $\widetilde{\boldsymbol{\mathcal{E}}} = \widetilde{\boldsymbol{\mathcal{E}}}_\theta + \widetilde{\boldsymbol{\mathcal{E}}}_\varphi$, where $\widetilde{\boldsymbol{\mathcal{E}}}_\theta$ and $\widetilde{\boldsymbol{\mathcal{E}}}_\varphi$ are the θ- and φ-components of the electric field vector, respectively. The component $\widetilde{\boldsymbol{\mathcal{E}}}_\theta = \widetilde{\mathcal{E}}_\theta \hat{\boldsymbol{\theta}}$ lies in the meridional plane (i.e., the plane through $\hat{\mathbf{n}}$ and the z-axis), whereas the component $\widetilde{\boldsymbol{\mathcal{E}}}_\varphi = \widetilde{\mathcal{E}}_\varphi \hat{\boldsymbol{\varphi}}$ is perpendicular to this plane.[1] The $\hat{\boldsymbol{\theta}}$ and $\hat{\boldsymbol{\varphi}}$ are the corresponding unit vectors such that $\hat{\mathbf{n}} = \hat{\boldsymbol{\theta}} \times \hat{\boldsymbol{\varphi}}$. The magnetic field can be decomposed similarly.

[1] In the microwave remote-sensing literature, $\widetilde{\boldsymbol{\mathcal{E}}}_\theta$ and $\widetilde{\boldsymbol{\mathcal{E}}}_\varphi$ are often denoted as $\widetilde{\boldsymbol{\mathcal{E}}}_\mathrm{v}$ and $\widetilde{\boldsymbol{\mathcal{E}}}_\mathrm{h}$ and called the vertical and horizontal electric field vector components, respectively (e.g., Ulaby and Elachi 1990; Tsang *et al.* 2000).

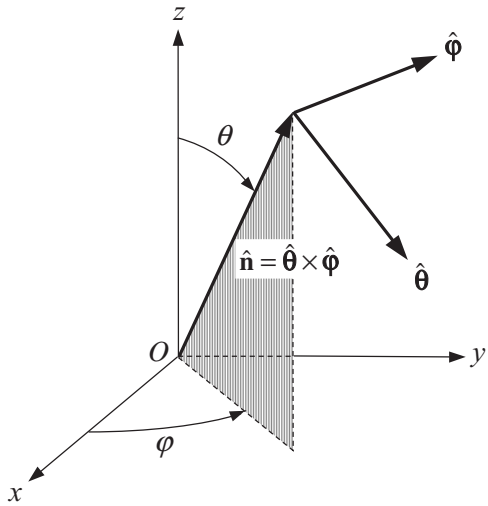

Fig. 7.1. Local coordinate system used to describe the direction of propagation and the polarization state of a plane electromagnetic wave at the observation point O.

The specification of a unit vector $\hat{\mathbf{n}}$ uniquely determines the meridional plane of the propagation direction, except when $\hat{\mathbf{n}}$ is oriented along the positive or negative direction of the z-axis. Although it may seem redundant to specify φ in addition to θ when $\theta = 0$ or π, the unit vectors $\hat{\boldsymbol{\theta}}$ and $\hat{\boldsymbol{\varphi}}$ and thus the electric field vector components $\widetilde{\boldsymbol{\mathcal{E}}}_\theta$ and $\widetilde{\boldsymbol{\mathcal{E}}}_\varphi$ still depend on the implicit orientation of the meridional plane. Therefore, we will always assume that the specification of $\hat{\mathbf{n}}$ implicitly includes the specification of the appropriate meridional plane in cases when $\hat{\mathbf{n}}$ is parallel to the z-axis. To minimize confusion, we will often specify explicitly the direction of propagation using the angles θ and φ; the latter uniquely defines the meridional plane when $\theta = 0$ or π.

Consider a plane electromagnetic wave propagating in a homogeneous medium without dispersion and losses and given by

$$\widetilde{\boldsymbol{\mathcal{E}}}(\mathbf{r}, t) = \mathbf{E}_0 \exp(\mathrm{i}k\hat{\mathbf{n}} \cdot \mathbf{r} - \mathrm{i}\omega t) \tag{7.2}$$

with a real-valued wave number k. The magnetic field is then given by $\widetilde{\boldsymbol{\mathcal{H}}}(\mathbf{r}, t) = (\epsilon/\mu)^{1/2}\, \hat{\mathbf{n}} \times \widetilde{\boldsymbol{\mathcal{E}}}(\mathbf{r}, t)$, which implies that $\widetilde{\mathcal{H}}_\theta(\mathbf{r}, t) = -(\epsilon/\mu)^{1/2}\, \widetilde{\mathcal{E}}_\varphi(\mathbf{r}, t)$ and $\widetilde{\mathcal{H}}_\varphi(\mathbf{r}, t) = (\epsilon/\mu)^{1/2}\, \widetilde{\mathcal{E}}_\theta(\mathbf{r}, t)$. Therefore, a simple complete set of linearly independent quadratic combinations of field components with nonzero time averages can consist of the following four quantities:

$$\widetilde{\mathcal{E}}_\theta(\mathbf{r}, t)[\widetilde{\mathcal{E}}_\theta(\mathbf{r}, t)]^* = E_{0\theta} E_{0\theta}^*, \quad \widetilde{\mathcal{E}}_\theta(\mathbf{r}, t)[\widetilde{\mathcal{E}}_\varphi(\mathbf{r}, t)]^* = E_{0\theta} E_{0\varphi}^*,$$
$$\widetilde{\mathcal{E}}_\varphi(\mathbf{r}, t)[\widetilde{\mathcal{E}}_\theta(\mathbf{r}, t)]^* = E_{0\varphi} E_{0\theta}^*, \quad \widetilde{\mathcal{E}}_\varphi(\mathbf{r}, t)[\widetilde{\mathcal{E}}_\varphi(\mathbf{r}, t)]^* = E_{0\varphi} E_{0\varphi}^*.$$

Furthermore, the products of these quantities and $\frac{1}{2}(\epsilon/\mu)^{1/2}$ have the requisite dimension of monochromatic energy flux. It is, therefore, natural to define the Stokes parameters using these products as building blocks.

Specifically, the real-valued Stokes parameters I, Q, U, and V are defined as the elements of a 4×1 Stokes column vector $\mathbf{I}$, as follows (MTL1, MTL2):

$$\mathbf{I} = \begin{bmatrix} I \\ Q \\ U \\ V \end{bmatrix} = \frac{1}{2}\sqrt{\frac{\epsilon}{\mu}} \begin{bmatrix} E_{0\theta}E_{0\theta}^* + E_{0\varphi}E_{0\varphi}^* \\ E_{0\theta}E_{0\theta}^* - E_{0\varphi}E_{0\varphi}^* \\ -E_{0\theta}E_{0\varphi}^* - E_{0\varphi}E_{0\theta}^* \\ \mathrm{i}(E_{0\varphi}E_{0\theta}^* - E_{0\theta}E_{0\varphi}^*) \end{bmatrix} = \frac{1}{2}\sqrt{\frac{\epsilon}{\mu}} \begin{bmatrix} E_{0\theta}E_{0\theta}^* + E_{0\varphi}E_{0\varphi}^* \\ E_{0\theta}E_{0\theta}^* - E_{0\varphi}E_{0\varphi}^* \\ -2\,\mathrm{Re}(E_{0\theta}E_{0\varphi}^*) \\ 2\,\mathrm{Im}(E_{0\theta}E_{0\varphi}^*) \end{bmatrix}. \tag{7.3}$$

Obviously, $I \geq 0$. By virtue of being real-valued and having the dimension of energy flux, the Stokes parameters form a complete set of quantities needed to characterize a plane electromagnetic wave, inasmuch as it is subject to actual optical analysis. This means that:

- Any other observable quantity is a linear combination of the four Stokes parameters.
- It is impossible to distinguish between two plane waves with the same values of the Stokes parameters and the same angular frequencies using a traditional optical device (the so-called principle of optical equivalence).

Indeed, the two complex amplitudes $E_{0\theta} = a_\theta \exp(\mathrm{i}\Delta_\theta)$ and $E_{0\varphi} = a_\varphi \exp(\mathrm{i}\Delta_\varphi)$ are characterized by four real numbers: the nonnegative amplitudes a_θ and a_φ and the phases Δ_θ and $\Delta_\varphi = \Delta_\theta - \Delta$. The Stokes parameters carry information about the amplitudes and the phase difference Δ, but not about Δ_θ. The latter is the only quantity that could be used to distinguish different waves with the same a_θ, a_φ, and Δ (and thus the same Stokes parameters), but it vanishes when a field vector component is multiplied by the complex conjugate value of the same or another field vector component.

Despite some differences in notation, our definition of the Stokes parameters (7.3) is consistent mathematically with that in Chandrasekhar (1950), van de Hulst (1957), Hansen and Travis (1974), Bohren and Huffman (1983), Kokhanovsky (2003), Hovenier *et al.* (2004), Doicu *et al.* (2006), and Borghese *et al.* (2007). The conventional definition of the Stokes parameter U in the microwave remote-sensing literature differs from ours by a minus sign (e.g., Tsang *et al.* 1985, 2000; Ulaby and Elachi 1990; Mätzler 2006; Cloude 2010).

The first Stokes parameter, I, is the intensity introduced in Section 3.1, with the explicit definition here applicable to a nonabsorbing homogeneous medium. The Stokes parameters Q, U, and V describe the polarization state of the wave, as will be discussed Section 7.3. It is easy to verify (see Problem 7.1) that the Stokes parameters of a plane monochromatic wave are not completely independent, but rather are related by the quadratic so-called Stokes identity

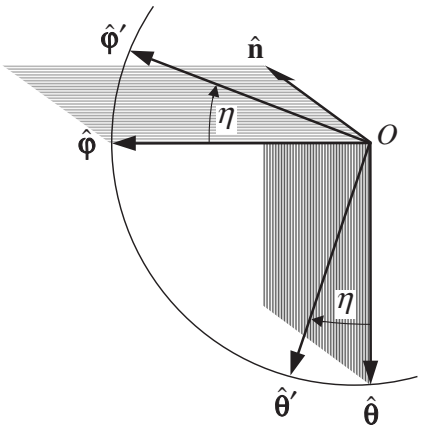

Fig. 7.2. Rotation of the θ- and φ-axes through an angle $\eta \geq 0$ around $\hat{\mathbf{n}}$ in the clockwise direction when looking in the direction of propagation.

$$I^2 = Q^2 + U^2 + V^2. \tag{7.4}$$

We will see in the following chapter, however, that this identity may not hold for a polychromatic beam of light.

7.2 Rotation transformation rule for the Stokes parameters

It is important to recognize that the Stokes parameters of a plane electromagnetic wave are always defined with respect to a specific reference plane containing the direction of wave propagation. If the reference plane is rotated about the direction of propagation then the Stokes parameters are modified according to a rotation transformation rule, which can be derived as follows. Consider a rotation of the coordinate axes θ and φ through an angle $0 \leq \eta < 2\pi$ in the *clockwise* direction, when looking in the direction of propagation (Fig. 7.2). The transformation rule for the rotation of a two-dimensional coordinate system yields the following transformation rule for the electric field vector components:

$$E'_{0\theta} = E_{0\theta} \cos\eta + E_{0\varphi} \sin\eta, \tag{7.5}$$

$$E'_{0\varphi} = -E_{0\theta} \sin\eta + E_{0\varphi} \cos\eta, \tag{7.6}$$

where the primes denote the vector components with respect to the new reference frame. It then follows from Eq. (7.3) that the rotation transformation rule for the Stokes column vector is

$$\mathbf{I}' = \mathbf{L}(\eta)\mathbf{I}, \tag{7.7}$$

where

$$\mathbf{L}(\eta) = \begin{bmatrix} 1 & 0 & 0 & 0 \\ 0 & \cos 2\eta & -\sin 2\eta & 0 \\ 0 & \sin 2\eta & \cos 2\eta & 0 \\ 0 & 0 & 0 & 1 \end{bmatrix} \tag{7.8}$$

is the so-called Stokes rotation matrix for angle η. It is easy to verify that an $\eta = \pi$ rotation does not change the Stokes parameters.

7.3 Ellipsometric content of the Stokes parameters

Writing, as before,

$$E_{0\theta} = a_\theta \exp(\mathrm{i}\Delta_\theta), \tag{7.9}$$

$$E_{0\varphi} = a_\varphi \exp(\mathrm{i}\Delta_\varphi) \tag{7.10}$$

with real nonnegative amplitudes a_θ and a_φ and real phases Δ_θ and Δ_φ, as well as recalling the definition (7.3), we obtain for the Stokes parameters

$$I = \frac{1}{2}\sqrt{\frac{\epsilon}{\mu}}\,(a_\theta^2 + a_\varphi^2), \tag{7.11}$$

$$Q = \frac{1}{2}\sqrt{\frac{\epsilon}{\mu}}\,(a_\theta^2 - a_\varphi^2), \tag{7.12}$$

$$U = -\sqrt{\frac{\epsilon}{\mu}}\,a_\theta a_\varphi \cos\Delta, \tag{7.13}$$

$$V = \sqrt{\frac{\epsilon}{\mu}}\,a_\theta a_\varphi \sin\Delta, \tag{7.14}$$

where

$$\Delta = \Delta_\theta - \Delta_\varphi. \tag{7.15}$$

Substituting Eqs. (7.9) and (7.10) in Eqs. (2.21) and (7.2), we derive for the real electric-field vector components:

$$\mathcal{E}_\theta(\mathbf{r}, t) = a_\theta \cos(\delta_\theta - \omega t), \tag{7.16}$$

$$\mathcal{E}_\varphi(\mathbf{r}, t) = a_\varphi \cos(\delta_\varphi - \omega t), \tag{7.17}$$

where

$$\delta_\theta = \Delta_\theta + k\hat{\mathbf{n}} \cdot \mathbf{r}, \tag{7.18}$$

$$\delta_\varphi = \Delta_\varphi + k\hat{\mathbf{n}} \cdot \mathbf{r}. \tag{7.19}$$

At any fixed point O in space, the endpoint of the real electric field vector given by Eqs. (7.16)–(7.19) describes an ellipse with specific major and minor axes and orientation (see Fig. 7.3a). The major axis of the ellipse makes an angle ζ with the positive direction of the φ-axis such that $\zeta \in [0, \pi)$. By definition, this orientation angle is obtained by rotating the φ-axis in the *clockwise* direction when looking in the direction of propagation, until it is directed along the major axis of the ellipse. The ellipticity is defined as the ratio of the minor to the major axes of the ellipse and is usually expressed as $|\tan\beta|$, where $\beta \in [-\pi/4, \pi/4]$. By definition, β is positive when the real electric field vector at O rotates clockwise, as viewed by an observer looking in the direction of propagation (Fig. 7.3a). The polarization for positive β is called right-handed, as opposed to the left-handed polarization corresponding to the anti-clockwise rotation of the electric field vector.

To express the orientation ζ of the ellipse and the ellipticity $|\tan\beta|$ in terms of the Stokes parameters, we first write the equations representing the rotation of the real electric field vector at O in the form

$$\mathcal{E}_q(\mathbf{r}, t) = a \sin\beta \sin(\delta - \omega t), \tag{7.20}$$

$$\mathcal{E}_p(\mathbf{r}, t) = a \cos\beta \cos(\delta - \omega t), \tag{7.21}$$

where $\mathcal{E}_p$ and $\mathcal{E}_q$ are the electric field vector components along the major and minor axes of the ellipse, respectively, Fig. 7.3a. One easily verifies that a positive (negative) β indeed corresponds to the right-handed (left-handed) polarization. The connection between Eqs. (7.16)–(7.19) and Eqs. (7.20)–(7.21) can be established by using the simple transformation rule for rotation of a two-dimensional coordinate system:

$$\mathcal{E}_\theta(\mathbf{r}, t) = -\mathcal{E}_q(\mathbf{r}, t) \cos\zeta + \mathcal{E}_p(\mathbf{r}, t) \sin\zeta, \tag{7.22}$$

$$\mathcal{E}_\varphi(\mathbf{r}, t) = -\mathcal{E}_q(\mathbf{r}, t) \sin\zeta - \mathcal{E}_p(\mathbf{r}, t) \cos\zeta. \tag{7.23}$$

By equating the coefficients of $\cos\omega t$ and $\sin\omega t$ in the expanded Eqs. (7.16) and (7.17) with those in Eqs. (7.22) and (7.23), we obtain

$$a_\theta \cos\delta_\theta = -a \sin\beta \sin\delta \cos\zeta + a \cos\beta \cos\delta \sin\zeta, \tag{7.24}$$

$$a_\theta \sin\delta_\theta = a \sin\beta \cos\delta \cos\zeta + a \cos\beta \sin\delta \sin\zeta, \tag{7.25}$$

$$a_\varphi \cos\delta_\varphi = -a \sin\beta \sin\delta \sin\zeta - a \cos\beta \cos\delta \cos\zeta, \tag{7.26}$$

$$a_\varphi \sin\delta_\varphi = a \sin\beta \cos\delta \sin\zeta - a \cos\beta \sin\delta \cos\zeta. \tag{7.27}$$

Squaring and adding Eqs. (7.24) and (7.25) as well as Eqs. (7.26) and (7.27) gives

$$a_\theta^2 = a^2(\sin^2\beta \cos^2\zeta + \cos^2\beta \sin^2\zeta), \tag{7.28}$$

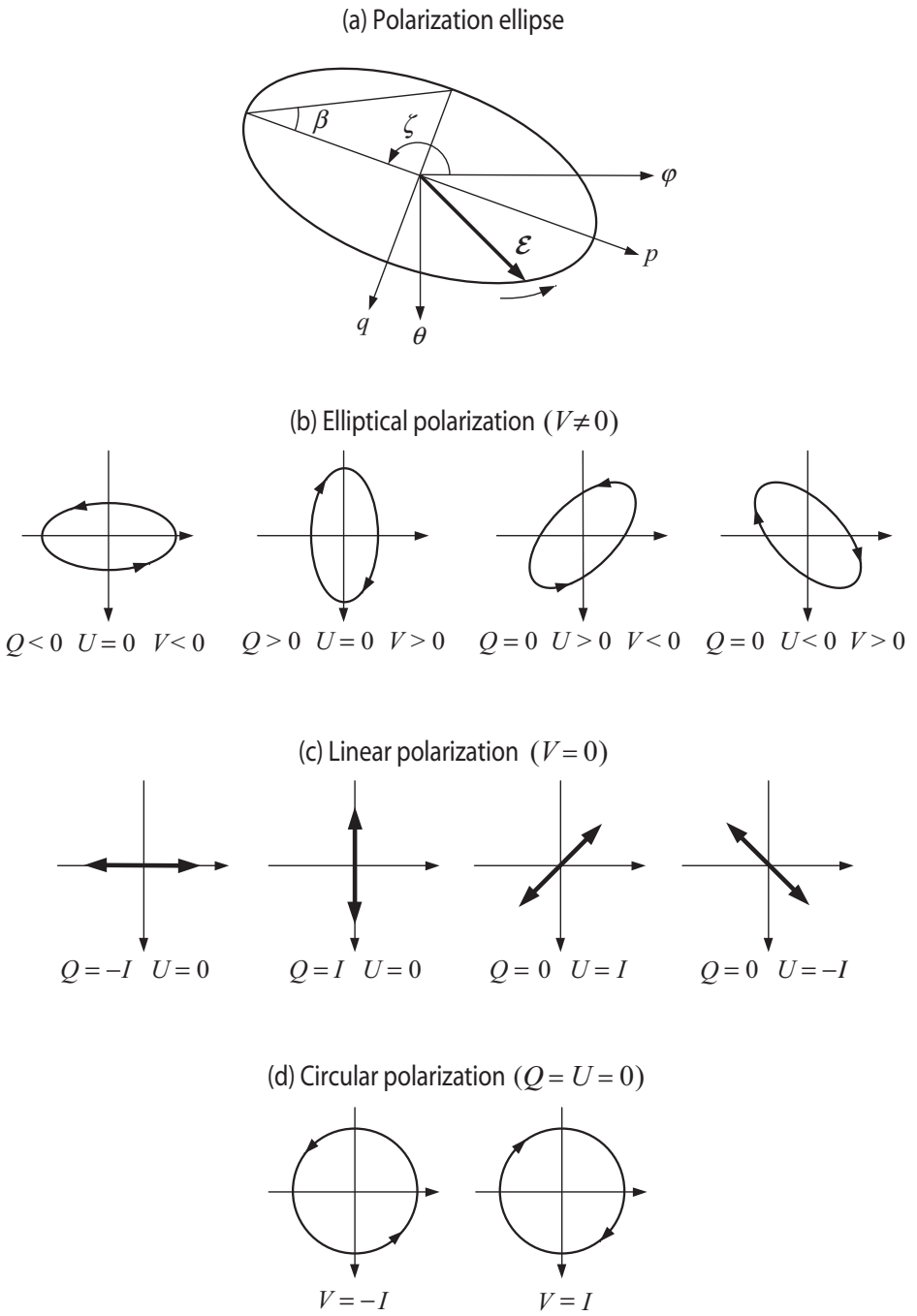

Fig. 7.3. Ellipse described by the tip of the real electric vector at a fixed point O in space (top panel) and particular cases of elliptical, linear, and circular polarization. The plane electromagnetic wave propagates towards the reader.

$$a_\varphi^2 = a^2(\sin^2\beta \sin^2\zeta + \cos^2\beta \cos^2\zeta). \tag{7.29}$$

Multiplying Eqs. (7.24) and (7.26) as well as Eqs. (7.25) and (7.27) and adding yields

$$a_\theta a_\varphi \cos\Delta = -\frac{1}{2}a^2 \cos 2\beta \sin 2\zeta. \tag{7.30}$$

Similarly, multiplying Eqs. (7.25) and (7.26) as well as Eqs. (7.24) and (7.27) and subtracting gives

$$a_\theta a_\varphi \sin\Delta = -\frac{1}{2}a^2 \sin 2\beta. \tag{7.31}$$

Comparing Eqs. (7.11)–(7.14) with Eqs. (7.28)–(7.31), we finally derive

$$I = \frac{1}{2}\sqrt{\frac{\epsilon}{\mu}}\, a^2, \tag{7.32}$$

$$Q = -I \cos 2\beta \cos 2\zeta, \tag{7.33}$$

$$U = I \cos 2\beta \sin 2\zeta, \tag{7.34}$$

$$V = -I \sin 2\beta \tag{7.35}$$

with

$$a^2 = a_\theta^2 + a_\varphi^2. \tag{7.36}$$

The parameters of the polarization ellipse are thus expressed in terms of the Stokes parameters as follows. The major and minor axes are given by $(2I\sqrt{\mu/\epsilon})^{1/2}\cos\beta$ and $(2I\sqrt{\mu/\epsilon})^{1/2}|\sin\beta|$, respectively (cf. Eqs. (7.20) and (7.21)). Equations (7.33) and (7.34) yield

$$\tan 2\zeta = -\frac{U}{Q}. \tag{7.37}$$

Since $|\beta| \le \pi/4$, we have $\cos 2\beta \ge 0$ so that $\cos 2\zeta$ has the same sign as $-Q$. Therefore, from the different values of ζ that satisfy Eq. (7.37), but differ by $\pi/2$, we must choose the one that makes the sign of $\cos 2\zeta$ to be the same as that of $-Q$. The ellipticity and handedness follow from

$$\tan 2\beta = -\frac{V}{\sqrt{Q^2 + U^2}}. \tag{7.38}$$

Thus, the polarization is left-handed if V is positive and is right-handed if V is negative (Fig. 7.3b).

The electromagnetic wave becomes linearly polarized when β vanishes; then the electric field vector vibrates along the line making the angle ζ with the

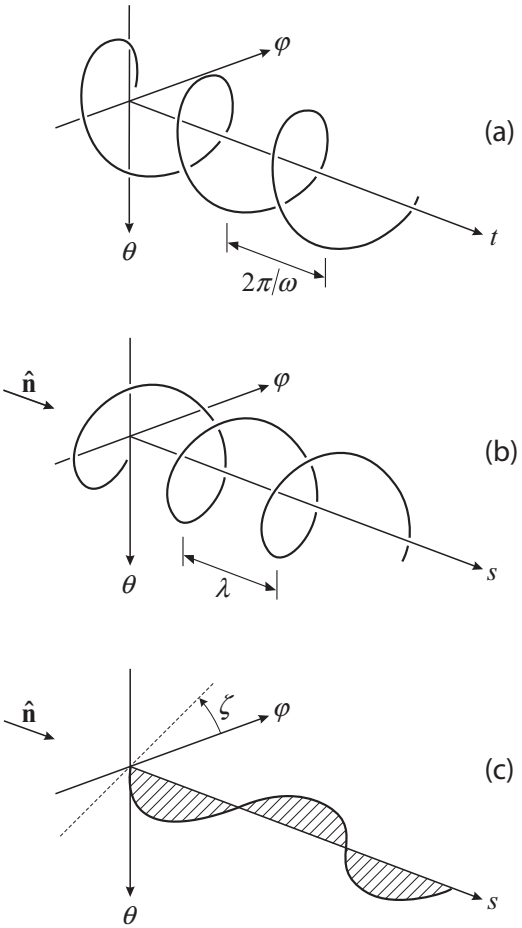

Fig. 7.4. **(a)** The helix described by the tip of the real electric field vector of a plane electromagnetic wave with right-handed polarization in the (θ, φ, t) coordinates at a fixed point in space. **(b)** As in (a), but in the (θ, φ, s) coordinates at a fixed moment in time. **(c)** As in (b), but for a linearly polarized wave.

φ-axis (Fig. 7.3a) and $V = 0$. Furthermore, if $\zeta = 0$ or $\zeta = \pi/2$ then U vanishes as well. This explains the usefulness of the modified Stokes representation of polarization given by Eq. (7.41) in situations involving linearly polarized light (Problem 7.3).

If, however, $\beta = \pm\pi/4$, then both Q and U vanish; the electric field vector describes a circle in the clockwise $(\beta = \pi/4,\ V = -I)$ or anti-clockwise $(\beta = -\pi/4,\ V = I)$ direction, if one is looking in the direction of propagation (Fig. 7.3d). In this case the electromagnetic wave is circularly polarized, which demonstrates the usefulness of the circular-polarization column vector defined by Eq. (7.42) (Problem 7.4).

The polarization ellipse, along with a designation of the rotation direction (right- or left-handed), fully describes the temporal evolution of the real electric field vector at a fixed point in space. This evolution can also be visualized by plotting the curve in (θ, φ, t) coordinates described by the tip of the electric field vector as a function of time. For example, in the case of an elliptically polarized plane wave with right-handed polarization, the curve is a right-handed helix with an elliptical projection onto the $\theta\varphi$-plane centered around the t-axis (see Fig. 7.4a). The pitch of the helix is simply $2\pi/\omega$, where ω is the angular frequency.

Another way to visualize a plane wave is to fix a moment in time and draw a three-dimensional curve in (θ, φ, s) coordinates described by the tip of the electric field vector as a function of a spatial coordinate $s = \hat{\mathbf{n}} \cdot \mathbf{r}$ oriented along the direction of propagation $\hat{\mathbf{n}}$. According to Eqs. (7.16)–(7.19), the electric field is the same for all {position, time} combinations with constant $ks - \omega t$. Therefore, at any instant of time (say, $t = 0$) the locus of the points described by the tip of the electric field vector originating at different points on the s-axis is also a helix, with the same projection onto the $\theta\varphi$-plane as the respective helix in the (θ, φ, t) coordinates, but with opposite handedness. For example, for the wave with right-handed elliptical polarization shown in Fig. 7.4a, the respective curve in the (θ, φ, s) coordinates is a left-handed elliptical helix, shown in Fig. 7.4b. The pitch of this helix is the wavelength λ. It is now clear that the propagation of the wave in time and space can be represented by progressive movement in time of the helix shown in Fig. 7.4b in the direction of $\hat{\mathbf{n}}$ with the speed of light. With increasing time, the intersection of the helix with any plane s = constant describes a right-handed vibration ellipse.

In the case of a circularly polarized wave, the elliptical helix becomes a helix with a circular projection onto the $\theta\varphi$-plane. If the wave is linearly polarized, then the helix degenerates into a simple sinusoidal curve in the plane making an angle ζ with the φ-axis (Fig. 7.4c).

Finally, we note that another choice of the time-harmonic factor (i.e., $\exp(\mathrm{i}\omega t)$ instead of $\exp(-\mathrm{i}\omega t)$) has a specific effect on the parameter V, as discussed in Problem 7.9.

7.4 The Stokes parameters of a spherical electromagnetic wave

In complete analogy with the case of a plane wave, the Stokes column vector of an outgoing spherical wave (3.30)–(3.31) propagating in a homogeneous lossless medium can be defined as

$$\mathbf{I}(\mathbf{r}) = \begin{bmatrix} I(\mathbf{r}) \\ Q(\mathbf{r}) \\ U(\mathbf{r}) \\ V(\mathbf{r}) \end{bmatrix} = \frac{1}{2}\sqrt{\frac{\epsilon}{\mu}}\frac{1}{r^2}\begin{bmatrix} E_{1\theta}(\hat{\mathbf{r}})[E_{1\theta}(\hat{\mathbf{r}})]^* + E_{1\varphi}(\hat{\mathbf{r}})[E_{1\varphi}(\hat{\mathbf{r}})]^* \\ E_{1\theta}(\hat{\mathbf{r}})[E_{1\theta}(\hat{\mathbf{r}})]^* - E_{1\varphi}(\hat{\mathbf{r}})[E_{1\varphi}(\hat{\mathbf{r}})]^* \\ -E_{1\theta}(\hat{\mathbf{r}})[E_{1\varphi}(\hat{\mathbf{r}})]^* - E_{1\varphi}(\hat{\mathbf{r}})[E_{1\theta}(\hat{\mathbf{r}})]^* \\ \mathrm{i}\{E_{1\varphi}(\hat{\mathbf{r}})[E_{1\theta}(\hat{\mathbf{r}})]^* - E_{1\theta}(\hat{\mathbf{r}})[E_{1\varphi}(\hat{\mathbf{r}})]^*\} \end{bmatrix}. \tag{7.39}$$

All elements of this column vector have the dimension of monochromatic energy flux. As before, the first Stokes parameter is the intensity, defined this time by Eq. (3.38).

Problems

7.1: Derive the Stokes identity (7.4).

7.2: The Stokes column vector is not the only representation of polarization and not always the most convenient one. Three other representations frequently used in practice are the complex coherency column vector

$$\mathbf{J} = \frac{1}{2}\sqrt{\frac{\epsilon}{\mu}}\begin{bmatrix} E_{0\theta}E_{0\theta}^* \\ E_{0\theta}E_{0\varphi}^* \\ E_{0\varphi}E_{0\theta}^* \\ E_{0\varphi}E_{0\varphi}^* \end{bmatrix}, \tag{7.40}$$

the real so-called modified Stokes column vector

$$\mathbf{I}^{\mathrm{MS}} = \begin{bmatrix} I_{\mathrm{v}} \\ I_{\mathrm{h}} \\ U \\ V \end{bmatrix} = \begin{bmatrix} \frac{1}{2}(I+Q) \\ \frac{1}{2}(I-Q) \\ U \\ V \end{bmatrix}, \tag{7.41}$$

and the complex-valued circular-polarization column vector

$$\mathbf{I}^{\mathrm{CP}} = \begin{bmatrix} I_2 \\ I_0 \\ I_{-0} \\ I_{-2} \end{bmatrix} = \frac{1}{2}\begin{bmatrix} Q+\mathrm{i}U \\ I+V \\ I-V \\ Q-\mathrm{i}U \end{bmatrix}. \tag{7.42}$$

Derive the explicit forms of 4×4 transformation matrices $\mathbf{B}$ and $\mathbf{A}$ such that

$$\mathbf{I} = \mathbf{D}\mathbf{J}, \tag{7.43}$$

$$\mathbf{I}^{\mathrm{MS}} = \mathbf{B}\mathbf{I}, \tag{7.44}$$

$$\mathbf{I}^{\mathrm{CP}} = \mathbf{A}\mathbf{I}. \tag{7.45}$$

Show that

$$\mathbf{J} = \mathbf{D}^{-1}\mathbf{I}, \tag{7.46}$$

$$\mathbf{I} = \mathbf{B}^{-1}\mathbf{I}^{\mathrm{MS}}, \tag{7.47}$$

$$\mathbf{I} = \mathbf{A}^{-1}\mathbf{I}^{\mathrm{CP}} \tag{7.48}$$

and derive the explicit forms of the inverse matrices $\mathbf{D}^{-1}$, $\mathbf{B}^{-1}$, and $\mathbf{A}^{-1}$.

7.3: What is I^{MS} for a plane electromagnetic wave polarized linearly in the θ- or φ-direction?

7.4: What is I^{CP} for a circularly polarized plane electromagnetic wave with right-handed (left-handed) polarization?

7.5: Derive the rotation matrices $\mathsf{L}^{\mathrm{MS}}(\eta)$ and $\mathsf{L}^{\mathrm{CP}}(\eta)$ for the modified Stokes and circular-polarization column vectors, respectively.

7.6: Derive the following properties of the rotation matrix in the circular-polarization representation:

$$\mathsf{L}^{\mathrm{CP}}(\eta_1+\eta_2) = \mathsf{L}^{\mathrm{CP}}(\eta_1)\mathsf{L}^{\mathrm{CP}}(\eta_2) = \mathsf{L}^{\mathrm{CP}}(\eta_2)\mathsf{L}^{\mathrm{CP}}(\eta_1), \tag{7.49}$$

$$\mathsf{L}^{\mathrm{CP}}(-\eta) = [\mathsf{L}^{\mathrm{CP}}(\eta)]^{-1}. \tag{7.50}$$

7.7: Derive the following properties of the Stokes rotation matrix:

$$\mathsf{L}(\eta_1+\eta_2) = \mathsf{L}(\eta_1)\mathsf{L}(\eta_2) = \mathsf{L}(\eta_2)\mathsf{L}(\eta_1), \tag{7.51}$$

$$\mathsf{L}(-\eta) = [\mathsf{L}(\eta)]^{-1}. \tag{7.52}$$

7.8: Derive the following properties of the rotation matrix in the modified Stokes representation:

$$\mathsf{L}^{\mathrm{MS}}(\eta_1+\eta_2) = \mathsf{L}^{\mathrm{MS}}(\eta_1)\mathsf{L}^{\mathrm{MS}}(\eta_2) = \mathsf{L}^{\mathrm{MS}}(\eta_2)\mathsf{L}^{\mathrm{MS}}(\eta_1), \tag{7.53}$$

$$\mathsf{L}^{\mathrm{MS}}(-\eta) = [\mathsf{L}^{\mathrm{MS}}(\eta)]^{-1}. \tag{7.54}$$

7.9: Our definition of the Stokes parameter V in Eq. (7.3) is mathematically the same as that in van de Hulst (1957) and Hovenier *et al.* (2004). However, their choice of the time-harmonic factor is $\exp(\mathrm{i}\omega t)$ instead of our choice $\exp(-\mathrm{i}\omega t)$. Show that this causes the numerical values of their complex electric and magnetic field vectors to be complex conjugates of ours. Then show that the numerical value of their Stokes parameter V is minus that of our Stokes parameter V. What sense of circular polarization (right-handed or left-handed) corresponds to a positive numerical value of their Stokes parameter V?

7.10: Let a plane electromagnetic wave be specified by the following real electric field vector components:

$$\mathcal{E}_\theta(\mathbf{r},t) = a_\theta \cos(\Delta_\theta + k\hat{\mathbf{n}}\cdot\mathbf{r} - \omega t), \tag{7.55}$$

$$\mathcal{E}_\varphi(\mathbf{r},t) = a_\varphi \cos(k\hat{\mathbf{n}}\cdot\mathbf{r} - \omega t). \tag{7.56}$$

What are the Stokes parameters and the polarization state of the wave for $\Delta_\theta = \pi/2$? Sketch the polarization ellipses for $\Delta_\theta = n\pi/4$ with $n = 0, 1, \ldots, 7$.

Notes and further reading

Even before the development of Maxwell's electromagnetics and his discovery of the electromagnetic nature of light, Sir George Gabriel Stokes (1819–1903) demonstrated that four quantities, now known as the Stokes parameters, could conveniently characterize the polarization state of any parallel beam of light, including partially polarized and unpolarized polychromatic light (Stokes 1852). Furthermore, he noted that, unlike the quantities entering the amplitude formulation of the optical field, these parameters could be directly measured by a suitable optical instrument.

The fascinating subject of polarization attracted the attention of many other great scientists before and after Stokes, including Thomas Young (1773–1829), Augustin Jean Fresnel (1788–1827), Dominique François Arago (1786–1853),

Thomas Young

Augustin Jean Fresnel

Dominique François Arago

Sir George Gabriel Stokes

Subrahmanyan Chandrasekhar (1910–95), and Hendrik Christoffel van de Hulst (1918–2000). Even Henri Poincaré, who is ranked by many as one the greatest and most transformative geniuses of all time (see, e.g., the scientific biographies of Poincaré by Verhulst (2012) and Gray (2013)), had found the time to contribute to this discipline by developing a useful polarization analysis tool known as the Poincaré sphere (Poincaré (1892); see also Kliger *et al.* (1990) and Collett (1992)). The early history of polarimetry (including its applications in astrophysics) is described by Brosseau (1998) and Clarke (2010).

Extensive treatments of theoretical and experimental aspects of polarimetry have been provided by Shurcliff (1962), Gehrels (1974), Coulson (1988), Kliger *et al.* (1990), Collett (1992), Brosseau (1998), Hovenier *et al*. (2004), and Cloude (2010). In Pye (2001), numerous manifestations of polarization in science and nature are described.

8

Poynting–Stokes tensor

We have already mentioned that different combinations of electric and magnetic field vectors can yield the same Poynting vector. This means that forming the vector product of the electric and magnetic field vectors results in a quantity that does not carry unique information about the participating fields. In particular, the Poynting vector contains no information about the polarization state of a transverse electromagnetic field. Thus, by its very definition, the Poynting vector cannot be used to describe the phenomenon of electromagnetic scattering by, for example, expressing the Poynting vector of the scattered field in that of the incident field.

We have seen in the preceding chapter that the standard descriptor of polarization is the Stokes column vector (7.3). However, this quantity contains no explicit information on the direction of the Poynting vector and can be defined only for a transverse (i.e., plane or spherical) electromagnetic wave, whereas the total electromagnetic field in the near zone of any object (e.g., at any observation point inside a cloud of particles) is never a transverse wave. It is, therefore, highly desirable to introduce an alternative quantity that:

- can be defined for any electromagnetic field;
- has the dimension of electromagnetic energy flux; and
- enables a complete and self-contained description of electromagnetic scattering in the context of practical optical analysis.

It has been shown by the author (Mishchenko 2010) that a quantity combining all these attributes is the PST defined as the dyadic product of the electric and magnetic field vectors:

$$\overleftrightarrow{\mathcal{P}}(\mathbf{r},t) = \boldsymbol{\mathcal{E}}(\mathbf{r},t) \otimes \boldsymbol{\mathcal{H}}(\mathbf{r},t). \tag{8.1}$$

Indeed, by its very construct, the PST is applicable to an arbitrary electromagnetic field. Furthermore, it can be used to find both the Poynting vector and,

whenever applicable, the Stokes parameters (Problems 8.1 and 8.2). Owing to its unique and convenient properties, the PST (8.1) will be central to the following discussion of electromagnetic scattering.

In the case of a monochromatic electromagnetic field with an angular frequency ω, we have, by analogy with Eq. (2.61),

$$\langle \overleftrightarrow{\mathcal{P}}(\mathbf{r},t)\rangle = \mathrm{Re}[\overleftrightarrow{P}(\mathbf{r})]^{\mathrm{T}}, \tag{8.2}$$

where the complex PST is defined by

$$\overleftrightarrow{P}(\mathbf{r}) = \frac{1}{2}\mathbf{H}(\mathbf{r}) \otimes [\mathbf{E}(\mathbf{r})]^{*}. \tag{8.3}$$

As before, the use of Eqs. (8.2) and (8.3) relies on averaging $\overleftrightarrow{\mathcal{P}}(\mathbf{r},t)$ over a period of time much longer than $T_{\mathrm{o}} = 2\pi/\omega$.

The complex PST (8.3) involves both the electric and the magnetic field at the observation point $\mathbf{r}$. It is sometimes convenient to have an alternative representation involving only the electric field. The reader can easily verify (Problem 8.3) that in the case of nonmagnetic materials, Eq. (8.3) everywhere in space can be written in the form

$$\overleftrightarrow{P}(\mathbf{r}) = \frac{1}{2\mathrm{i}\omega\mu_0}[\nabla_{\mathbf{r}'}\times\overleftrightarrow{C}(\mathbf{r}',\mathbf{r})]\Big|_{\mathbf{r}'=\mathbf{r}}, \tag{8.4}$$

where

$$\overleftrightarrow{C}(\mathbf{r}',\mathbf{r}) = \mathbf{E}(\mathbf{r}') \otimes [\mathbf{E}(\mathbf{r})]^{*} \tag{8.5}$$

is the so-called dyadic correlation function involving the electric field at two different points in space. The subscript $\mathbf{r}'$ means that the ∇ operator acts only on $\mathbf{E}(\mathbf{r}')$.

Problems

8.1: Express the complex Poynting vector in terms of the complex PST (8.3) using Cartesian coordinates.

8.2: Consider a transverse electromagnetic wave propagating in a homogeneous nonabsorbing medium and express its complex Poynting vector and Stokes column vector in terms of the complex PST (8.3), using local spherical coordinates.

8.3: Derive Eq. (8.4).

9

Polychromatic electromagnetic fields

The definition of a purely monochromatic electromagnetic field given in Section 2.3 implies that the time dependence of the complex vectors $\widetilde{\boldsymbol{\mathcal{E}}}(\mathbf{r}, t)$ and $\widetilde{\boldsymbol{\mathcal{H}}}(\mathbf{r}, t)$ is fully described by the complex-exponential factor $\exp(-\mathrm{i}\omega t)$ with a fixed angular frequency ω. This can be a good model for beams generated by certain types of laser, but not for the majority of natural and artificial electromagnetic fields. In reality, the electromagnetic field is typically polychromatic, i.e., is a superposition of a (possibly very large) number of monochromatic fields with different angular frequencies distributed over a given range $[\omega_{\min}, \omega_{\max}]$. Furthermore, in many cases the amplitudes of the complex electric and magnetic fields representing the component with an angular frequency ω are not constant but rather fluctuate in time, albeit much more slowly than the factor $\exp(-\mathrm{i}\omega t)$. Then the resulting polychromatic field is said to consist of quasi-monochromatic components. The range of angular frequencies $[\omega_{\min}, \omega_{\max}]$ of monochromatic or quasi-monochromatic components can be relatively narrow for some artificial sources of light. However, it can also be very wide, the solar radiation and the light produced by incandescent lamps being prime examples.

Given the ubiquity of polychromatic electromagnetic fields in natural and artificial environments, it is essential to analyze how the results of Chapters 7 and 8 can be generalized to account for a mix of different angular frequencies and/or random fluctuations of the amplitudes of the constituent complex fields. We will see that this generalization is, in fact, quite straightforward provided that we apply averaging over a sufficiently long period of time.

9.1 Time-averaged Poynting–Stokes tensor and Poynting vector of a polychromatic field with monochromatic components

A simple polychromatic electromagnetic field exactly satisfying the MMEs everywhere in space is a vector superposition of a number N of monochromatic fields with a range of angular frequencies:

$$\mathcal{E}(\mathbf{r},t) = \mathrm{Re}\sum_{n=1}^{N}\mathbf{E}_n(\mathbf{r})\exp(-\mathrm{i}\omega_n t), \tag{9.1}$$

$$\mathcal{H}(\mathbf{r},t) = \mathrm{Re}\sum_{n=1}^{N}\mathbf{H}_n(\mathbf{r})\exp(-\mathrm{i}\omega_n t), \tag{9.2}$$

where each couple $[\mathbf{E}_n(\mathbf{r}), \mathbf{H}_n(\mathbf{r})]$ is a solution of the frequency-domain MMEs,

$$\omega_{\min} \le \omega_n \le \omega_{\max}, \tag{9.3}$$

and

$$\omega_n \ne \omega_{n'} \text{ for any } n \ne n'. \tag{9.4}$$

Recalling the definition (8.1), we have:

$$\begin{aligned}
\overleftrightarrow{\mathcal{P}}(\mathbf{r},t) &= \mathcal{E}(\mathbf{r},t)\otimes\mathcal{H}(\mathbf{r},t) && (9.5)\\
&= \frac{1}{4}\sum_{n,n'=1}^{N}\{\mathbf{E}_n(\mathbf{r})\exp(-\mathrm{i}\omega_n t)+[\mathbf{E}_n(\mathbf{r})]^*\exp(\mathrm{i}\omega_n t)\}\\
&\qquad\otimes\{\mathbf{H}_{n'}(\mathbf{r})\exp(-\mathrm{i}\omega_{n'} t)+[\mathbf{H}_{n'}(\mathbf{r})]^*\exp(\mathrm{i}\omega_{n'} t)\}\\
&= \frac{1}{2}\mathrm{Re}\sum_{n,n'=1}^{N}\mathbf{E}_n(\mathbf{r})\otimes\mathbf{H}_{n'}(\mathbf{r})\exp[-\mathrm{i}(\omega_n+\omega_{n'})t] && (9.5\text{a})\\
&\quad+\frac{1}{2}\mathrm{Re}\sum_{n,n'=1}^{N}[\mathbf{E}_n(\mathbf{r})]^*\otimes\mathbf{H}_{n'}(\mathbf{r})\exp[\mathrm{i}(\omega_n-\omega_{n'})t]. && (9.5\text{b})
\end{aligned}$$

Averaging the complex exponentials over a time interval

$$T \gg \max_{1\le n<n'\le N}\frac{2\pi}{|\omega_n-\omega_{n'}|} \tag{9.6}$$

yields

$$\frac{1}{T}\left|\int_{t-T/2}^{t+T/2}\mathrm{d}t'\exp[-\mathrm{i}(\omega_n+\omega_{n'})t']\right| = O\left(\frac{1}{T(\omega_n+\omega_{n'})}\right) \text{ for any } n \text{ and } n' \tag{9.7}$$

and

$$\frac{1}{T}\left|\int_{t-T/2}^{t+T/2}\mathrm{d}t'\exp[\mathrm{i}(\omega_n-\omega_{n'})t']\right| = O\left(\frac{1}{T\,|\omega_n-\omega_{n'}|}\right) \text{ for any } n \ne n', \tag{9.8}$$

where O stands for "of the order of." We can thus conclude that averaging the right-hand side of Eq. (9.5) over a sufficiently long time interval zeros out the entire sum (9.5a), as well as the $n \ne n'$ terms in the sum (9.5b). Hence,

$$\langle\langle\overleftrightarrow{\mathcal{P}}(\mathbf{r},t)\rangle\rangle = \mathrm{Re}[\overleftrightarrow{P}(\mathbf{r})]^{\mathrm{T}}, \tag{9.9}$$

where $\langle\langle\cdots\rangle\rangle$ hereinafter denotes averaging over an appropriately long time inter-

val that can potentially be much longer than that in Eqs. (2.40), (2.61), and (8.2);

$$\ddot{P}(\mathbf{r}) = \sum_{n=1}^{N} \ddot{P}_n(\mathbf{r}) \tag{9.10}$$

is the complex PST of the polychromatic field; and, according to Eq. (8.3),

$$\ddot{P}_n(\mathbf{r}) = \frac{1}{2}\mathbf{H}_n(\mathbf{r}) \otimes [\mathbf{E}_n(\mathbf{r})]^* \tag{9.11}$$

is the complex PST of the nth monochromatic component. Thus, the time-averaged PST of the polychromatic electromagnetic field (9.1)–(9.2) is independent of t and is obtained by transposing the real part of the sum of the complex PSTs of the participating monochromatic fields.

This simple additivity rule has great practical importance. However, it is imperative to remember that its validity relies on averaging Eq. (9.5b) over a sufficiently long period of time, especially when N is very large and $|\omega_n - \omega_{n'}|$ is much smaller than either ω_n or $\omega_{n'}$ for many combinations of n and n'. Indeed, in such cases much longer averaging time can be necessary to make the sum of the $N(N-1)$ terms with $n \neq n'$ much smaller (in the absolute-value sense) than that of the N terms with $n = n'$. While this can typically be expected to be less of a problem at infrared and shorter wavelengths, special care is called for when dealing with micro- and radiowaves.

An immediate consequence of Eqs. (9.9)–(9.11) and (H.14) is the respective additivity rule for the time-averaged Poynting vector of a polychromatic field with monochromatic components:

$$\langle\langle \boldsymbol{\mathcal{S}}(\mathbf{r}, t)\rangle\rangle = \mathrm{Re}\,\mathbf{S}(\mathbf{r}), \tag{9.12}$$

where $\langle\langle \boldsymbol{\mathcal{S}}(\mathbf{r}, t)\rangle\rangle$ is independent of t;

$$\mathbf{S}(\mathbf{r}) = \sum_{n=1}^{N} \mathbf{S}_n(\mathbf{r}); \tag{9.13}$$

and

$$\mathbf{S}_n(\mathbf{r}) = \frac{1}{2}\mathbf{E}_n(\mathbf{r}) \times [\mathbf{H}_n(\mathbf{r})]^* \tag{9.14}$$

is the complex Poynting vector of the nth monochromatic component.

9.2 Time-averaged Stokes parameters of a parallel polychromatic beam with monochromatic components

The simplest example of a polychromatic field is a parallel beam of infinite lateral extent consisting of plane waves propagating through a homogeneous lossless medium in the same direction $\hat{\mathbf{n}}$. In the complex-field representation, the resulting electric and magnetic fields everywhere in space are then given by

$$\widetilde{\mathcal{E}}(\mathbf{r},t) = \sum_{n=1}^{N} \mathbf{E}_{0n} \exp(\mathrm{i}k_n \hat{\mathbf{n}} \cdot \mathbf{r} - \mathrm{i}\omega_n t), \tag{9.15}$$

$$\widetilde{\mathcal{H}}(\mathbf{r},t) = \sum_{n=1}^{N} \mathbf{H}_{0n} \exp(\mathrm{i}k_n \hat{\mathbf{n}} \cdot \mathbf{r} - \mathrm{i}\omega_n t). \tag{9.16}$$

Equations (9.9)–(9.11) and (H.16) then imply the following additivity rule for the resulting time-averaged (and, thus, t-independent) Stokes parameters:

$$\langle\langle I \rangle\rangle = \sum_{n=1}^{N} I_n, \quad \langle\langle Q \rangle\rangle = \sum_{n=1}^{N} Q_n, \quad \langle\langle U \rangle\rangle = \sum_{n=1}^{N} U_n, \quad \langle\langle V \rangle\rangle = \sum_{n=1}^{N} V_n, \tag{9.17}$$

where I_n, Q_n, U_n, and V_n are the Stokes parameters of the nth monochromatic component. The additivity rule implies that the time-averaged Stokes parameters of the polychromatic beam are independent of $\mathbf{r}$; in other words, they do not change upon propagation of the beam.

The Stokes identity (7.4) is not valid, in general, for a polychromatic beam and must be replaced by the so-called Stokes–Verdet inequality

$$\langle\langle I \rangle\rangle^2 \geq \langle\langle Q \rangle\rangle^2 + \langle\langle U \rangle\rangle^2 + \langle\langle V \rangle\rangle^2 \tag{9.18}$$

(see Problem 9.1). The beam is said to be fully polarized if the equality holds: $\langle\langle I \rangle\rangle^2 = \langle\langle Q \rangle\rangle^2 + \langle\langle U \rangle\rangle^2 + \langle\langle V \rangle\rangle^2$. This definition includes a single monochromatic plane wave (which is always fully polarized), but is, of course, more general. It can be shown (see Problem 9.2) that a polychromatic parallel beam defined by Eqs. (9.15) and (9.16) is fully polarized if and only if

$$\begin{bmatrix} I_n \\ Q_n \\ U_n \\ V_n \end{bmatrix} = \alpha_{nn'} \begin{bmatrix} I_{n'} \\ Q_{n'} \\ U_{n'} \\ V_{n'} \end{bmatrix} \text{ for any } n \text{ and } n', \tag{9.19}$$

where $\alpha_{nn'}$ is a positive real number. This means that all the ellipses described by the electric field vectors of the individual monochromatic plane waves have the same ellipticity, handedness, and orientation; only their sizes can be different.

If $\langle\langle Q \rangle\rangle^2 = \langle\langle U \rangle\rangle^2 = \langle\langle V \rangle\rangle^2 = 0$ then the polychromatic beam is said to be unpolarized (or natural). If $\langle\langle I \rangle\rangle^2 > \langle\langle Q \rangle\rangle^2 + \langle\langle U \rangle\rangle^2 + \langle\langle V \rangle\rangle^2$ and at least one of the Stokes parameters $\langle\langle Q \rangle\rangle, \langle\langle U \rangle\rangle$, and $\langle\langle V \rangle\rangle$ is not equal to zero, then the beam is partially polarized; a beam with $\langle\langle V \rangle\rangle = 0$ is called linearly polarized, while that with $\langle\langle Q \rangle\rangle = \langle\langle U \rangle\rangle = 0$ is said to be circularly polarized.

9.3 Polychromatic field with quasi-monochromatic components

The important property of the polychromatic field with monochromatic components as defined by Eqs. (9.1) and (9.2) is that it satisfies the frequency-domain

MMEs exactly. However, this model can often be criticized as being unrealistic in that it ignores the nature of physical processes generating electromagnetic fields. Indeed, in many practical situations, each component of the polychromatic field (9.1)–(9.2) is in turn a superposition of many monochromatic subcomponents, all having the same angular frequency, but different complex amplitudes. More often than not, the specific set of subcomponents contributing to an nth component and their number fluctuate in time, thereby making the resulting complex amplitudes $\mathbf{E}_n$ and $\mathbf{H}_n$ random functions of time. We thus have:

$$\boldsymbol{\mathcal{E}}(\mathbf{r},t) = \mathrm{Re}\sum_{n=1}^{N}\mathbf{E}_n(\mathbf{r},t)\exp(-\mathrm{i}\omega_n t), \tag{9.20}$$

$$\boldsymbol{\mathcal{H}}(\mathbf{r},t) = \mathrm{Re}\sum_{n=1}^{N}\mathbf{H}_n(\mathbf{r},t)\exp(-\mathrm{i}\omega_n t). \tag{9.21}$$

If the typical period of fluctuations $T_{\mathrm{f}n}$ of the amplitudes $\mathbf{E}_n(\mathbf{r},t)$ and $\mathbf{H}_n(\mathbf{r},t)$ is much longer than the period of time-harmonic oscillations $T_{\mathrm{o}n} = 2\pi/\omega_n$ then the random vector field given by

$$\begin{cases}\mathbf{E}_n(\mathbf{r},t)\exp(-\mathrm{i}\omega_n t)\\ \mathbf{H}_n(\mathbf{r},t)\exp(-\mathrm{i}\omega_n t)\end{cases} \tag{9.22}$$

is said to represent a *quasi-monochromatic* electromagnetic field. Note that the temporal fluctuations of the complex amplitudes $\mathbf{E}_n(\mathbf{r},t)$ and $\mathbf{H}_n(\mathbf{r},t)$ imply fluctuations of both the amplitudes and the phases of the real electric and magnetic fields. Although $T_{\mathrm{f}n} \gg T_{\mathrm{o}n}$, these random fluctuations usually occur too fast to be traced by traditional optical instruments.

Strictly speaking, the field (9.22) does not satisfy the frequency-domain MMEs. However, by its very construct, each quasi-monochromatic component can be considered monochromatic (and hence can be found by solving the frequency-domain MMEs) over time intervals that are much longer than $T_{\mathrm{o}n}$ yet significantly shorter than $T_{\mathrm{f}n}$. This makes the concept of a quasi-monochromatic field a useful compromise allowing one to combine the simplicity of the frequency-domain formalism with a more realistic representation of many natural and artificial electromagnetic fields.

The instantaneous PST of the polychromatic field (9.20)–(9.21) is given by

$$\overleftrightarrow{\mathcal{P}}(\mathbf{r},t) = \frac{1}{2}\mathrm{Re}\sum_{n,n'=1}^{N}\mathbf{E}_n(\mathbf{r},t)\exp(-\mathrm{i}\omega_n t)\otimes\mathbf{H}_{n'}(\mathbf{r},t)\exp(-\mathrm{i}\omega_{n'} t) \tag{9.23a}$$

$$+\frac{1}{2}\mathrm{Re}\sum_{n,n'=1}^{N}[\mathbf{E}_n(\mathbf{r},t)\exp(-\mathrm{i}\omega_n t)]^{*}\otimes\mathbf{H}_{n'}(\mathbf{r},t)\exp(-\mathrm{i}\omega_{n'} t). \tag{9.23b}$$

It is quite reasonable in most cases to assume that for any $n \neq n'$, $\mathbf{E}_n(\mathbf{r},t) \times \exp(-\mathrm{i}\omega_n t)$ and $\mathbf{H}_{n'}(\mathbf{r},t)\exp(-\mathrm{i}\omega_{n'} t)$ are independent and, thus, uncorrelated random processes. This implies that the time average of the dyadic product of

these random fields is equal to the dyadic product of the time averages of the fields (Priestley 1992). Since the complex amplitudes $\mathbf{E}_n(\mathbf{r},t)$ and $\mathbf{H}_n(\mathbf{r},t)$ vary in time much more slowly than the respective time-harmonic factors, we have

$$\langle \mathbf{E}_n(\mathbf{r},t)\exp(-\mathrm{i}\omega_n t)\rangle = \langle \mathbf{H}_n(\mathbf{r},t)\exp(-\mathrm{i}\omega_n t)\rangle = \mathbf{0}. \tag{9.24}$$

As a consequence, only the $n = n'$ terms in Eq. (9.23b) survive averaging over time, thereby yielding a modified version of Eqs. Eq. (9.9)–(9.11) in which the total and component complex PSTs are now obtained by averaging over a sufficiently long period of time:

$$\langle\langle \ddot{\mathcal{P}}(\mathbf{r},t)\rangle\rangle = \mathrm{Re}\langle\langle \ddot{P}(\mathbf{r},t)\rangle\rangle^{\mathrm{T}}, \tag{9.25}$$

$$\langle\langle \ddot{P}(\mathbf{r},t)\rangle\rangle = \sum_{n=1}^{N}\langle\langle \ddot{P}_n(\mathbf{r},t)\rangle\rangle, \tag{9.26}$$

$$\langle\langle \ddot{P}_n(\mathbf{r},t)\rangle\rangle = \frac{1}{2}\langle\langle \mathbf{H}_n(\mathbf{r},t)\otimes[\mathbf{E}_n(\mathbf{r},t)]^*\rangle\rangle. \tag{9.27}$$

Note that all time averages in Eqs. (9.25)–(9.27) are independent of t owing to the presumed stationarity of the random processes $\mathbf{H}_n(\mathbf{r},t)\otimes[\mathbf{E}_n(\mathbf{r},t)]^*$ (cf. Priestley 1992). Also, the requisite averaging time is now much longer than $T_{\mathrm{f}n}$ (i.e., not just much longer than $T_{\mathrm{o}n}$) for any n. The time-averaged Poynting vector of the polychromatic field (9.20)–(9.21) is now given by

$$\langle\langle \boldsymbol{\mathcal{S}}(\mathbf{r},t)\rangle\rangle = \mathrm{Re}\langle\langle \mathbf{S}(\mathbf{r},t)\rangle\rangle, \tag{9.28}$$

in which

$$\langle\langle \mathbf{S}(\mathbf{r},t)\rangle\rangle = \sum_{n=1}^{N}\langle\langle \mathbf{S}_n(\mathbf{r},t)\rangle\rangle, \tag{9.29}$$

$$\langle\langle \mathbf{S}_n(\mathbf{r},t)\rangle\rangle = \frac{1}{2}\langle\langle \mathbf{E}_n(\mathbf{r},t)\times[\mathbf{H}_n(\mathbf{r},t)]^*\rangle\rangle. \tag{9.30}$$

A parallel beam of infinite lateral extent consisting of quasi-monochromatic plane waves propagating in the direction $\hat{\mathbf{n}}$ is defined by

$$\widetilde{\boldsymbol{\mathcal{E}}}(\mathbf{r},t) = \sum_{n=1}^{N}\mathbf{E}_{0n}(t)\exp(\mathrm{i}k_n\hat{\mathbf{n}}\cdot\mathbf{r} - \mathrm{i}\omega_n t), \tag{9.31}$$

$$\widetilde{\boldsymbol{\mathcal{H}}}(\mathbf{r},t) = \sum_{n=1}^{N}\mathbf{H}_{0n}(t)\exp(\mathrm{i}k_n\hat{\mathbf{n}}\cdot\mathbf{r} - \mathrm{i}\omega_n t), \tag{9.32}$$

where $\mathbf{E}_{0n}(t)$ and $\mathbf{H}_{0n}(t)$ are "slowly" fluctuating complex amplitudes. According to Eqs. (9.25)–(9.27), Eq. (9.17) is now modified as follows:

$$\langle\langle I(t)\rangle\rangle = \sum_{n=1}^{N}\langle\langle I_n(t)\rangle\rangle, \qquad \langle\langle Q(t)\rangle\rangle = \sum_{n=1}^{N}\langle\langle Q_n(t)\rangle\rangle,$$

$$\langle\langle U(t)\rangle\rangle = \sum_{n=1}^{N} \langle\langle U_n(t)\rangle\rangle, \quad \langle\langle V(t)\rangle\rangle = \sum_{n=1}^{N} \langle\langle V_n(t)\rangle\rangle, \tag{9.33}$$

where $I_n(t)$, $Q_n(t)$, $U_n(t)$, and $V_n(t)$ are the "quasi-instantaneous" Stokes parameters of the nth quasi-monochromatic component, and all time averages are independent of t.

The time-integrated Stokes parameters of each quasi-monochromatic component are essentially obtained by summing up the Stokes parameters of a temporal sequence of "quasi-instantaneous" monochromatic plane waves. Therefore, the Stokes–Verdet inequality now applies to each quasi-monochromatic component:

$$\langle\langle I_n(t)\rangle\rangle^2 \geq \langle\langle Q_n(t)\rangle\rangle^2 + \langle\langle U_n(t)\rangle\rangle^2 + \langle\langle V_n(t)\rangle\rangle^2. \tag{9.34}$$

The equality holds if and only if

$$\begin{bmatrix} I_n(t') \\ Q_n(t') \\ U_n(t') \\ V_n(t') \end{bmatrix} = \beta_n \begin{bmatrix} I_n(t) \\ Q_n(t) \\ U_n(t) \\ V_n(t) \end{bmatrix} \text{ for any } t \text{ and } t', \tag{9.35}$$

where β_n is a positive real-valued function of t and t'. This implies that the ellipticity, handedness, and orientation of the "instantaneous" ellipse described by the electric field vector of the quasi-monochromatic plane wave do not change in time. It follows from Eq. (9.34) that unlike a monochromatic plane electromagnetic wave, a quasi-monochromatic wave can be partially polarized and even unpolarized.

It is straightforward to show that the total time-averaged Stokes parameters (9.33) of the polychromatic beam with quasi-monochromatic components also satisfy the Stokes–Verdet inequality (9.18). The equality holds if and only if each quasi-monochromatic component is fully polarized and

$$\begin{bmatrix} \langle\langle I_n(t)\rangle\rangle \\ \langle\langle Q_n(t)\rangle\rangle \\ \langle\langle U_n(t)\rangle\rangle \\ \langle\langle V_n(t)\rangle\rangle \end{bmatrix} = \alpha_{nn'} \begin{bmatrix} \langle\langle I_{n'}(t)\rangle\rangle \\ \langle\langle Q_{n'}(t)\rangle\rangle \\ \langle\langle U_{n'}(t)\rangle\rangle \\ \langle\langle V_{n'}(t)\rangle\rangle \end{bmatrix} \text{ for any } n \text{ and } n', \tag{9.36}$$

where $\alpha_{nn'}$ is a positive real number (see Problem 9.3).

As we have already mentioned, traditional optical instruments are incapable of tracing the temporal fluctuations of the amplitude and phase of a quasi-monochromatic plane wave. Therefore, the principle of optical equivalence introduced in Section 7.1 can be generalized as follows: it is impossible by means of a traditional optical instrument to distinguish between two different quasi-monochromatic waves having the same angular frequency and the same time-averaged Stokes parameters. For example, there is only one kind of unpolarized quasi-

monochromatic light, although it can be represented by temporal sequences of "instantaneous" monochromatic waves in an infinite variety of optically indistinguishable ways.

9.4 Derivative polarimetric characteristics of a polychromatic beam

The resulting electric field vector of a polychromatic parallel beam (9.15)–(9.16) or (9.31)–(9.32) does not describe an ellipse in a plane perpendicular to the propagation direction. Therefore, the ellipsometric analysis of Section 7.3 becomes inapplicable, and the complete optical specification of the beam is provided by the time-averaged Stokes parameters. In other words, one does not need any quantity other than $\langle\langle I(t)\rangle\rangle$, $\langle\langle Q(t)\rangle\rangle$, $\langle\langle U(t)\rangle\rangle$, and $\langle\langle V(t)\rangle\rangle$ in order to fully characterize a polychromatic beam in the majority of practical applications. Yet there are several derivative descriptors of the polarization state of the beam that are commonly used in the literature and allegedly provide a more intuitive representation of polarization than the Stokes parameters themselves. Not surprisingly, some of these descriptors are rooted in the ellipsometric analysis of a monochromatic plane wave. Prime examples of such derivative polarimetric characteristics are given below.

Upon recalling the definitions of unpolarized and fully polarized beams given in Section 9.2, it is natural to define the degree of *elliptical* polarization of a polychromatic beam as

$$P = \frac{\sqrt{Q^2 + U^2 + V^2}}{I} \geq 0, \tag{9.37}$$

where the angular brackets $\langle\langle\cdots\rangle\rangle$ around the Stokes parameters are omitted for the sake of brevity. Similarly, the degree of *linear* polarization is defined as

$$P_{\mathrm{L}} = \frac{\sqrt{Q^2 + U^2}}{I} \geq 0 \tag{9.38}$$

and the degree of *circular* polarization as

$$P_{\mathrm{C}} = V/I. \tag{9.39}$$

P vanishes for unpolarized light and is equal to unity for fully polarized light. For a partially polarized beam $(0 < P < 1)$ with $V \neq 0$, the sign of V can be interpreted to indicate the preferential handedness of the vibration ellipses described by the endpoints of the electric field vectors of the individual (or instantaneous) monochromatic waves constituting the beam. Specifically, a positive V indicates left-handed resulting polarization and a negative V indicates right-handed resulting polarization. By analogy with Eqs. (7.37) and (7.38), the quantities $-U/Q$ and $|V|/(Q^2 + U^2)^{1/2}$ can be interpreted as specifying the orientation and ellipticity, respectively, of an imaginary "preferential" vibration ellipse of the poly-

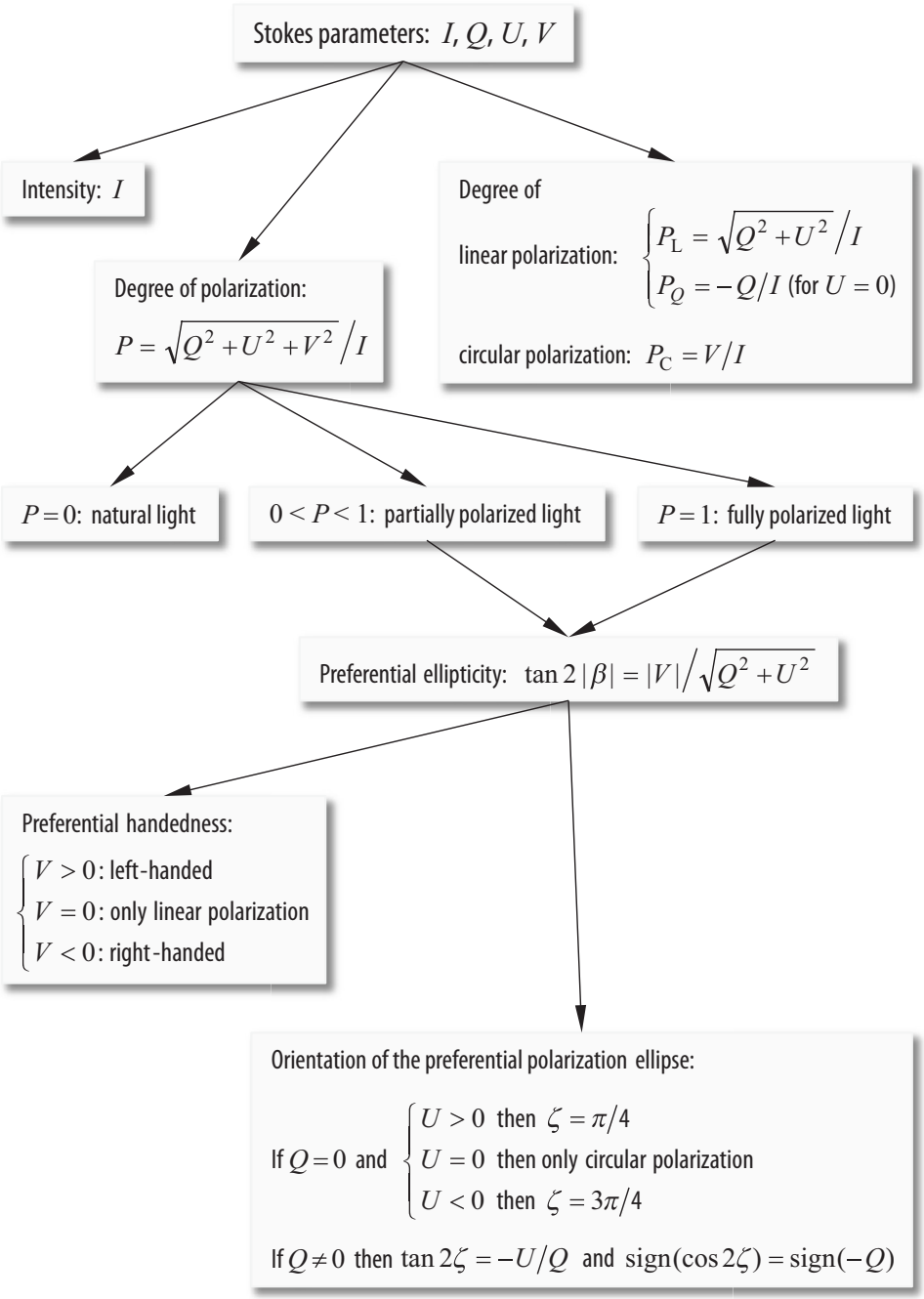

Fig. 9.1. Analysis of a parallel polychromatic beam characterized by the time-averaged Stokes parameters I, Q, U, and V. The angular brackets $\langle\langle\cdots\rangle\rangle$ around the Stokes parameters are omitted for the sake of brevity.

chromatic beam. It is important to remember, however, that unlike the Stokes parameters, these quantities are not additive. It is straightforward to show (see Problem 9.4) that P, P_L, and P_C are invariant with respect to rotations of the reference frame around the direction of propagation.

When $U = 0$, the ratio

$$P_Q = -Q/I \tag{9.40}$$

is called the *signed* degree of linear polarization. P_Q is positive when the vibrations of the total electric field vector in the φ-direction (i.e., in the direction perpendicular to the meridional plane of the beam) dominate those in the θ-direction, and is negative otherwise.

The standard polarimetric analysis of a general polychromatic beam with time-averaged Stokes parameters I, Q, U, and V is summarized in Fig. 9.1. All results of this section also apply to the time-averaged Stokes parameters of a single quasi-monochromatic plane wave.

Problems

9.1: Derive the Stokes–Verdet inequality (9.18).

9.2: Prove that a polychromatic parallel beam with monochromatic components is fully polarized if and only if the condition (9.19) is satisfied.

9.3: Prove that if at least one quasi-monochromatic component in Eqs. (9.31)–(9.32) is partially polarized then the entire polychromatic beam is partially polarized.

9.4: Prove that P, P_L, and P_C are invariant with respect to rotations of the reference frame around the direction of propagation.

Further reading

Intelligible introductions to the theory of random processes can be found in Priestley (1992) and Mandel and Wolf (1995).

10

Polychromatic scattering by fixed and randomly changing objects

Equation (4.24) expresses the scattered (and thus the total) monochromatic field in terms of the incident monochromatic field (we remind the reader that the incident field is the total field in the absence of the scattering object). However, neither field can be measured directly with conventional optical instruments, which obviously calls for the derivation of the corresponding relationships between *observable* characteristics of the total and incident fields. In view of the discussion in Chapter 8, all such relationships should be particular cases of a general expression of the PST of the total field in the presence of the scattering object in terms of that of the incident field. This general expression will be derived below.

There are two other important practical issues to consider. Indeed, our previous discussion of electromagnetic scattering has been based on the assumptions that: (i) the electromagnetic field is purely monochromatic, and (ii) the scattering object does not change with time. However, in the majority of actual applications the electromagnetic field is polychromatic and the scattering object changes in time randomly or quasi-randomly. Furthermore, the temporal variability of the object can be rapid enough to affect the result of averaging an actual optical observable over the time interval required to take a measurement.

To address these key practical aspects of electromagnetic scattering, another goal of this chapter is to develop a simple yet general formalism that can be used to express the time-averaged PST of the total polychromatic field in terms of that of the incident polychromatic field for both fixed and randomly changing objects. We will also introduce the concept of ergodicity and explain its importance in dealing with stochastic scatterers.

10.1 Monochromatic scattering by a fixed object

Let us first consider monochromatic scattering by a fixed object. To include explicitly the time-harmonic factor, we rewrite Eq. (4.24) as follows:

$$\widetilde{\boldsymbol{\mathcal{E}}}^{\mathrm{sca}}(\mathbf{r},t) = \int_{V_{\mathrm{INT}}} \mathrm{d}^3\mathbf{r}'\,\overleftrightarrow{G}(\mathbf{r},\mathbf{r}',k_1)\cdot\int_{V_{\mathrm{INT}}} \mathrm{d}^3\mathbf{r}''\exp(\mathrm{i}k_1\hat{\mathbf{n}}^{\mathrm{inc}}\cdot\mathbf{r}'')$$
$$\times\overleftrightarrow{T}(\mathbf{r}',\mathbf{r}'',\omega)\cdot\mathbf{E}_0^{\mathrm{inc}}\exp(-\mathrm{i}\omega t),\quad \mathbf{r}\in\Re^3, \tag{10.1}$$

where we assume that the incident field is a plane electromagnetic wave propagating in the direction of the unit vector $\hat{\mathbf{n}}^{\mathrm{inc}}$:

$$\widetilde{\boldsymbol{\mathcal{E}}}^{\mathrm{inc}}(\mathbf{r},t) = \mathbf{E}_0^{\mathrm{inc}}\exp(\mathrm{i}k_1\hat{\mathbf{n}}^{\mathrm{inc}}\cdot\mathbf{r}-\mathrm{i}\omega t). \tag{10.2}$$

Hence, the total field can be expressed as

$$\widetilde{\boldsymbol{\mathcal{E}}}(\mathbf{r},t) = \overleftrightarrow{\mathcal{T}}_{\mathcal{E}}(\mathbf{r},\hat{\mathbf{n}}^{\mathrm{inc}},\omega)\cdot\mathbf{E}_0^{\mathrm{inc}}\exp(-\mathrm{i}\omega t),\quad \mathbf{r}\in\Re^3, \tag{10.3}$$

where $\overleftrightarrow{\mathcal{T}}_{\mathcal{E}}$ is a transformation dyadic independent of $\mathbf{E}_0^{\mathrm{inc}}$ and given by

$$\overleftrightarrow{\mathcal{T}}_{\mathcal{E}}(\mathbf{r},\hat{\mathbf{n}}^{\mathrm{inc}},\omega) = \exp(\mathrm{i}k_1\hat{\mathbf{n}}^{\mathrm{inc}}\cdot\mathbf{r})\overleftrightarrow{I} + \int_{V_{\mathrm{INT}}} \mathrm{d}^3\mathbf{r}'\,\overleftrightarrow{G}(\mathbf{r},\mathbf{r}',k_1)\cdot\int_{V_{\mathrm{INT}}} \mathrm{d}^3\mathbf{r}''$$
$$\times\exp(\mathrm{i}k_1\hat{\mathbf{n}}^{\mathrm{inc}}\cdot\mathbf{r}'')\,\overleftrightarrow{T}(\mathbf{r}',\mathbf{r}'',\omega). \tag{10.4}$$

Note that we explicitly indicate the dependence of the dyadic transition operator on the angular frequency and the dependence of the dyadic Green's function on the wave number $k_1 = \omega(\epsilon_1\mu_0)^{1/2}$. It follows from Eqs. (3.12), (4.2), and (4.3) that a relationship similar to Eq. (10.3) must exist for the magnetic field as well:

$$\widetilde{\boldsymbol{\mathcal{H}}}(\mathbf{r},t) = \overleftrightarrow{\mathcal{T}}_{\mathcal{H}}(\mathbf{r},\hat{\mathbf{n}}^{\mathrm{inc}},\omega)\cdot\mathbf{H}_0^{\mathrm{inc}}\exp(-\mathrm{i}\omega t),\quad \mathbf{r}\in\Re^3, \tag{10.5}$$

where the transformation dyadic $\overleftrightarrow{\mathcal{T}}_{\mathcal{H}}$ is independent of $\mathbf{H}_0^{\mathrm{inc}}$, the latter being the complex amplitude of the incident plane wave:

$$\widetilde{\boldsymbol{\mathcal{H}}}^{\mathrm{inc}}(\mathbf{r},t) = \mathbf{H}_0^{\mathrm{inc}}\exp(\mathrm{i}k_1\hat{\mathbf{n}}^{\mathrm{inc}}\cdot\mathbf{r}-\mathrm{i}\omega t). \tag{10.6}$$

Let us now recall Eqs. (8.2) and (8.3), valid for any monochromatic field, and apply them separately to the total field $\{\boldsymbol{\mathcal{E}}(\mathbf{r},t),\boldsymbol{\mathcal{H}}(\mathbf{r},t)\}$ and the incident field $\{\boldsymbol{\mathcal{E}}^{\mathrm{inc}}(\mathbf{r},t),\boldsymbol{\mathcal{H}}^{\mathrm{inc}}(\mathbf{r},t)\}$. Then Eqs. (10.3) and (10.5) imply the following formula for the complex PST of the total field (Problem 10.1):

$$\overleftrightarrow{P}(\mathbf{r}) = \overleftrightarrow{\mathcal{T}}_{\mathcal{H}}(\mathbf{r},\hat{\mathbf{n}}^{\mathrm{inc}},\omega)\cdot\overleftrightarrow{P}^{\mathrm{inc}}\cdot[\overleftrightarrow{\mathcal{T}}_{\mathcal{E}}(\mathbf{r},\hat{\mathbf{n}}^{\mathrm{inc}},\omega)]^{\mathrm{T}*},\quad \mathbf{r}\in\Re^3, \tag{10.7}$$

where

$$\overleftrightarrow{P}^{\mathrm{inc}} = \frac{1}{2}\mathbf{H}_0^{\mathrm{inc}}\otimes[\mathbf{E}_0^{\mathrm{inc}}]^* \tag{10.8}$$

is the complex PST of the incident plane wave.

Equation (10.7) is the sought relationship between the complex PSTs of the total and incident fields. We will see in what follows that this formula is a template for many useful relationships between observable characteristics of the incident and total fields. Importantly, Eq. (10.7) demonstrates that, in general, the elements of the tensor $\overleftrightarrow{P}(\mathbf{r})$ depend on all the elements of the tensor $\overleftrightarrow{P}^{\mathrm{inc}}$. As a consequence, the complex Poynting vector of the total field cannot be uniquely

expressed in that of the incident field (Problem 10.2), which illustrates that electromagnetic scattering is a profoundly "vectorial" rather than "scalar" phenomenon. In other words, any characterization of electromagnetic scattering as a phenomenon resulting in the transformation of the intensity of the incident light into that of the scattered light is fundamentally wrong.

Equation (10.7) implies the existence of a linear (but not necessarily tensorial) operator which relates $\overleftrightarrow{P}(\mathbf{r})$ and $\overleftrightarrow{P}^{\text{inc}}$ while being independent of $\overleftrightarrow{P}^{\text{inc}}$. We will denote this operator by $\hat{\mathcal{T}}$ and write symbolically:

$$\overleftrightarrow{P}(\mathbf{r}) = \hat{\mathcal{T}}(\mathbf{r}, \hat{\mathbf{n}}^{\text{inc}}, \omega)\overleftrightarrow{P}^{\text{inc}}. \tag{10.9}$$

10.2 Polychromatic scattering by a fixed object

Our next step is to consider the incident field in the form of a polychromatic parallel beam with monochromatic components:

$$\widetilde{\boldsymbol{\mathcal{E}}}^{\text{inc}}(\mathbf{r}, t) = \sum_{n=1}^{N} \mathbf{E}_{0n}^{\text{inc}} \exp(\mathrm{i}k_1 \hat{\mathbf{n}}^{\text{inc}} \cdot \mathbf{r} - \mathrm{i}\omega_n t), \tag{10.10}$$

$$\widetilde{\boldsymbol{\mathcal{H}}}^{\text{inc}}(\mathbf{r}, t) = \sum_{n=1}^{N} \mathbf{H}_{0n}^{\text{inc}} \exp(\mathrm{i}k_1 \hat{\mathbf{n}}^{\text{inc}} \cdot \mathbf{r} - \mathrm{i}\omega_n t). \tag{10.11}$$

According to Section 4.2, the total complex polychromatic field everywhere in space is now given by

$$\widetilde{\boldsymbol{\mathcal{E}}}(\mathbf{r}, t) = \sum_{n=1}^{N} \overleftrightarrow{\mathcal{T}}_{\mathcal{E}}(\mathbf{r}, \hat{\mathbf{n}}^{\text{inc}}, \omega_n) \cdot \mathbf{E}_{0n}^{\text{inc}} \exp(-\mathrm{i}\omega_n t), \tag{10.12}$$

$$\widetilde{\boldsymbol{\mathcal{H}}}(\mathbf{r}, t) = \sum_{n=1}^{N} \overleftrightarrow{\mathcal{T}}_{\mathcal{H}}(\mathbf{r}, \hat{\mathbf{n}}^{\text{inc}}, \omega_n) \cdot \mathbf{H}_{0n}^{\text{inc}} \exp(-\mathrm{i}\omega_n t). \tag{10.13}$$

Applying the results of Section 9.1 separately to the total and incident polychromatic fields $\{\boldsymbol{\mathcal{E}}(\mathbf{r}, t), \boldsymbol{\mathcal{H}}(\mathbf{r}, t)\}$ and $\{\boldsymbol{\mathcal{E}}^{\text{inc}}(\mathbf{r}, t), \boldsymbol{\mathcal{H}}^{\text{inc}}(\mathbf{r}, t)\}$ implies that the time-averaged PST of the total polychromatic field is given by Eqs. (9.9) and (9.10), in which

$$\overleftrightarrow{P}_n(\mathbf{r}) = \overleftrightarrow{\mathcal{T}}_{\mathcal{H}}(\mathbf{r}, \hat{\mathbf{n}}^{\text{inc}}, \omega_n) \cdot \overleftrightarrow{P}_n^{\text{inc}} \cdot [\overleftrightarrow{\mathcal{T}}_{\mathcal{E}}(\mathbf{r}, \hat{\mathbf{n}}^{\text{inc}}, \omega_n)]^{\mathrm{T}*} \tag{10.14}$$

is the complex PST of the nth monochoromatic component of the total field, while

$$\overleftrightarrow{P}_n^{\text{inc}} = \frac{1}{2} \mathbf{H}_{0n}^{\text{inc}} \otimes [\mathbf{E}_{0n}^{\text{inc}}]^* \tag{10.15}$$

is the complex PST of the nth monochromatic component of the incident parallel beam. Equation (10.9) now takes the form

$$\ddot{P}(\mathbf{r}) = \sum_{n=1}^{N} \hat{\mathcal{T}}(\mathbf{r}, \hat{\mathbf{n}}^{\text{inc}}, \omega_n) \ddot{P}_n^{\text{inc}}. \tag{10.16}$$

Finally, consider the incident field in the form of a polychromatic parallel beam with quasi-monochromatic components:

$$\widetilde{\boldsymbol{\mathcal{E}}}^{\text{inc}}(\mathbf{r}, t) = \sum_{n=1}^{N} \mathbf{E}_{0n}^{\text{inc}}(t) \exp(\mathrm{i}k_1 \hat{\mathbf{n}}^{\text{inc}} \cdot \mathbf{r} - \mathrm{i}\omega_n t), \tag{10.17}$$

$$\widetilde{\boldsymbol{\mathcal{H}}}^{\text{inc}}(\mathbf{r}, t) = \sum_{n=1}^{N} \mathbf{H}_{0n}^{\text{inc}}(t) \exp(\mathrm{i}k_1 \hat{\mathbf{n}}^{\text{inc}} \cdot \mathbf{r} - \mathrm{i}\omega_n t). \tag{10.18}$$

For the total complex field everywhere in space, we now have:

$$\widetilde{\boldsymbol{\mathcal{E}}}(\mathbf{r}, t) = \sum_{n=1}^{N} \ddot{\mathcal{T}}_{\mathcal{E}}(\mathbf{r}, \hat{\mathbf{n}}^{\text{inc}}, \omega_n) \cdot \mathbf{E}_{0n}^{\text{inc}}(t) \exp(-\mathrm{i}\omega_n t), \tag{10.19}$$

$$\widetilde{\boldsymbol{\mathcal{H}}}(\mathbf{r}, t) = \sum_{n=1}^{N} \ddot{\mathcal{T}}_{\mathcal{H}}(\mathbf{r}, \hat{\mathbf{n}}^{\text{inc}}, \omega_n) \cdot \mathbf{H}_{0n}^{\text{inc}}(t) \exp(-\mathrm{i}\omega_n t). \tag{10.20}$$

As in Section 9.3, we assume that $\mathbf{E}_{0n}^{\text{inc}}(t)\exp(-\mathrm{i}\omega_n t)$ and $\mathbf{H}_{0n'}^{\text{inc}}(t)\exp(-\mathrm{i}\omega_{n'} t)$ for any $n \neq n'$ are independent and, thus, uncorrelated random processes with zero time averages. The time-averaged PST of the total polychromatic field is then given by Eqs. (9.25) and (9.26), in which

$$\langle\langle \ddot{P}_n(\mathbf{r}, t) \rangle\rangle = \ddot{\mathcal{T}}_{\mathcal{H}}(\mathbf{r}, \hat{\mathbf{n}}^{\text{inc}}, \omega_n) \cdot \langle\langle \ddot{P}_n^{\text{inc}}(t) \rangle\rangle \cdot [\ddot{\mathcal{T}}_{\mathcal{E}}(\mathbf{r}, \hat{\mathbf{n}}^{\text{inc}}, \omega_n)]^{\mathrm{T}*} \tag{10.21}$$

is the time-averaged complex PST of the nth quasi-monochromatic component of the total field and

$$\ddot{P}_n^{\text{inc}}(t) = \frac{1}{2} \mathbf{H}_{0n}^{\text{inc}}(t) \otimes [\mathbf{E}_{0n}^{\text{inc}}(t)]^* \tag{10.22}$$

is the time-dependent complex PST of the nth quasi-monochromatic component of the incident parallel beam. Note that $\langle\langle \ddot{P}_n^{\text{inc}}(t) \rangle\rangle$ and hence $\langle\langle \ddot{P}_n(\mathbf{r}, t) \rangle\rangle$ are independent of time owing to the presumed stationarity of the random functions $\mathbf{H}_{0n}^{\text{inc}}(t) \otimes [\mathbf{E}_{0n}^{\text{inc}}(t)]^*$. Equation (10.9) takes the form

$$\langle\langle \ddot{P}(\mathbf{r}, t) \rangle\rangle = \sum_{n=1}^{N} \hat{\mathcal{T}}(\mathbf{r}, \hat{\mathbf{n}}^{\text{inc}}, \omega_n) \langle\langle \ddot{P}_n^{\text{inc}}(t) \rangle\rangle. \tag{10.23}$$

Equations (10.14)–(10.16) and (10.21)–(10.23) are in fact quite remarkable. Indeed, they imply that to express any time-averaged observable characteristic of the total polychromatic field in terms of those of the incident field, all one needs to do is solve N independent monochromatic scattering problems (corresponding to the N participating angular frequencies ω_n) and then use the appropriate additivity rule for the total complex PST. The averaging time must be sufficiently long, as discussed in Sections 9.1 and 9.3.

10.3 Stochastic scattering object

The theory of electromagnetic scattering by a fixed object can be used directly to analyze the results of measurements with a microwave laboratory setup, such as the one shown in Fig. 1.6d. In most cases, however, the scattering object is stochastic in that its size, morphology, position, and/or orientation randomly change in time. We will see in Section 17.1 that changing the size and/or shape of an individual particle (such as the one shown in Plate 1.1a), even by a fraction of a wavelength, can modify the solution of the MMEs quite significantly. Morphological changes of a large scattering object such as a cloud of water droplets (Plate 1.1b) that occur over a small fraction of a second can be orders of magnitude greater and result in much more dramatic changes in the corresponding solution of the MMEs. In most cases, however, one is interested in time-averaged characteristics of the total electromagnetic field rather than in their detailed evolution caused by specific temporal changes of the scattering object.

To illustrate this point, let us consider a stochastic scatterer in the form of a cloud of particles, as shown in Fig. 10.1, and assume that the incident field is a monochromatic plane electromagnetic wave. Let us also assume that the cloud

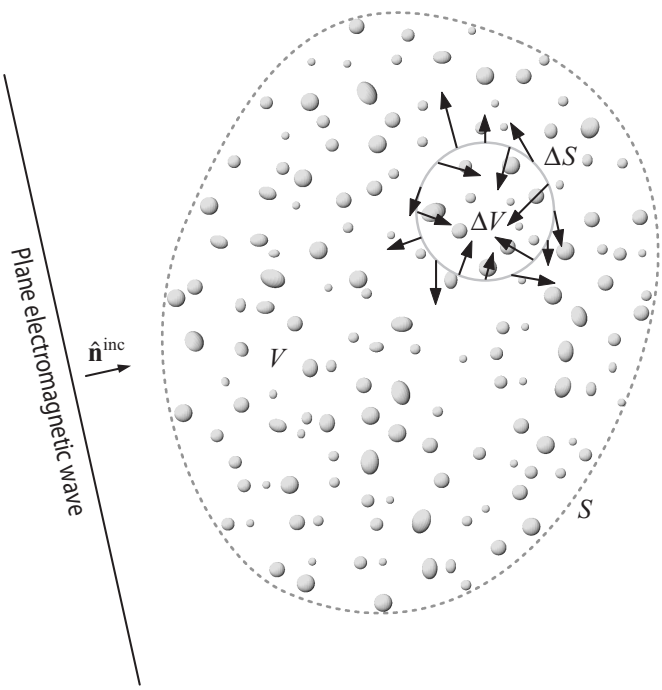

Fig. 10.1. Quasi-instantaneous energy budget of a volume element ΔV bounded by the closed surface ΔS. The arrows represent the distribution of $\langle \boldsymbol{\mathcal{S}}(\mathbf{r},t)\rangle$ over ΔS obtained by solving the MMEs for the specific instantaneous multiparticle configuration.

varies in time, but does it slowly enough that any *significant* (i.e., modifying the solution of the MMEs) changes of the cloud occur over time intervals T_v much longer than the period of time-harmonic oscillations of the electromagnetic field $T_o = 2\pi/\omega$. This allows us to compute the total field over any time interval much longer than T_o yet shorter than T_v by solving the frequency-domain MMEs (or, equivalently, the FEs). We can then use Eq. (2.61) to find the spatial distribution of the quasi-instantaneous Poynting vector obtained by averaging over a time interval T such that $T_o \ll T \ll T_v$ (see Section 2.3).

Given the morphological complexity of the cloud, this spatial distribution can be expected to be quite intricate and form a quasi-random speckle pattern. Figure 10.1 depicts schematically the distribution of the quasi-instantaneous Poynting vector $\langle \boldsymbol{\mathcal{S}}(\mathbf{r},t)\rangle$ over the closed boundary ΔS of a macroscopic volume element ΔV. This distribution depends on time, owing to temporal changes of the cloud, and fluctuates over time intervals of the order of T_v. According to Eq. (2.62), the quasi-instantaneous energy budget of the volume element ΔV is determined by integrating $\langle \boldsymbol{\mathcal{S}}(\mathbf{r},t)\rangle$ over ΔS:

$$\langle W_{\Delta S}(t)\rangle = -\oint_{\Delta S} \mathrm{d}^2\mathbf{r}\,\langle \boldsymbol{\mathcal{S}}(\mathbf{r},t)\rangle \cdot \hat{\mathbf{n}}(\mathbf{r}), \tag{10.24}$$

where $\langle W_{\Delta S}(t)\rangle \geq 0$ is the net amount of electromagnetic energy entering the volume element ΔV per unit time and $\hat{\mathbf{n}}(\mathbf{r})$ is the local outward normal to the boundary. If $\langle W_{\Delta S}(t)\rangle = 0$ then the incoming energy is balanced by the outgoing energy. Otherwise there is absorption of electromagnetic energy inside the volume element. The energy budget of the entire volume V occupied by the cloud is evaluated similarly, except now the integral in Eq. (10.24) is taken over the closed boundary S (Fig. 10.1).

In the majority of applications, one is interested in the energy budget averaged over a much longer period of time. This is because: (i) any actual measurement typically takes an amount of time much greater than T_v and/or (ii) the reaction of the cloud as a physical system to the incoming electromagnetic energy occurs on time scales much longer than T_v. To suppress the quasi-instantaneous speckle and thereby isolate the static pattern relevant to actual energy-budget applications, one must average $\boldsymbol{\mathcal{S}}(\mathbf{r},t)$ over an appropriately long time interval. The result is a much smoother distribution of the Poynting vector $\langle\langle \boldsymbol{\mathcal{S}}(\mathbf{r},t)\rangle\rangle$, as shown schematically in Fig. 10.2. Equation (10.24) now takes the form

$$\langle\langle W_{\Delta S}(t)\rangle\rangle = -\oint_{\Delta S} \mathrm{d}^2\mathbf{r}\,\langle\langle \boldsymbol{\mathcal{S}}(\mathbf{r},t)\rangle\rangle \cdot \hat{\mathbf{n}}(\mathbf{r}). \tag{10.25}$$

This example suggests that in the framework of typical applications of the theory of electromagnetic scattering, the basic quantity of actual relevance is the average of the PST over a relatively long time interval encompassing a representative set of physical states of a time-variable scattering object. It is therefore im-

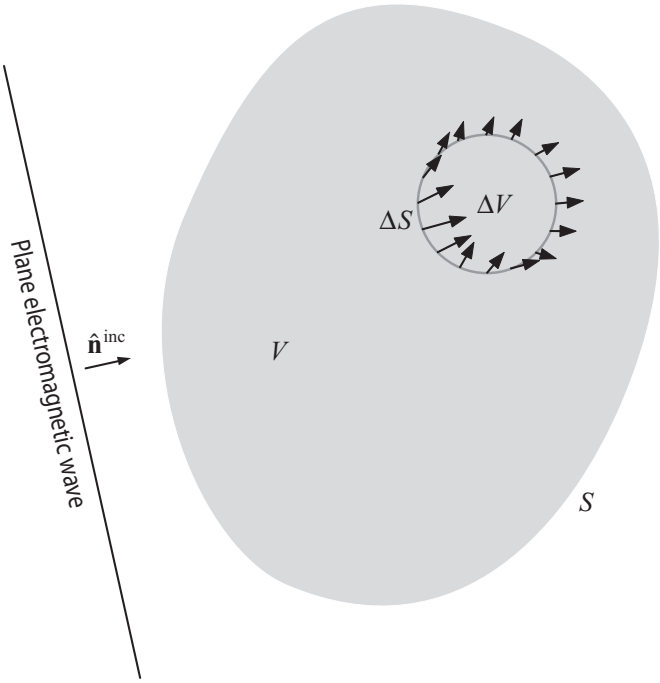

Fig. 10.2. Time-averaged energy budget of a volume element ΔV bounded by the closed surface ΔS. The arrows symbolize the distribution of $\langle\langle \boldsymbol{\mathcal{S}}(\mathbf{r}, t)\rangle\rangle$ over the boundary ΔS, while the uniform shading is intended to emphasize that cloud particles move randomly throughout the volume V during a time interval much longer than T_{v}.

portant to generalize the results of Sections 10.1 and 10.2 by explicitly allowing the scattering object to randomly change in time.

Assuming first that the incident field is a plane electromagnetic wave given by Eqs. (10.2) and (10.6), we have instead of Eqs. (10.1), (10.3), and (10.4):

$$\widetilde{\boldsymbol{\mathcal{E}}}^{\text{sca}}(\mathbf{r}, t) = \int_{V_{\text{INT}}(t)} \mathrm{d}^3\mathbf{r}' \overleftrightarrow{G}(\mathbf{r}, \mathbf{r}', k_1) \cdot \int_{V_{\text{INT}}(t)} \mathrm{d}^3\mathbf{r}'' \exp(\mathrm{i}k_1 \hat{\mathbf{n}}^{\text{inc}} \cdot \mathbf{r}'') \times \overleftrightarrow{T}(\mathbf{r}', \mathbf{r}'', \omega, t) \cdot \mathbf{E}_0^{\text{inc}} \exp(-\mathrm{i}\omega t), \quad \mathbf{r} \in \Re^3, \tag{10.26}$$

$$\widetilde{\boldsymbol{\mathcal{E}}}(\mathbf{r}, t) = \overleftrightarrow{\mathcal{T}}_{\mathcal{E}}(\mathbf{r}, \hat{\mathbf{n}}^{\text{inc}}, \omega, t) \cdot \mathbf{E}_0^{\text{inc}} \exp(-\mathrm{i}\omega t), \quad \mathbf{r} \in \Re^3, \tag{10.27}$$

$$\overleftrightarrow{\mathcal{T}}_{\mathcal{E}}(\mathbf{r}, \hat{\mathbf{n}}^{\text{inc}}, \omega, t) = \exp(\mathrm{i}k_1 \hat{\mathbf{n}}^{\text{inc}} \cdot \mathbf{r}) \overleftrightarrow{I} + \int_{V_{\text{INT}}(t)} \mathrm{d}^3\mathbf{r}' \overleftrightarrow{G}(\mathbf{r}, \mathbf{r}', k_1) \cdot \int_{V_{\text{INT}}(t)} \mathrm{d}^3\mathbf{r}'' \times \exp(\mathrm{i}k_1 \hat{\mathbf{n}}^{\text{inc}} \cdot \mathbf{r}'') \overleftrightarrow{T}(\mathbf{r}', \mathbf{r}'', \omega, t), \tag{10.28}$$

where at any moment t the transition dyadic operator is the solution of the following equation:

$$\begin{aligned}\ddot{T}(\mathbf{r},\mathbf{r}',\omega,t) &= k_1^2[m^2(\mathbf{r},\omega,t)-1]\,\delta(\mathbf{r}-\mathbf{r}')\ddot{I}\\ &\quad + k_1^2[m^2(\mathbf{r},\omega,t)-1]\int_{V_{\mathrm{INT}}(t)} \mathrm{d}^3\mathbf{r}''\,\ddot{G}(\mathbf{r},\mathbf{r}'',k_1)\cdot\ddot{T}(\mathbf{r}'',\mathbf{r}',\omega,t),\\ &\quad \mathbf{r},\mathbf{r}'\in V_{\mathrm{INT}}(t).\end{aligned} \tag{10.29}$$

Note that the relatively slow changes of the scattering object are accounted for by the explicit time dependence of the internal volume V_{INT} and the relative refractive index m. Similarly,

$$\widetilde{\mathcal{H}}(\mathbf{r},t) = \ddot{\mathcal{T}}_{\mathcal{H}}(\mathbf{r},\hat{\mathbf{n}}^{\mathrm{inc}},\omega,t)\cdot\mathbf{H}_0^{\mathrm{inc}}\exp(-\mathrm{i}\omega t), \quad \mathbf{r}\in\Re^3. \tag{10.30}$$

This means that the quasi-instantaneous Poynting vector obtained by averaging over a time interval $T_{\mathrm{o}} \ll T \ll T_{\mathrm{v}}$ is now time-dependent and given by

$$\langle\ddot{\mathcal{P}}(\mathbf{r},t)\rangle = \mathrm{Re}[\ddot{P}(\mathbf{r},t)]^{\mathrm{T}}, \tag{10.31}$$

where

$$\ddot{P}(\mathbf{r},t) = \hat{\mathcal{T}}(\mathbf{r},\hat{\mathbf{n}}^{\mathrm{inc}},\omega,t)\,\ddot{P}^{\mathrm{inc}}. \tag{10.32}$$

Averaging Eqs. (10.31) and (10.32) over a time interval $T \gg T_{\mathrm{v}}$ yields Eq. (9.25) in which

$$\langle\langle\ddot{P}(\mathbf{r},t)\rangle\rangle = \langle\langle\hat{\mathcal{T}}(\mathbf{r},\hat{\mathbf{n}}^{\mathrm{inc}},\omega,t)\rangle\rangle\,\ddot{P}^{\mathrm{inc}}. \tag{10.33}$$

Assuming that the actual temporal variability of the stochastic scattering object causes $\hat{\mathcal{T}}(\mathbf{r},\hat{\mathbf{n}}^{\mathrm{inc}},\omega,t)$ to be a stationary random process and that T is sufficiently long implies that $\langle\langle\ddot{P}(\mathbf{r},t)\rangle\rangle$ and thus $\langle\langle\ddot{\mathcal{P}}(\mathbf{r},t)\rangle\rangle$ are independent of t.

Finally, let us consider the incident field in the form of a polychromatic parallel beam with quasi-monochromatic components, as defined by Eqs. (10.17) and (10.18). The total complex field is now given by

$$\widetilde{\mathcal{E}}(\mathbf{r},t) = \sum_{n=1}^{N}\ddot{\mathcal{T}}_{\mathcal{E}}(\mathbf{r},\hat{\mathbf{n}}^{\mathrm{inc}},\omega_n,t)\cdot\mathbf{E}_{0n}^{\mathrm{inc}}(t)\exp(-\mathrm{i}\omega_n t), \tag{10.34}$$

$$\widetilde{\mathcal{H}}(\mathbf{r},t) = \sum_{n=1}^{N}\ddot{\mathcal{T}}_{\mathcal{H}}(\mathbf{r},\hat{\mathbf{n}}^{\mathrm{inc}},\omega_n,t)\cdot\mathbf{H}_{0n}^{\mathrm{inc}}(t)\exp(-\mathrm{i}\omega_n t) \tag{10.35}$$

and is also a polychromatic field with quasi-monochromatic components. Furthermore, each quasi-monochromatic component of the total field has a zero time average:

$$\begin{aligned}&\langle\ddot{\mathcal{T}}_{\mathcal{E}}(\mathbf{r},\hat{\mathbf{n}}^{\mathrm{inc}},\omega_n,t)\cdot\mathbf{E}_{0n}^{\mathrm{inc}}(t)\exp(-\mathrm{i}\omega_n t)\rangle\\ &= \langle\ddot{\mathcal{T}}_{\mathcal{H}}(\mathbf{r},\hat{\mathbf{n}}^{\mathrm{inc}},\omega_n,t)\cdot\mathbf{H}_{0n}^{\mathrm{inc}}(t)\exp(-\mathrm{i}\omega_n t)\rangle = \mathbf{0}\end{aligned} \tag{10.36}$$

(cf. Eq. (9.24)). Therefore, the corresponding results of Section 9.3 can be applied to both the incident and the total field. It is easy to verify that the time-averaged PST of the total field is again given by Eqs. (9.25) and (9.26), in which

$$\langle\langle \vec{P}_n(\mathbf{r},t)\rangle\rangle = \langle\langle \overleftrightarrow{\mathcal{T}}_{\mathcal{H}}(\mathbf{r},\hat{\mathbf{n}}^{\text{inc}},\omega_n,t)\cdot \vec{P}_n^{\text{inc}}(t)\cdot[\overleftrightarrow{\mathcal{T}}_{\mathcal{E}}(\mathbf{r},\hat{\mathbf{n}}^{\text{inc}},\omega_n,t)]^{\text{T}*}\rangle\rangle$$
$$= \langle\langle \hat{\mathcal{T}}(\mathbf{r},\hat{\mathbf{n}}^{\text{inc}},\omega_n,t)\vec{P}_n^{\text{inc}}(t)\rangle\rangle. \tag{10.37}$$

Making the reasonable assumption that $\hat{\mathcal{T}}(\mathbf{r},\hat{\mathbf{n}}^{\text{inc}},\omega_n,t)$ and $\vec{P}_n^{\text{inc}}(t)$ for any n are independent stationary random processes, we finally derive:

$$\langle\langle \vec{P}(\mathbf{r},t)\rangle\rangle = \sum_{n=1}^{N}\langle\langle \hat{\mathcal{T}}(\mathbf{r},\hat{\mathbf{n}}^{\text{inc}},\omega_n,t)\rangle\rangle\langle\langle \vec{P}_n^{\text{inc}}(t)\rangle\rangle, \tag{10.38}$$

where all time averages are independent of t provided that averaging is performed over a time interval T such that $T \gg T_{\text{v}}$ and $T \gg T_{\text{f}n}$ for any n.

The only difference of the latter formula from Eq. (10.23) valid for a fixed scattering object is that the constant operator $\hat{\mathcal{T}}(\mathbf{r},\hat{\mathbf{n}}^{\text{inc}},\omega_n)$ is replaced by the time-averaged operator $\langle\langle \hat{\mathcal{T}}(\mathbf{r},\hat{\mathbf{n}}^{\text{inc}},\omega_n,t)\rangle\rangle$. In other words, the averaging over time of the complex PST of the incident polychromatic beam is completely separated from the averaging over time of the transformation operator $\hat{\mathcal{T}}$. We will see in what follows that this separation offers substantial simplifications in many theoretical derivations.

10.4 Ergodicity

The time average of the transformation operator $\hat{\mathcal{T}}$ in Eqs. (10.33) and (10.38) is formally defined by

$$\langle\langle \hat{\mathcal{T}}(\mathbf{r},\hat{\mathbf{n}}^{\text{inc}},\omega,t)\rangle\rangle = \frac{1}{T}\int_{t-T/2}^{t+T/2} \mathrm{d}t'\,\hat{\mathcal{T}}(\mathbf{r},\hat{\mathbf{n}}^{\text{inc}},\omega,t'), \tag{10.39}$$

where the time interval T is much longer than T_{v}. During this time interval a variable scattering object goes through an infinite sequence of evolving discrete states governed by relevant physical and chemical processes. Therefore, the right-hand side of Eq. (10.39) must be evaluated by: (i) tracing the temporal evolution of the internal volume $V_{\text{INT}}(t)$ and the relative refractive index $m(\mathbf{r},\omega,t)$ and (ii) computing $\hat{\mathcal{T}}(\mathbf{r},\hat{\mathbf{n}}^{\text{inc}},\omega,t')$ for a sufficiently representative set of moments $t' \in [t-T/2, t+T/2]$. A computer implementation of this averaging procedure is not totally inconceivable, at least in some special cases. However, the direct use of the definition (10.39) in analytical derivations – such as the derivation of the radiative transfer equation for a cloud of water droplets – typically leads to insurmountable technical difficulties. A far more practical approach in such cases is based on the assumption of ergodicity.

Specifically, all further discussion of electromagnetic scattering by a time-variable object will be based on the following two fundamental premises:

- The scattering object can be uniquely characterized at any moment by a finite set of physical parameters.

- The scattering object is statistically random and sufficiently variable in time, and the time interval T is sufficiently long that averaging $\hat{\mathcal{T}}$ over this interval is essentially equivalent to averaging $\hat{\mathcal{T}}$ over an appropriate analytical probability distribution of the physical parameters characterizing the scattering object.

In other words, we will assume in what follows that averaging over time for one specific realization of a random scattering process is equivalent to ensemble averaging. The equivalence of the time and ensemble averages is traditionally called *ergodicity*.

To better understand the meaning of ergodicity, let us denote by $\psi(t)$ the set of parameters providing the complete optical specification (or the state) of the stochastic scattering object at the moment t, i.e., the internal volume $V_{\mathrm{INT}}(t)$ and the relative refractive index $m(\mathbf{r}, \omega, t)$. $\hat{\mathcal{T}}$ depends on time by being a function of $\psi(t)$. It is convenient to rewrite Eq. (10.39) in a condensed form:

$$\langle\langle \hat{\mathcal{T}}(t) \rangle\rangle = \frac{1}{T}\int_{t-T/2}^{t+T/2} \mathrm{d}t' \hat{\mathcal{T}}[\psi(t')]. \tag{10.40}$$

Although the temporal variation of ψ is assumed to be a random process, the explicit calculation of the integral in Eq. (10.40) requires the use of a particular realization of this process in the form of a specific – albeit fluctuating and "random-looking" – function of time $\psi_1(t')$. The use of another realization of the same random process, $\psi_2(t')$, may result in a somewhat different value of $\langle\langle \hat{\mathcal{T}}(t) \rangle\rangle$. However, with increasing T the range of instantaneous states of the object captured by the time interval $[t - T/2, t + T/2]$ eventually becomes representative of that captured by an infinitely long time interval, thereby yielding a t-independent and realization-independent average $\langle\langle \hat{\mathcal{T}} \rangle\rangle$:

$$\lim_{T\to\infty} \frac{1}{T}\int_{t_1-T/2}^{t_1+T/2} \mathrm{d}t' \hat{\mathcal{T}}[\psi_1(t')] = \lim_{T\to\infty} \frac{1}{T}\int_{t_2-T/2}^{t_2+T/2} \mathrm{d}t' \hat{\mathcal{T}}[\psi_2(t')] = \langle\langle \hat{\mathcal{T}} \rangle\rangle. \tag{10.41}$$

Notice now that in the limit $T \to \infty$, the integrals in Eq. (10.41) can be expected to "sample" virtually every physically realizable state ψ of the object. Furthermore, this sampling becomes statistically representative in that the number of times each state is sampled is large and tends to infinity in the limit $T \to \infty$. Most importantly, the cumulative contribution of a state ψ to $\langle\langle \hat{\mathcal{T}} \rangle\rangle$ is independent of the specific moment in time when this state actually occurred in the process of the temporal evolution of the scattering object. Rather, it depends on how many times this state was sampled. Therefore, this cumulative contribution can be thought of as being proportional to the probability of occurrence of the state ψ at *any* moment of time. This means that instead of specifying the state of the cloud at each moment t' and integrating over all t', one can introduce an appropriate time-independent probability density function $p(\psi)$ and integrate over the entire physically realizable range of states:

$$\langle\langle \hat{\mathcal{T}} \rangle\rangle \approx \int \mathrm{d}\psi\, p(\psi)\hat{\mathcal{T}}(\psi) = \langle \hat{\mathcal{T}} \rangle_{\psi}, \tag{10.42}$$

where $p(\psi)$ is normalized according to

$$\int \mathrm{d}\psi\, p(\psi) = 1. \tag{10.43}$$

Equation (10.42) is the formal mathematical expression of the principle of ergodicity introduced above.

It should be kept in mind that for the assumption of ergodicity to yield an accurate estimate of the time average $\langle\langle \hat{\mathcal{T}} \rangle\rangle$, the time interval T must be sufficiently long. Physical processes such as Brownian motion and turbulence often help to establish a significant degree of randomness of particle positions and orientations in a multi-particle scattering object, which seems to explain why many theoretical predictions based on the assumption of ergodicity have agreed well with experimental data (Berne and Pecora 1976). The assumption of ergodicity may appear to be far-fetched in the case of a large complex scattering object such as a cloud. However, there are factors making ergodicity more plausible in the practical rather than strictly mathematical sense. They will be discussed specifically in Section 19.13.

Problems

10.1: Derive Eq. (10.7).

10.2: Show that in general, the complex Poynting vector of the total (and hence scattered) monochromatic field cannot be expressed uniquely in that of the incident monochromatic field.

10.3: How do Eqs. (10.16), (10.23), and (10.38) change if the various monochromatic or quasi-monochromatic components of the incident field are allowed to have different incidence directions?

Notes and further reading

The ergodic hypothesis was introduced by James Clerk Maxwell and the great Austrian physicist Ludwig Boltzmann (1844–1906) as a basic underlying principle of statistical mechanics and kinetic theory. The mathematical aspects of the ergodic theory, its relation to the famous Poincaré recurrence theorem (Poincaré 1890), and its applications to statistical physics are described by Khinchin (1949), Uhlenbeck and Ford (1963), and Farquhar

Ludwig Boltzmann

(1964). Instructive discussions of the ergodic hypothesis and specific examples of nonergodic scattering media can be found in Pusey and van Megen (1989), Joosten *et al.* (1990), Xue *et al.* (1992), Nisato *et al.* (2000), and Scheffold *et al.* (2001).

11

Measurement of electromagnetic energy flow

Measurements of electromagnetic energy flow are an integral part of solving various energy-budget and optical-characterization problems. For example, the physical state of a cloud of water droplets or ice crystals in the terrestrial atmosphere can be affected by an imbalance between the incoming and outgoing electromagnetic energy, while measurements of specific manifestations of electromagnetic energy flow with a suitable device can potentially be analyzed to infer useful information about the cloud. Conceptually similar problems are encountered in many other areas of science and engineering. It is therefore very important to understand clearly what specific measurement is afforded by an optical instrument and how to model this measurement theoretically.

Let us recall, for example, the energy-budget problem for a macroscopic volume element of an idealized liquid-water cloud discussed in Section 1.4. Suppose that we have at our disposal a Poynting-meter, i.e., a device that can determine both the direction and the absolute value of the time-averaged local Poynting vector. Then measuring $\langle\langle \boldsymbol{\mathcal{S}}(\mathbf{r}, t)\rangle\rangle$ at a sufficiently representative number of points densely distributed over the boundary ΔS would enable one to evaluate the integral in Eq. (1.12) numerically and thereby quantify the degree of electromagnetic energy imbalance of the volume element ΔV.

Unfortunately, none of the existing photometers can, strictly speaking, be considered a Poynting-meter. Despite the wide variety of specific designs and the alleged ability to quantify the electromagnetic energy flow (e.g., Bukshtab 2012), the actual physical nature of the measurements afforded by these instruments had remained poorly understood and had rarely been formulated in the context of advanced theories of light–matter interactions. Furthermore, it had hardly been recognized that the physical meaning of the signal generated by these instruments depends critically on the very nature of the electromagnetic field transporting radiative energy and hence on the object creating the electromagnetic field.

The goal of this chapter is to clarify the physical framework of the measurement with instruments that can be called "well-collimated radiometers" (WCRs).

They represent by far the most widely used class of photometers, which makes it imperative to have a clear understanding of what these instruments can really measure. In particular, the following sections are intended to:

- summarize the basic operational principle of photoelectric detectors in the context of the QED theory of the photoelectric effect;
- clarify the actual role of the optical tract of a WCR;
- analyze the interaction of the electromagnetic radiation filtered out by the optical tract of a WCR with the end photodetector;
- identify quantitative attributes of the electromagnetic energy flow that can be captured by a WCR, depending on the specific measurement setting; and
- discuss how these attributes can be modeled theoretically for morphologically complex scattering objects and thereby enter the solution of energy-budget as well as optical-characterization problems.

As was pointed out in Section 2.4, the Poynting vector does not, strictly speaking, characterize the direction and rate of the local electromagnetic energy flow. It is, however, important to recognize that if one can measure the local time-averaged Poynting vector then Eq. (1.12) (or Eq. (2.62)) can be used to evaluate the radiative energy budget of the object in question, irrespective of the physical meaning of the vector product $\boldsymbol{\mathcal{E}}(\mathbf{r},t)\times\boldsymbol{\mathcal{H}}(\mathbf{r},t)$. Therefore, it is the practical measurability of the Poynting vector that will be one of the foci of the following discussion. We will not consider technical and technological issues related to the development of sensitive and efficient detectors of light. Instead, we will concentrate on the precise definitions of general measurement principles and their specific practical implications in the framework of electromagnetic scattering by particles and particle groups.

11.1 Direction-insensitive detectors

Typical devices used for the detection and quantification of electromagnetic energy flow are photomultipliers, photodiodes, and photoelectric charge-coupled

(a) (b) (c)

Fig. 11.1. Typical detectors of electromagnetic energy flow based on the photoelectric effect: **(a)** a photomultiplier, **(b)** a photodiode, and **(c)** a CCD.

devices (CCDs) illustrated in Fig. 11.1. A photomultiplier or a photodiode is a single photodetector reacting to the electromagnetic field "impinging" anywhere on its relatively large sensitive surface, whereas a photoelectric CCD is a two-dimensional array of smaller detectors (pixels) that are designed to react to the incoming electromagnetic field independently of each other. All these devices are based on the absorption of electromagnetic energy via the photoelectric effect. The physical nature of this phenomenon is well understood, both in the framework of the semi-classical approach, wherein only the matter is quantized, while the electromagnetic field is treated classically (Dodd 1991), and in the framework of QED, wherein one quantizes both the matter and the electromagnetic field (Mandel and Wolf 1995).

The essential property of the photoelectric effect is the Stoletov law, according to which the photoelectric current is proportional to the intensity of the incident light. Although this law was discovered experimentally in 1889, it has since been confirmed and refined theoretically. The principal result of the most general QED treatment today can be formulated as follows (Kimble and Mandel 1984). Let us model the sensitive element of a photodetector as a thin plane-parallel layer. The outer flat surface of this layer S_{pd} is exposed to a parallel beam of light that has an effectively infinite lateral extent, propagates normally to the surface, and consists of $N \geq 1$ quasi-monochromatic components with different angular frequencies ω_n, where n numbers the quasi-monochromatic beams, so that $1 \leq n \leq N$. The local sensitivity of the detector is assumed to be uniform over S_{pd} and axially symmetric with respect to the local normal to S_{pd}. Then the total number of photoelectrons recorded by the photodetector during a sufficiently long time interval T is given by

$$N_{\mathrm{pe}}(T) = T S_{\mathrm{pd}} \sum_{n=1}^{N} K^{\mathrm{pd}}(\omega_n) \langle\langle I_n(t) \rangle\rangle, \tag{11.1}$$

where $\langle\langle I_n(t) \rangle\rangle$ is the time-averaged intensity of the nth quasi-monochromatic component and $K^{\mathrm{pd}}(\omega_n)$ is the quantum efficiency of the photodetector at the frequency ω_n.

Despite the great practical importance of Eq. (11.1), it is imperative to always remember the specific conditions of its applicability formulated in the preceding paragraph. Any violation of these conditions may lead to complications and potentially significant uncertainties. Indeed, the angular distribution of the emitted photoelectrons is not isotropic and, furthermore, can depend on the polarization state of the incident beam (Lee 1974; Huang 1980). The efficiency with which the photodetector collects the emitted photoelectrons propagating in various directions can never be perfectly uniform and, in reality, can be substantially anisotropic. This anisotropy can be expected to be especially pronounced for thicker sensitive layers (Berglund and Spicer 1964). As a consequence, real photodetectors can exhibit strong sensitivity to the direction of propagation and

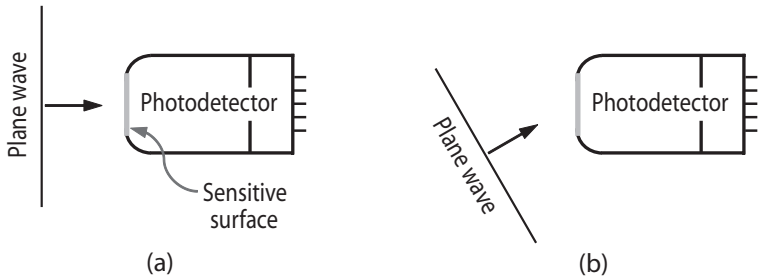

Fig. 11.2. A photodetector exposed to a plane electromagnetic wave.

polarization state of the incident beam (Munz 1975; Chyba and Mandel 1988). The polarization sensitivity can often be mitigated by placing a depolarizer in front of the photodetector, but the angular sensitivity may be more difficult to compensate for. It is, therefore, essential to limit the practical use of photoelectric detectors to the case of parallel-beam illumination in the direction normal to the detector sensitive surface.

It is important to remember that Eq. (11.1) was specifically derived for a parallel polychromatic incident beam with quasi-monochromatic components propagating in the same direction, which makes it inapplicable to the case of uncollimated incident light.

11.2 Photoelectric detector as a Poynting-meter

The simplest photometer is a "bare" photoelectric detector with no optical elements – except, perhaps, a depolarizer – placed in front of its sensitive surface. Let us first assume that the detector is exposed to a plane electromagnetic wave propagating perpendicularly to its sensitive surface, as shown schematically in Fig. 11.2a. At any point of the sensitive surface, the direction of the instantaneous local Poynting vector is normal to the surface. Furthermore, the magnitude of the Poynting vector is uniform across the sensitive surface. We have seen in Section 3.1 that the time-averaged Poynting vector of a plane electromagnetic wave is given by

$$\langle \boldsymbol{\mathcal{S}}(\mathbf{r},t)\rangle = \hat{\mathbf{n}} I, \tag{11.2}$$

where the unit vector $\hat{\mathbf{n}}$ specifies the direction of wave propagation and I is the intensity of the wave. Since the direction $\hat{\mathbf{n}}$ is assumed to be known, the measurement illustrated in Fig. 11.2a can be thought of as yielding the time-averaged Poynting vector of the plane wave:

$$\langle \boldsymbol{\mathcal{S}}(\mathbf{r},t)\rangle = \frac{N_{\mathrm{pe}}(T)}{T S_{\mathrm{pd}} K^{\mathrm{pd}}(\omega)} \hat{\mathbf{n}}, \tag{11.3}$$

where ω is the corresponding angular frequency.

More generally, let us assume that the detector is illuminated by a superposition of N parallel quasi-monochromatic beams propagating in the same direction $\hat{\mathbf{n}}$ and having angular frequencies close enough so that for any $1 \le n \le N$,

$$K^{\mathrm{pd}}(\omega_n) \approx K^{\mathrm{pd}}. \tag{11.4}$$

Then Eq. (11.1) implies that

$$\langle\langle \boldsymbol{\mathcal{S}}(\mathbf{r},t)\rangle\rangle = \frac{N_{\mathrm{pe}}(T)}{T S_{\mathrm{pd}} K^{\mathrm{pd}}}\hat{\mathbf{n}}, \tag{11.5}$$

where

$$\langle\langle \boldsymbol{\mathcal{S}}(\mathbf{r},t)\rangle\rangle = \sum_{n=1}^{N} \langle\langle \boldsymbol{\mathcal{S}}_n(\mathbf{r},t)\rangle\rangle \tag{11.6}$$

is the time-averaged Poynting vector of the total beam and $\langle\langle \boldsymbol{\mathcal{S}}_n(\mathbf{r},t)\rangle\rangle$ is that of the nth quasi-monochromatic component (see Eq. (9.29)). Thus, in the limited measurement setting, wherein the direction of the Poynting vector is constant and is assumed to be known, the photodetector can be said to serve as the Poynting-meter.

In practice, the active surface of the photodetector may be polarization sensitive, in which case the actual reading of the detector is proportional to $\langle\langle I\rangle\rangle + \alpha_Q\langle\langle Q\rangle\rangle + \alpha_U\langle\langle U\rangle\rangle + \alpha_V\langle\langle V\rangle\rangle$, where one or more of the proportionality factors α_Q, α_U, and α_V is not equal to zero. In order to make the intensity measurement depicted in Fig. 11.2a useful, one must ensure that α_Q, α_U, and α_V are much smaller (in the absolute-value sense) than unity. As we have indicated previously, this can often be accomplished by placing a depolarizer in front of the photodetector.

The interpretation of the measurement with the photodetector becomes more uncertain if the propagation direction of the plane electromagnetic wave or the parallel polychromatic beam of light is arbitrary and is not known *a priori* (see Fig. 11.2b). In this case the electromagnetic power intercepted by the active surface scales as $\cos\theta$, where θ is the (unknown) angle between the propagation direction and the normal to the surface. Furthermore, the proportionality coefficients can also be expected to have a complex dependence on θ. As a consequence, the reading of the photodetector is now proportional to $\cos\theta[\alpha_I(\theta) \times\langle\langle I\rangle\rangle + \alpha_Q(\theta)\langle\langle Q\rangle\rangle + \alpha_U(\theta)\langle\langle U\rangle\rangle + \alpha_V(\theta)\langle\langle V\rangle\rangle]$, where $\alpha_I(\theta)$ is not necessarily equal to unity and θ is unknown. These factors make problematic the use of the photodetector as a Poynting-meter, even if a high-quality depolarizer is placed in front of the sensitive surface.

Even more problematic is the situation depicted in Fig. 11.3. Now the photodetector is placed inside a cloud composed of M randomly positioned and randomly moving particles. This implies that the detector is located in the near zone of the entire scattering object and that the electromagnetic field impinging on the

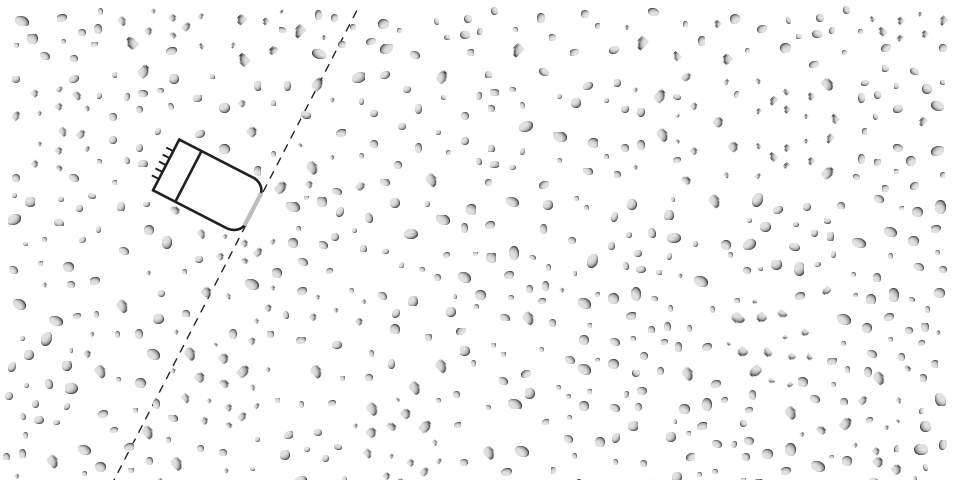

Fig. 11.3. A "near-zone" photodetector placed inside the scattering object in the form of a cloud of M randomly moving discrete particles.

sensitive surface is not a locally unidirectional transverse electromagnetic wave or a parallel polychromatic beam. The direction and magnitude of the instantaneous Poynting vector are now intricate functions of time and are also quite variable across the sensitive surface of the detector. As a consequence, the measurement afforded by the photodetector becomes essentially useless.

Even more fundamentally, the local Poynting vector at any point $\mathbf{r}$ of the sensitive surface at any moment in time is not the same as it would be in the absence of the detector. Indeed, let us assume for simplicity that the particles are separated widely enough to satisfy the conditions of applicability of the far-field FEs. Then, according to Eqs. (6.34)–(6.35), the total instantaneous electric and magnetic fields at $\mathbf{r}$ in the absence of the detector are superpositions of the respective incident and M scattered fields:

$$\boldsymbol{\mathcal{E}}(\mathbf{r},t) = \boldsymbol{\mathcal{E}}^{\text{inc}}(\mathbf{r},t) + \sum_{i=1}^{M} \boldsymbol{\mathcal{E}}_i^{\text{sca}}(\mathbf{r},t), \qquad \boldsymbol{\mathcal{H}}(\mathbf{r},t) = \boldsymbol{\mathcal{H}}^{\text{inc}}(\mathbf{r},t) + \sum_{i=1}^{M} \boldsymbol{\mathcal{H}}_i^{\text{sca}}(\mathbf{r},t), \quad (11.7)$$

where $\boldsymbol{\mathcal{E}}_i^{\text{sca}}(\mathbf{r},t)$ and $\boldsymbol{\mathcal{H}}_i^{\text{sca}}(\mathbf{r},t)$ describe an outgoing spherical wavelet centered at the origin of particle i. The corresponding local instantaneous Poynting vector is given by the vector product $\boldsymbol{\mathcal{S}}(\mathbf{r},t) = \boldsymbol{\mathcal{E}}(\mathbf{r},t)\times\boldsymbol{\mathcal{H}}(\mathbf{r},t)$. The major side effect of the presence of the detector is to block the spherical wavelets generated by the M' particles located to the left of the plane through the sensitive surface shown schematically by the dashed line in Fig. 11.3. The resulting "truncated" electric and magnetic fields at $\mathbf{r}$ are now given by

$$\boldsymbol{\mathcal{E}}'(\mathbf{r},t) = \sum_{i=1}^{M-M'} \boldsymbol{\mathcal{E}}_i^{\text{sca}}(\mathbf{r},t), \qquad \boldsymbol{\mathcal{H}}'(\mathbf{r},t) = \sum_{i=1}^{M-M'} \boldsymbol{\mathcal{H}}_i^{\text{sca}}(\mathbf{r},t), \quad (11.8)$$

where the sums include only the contributions from the $M - M'$ "unblocked" particles, and we assume that the detector blocks the incident plane wave as well. It is quite obvious that the corresponding "truncated" Poynting vector is not equal to the original Poynting vector: $\boldsymbol{\mathcal{S}}'(\mathbf{r}, t) = \boldsymbol{\mathcal{E}}'(\mathbf{r}, t) \times \boldsymbol{\mathcal{H}}'(\mathbf{r}, t) \neq \boldsymbol{\mathcal{S}}(\mathbf{r}, t)$.

The photodetectors shown in Fig. 11.1 can be called direction insensitive owing to their inability to accurately decouple the direction and magnitude of the Poynting vector. The applicability of such instruments to the measurement of the Poynting vector is quite limited and relies on the following assumptions:

- the incoming radiation is a plane electromagnetic wave or a parallel polychromatic beam of light known to propagate perpendicularly to the sensitive surface of the photodetector;
- the incoming radiation is (or is made) unpolarized; and
- the range of constituent angular frequencies of the incoming polychromatic beam is narrow enough that the quantum efficiency of the photodetector can be considered frequency independent.

11.3 Preisendorfer's radiance-function meter

In his search of a connection between the "mainland" of fundamental electromagnetics and the "island" of phenomenological photometry, Preisendorfer (1965) suggested a thought experiment allegedly yielding a direct measurement of the time-averaged Poynting vector. Although it turns out that this thought experiment cannot be realized in practice, an analysis of its deficiencies is quite instructive and exposes the nature of major problems encountered in near-field measurements of directional electromagnetic energy flow, as exemplified by Fig. 11.3.

A hypothetical instrument capable of measuring both the direction and the magnitude of the Poynting vector of a plane electromagnetic wave (or a parallel polychromatic beam of light) is shown schematically in Plate 11.1a. The sensitive surface of this detector S_d is polarization insensitive, is exposed directly to the incoming radiation, and is assumed to react to the local instantaneous Poynting vector only if this vector is directed along or almost along the optical axis of the instrument defined by the unit vector $\hat{\mathbf{q}}$ normal to S_d. Specifically, if the direction of $\boldsymbol{\mathcal{S}}(\mathbf{r}', t)$ at any point $\mathbf{r}'$ of the sensitive surface at any moment t is within the small acceptance solid angle $\Delta\Omega_{\hat{\mathbf{q}}}$ of the detector (e.g., vector $\boldsymbol{\mathcal{S}}_1$ in Plate 11.1a) then this vector contributes to the cumulative reading of the instrument. Instantaneous local Poynting vectors with directions outside $\Delta\Omega_{\hat{\mathbf{q}}}$ (e.g., vectors $\boldsymbol{\mathcal{S}}_2$ and $\boldsymbol{\mathcal{S}}_3$) are ignored by the instrument and do not contribute to its reading.

Let us first assume that this hypothetical directional detector of electromagnetic energy flow is exposed to a monochromatic or quasi-monochromatic plane electromagnetic wave (Fig. 11.4) or, more generally, a parallel polychromatic

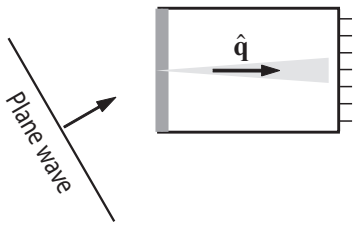

Fig. 11.4. A hypothetical directional detector exposed to a plane electromagnetic wave.

beam of light. It is clear that even if the propagation direction of the incoming light is unknown, it can be determined accurately by scanning all directions $\hat{\mathbf{q}} \in 4\pi$. As a result, both the direction and the magnitude of the Poynting vector can be determined.

The near-field situation shown in Fig. 11.5 is much more complex. In this case the instantaneous local Poynting vector varies very rapidly both in time and across the sensitive area of the detector. At any given moment t' and for any given orientation of the detector $\hat{\mathbf{q}}$, there can be differential elements of the sensitive surface S_d at which the direction of the local instantaneous Poynting vector is very close to $\hat{\mathbf{q}}$. Therefore, the time average of the signal generated by the directional detector is proportional to the following double integral:

$$\frac{1}{T}\int_{S_\mathrm{d}} \mathrm{d}^2\mathbf{r}' \int_{t-T/2}^{t+T/2} \mathrm{d}t' \,|\boldsymbol{\mathcal{S}}(\mathbf{r}', t')|\, \chi[\Delta\Omega_{\hat{\mathbf{q}}}, \hat{\boldsymbol{s}}(\mathbf{r}', t')], \tag{11.9}$$

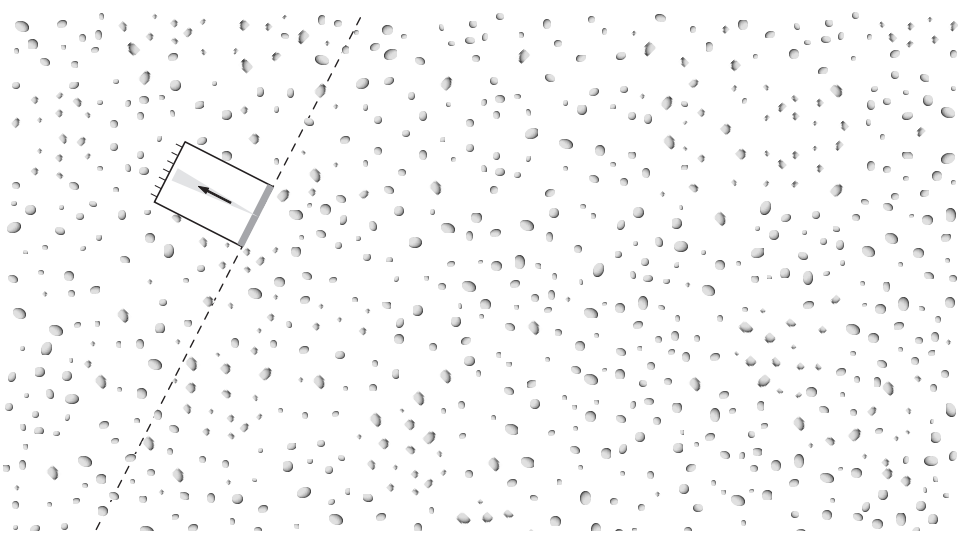

Fig. 11.5. The hypothetical directional detector is placed inside a cloud of randomly moving particles.

where $\hat{\mathbf{s}}(\mathbf{r}', t') = \boldsymbol{\mathcal{S}}(\mathbf{r}', t')/|\boldsymbol{\mathcal{S}}(\mathbf{r}', t')|$ is the unit vector in the direction of the local instantaneous Poynting vector $\boldsymbol{\mathcal{S}}(\mathbf{r}', t')$, while the step function

$$\chi[\Delta\Omega_{\hat{\mathbf{q}}}, \hat{\mathbf{s}}(\mathbf{r}', t')] = \begin{cases} 1 \text{ if } \hat{\mathbf{s}}(\mathbf{r}', t') \in \Delta\Omega_{\hat{\mathbf{q}}}, \\ 0 \text{ otherwise} \end{cases} \tag{11.10}$$

describes the directional selectivity of the instrument. It is now appropriate to introduce the quantity

$$\widetilde{N}(\mathbf{r}, \hat{\mathbf{q}}) = \lim_{\substack{\Delta\Omega_{\hat{\mathbf{q}}} \to 0 \\ T \to \infty}} \frac{1}{\Delta\Omega_{\hat{\mathbf{q}}}} \frac{1}{T} \int_{t-T/2}^{t+T/2} \mathrm{d}t' \, |\boldsymbol{\mathcal{S}}(\mathbf{r}, t')| \, \chi[\Delta\Omega_{\hat{\mathbf{q}}}, \hat{\mathbf{s}}(\mathbf{r}, t')] \tag{11.11a}$$

$$\approx \frac{1}{S_{\mathrm{d}}} \frac{1}{\Delta\Omega_{\hat{\mathbf{q}}}} \frac{1}{T} \int_{S_{\mathrm{d}}} \mathrm{d}^2\mathbf{r}' \int_{t-T/2}^{t+T/2} \mathrm{d}t' \, |\boldsymbol{\mathcal{S}}(\mathbf{r}', t')| \, \chi[\Delta\Omega_{\hat{\mathbf{q}}}, \hat{\mathbf{s}}(\mathbf{r}', t')] \tag{11.11b}$$

essentially measured by the hypothetical directional detector, where the observation point $\mathbf{r}$ coincides with the center of the detector surface S_{d}. Note that the dependence on $\mathbf{r}'$ over S_{d} in Eq. (11.11b) vanishes upon averaging over a sufficiently long time interval T and assuming that the diameter of the sensitive surface is much smaller than any dimension of the particulate scattering medium. The quantity (11.11a) was introduced by Preisendorfer (1965) and will therefore be called the Preisendorfer radiance function. Importantly, the dimension of $\widetilde{N}(\mathbf{r}, \hat{\mathbf{q}})$ is different from that of the Poynting vector $\boldsymbol{\mathcal{S}}$: it is $\mathrm{W\,m^{-2}\,sr^{-1}}$ rather than $\mathrm{W\,m^{-2}}$. It is now clear that to find the time average of the Poynting vector at the observation point $\mathbf{r}$, we need to integrate the reading of the hypothetical directional detector over all directions $\{\theta, \varphi\}$ of the unit vector $\hat{\mathbf{q}}$:

$$\langle\langle \boldsymbol{\mathcal{S}}(\mathbf{r}, t) \rangle\rangle = \int_{4\pi} \mathrm{d}\hat{\mathbf{q}} \, \hat{\mathbf{q}} \, \widetilde{N}(\mathbf{r}, \hat{\mathbf{q}}) = \int_0^{2\pi} \mathrm{d}\varphi \int_0^{\pi} \mathrm{d}\theta \sin\theta \, \hat{\mathbf{q}} \, \widetilde{N}(\mathbf{r}, \hat{\mathbf{q}}). \tag{11.12}$$

Thus, if this thought experiment were possible then it would serve to yield the direct measurement of the Preisendorfer radiance function (11.11a) and the determination of the local time-averaged Poynting vector via Eq. (11.12). Unfortunately, a practical implementation of this measurement methodology faces two major obstacles. First of all, to the best of the author's knowledge, a directional detector of electromagnetic energy flow depicted schematically in Plate 11.1a has never been built, and it remains quite questionable whether it can be built in principle. Obviously, assessing the very feasibility of a detector with directional sensitivity to the local instantaneous Poynting vector requires an advanced quantum-mechanical analysis of light–matter interaction. It is possible that there exists a variant of the Heisenberg uncertainty principle that fundamentally prohibits such a measurement. Second of all, as we have already pointed out, the instrument blocks the spherical wavelets generated by the particles located to the left of the plane through the sensitive surface shown schematically by the dashed line in Fig. 11.5. As a consequence, the "truncated" instantaneous local Poynting vector

entering the right-hand side of Eq. (11.11b) is fundamentally different from what it would be in the absence of the detector.

11.4 Well-collimated radiometers

The majority of actual directional radiometers in use today are WCRs based on a profoundly different physical principle, as illustrated schematically in Plate 11.1b. The main functional elements of a WCR are the objective and relay lenses, the diaphragm, and the photoelectric detector. Let us consider the reaction of a WCR to the electromagnetic field formed by superposing two plane waves propagating in directions $\hat{\mathbf{q}}$ and $\hat{\mathbf{q}}'$, respectively. The objective lens acts as a linear optical transformer in that its effect on the total field is a superposition of its effects on each plane-wave component. Specifically, the well-known paraxial approximation (see, e.g., Section 5.1 of Goodman (2005)) implies that in the near zone of the objective lens either plane wavefront is transformed into a converging spherical wavefront (Plate 11.1e) with its respective focal point located in the plane of the diaphragm. However, the ultimate fates of the two spherical wavefronts in Plate 11.1b are different. The pink spherical wavefront passes freely through the pinhole, is converted back into a plane wavefront, and is relayed onto the sensitive surface of the photodetector, thereby contributing to the cumulative reading of the WCR. The blue spherical wavefront gets annihilated by the diaphragm and does not contribute to the reading of the photodetector.

Thus the combination {objective lens, diaphragm} serves to select only plane (or near-plane) wavefronts propagating in directions very close to the optical axis of the instrument and falling within its small acceptance solid angle

$$\Delta\Omega = \frac{\pi d^2}{4f^2}, \tag{11.13}$$

where d is the diameter of the pinhole and f is the focal length of the objective lens. The fundamental difference between the two instruments shown in Plates 11.1a and 11.1b is that the latter selects appropriately directed wavefronts, whereas the former is assumed to select appropriately directed instantaneous Poynting vectors (Mishchenko 2010). It can thus be said that *the hypothetical directional meter of electromagnetic energy flow shown in Plate 11.1a is intended to operate in the Poynting-vector domain, whereas the conventional WCR acts as a wave-domain filter*.

This analysis implies that the typical WCR does not necessarily react to the local Poynting vector at a point on the exterior surface of the objective lens, even if this vector is directed along the optical axis of the instrument. To demonstrate this, let us consider the electromagnetic field formed by a superposition of two plane electromagnetic waves propagating in directions $\hat{\mathbf{q}}_1$ and $\hat{\mathbf{q}}_2$ such that both form a 45° angle with the optical axis of the WCR (Plate 11.1c). The waves are linearly polarized, with their electric vectors $\boldsymbol{\mathcal{E}}_1$ and $\boldsymbol{\mathcal{E}}_2$ oscillating perpendicularly

to the paper, and fully coherent in that at any moment in time $\boldsymbol{\mathcal{E}}_1 = \boldsymbol{\mathcal{E}}_2$ at the central point of the objective lens. Let the local instantaneous magnetic vectors of the waves be $\boldsymbol{\mathcal{H}}_1$ and $\boldsymbol{\mathcal{H}}_2$, respectively, as shown by the magenta arrows, while the corresponding instantaneous electric vectors $\boldsymbol{\mathcal{E}}_1 = \boldsymbol{\mathcal{E}}_2$ are directed towards the reader. The cumulative local instantaneous field is represented by the vectors $\boldsymbol{\mathcal{E}} = 2\boldsymbol{\mathcal{E}}_1$ and $\boldsymbol{\mathcal{H}} = \boldsymbol{\mathcal{H}}_1 + \boldsymbol{\mathcal{H}}_2$, the former again being directed towards the reader. One can see that the resulting local instantaneous Poynting vector $\boldsymbol{\mathcal{S}} = \boldsymbol{\mathcal{E}} \times \boldsymbol{\mathcal{H}}$, shown by the green arrow, is directed along the optical axis of the instrument. Moreover, it is easily verified that the Poynting vector at the central point is always directed along the optical axis of the WCR. Yet the reading of the detector is identically equal to zero since neither plane wavefront is passed by the {objective lens, diaphragm} filter.

Conversely, a WCR can generate a nonzero signal when the local Poynting vector is zero. Indeed, let us consider the superposition of two plane waves propagating in opposite directions along the y-axis, as shown in Fig. 11.6a. The corresponding electric and magnetic fields are given by

$$\boldsymbol{\mathcal{E}}_1(\mathbf{r}, t) = \mathcal{E}\cos(ky - \omega t)\,\hat{\mathbf{z}}, \quad \boldsymbol{\mathcal{H}}_1(\mathbf{r}, t) = \mathcal{H}\cos(ky - \omega t)\,\hat{\mathbf{x}}, \tag{11.14}$$

$$\boldsymbol{\mathcal{E}}_2(\mathbf{r}, t) = \mathcal{E}\cos(ky - \omega t)\,\hat{\mathbf{z}}, \quad \boldsymbol{\mathcal{H}}_2(\mathbf{r}, t) = -\mathcal{H}\cos(ky - \omega t)\,\hat{\mathbf{x}}, \tag{11.15}$$

respectively. One can see that at the origin ($y = 0$), the total magnetic field and, as a consequence, the Poynting vector are identically equal to zero. Yet the WCRs in Figs. 11.6b and 11.6c block one of the waves and thereby record a nonzero "Poynting vector" directed along the positive (Fig. 11.6b) or negative (Fig. 11.6c) y-axis.

The failure of the WCR to react to the instantaneous Poynting vector in Plate 11.1c can be traced to the following fundamental fact: although the Poynting vector is sought at points on the exterior surface of the objective lens, the actual photodetector is invariably located very far (compared to the wavelength) from these points. What the optical scheme of the WCR can relay from the entrance plane onto the sensitive surface of the photodetector is a suitable plane (or quasi-plane) wavefront, but not the Poynting vector of the *total* field. The only circumstance in which the WCR relays the Poynting vector itself is when the total field consists only of one or several plane or near-plane wavefronts propagating in the same direction along the optical axis of the instrument. In fact, it is the very principle of serving as a *wavefront angular filter* (rather than a Poynting-vector angular filter) that allows one to build a WCR by using easy-to-fabricate macroscopic optical elements (such as lenses, mirrors, polarizers, prisms, diffraction gratings, etc.). In some cases these elements can be very large, as exemplified by modern astronomical telescopes (see, e.g., Figs. 1.6a and 1.6b).

Thus, contrary to a widespread belief, a WCR cannot be said to measure the directional distribution of the electromagnetic energy flow at an observation point. It is therefore imperative to formulate precisely what a WCR does in actuality. Let us assume that it is exposed to an electromagnetic field in the form of a

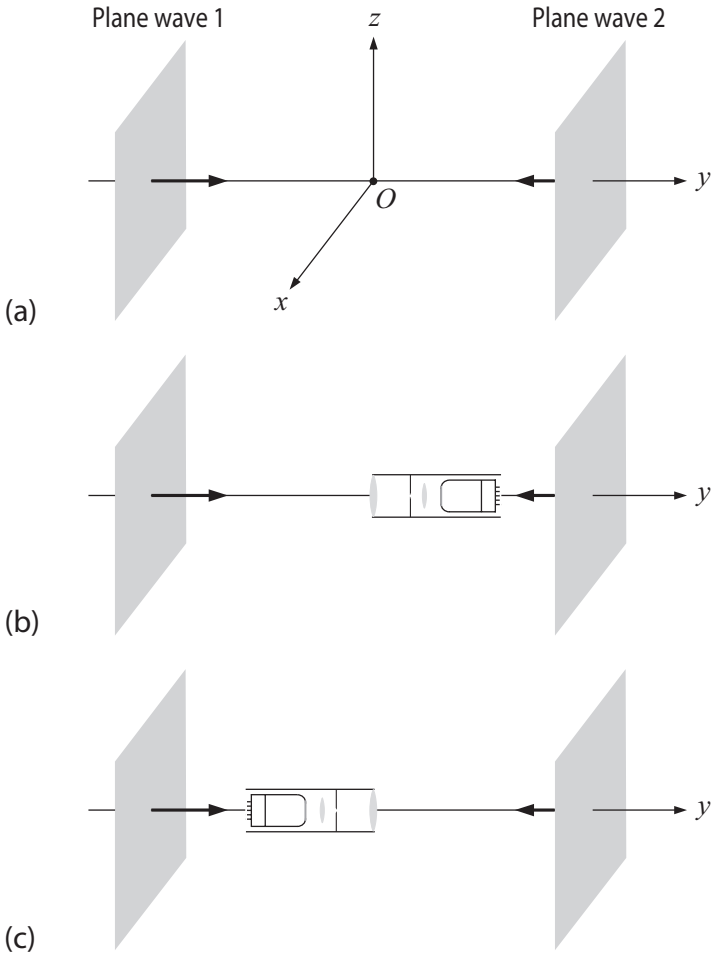

Fig. 11.6. A WCR can register a nonzero signal even if the local Poynting vector is identically equal to zero.

superposition of several plane wavefronts, as depicted schematically in Fig. 11.7. According to the above discussion, the WCR does the following:

- selects only those wavefronts whose propagation directions fall within its small acceptance solid angle $\Delta\Omega_{\hat{\mathbf{q}}}$ (i.e., $\hat{\mathbf{q}}_3, \hat{\mathbf{q}}_4$, and $\hat{\mathbf{q}}_5$, but not $\hat{\mathbf{q}}_1, \hat{\mathbf{q}}_2, \hat{\mathbf{q}}_6$, and $\hat{\mathbf{q}}_7$);
- sums up the respective instantaneous electric and magnetic field vectors: $\mathcal{E}' = \mathcal{E}_3 + \mathcal{E}_4 + \mathcal{E}_5$ and $\mathcal{H}' = \mathcal{H}_3 + \mathcal{H}_4 + \mathcal{H}_5$; and finally
- integrates the modulus of the vector product $\mathcal{E}' \times \mathcal{H}'$ (which, by its very construct, is always directed along – or very close to – the optical axis of the WCR; see Problem 11.1) over the entrance pupil S_{ep} as well as over time.

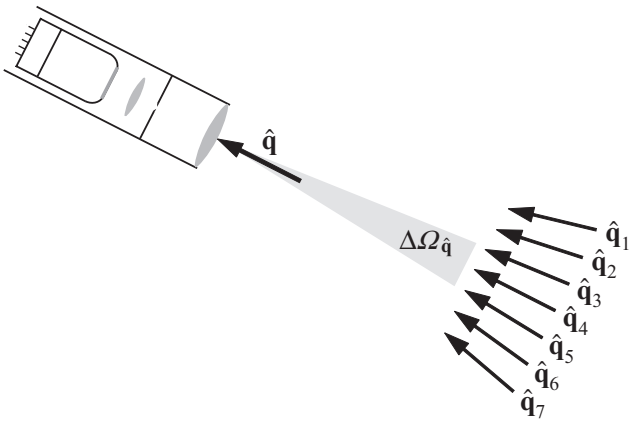

Fig. 11.7. Response of a WCR to a superposition of several plane electromagnetic waves.

Importantly, invoking the concept of the flat entrance pupil of a WCR, shown in Plate 11.1d, helps to accommodate the following two facts:

- the electromagnetic power enters the WCR through the objective lens and is, therefore, proportional to the area of this lens; and
- the actual registration of the resulting Poynting vector of the superposition of transmitted wavefronts occurs at the sensitive surface of the end photodetector.

Indeed, the optical scheme of the WCR serves to preserve the phase relations between the incoming wavefronts as they are relayed onto the sensitive surface of the detector. Suppose, for example, that one of two wavefronts propagating along the WCR axis is a plane electromagnetic wave $\{\boldsymbol{\mathcal{E}}_1, \boldsymbol{\mathcal{H}}_1\}$, while the other one is a spherical wave $\{\boldsymbol{\mathcal{E}}_2, \boldsymbol{\mathcal{H}}_2\}$ with a large, but finite, radius of curvature. The phase difference between these wavefronts varies over a plane perpendicular to the direction of propagation, thereby causing lateral variations of the resulting vector product $(\boldsymbol{\mathcal{E}}_1 + \boldsymbol{\mathcal{E}}_2) \times (\boldsymbol{\mathcal{H}}_1 + \boldsymbol{\mathcal{H}}_2)$. It is easy to see that the combination of the objective and relay lenses in Plate 11.1b yields the same phase-difference distribution over the sensitive surface of the detector as that over the flat entrance pupil. We will see in Chapter 13 that this functional feature of a WCR is essential in the practical measurement of extinction.

Another fundamental feature of the basic optical scheme of a WCR is that the wavefronts impinging on the sensitive surface of the end photodetector always propagate normally to the surface, thereby eliminating one of the drawbacks of uncollimated radiometers discussed in Section 11.2. Although the photodetector can still have residual polarimetric sensitivity, this problem can be mitigated by inserting a depolarizer between the relay lens and the detector.

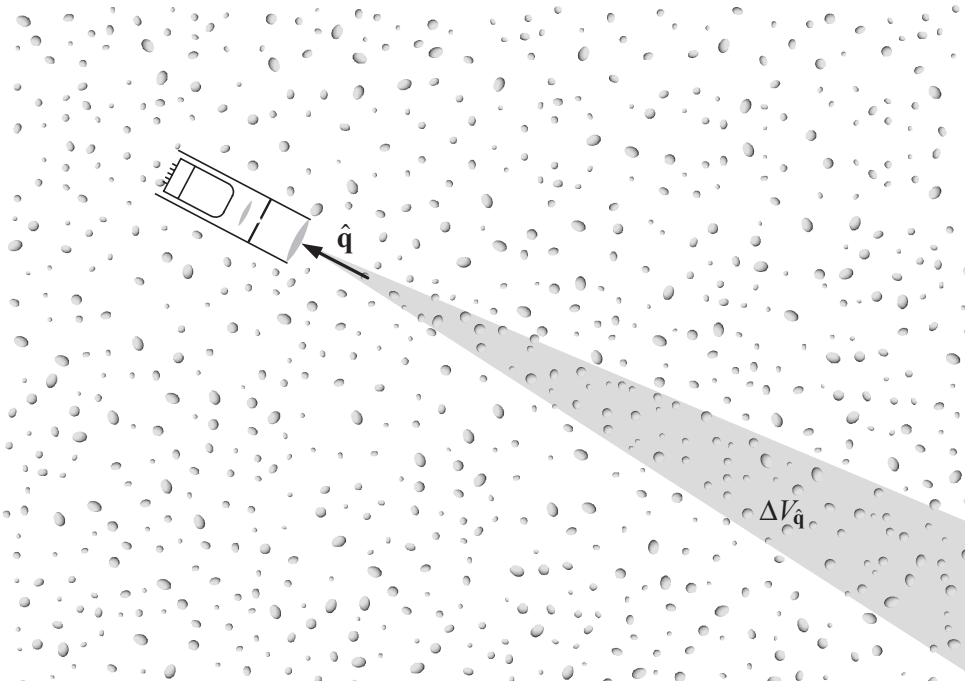

Fig. 11.8. A WCR placed inside a random cloud of particles.

Thus, the operation performed by a WCR is by no means equivalent to accumulating appropriately directed local instantaneous Poynting vectors of the *total field over the entrance pupil* (cf. Plate 11.1a). Despite this fundamental limitation, the above discussion shows that the measurement afforded by a WCR is well defined and thus can be modeled theoretically. This, as will be described in later chapters, makes WCRs very useful tools in solving energy-budget and particle-characterization problems. Furthermore, we will demonstrate in the following chapter that a WCR can be upgraded to measure even the state of polarization of the superposition of wavefronts filtered out by its {objective lens, diaphragm} combination. This further increases the utility of WCRs in optical particle characterization.

The very fact that a WCR serves as a directional filter of plane or near-plane wavefronts imposes strict limitations on its practical use. For example, a WCR having a centimeter-sized or larger entrance pupil cannot be used to characterize the near field created by a micrometer-sized particle, such as that shown in Fig. 1.3c. Solving this problem requires specifically designed nano-optical probes (Novotny and Hecht 2012) and is beyond the scope of this book. Instead, our discussion of FFS in Chapter 5 suggests that a WCR should ideally be located in the far zone of the entire scattering object and at a distance from the object much greater than the diameter of the entrance pupil. Then the part of the scattered

spherical wavefront cut out by the entrance pupil becomes sufficiently flat to pass in its entirety the {objective lens, diaphragm} filter.

The WCR shown in Fig. 11.8 is located in the near zone of the cloud. We have seen, however, that if the cloud is formed by widely separated particles then the total field at any observation point located in the far zones of all the constituent particles is a superposition of the incident field and individual spherical wavelets contributed by all the cloud particles. If the size of the cloud is much greater than the diameter of the entrance pupil then the majority of these wavelets are contributed by remote particles and develop into near-plane wavefronts at the location of the WCR. Therefore, the use of the WCR appears to be justified, as long as these wavefronts dominate the total local field.

An implicit advantage of a WCR over the hypothetical directional meter of electromagnetic energy flow shown in Plate 11.1a is that the specific measurement afforded by the WCR is much less affected by the WCR's very presence. Indeed, we have seen in Section 11.3 that placing the directional meter inside a cloud of particles changes the local Poynting vector dramatically by blocking a large fraction of incoming spherical wavefronts (Fig. 11.5). The measurement afforded by the WCR is fundamentally different in that, by definition, the WCR selects only those incoming wavefronts that are generated by particles residing in the narrow conical volume $\Delta V_{\hat{\mathbf{q}}}$ defined by the WCR's acceptance solid angle $\Delta\Omega_{\hat{\mathbf{q}}}$ (Fig. 11.8). It is obvious that placing the WCR inside the cloud blocks none of these wavefronts.

Admittedly, the addition of a foreign body such as a WCR modifies the partial wavelets created at the observation point by the particles residing in the conical volume $\Delta V_{\hat{\mathbf{q}}}$. However, the WCR can be expected to affect only the wavelets coming from particles located in the close vicinity of the WCR. If the size of the WCR is much smaller than that of the cloud then the fraction of such particles in the conical volume $\Delta V_{\hat{\mathbf{q}}}$ is relatively small, thereby making the actual signal measured by the WCR close to the imaginary signal caused by the same particles in the absence of the WCR. The situation depicted in Fig. 11.5 is fundamentally different in that the directional detector essentially destroys the signal that it is supposed to measure.

11.5 Response of a well-collimated radiometer to polychromatic light

Since in practice one usually deals with polychromatic rather than monochromatic light, accounting for spectral dependence of WCR's sensitivity becomes an essential part of the theoretical modeling of an actual photometric measurement. Let us consider the most general situation wherein a WCR is exposed to polychromatic light with quasi-monochromatic components. This implies that electromagnetic radiation reaching the photodetector in Plate 11.1b is a superposition of plane wavefronts essentially parallel to the sensitive surface of the detector and

given by the complex fields

$$\widetilde{\boldsymbol{\mathcal{E}}}^{\mathrm{d}}(\mathbf{r},t) = \sum_{n=1}^{N} \mathbf{E}_{0n}^{\mathrm{d}}(t)\exp(\mathrm{i}k_n\hat{\mathbf{q}}\cdot\mathbf{r} - \mathrm{i}\omega_n t), \tag{11.16}$$

$$\widetilde{\boldsymbol{\mathcal{H}}}^{\mathrm{d}}(\mathbf{r},t) = \sum_{n=1}^{N} \mathbf{H}_{0n}^{\mathrm{d}}(t)\exp(\mathrm{i}k_n\hat{\mathbf{q}}\cdot\mathbf{r} - \mathrm{i}\omega_n t), \tag{11.17}$$

where the unit vector $\hat{\mathbf{q}}$ is directed along the inward normal to the sensitive surface. The photoelectric response of the detector can now be modeled in the framework of the quantum theory of photodetection discussed in Section 11.1. Specifically, the total number of photoelectrons $N_{\mathrm{pe}}(T)$ generated by the detector during a time interval T is now given by

$$N_{\mathrm{pe}}(T) = TS_{\mathrm{ill}}\sum_{n=1}^{N} K^{\mathrm{d}}(\omega_n)\langle\langle I_n^{\mathrm{d}}(t)\rangle\rangle, \tag{11.18}$$

where S_{ill} is the illuminated area of the sensitive surface, $K^{\mathrm{d}}(\omega_n)$ is the quantum efficiency of the photodetector at the frequency ω_n, and $\langle\langle I_n^{\mathrm{d}}(t)\rangle\rangle$ is the time-averaged intensity of the nth quasi-monochromatic component.

In the absence of absorption of light by the objective and relay lenses, we would have $S_{\mathrm{ill}}\langle\langle I_n^{\mathrm{d}}(t)\rangle\rangle = S_{\mathrm{ep}}\langle\langle I_n(t)\rangle\rangle$, where $\langle\langle I_n(t)\rangle\rangle$ is the time-averaged intensity of the nth quasi-monochromatic wavefront *at the entrance pupil*. However, the spectrally varying absorption by both lenses must be taken into account by introducing an additional attenuation factor $K^{\mathrm{ol+rl}}(\omega_n)$. We thus have the following final formula for $N_{\mathrm{pe}}(T)$:

$$N_{\mathrm{pe}}(T) = TS_{\mathrm{ep}}\sum_{n=1}^{N} K^{\mathrm{WCR}}(\omega_n)\langle\langle I_n(t)\rangle\rangle, \tag{11.19}$$

where

$$K^{\mathrm{WCR}}(\omega_n) = K^{\mathrm{d}}(\omega_n)K^{\mathrm{ol+rl}}(\omega_n) \tag{11.20}$$

is the cumulative spectrally dependent detection efficiency of the WCR. If the WCR is also capable of measuring the other Stokes parameters then, by analogy with Eq. (11.19), we can write the following symbolic expression:

$$\begin{bmatrix} N_{\mathrm{pe},I}(T) \\ N_{\mathrm{pe},Q}(T) \\ N_{\mathrm{pe},U}(T) \\ N_{\mathrm{pe},V}(T) \end{bmatrix} = TS_{\mathrm{ep}}\sum_{n=1}^{N}\begin{bmatrix} K_I^{\mathrm{WCR}}(\omega_n)\langle\langle I_n(t)\rangle\rangle \\ K_Q^{\mathrm{WCR}}(\omega_n)\langle\langle Q_n(t)\rangle\rangle \\ K_U^{\mathrm{WCR}}(\omega_n)\langle\langle U_n(t)\rangle\rangle \\ K_V^{\mathrm{WCR}}(\omega_n)\langle\langle V_n(t)\rangle\rangle \end{bmatrix}, \tag{11.21}$$

where the four K^{WCR} coefficients now incorporate the spectrally varying attenuation by additional optical elements required to perform polarization measurements, as described in the following chapter. Note that the nominal "photoelect-

ron counts" $N_{\mathrm{pe},Q}$, $N_{\mathrm{pe},U}$, and $N_{\mathrm{pe},V}$ in Eq. (11.21) are obtained by subtracting real photoelectron counts registered with different orientations of polarizers and retarders (see Section 12.3) and therefore can be negative.

In many cases of practical interest the polychromatic field in question is a superposition of a very large number of quasi-monochromatic components with a quasi-continuous distribution of frequencies ranging from $\omega_{\min}$ to $\omega_{\max}$. Then Eq. (11.21) takes the form

$$\begin{bmatrix} N_{\mathrm{pe},I}(T) \\ N_{\mathrm{pe},Q}(T) \\ N_{\mathrm{pe},U}(T) \\ N_{\mathrm{pe},V}(T) \end{bmatrix} = T S_{\mathrm{ep}} \int_{\omega_{\min}}^{\omega_{\max}} \mathrm{d}\omega \begin{bmatrix} K_I^{\mathrm{WCR}}(\omega)\langle\langle I_\omega(t)\rangle\rangle \\ K_Q^{\mathrm{WCR}}(\omega)\langle\langle Q_\omega(t)\rangle\rangle \\ K_U^{\mathrm{WCR}}(\omega)\langle\langle U_\omega(t)\rangle\rangle \\ K_V^{\mathrm{WCR}}(\omega)\langle\langle V_\omega(t)\rangle\rangle \end{bmatrix}. \tag{11.22}$$

Comparison of Eq. (9.33) with Eq. (11.21) shows that a WCR can be used to measure the cumulative Stokes parameters of the superposition of wavefronts selected by the WCR's {objective lens, diaphragm} filter only if the total spectral range $[\omega_{\min}; \omega_{\max}]$ is narrow enough to ensure nearly constant coefficients K_I^{WCR}, K_Q^{WCR}, K_U^{WCR}, and K_V^{WCR}. Otherwise the measurement convolves the spectral diversity of the electromagnetic field with the spectrally varying sensitivity of the WCR, thereby yielding a signal that may be difficult, if even possible, to decipher. This explains the frequent use of narrow spectral filters and optical monochromators in the optical tract of a WCR intended to cut out a sufficiently narrow range of angular frequencies. Accordingly, we will always assume in what follows that the range $[\omega_{\min}; \omega_{\max}]$ is narrow enough that Eq. (11.21) can be simplified as follows:

$$\begin{bmatrix} N_{\mathrm{pe},I}(T) \\ N_{\mathrm{pe},Q}(T) \\ N_{\mathrm{pe},U}(T) \\ N_{\mathrm{pe},V}(T) \end{bmatrix} = T S_{\mathrm{ep}} \sum_{n=1}^{N} \begin{bmatrix} K_I^{\mathrm{WCR}}\langle\langle I_n(t)\rangle\rangle \\ K_Q^{\mathrm{WCR}}\langle\langle Q_n(t)\rangle\rangle \\ K_U^{\mathrm{WCR}}\langle\langle U_n(t)\rangle\rangle \\ K_V^{\mathrm{WCR}}\langle\langle V_n(t)\rangle\rangle \end{bmatrix}. \tag{11.23}$$

Furthermore, we will assume that the frequency-independent coefficients K_I^{WCR}, K_Q^{WCR}, K_U^{WCR}, and $K_I^{\mathrm{WCR}}, K_V^{\mathrm{WCR}}$ are known beforehand. This allows us to move them to the left-hand side,

$$\frac{1}{T}\begin{bmatrix} N_{\mathrm{pe},I}(T)/K_I^{\mathrm{WCR}} \\ N_{\mathrm{pe},Q}(T)/K_Q^{\mathrm{WCR}} \\ N_{\mathrm{pe},U}(T)/K_U^{\mathrm{WCR}} \\ N_{\mathrm{pe},V}(T)/K_V^{\mathrm{WCR}} \end{bmatrix} = S_{\mathrm{ep}} \sum_{n=1}^{N} \begin{bmatrix} \langle\langle I_n(t)\rangle\rangle \\ \langle\langle Q_n(t)\rangle\rangle \\ \langle\langle U_n(t)\rangle\rangle \\ \langle\langle V_n(t)\rangle\rangle \end{bmatrix}, \tag{11.24}$$

and refer to the right-hand side of Eq. (11.24) as the *net signal recorded by the WCR per unit time*.

11.6 Panoramic radiometers

A WCR is an inherently monodirectional instrument. The basic optical scheme of a multidirectional panoramic radiometer is depicted in Plate 11.1f. In this case the role of the diaphragm is played by each individual pixel of the L-pixel CCD. For example, the pink wavefront propagating along the optical axis in the direction $\hat{\mathbf{q}}$ is detected by the central pixel of the CCD, while the blue wavefront propagating in the direction $\hat{\mathbf{q}}'$ is not annihilated (cf. Plate 11.1b), but is rather detected by an off-center pixel. In other words, each pixel is expected to measure the cumulative Poynting vector of the superposition of plane or near-plane wavefronts propagating in the direction defined by the corresponding {objective lens, pixel} filter. As a result, a single exposure of the CCD yields L simultaneous measurements that are often thought of as forming a two-dimensional image.

For a host of technical reasons not discussed here specifically, accurate radiometric measurements with CCDs are more problematic than those with photomultipliers and photodiodes. However, the following note is of a more basic nature. The quantum theory of the photoelectric effect is well established in the case of photodetection of a plane electromagnetic wave or a parallel polychromatic beam propagating perpendicularly to the plane sensitive surface of the photodetector (Kimble and Mandel 1984; Mandel and Wolf 1995). The main practical result of this theory is summarized by Eq. (11.1) and helps in making the measurement with a WCR a well-characterized and theoretically interpretable procedure. It also further illustrates the essential role played by the relay lens in Plate 11.1b.

Unlike the optical scheme of a WCR shown in Plate 11.1b, that of a panoramic radiometer shown in Plate 11.1f implies that each pixel is located in the focal point of a converging spherical wavefront rather than being exposed to a plane wavefront. Furthermore, the angle between the symmetry axis of a spherical wavefront and the normal to the sensitive surface varies over the CCD and can deviate from zero quite substantially. To the best of the author's knowledge, the quantum theory of photodetection of a converging spherical wave has not been developed yet. As a consequence, the quantitative relationship between the individual intensities of the plane wavefronts in Plate 11.1f and the signals generated by the respective CCD pixels remains poorly characterized. This makes theoretical interpretations of measurements with panoramic radiometers more uncertain than those with WCRs.

Problems

11.1: Consider a superposition of N transverse electromagnetic waves with all individual vector products $\boldsymbol{\mathcal{E}}_i \times \boldsymbol{\mathcal{H}}_i$ pointing in the same direction $\hat{\mathbf{n}}$. Prove that the corresponding product $\sum_{i=1}^{N} \boldsymbol{\mathcal{E}}_i \times \sum_{i'=1}^{N} \boldsymbol{\mathcal{H}}_{i'}$ for the superposition of these waves also points in the direction $\hat{\mathbf{n}}$.

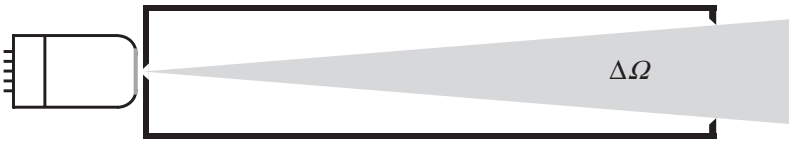

Fig. 11.9. The Gershun tube.

11.2: The so-called Gershun tube (e.g., McCluney 1994; Eppeldauer *et al.* 2005) is a simple optical device claimed by Preisendorfer (1965) to be a radiance-function meter. This device is sketched in Fig. 11.9 and consists of a long tube with entrance and exit apertures followed by a photodetector. Show that the Gershun tube is, in fact, a wavefront-filtering WCR rather than a radiance-function meter. Express the acceptance solid angle of this device $\Delta\Omega$ in terms of the tube length L and the diameters D and d of the entrance and exit apertures, respectively, assuming that $D \gg d$. Show that the acceptance solid angle increases and becomes partially vignetted with increasing d. Compare the energy collection efficiency of the Gershun tube and the WCR sketched in Plate 11.1b by taking into account that the former is defined only by d.

Notes and further reading

The photoelectric effect was discovered experimentally in 1887 by Heinrich Hertz (1857–94) (see Hertz 1887) and studied systematically by Aleksandr Stoletov (1839–96). Stoletov's experimental results were reported in a series of papers published in *Comptes Rendus* and *Journal de Physique*; a summary appeared in the form of a Russian-language monograph (Stoletov 1889). The experimentally established proportionality of the photoelectric current to the intensity of the incident light is the famous Stoletov law.

Albert Einstein (1879–1955) attempted to explain the photoelectric effect by resurrecting the idea of light corpuscles advocated by Sir Isaac Newton (1642–1727). Specifically, Einstein suggested that "the energy of a light ray spreading out from a point source is not continuously distributed over an increasing space but consists of a finite number of energy quanta which are localized at points in space, which move without dividing, and which can only be produced and absorbed as complete units" (see Arons and Peppard 1965).

The obsolete phenomenological nature of Einstein's localized light quanta (Kidd *et al.* 1989; Roychoudhuri *et al.* 2008) becomes obvious upon opening virtually any advanced textbook on QED or quantum optics (e.g., Bohm 1951; Kramers 1957; Power 1964; Akhiezer and Berestetskii 1965; Mandel and Wolf 1995; Meystre and Sargent 1999). Nevertheless, the lasting misinterpretation of the actual QED photons as localized particles of light has been kept flourishing by authors of many school and college textbooks, as well as by scores of incom-

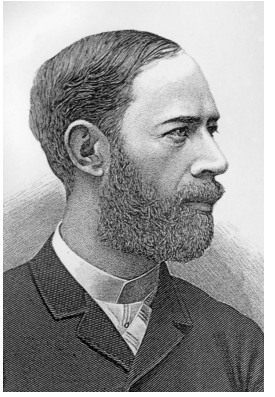
Heinrich Hertz

Aleksandr Stoletov

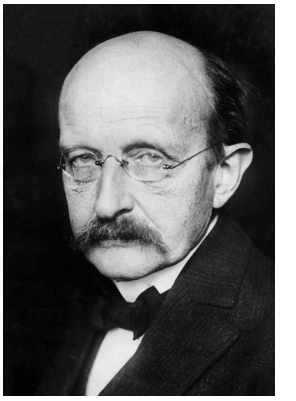
Max Planck

petent popularizers of science. A typical example is the textbook by Taylor *et al.* (2004, p. 125), where one can find the following false statement: "It was found that an electromagnetic wave consists of tiny localized bundles of energy. These bundles, or quanta of light, have come to be called photons." Similarly, Petty (2006, p. 32) defines electromagnetic radiation as a "shower of particles."

Although the term "photon" is ubiquitous in QED and quantum optics (e.g., Scully and Zubairy 1997), it is well known that there is no position operator for a photon and that it is impossible to introduce a photon wave function in the coordinate representation (e.g., Section 2.2 of Akhiezer and Berestetskii (1965)). The actual QED photons are quantum excitations of the normal modes of the electromagnetic field and as such are associated with plane waves of definite wave vector and definite polarization, but infinite lateral extent (Mandel and Wolf 1995). This implies, of course, that photons are not localized point-like particles of light (Lamb 1995).

Contrary to the widespread misrepresentation of the true nature of QED photons in many entry-level textbooks and superficial popularizations of physics, the photoelectric and the Compton effects do not prove the existence of Newtonian corpuscles or Einstein's localized light quanta. The main traits of either effect can be explained on the basis of the semi-classical approach pioneered by Max Planck (1858–1947) (see Planck 1906) wherein only matter is quantized, while the electromagnetic field remains classical (Kidd *et al.* 1989; Dodd 1991; Mandel and Wolf 1995). Even if quantization of the electromagnetic field proves to be necessary, it yields QED photons occupying the entire quantization domain rather than particles of light localized at points in space. Furthermore, based on the advanced QED theory of the photoelectric effect, Kimble and Mandel (1984) concluded that *photodetectors do not count photons in any precise sense*.

12

Measurement of the Stokes parameters

We have seen in the preceding chapter that a WCR directly measures the absolute value of the time-averaged Poynting vector (i.e., the intensity) for the superposition of plane or near-plane wavefronts filtered out by the {objective lens, diaphragm} combination, by relaying it onto the sensitive surface of the photodetector. Since all these wavefronts propagate in essentially the same direction, i.e., along the optical axis of the instrument, they can be thought of as forming a parallel beam that can be characterized by all four Stokes parameters rather than only by the first one, i.e., the intensity (Sections 9.2 and 9.3). It turns out that by inserting special optical elements between the relay lens and the detector, it is possible to modify this beam in such a way that the new first Stokes parameter of the beam reaching the photodetector contains information about the second, third, or fourth Stokes parameters of the original beam. This is usually done by using so-called polarizers and retarders, and typically involves a succession of several measurements to fully characterize the four-component Stokes column vector.

The following discussion will be based on the assumption that the WCR faces a monochromatic plane wave. However, the additivity of the Stokes parameters derived in Sections 9.2 and 9.3 allows for a straightforward generalization of the results to polychromatic light assuming that, according to Section 11.5, the range of angular frequencies involved is sufficiently narrow.

12.1 Polarizers

A polarizer is an optical element that attenuates the orthogonal components of the electric field vector of a plane electromagnetic wave unevenly. Let us denote the corresponding attenuation coefficients as p_θ and p_φ and consider first the situation when the two orthogonal transmission axes of a polarizer coincide with the θ- and φ-axes of the laboratory coordinate system (see Fig. 12.1). This means that after the electromagnetic wave has propagated through the polarizer, the orthogonal components of the electric field change as follows:

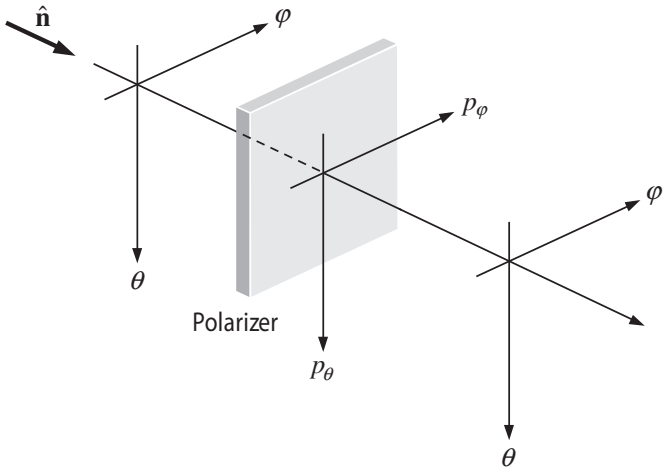

Fig. 12.1. Propagation of a plane wave through a polarizer. The transmission axes of the polarizer coincide with those of the laboratory reference frame. The wave propagates in the direction of the unit vector $\hat{\mathbf{n}}$.

$$E'_\theta = p_\theta E_\theta, \quad 0 \le p_\theta \le 1, \tag{12.1}$$

$$E'_\varphi = p_\varphi E_\varphi, \quad 0 \le p_\varphi \le 1. \tag{12.2}$$

It then follows from the definition of the Stokes parameters, Eq. (7.3), that the Stokes column vector of the wave modifies according to

$$\mathbf{I}' = \mathbf{P}\mathbf{I}, \tag{12.3}$$

where

$$\mathbf{P} = \frac{1}{2}\begin{bmatrix} p_\theta^2 + p_\varphi^2 & p_\theta^2 - p_\varphi^2 & 0 & 0 \\ p_\theta^2 - p_\varphi^2 & p_\theta^2 + p_\varphi^2 & 0 & 0 \\ 0 & 0 & 2p_\theta p_\varphi & 0 \\ 0 & 0 & 0 & 2p_\theta p_\varphi \end{bmatrix} \tag{12.4}$$

is the so-called Mueller matrix representing the effect of the polarizer on the transmitted wave (Problem 12.1).

An important example of a polarizer is a neutral filter with $p_\theta = p_\varphi = p$ which equally attenuates the orthogonal components of the electric field vector and does not change the polarization state of the wave:

$$\mathbf{P} = p^2 \operatorname{diag}[1, 1, 1, 1]. \tag{12.5}$$

In contrast, an ideal linear polarizer transmits only one orthogonal component of the wave, say, the θ-component, and completely blocks the other one, thereby implying that $p_\varphi = 0$. We thus have:

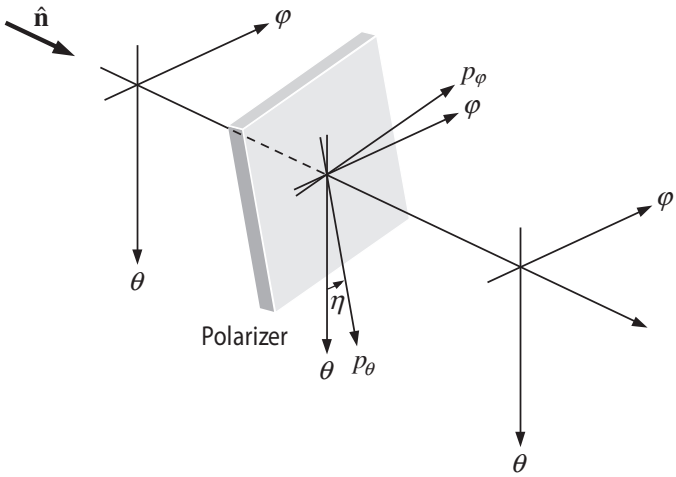

Fig. 12.2. The polarizer transmission axes are rotated through an angle $\eta \geq 0$ around $\hat{\mathbf{n}}$ in the clockwise direction when looking in the direction of $\hat{\mathbf{n}}$.

$$\mathbf{P} = \frac{p_\theta^2}{2}\begin{bmatrix} 1 & 1 & 0 & 0 \\ 1 & 1 & 0 & 0 \\ 0 & 0 & 0 & 0 \\ 0 & 0 & 0 & 0 \end{bmatrix}. \tag{12.6}$$

An ideal perfect linear polarizer does not change one orthogonal component $(p_\theta = 1)$ and completely blocks the other one $(p_\varphi = 0)$:

$$\mathbf{P} = \frac{1}{2}\begin{bmatrix} 1 & 1 & 0 & 0 \\ 1 & 1 & 0 & 0 \\ 0 & 0 & 0 & 0 \\ 0 & 0 & 0 & 0 \end{bmatrix}. \tag{12.7}$$

If the transmission axes of a polarizer are rotated relative to the laboratory coordinate system (Fig. 12.2) then its Mueller matrix with respect to the laboratory coordinate system also changes. To obtain the resulting Stokes column vector with respect to the laboratory coordinate system, we need to:

- "Rotate" the initial Stokes column vector through the angle η in the clockwise direction in order to obtain the Stokes parameters of the original beam with respect to the polarizer axes.
- Multiply the "rotated" Stokes column vector by the original (nonrotated) polarizer Mueller matrix.
- "Rotate" the Stokes column vector thus obtained through the angle $-\eta$ in order to calculate the Stokes parameters of the resulting beam with respect to the laboratory coordinate system.

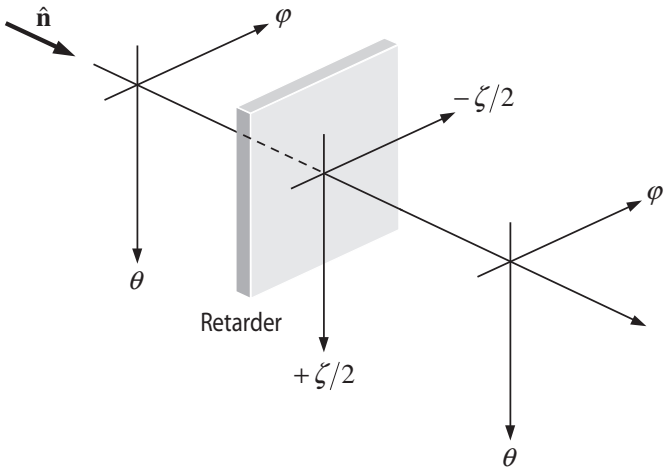

Fig. 12.3. Propagation of a plane wave through a retarder.

The final result is as follows:

$$\mathbf{I}' = \mathbf{L}(-\eta)\mathbf{P}\mathbf{L}(\eta)\mathbf{I}, \tag{12.8}$$

where $\mathbf{L}$ is the rotation matrix (7.8). Hence, the Mueller matrix of the rotated polarizer computed with respect to the laboratory coordinate system is given by

$$\mathbf{P}(\eta) = \mathbf{L}(-\eta)\mathbf{P}\mathbf{L}(\eta) \tag{12.9}$$

with $\mathbf{P}(0) = \mathbf{P}$.

12.2 Retarders

A retarder is an optical element that changes the phase of the plane electromagnetic wave by causing a phase shift of $+\zeta/2$ along the θ-axis and a phase shift of $-\zeta/2$ along the φ-axis (Fig. 12.3). We thus have

$$E'_\theta = \exp(+\mathrm{i}\zeta/2)E_\theta, \tag{12.10}$$

$$E'_\varphi = \exp(-\mathrm{i}\zeta/2)E_\varphi, \tag{12.11}$$

which yields

$$\mathbf{I}' = \mathbf{R}(\zeta)\mathbf{I}, \tag{12.12}$$

where the Mueller matrix of the retarder is given by (Problem 12.3)

$$\mathbf{R}(\zeta) = \begin{bmatrix} 1 & 0 & 0 & 0 \\ 0 & 1 & 0 & 0 \\ 0 & 0 & \cos\zeta & \sin\zeta \\ 0 & 0 & -\sin\zeta & \cos\zeta \end{bmatrix}. \tag{12.13}$$

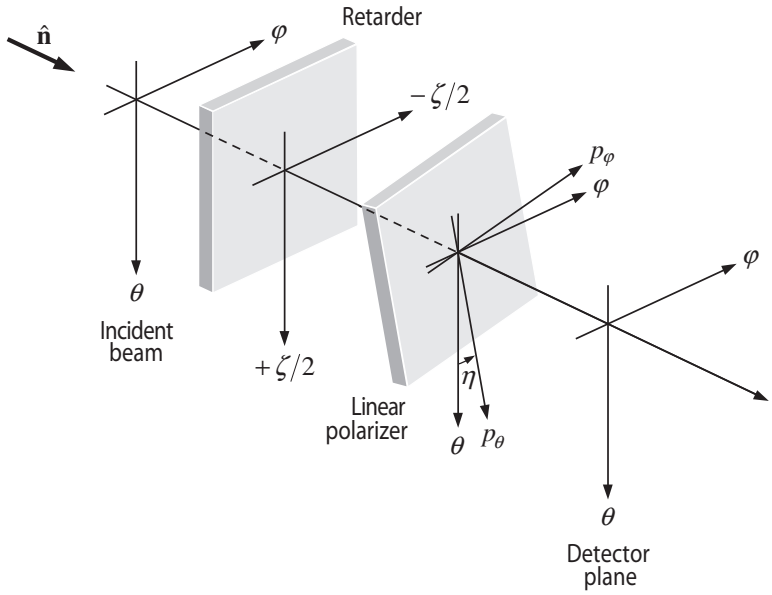

Fig. 12.4. Measurement of the Stokes parameters with a retarder and an ideal perfect linear polarizer rotated with respect to the laboratory reference frame.

12.3 Measurement of the Stokes parameters

Consider now the optical path shown in Fig. 12.4. The plane electromagnetic wave propagates through a retarder and a rotated ideal perfect linear polarizer and then impinges on the surface of a polarization-insensitive detector. The Stokes column vector of the resulting wave impinging on the detector surface is given by

$$\mathbf{I}' = \mathbf{P}(\eta)\mathbf{R}(\zeta)\mathbf{I}, \tag{12.14}$$

where the polarizer Mueller matrix is

$$\mathbf{P}(\eta) = \frac{1}{2}\begin{bmatrix} 1 & \cos 2\eta & -\sin 2\eta & 0 \\ \cos 2\eta & \cos^2 2\eta & -\cos 2\eta \sin 2\eta & 0 \\ -\sin 2\eta & -\cos 2\eta \sin 2\eta & \sin^2 2\eta & 0 \\ 0 & 0 & 0 & 0 \end{bmatrix} \tag{12.15}$$

(Problem 12.4). Hence the intensity of the resulting beam as a function of η and ζ is given by

$$I'(\eta, \zeta) = \tfrac{1}{2}(I + Q\cos 2\eta - U\sin 2\eta \cos\zeta - V\sin 2\eta \sin\zeta). \tag{12.16}$$

This formula suggests a simple way to determine the Stokes parameters of the original beam by measuring the intensity of the resulting beam using four different combinations of η and ζ:

$$I = I'(0°, 0°) + I'(90°, 0°), \tag{12.17}$$

$$Q = I'(0°, 0°) - I'(90°, 0°), \tag{12.18}$$

$$U = -2I'(45°, 0°) + I, \tag{12.19}$$

$$V = I - 2I'(45°, 90°) \tag{12.20}$$

(Problem 12.5).

Problems

12.1: Derive Eqs. (12.4).

12.2: Derive the explicit form of $\mathbf{P}(\eta)$ assuming the general form of $\mathbf{P}$ given by Eq. (12.4). What is the result for a neutral filter described by Eq. (12.5)?

12.3: Derive Eq. (12.13).

12.4: Derive Eq. (12.15).

12.5: Verify Eqs. (12.17)–(12.20).

Further reading

Other methods for measuring the Stokes parameters and practical aspects of polarimetry are discussed in detail in the books by Shurcliff (1962), Clarke and Grainger (1971), Azzam and Bashara (1977), Kliger *et al*. (1990), and Collett (1992). Clarke (2010) and Mishchenko *et al.* (2010) discuss issues specific to polarimetric observations in astrophysics.

13

Description of far-field scattering in terms of actual optical observables

As discussed in Chapter 5, scattering in the far zone is unique in that the scattered field always evolves into a simple outgoing spherical wave, irrespective of the physical nature of the scatterer. It should therefore be important, as well as instructive, to analyze how the general concepts introduced in Chapters 7–12 apply to this simplest type of electromagnetic scattering. Indeed, electromagnetic scattering in the far zone of an object was previously described in terms of the incident and scattered fields related by the amplitude scattering matrix, that is, in terms of typically unobservable quantities. The aim of this chapter is to describe FFS in terms of quantities directly measurable with a WCR and/or directly quantifying the electromagnetic energy budget of a finite volume element enclosing the scattering object.

We will begin by considering the simplest case of monochromatic scattering by a fixed object imbedded in a lossless homogeneous medium and then generalize the results by allowing the incident field to be a polychromatic parallel beam and the object to change randomly in time. The main results of this chapter will be straightforward mathematical corollaries of the total field in the far zone being a superposition of plane and spherical wavefronts. Unlike the more complex case of near-field scattering by a large multi-particle group, the relative mathematical simplicity of FFS will allow us to bypass the computation of the PST and work directly with the Poynting vector and the Stokes parameters.

13.1 Electromagnetic response of a well-collimated radiometer

Consider the measurement configuration involving polarization-insensitive WCRs located at a distance r from the origin O in the far zone of the entire scattering object, as shown in Fig. 13.1. The origin of the laboratory coordinate system is assumed to be close to the geometrical center of the object, but otherwise

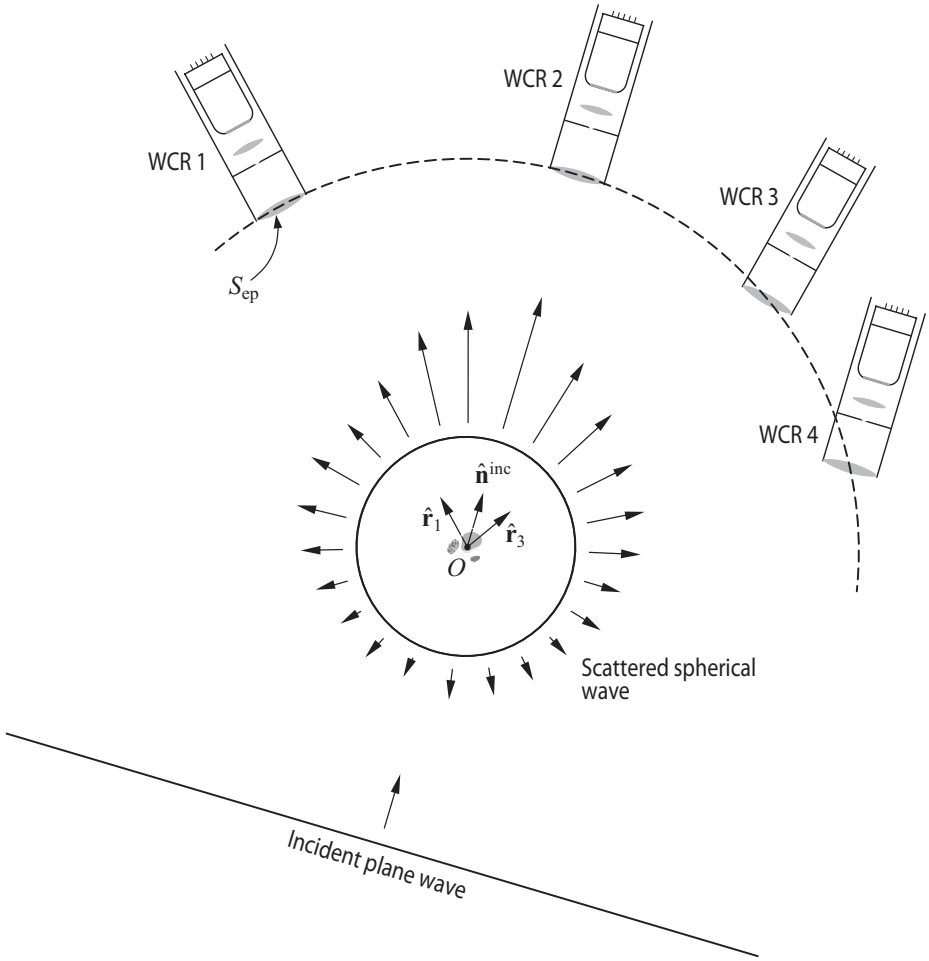

Fig. 13.1. The net signal recorded by a well-collimated radiometer depends on its line of sight.

it is arbitrary. According to Section 5.1, the total electromagnetic field at the location of a WCR is mathematically represented as a superposition of the incident field in the form of a plane electromagnetic wave propagating in the direction of the unit vector $\hat{\mathbf{n}}^{inc}$ and the scattered field in the form of an outgoing spherical wave centered at O. We remind the reader that the total field is the only real physical field, while the separation of this field into the incident and scattered components is notional only. We thus have for a far-zone point $\mathbf{r}'$:

$$\mathbf{E}^{inc}(\mathbf{r}') = \mathbf{E}_0^{inc}\exp(\mathrm{i}k_1\hat{\mathbf{n}}^{inc}\cdot\mathbf{r}'), \quad \mathbf{E}_0^{inc}\cdot\hat{\mathbf{n}}^{inc} = 0, \tag{13.1}$$

$$\mathbf{H}^{inc}(\mathbf{r}') = \sqrt{\frac{\epsilon_1}{\mu_0}}\exp(\mathrm{i}k_1\hat{\mathbf{n}}^{inc}\cdot\mathbf{r}')\hat{\mathbf{n}}^{inc}\times\mathbf{E}_0^{inc}, \tag{13.2}$$

$$\mathbf{E}^{\text{sca}}(\mathbf{r}') = \frac{\exp(\mathrm{i}k_1 r')}{r'}\mathbf{E}_1^{\text{sca}}(\hat{\mathbf{r}}'), \quad \mathbf{E}_1^{\text{sca}}(\hat{\mathbf{r}}')\cdot\hat{\mathbf{r}}' = 0, \tag{13.3}$$

$$\mathbf{H}^{\text{sca}}(\mathbf{r}') = \sqrt{\frac{\epsilon_1}{\mu_0}}\frac{\exp(\mathrm{i}k_1 r')}{r'}\hat{\mathbf{r}}'\times\mathbf{E}_1^{\text{sca}}(\hat{\mathbf{r}}'). \tag{13.4}$$

The entrance pupils of the four WCRs shown in Fig. 13.1 are centered at the endpoints of the respective position vectors $\mathbf{r}_1 = r\hat{\mathbf{r}}_1$, $\mathbf{r}_2 = r\hat{\mathbf{r}}_2 = r\hat{\mathbf{n}}^{\text{inc}}$, $\mathbf{r}_3 = r\hat{\mathbf{r}}_3$, and $\mathbf{r}_4 = r\hat{\mathbf{r}}_4$. The distance r from the origin is assumed to be much greater than the diameter D of the entrance pupils to ensure that the part of the scattered wavefront (shown by the dashed curve in Fig. 13.1) cut out by an entrance pupil is essentially flat. Specifically, it satisfies the inequality

$$\frac{S_{\text{ep}}}{r^2} < \Delta\Omega \tag{13.5}$$

(see Problem 13.1), where, as before, S_{ep} is the area of the entrance pupil and $\Delta\Omega$ is the WCR acceptance solid angle defined by Eq. (11.13).

The optical axis of WCR 3 coincides neither with the respective radial direction $\hat{\mathbf{r}}_3$ nor with the incidence direction $\hat{\mathbf{n}}^{\text{inc}}$. According to the discussion in Section 11.4, this implies that neither the incident plane wave nor the locally flat scattered wavefront can pass the {objective lens, diaphragm} filter, which makes the reading of WCR 3 identically equal to zero. In other words, if the optical axis of a WCR does not go through the origin O and is not parallel to $\hat{\mathbf{n}}^{\text{inc}}$ then the WCR records no signal.

The optical axis of WCR 4 is parallel to the incidence direction, but does not coincide with the respective radial direction $\hat{\mathbf{r}}_4$, which implies that only the incident plane-wave component passes the {objective lens, diaphragm} filter. Therefore, the time-averaged net power recorded by WCR 4 is given by

$$\langle W_4\rangle = S_{\text{ep}} I^{\text{inc}}, \tag{13.6}$$

where

$$I^{\text{inc}} = \frac{1}{2}\sqrt{\frac{\epsilon_1}{\mu_0}}\,|\mathbf{E}_0^{\text{inc}}|^2 \tag{13. 7}$$

is the nominal intensity of the incident plane-wave component, i.e., computed as if the scattered spherical-wave component of the total field were zero (see Eq. (3.20) with $m_1 = 0$).

The optical axis of WCR 1 coincides with the corresponding radial direction $\hat{\mathbf{r}}_1$, but not with the incidence direction $\hat{\mathbf{n}}^{\text{inc}}$. Therefore, the {objective lens, diaphragm} filter of WCR 1 passes only the scattered wavefront. According to Section 11.4, the net time-averaged electromagnetic power recorded by WCR 1 is

$$\langle W_1\rangle = \frac{1}{2}\mathrm{Re}\int_{S_{\text{ep1}}} \mathrm{d}^2\mathbf{r}'\,\hat{\mathbf{r}}'\cdot\{\mathbf{E}^{\text{sca}}(\mathbf{r}')\times[\mathbf{H}^{\text{sca}}(\mathbf{r}')]^*\} \approx S_{\text{ep}} I^{\text{sca}}(r\hat{\mathbf{r}}_1), \tag{13.8}$$

where

$$I^{\mathrm{sca}}(r\hat{\mathbf{r}}_1) = \frac{1}{2}\sqrt{\frac{\epsilon_1}{\mu_0}}\,\frac{1}{r^2}\,|\mathbf{E}_1^{\mathrm{sca}}(\hat{\mathbf{r}}_1)|^2 \tag{13.9}$$

is the nominal intensity of the scattered spherical-wave component, i.e., computed as if the incident plane-wave component of the total field were zero (see Eq. (3.38) with $m_{\mathrm{I}} = 0$).

The computation of the electromagnetic response of WCR 2 oriented along the incidence direction is more involved because the corresponding {objective lens, diaphragm} filter passes both the incident and the forward-scattered wavefront. The time-averaged Poynting vector $\langle \boldsymbol{\mathcal{S}}(\mathbf{r}', t)\rangle$ at any point $\mathbf{r}'$ of the entrance pupil of WCR 2 is the sum of three terms:

$$\begin{aligned}\langle \boldsymbol{\mathcal{S}}(\mathbf{r}', t)\rangle &= \frac{1}{2}\mathrm{Re}\{\mathbf{E}(\mathbf{r}')\times[\mathbf{H}(\mathbf{r}')]^*\}\\ &= \langle \boldsymbol{\mathcal{S}}^{\mathrm{inc}}(\mathbf{r}', t)\rangle + \langle \boldsymbol{\mathcal{S}}^{\mathrm{sca}}(\mathbf{r}', t)\rangle + \langle \boldsymbol{\mathcal{S}}^{\mathrm{ext}}(\mathbf{r}', t)\rangle,\end{aligned} \tag{13.10}$$

where

$$\langle \boldsymbol{\mathcal{S}}^{\mathrm{inc}}(\mathbf{r}', t)\rangle = \frac{1}{2}\mathrm{Re}\{\mathbf{E}^{\mathrm{inc}}(\mathbf{r}')\times[\mathbf{H}^{\mathrm{inc}}(\mathbf{r}')]^*\} \tag{13.11}$$

and

$$\langle \boldsymbol{\mathcal{S}}^{\mathrm{sca}}(\mathbf{r}', t)\rangle = \frac{1}{2}\mathrm{Re}\{\mathbf{E}^{\mathrm{sca}}(\mathbf{r}')\times[\mathbf{H}^{\mathrm{sca}}(\mathbf{r}')]^*\} \tag{13.12}$$

are the Poynting vector components associated with the incident and the scattered wavefront, respectively, and

$$\langle \boldsymbol{\mathcal{S}}^{\mathrm{ext}}(\mathbf{r}', t)\rangle = \frac{1}{2}\mathrm{Re}\{\mathbf{E}^{\mathrm{inc}}(\mathbf{r}')\times[\mathbf{H}^{\mathrm{sca}}(\mathbf{r}')]^* + \mathbf{E}^{\mathrm{sca}}(\mathbf{r}')\times[\mathbf{H}^{\mathrm{inc}}(\mathbf{r}')]^*\} \tag{13.13}$$

quantifies the "interaction" between the incident and scattered wavefronts. The resulting electromagnetic response is obtained by integrating the absolute value of the Poynting vector (13.10) over the entrance pupil of WCR 2.

It is convenient at this point to make use of the following far-zone decomposition of the incident electric field into incoming and outgoing spherical-wave components centered at the origin O:

$$\mathbf{E}^{\mathrm{inc}}(\mathbf{r}') \underset{k_1 r'\to\infty}{=} \frac{\mathrm{i}2\pi}{k_1}\left[\delta(\hat{\mathbf{n}}^{\mathrm{inc}} + \hat{\mathbf{r}}')\frac{\exp(-\mathrm{i}k_1 r')}{r'} - \delta(\hat{\mathbf{n}}^{\mathrm{inc}} - \hat{\mathbf{r}}')\frac{\exp(\mathrm{i}k_1 r')}{r'}\right]\mathbf{E}_0^{\mathrm{inc}}, \tag{13.14}$$

where $r' = |\mathbf{r}'|$, $\hat{\mathbf{r}}' = \mathbf{r}'/r'$, and

$$\delta(\hat{\mathbf{r}} - \hat{\mathbf{r}}') = \delta(\cos\theta - \cos\theta')\,\delta(\varphi - \varphi') \tag{13.15}$$

is the solid-angle delta function (see Appendix D). Similarly, the incident magnetic field is given by

$$\mathbf{H}^{\text{inc}}(\mathbf{r}') \underset{k_1 r' \to \infty}{=} \frac{\mathrm{i}2\pi}{k_1}\Bigg[\delta(\hat{\mathbf{n}}^{\text{inc}} + \hat{\mathbf{r}}')\frac{\exp(-\mathrm{i}k_1 r')}{r'} - \delta(\hat{\mathbf{n}}^{\text{inc}} - \hat{\mathbf{r}}')\frac{\exp(\mathrm{i}k_1 r')}{r'}\Bigg]\sqrt{\frac{\epsilon_1}{\mu_0}}\,\hat{\mathbf{n}}^{\text{inc}} \times \mathbf{E}_0^{\text{inc}}. \quad (13.16)$$

Substituting these decompositions in Eq. (13.13) and integrating the absolute value of the Poynting vector (13.10) over the entrance pupil of WCR 2 yields (Problem 13.2):

$$\langle W_2 \rangle \approx S_{\text{ep}}[I^{\text{inc}} + I^{\text{sca}}(r\hat{\mathbf{r}}_1)] - \frac{2\pi}{k_1}\sqrt{\frac{\epsilon_1}{\mu_0}}\,\text{Im}[\mathbf{E}_1^{\text{sca}}(\hat{\mathbf{n}}^{\text{inc}}) \cdot (\mathbf{E}_0^{\text{inc}})^*] \quad (13.17a)$$

$$= S_{\text{ep}} I^{\text{inc}} - \frac{2\pi}{k_1}\sqrt{\frac{\epsilon_1}{\mu_0}}\,\text{Im}[\mathbf{E}_1^{\text{sca}}(\hat{\mathbf{n}}^{\text{inc}}) \cdot (\mathbf{E}_0^{\text{inc}})^*] + O(r^{-2}). \quad (13.17b)$$

Equations (13.17) represent the so-called optical theorem. The first term on the right-hand side of Eq. (13.17b) is proportional to S_{ep} and is equal to the net electromagnetic power that would be recorded by WCR 2 in the absence of the scattering object. The second term is independent of S_{ep} and describes attenuation caused by interposing the object between the light source and the WCR. Thus, the WCR centered at the object along the forward-scattering direction can be said to measure the nominal power of the incident plane wave attenuated by the interference of the incident and scattered wavefronts, plus a relatively small contribution from the scattered wavefront. The detector centered at the object along any other radial direction reacts only to the scattered wavefront.

The fact that the extinction term in Eqs. (13.17) is independent of S_{ep} has a simple qualitative explanation. Although the radius of curvature of the spherical wave at WCR 2 is large, it is still finite. Because of that, the phase difference between the incident and scattered wavefronts varies over the flat entrance pupil (see Fig. 13.2), thereby causing the Poynting vector component $\langle \boldsymbol{\mathcal{S}}^{\text{ext}}(\mathbf{r}', t)\rangle$ to oscillate with increasing frequency as the distance of the observation point $\mathbf{r}'$ from the center of the entrance pupil increases. These high-frequency oscillations between positive and negative values effectively cancel each other upon the integration over the entrance pupil. The only exception is the immediate vicinity of the exact forward-scattering direction, where the phase difference between the incident and scattered wavefronts remains approximately constant. Hence the appearance of a delta-function term on the right-hand side of Eq. (13.13), causing a nonzero extinction term in Eqs. (13.17). This explanation also demonstrates the importance of the optical scheme of WCR 2 preserving the lateral distribution of the phase difference between the incident and scattered wavefronts as they are relayed onto the sensitive surface of the photodetector (recall the discussion in Section 11.4).

The ratio of minus the second term on the right-hand side of Eq. (13.17b) to the nominal intensity of the incident plane wave has the dimension of area and is

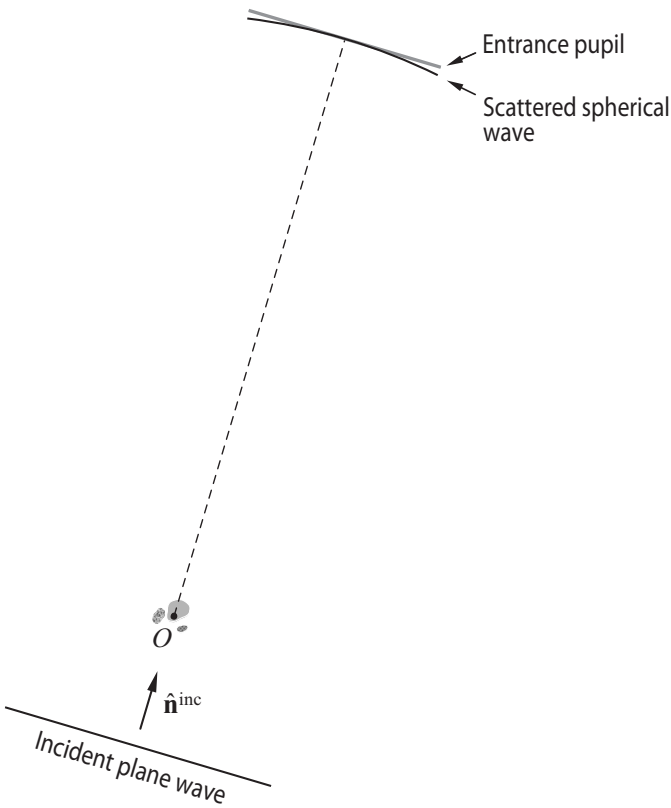

Fig. 13.2. The scattered spherical wavefront "interacts" with the incident plane wavefront only in the immediate vicinity of the exact forward-scattering direction.

called the extinction cross section, C_{ext}. Therefore, Eq. (13.17b) can be written as

$$\langle W_2 \rangle \approx (S_{\text{ep}} - C_{\text{ext}}) I^{\text{inc}} + O(r^{-2}), \tag{13.18}$$

where

$$C_{\text{ext}} = \frac{4\pi}{k_1 |\mathbf{E}_0^{\text{inc}}|^2} \operatorname{Im}\left[\mathbf{E}_1^{\text{sca}}(\hat{\mathbf{n}}^{\text{inc}}) \cdot (\mathbf{E}_0^{\text{inc}})^*\right]. \tag{13.19}$$

We will see in later chapters that the extinction cross section can exceed the area of the object's geometrical projection by a factor of several. Therefore, it is imperative to satisfy the following requirement:

$$D_{\text{ep}} \gg 2a, \tag{13.20}$$

where D_{ep} is the diameter of the entrance pupil and a is the radius of the smallest circumscribing sphere of the scattering object. Indeed, this requirement implies that the signal measured by WCR 2 is positive and, thus, physically meaningful. In general, this requirement does not apply to WCR 1 in Fig. 13.1.

There is another fundamental reason for imposing the requirement (13.20). As we have already emphasized, the far-field approximation implies the treatment of the scatterer as a point-like object. This treatment is justified for the derivation of the above formulas, but becomes too crude when one attempts to describe the interaction of the incident plane wave and the scattered field *over* the entrance pupil of the WCR facing the incident light. To do that properly, we should recall that the actual scattered field is a superposition of spherical wavelets generated by elementary volume elements of the scattering object (Section 5.1). It is clear from the previous discussion that each wavelet "interacts" with the incident plane wave only along the straight line drawn through the center of the corresponding volume element and parallel to the incidence direction $\hat{\mathbf{n}}^{\text{inc}}$ (Fig. 13.3a). Therefore, to capture each individual interaction, the surface of the entrance pupil must exceed the area of the shadow cast by the scatterer onto the plane normal to $\hat{\mathbf{n}}^{\text{inc}}$, Fig. 13.3b.

Another important practical aspect of FFS measurements is that the angular scattering pattern, as measured by WCR 1, for an object comparable to and larger than the wavelength is known to vary dramatically with scattering direction. This angular variability can be traced back to the complex exponential factor $\exp(-\mathrm{i}k_1\hat{\mathbf{r}}\cdot\mathbf{r}')$ on the right-hand side of Eq. (5.9). Indeed, the electric field contributions from two arbitrary elementary volumes of the scattering object centered at $\mathbf{r}'$ and $\mathbf{r}''$ interfere in the far zone, the result of the interference being controlled by the product

$$\exp(-\mathrm{i}k_1\hat{\mathbf{r}}\cdot\mathbf{r}')[\exp(-\mathrm{i}k_1\hat{\mathbf{r}}\cdot\mathbf{r}'')]^* = \exp[-\mathrm{i}k_1\hat{\mathbf{r}}\cdot(\mathbf{r}'-\mathbf{r}'')]. \tag{13.21}$$

Obviously, depending on the angle between $\hat{\mathbf{r}}$ and $\mathbf{r}'-\mathbf{r}''$ and on $|\mathbf{r}'-\mathbf{r}''|$, this complex exponential can be a rapidly varying function of $\hat{\mathbf{r}}$. As a result, the angular scattering pattern in the far zone can be expected to be a superposition of multiple maxima and minima generated by different pairs of elementary volume elements of the scatterer. The most rapidly changing component of the scattering pattern should be caused by the pairs of volume elements with $(\mathbf{r}'-\mathbf{r}'')\perp\hat{\mathbf{r}}$ and $|\mathbf{r}'-\mathbf{r}''|\approx 2a$. Therefore, the far-field angular pattern can be expected to vary quite significantly, even when the scattering direction changes by as little as $\pi/(2k_1a)$ (rad) since this change corresponds to a change of the phase $k_1\hat{\mathbf{r}}\cdot(\mathbf{r}'-\mathbf{r}'')$ equal to π. An example of this strong angular variability can be seen in Plate 17.1, discussed in Section 17.1.

Thus, for a WCR to fully resolve this angular variability, the distance r from the scattering object to the detector must satisfy the following inequality:

$$r \gg \frac{D_{\text{ep}}k_1a}{\pi}. \tag{13.22}$$

If this requirement is not met then WCR 1 records a complex convolution of the angular scattering pattern with the instrument angular aperture. For particles

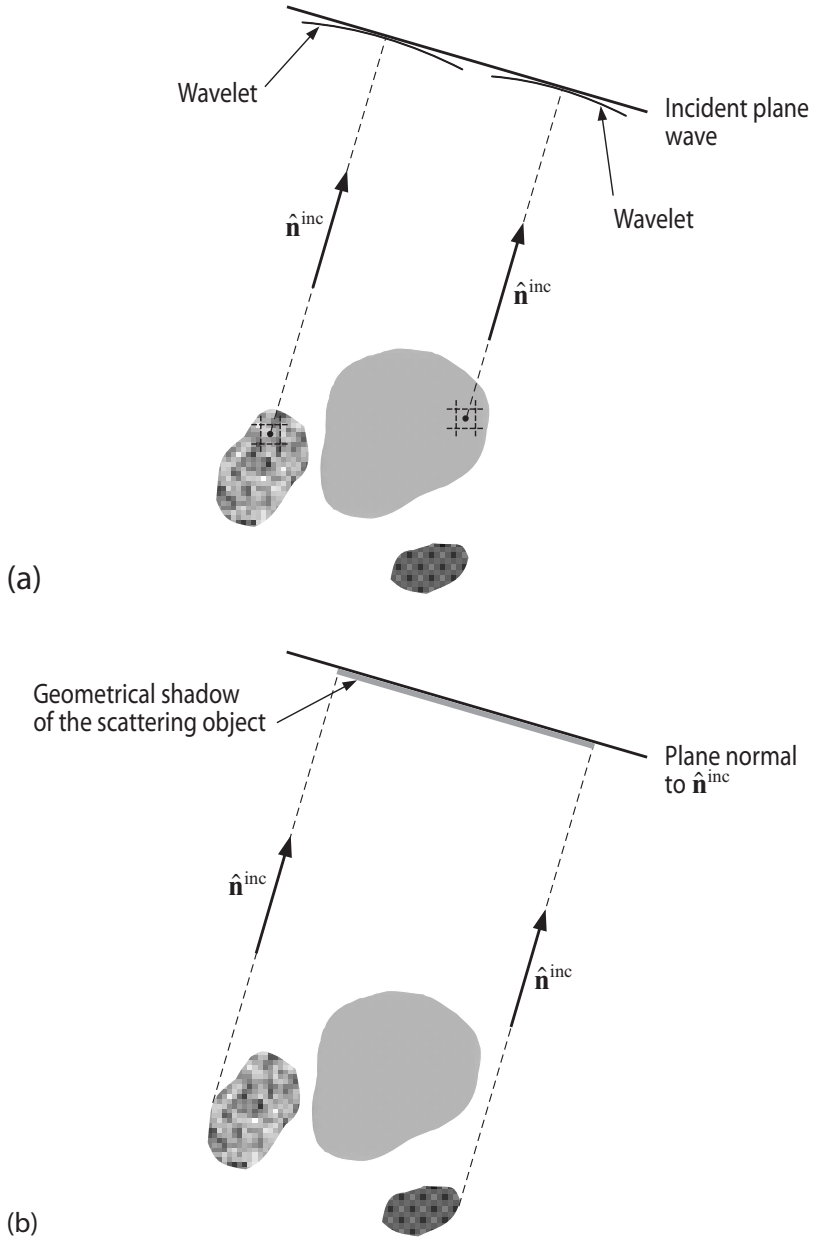

Fig. 13.3. **(a)** The spherical wavelets generated by different elementary volume elements interact with the incident plane wave along the respective straight lines parallel to $\hat{\mathbf{n}}^{\text{inc}}$. **(b)** To capture the interaction of all spherical wavelets generated by different elementary volume elements with the incident plane wave, the entrance pupil of a WCR must be larger than the object's geometrical projection onto the pupil.

greater than the wavelength, the condition (13.22) can become more demanding than the condition (13.5).

To conclude this section, let us go back to Fig. 13.1. It is easily seen that the time-averaged Poynting vector (13.10) at any point $\mathbf{r}'$ of the entrance pupil of WCR 1 is not directed along the optical axis of the instrument, since the complex electric and magnetic field vectors $\mathbf{E}(\mathbf{r}')$ and $\mathbf{H}(\mathbf{r}')$ of the total field are not parallel to the pupil plane. Yet, WCR 1 records a nonzero time-averaged signal described by Eq. (13.8). Similarly, the time-averaged Poynting vector $\langle \boldsymbol{\mathcal{S}}(\mathbf{r}', t)\rangle$ at any point $\mathbf{r}'$ of the entrance pupil of WCR 4 is not directed along the incidence direction, and yet WCR 4 registers a nonzero time-averaged signal given by Eq. (13.6). On the other hand, depending on the orientation of WCR 3, the Poynting vector $\langle \boldsymbol{\mathcal{S}}(\mathbf{r}', t)\rangle$ can be directed along its optical axis at certain points of its entrance pupil. Despite that, WCR 3 records no signal whatsoever. These facts demonstrate again that, in general, a WCR does not measure the directional flow of electromagnetic energy, but rather generates a certain signal defined by its specific optical design. The only exception is the case when all the wavefronts constituting the local electromagnetic field are parallel to the entrance pupil of the WCR. Only WCR 2 in Fig. 13.1 satisfies this condition and hence integrates over its entrance pupil the actual time-averaged Poynting vector of the total electromagnetic field. Thus, Fig. 13.1 demonstrates again that it is imperative to understand the physical nature of the *actual* measurement afforded by a WCR rather than to ascribe to the WCR a *desirable* measurement capability.

Despite the inherent inability of WCRs 1 and 4 to react to the local time-averaged Poynting vector, the readings of these two instruments can be used to calculate $\langle \boldsymbol{\mathcal{S}}(\mathbf{r}_1, t)\rangle$ in the particular setting of FFS. Indeed, owing to Eqs. (13.14) and (13.16) and the fact that $\hat{\mathbf{r}}_1 \neq \hat{\mathbf{n}}^{\text{inc}}$, the time-averaged interaction component $\langle \boldsymbol{\mathcal{S}}^{\text{ext}}(\mathbf{r}_1, t)\rangle$ in Eq. (13.10) must vanish. Therefore, summing the measured vectors $\langle \boldsymbol{\mathcal{S}}^{\text{inc}}(\mathbf{r}_1, t)\rangle \equiv \langle \boldsymbol{\mathcal{S}}^{\text{inc}}(\mathbf{r}_4, t)\rangle$ and $\langle \boldsymbol{\mathcal{S}}^{\text{sca}}(\mathbf{r}_1, t)\rangle$ yields the total time-averaged Poynting vector at $\mathbf{r}_1$:

$$\langle \boldsymbol{\mathcal{S}}(\mathbf{r}_1, t)\rangle = \frac{1}{S_{\text{ep}}}\left(\langle W_4\rangle \hat{\mathbf{n}}^{\text{inc}} + \langle W_1\rangle \hat{\mathbf{r}}_1\right). \tag{13.23}$$

13.2 Phase matrix

The fact that WCR 1 in Fig. 13.1 faces a quasi-plane wavefront, while WCR 2 faces a superposition of plane and quasi-plane wavefronts propagating in essentially the same direction allows us to apply directly the concepts introduced in Chapters 7 and 12. Indeed, we have assumed in the preceding section that the WCRs can measure only the total power of electromagnetic radiation impinging on their photodetectors and make no distinction between electromagnetic waves with different states of polarization. A WCR can indeed be made polarization-insensitive. However, we have seen in Chapter 12 that by interposing one or

more optical elements, such as polarizers and retarders, before the scattering object, one can generate the incident field with a specific state of polarization, whereas interposing one or more optical elements following the relay lens enables the WCR to measure the power corresponding to particular polarization components of the field impinging on the sensitive surface of the photodetector. By repeating the measurement for a number of different combinations and/or orientations of the optical elements, one can, in principle, determine the specific mathematical relationship between a complete set of polarization characteristics of the incident field and that of the field impinging on the entrance pupil of a WCR. This relationship is usually formulated in terms of the Stokes parameters and the so-called phase and extinction matrices.

Let us first consider the situation when the scattering direction is *away from the incidence direction* ($\hat{\mathbf{r}} \neq \hat{\mathbf{n}}^{\text{inc}}$). According to the previous discussion, WCR 1 in Fig. 13.1 reacts only to the outgoing spherical wave. Therefore, one can express the net polarization response of WCR 1 in terms of the Stokes column vector of the scattered wave as follows:

$$\langle \textbf{Signal 1} \rangle = S_{\text{ep}}\, \mathbf{I}^{\text{sca}}(r\hat{\mathbf{n}}^{\text{sca}}), \tag{13.24}$$

where $\hat{\mathbf{n}}^{\text{sca}} = \hat{\mathbf{r}}_1$. Recalling Eqs. (5.11) and (7.3), we have

$$\mathbf{I}^{\text{sca}}(r\hat{\mathbf{n}}^{\text{sca}}) = \frac{1}{2r^2}\sqrt{\frac{\epsilon_1}{\mu_0}} \begin{bmatrix} E_{1\theta}^{\text{sca}}(\hat{\mathbf{n}}^{\text{sca}})[E_{1\theta}^{\text{sca}}(\hat{\mathbf{n}}^{\text{sca}})]^* + E_{1\varphi}^{\text{sca}}(\hat{\mathbf{n}}^{\text{sca}})[E_{1\varphi}^{\text{sca}}(\hat{\mathbf{n}}^{\text{sca}})]^* \\ E_{1\theta}^{\text{sca}}(\hat{\mathbf{n}}^{\text{sca}})[E_{1\theta}^{\text{sca}}(\hat{\mathbf{n}}^{\text{sca}})]^* - E_{1\varphi}^{\text{sca}}(\hat{\mathbf{n}}^{\text{sca}})[E_{1\varphi}^{\text{sca}}(\hat{\mathbf{n}}^{\text{sca}})]^* \\ -E_{1\theta}^{\text{sca}}(\hat{\mathbf{n}}^{\text{sca}})[E_{1\varphi}^{\text{sca}}(\hat{\mathbf{n}}^{\text{sca}})]^* - E_{1\varphi}^{\text{sca}}(\hat{\mathbf{n}}^{\text{sca}})[E_{1\theta}^{\text{sca}}(\hat{\mathbf{n}}^{\text{sca}})]^* \\ \mathrm{i}\{E_{1\varphi}^{\text{sca}}(\hat{\mathbf{n}}^{\text{sca}})[E_{1\theta}^{\text{sca}}(\hat{\mathbf{n}}^{\text{sca}})]^* - E_{1\theta}^{\text{sca}}(\hat{\mathbf{n}}^{\text{sca}})[E_{1\varphi}^{\text{sca}}(\hat{\mathbf{n}}^{\text{sca}})]^*\} \end{bmatrix}. \tag{13.25}$$

An equivalent, but mathematically more convenient, form of Eq. (13.25) is that in terms of the coherency column vector defined by Eq. (7.40):

$$\langle \textbf{Signal 1} \rangle^J = S_{\text{ep}}\, \mathbf{J}^{\text{sca}}(r\hat{\mathbf{n}}^{\text{sca}}), \tag{13.26}$$

where

$$\mathbf{J}^{\text{sca}}(r\hat{\mathbf{n}}^{\text{sca}}) = \frac{1}{2r^2}\sqrt{\frac{\epsilon_1}{\mu_0}} \begin{bmatrix} E_{1\theta}^{\text{sca}}(\hat{\mathbf{n}}^{\text{sca}})[E_{1\theta}^{\text{sca}}(\hat{\mathbf{n}}^{\text{sca}})]^* \\ E_{1\theta}^{\text{sca}}(\hat{\mathbf{n}}^{\text{sca}})[E_{1\varphi}^{\text{sca}}(\hat{\mathbf{n}}^{\text{sca}})]^* \\ E_{1\varphi}^{\text{sca}}(\hat{\mathbf{n}}^{\text{sca}})[E_{1\theta}^{\text{sca}}(\hat{\mathbf{n}}^{\text{sca}})]^* \\ E_{1\varphi}^{\text{sca}}(\hat{\mathbf{n}}^{\text{sca}})[E_{1\varphi}^{\text{sca}}(\hat{\mathbf{n}}^{\text{sca}})]^* \end{bmatrix}. \tag{13.27}$$

Recalling that the coherency column vector of the incident plane wave is given by

$$\mathbf{J}^{\text{inc}} = \frac{1}{2}\sqrt{\frac{\epsilon_1}{\mu_0}} \begin{bmatrix} E_{0\theta}^{\text{inc}}(E_{0\theta}^{\text{inc}})^* \\ E_{0\theta}^{\text{inc}}(E_{0\varphi}^{\text{inc}})^* \\ E_{0\varphi}^{\text{inc}}(E_{0\theta}^{\text{inc}})^* \\ E_{0\varphi}^{\text{inc}}(E_{0\varphi}^{\text{inc}})^* \end{bmatrix}, \tag{13.28}$$

it is straightforward to derive the following mathematical relationship between the coherency column vectors of the incident and scattered waves:

$$\mathbf{J}^{\text{sca}}(r\hat{\mathbf{n}}^{\text{sca}}) = \frac{1}{r^2}\mathbf{Z}^J(\hat{\mathbf{n}}^{\text{sca}}, \hat{\mathbf{n}}^{\text{inc}})\mathbf{J}^{\text{inc}}, \tag{13.29}$$

where the elements of the 4×4 coherency phase matrix $\mathbf{Z}^J(\hat{\mathbf{n}}^{\text{sca}}, \hat{\mathbf{n}}^{\text{inc}})$ have the dimension of area and are quadratic combinations of the elements of the amplitude scattering matrix $\mathbf{S}(\hat{\mathbf{n}}^{\text{sca}}, \hat{\mathbf{n}}^{\text{inc}})$ defined by Eq. (5.24):

$$\mathbf{Z}^J = \begin{bmatrix} |S_{11}|^2 & S_{11}S_{12}^* & S_{12}S_{11}^* & |S_{12}|^2 \\ S_{11}S_{21}^* & S_{11}S_{22}^* & S_{12}S_{21}^* & S_{12}S_{22}^* \\ S_{21}S_{11}^* & S_{21}S_{12}^* & S_{22}S_{11}^* & S_{22}S_{12}^* \\ |S_{21}|^2 & S_{21}S_{22}^* & S_{22}S_{21}^* & |S_{22}|^2 \end{bmatrix}. \tag{13.30}$$

The Stokes column vector of the plane incident wave is given by

$$\mathbf{I}^{\text{inc}} = \frac{1}{2}\sqrt{\frac{\epsilon_1}{\mu_0}}\begin{bmatrix} E_{0\theta}^{\text{inc}}(E_{0\theta}^{\text{inc}})^* + E_{0\varphi}^{\text{inc}}(E_{0\varphi}^{\text{inc}})^* \\ E_{0\theta}^{\text{inc}}(E_{0\theta}^{\text{inc}})^* - E_{0\varphi}^{\text{inc}}(E_{0\varphi}^{\text{inc}})^* \\ -E_{0\theta}^{\text{inc}}(E_{0\varphi}^{\text{inc}})^* - E_{0\varphi}^{\text{inc}}(E_{0\theta}^{\text{inc}})^* \\ \mathrm{i}\left[E_{0\varphi}^{\text{inc}}(E_{0\theta}^{\text{inc}})^* - E_{0\theta}^{\text{inc}}(E_{0\varphi}^{\text{inc}})^*\right] \end{bmatrix}. \tag{13.31}$$

The corresponding scattering relationship now reads:

$$\mathbf{I}^{\text{sca}}(r\hat{\mathbf{n}}^{\text{sca}}) = \frac{1}{r^2}\mathbf{Z}(\hat{\mathbf{n}}^{\text{sca}}, \hat{\mathbf{n}}^{\text{inc}})\mathbf{I}^{\text{inc}}, \tag{13.32}$$

where $\mathbf{Z}(\hat{\mathbf{n}}^{\text{sca}}, \hat{\mathbf{n}}^{\text{inc}})$ is the 4×4 Stokes phase matrix. Explicit formulas for the elements of the Stokes phase matrix in terms of the amplitude scattering matrix elements result from

$$\mathbf{Z}(\hat{\mathbf{n}}^{\text{sca}}, \hat{\mathbf{n}}^{\text{inc}}) = \mathbf{D}\mathbf{Z}^J(\hat{\mathbf{n}}^{\text{sca}}, \hat{\mathbf{n}}^{\text{inc}})\mathbf{D}^{-1} \tag{13.33}$$

(Problem 13.3), where the matrices $\mathbf{D}$ and $\mathbf{D}^{-1}$ are given by Eq. (H.9), and are as follows (Problem 13.4):

$$Z_{11} = \frac{1}{2}\left(|S_{11}|^2 + |S_{12}|^2 + |S_{21}|^2 + |S_{22}|^2\right), \tag{13.34}$$

$$Z_{12} = \frac{1}{2}\left(|S_{11}|^2 - |S_{12}|^2 + |S_{21}|^2 - |S_{22}|^2\right), \tag{13.35}$$

$$Z_{13} = -\mathrm{Re}\left(S_{11}S_{12}^* + S_{22}S_{21}^*\right), \tag{13.36}$$

$$Z_{14} = -\mathrm{Im}\left(S_{11}S_{12}^* - S_{22}S_{21}^*\right), \tag{13.37}$$

$$Z_{21} = \frac{1}{2}\left(|S_{11}|^2 + |S_{12}|^2 - |S_{21}|^2 - |S_{22}|^2\right), \tag{13.38}$$

$$Z_{22} = \frac{1}{2}\left(|S_{11}|^2 - |S_{12}|^2 - |S_{21}|^2 + |S_{22}|^2\right), \tag{13.39}$$

$$Z_{23} = -\mathrm{Re}(S_{11}S_{12}^* - S_{22}S_{21}^*), \tag{13.40}$$

$$Z_{24} = -\mathrm{Im}(S_{11}S_{12}^* + S_{22}S_{21}^*), \tag{13.41}$$

$$Z_{31} = -\mathrm{Re}(S_{11}S_{21}^* + S_{22}S_{12}^*), \tag{13.42}$$

$$Z_{32} = -\mathrm{Re}(S_{11}S_{21}^* - S_{22}S_{12}^*), \tag{13.43}$$

$$Z_{33} = \mathrm{Re}(S_{11}S_{22}^* + S_{12}S_{21}^*), \tag{13.44}$$

$$Z_{34} = \mathrm{Im}(S_{11}S_{22}^* + S_{21}S_{12}^*), \tag{13.45}$$

$$Z_{41} = -\mathrm{Im}(S_{21}S_{11}^* + S_{22}S_{12}^*), \tag{13.46}$$

$$Z_{42} = -\mathrm{Im}(S_{21}S_{11}^* - S_{22}S_{12}^*), \tag{13.47}$$

$$Z_{43} = \mathrm{Im}(S_{22}S_{11}^* - S_{12}S_{21}^*), \tag{13.48}$$

$$Z_{44} = \mathrm{Re}(S_{22}S_{11}^* - S_{12}S_{21}^*). \tag{13.49}$$

The elements of the Stokes phase matrix $\mathbf{Z}$ are real-valued. Like the amplitude scattering matrix, the Stokes and coherency phase matrices depend on φ^{inc} and φ^{sca} explicitly, even when the incident and/or scattered light propagates along the z-axis of the laboratory coordinate system.

The elements of both phase matrices $\mathbf{Z}$ and $\mathbf{Z}^J$ have the dimension of area. It is easy to see that the dimensionless products of k_1^2 and the phase matrix elements satisfy the scale invariance rule (see Section 5.5). Another way to create scale-invariant quantities is to divide the phase matrix elements by a^2.

In general, all 16 elements of the Stokes phase matrix are nonzero. However, the phase matrix elements are expressed in terms of only seven independent real numbers resulting from the four moduli $|S_{ij}|$ $(i,j = 1, 2)$ and three differences in phase between the S_{ij}. Therefore, only seven of the phase matrix elements are actually independent, and there must exist nine independent relations among the sixteen phase matrix elements. Furthermore, the specific mathematical structure of the phase matrix can also be used to derive many useful linear and quadratic inequalities for the Stokes phase matrix elements. The most important of these inequalities are

$$Z_{11} \geq 0 \tag{13.50}$$

(this property follows directly from Eq. (13.34)) and

$$|Z_{ij}| \leq Z_{11} \quad (i, j = 1, \ldots, 4). \tag{13.51}$$

Hovenier and van der Mee (2000) review this subject and discuss how the general properties of the phase matrix can be used for testing the results of theoretical computations and laboratory measurements.

Equations (13.34)–(13.49) and (5.31) imply the following reciprocity relation for the Stokes phase matrix:

$$\mathbf{Z}(-\hat{\mathbf{n}}^{\mathrm{inc}}, -\hat{\mathbf{n}}^{\mathrm{sca}}) = \mathbf{\Delta}_3[\mathbf{Z}(\hat{\mathbf{n}}^{\mathrm{sca}}, \hat{\mathbf{n}}^{\mathrm{inc}})]^{\mathrm{T}}\mathbf{\Delta}_3, \tag{13.52}$$

where T denotes a transposed matrix and the 4×4 diagonal matrix $\boldsymbol{\Delta}_3$ is given by

$$\boldsymbol{\Delta}_3 = \boldsymbol{\Delta}_3^{\mathrm{T}} = \boldsymbol{\Delta}_3^{-1} = \mathrm{diag}[1, 1, -1, 1]. \tag{13.53}$$

The backscattering theorem (5.32) along with Eqs. (13.34), (13.39), (13.44), and (13.49) yields the following general property of the backscattering Stokes phase matrix (Mishchenko *et al*. 2000, p. 15):

$$Z_{11}(-\hat{\mathbf{n}}, \hat{\mathbf{n}}) - Z_{22}(-\hat{\mathbf{n}}, \hat{\mathbf{n}}) + Z_{33}(-\hat{\mathbf{n}}, \hat{\mathbf{n}}) - Z_{44}(-\hat{\mathbf{n}}, \hat{\mathbf{n}}) = 0. \tag{13.54}$$

13.3 Extinction matrix

Let us now consider the case of a polarimetric WCR centered at the *exact forward-scattering direction* ($\hat{\mathbf{r}} = \hat{\mathbf{n}}^{\mathrm{inc}}$), i.e., WCR 2 in Fig. 13.1. Because now both the incident plane wave and the scattered outgoing spherical wave propagate in essentially the same direction and are transverse, their superposition is also a transverse wave propagating in the forward direction. Therefore, we can define the coherency column vector of the total field for propagation directions $\hat{\mathbf{r}}'$ very close to $\hat{\mathbf{n}}^{\mathrm{inc}}$ as follows:

$$\mathbf{J}(r'\hat{\mathbf{r}}') = \frac{1}{2}\sqrt{\frac{\epsilon_1}{\mu_0}} \begin{bmatrix} E_\theta(r'\hat{\mathbf{r}}')[E_\theta(r'\hat{\mathbf{r}}')]^* \\ E_\theta(r'\hat{\mathbf{r}}')[E_\varphi(r'\hat{\mathbf{r}}')]^* \\ E_\varphi(r'\hat{\mathbf{r}}')[E_\theta(r'\hat{\mathbf{r}}')]^* \\ E_\varphi(r'\hat{\mathbf{r}}')[E_\varphi(r'\hat{\mathbf{r}}')]^* \end{bmatrix}, \tag{13.55}$$

where the total electric field is given by

$$\mathbf{E}(r'\hat{\mathbf{r}}') = \mathbf{E}^{\mathrm{inc}}(r'\hat{\mathbf{r}}') + \mathbf{E}^{\mathrm{sca}}(r'\hat{\mathbf{r}}'). \tag{13.56}$$

Integrating the elements of $\mathbf{J}(r'\hat{\mathbf{r}}')$ over the entrance pupil of WCR 2 and using Eqs. (13.3) and (13.14), we derive for the coherency-vector representation of the recorded net polarized signal (Problem 13.6):

$$\begin{aligned} \langle \textbf{Signal 2} \rangle^J &= \int_{S_{\mathrm{ep2}}} \mathrm{d}^2\mathbf{r}'\,\mathbf{J}(r'\hat{\mathbf{r}}') \\ &= S_{\mathrm{ep}}\mathbf{J}^{\mathrm{inc}} - \mathbf{K}^J(\hat{\mathbf{n}}^{\mathrm{inc}})\mathbf{J}^{\mathrm{inc}} + \frac{S_{\mathrm{ep}}}{r^2}\mathbf{Z}^J(\hat{\mathbf{n}}^{\mathrm{inc}}, \hat{\mathbf{n}}^{\mathrm{inc}})\mathbf{J}^{\mathrm{inc}} \qquad (13.57\text{a}) \\ &= S_{\mathrm{ep}}\mathbf{J}^{\mathrm{inc}} - \mathbf{K}^J(\hat{\mathbf{n}}^{\mathrm{inc}})\mathbf{J}^{\mathrm{inc}} + \boldsymbol{O}(r^{-2}), \qquad (13.57\text{b}) \end{aligned}$$

where $\mathbf{Z}^J(\hat{\mathbf{n}}^{\mathrm{inc}}, \hat{\mathbf{n}}^{\mathrm{inc}})$ is the forward-scattering coherency phase matrix, $\boldsymbol{O}(r^{-2})$ is a 4×4 matrix with all elements vanishing at infinity as r^{-2}, and the elements of the 4×4 coherency extinction matrix $\mathbf{K}^J(\theta^{\mathrm{inc}}, \varphi^{\mathrm{inc}})$ are expressed in the elements of the forward-scattering amplitude matrix $\mathbf{S}(\theta^{\mathrm{inc}}, \varphi^{\mathrm{inc}}; \theta^{\mathrm{inc}}, \varphi^{\mathrm{inc}})$ according to the following formula:

$$\mathbf{K}^J = \frac{\mathrm{i}2\pi}{k_1}\begin{bmatrix} S_{11}^* - S_{11} & S_{12}^* & -S_{12} & 0 \\ S_{21}^* & S_{22}^* - S_{11} & 0 & -S_{12} \\ -S_{21} & 0 & S_{11}^* - S_{22} & S_{12}^* \\ 0 & -S_{21} & S_{21}^* & S_{22}^* - S_{22} \end{bmatrix}. \tag{13.58}$$

In the Stokes-vector representation,

$$\langle \textbf{Signal 2} \rangle = \int_{S_{\mathrm{ep2}}} \mathrm{d}^2\mathbf{r}'\, \mathbf{I}(r'\hat{\mathbf{r}}')$$

$$= S_{\mathrm{ep}}\mathbf{I}^{\mathrm{inc}} - \mathbf{K}(\hat{\mathbf{n}}^{\mathrm{inc}})\mathbf{I}^{\mathrm{inc}} + \frac{S_{\mathrm{ep}}}{r^2}\mathbf{Z}(\hat{\mathbf{n}}^{\mathrm{inc}}, \hat{\mathbf{n}}^{\mathrm{inc}})\mathbf{I}^{\mathrm{inc}} \tag{13.59a}$$

$$= S_{\mathrm{ep}}\mathbf{I}^{\mathrm{inc}} - \mathbf{K}(\hat{\mathbf{n}}^{\mathrm{inc}})\mathbf{I}^{\mathrm{inc}} + \boldsymbol{O}(r^{-2}), \tag{13.59b}$$

where

$$\mathbf{I}(r\hat{\mathbf{n}}^{\mathrm{inc}}) = \mathbf{D}\,\mathbf{J}(r\hat{\mathbf{n}}^{\mathrm{inc}}), \tag{13.60}$$

and the 4×4 Stokes extinction matrix $\mathbf{K}(\hat{\mathbf{n}}^{\mathrm{inc}})$ is given by

$$\mathbf{K}(\hat{\mathbf{n}}^{\mathrm{inc}}) = \mathbf{D}\mathbf{K}^J(\hat{\mathbf{n}}^{\mathrm{inc}})\mathbf{D}^{-1}. \tag{13.61}$$

The explicit formulas for the elements of this matrix in terms of the elements of the forward-scattering amplitude matrix $\mathbf{S}(\theta^{\mathrm{inc}}, \varphi^{\mathrm{inc}};\ \theta^{\mathrm{inc}}, \varphi^{\mathrm{inc}})$ are as follows (Problem 13.7):

$$K_{jj} = \frac{2\pi}{k_1}\,\mathrm{Im}(S_{11} + S_{22}), \quad j = 1, \ldots, 4, \tag{13.62}$$

$$K_{12} = K_{21} = \frac{2\pi}{k_1}\,\mathrm{Im}(S_{11} - S_{22}), \tag{13.63}$$

$$K_{13} = K_{31} = -\frac{2\pi}{k_1}\,\mathrm{Im}(S_{12} + S_{21}), \tag{13.64}$$

$$K_{14} = K_{41} = \frac{2\pi}{k_1}\,\mathrm{Re}(S_{21} - S_{12}), \tag{13.65}$$

$$K_{23} = -K_{32} = \frac{2\pi}{k_1}\,\mathrm{Im}(S_{21} - S_{12}), \tag{13.66}$$

$$K_{24} = -K_{42} = -\frac{2\pi}{k_1}\,\mathrm{Re}(S_{12} + S_{21}), \tag{13.67}$$

$$K_{34} = -K_{43} = \frac{2\pi}{k_1}\,\mathrm{Re}(S_{22} - S_{11}). \tag{13.68}$$

The elements of the coherency and Stokes extinction matrices have the dimension of area. The dimensionless products of k_1^2 and elements of either extinction matrix, as well as the dimensionless ratios of the extinction matrix ele-

ments and a^2 satisfy the scale invariance rule (Section 5.5).

Equations (13.59) generalize the optical theorem. They show that the presence of the scattering object changes not only the total power of the electromagnetic radiation recorded by the WCR facing the incident wave (WCR 2 in Fig. 13.1), but also, perhaps, its state of polarization. The latter phenomenon is called dichroism and results from different attenuation rates for different polarization components of the incident wave.

By placing WCR 2 appropriately far from the scatterer, one can make the contribution of the third term on the right-hand side of Eq. (13.59b) negligibly small:

$$\langle \textbf{Signal 2} \rangle \underset{r \to \infty}{=} S_{\rm ep} \mathbf{I}^{\rm inc} - \mathbf{K}(\hat{\mathbf{n}}^{\rm inc}) \mathbf{I}^{\rm inc}. \tag{13.69}$$

As a consequence, the extinction matrix becomes a directly measurable quantity.

It is clear from Eqs. (13.62)–(13.68) that only seven of the sixteen elements of the Stokes extinction matrix are independent. It is easy to verify that this is also true of the coherency extinction matrix. The elements of both matrices explicitly depend on $\varphi^{\rm inc}$, even when the incident wave propagates along the positive or negative direction of the z-axis.

From Eqs. (5.31) and (13.62)–(13.68) we obtain the reciprocity relation for the Stokes extinction matrix:

$$\mathbf{K}(-\hat{\mathbf{n}}^{\rm inc}) = \mathbf{\Delta}_3 [\mathbf{K}(\hat{\mathbf{n}}^{\rm inc})]^{\rm T} \mathbf{\Delta}_3. \tag{13.70}$$

It is also straightforward to derive a closely related symmetry property (Problem 13.8):

$$\mathbf{K}(-\hat{\mathbf{n}}^{\rm inc}) = \begin{bmatrix} K_{11}(\hat{\mathbf{n}}^{\rm inc}) & K_{12}(\hat{\mathbf{n}}^{\rm inc}) & -K_{13}(\hat{\mathbf{n}}^{\rm inc}) & K_{14}(\hat{\mathbf{n}}^{\rm inc}) \\ K_{21}(\hat{\mathbf{n}}^{\rm inc}) & K_{22}(\hat{\mathbf{n}}^{\rm inc}) & K_{23}(\hat{\mathbf{n}}^{\rm inc}) & -K_{24}(\hat{\mathbf{n}}^{\rm inc}) \\ -K_{31}(\hat{\mathbf{n}}^{\rm inc}) & K_{32}(\hat{\mathbf{n}}^{\rm inc}) & K_{33}(\hat{\mathbf{n}}^{\rm inc}) & K_{34}(\hat{\mathbf{n}}^{\rm inc}) \\ K_{41}(\hat{\mathbf{n}}^{\rm inc}) & -K_{42}(\hat{\mathbf{n}}^{\rm inc}) & K_{43}(\hat{\mathbf{n}}^{\rm inc}) & K_{44}(\hat{\mathbf{n}}^{\rm inc}) \end{bmatrix}. \tag{13.71}$$

Thus, the only effect of reversing the direction of propagation is to change the sign of four elements of the Stokes extinction matrix.

13.4 Energy-budget problem

In the preceding three sections, we have discussed how the knowledge of the total electromagnetic field in the far zone can be used to quantify the electromagnetic response of an arbitrarily oriented WCR. In this section we will discuss the theoretical as well as experimental solution of the energy-budget problem for a volume enclosing the scattering object. Let us first surround the object by an imaginary sphere S of radius r large enough to be in the far zone. Since the host medium is assumed to be nonabsorbing and the scattering object is assumed to be

composed of passive materials (Section 2.5), the net rate at which the electromagnetic energy crosses the surface S of the sphere is always nonnegative and is equal to the power absorbed by the object:

$$\langle W^{\text{abs}}\rangle = -\oint_S \mathrm{d}^2\mathbf{r}\,\langle \boldsymbol{\mathcal{S}}(\mathbf{r},t)\rangle\cdot\hat{\mathbf{r}} = -r^2\int_{4\pi}\mathrm{d}\hat{\mathbf{r}}\,\langle \boldsymbol{\mathcal{S}}(\mathbf{r},t)\rangle\cdot\hat{\mathbf{r}} \tag{13.72}$$

(see Eq. (2.62)). According to Eq. (13.10), $\langle W^{\text{abs}}\rangle$ can be written as a combination of three terms:

$$\langle W^{\text{abs}}\rangle = \langle W^{\text{inc}}\rangle - \langle W^{\text{sca}}\rangle + \langle W^{\text{ext}}\rangle, \tag{13.73}$$

where

$$\langle W^{\text{inc}}\rangle = -r^2\int_{4\pi}\mathrm{d}\hat{\mathbf{r}}\,\langle \boldsymbol{\mathcal{S}}^{\text{inc}}(\mathbf{r},t)\rangle\cdot\hat{\mathbf{r}}, \tag{13.74}$$

$$\langle W^{\text{sca}}\rangle = r^2\int_{4\pi}\mathrm{d}\hat{\mathbf{r}}\,\langle \boldsymbol{\mathcal{S}}^{\text{sca}}(\mathbf{r},t)\rangle\cdot\hat{\mathbf{r}}, \tag{13.75}$$

$$\langle W^{\text{ext}}\rangle = -r^2\int_{4\pi}\mathrm{d}\hat{\mathbf{r}}\,\langle \boldsymbol{\mathcal{S}}^{\text{ext}}(\mathbf{r},t)\rangle\cdot\hat{\mathbf{r}}. \tag{13.76}$$

$\langle W^{\text{inc}}\rangle$ vanishes identically because the surrounding medium is nonabsorbing and $\langle \boldsymbol{\mathcal{S}}^{\text{inc}}(\mathbf{r},t)\rangle$ is a constant vector independent of $\mathbf{r}$. Therefore, $\langle W^{\text{abs}}\rangle$ is equal to the difference between the energy extinction rate and the energy scattering rate:

$$\langle W^{\text{abs}}\rangle = \langle W^{\text{ext}}\rangle - \langle W^{\text{sca}}\rangle. \tag{13.77}$$

Substituting Eqs. (13.12)–(13.16) in Eqs. (13.75) and (13.76) and recalling the definitions of the extinction and scattering cross sections, we derive, after some algebra:

$$\langle W^{\text{ext}}\rangle = \frac{2\pi}{k_1}\sqrt{\frac{\epsilon_1}{\mu_0}}\,\mathrm{Im}\big[\mathbf{E}_1^{\text{sca}}(\hat{\mathbf{n}}^{\text{inc}})\cdot(\mathbf{E}_0^{\text{inc}})^*\big], \tag{13.78}$$

$$\langle W^{\text{sca}}\rangle = \frac{1}{2}\sqrt{\frac{\epsilon_1}{\mu_0}}\int_{4\pi}\mathrm{d}\hat{\mathbf{r}}\,|\mathbf{E}_1^{\text{sca}}(\hat{\mathbf{r}})|^2. \tag{13.79}$$

In view of Eqs. (5.11) and (5.24), the last two formulas can be rewritten as follows (Problem 13.9):

$$\langle W^{\text{ext}}\rangle = K_{11}(\hat{\mathbf{n}}^{\text{inc}})I^{\text{inc}} + K_{12}(\hat{\mathbf{n}}^{\text{inc}})Q^{\text{inc}} + K_{13}(\hat{\mathbf{n}}^{\text{inc}})U^{\text{inc}} + K_{14}(\hat{\mathbf{n}}^{\text{inc}})V^{\text{inc}}, \tag{13.80}$$

$$\langle W^{\text{sca}}\rangle = r^2\int_{4\pi}\mathrm{d}\hat{\mathbf{r}}\,I^{\text{sca}}(r\hat{\mathbf{r}}) \tag{13.81a}$$

$$= \int_{4\pi}\mathrm{d}\hat{\mathbf{r}}\,[Z_{11}(\hat{\mathbf{r}},\hat{\mathbf{n}}^{\text{inc}})I^{\text{inc}} + Z_{12}(\hat{\mathbf{r}},\hat{\mathbf{n}}^{\text{inc}})Q^{\text{inc}} + Z_{13}(\hat{\mathbf{r}},\hat{\mathbf{n}}^{\text{inc}})U^{\text{inc}} + Z_{14}(\hat{\mathbf{r}},\hat{\mathbf{n}}^{\text{inc}})V^{\text{inc}}]. \tag{13.81b}$$

Equation (13.80) is another representation of the optical theorem and, along with Eqs. (13.62)–(13.68), shows that extinction is determined only by the amp-

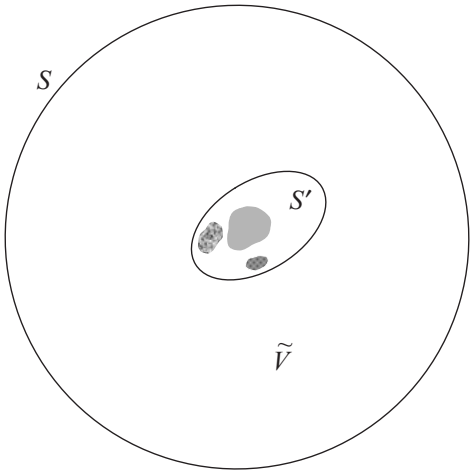

Fig. 13.4. Energy budget of a finite volume enclosing the scattering object.

litude scattering matrix corresponding to the exact forward direction. This is a direct consequence of the fact that extinction results from the interference between the incident and scattered wavefronts (Eq. (13.13)) and the presence of delta-function terms in Eqs. (13.14) and (13.16).

Note that the presence of the terms proportional to the delta function $\delta(\hat{\mathbf{n}}^{\text{inc}} + \hat{\mathbf{r}})$ on the right-hand sides of Eqs. (13.14) and (13.16) seems to indicate that there is interference of the incident field and the field scattered in the exact backscattering direction. It is easy to verify, however, that the backscattering contribution of the interference term $\langle \boldsymbol{\mathcal{S}}^{\text{ext}}(\mathbf{r}, t)\rangle$ to W^{ext} vanishes upon taking the real part of the right-hand side of Eq. (13.13).

Although we have derived Eqs. (13.80) and (13.81b) by considering a spherical far-field boundary S enclosing the object, the corresponding energy absorption rate (13.77) applies to any finite volume, as long as its boundary S' encloses the object completely (Fig. 13.4). Indeed, since the host medium is nonabsorbing, there is no energy loss in the volume $\widetilde{V}$ bounded by the surfaces S and S'. Therefore, the net rate at which the electromagnetic energy crosses the surface S' must exactly equal the flow of energy through the spherical surface S.

This result, along with Eqs. (13.80) and (13.81a), implies that the energy budget of any volume enclosing the object can be determined by using a far-field WCR. Indeed, it follows from Eqs. (13.24) and (13.69) that all one needs to do is to scan all outgoing propagation directions with a WCR pointed at the object. Of course, in real practice this procedure can be quite cumbersome.

13.5 Derivative characteristics of far-field scattering

Like the amplitude scattering matrix, the phase and extinction matrices are intrinsic far-field properties of the scattering object and are independent of the incident

field, besides being functions of the direction of incidence and of the angular frequency. The knowledge of these matrices allows one to model the response of an arbitrarily oriented far-zone WCR via Eqs. (13.24), (13.32), and (13.59), as well as to evaluate the energy budget of an arbitrary volume enclosing the object via Eqs. (13.77), (13.80), and (13.81b). Conversely, a far-zone WCR can be used to measure the phase and extinction matrices and, thus, to solve the energy-budget problem experimentally. We will see in later chapters that $\mathbf{Z}$ and $\mathbf{K}$ are sensitive functions of the object's size, morphology, composition, and orientation. Therefore, the very fact that the measurement of these matrices with a far-zone WCR can be modeled theoretically enables one to solve the inverse scattering problem and use WCRs – especially those with a polarimetric capability – as useful optical-characterization tools.

Although the phase and extinction matrices are the most general measurable descriptors of FFS and are independent of the Stokes parameters of the incident field, several derivative quantities have also been used, despite their potential dependence on $Q^{\rm inc}$, $U^{\rm inc}$, and/or $V^{\rm inc}$. For example, Eqs. (13.78)–(13.81) are often re-written in terms of the respective optical cross sections:

$$\langle W^{\rm ext}\rangle = C_{\rm ext} I^{\rm inc}, \tag{13.82}$$

$$\langle W^{\rm sca}\rangle = C_{\rm sca} I^{\rm inc}, \tag{13.83}$$

where the extinction cross section is given by Eq. (13.19) or, equivalently, by

$$C_{\rm ext} = \frac{1}{I^{\rm inc}}\left[K_{11}(\hat{\mathbf{n}}^{\rm inc})I^{\rm inc} + K_{12}(\hat{\mathbf{n}}^{\rm inc})Q^{\rm inc} + K_{13}(\hat{\mathbf{n}}^{\rm inc})U^{\rm inc} + K_{14}(\hat{\mathbf{n}}^{\rm inc})V^{\rm inc}\right], \tag{13.84}$$

while the scattering cross section is given by

$$\begin{aligned} C_{\rm sca} &= \frac{r^2}{I^{\rm inc}}\int_{4\pi} {\rm d}\hat{\mathbf{r}}\, I^{\rm sca}(r\hat{\mathbf{r}}) \\ &= \frac{1}{I^{\rm inc}}\int_{4\pi} {\rm d}\hat{\mathbf{r}}\left[Z_{11}(\hat{\mathbf{r}},\hat{\mathbf{n}}^{\rm inc})I^{\rm inc} + Z_{12}(\hat{\mathbf{r}},\hat{\mathbf{n}}^{\rm inc})Q^{\rm inc}\right. \\ &\qquad \left. + Z_{13}(\hat{\mathbf{r}},\hat{\mathbf{n}}^{\rm inc})U^{\rm inc} + Z_{14}(\hat{\mathbf{r}},\hat{\mathbf{n}}^{\rm inc})V^{\rm inc}\right]. \end{aligned} \tag{13.85}$$

The absorption cross section is defined as the difference of the extinction and scattering cross sections:

$$C_{\rm abs} = C_{\rm ext} - C_{\rm sca} \geq 0, \tag{13.86}$$

while the single-scattering albedo is defined as the ratio of the scattering and extinction cross sections:

$$\varpi = \frac{C_{\rm sca}}{C_{\rm ext}} \leq 1. \tag{13.87}$$

Obviously, $C_{\rm abs} = 0$ and $\varpi = 1$ for a lossless (nonabsorbing) object.

All optical cross sections are inherently nonnegative real-valued quantities and have the dimension of area. Unless the scattering object is spherically symmetric, they depend on the propagation direction, polarization state, and wavelength of the incident wave, as well as on the object's size, morphology, relative refractive index, and orientation with respect to the laboratory reference frame. The products of all three optical cross sections and k_1^2 obey the scale invariance rule.

Equation (13.18) shows that the extinction cross section is a well-defined, observable quantity that can be determined by measuring $\langle W_2 \rangle$ without and with the scattering object interposed between the source of light and WCR 2. The nominal effect of the object is to reduce the area of the entrance pupil by "casting a shadow" of area C_{ext}. Of course, this does not mean that C_{ext} is merely given by the area G of the object's geometrical projection on the detector surface. However, this geometrical interpretation of the extinction cross section illustrates the rationale for introducing the dimensionless efficiency factor for extinction as the ratio of the extinction cross section and the geometrical cross section:

$$Q_{\text{ext}} = \frac{C_{\text{ext}}}{G}. \tag{13.88}$$

We will see later that, depending on the object's physical parameters, Q_{ext} can be considerably greater or much less than unity. The efficiency factors for scattering and absorption are defined analogously:

$$Q_{\text{sca}} = \frac{C_{\text{sca}}}{G}, \quad Q_{\text{abs}} = \frac{C_{\text{abs}}}{G}. \tag{13.89}$$

It is easy to verify that all three efficiency factors obey the scale invariance rule.

The quantity

$$\begin{aligned}\frac{\mathrm{d}C_{\text{sca}}}{\mathrm{d}\Omega} &= \frac{I^{\text{sca}}(r\hat{\mathbf{r}})r^2}{I^{\text{inc}}} \\ &= \frac{1}{I^{\text{inc}}}[Z_{11}(\hat{\mathbf{r}},\hat{\mathbf{n}}^{\text{inc}})I^{\text{inc}} + Z_{12}(\hat{\mathbf{r}},\hat{\mathbf{n}}^{\text{inc}})Q^{\text{inc}} + Z_{13}(\hat{\mathbf{r}},\hat{\mathbf{n}}^{\text{inc}})U^{\text{inc}} + Z_{14}(\hat{\mathbf{r}},\hat{\mathbf{n}}^{\text{inc}})V^{\text{inc}}]\end{aligned} \tag{13.90}$$

has the dimension of area and is called the differential scattering cross section. It characterizes the angular dependence of the electromagnetic response of WCR 1 in Fig. 13.1 by specifying nominally the electromagnetic power scattered into a unit solid angle about a given direction per unit incident intensity.[1] The differential scattering cross section depends on the polarization state of the incident light as well as on the incidence and scattering directions. It is easily seen that

$$C_{\text{sca}} = \int_{4\pi} \mathrm{d}\hat{\mathbf{r}}\, \frac{\mathrm{d}C_{\text{sca}}}{\mathrm{d}\Omega}. \tag{13.91}$$

[1] Note that the symbol $\mathrm{d}C_{\text{sca}}/\mathrm{d}\Omega$ should not be interpreted as a derivative.

A quantity related to the differential scattering cross section is the phase function $p(\hat{\mathbf{r}}, \hat{\mathbf{n}}^{\text{inc}})$ defined by

$$p(\hat{\mathbf{r}}, \hat{\mathbf{n}}^{\text{inc}}) = \frac{4\pi}{C_{\text{sca}}} \frac{\mathrm{d}C_{\text{sca}}}{\mathrm{d}\Omega}. \tag{13.92}$$

The convenience of the phase function is that it is dimensionless and normalized:

$$\frac{1}{4\pi} \int_{4\pi} \mathrm{d}\hat{\mathbf{r}}\, p(\hat{\mathbf{r}}, \hat{\mathbf{n}}^{\text{inc}}) = 1. \tag{13.93}$$

The asymmetry parameter g is defined as the average cosine of the scattering angle $\Theta = \arccos(\hat{\mathbf{r}} \cdot \hat{\mathbf{n}}^{\text{inc}})$ (i.e., the angle between the incidence and scattering directions):

$$g = \frac{1}{4\pi} \int_{4\pi} \mathrm{d}\hat{\mathbf{r}}\, p(\hat{\mathbf{r}}, \hat{\mathbf{n}}^{\text{inc}}) \hat{\mathbf{r}} \cdot \hat{\mathbf{n}}^{\text{inc}} = \frac{1}{C_{\text{sca}}} \int_{4\pi} \mathrm{d}\hat{\mathbf{r}}\, \frac{\mathrm{d}C_{\text{sca}}}{\mathrm{d}\Omega}\, \hat{\mathbf{r}} \cdot \hat{\mathbf{n}}^{\text{inc}}. \tag{13.94}$$

The asymmetry parameter is positive if the phase function is peaked more toward the forward-scattering direction $\hat{\mathbf{r}} = \hat{\mathbf{n}}^{\text{inc}}$, is negative if $p(\hat{\mathbf{r}}, \hat{\mathbf{n}}^{\text{inc}})$ is peaked more toward the backscattering direction $\hat{\mathbf{r}} = -\hat{\mathbf{n}}^{\text{inc}}$, and vanishes if the phase function is symmetric with respect to the plane perpendicular to the incidence direction. It is easily seen that $g \in [-1, +1]$. The limiting values correspond to the (artificial) phase functions $4\pi\delta(\hat{\mathbf{r}} + \hat{\mathbf{n}}^{\text{inc}})$ and $4\pi\delta(\hat{\mathbf{r}} - \hat{\mathbf{n}}^{\text{inc}})$, respectively.

13.6 Polychromatic far-field scattering by a fixed object

Up until now we have been discussing only the case of monochromatic scattering. Let us now consider the incident field in the form of a parallel polychromatic beam with N monochromatic components, as described by Eqs. (10.10) and (10.11), while still assuming that the scattering object is fixed. It should be recognized that in the final analysis, Eqs. (13.32) and (13.59a) are particular coordinate-specific cases of Eq. (10.9). Therefore, similarly to Eq. (10.16), we can generalize Eqs. (13.24), (13.32), and (13.59a) as follows (Problem 13.10):

$$\langle\langle \textbf{Signal 1} \rangle\rangle = \frac{S_{\text{ep}}}{r^2} \sum_{n=1}^{N} \mathbf{Z}(\hat{\mathbf{n}}^{\text{sca}}, \hat{\mathbf{n}}^{\text{inc}}; \omega_n) \mathbf{I}_n^{\text{inc}}, \tag{13.95}$$

$$\langle\langle \textbf{Signal 2} \rangle\rangle = S_{\text{ep}} \sum_{n=1}^{N} \mathbf{I}_n^{\text{inc}} - \sum_{n=1}^{N} \mathbf{K}(\hat{\mathbf{n}}^{\text{inc}}; \omega_n) \mathbf{I}_n^{\text{inc}} + \frac{S_{\text{ep}}}{r^2} \sum_{n=1}^{N} \mathbf{Z}(\hat{\mathbf{n}}^{\text{inc}}, \hat{\mathbf{n}}^{\text{inc}}; \omega_n) \mathbf{I}_n^{\text{inc}}, \tag{13.96}$$

where the phase and extinction matrices are explicit functions of the angular frequency, the double angular brackets denote averaging over a time interval long enough to satisfy the inequality (9.6), and $\mathbf{I}_n^{\text{inc}}$ is the Stokes column vector of the nth monochromatic component. Similarly, Eqs. (13.80) and (13.81b) take the form

$$\langle\langle W^{\rm ext}\rangle\rangle = \sum_{n=1}^{N}\big[K_{11}(\hat{\mathbf{n}}^{\rm inc};\omega_n)I_n^{\rm inc} + K_{12}(\hat{\mathbf{n}}^{\rm inc};\omega_n)Q_n^{\rm inc} + K_{13}(\hat{\mathbf{n}}^{\rm inc};\omega_n)U_n^{\rm inc} + K_{14}(\hat{\mathbf{n}}^{\rm inc};\omega_n)V_n^{\rm inc}\big], \tag{13.97}$$

$$\langle\langle W^{\rm sca}\rangle\rangle = \sum_{n=1}^{N}\int_{4\pi}{\rm d}\hat{\mathbf{r}}\,\big[Z_{11}(\hat{\mathbf{r}},\hat{\mathbf{n}}^{\rm inc};\omega_n)I_n^{\rm inc} + Z_{12}(\hat{\mathbf{r}},\hat{\mathbf{n}}^{\rm inc};\omega_n)Q_n^{\rm inc} + Z_{13}(\hat{\mathbf{r}},\hat{\mathbf{n}}^{\rm inc};\omega_n)U_n^{\rm inc} + Z_{14}(\hat{\mathbf{r}},\hat{\mathbf{n}}^{\rm inc};\omega_n)V_n^{\rm inc}\big]. \tag{13.98}$$

Consistent with the discussion in Section 11.5, the formulas (13.95) and (13.96) (but not Eqs. (13.97) and (13.98)) are based on the assumption that the detection efficiency of the WCRs is frequency-independent, which implies a sufficiently narrow range of constituent angular frequencies.

Let us now consider the incident field in the form of a polychromatic parallel beam with quasi-monochromatic components given by Eqs. (10.17) and (10.18). A straightforward derivation analogous to that in Section 10.2 then yields the following generalized version of Eqs. (13.95)–(13.98) (Problem 13.11):

$$\langle\langle\textbf{Signal 1}\rangle\rangle = \frac{S_{\rm ep}}{r^2}\sum_{n=1}^{N}\mathbf{Z}(\hat{\mathbf{n}}^{\rm sca},\hat{\mathbf{n}}^{\rm inc};\omega_n)\langle\langle\mathbf{I}_n^{\rm inc}\rangle\rangle, \tag{13.99}$$

$$\langle\langle\textbf{Signal 2}\rangle\rangle = S_{\rm ep}\sum_{n=1}^{N}\langle\langle\mathbf{I}_n^{\rm inc}\rangle\rangle - \sum_{n=1}^{N}\mathbf{K}(\hat{\mathbf{n}}^{\rm inc};\omega_n)\langle\langle\mathbf{I}_n^{\rm inc}\rangle\rangle + \frac{S_{\rm ep}}{r^2}\sum_{n=1}^{N}\mathbf{Z}(\hat{\mathbf{n}}^{\rm inc},\hat{\mathbf{n}}^{\rm inc};\omega_n)\langle\langle\mathbf{I}_n^{\rm inc}\rangle\rangle, \tag{13.100}$$

$$\langle\langle W^{\rm ext}\rangle\rangle = \sum_{n=1}^{N}\big[K_{11}(\hat{\mathbf{n}}^{\rm inc};\omega_n)\langle\langle I_n^{\rm inc}\rangle\rangle + K_{12}(\hat{\mathbf{n}}^{\rm inc};\omega_n)\langle\langle Q_n^{\rm inc}\rangle\rangle + K_{13}(\hat{\mathbf{n}}^{\rm inc};\omega_n)\langle\langle U_n^{\rm inc}\rangle\rangle + K_{14}(\hat{\mathbf{n}}^{\rm inc};\omega_n)\langle\langle V_n^{\rm inc}\rangle\rangle\big], \tag{13.101}$$

$$\langle\langle W^{\rm sca}\rangle\rangle = \sum_{n=1}^{N}\int_{4\pi}{\rm d}\hat{\mathbf{r}}\,\big[Z_{11}(\hat{\mathbf{r}},\hat{\mathbf{n}}^{\rm inc};\omega_n)\langle\langle I_n^{\rm inc}\rangle\rangle + Z_{12}(\hat{\mathbf{r}},\hat{\mathbf{n}}^{\rm inc};\omega_n)\langle\langle Q_n^{\rm inc}\rangle\rangle + Z_{13}(\hat{\mathbf{r}},\hat{\mathbf{n}}^{\rm inc};\omega_n)\langle\langle U_n^{\rm inc}\rangle\rangle + Z_{14}(\hat{\mathbf{r}},\hat{\mathbf{n}}^{\rm inc};\omega_n)\langle\langle V_n^{\rm inc}\rangle\rangle\big], \tag{13.102}$$

where $\langle\langle\cdots\rangle\rangle$ denotes averaging over a time interval much longer than $T_{{\rm f}n}$ for any n. As before, the range of constituent angular frequencies in Eqs. (13.99) and (13.100) is assumed to be appropriately narrow.

13.7 Far-field scattering by a stochastic object

Let us now allow the size, morphology, refractive index, and orientation of the scattering object to change randomly in time. We will assume, however, that the object is always centered at (or very close to) the origin O of the laboratory coor-

dinate system and that the observation point is sufficiently far from the origin. This ensures that the formal criteria of FFS (5.15)–(5.17) are satisfied at all times. Furthermore, consistent with the discussion in Section 10.3, the temporal fluctuations of the object are assumed to occur much more slowly than the time-harmonic oscillations of the electromagnetic field. The above assumptions describe, for example, the scattering configuration shown in Plate 1.1a, wherein the position, size, shape, and orientation of the levitated micro-droplet can fluctuate in time.

Consider first the incident field in the form of a monochromatic plane wave given by Eqs. (10.2) and (10.6). Then, by analogy with Eq. (10.33), the formulas (13.24), (13.32), and (13.59a) can be generalized as follows (Problem 13.12):

$$\langle\langle \textbf{Signal 1} \rangle\rangle = \frac{S_{\rm ep}}{r^2} \langle\langle \mathbf{Z}(\hat{\mathbf{n}}^{\rm sca}, \hat{\mathbf{n}}^{\rm inc}; t) \rangle\rangle \mathbf{I}^{\rm inc}, \tag{13.103}$$

$$\langle\langle \textbf{Signal 2} \rangle\rangle = S_{\rm ep} \mathbf{I}^{\rm inc} - \langle\langle \mathbf{K}(\hat{\mathbf{n}}^{\rm inc}; t) \rangle\rangle \mathbf{I}^{\rm inc} + \frac{S_{\rm ep}}{r^2} \langle\langle \mathbf{Z}(\hat{\mathbf{n}}^{\rm inc}, \hat{\mathbf{n}}^{\rm inc}; t) \rangle\rangle \mathbf{I}^{\rm inc}, \tag{13.104}$$

$$\begin{aligned} \langle\langle W^{\rm ext} \rangle\rangle = {} & \langle\langle K_{11}(\hat{\mathbf{n}}^{\rm inc}; t) \rangle\rangle I^{\rm inc} + \langle\langle K_{12}(\hat{\mathbf{n}}^{\rm inc}; t) \rangle\rangle Q^{\rm inc} + \langle\langle K_{13}(\hat{\mathbf{n}}^{\rm inc}; t) \rangle\rangle U^{\rm inc} \\ & + \langle\langle K_{14}(\hat{\mathbf{n}}^{\rm inc}; t) \rangle\rangle V^{\rm inc}, \end{aligned} \tag{13.105}$$

$$\begin{aligned} \langle\langle W^{\rm sca} \rangle\rangle = \int_{4\pi} {\rm d}\hat{\mathbf{r}} \, [& \langle\langle Z_{11}(\hat{\mathbf{r}}, \hat{\mathbf{n}}^{\rm inc}; t) \rangle\rangle I^{\rm inc} + \langle\langle Z_{12}(\hat{\mathbf{r}}, \hat{\mathbf{n}}^{\rm inc}; t) \rangle\rangle Q^{\rm inc} \\ & + \langle\langle Z_{13}(\hat{\mathbf{r}}, \hat{\mathbf{n}}^{\rm inc}; t) \rangle\rangle U^{\rm inc} + \langle\langle Z_{14}(\hat{\mathbf{r}}, \hat{\mathbf{n}}^{\rm inc}; t) \rangle\rangle V^{\rm inc}], \end{aligned} \tag{13.106}$$

where the phase and extinction matrices are now explicit functions of time and the double angular brackets denote averaging over a time interval much longer than $T_{\rm v}$.

Assume now that the incident field is a polychromatic parallel beam with statistically independent quasi-monochromatic components given by Eqs. (10.17) and (10.18). Consistent with the discussion in Section 10.3, we also assume that the extinction and phase matrices corresponding to any ω_n on one hand and the quasi-instantaneous Stokes parameters of the corresponding quasi-monochromatic component of the incident field on the other hand are independent stationary random processes. Then Eqs. (13.99)–(13.102) take the following more general form (Problem 13.13):

$$\langle\langle \textbf{Signal 1} \rangle\rangle = \frac{S_{\rm ep}}{r^2} \sum_{n=1}^{N} \langle\langle \mathbf{Z}(\hat{\mathbf{n}}^{\rm sca}, \hat{\mathbf{n}}^{\rm inc}; \omega_n, t) \rangle\rangle \langle\langle \mathbf{I}_n^{\rm inc} \rangle\rangle, \tag{13.107}$$

$$\begin{aligned} \langle\langle \textbf{Signal 2} \rangle\rangle = {} & S_{\rm ep} \sum_{n=1}^{N} \langle\langle \mathbf{I}_n^{\rm inc} \rangle\rangle - \sum_{n=1}^{N} \langle\langle \mathbf{K}(\hat{\mathbf{n}}^{\rm inc}; \omega_n, t) \rangle\rangle \langle\langle \mathbf{I}_n^{\rm inc} \rangle\rangle \\ & + \frac{S_{\rm ep}}{r^2} \sum_{n=1}^{N} \langle\langle \mathbf{Z}(\hat{\mathbf{n}}^{\rm inc}, \hat{\mathbf{n}}^{\rm inc}; \omega_n, t) \rangle\rangle \langle\langle \mathbf{I}_n^{\rm inc} \rangle\rangle, \end{aligned} \tag{13.108}$$

$$\langle\langle W^{\text{ext}}\rangle\rangle = \sum_{n=1}^{N}\big[\langle\langle K_{11}(\hat{\mathbf{n}}^{\text{inc}};\omega_n,t)\rangle\rangle\langle\langle I_n^{\text{inc}}\rangle\rangle + \langle\langle K_{12}(\hat{\mathbf{n}}^{\text{inc}};\omega_n,t)\rangle\rangle\langle\langle Q_n^{\text{inc}}\rangle\rangle + \langle\langle K_{13}(\hat{\mathbf{n}}^{\text{inc}};\omega_n,t)\rangle\rangle\langle\langle U_n^{\text{inc}}\rangle\rangle + \langle\langle K_{14}(\hat{\mathbf{n}}^{\text{inc}};\omega_n,t)\rangle\rangle\langle\langle V_n^{\text{inc}}\rangle\rangle\big], \quad (13.109)$$

$$\langle\langle W^{\text{sca}}\rangle\rangle = \sum_{n=1}^{N}\int_{4\pi}\mathrm{d}\hat{\mathbf{r}}\,\big[\langle\langle Z_{11}(\hat{\mathbf{r}},\hat{\mathbf{n}}^{\text{inc}};\omega_n,t)\rangle\rangle\langle\langle I_n^{\text{inc}}\rangle\rangle + \langle\langle Z_{12}(\hat{\mathbf{r}},\hat{\mathbf{n}}^{\text{inc}};\omega_n,t)\rangle\rangle\langle\langle Q_n^{\text{inc}}\rangle\rangle + \langle\langle Z_{13}(\hat{\mathbf{r}},\hat{\mathbf{n}}^{\text{inc}};\omega_n,t)\rangle\rangle\langle\langle U_n^{\text{inc}}\rangle\rangle + \langle\langle Z_{14}(\hat{\mathbf{r}},\hat{\mathbf{n}}^{\text{inc}};\omega_n,t)\rangle\rangle\langle\langle V_n^{\text{inc}}\rangle\rangle\big], \quad (13.110)$$

where double angular brackets denote averaging over a time interval T such that $T \gg T_{\text{v}}$ and $T \gg T_{\text{f}n}$ for any n. These formulas are very important, since they show that averaging over time the extinction and phase matrices can be completely separated from averaging over time the Stokes parameters of the polychromatic incident field. This will allow us to use the principle of ergodicity in the following section. As before, Eqs. (13.107) and (13.108) are derived under the assumption that the detection efficiency of the WCR is frequency independent, which dictates a sufficiently narrow range of constituent angular frequencies.

13.8 Far-field scattering by an ergodic random object

Our final step is to assume that the random scattering object is ergodic and replace time averages of the extinction and phase matrices by appropriate ensemble averages, according to the discussion in Section 10.4. Then Eqs. (3.103)–(3.106) become

$$\langle\langle \textbf{Signal 1}\rangle\rangle = \frac{S_{\text{ep}}}{r^2}\langle\mathbf{Z}(\hat{\mathbf{n}}^{\text{sca}},\hat{\mathbf{n}}^{\text{inc}};\psi)\rangle_\psi\,\mathbf{I}^{\text{inc}}, \quad (13.111)$$

$$\langle\langle \textbf{Signal 2}\rangle\rangle = S_{\text{ep}}\mathbf{I}^{\text{inc}} - \langle\mathbf{K}(\hat{\mathbf{n}}^{\text{inc}};\psi)\rangle_\psi\,\mathbf{I}^{\text{inc}} + \frac{S_{\text{ep}}}{r^2}\langle\mathbf{Z}(\hat{\mathbf{n}}^{\text{inc}},\hat{\mathbf{n}}^{\text{inc}};\psi)\rangle_\psi\,\mathbf{I}^{\text{inc}}, \quad (13.112)$$

$$\langle\langle W^{\text{ext}}\rangle\rangle = \langle K_{11}(\hat{\mathbf{n}}^{\text{inc}};\psi)\rangle_\psi I^{\text{inc}} + \langle K_{12}(\hat{\mathbf{n}}^{\text{inc}};\psi)\rangle_\psi Q^{\text{inc}} + \langle K_{13}(\hat{\mathbf{n}}^{\text{inc}};\psi)\rangle_\psi U^{\text{inc}} + \langle K_{14}(\hat{\mathbf{n}}^{\text{inc}};\psi)\rangle_\psi V^{\text{inc}}, \quad (13.113)$$

$$\langle\langle W^{\text{sca}}\rangle\rangle = \int_{4\pi}\mathrm{d}\hat{\mathbf{r}}\,\big[\langle Z_{11}(\hat{\mathbf{r}},\hat{\mathbf{n}}^{\text{inc}};\psi)\rangle_\psi I^{\text{inc}} + \langle Z_{12}(\hat{\mathbf{r}},\hat{\mathbf{n}}^{\text{inc}};\psi)\rangle_\psi Q^{\text{inc}} + \langle Z_{13}(\hat{\mathbf{r}},\hat{\mathbf{n}}^{\text{inc}};\psi)\rangle_\psi U^{\text{inc}} + \langle Z_{14}(\hat{\mathbf{r}},\hat{\mathbf{n}}^{\text{inc}};\psi)\rangle_\psi V^{\text{inc}}\big], \quad (13.114)$$

where the state of the object ψ includes its size, morphology, relative refractive index, and shape, as well as its orientation and position with respect to the laboratory reference frame. Similarly, Eqs. (3.107)–(3.110) are modified as follows:

$$\langle\langle \textbf{Signal 1}\rangle\rangle = \frac{S_{\text{ep}}}{r^2}\sum_{n=1}^{N}\langle\mathbf{Z}(\hat{\mathbf{n}}^{\text{sca}},\hat{\mathbf{n}}^{\text{inc}};\omega_n,\psi)\rangle_\psi\,\langle\langle\mathbf{I}_n^{\text{inc}}\rangle\rangle, \quad (13.115)$$

$$\langle\langle \textbf{Signal 2} \rangle\rangle = S_{\rm ep} \sum_{n=1}^{N} \langle\langle \mathbf{I}_n^{\rm inc} \rangle\rangle - \sum_{n=1}^{N} \langle \mathbf{K}(\hat{\mathbf{n}}^{\rm inc}; \omega_n, \psi) \rangle_\psi \langle\langle \mathbf{I}_n^{\rm inc} \rangle\rangle + \frac{S_{\rm ep}}{r^2} \sum_{n=1}^{N} \langle \mathbf{Z}(\hat{\mathbf{n}}^{\rm inc}, \hat{\mathbf{n}}^{\rm inc}; \omega_n, \psi) \rangle_\psi \langle\langle \mathbf{I}_n^{\rm inc} \rangle\rangle, \tag{13.116}$$

$$\begin{aligned}\langle\langle W^{\rm ext} \rangle\rangle = \sum_{n=1}^{N} \big[& \langle K_{11}(\hat{\mathbf{n}}^{\rm inc}; \omega_n, \psi) \rangle_\psi \langle\langle I_n^{\rm inc} \rangle\rangle + \langle K_{12}(\hat{\mathbf{n}}^{\rm inc}; \omega_n, \psi) \rangle_\psi \langle\langle Q_n^{\rm inc} \rangle\rangle \\ & + \langle K_{13}(\hat{\mathbf{n}}^{\rm inc}; \omega_n, \psi) \rangle_\psi \langle\langle U_n^{\rm inc} \rangle\rangle \\ & + \langle K_{14}(\hat{\mathbf{n}}^{\rm inc}; \omega_n, \psi) \rangle_\psi \langle\langle V_n^{\rm inc} \rangle\rangle \big],\end{aligned} \tag{13.117}$$

$$\begin{aligned}\langle\langle W^{\rm sca} \rangle\rangle = \sum_{n=1}^{N} \int_{4\pi} {\rm d}\hat{\mathbf{r}} \big[& \langle Z_{11}(\hat{\mathbf{r}}, \hat{\mathbf{n}}^{\rm inc}; \omega_n, \psi) \rangle_\psi \langle\langle I_n^{\rm inc} \rangle\rangle + \langle Z_{12}(\hat{\mathbf{r}}, \hat{\mathbf{n}}^{\rm inc}; \omega_n, \psi) \rangle_\psi \langle\langle Q_n^{\rm inc} \rangle\rangle \\ & + \langle Z_{13}(\hat{\mathbf{r}}, \hat{\mathbf{n}}^{\rm inc}; \omega_n, \psi) \rangle_\psi \langle\langle U_n^{\rm inc} \rangle\rangle \\ & + \langle Z_{14}(\hat{\mathbf{r}}, \hat{\mathbf{n}}^{\rm inc}; \omega_n, \psi) \rangle_\psi \langle\langle V_n^{\rm inc} \rangle\rangle \big].\end{aligned} \tag{13.118}$$

Again, the use of Eqs. (13.115) and (13.116) implies an appropriately narrow range of constituent angular frequencies.

The practical importance of Eqs. (13.111)–(13.118) is hard to overstate. Although these formulas or their adaptations have usually been taken for granted, our detailed analysis shows that their explicit derivation is quite involved and is based on a number of specific assumptions that ultimately define the range of their applicability.

13.9 Ensemble averaging

Ensemble averaging of the extinction and phase matrices is, in principle, rather straightforward, provided that both matrices can be computed by solving the MMEs for a given scattering object characterized by the state $\psi = \{\mathbf{R}; \xi\}$, where $\mathbf{R}$ is the position vector of the object's origin and ξ denotes collectively the object's microphysical state, i.e., all physical characteristics of the object except for its coordinates. By analogy with Eq. (10.42), we have

$$\begin{Bmatrix} \langle \mathbf{K}(\hat{\mathbf{n}}^{\rm inc}; \psi) \rangle_\psi \\ \langle \mathbf{Z}(\hat{\mathbf{n}}^{\rm sca}, \hat{\mathbf{n}}^{\rm inc}; \psi) \rangle_\psi \end{Bmatrix} = \int {\rm d}\psi\, p(\psi) \begin{Bmatrix} \mathbf{K}(\hat{\mathbf{n}}^{\rm inc}; \psi) \\ \mathbf{Z}(\hat{\mathbf{n}}^{\rm sca}, \hat{\mathbf{n}}^{\rm inc}; \psi) \end{Bmatrix}, \tag{13.119}$$

where $p(\psi)$ is the corresponding probability density function.

As an example, let us assume that the droplet shown in Plate 1.1a can be modeled as a homogeneous ellipsoidal particle with semi-axes fluctuating within the ranges $a \in [a_{\rm min}, a_{\rm max}]$, $b \in [b_{\rm min}, b_{\rm max}]$, and $c \in [c_{\rm min}, c_{\rm max}]$ and with its geometrical center O' being confined to a spherical volume V around the origin O of the laboratory coordinate system (Fig. 13.5). The orientation of the particle with respect to the laboratory coordinate system can be parameterized by affixing a

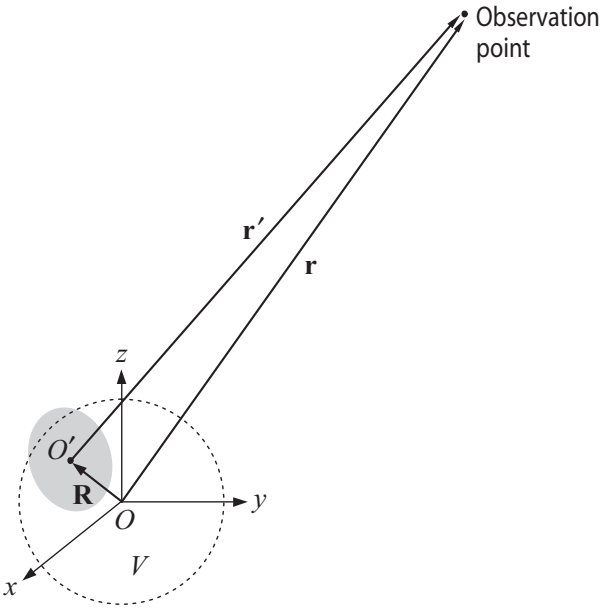

Fig. 13.5. The origin of the particle reference frame does not coincide with that of the laboratory reference frame.

Cartesian coordinate system to the particle and specifying the Euler angles α, β, and γ that transform the laboratory coordinate system into the particle coordinate system (see Appendix C). Then the ensemble average of the extinction matrix is given by

$$\langle \mathbf{K}(\hat{\mathbf{n}}^{\rm inc};\psi)\rangle_\psi = \int_V {\rm d}^3\mathbf{R}\int_0^{2\pi}{\rm d}\alpha\int_0^{\pi}{\rm d}\beta\,\sin\beta\int_0^{2\pi}{\rm d}\gamma\int_{a_{\rm min}}^{a_{\rm max}}{\rm d}a\int_{b_{\rm min}}^{b_{\rm max}}{\rm d}b\int_{c_{\rm min}}^{c_{\rm max}}{\rm d}c$$
$$\times\, p(\mathbf{R};\alpha,\beta,\gamma,a,b,c)\mathbf{K}(\hat{\mathbf{n}}^{\rm inc};\mathbf{R};\alpha,\beta,\gamma,a,b,c), \qquad (13.120)$$

where $\mathbf{R}$ is the position vector of the particle origin O' and the probability density function $p(\mathbf{R};\alpha,\beta,\gamma,a,b,c)$ satisfies the following normalization condition:

$$\int_V {\rm d}^3\mathbf{R}\int_0^{2\pi}{\rm d}\alpha\int_0^{\pi}{\rm d}\beta\,\sin\beta\int_0^{2\pi}{\rm d}\gamma\int_{a_{\rm min}}^{a_{\rm max}}{\rm d}a\int_{b_{\rm min}}^{b_{\rm max}}{\rm d}b\int_{c_{\rm min}}^{c_{\rm max}}{\rm d}c\; p(\mathbf{R};\alpha,\beta,\gamma,a,b,c) = 1. \qquad (13.121)$$

The integrals in Eq. (13.120) can be evaluated numerically by using an appropriate quadrature formula (Appendix E). Similarly,

$$\langle \mathbf{Z}(\hat{\mathbf{n}}^{\rm sca},\hat{\mathbf{n}}^{\rm inc};\psi)\rangle_\psi = \int_V {\rm d}^3\mathbf{R}\int_0^{2\pi}{\rm d}\alpha\int_0^{\pi}{\rm d}\beta\,\sin\beta\int_0^{2\pi}{\rm d}\gamma\int_{a_{\rm min}}^{a_{\rm max}}{\rm d}a\int_{b_{\rm min}}^{b_{\rm max}}{\rm d}b\int_{c_{\rm min}}^{c_{\rm max}}{\rm d}c$$
$$\times p(\mathbf{R};\alpha,\beta,\gamma,a,b,c)\mathbf{Z}(\hat{\mathbf{n}}^{\rm sca},\hat{\mathbf{n}}^{\rm inc};\mathbf{R};\alpha,\beta,\gamma,a,b,c). \qquad (13.122)$$

Equation (13.119) can often be simplified. For example, if the residence volume V is sufficiently small, then the need to average over particle positions can be obviated. Indeed, let the electric field of the incident plane wave be given by the usual expression

$$\mathbf{E}^{\text{inc}}(\mathbf{r}) = \mathbf{E}_0^{\text{inc}} \exp(\mathrm{i}k_1 \hat{\mathbf{n}}^{\text{inc}} \cdot \mathbf{r}), \tag{13.123}$$

where $\mathbf{r}$ is the position vector originating at O, and let $\mathbf{r}'$ be the position vector of the same observation point, but originating at the particle origin O' (Fig. 13.5). Since $\mathbf{r} = \mathbf{r}' + \mathbf{R}$, the incident electric field at the observation point can also be written as follows:

$$\mathbf{E}^{\text{inc}}(\mathbf{r}) = \mathbf{E}_0^{\text{inc}} \exp(\mathrm{i}k_1 \hat{\mathbf{n}}^{\text{inc}} \cdot \mathbf{r}') \exp(\mathrm{i}k_1 \hat{\mathbf{n}}^{\text{inc}} \cdot \mathbf{R}). \tag{13.124}$$

We know that the outgoing spherical wave generated by the particle in response to a plane-wave excitation of the form $\mathbf{E}_0^{\text{inc}} \exp(\mathrm{i}k_1 \hat{\mathbf{n}}^{\text{inc}} \cdot \mathbf{r}')$ in the far zone is given by

$$\frac{\exp(\mathrm{i}k_1 r')}{r'} \vec{A}(\hat{\mathbf{r}}', \hat{\mathbf{n}}^{\text{inc}}; \xi) \cdot \mathbf{E}_0^{\text{inc}},$$

where $\hat{\mathbf{r}}' = \mathbf{r}'/r'$ is the scattering direction originating at the particle origin O' and $\vec{A}(\hat{\mathbf{r}}', \hat{\mathbf{n}}^{\text{inc}}; \xi)$ is the scattering dyadic with respect to the particle reference frame. Therefore, the incident field (13.123) results in the following scattered field:

$$\mathbf{E}^{\text{sca}}(\mathbf{r}) = \frac{\exp(\mathrm{i}k_1 r')}{r'} \exp(\mathrm{i}k_1 \hat{\mathbf{n}}^{\text{inc}} \cdot \mathbf{R}) \vec{A}(\hat{\mathbf{r}}', \hat{\mathbf{n}}^{\text{inc}}; \xi) \cdot \mathbf{E}_0^{\text{inc}}. \tag{13.125}$$

Using the law of cosines,

$$r'^2 = r^2 + R^2 - 2\mathbf{r} \cdot \mathbf{R}, \tag{13.126}$$

we finally obtain

$$\mathbf{E}^{\text{sca}}(\mathbf{r}) = \frac{\exp(\mathrm{i}k_1 r)}{r} \vec{A}(\hat{\mathbf{r}}, \hat{\mathbf{n}}^{\text{inc}}; \mathbf{R}; \xi) \cdot \mathbf{E}_0^{\text{inc}}, \tag{13.127}$$

where $\hat{\mathbf{r}} = \mathbf{r}/r$ is the scattering direction originating at O,

$$\vec{A}(\hat{\mathbf{r}}, \hat{\mathbf{n}}^{\text{inc}}; \mathbf{R}; \xi) = \exp(\mathrm{i}\Delta) \vec{A}(\hat{\mathbf{r}}, \hat{\mathbf{n}}^{\text{inc}}; \xi) \tag{13.128}$$

is the scattering dyadic of the particle with respect to the laboratory coordinate system,

$$\Delta = k_1(\hat{\mathbf{n}}^{\text{inc}} - \hat{\mathbf{r}}) \cdot \mathbf{R}, \tag{13.129}$$

and we have further assumed that the following inequalities hold:

$$R \ll r, \tag{13.130}$$

$$k_1 R^2 \ll 2r, \tag{13.131}$$

and

$$\vec{A}(\hat{\mathbf{r}}', \hat{\mathbf{n}}^{\rm inc}; \xi) \approx \vec{A}(\hat{\mathbf{r}}, \hat{\mathbf{n}}^{\rm inc}; \xi). \tag{13.132}$$

Equation (13.127) describes a transverse outgoing spherical wave centered at the origin of the laboratory reference frame. This allows us to proceed in exactly the same way as we did in Section 5.3. Specifically, exploiting the transverse character of the wave yields

$$\mathbf{E}^{\rm sca}(\mathbf{r}) = \frac{\exp({\rm i}k_1 r)}{r}\mathbf{S}(\hat{\mathbf{r}}, \hat{\mathbf{n}}^{\rm inc}; \mathbf{R}; \xi)\mathbf{E}_0^{\rm inc}, \tag{13.133}$$

where we have used the notation of Eq. (5.25). The amplitude scattering matrix of the particle with respect to the laboratory coordinate system, $\mathbf{S}(\hat{\mathbf{r}}, \hat{\mathbf{n}}^{\rm inc}; \mathbf{R}; \xi)$, is expressed in terms of that with respect to the particle coordinate system, $\mathbf{S}(\hat{\mathbf{r}}, \hat{\mathbf{n}}^{\rm inc}; \xi)$, as follows:

$$\mathbf{S}(\hat{\mathbf{r}}, \hat{\mathbf{n}}^{\rm inc}; \mathbf{R}; \xi) = \exp({\rm i}\Delta)\mathbf{S}(\hat{\mathbf{r}}, \hat{\mathbf{n}}^{\rm inc}; \xi), \tag{13.134}$$

where it is assumed that the spatial orientations of the two coordinate systems are identical. An obvious consequence of this latter formula is that, irrespective of the particle's position within the residence volume V, the phase and extinction matrices of the particle with respect to the laboratory reference frame remain the same and are equal to those with respect to the particle reference frame (Problem 13.15):

$$\mathbf{Z}(\hat{\mathbf{r}}, \hat{\mathbf{n}}^{\rm inc}; \mathbf{R}; \xi) \equiv \mathbf{Z}(\hat{\mathbf{r}}, \hat{\mathbf{n}}^{\rm inc}; \mathbf{0}; \xi) = \mathbf{Z}(\hat{\mathbf{r}}, \hat{\mathbf{n}}^{\rm inc}; \xi), \tag{13.135}$$

$$\mathbf{K}(\hat{\mathbf{n}}^{\rm inc}; \mathbf{R}; \xi) \equiv \mathbf{K}(\hat{\mathbf{n}}^{\rm inc}; \mathbf{0}; \xi) = \mathbf{K}(\hat{\mathbf{n}}^{\rm inc}; \xi). \tag{13.136}$$

This result obviously eliminates the need to integrate over V in Eqs. (13.120) and (13.122), albeit at the expense of requiring that the criteria (13.130)–(13.132) be satisfied. The first two criteria imply that the observation point must be in the far zone of the entire residence volume in addition to being in the far zone of the particle itself. The requirement (13.20) must also be modified accordingly. Then Eqs. (13.111)–(13.114) take the form

$$\langle\langle \textbf{Signal 1} \rangle\rangle = \frac{S_{\rm ep}}{r^2}\langle \mathbf{Z}(\hat{\mathbf{n}}^{\rm sca}, \hat{\mathbf{n}}^{\rm inc}; \xi)\rangle_\xi \mathbf{I}^{\rm inc}, \tag{13.137}$$

$$\langle\langle \textbf{Signal 2} \rangle\rangle = S_{\rm ep}\mathbf{I}^{\rm inc} - \langle \mathbf{K}(\hat{\mathbf{n}}^{\rm inc}; \xi)\rangle_\xi \mathbf{I}^{\rm inc} + \frac{S_{\rm ep}}{r^2}\langle \mathbf{Z}(\hat{\mathbf{n}}^{\rm inc}, \hat{\mathbf{n}}^{\rm inc}; \xi)\rangle_\xi \mathbf{I}^{\rm inc}, \tag{13.138}$$

$$\begin{aligned}\langle\langle W^{\rm ext}\rangle\rangle = {}& \langle K_{11}(\hat{\mathbf{n}}^{\rm inc}; \xi)\rangle_\xi I^{\rm inc} + \langle K_{12}(\hat{\mathbf{n}}^{\rm inc}; \xi)\rangle_\xi Q^{\rm inc} + \langle K_{13}(\hat{\mathbf{n}}^{\rm inc}; \xi)\rangle_\xi U^{\rm inc} \\ & + \langle K_{14}(\hat{\mathbf{n}}^{\rm inc}; \xi)\rangle_\xi V^{\rm inc},\end{aligned} \tag{13.139}$$

$$\begin{aligned}\langle\langle W^{\rm sca}\rangle\rangle = {}& \int_{4\pi} {\rm d}\hat{\mathbf{r}}\,[\langle Z_{11}(\hat{\mathbf{r}}, \hat{\mathbf{n}}^{\rm inc}; \xi)\rangle_\xi I^{\rm inc} + \langle Z_{12}(\hat{\mathbf{r}}, \hat{\mathbf{n}}^{\rm inc}; \xi)\rangle_\xi Q^{\rm inc} \\ & + \langle Z_{13}(\hat{\mathbf{r}}, \hat{\mathbf{n}}^{\rm inc}; \xi)\rangle_\xi U^{\rm inc} + \langle Z_{14}(\hat{\mathbf{r}}, \hat{\mathbf{n}}^{\rm inc}; \xi)\rangle_\xi V^{\rm inc}],\end{aligned} \tag{13.140}$$

where

$$\begin{Bmatrix} \langle \mathbf{K}(\hat{\mathbf{n}}^{\text{inc}};\xi)\rangle_\xi \\ \langle \mathbf{Z}(\hat{\mathbf{n}}^{\text{sca}},\hat{\mathbf{n}}^{\text{inc}};\xi)\rangle_\xi \end{Bmatrix} = \int \mathrm{d}\xi\, p_\xi(\xi) \begin{Bmatrix} \mathbf{K}(\hat{\mathbf{n}}^{\text{inc}};\xi) \\ \mathbf{Z}(\hat{\mathbf{n}}^{\text{sca}},\hat{\mathbf{n}}^{\text{inc}};\xi) \end{Bmatrix}, \tag{13.141}$$

the $p_\xi(\xi)$ being the corresponding probability density function normalized to unity:

$$\int \mathrm{d}\xi\, p_\xi(\xi) = 1. \tag{13.142}$$

Similarly, Eqs. (13.115)–(13.118) take the form

$$\langle\langle \textbf{Signal 1} \rangle\rangle = \frac{S_{\text{ep}}}{r^2} \sum_{n=1}^{N} \langle \mathbf{Z}(\hat{\mathbf{n}}^{\text{sca}},\hat{\mathbf{n}}^{\text{inc}};\omega_n,\xi)\rangle_\xi \langle\langle \mathbf{I}_n^{\text{inc}} \rangle\rangle, \tag{13.143}$$

$$\begin{aligned} \langle\langle \textbf{Signal 2} \rangle\rangle = {} & S_{\text{ep}} \sum_{n=1}^{N} \langle\langle \mathbf{I}_n^{\text{inc}} \rangle\rangle - \sum_{n=1}^{N} \langle \mathbf{K}(\hat{\mathbf{n}}^{\text{inc}};\omega_n,\xi)\rangle_\xi \langle\langle \mathbf{I}_n^{\text{inc}} \rangle\rangle \\ & + \frac{S_{\text{ep}}}{r^2} \sum_{n=1}^{N} \langle \mathbf{Z}(\hat{\mathbf{n}}^{\text{inc}},\hat{\mathbf{n}}^{\text{inc}};\omega_n,\xi)\rangle_\xi \langle\langle \mathbf{I}_n^{\text{inc}} \rangle\rangle, \end{aligned} \tag{13.144}$$

$$\begin{aligned} \langle\langle W^{\text{ext}} \rangle\rangle = \sum_{n=1}^{N} \big[& \langle K_{11}(\hat{\mathbf{n}}^{\text{inc}};\omega_n,\xi)\rangle_\xi \langle\langle I_n^{\text{inc}} \rangle\rangle + \langle K_{12}(\hat{\mathbf{n}}^{\text{inc}};\omega_n,\xi)\rangle_\xi \langle\langle Q_n^{\text{inc}} \rangle\rangle \\ & + \langle K_{13}(\hat{\mathbf{n}}^{\text{inc}};\omega_n,\xi)\rangle_\xi \langle\langle U_n^{\text{inc}} \rangle\rangle \\ & + \langle K_{14}(\hat{\mathbf{n}}^{\text{inc}};\omega_n,\xi)\rangle_\xi \langle\langle V_n^{\text{inc}} \rangle\rangle \big], \end{aligned} \tag{13.145}$$

$$\begin{aligned} \langle\langle W^{\text{sca}} \rangle\rangle = \sum_{n=1}^{N} \int_{4\pi} \mathrm{d}\hat{\mathbf{r}}\, \big[& \langle Z_{11}(\hat{\mathbf{r}},\hat{\mathbf{n}}^{\text{inc}};\omega_n,\xi)\rangle_\xi \langle\langle I_n^{\text{inc}} \rangle\rangle + \langle Z_{12}(\hat{\mathbf{r}},\hat{\mathbf{n}}^{\text{inc}};\omega_n,\xi)\rangle_\xi \langle\langle Q_n^{\text{inc}} \rangle\rangle \\ & + \langle Z_{13}(\hat{\mathbf{r}},\hat{\mathbf{n}}^{\text{inc}};\omega_n,\xi)\rangle_\xi \langle\langle U_n^{\text{inc}} \rangle\rangle \\ & + \langle Z_{14}(\hat{\mathbf{r}},\hat{\mathbf{n}}^{\text{inc}};\omega_n,\xi)\rangle_\xi \langle\langle V_n^{\text{inc}} \rangle\rangle \big]. \end{aligned} \tag{13.146}$$

Further simplifications of the ensemble averaging procedure are possible if the shape/size and orientation probability distributions are statistically independent of each other. The total probability density function $p_\xi(\xi)$ can then be represented as a product of two functions, one of which describes the distribution of particle orientations, and the other describes the particle shape/size distribution. For example, in the case of the ellipsoidal droplet,

$$p_\xi(\alpha,\beta,\gamma,a,b,c) = p_{\text{o}}(\alpha,\beta,\gamma)\, p_{\text{s}}(a,b,c), \tag{13.147}$$

where the orientation, $p_{\text{o}}(\alpha,\beta,\gamma)$, and shape/size, $p_{\text{s}}(a,b,c)$, probability density functions are each normalized to unity:

$$\int_0^{2\pi} \mathrm{d}\alpha \int_0^{\pi} \mathrm{d}\beta \sin\beta \int_0^{2\pi} \mathrm{d}\gamma\, p_{\text{o}}(\alpha,\beta,\gamma) = 1, \tag{13.148}$$

$$\int_{a_{\min}}^{a_{\max}} \mathrm{d}a \int_{b_{\min}}^{b_{\max}} \mathrm{d}b \int_{c_{\min}}^{c_{\max}} \mathrm{d}c\, p_{\mathrm{s}}(a,b,c) = 1. \tag{13.149}$$

As a consequence, the tasks of computing orientation and shape/size averages are separated.

Similarly, it is often convenient to separate averaging over shapes and sizes by assuming that these microphysical parameters are statistically independent of each other. For example, the shape of a spheroidal particle can be specified by its aspect ratio ε (i.e., the ratio of the largest to the smallest axes) along with the designation of either prolate or oblate, whereas the particle size can be specified by an equivalent-sphere radius r. Then the shape/size probability density function $p_{\mathrm{s}}(\varepsilon, r)$ can be represented as a product

$$p_{\mathrm{s}}(\varepsilon, r) = p_{\varepsilon}(\varepsilon)\, n(r), \tag{13.150}$$

where $p_{\varepsilon}(\varepsilon)$ describes the distribution of spheroid aspect ratios and $n(r)$ is the distribution of equivalent-sphere radii. Again, both $p_{\varepsilon}(\varepsilon)$ and $n(r)$ are normalized to unity:

$$\int_{\varepsilon_{\min}}^{\varepsilon_{\max}} \mathrm{d}\varepsilon\, p(\varepsilon) = 1, \tag{13.151}$$

$$\int_{r_{\min}}^{r_{\max}} \mathrm{d}r\, n(r) = 1. \tag{13.152}$$

In the absence of external forces such as magnetic, electrostatic, or aerodynamic forces, all orientations of a stochastic nonspherical particle are equiprobable. In this practically important case of random orientation, the orientation distribution function is uniform with respect to the Euler angles of rotation, and we have

$$p_{\mathrm{o,random}}(\alpha, \beta, \gamma) = \frac{1}{8\pi^2} \tag{13.153}$$

(Problem 13.18). Particular details of the particle shape can also simplify the orientation distribution function. For example, for a rotationally symmetric body, it is convenient to direct the z-axis of the particle reference frame along the axis of rotation, in which case the orientation distribution function in the laboratory reference frame becomes independent of the Euler angle γ (Problem 13.19):

$$p_{\mathrm{o}}(\alpha, \beta, \gamma) = \frac{1}{2\pi}\, p_{\mathrm{o}}(\alpha, \beta). \tag{13.154}$$

Problems

13.1: Derive the inequality (13.5).

13.2: Derive Eq. (13.17a).

13.3: Derive Eq. (13.33).

13.4: Derive Eqs. (13.34)–(13.49).

13.5: Derive the reciprocity relation for the coherency phase matrix $\mathbf{Z}^J$ given by Eq. (13.30).

13.6: Derive Eqs. (13.57) and (13.58).

13.7: Derive Eqs. (13.62)–(13.68).

13.8: Derive Eq. (13.71).

13.9: Derive Eqs. (13.80) and (13.81).

13.10: Derive Eqs. (13.95)–(13.98).

13.11: Derive Eqs. (13.99)–(13.102).

13.12: Derive Eqs. (13.103)–(13.106).

13.13: Derive Eqs. (13.107)–(13.110).

13.14: What should be the minimal distance from the origin O in Fig. 13.5 to a WCR having an acceptance solid angle $\Delta\Omega$? Express this distance in terms of the radius of the spherical volume V and the maximal linear dimension L of the droplet. Keep in mind the discussion following Eq. (5.2) in Section 5.1.

13.15: Derive Eqs. (13.135) and (13.136).

13.16: Consider a WCR with its optical axis centered at the origin O (Fig. 13.5) along the radial direction $\hat{\mathbf{q}}$. Show that the pair of Eqs. (13.143) and (13.144) can be combined into the following single formula:

$$\langle\langle \mathbf{Signal}(\hat{\mathbf{q}})\rangle\rangle = \frac{S_{\text{ep}}}{r^2}\sum_{n=1}^{N}\langle \mathbf{Z}(\hat{\mathbf{q}},\hat{\mathbf{n}}^{\text{inc}};\omega_n,\xi)\rangle_\xi\,\langle\langle \mathbf{I}_n^{\text{inc}}\rangle\rangle$$
$$+\ \chi(\Delta\Omega_{\hat{\mathbf{q}}},\hat{\mathbf{n}}^{\text{inc}})\sum_{n=1}^{N}\left(S_{\text{ep}}-\langle \mathbf{K}(\hat{\mathbf{n}}^{\text{inc}};\omega_n,\xi)\rangle_\xi\right)\langle\langle \mathbf{I}_n^{\text{inc}}\rangle\rangle, \qquad (13.155)$$

where the angular step function $\chi(\Delta\Omega_{\hat{\mathbf{q}}},\hat{\mathbf{n}}^{\text{inc}})$ is defined by Eq. (11.10). Generalize this formula by allowing the incident electromagnetic field to be a superposition of several polychromatic beams with different propagation directions.

13.17: Generalize Eqs. (13.145) and (13.146) by allowing the incident field to be a superposition of several polychromatic beams with different propagation directions.

13.18: Verify Eq. (13.153).

13.19: Verify Eq. (13.154).

Notes and further reading

Instructive discussions of the optical theorem can be found in Berg *et al.* (2008) and Mishchenko *et al.* (2009a). They demonstrate that practical measurements of the extinction cross section can be a nontrivial problem. A more detailed discussion of electromagnetic scattering by a single random particle can be found in Chapter 6 of MTL2.

14

Electromagnetic scattering by a small random group of sparsely distributed particles

Although the far-field formulas derived in Chapter 13 for a stochastic scattering object are attractively simple, they have a rather limited range of applicability. Indeed, one of the criteria of the far zone, Eq. (5.14), becomes quite challenging for an object significantly greater than the wavelength (Problems 14.1 and 14.2) and often prohibits direct use of the far-field approximation. It turns out, however, that many aspects of the far-field formalism can be preserved if the stochastic scattering object belongs to a particular morphological type. Specifically, in this chapter we will assume that the object can be defined as a group of N distinct particles separated from each other and distributed throughout an imaginary volume element V. Accordingly, the starting point of the analysis of electromagnetic scattering by this object will be the FEs derived in Section 6.1 rather than the VIE. In addition, we will assume that:

- the total number of particles forming the object is sufficiently small and the average distance between them is sufficiently large that in the framework of the FEs (Section 6.1), each particle can be assumed to be "excited" only by the incident field;
- the N-particle object is observed from a distance much greater than any linear dimension of the volume element V;
- although the observation point is allowed to be in the near zone of the entire object, it is remote enough to be in the far zone of any of the N distinct particles forming the object; and
- the N particles are moving randomly and independently of each other throughout the volume element V.

The prime example of an application satisfying these requirements is the analysis of laboratory measurements of light scattering by tenuous collections of natural and artificial small particles, as discussed in Section 16.3.1.

As usual, we will first consider the scattering of a plane electromagnetic wave and then discuss the more general case of polychromatic scattering.

14.1 Single-scattering approximation for a fixed group of particles

We have seen in Section 6.1 that electromagnetic scattering by the object in the form of an arbitrary fixed group of N distinct finite particles is rigorously described by the vector form of the FEs (6.5)–(6.7). Let us now assume that the second term on the right-hand side of Eq. (6.6) is negligibly small in comparison with the first term. This means that each particle is excited only by the incident field, which is the gist of the so-called single-scattering approximation (SSA) for the fixed N-particle object. We then have instead of Eq. (6.5):

$$\mathbf{E}(\mathbf{r}) = \mathbf{E}^{\rm inc}(\mathbf{r}) + \mathbf{E}^{\rm sca}(\mathbf{r}), \quad \mathbf{r} \in \Re^3, \tag{14.1}$$

where the total scattered field is a vector sum of the partial scattered fields contributed by the individual particles:

$$\mathbf{E}^{\rm sca}(\mathbf{r}) = \sum_{i=1}^{N} \mathbf{E}_i^{\rm sca}(\mathbf{r}), \tag{14.2}$$

$$\mathbf{E}_i^{\rm sca}(\mathbf{r}) = \int_{V_i} {\rm d}^3\mathbf{r}' \overleftrightarrow{G}(\mathbf{r}, \mathbf{r}') \cdot \int_{V_i} {\rm d}^3\mathbf{r}'' \overleftrightarrow{T}_i(\mathbf{r}', \mathbf{r}'') \cdot \mathbf{E}^{\rm inc}(\mathbf{r}''). \tag{14.3}$$

It is easily seen that each partial field is independent of the partial fields scattered by all the other particles forming the object (see Eq. (4.24)).

Let us now choose the origin O of the laboratory coordinate system close to the geometrical center of the entire object, assume that the incident field is a plane electromagnetic wave with the propagation direction given by the unit vector $\hat{\mathbf{s}}$,

$$\mathbf{E}^{\rm inc}(\mathbf{r}) = \mathbf{E}_0^{\rm inc} \exp({\rm i}k_1 \hat{\mathbf{s}} \cdot \mathbf{r}), \quad \mathbf{E}_0^{\rm inc} \cdot \hat{\mathbf{s}} = 0, \tag{14.4}$$

$$\mathbf{H}^{\rm inc}(\mathbf{r}) = \sqrt{\frac{\epsilon_1}{\mu_0}}\, \hat{\mathbf{s}} \times \mathbf{E}_0^{\rm inc} \exp({\rm i}k_1 \hat{\mathbf{s}} \cdot \mathbf{r}), \tag{14.5}$$

and consider an external observation point that is located close enough to be in the near zone of the N-particle object, yet far enough to be in the far zone of any particle from the group, as shown in Fig. 14.1. Recall now Eqs. (5.19) and (5.20), which imply that the outgoing spherical wave generated by particle i in response to a plane-wave excitation of the form $\mathbf{E}_0^{\rm inc} \exp({\rm i}k_1 \hat{\mathbf{s}} \cdot \mathbf{r}_i)$ in the far zone of this particle is given by

$$\frac{\exp({\rm i}k_1 r_i)}{r_i}\, \overleftrightarrow{A}_i(\hat{\mathbf{r}}_i, \hat{\mathbf{s}}) \cdot \mathbf{E}_0^{\rm inc},$$

where $\mathbf{r}_i$ originates inside particle i (Fig. 14.1), $\overleftrightarrow{A}_i(\hat{\mathbf{r}}_i, \hat{\mathbf{s}})$ is the ith particle scattering dyadic centered at the particle origin, and $\hat{\mathbf{r}}_i = \mathbf{r}_i / r_i$ is the unit vector in

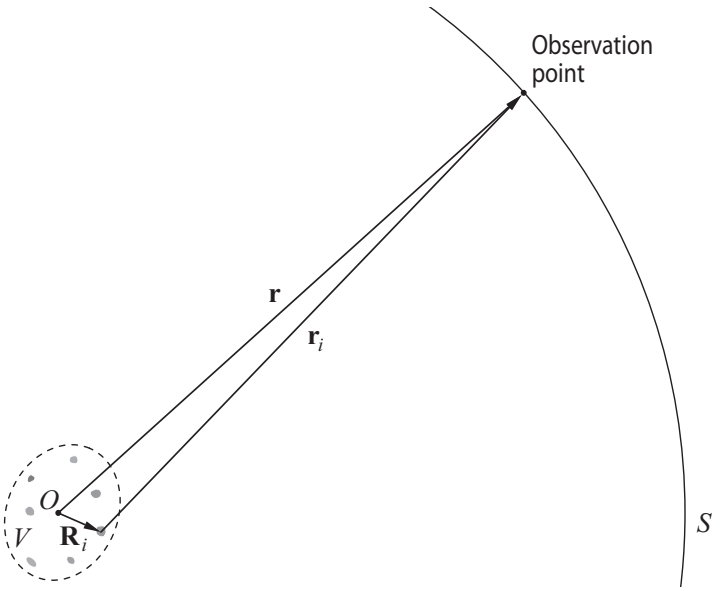

Fig. 14.1. A fixed group of N particles distributed throughout a volume element V is observed from a large distance r.

the scattering direction. To make use of this fact, we must rewrite Eq. (14.4) as follows:

$$\mathbf{E}^{\text{inc}}(\mathbf{r}) = \mathbf{E}_0^{\text{inc}} \exp(\mathrm{i}k_1 \hat{\mathbf{s}} \cdot \mathbf{r}_i) \exp(\mathrm{i}k_1 \hat{\mathbf{s}} \cdot \mathbf{R}_i), \tag{14.6}$$

where $\mathbf{R}_i$ connects the origin of the laboratory coordinate system with the origin of particle i (Fig. 14.1). We then have:

$$\mathbf{E}_i^{\text{sca}}(\mathbf{r}) = \exp(\mathrm{i}k_1 \hat{\mathbf{s}} \cdot \mathbf{R}_i) \frac{\exp(\mathrm{i}k_1 r_i)}{r_i} \overleftrightarrow{A}_i(\hat{\mathbf{r}}_i, \hat{\mathbf{s}}) \cdot \mathbf{E}_0^{\text{inc}}. \tag{14.7}$$

This formula is valid provided that the following inequalities hold for each particle from the group:

$$k_1(r_i - a_i) \gg 1, \tag{14.8}$$

$$r_i \gg a_i, \tag{14.9}$$

$$r_i \gg \frac{k_1 a_i^2}{2}, \tag{14.10}$$

where a_i is the radius of the smallest circumscribing sphere of particle i centered at its origin (cf. Eqs. (5.12)–(5.14)). The corresponding partial magnetic field is given by

$$\mathbf{H}_i^{\text{sca}}(\mathbf{r}) = \sqrt{\frac{\epsilon_1}{\mu_0}}\, \hat{\mathbf{r}}_i \times \mathbf{E}_i^{\text{sca}}(\mathbf{r}). \tag{14.11}$$

The reader can easily verify that Eqs. (14.2) and (14.7) could also be derived by keeping only the first sum on the right-hand side of the far-field Neumann expansion (6.48).

The above formulas, coupled with Eqs. (8.2) and (8.3), imply that the average of the PST of the total electromagnetic field at the remote observation point over a time interval much longer that the period of time-harmonic oscillations T_o is given by the real part of the following complex PST:

$$\vec{\vec{P}}(\mathbf{r}) = \frac{1}{2}\mathbf{H}(\mathbf{r}) \otimes [\mathbf{E}(\mathbf{r})]^* \tag{14.12a}$$

$$\begin{aligned} &= \vec{\vec{P}}^{\text{inc}} + \frac{1}{2}\sqrt{\frac{\epsilon_1}{\mu_0}}[\hat{\mathbf{s}} \times \mathbf{E}^{\text{inc}}(\mathbf{r})] \otimes \sum_{i=1}^{N} [\mathbf{E}_i^{\text{sca}}(\mathbf{r})]^* \\ &\quad + \frac{1}{2}\sqrt{\frac{\epsilon_1}{\mu_0}} \sum_{i=1}^{N} [\hat{\mathbf{r}}_i \times \mathbf{E}_i^{\text{sca}}(\mathbf{r})] \otimes [\mathbf{E}^{\text{inc}}(\mathbf{r})]^* \\ &\quad + \frac{1}{2}\sqrt{\frac{\epsilon_1}{\mu_0}} \sum_{i=1}^{N} [\hat{\mathbf{r}}_i \times \mathbf{E}_i^{\text{sca}}(\mathbf{r})] \otimes \sum_{j(\neq i)=1}^{N} [\mathbf{E}_j^{\text{sca}}(\mathbf{r})]^* \\ &\quad + \frac{1}{2}\sqrt{\frac{\epsilon_1}{\mu_0}} \sum_{i=1}^{N} [\hat{\mathbf{r}}_i \times \mathbf{E}_i^{\text{sca}}(\mathbf{r})] \otimes [\mathbf{E}_i^{\text{sca}}(\mathbf{r})]^*. \end{aligned} \tag{14.12b}$$

14.2 Ensemble-averaged Poynting–Stokes tensor of the total field

Let us now assume that the N-particle object is random and ergodic. Specifically, we assume that:

- averaging the complex PST of the entire object over a period of time much longer than T_v can be replaced by ensemble averaging:

$$\langle\langle \vec{\vec{P}}(\mathbf{r}) \rangle\rangle = \langle \vec{\vec{P}}(\mathbf{r}) \rangle_\psi; \tag{14.13}$$

- all particle positions $\mathbf{R}_i$, as well as all particle microphysical states ξ_i (and hence the corresponding particle-centered scattering dyadics $\vec{\vec{A}}_i(\hat{\mathbf{r}}_i, \hat{\mathbf{s}})$) as functions of time are independent random processes.

The latter assumption implies that averaging over all the individual-particle coordinates and all the individual-particle microphysical states can be performed independently:

$$\langle \vec{\vec{P}}(\mathbf{r}) \rangle_\psi = \langle \langle \vec{\vec{P}}(\mathbf{r}) \rangle_{\mathbf{R}} \rangle_\xi, \tag{14.14}$$

where

$$\langle \vec{\vec{P}}(\mathbf{r}) \rangle_{\mathbf{R}} = \vec{\vec{P}}^{\text{inc}} + \frac{1}{2}\sqrt{\frac{\epsilon_1}{\mu_0}}[\hat{\mathbf{s}} \times \mathbf{E}^{\text{inc}}(\mathbf{r})] \otimes \sum_{i=1}^{N} \langle \mathbf{E}_i^{\text{sca}}(\mathbf{r}) \rangle_{\mathbf{R}_i}^*$$

$$+\frac{1}{2}\sqrt{\frac{\epsilon_1}{\mu_0}}\sum_{i=1}^{N}\langle\hat{\mathbf{r}}_i\times\mathbf{E}_i^{\mathrm{sca}}(\mathbf{r})\rangle_{\mathbf{R}_i}\otimes[\mathbf{E}^{\mathrm{inc}}(\mathbf{r})]^*$$

$$+\frac{1}{2}\sqrt{\frac{\epsilon_1}{\mu_0}}\sum_{i=1}^{N}\langle\hat{\mathbf{r}}_i\times\mathbf{E}_i^{\mathrm{sca}}(\mathbf{r})\rangle_{\mathbf{R}_i}\otimes\sum_{j(\neq i)=1}^{N}\langle\mathbf{E}_j^{\mathrm{sca}}(\mathbf{r})\rangle_{\mathbf{R}_j}^*$$

$$+\frac{1}{2}\sqrt{\frac{\epsilon_1}{\mu_0}}\sum_{i=1}^{N}\langle\hat{\mathbf{r}}_i\times\mathbf{E}_i^{\mathrm{sca}}(\mathbf{r})\otimes[\mathbf{E}_i^{\mathrm{sca}}(\mathbf{r})]^*\rangle_{\mathbf{R}_i}. \tag{14.15}$$

To perform the averaging over the individual positions of the N particles, we assume that the corresponding coordinate probability density functions are given by

$$p_{\mathbf{R}}(\mathbf{R}_i)=\begin{cases}1/V & \text{if } \mathbf{R}_i\in V,\\ 0 & \text{if } \mathbf{R}_i\notin V\end{cases}\quad\text{for any } i, \tag{14.16}$$

which means that the individual spatial distributions of all the N particles throughout the entire volume element V are mutually independent and statistically uniform. This implies, of course, that the average particle packing density must be sufficiently small.

Let us first consider the last term on the right-hand side of Eq. (14.15) and make the following two assumptions: (i) the distance r from the origin of the laboratory coordinate system to the observation point (Fig. 14.1) is much greater than the characteristic linear dimension L of the volume V,

$$r\gg L, \tag{14.17}$$

and (ii) the angular variability of the individual particle-centered scattering dyadics is sufficiently weak:

$$\overleftrightarrow{A}_i(\hat{\mathbf{r}}_i,\hat{\mathbf{s}})\approx\overleftrightarrow{A}_i(\hat{\mathbf{r}},\hat{\mathbf{s}})\ \text{ for any } i. \tag{14.18}$$

Then integrating the last term over all particle positions yields

$$\frac{1}{2}\sqrt{\frac{\epsilon_1}{\mu_0}}\frac{1}{r^2}\sum_{i=1}^{N}\hat{\mathbf{r}}\times[\overleftrightarrow{A}_i(\hat{\mathbf{r}},\hat{\mathbf{s}})\cdot\mathbf{E}_0^{\mathrm{inc}}]\otimes[\overleftrightarrow{A}_i(\hat{\mathbf{r}},\hat{\mathbf{s}})\cdot\mathbf{E}_0^{\mathrm{inc}}]^* \tag{14.19}$$

for any observation point $\mathbf{r}$ located at a sufficiently large distance from the volume element V.

To determine the contributions of the second, third, and fourth terms on the right-hand side of Eq. (14.15), we need to know the averages $\langle\mathbf{E}_i^{\mathrm{sca}}(\mathbf{r})\rangle_{\mathbf{R}_i}$ and $\langle\hat{\mathbf{r}}_i\times\mathbf{E}_i^{\mathrm{sca}}(\mathbf{r})\rangle_{\mathbf{R}_i}$. Either average can be conveniently calculated using the spherical coordinate system originating at the observation point, as shown in Fig. 14.2a. For example, taking into account that $\mathbf{R}_i=\mathbf{r}+\mathbf{R}_i'$, where the vector $\mathbf{R}_i'$ connects the observation point and the origin of particle i, and recalling Eq. (14.7), we have:

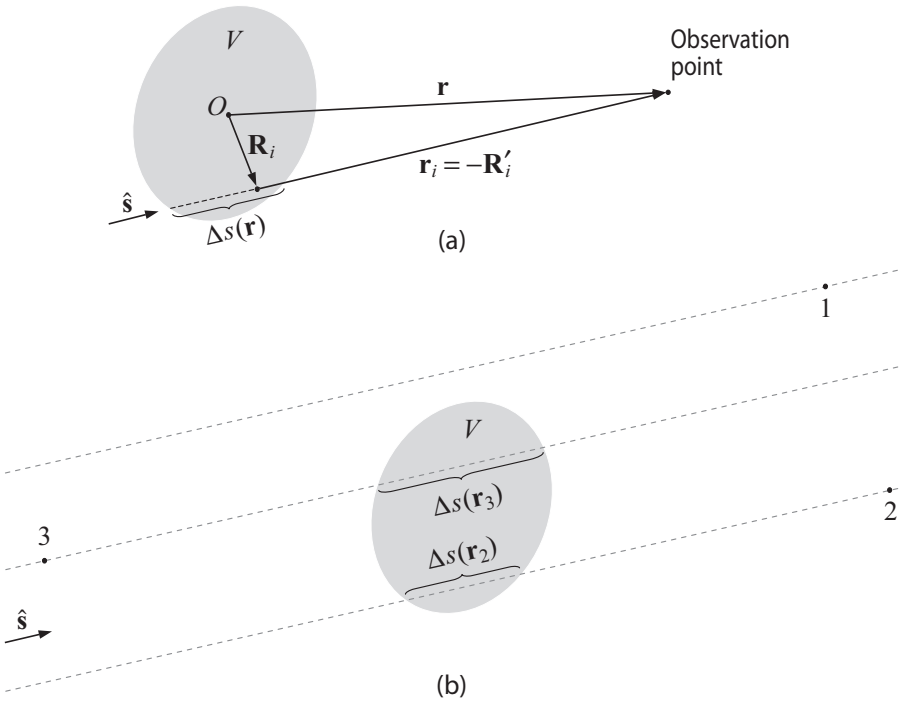

Fig. 14.2. Near-field scattering geometry.

$$\langle \mathbf{E}_i^{\mathrm{sca}}(\mathbf{r})\rangle_{\mathbf{R}_i} = \int_{\Re^3} \mathrm{d}\mathbf{R}_i\, p_{\mathbf{R}}(\mathbf{R}_i)\, \mathbf{E}_i^{\mathrm{sca}}(\mathbf{r})$$
$$= \int_{\Re^3} \mathrm{d}\mathbf{R}_i\, p_{\mathbf{R}}(\mathbf{R}_i) \exp(\mathrm{i}k_1 \hat{\mathbf{s}}\cdot\mathbf{R}'_i)\, \frac{\exp(\mathrm{i}k_1 r_i)}{r_i}\, \overleftrightarrow{A}_i(\hat{\mathbf{r}}_i, \hat{\mathbf{s}})\cdot \mathbf{E}^{\mathrm{inc}}(\mathbf{r}). \qquad (14.20)$$

Applying then the Saxon asymptotic expression (D.10) to the complex exponential $\exp(\mathrm{i}k_1 \hat{\mathbf{s}}\cdot\mathbf{R}'_i)$ yields

$$\langle \mathbf{E}_i^{\mathrm{sca}}(\mathbf{r})\rangle_{\mathbf{R}_i} = \frac{\mathrm{i}2\pi}{k_1} \int_{4\pi} \mathrm{d}\hat{\mathbf{R}}'_i \int_0^{\infty} \mathrm{d}R'_i\, [\delta(\hat{\mathbf{s}} + \hat{\mathbf{R}}'_i) - \delta(\hat{\mathbf{s}} - \hat{\mathbf{R}}'_i)\exp(2\mathrm{i}k_1 R'_i)]$$
$$\times\, p_{\mathbf{R}}(\mathbf{R}_i)\, \overleftrightarrow{A}_i(-\hat{\mathbf{R}}'_i, \hat{\mathbf{s}})\cdot \mathbf{E}^{\mathrm{inc}}(\mathbf{r}). \qquad (14.21)$$

The presence of two solid-angle delta functions in this formula implies that each average partial field $\langle \mathbf{E}_i^{\mathrm{sca}}(\mathbf{r})\rangle_{\mathbf{R}_i}$ is contributed to only by those points of the volume element V that belong to the segment $\Delta s(\mathbf{r})$ of the infinite straight line parallel to the unit vector $\hat{\mathbf{s}}$ and going through the observation point (Figs. 14.2a and 14.2b). Therefore, the following three scenarios must be considered in the computation of $\langle \mathbf{E}_i^{\mathrm{sca}}(\mathbf{r})\rangle_{\mathbf{R}_i}$:

- the observation point lies on a line that is parallel to the incidence direction and does not go through V (point 1 in Fig. 14.2b);

- the observation point is "shadowed" by V (point 2); or
- the observation point is located in front of V with respect to the incidence direction (point 3).

It is easily seen that the same scenarios must be considered in the computation of the average $\langle \hat{\mathbf{r}}_i \times \mathbf{E}_i^{\text{sca}}(\mathbf{r})\rangle_{\mathbf{R}_i}$.

First of all, it is quite obvious that for any point 1,

$$\langle \mathbf{E}_i^{\text{sca}}(\mathbf{r}_1)\rangle_{\mathbf{R}_i} = \langle \hat{\mathbf{r}}_i \times \mathbf{E}_i^{\text{sca}}(\mathbf{r})\rangle_{\mathbf{R}_i} = \mathbf{0}, \tag{14.22}$$

which, along with Eq. (14.19), yields

$$\langle \overleftrightarrow{P}(\mathbf{r}_1)\rangle_{\mathbf{R}} = \overleftrightarrow{P}^{\text{inc}} + \frac{1}{2}\sqrt{\frac{\epsilon_1}{\mu_0}}\frac{1}{r^2}\sum_{i=1}^{N} \hat{\mathbf{r}}_1 \times [\overleftrightarrow{A}_i(\hat{\mathbf{r}}_1, \hat{\mathbf{s}}) \cdot \mathbf{E}_0^{\text{inc}}] \otimes [\overleftrightarrow{A}_i(\hat{\mathbf{r}}_1, \hat{\mathbf{s}}) \cdot \mathbf{E}_0^{\text{inc}}]^*. \tag{14.23}$$

Second of all, it is straightforward to show that for any point 2,

$$\langle \mathbf{E}_i^{\text{sca}}(\mathbf{r}_2)\rangle_{\mathbf{R}_i} = \frac{\mathrm{i}\,2\pi}{k_1 V}\Delta s(\mathbf{r}_2)\,\overleftrightarrow{A}_i(\hat{\mathbf{s}}, \hat{\mathbf{s}}) \cdot \mathbf{E}^{\text{inc}}(\mathbf{r}_2), \tag{14.24}$$

$$\langle \hat{\mathbf{r}}_i \times \mathbf{E}_i^{\text{sca}}(\mathbf{r}_2)\rangle_{\mathbf{R}_i} = \frac{\mathrm{i}\,2\pi}{k_1 V}\Delta s(\mathbf{r}_2)\,\hat{\mathbf{s}} \times [\overleftrightarrow{A}_i(\hat{\mathbf{s}}, \hat{\mathbf{s}}) \cdot \mathbf{E}^{\text{inc}}(\mathbf{r}_2)]. \tag{14.25}$$

Furthermore, it follows from Eqs. (5.26)–(5.29), (13.62)–(13.65), and (13.84) that the factor

$$\frac{2\pi}{k_1 V}\Delta s(\mathbf{r}_2)\sum_{i=1}^{N} \overleftrightarrow{A}_i(\hat{\mathbf{s}}, \hat{\mathbf{s}})$$

is of the same order of magnitude as the sum of the extinction cross sections of all the particles filling the volume V divided by the volume's geometrical cross section:

$$\frac{1}{L^2}\sum_{i=1}^{N} C_{\text{ext},i}.$$

Assuming that this ratio is much smaller than unity,

$$\sum_{i=1}^{N} C_{\text{ext},i} \ll L^2, \tag{14.26}$$

we can neglect the fourth term on the right-hand side of Eq. (14.15) in comparison with the second and third terms at any observation point shadowed by the volume V. As a consequence,

$$\langle \overleftrightarrow{P}(\mathbf{r}_2)\rangle_{\mathbf{R}} = \overleftrightarrow{P}^{\text{inc}} + \frac{1}{2}\sqrt{\frac{\epsilon_1}{\mu_0}}\frac{\mathrm{i}\,2\pi}{k_1 V}\Delta s(\mathbf{r}_2)\sum_{i=1}^{N} \hat{\mathbf{s}} \times \{-\mathbf{E}_0^{\text{inc}} \otimes [\overleftrightarrow{A}_i(\hat{\mathbf{s}}, \hat{\mathbf{s}}) \cdot \mathbf{E}_0^{\text{inc}}]^* + [\overleftrightarrow{A}_i(\hat{\mathbf{s}}, \hat{\mathbf{s}}) \cdot \mathbf{E}_0^{\text{inc}}] \otimes [\mathbf{E}_0^{\text{inc}}]^*\}$$

$$+\frac{1}{2}\sqrt{\frac{\epsilon_1}{\mu_0}}\frac{1}{r^2}\sum_{i=1}^{N}\hat{\mathbf{r}}_2\times[\overleftrightarrow{A}_i(\hat{\mathbf{r}}_2,\hat{\mathbf{s}})\cdot\mathbf{E}_0^{\rm inc}]\otimes[\overleftrightarrow{A}_i(\hat{\mathbf{r}}_2,\hat{\mathbf{s}})\cdot\mathbf{E}_0^{\rm inc}]^*. \qquad (14.27)$$

Finally, let us consider point 3. It can be shown (Problem 14.3) that the contributions of the second and third terms on the right-hand side of Eq. (14.15) to $\mathrm{Re}\langle\overleftrightarrow{P}(\mathbf{r}_3)\rangle_{\mathbf{R}}$ cancel each other:

$$\mathrm{Re}\left\{[\hat{\mathbf{s}}\times\mathbf{E}^{\rm inc}(\mathbf{r}_3)]\otimes\langle\mathbf{E}_i^{\rm sca}(\mathbf{r}_3)\rangle_{\mathbf{R}_i}^*+\langle\hat{\mathbf{r}}_i\times\mathbf{E}_i^{\rm sca}(\mathbf{r}_3)\rangle_{\mathbf{R}_i}\otimes[\mathbf{E}^{\rm inc}(\mathbf{r}_3)]^*\right\}=\overleftrightarrow{0}. \qquad (14.28)$$

Also, we should take into account that the radial integral in Eq. (14.21) now contains a rapidly oscillating factor $\exp(2\mathrm{i}k_1R_i')$, which makes $\langle\mathbf{E}_i^{\rm sca}(\mathbf{r}_3)\rangle_{\mathbf{R}_i}$ much smaller than $\langle\mathbf{E}_i^{\rm sca}(\mathbf{r}_2)\rangle_{\mathbf{R}_i}$ provided that $k_1\Delta s(\mathbf{r}_3)\gg 1$. The latter condition is equivalent to the inequality

$$k_1L\gg 1, \qquad (14.29)$$

where L is the characteristic linear dimension of the volume element V. The same arguments apply to the average $\langle\hat{\mathbf{r}}_i\times\mathbf{E}_i^{\rm sca}(\mathbf{r}_3)\rangle_{\mathbf{R}_i}$. Thus we can conclude that the contribution of the fourth term on the right-hand side of Eq. (14.15) to $\langle\overleftrightarrow{P}(\mathbf{r}_3)\rangle_{\mathbf{R}}$ (and thus to the electromagnetic energy budget of the volume element V) is even smaller than that to $\langle\overleftrightarrow{P}(\mathbf{r}_2)\rangle_{\mathbf{R}}$. Thus,

$$\mathrm{Re}\langle\overleftrightarrow{P}(\mathbf{r}_3)\rangle_{\mathbf{R}}=\mathrm{Re}\,\overleftrightarrow{P}^{\rm inc}+\frac{1}{2}\sqrt{\frac{\epsilon_1}{\mu_0}}\frac{1}{r^2}\mathrm{Re}\sum_{i=1}^{N}\hat{\mathbf{r}}_3\times[\overleftrightarrow{A}_i(\hat{\mathbf{r}}_3,\hat{\mathbf{s}})\cdot\mathbf{E}_0^{\rm inc}]\otimes[\overleftrightarrow{A}_i(\hat{\mathbf{r}}_3,\hat{\mathbf{s}})\cdot\mathbf{E}_0^{\rm inc}]^*. \qquad (14.30)$$

14.3 Energy-budget problem

Let us now apply Eqs. (14.23), (14.27), and (14.30) to solving the standard energy-budget problem for the random N-particle object. Specifically, we surround the volume element V by an imaginary sphere S having a radius r much greater than the volume's typical linear dimension L, as shown in Fig. 14.1, and evaluate the integral

$$\langle W^{\rm abs}\rangle_{\mathbf{R}}=-\mathrm{Re}\oint_S \mathrm{d}^2\mathbf{r}\,\langle\mathbf{S}(\mathbf{r})\rangle_{\mathbf{R}}\cdot\hat{\mathbf{r}}. \qquad (14.31)$$

Equation (H.15) implies that the component $\mathbf{S}^{\rm inc}$ of the average Poynting vector contributed by $\overleftrightarrow{P}^{\rm inc}$ is always directed along the unit vector $\hat{\mathbf{s}}$. The same is true of the component $\langle\mathbf{S}^{\rm ext}(\mathbf{r})\rangle_{\mathbf{R}}$ contributed by the second term on the right-hand side of Eq. (14.27), whereas the component $\langle\mathbf{S}^{\rm sca}(\mathbf{r})\rangle_{\mathbf{R}}$ contributed by the term (14.19) is always directed along the unit vector $\hat{\mathbf{r}}$. It is easily seen that the integral of $\mathbf{S}^{\rm inc}\cdot\hat{\mathbf{r}}$ vanishes identically, while the component $\langle\mathbf{S}^{\rm ext}(\mathbf{r})\rangle_{\mathbf{R}}$ deviates from zero only over the shadow cast by the volume V on the spherical surface S. Performing the requisite integrations and recalling Eqs. (5.24) and (13.62)–(13.65), we finally obtain (Problem 14.4):

$$\langle W^{\text{abs}}\rangle_{\mathbf{R}} = \langle W^{\text{ext}}\rangle_{\mathbf{R}} - \langle W^{\text{sca}}\rangle_{\mathbf{R}}, \tag{14.32}$$

where

$$\langle W^{\text{ext}}\rangle_{\mathbf{R}} = \sum_{i=1}^{N}[K_{11}(\hat{\mathbf{s}};i)I^{\text{inc}} + K_{12}(\hat{\mathbf{s}};i)Q^{\text{inc}} + K_{13}(\hat{\mathbf{s}};i)U^{\text{inc}} + K_{14}(\hat{\mathbf{s}};i)V^{\text{inc}}], \tag{14.33}$$

$$\langle W^{\text{sca}}\rangle_{\mathbf{R}} = \int_{4\pi} \mathrm{d}\hat{\mathbf{r}} \sum_{i=1}^{N}[Z_{11}(\hat{\mathbf{r}},\hat{\mathbf{s}};i)I^{\text{inc}} + Z_{12}(\hat{\mathbf{r}},\hat{\mathbf{s}};i)Q^{\text{inc}} + Z_{13}(\hat{\mathbf{r}},\hat{\mathbf{s}};i)U^{\text{inc}} + Z_{14}(\hat{\mathbf{r}},\hat{\mathbf{s}};i)V^{\text{inc}}]. \tag{14.34}$$

In the above formulas, $\mathbf{K}(\hat{\mathbf{s}};i)$ and $\mathbf{Z}(\hat{\mathbf{r}},\hat{\mathbf{s}};i)$ are the particle-centered extinction and phase matrices of particle i, respectively, while $\mathbf{I}^{\text{inc}} = [I^{\text{inc}}, Q^{\text{inc}}, U^{\text{inc}}, V^{\text{inc}}]^{\text{T}}$ is the Stokes column vector of the incident field.

14.4 Response of a remote well-collimated radiometer

Let us now quantify the electromagnetic response of the two remote polarimetric WCRs shown in Fig. 14.3 and having their optical axes centered at the volume element V. We assume that both instruments are located in the near zone of the scattering object, yet sufficiently far from it. Specifically, we assume that either WCR is located in the far zones of all the N particles occupying the volume element V, which implies that the partial wavelets scattered by the particles become locally flat by the time they reach a WCR. Furthermore, although the acceptance solid angle $\Delta\Omega$ of either WCR is very small, its distance r from the center of the volume element V is sufficiently large that the solid angle subtended by V, as viewed from the WCR, is smaller than $\Delta\Omega$:

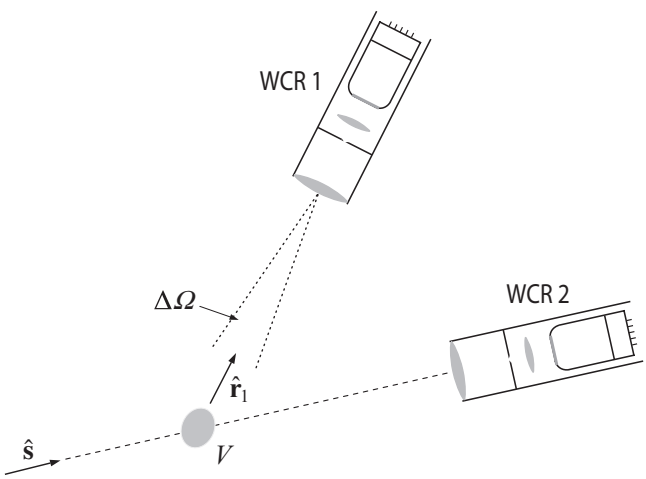

Fig. 14.3. Near-field measurement configuration.

$$\frac{\pi L^2}{4r^2} < \Delta\Omega. \tag{14.35}$$

As a consequence, either WCR captures all partial wavelets scattered by the N particles, irrespective of particles' locations within V, while WCR 2 also captures the incident plane wave. We also assume that the entrance pupil $S_{\rm ep}$ of WCR 2 is larger that than the geometrical shadow cast by the volume:

$$\frac{\pi L^2}{4} < S_{\rm ep}. \tag{14.36}$$

We will also assume that the inequalities (13.5), (14.17), and (14.18) hold.

Let us first consider the response of WCR 1. According to Section 11.4, this instrument integrates over its entrance pupil the time-averaged Stokes column vector of the superposition of the N near-plane wavelets propagating essentially in the same direction $\hat{\mathbf{r}}_1$. This Stokes column vector can be expressed in the corresponding time-averaged complex PST according to Eq. (H.16). Since the {objective lens, diaphragm} filter of WCR 1 does not pass the incident plane wave, the resulting PST averaged over all particle positions is given by Eq. (14.23), but without the incident-field term on the right-hand side:

$$\frac{1}{2}\sqrt{\frac{\epsilon_1}{\mu_0}}\,\frac{1}{r^2}\sum_{i=1}^{N}\hat{\mathbf{r}}_1\times[\ddot{A}_i(\hat{\mathbf{r}}_1,\hat{\mathbf{s}})\cdot\mathbf{E}_0^{\rm inc}]\otimes[\ddot{A}_i(\hat{\mathbf{r}}_1,\hat{\mathbf{s}})\cdot\mathbf{E}_0^{\rm inc}]^*. \tag{14.37}$$

After recalling Eqs. (13.34)–(13.49), it is straightforward to show (Problem 14.5) that the polarized response of WCR 1 averaged over all particle positions is given by

$$\langle\textbf{Signal 1}\rangle_{\mathbf{R}} = \frac{S_{\rm ep}}{r^2}\sum_{i=1}^{N}\mathbf{Z}(\hat{\mathbf{r}}_1,\hat{\mathbf{s}};i)\mathbf{I}^{\rm inc}. \tag{14.38}$$

Unlike the situation with WCR 1, the {objective lens, diaphragm} filter of WCR 2 does pass the incident plane wave as well as the N partial near-plane wavelets. As a consequence, the corresponding PST averaged over all particle positions is given by Eq. (14.27). The integration of this PST over the entrance pupil of WCR 2 finally yields (Problem 14.6):

$$\langle\textbf{Signal 2}\rangle_{\mathbf{R}} = S_{\rm ep}\mathbf{I}^{\rm inc} - \sum_{i=1}^{N}\mathbf{K}(\hat{\mathbf{s}};i)\mathbf{I}^{\rm inc} + \frac{S_{\rm ep}}{r^2}\sum_{i=1}^{N}\mathbf{Z}(\hat{\mathbf{s}},\hat{\mathbf{s}};i)\mathbf{I}^{\rm inc}. \tag{14.39}$$

14.5 First-order-scattering approximation

Equations (14.32)–(14.34), (14.38) and (14.39) summarize the so-called first-order-scattering approximation (FOSA) for the object in the form of a small group of sparsely distributed, randomly moving particles. Comparison of these formu-

las with their far-field counterparts (13.77), (13.80), and (13.81b) is quite instructive and shows that: (i) the energy budget of the small random group is a simple "incoherent" sum of the individual-particle energy budgets, and (ii) the polarized readings of near-field yet sufficiently distant WCRs can be modeled by summing up the corresponding single-particle far-field readings.

An important and convenient feature of the FOSA is that it satisfies the energy conservation law. Indeed, comparison of Eqs. (14.32)–(14.34) with Eqs. (13.77), (13.80), and (13.81b) shows that $\langle W^{\rm abs}\rangle_{\mathbf{R}}$ for the entire volume element V vanishes, provided that each member of the N-particle group is nonabsorbing.

The main results of the FOSA can be generalized by assuming that the microphysical states of the N particles change randomly and independently of each other as well as independently of the particle positions. Then invoking Eqs. (14.13) and (14.14) yields:

$$\langle\langle W^{\rm ext}\rangle\rangle = \sum_{i=1}^{N}[\langle K_{11}(\hat{\mathbf{s}};\xi_i)\rangle_{\xi_i} I^{\rm inc} + \langle K_{12}(\hat{\mathbf{s}};\xi_i)\rangle_{\xi_i} Q^{\rm inc} + \langle K_{13}(\hat{\mathbf{s}};\xi_i)\rangle_{\xi_i} U^{\rm inc} + \langle K_{14}(\hat{\mathbf{s}};\xi_i)\rangle_{\xi_i} V^{\rm inc}], \tag{14.40}$$

$$\langle\langle W^{\rm sca}\rangle\rangle = \int_{4\pi} {\rm d}\hat{\mathbf{r}} \sum_{i=1}^{N}[\langle Z_{11}(\hat{\mathbf{r}},\hat{\mathbf{s}};\xi_i)\rangle_{\xi_i} I^{\rm inc} + \langle Z_{12}(\hat{\mathbf{r}},\hat{\mathbf{s}};\xi_i)\rangle_{\xi_i} Q^{\rm inc} + \langle Z_{13}(\hat{\mathbf{r}},\hat{\mathbf{s}};\xi_i)\rangle_{\xi_i} U^{\rm inc} + \langle Z_{14}(\hat{\mathbf{r}},\hat{\mathbf{s}};\xi_i)\rangle_{\xi_i} V^{\rm inc}], \tag{14.41}$$

$$\langle\langle \textbf{Signal 1}\rangle\rangle = \frac{S_{\rm ep}}{r^2}\sum_{i=1}^{N}\langle \mathbf{Z}(\hat{\mathbf{r}}_1,\hat{\mathbf{s}};\xi_i)\rangle_{\xi_i}\mathbf{I}^{\rm inc}, \tag{14.42}$$

$$\langle\langle \textbf{Signal 2}\rangle\rangle = S_{\rm ep}\mathbf{I}^{\rm inc} - \sum_{i=1}^{N}\langle \mathbf{K}(\hat{\mathbf{s}};\xi_i)\rangle_{\xi_i}\mathbf{I}^{\rm inc} + \frac{S_{\rm ep}}{r^2}\sum_{i=1}^{N}\langle \mathbf{Z}(\hat{\mathbf{s}},\hat{\mathbf{s}};\xi_i)\rangle_{\xi_i}\mathbf{I}^{\rm inc}. \tag{14.43}$$

A fundamental consequence of the "additivity" of the extinction and phase matrices in Eqs. (14.40)–(14.43) is that the actual random N-particle ensemble is optically indistinguishable from an ensemble composed of N statistically identical particles each having the same average extinction and phase matrices given by

$$\begin{cases} \langle \mathbf{K}(\hat{\mathbf{s}};\xi)\rangle_{\xi} = \dfrac{1}{N}\displaystyle\sum_{i=1}^{N}\langle \mathbf{K}(\hat{\mathbf{s}};\xi_i)\rangle_{\xi_i}, \\ \langle \mathbf{Z}(\hat{\mathbf{r}},\hat{\mathbf{s}};\xi)\rangle_{\xi} = \dfrac{1}{N}\displaystyle\sum_{i=1}^{N}\langle \mathbf{Z}(\hat{\mathbf{r}},\hat{\mathbf{s}};\xi_i)\rangle_{\xi_i}. \end{cases} \tag{14.44}$$

The matrices $\langle \mathbf{K}(\hat{\mathbf{s}};\xi)\rangle_{\xi}$ and $\langle \mathbf{Z}(\hat{\mathbf{r}},\hat{\mathbf{s}};\xi)\rangle_{\xi}$ can be thought of as being averaged according to Eq. (13.141) over a synthetic probability distribution of microphysical states of one particle $p_{\xi}(\xi)$ derived from the N individual-particle distributions $p_{\xi_i}(\xi_i)$. Then Eqs. (14.40)–(14.43) take a much simpler form, essentially replicating that of Eqs. (13.137)–(13.140), the principal difference being the extra factor N:

$$\langle\langle W^{\rm ext}\rangle\rangle = N\big[\langle K_{11}(\hat{\mathbf{s}};\xi)\rangle_\xi I^{\rm inc} + \langle K_{12}(\hat{\mathbf{s}};\xi)\rangle_\xi Q^{\rm inc} + \langle K_{13}(\hat{\mathbf{s}};\xi)\rangle_\xi U^{\rm inc} + \langle K_{14}(\hat{\mathbf{s}};\xi)\rangle_\xi V^{\rm inc}\big], \tag{14.45}$$

$$\langle\langle W^{\rm sca}\rangle\rangle = N\int_{4\pi} {\rm d}\hat{\mathbf{r}}\,\big[\langle Z_{11}(\hat{\mathbf{r}},\hat{\mathbf{s}};\xi)\rangle_\xi I^{\rm inc} + \langle Z_{12}(\hat{\mathbf{r}},\hat{\mathbf{s}};\xi)\rangle_\xi Q^{\rm inc} + \langle Z_{13}(\hat{\mathbf{r}},\hat{\mathbf{s}};\xi)\rangle_\xi U^{\rm inc} + \langle Z_{14}(\hat{\mathbf{r}},\hat{\mathbf{s}};\xi)\rangle_\xi V^{\rm inc}\big], \tag{14.46}$$

$$\langle\langle \textbf{Signal 1}\rangle\rangle = \frac{S_{\rm ep}}{r^2} N\langle \mathbf{Z}(\hat{\mathbf{r}}_1,\hat{\mathbf{s}};\xi)\rangle_\xi \mathbf{I}^{\rm inc}, \tag{14.47}$$

$$\langle\langle \textbf{Signal 2}\rangle\rangle = S_{\rm ep}\mathbf{I}^{\rm inc} - N\langle \mathbf{K}(\hat{\mathbf{s}};\xi)\rangle_\xi \mathbf{I}^{\rm inc} + \frac{S_{\rm ep}}{r^2} N\langle \mathbf{Z}(\hat{\mathbf{s}},\hat{\mathbf{s}};\xi)\rangle_\xi \mathbf{I}^{\rm inc}. \tag{14.48}$$

Finally, Eqs. (14.40)–(14.43) and (14.45)–(14.48) can be generalized to allow for the case of polychromatic light with M quasi-monochromatic components. For example, Eqs. (14.45)–(14.48) become

$$\langle\langle W^{\rm ext}\rangle\rangle = N\sum_{m=1}^{M}\big[\langle K_{11}(\hat{\mathbf{s}};\omega_m,\xi)\rangle_\xi\langle\langle I_m^{\rm inc}\rangle\rangle + \langle K_{12}(\hat{\mathbf{s}};\omega_m,\xi)\rangle_\xi\langle\langle Q_m^{\rm inc}\rangle\rangle + \langle K_{13}(\hat{\mathbf{s}};\omega_m,\xi)\rangle_\xi\langle\langle U_m^{\rm inc}\rangle\rangle + \langle K_{14}(\hat{\mathbf{s}};\omega_m,\xi)\rangle_\xi\langle\langle V_m^{\rm inc}\rangle\rangle\big], \tag{14.49}$$

$$\langle\langle W^{\rm sca}\rangle\rangle = N\int_{4\pi} {\rm d}\hat{\mathbf{r}}\sum_{m=1}^{M}\big[\langle Z_{11}(\hat{\mathbf{r}},\hat{\mathbf{s}};\omega_m,\xi)\rangle_\xi\langle\langle I_m^{\rm inc}\rangle\rangle + \langle Z_{12}(\hat{\mathbf{r}},\hat{\mathbf{s}};\omega_m,\xi)\rangle_\xi\langle\langle Q_m^{\rm inc}\rangle\rangle + \langle Z_{13}(\hat{\mathbf{r}},\hat{\mathbf{s}};\omega_m,\xi)\rangle_\xi\langle\langle U_m^{\rm inc}\rangle\rangle + \langle Z_{14}(\hat{\mathbf{r}},\hat{\mathbf{s}};\omega_m,\xi)\rangle_\xi\langle\langle V_m^{\rm inc}\rangle\rangle\big], \tag{14.50}$$

$$\langle\langle \textbf{Signal 1}\rangle\rangle = \frac{S_{\rm ep}}{r^2} N\sum_{m=1}^{M}\langle \mathbf{Z}(\hat{\mathbf{r}}_1,\hat{\mathbf{s}};\omega_m,\xi)\rangle_\xi\langle\langle \mathbf{I}_m^{\rm inc}\rangle\rangle, \tag{14.51}$$

$$\langle\langle \textbf{Signal 2}\rangle\rangle = S_{\rm ep}\sum_{m=1}^{M}\langle\langle \mathbf{I}_m^{\rm inc}\rangle\rangle - N\sum_{m=1}^{M}\langle \mathbf{K}(\hat{\mathbf{s}};\omega_m,\xi)\rangle_\xi\langle\langle \mathbf{I}_m^{\rm inc}\rangle\rangle + \frac{S_{\rm ep}}{r^2} N\sum_{m=1}^{M}\langle \mathbf{Z}(\hat{\mathbf{s}},\hat{\mathbf{s}};\omega_m,\xi)\rangle_\xi\langle\langle \mathbf{I}_m^{\rm inc}\rangle\rangle, \tag{14.52}$$

where the index m numbers the quasi-monochromatic components and, as usual, the detection efficiency of the WCRs is assumed to be frequency independent. Again, it is instructive to compare Eqs. (14.49)–(14.52) with Eqs. (13.143)–(13.146).

14.6 Analysis of the first-order-scattering approximation

The main attraction of the FOSA is that it obviates the need to solve the MMEs for a statistically representative set of sparse N-particle configurations explicitly and reduces this complicated (if not impracticable) task to the much simpler

problem of solving the MMEs for only one particle, followed by averaging over a representative distribution of the particle microphysical states. Even though this approximation has traditionally been taken for granted and used in countless applications, our discussion demonstrates that its explicit derivation from the MMEs is not necessarily trivial and rests on several specific assumptions. Indeed, the use of the FOSA to solve the energy-budget problem for a random N-particle object requires that the following conditions be met:

- Each particle in the group is effectively excited by the incident field only, which allows one to replace the exact FEs by the approximate versions (14.1)–(14.3).
- The observation point is located sufficiently far from the volume element V to ensure that the inequalities (14.8)–(14.10) and (14.17), as well as the approximate equality (14.18), hold.
- The random N-particle object is fully ergodic, thereby making it possible to replace averaging over time by ensemble averaging. According to Section 10.4, this condition implies that the averaging time must be much longer than the typical temporal scale of variability of the N-particle object.
- All particle positions and all particle microphysical states as functions of time are mutually independent random processes. All positions of any of the N particles throughout the volume element V are equally probable, thereby justifying the use of the uniform probability density function (14.16). These conditions imply that the average distance $\langle d_{\rm np}\rangle_{\mathbf{R}}$ between neighboring particles must be much greater than their sizes:

$$\langle d_{\rm np}\rangle_{\mathbf{R}} \gg a_i \ \text{ for } \ i = 1, ..., N. \tag{14.53}$$

- The sum of the extinction cross sections of the particles filling the volume element V is much smaller than the volume's geometrical cross section, Eq. (14.26).
- The size parameter of the volume element V is much greater than unity, Eq. (14.29).

Should the FOSA also be used to quantify the (polarized) reading of a remote WCR, the inequalities (13.5), (14.35), and (14.36) must be satisfied as well. Furthermore, in this case the condition (14.18) implies the inequality

$$r \gg \frac{D_{\rm ep} k_1 a_i}{\pi} \ \text{ for } \ i = 1, ..., N, \tag{14.54}$$

where, as before, $D_{\rm ep}$ is the diameter of the entrance pupil of the WCR (cf. Eq. (13.22)).

The qualitatively obvious implication of the SSA is that the average separation between the particles must be appropriately large and their total number N must be sufficiently small. Although it is difficult to formulate universal quanti-

tative criteria of applicability of the SSA, comparisons of the FOSA predictions with the results of numerically exact computer solutions of the MMEs for random multi-particle objects can provide useful guidance. Such comparisons will be described and discussed in Section 18.5.

By explicitly allowing the remote observation point to be located in the near zone of the volume element V, the FOSA obviates the need to satisfy the most demanding requirement of the far-field approximation, i.e., the inequality (5.14) with $a = L$. It is therefore interesting to analyze what would happen if the observation point were moved to the far zone of the entire volume element. A direct consequence of taking the limit $r \to \infty$ is that $\mathbf{R}_i'$ becomes parallel to $\hat{\mathbf{s}}$, which causes the factor $\exp(\mathrm{i}k_1\hat{\mathbf{s}}\cdot\mathbf{R}_i')\exp(\mathrm{i}k_1 r_i)$ in Eq. (14.20) and in the analogous formula for $\langle\hat{\mathbf{r}}_i\times\mathbf{E}_i^{\mathrm{sca}}(\mathbf{r})\rangle_{\mathbf{R}_i}$ to vanish. Although this requires a tedious derivation, it can be shown by inspection that the contributions of the second, third, and fifth terms on the right-hand side of Eq. (14.15) to $\langle\langle W^{\mathrm{ext}}\rangle\rangle$, $\langle\langle W^{\mathrm{sca}}\rangle\rangle$, $\langle\langle\textbf{Signal 1}\rangle\rangle$, and $\langle\langle\textbf{Signal 2}\rangle\rangle$ do not change. However, the fourth term changes dramatically at far-zone observation points in the immediate vicinity of the exact forward-scattering direction. To demonstrate the most striking consequence of this change, let us assume that the N particles have identical and time-independent scattering dyadics. Then the reader can verify that

$$\lim_{\substack{r\to\infty\\ \hat{\mathbf{r}}_1\to\hat{\mathbf{s}}}}\langle\langle\textbf{Signal 1}\rangle\rangle = \frac{S_{\mathrm{ep}}}{r^2}N^2\langle\mathbf{Z}(\hat{\mathbf{s}},\hat{\mathbf{s}})\rangle_\xi\mathbf{I}^{\mathrm{inc}}, \tag{14.55}$$

which, obviously, is N times greater than the FOSA prediction (14.47) (Problem 14.7).

The result (14.55) can be interpreted as being a consequence of the so-called forward-scattering interference effect illustrated in Fig. 14.4. Panel 14.4a shows that irrespective of the instantaneous positions of particles i and j within the vol-

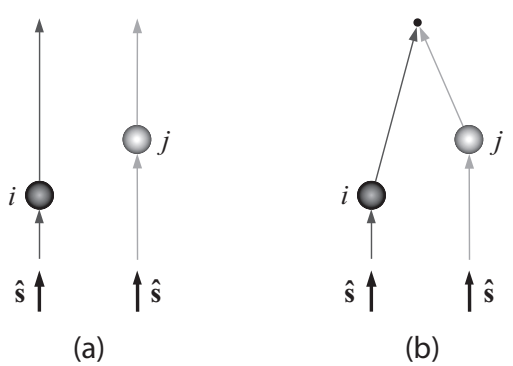

Fig. 14.4. Forward-scattering interference. **(a)** The observation point is located in the far zone of the entire N-particle object. **(b)** The observation point is located in the far zone of each individual particle, yet in the near zone of the entire N-particle object.

ume element V, the phases of the respective partial wavelets arriving at a far-zone observation point corresponding to the exact forward-scattering direction are always the same, thereby causing a consistently constructive interference. If both particles have identical microphysical properties then averaging the term $\hat{\mathbf{r}}_i \times \mathbf{E}_i^{\text{sca}}(\mathbf{r}_2) \otimes \mathbf{E}_j^{\text{sca}}(\mathbf{r}_2)^*$ over all particle positions yields the same contribution to $\langle \ddot{P}(\mathbf{r}_2) \rangle_{\mathbf{R}}$ as the term $\hat{\mathbf{r}}_i \times \mathbf{E}_i^{\text{sca}}(\mathbf{r}_2) \otimes \mathbf{E}_i^{\text{sca}}(\mathbf{r}_2)^*$, which explains the factor N^2 in Eq. (14.55). In the case of a near-field observation point, the phase difference between the two partial wavelets oscillates rapidly as particles i and j move, thereby resulting in a much weaker contribution of the position-averaged product $\hat{\mathbf{r}}_i \times \mathbf{E}_i^{\text{sca}}(\mathbf{r}_2) \otimes \mathbf{E}_j^{\text{sca}}(\mathbf{r}_2)^*$ to $\langle \ddot{P}(\mathbf{r}_2) \rangle_{\mathbf{R}}$.

Although the far-zone value of $\langle\langle \textbf{Signal 1} \rangle\rangle$ in the limit $\hat{\mathbf{r}}_1 \to \hat{\mathbf{s}}$ is N times greater than the near-zone value, the angular width of the forward-scattering interference peak can be expected to be of the order $\lambda_1 / k_1 L$. As a consequence, the contribution of this peak to $\langle\langle W^{\text{sca}} \rangle\rangle$ is usually very small and can typically be neglected. The forward-scattering interference effect will be further discussed in Section 18.4.

Problems

14.1: Consider the measurement arrangement shown in Fig. 16.8 and assume that the laser beam illuminates a 5-mm-radius volume filled with particles. What should be the distance from the particulate volume to the monitors in order to satisfy the FFS criteria (5.12)–(5.14) for the entire volume, provided that the laser wavelength is 600 nm?

14.2: What should be the minimal distance from a 100-m-radius cloud of water droplets to an observation point in order to satisfy the FFS criteria (5.12)–(5.14) for the entire cloud, provided that the wavelength of observation is 600 nm?

14.3: Derive Eq. (14.28).

14.4: Derive Eqs. (14.32)–(14.34).

14.5: Derive Eq. (14.38).

14.6: Derive Eq. (14.39).

14.7: Derive the far-field limit (14.55).

14.8: Generalize Eqs. (14.49) and (14.50) by allowing the incident field to be a superposition of several polychromatic beams with different propagation directions.

14.9: Consider a WCR with its optical axis centered at the volume element V in the direction $\hat{\mathbf{q}}$ and rewrite Eqs. (14.51) and (14.52) in the form of a single formula

$$\langle\langle \mathbf{Signal}(\hat{\mathbf{q}})\rangle\rangle = \frac{S_{\mathrm{ep}}}{r^2} N \sum_{m=1}^{M} \langle \mathbf{Z}(\hat{\mathbf{q}}, \hat{\mathbf{s}}; \omega_m, \xi)\rangle_\xi \langle\langle \mathbf{I}_m^{\mathrm{inc}}\rangle\rangle$$
$$+ \chi(\Delta\Omega_{\hat{\mathbf{q}}}, \hat{\mathbf{s}}) \sum_{n=1}^{N} \left(S_{\mathrm{ep}} - N\langle \mathbf{K}(\hat{\mathbf{s}}; \omega_m, \xi)\rangle_\xi\right)\langle\langle \mathbf{I}_m^{\mathrm{inc}}\rangle\rangle, \qquad (14.56)$$

where the angular step function $\chi(\Delta\Omega_{\hat{\mathbf{q}}}, \hat{\mathbf{s}})$ is defined by Eq. (11.10). Generalize this formula by allowing the incident field to be a superposition of several polychromatic beams with different propagation directions.

15

Statistically isotropic and mirror-symmetric random particles

Equations (13.52), (13.54), (13.70), and (13.71) are the most general symmetry properties of the phase and extinction matrices appearing in the far-field limit of electromagnetic scattering by a fixed object. It is obvious that they also apply to the matrices $\langle \mathbf{K}(\hat{\mathbf{n}}^{\rm inc};\xi)\rangle_\xi$ and $\langle \mathbf{Z}(\hat{\mathbf{n}}^{\rm sca},\hat{\mathbf{n}}^{\rm inc};\xi)\rangle_\xi$ entering the far-field formulas (13.137)–(13.146) and the FOSA formulas (14.45)–(14.52) derived for ergodic random scatterers. The reader should recall that in the far-field formulation these matrices, defined by Eq. (13.141), characterize the entire random object, while in the framework of the FOSA they characterize the "virtual" random particle that *de facto* replaces each random member of the N-particle group. In what follows, we will often refer to either an FFS object or a FOSA particle as a "particle".

The matrices $\langle \mathbf{K}(\hat{\mathbf{n}}^{\rm inc};\xi)\rangle_\xi$ and $\langle \mathbf{Z}(\hat{\mathbf{n}}^{\rm sca},\hat{\mathbf{n}}^{\rm inc};\xi)\rangle_\xi$ can possess additional symmetries depending on the specific form of the probability density function $p_\xi(\xi)$. A particularly important class of functions $p_\xi(\xi)$ represents so-called statistically isotropic and mirror-symmetric random particles (hereinafter ISRPs). By definition, $p_\xi(\xi)$ represents an ISRP if it possesses the following properties:

- $p_\xi(\xi)$ is a product of morphology and orientation probability density functions,

$$p_\xi(\xi) \equiv p_\varsigma(\varsigma)\, p_{\rm o}(\alpha,\beta,\gamma), \tag{15.1}$$

both $p_\varsigma(\varsigma)$ and $p_{\rm o}(\alpha,\beta,\gamma)$ being normalized to unity:

$$\int {\rm d}\varsigma\, p_\varsigma(\varsigma) = 1, \tag{15.2}$$

$$\int_0^{2\pi} {\rm d}\alpha \int_0^{\pi} {\rm d}\beta \sin\beta \int_0^{2\pi} {\rm d}\gamma\, p_{\rm o}(\alpha,\beta,\gamma) = 1. \tag{15.3}$$

The morphology ς can be thought of as specifying the spatial distribution of the relative refractive index with respect to the "particle reference frame"

affixed to either the entire FFS object or the virtual FOSA particle, while the Euler rotation angles (α, β, γ) specify the orientation of the particle reference frame relative to the laboratory reference frame according to Appendix C. Note that ς includes implicitly the overall size of either the FFS object or the virtual FOSA particle. Equation (15.1) implies that the random morphologies ς and orientations (α, β, γ) are statistically independent of each other.

- $p_\varsigma(\varsigma)$ is such that the probability of occurrence of any morphology ς is equal to the probability of occurrence of its mirror image:

$$p_\varsigma(\varsigma) \equiv p_\varsigma(\text{mirror image of } \varsigma). \tag{15.4}$$

- All particle orientations are completely random (equiprobable), thereby implying that the orientation probability density function amounts to a constant:

$$p_o(\alpha, \beta, \gamma) \equiv \frac{1}{8\pi^2}. \tag{15.5}$$

Although this class of functions $p_\xi(\xi)$ might be viewed as being rather special, it nonetheless results in sufficiently accurate optical parameterizations of many random scatterers encountered in practice and is by far the most frequently used theoretical model. Moreover, we shall see below that the assumptions of isotropy and mirror symmetry lead to significant mathematical simplifications and allows one to develop efficient computer algorithms.

In particular, it turns out that a convenient concept in the analysis of electromagnetic scattering by an ISRP is that of the 4×4 scattering matrix. As we have seen in Chapter 13, the phase matrix is defined such that it links the Stokes parameters of the incident and scattered fields defined relative to their respective meridional planes. In contrast, the scattering matrix $\mathbf{F}$ links the Stokes parameters of the incident and scattered fields defined with respect to the scattering plane, that is, the plane through the unit vectors $\hat{\mathbf{n}}^{\text{inc}}$ and $\hat{\mathbf{n}}^{\text{sca}}$ (Perrin 1942; van de Hulst 1957).

A simple way to introduce the scattering matrix is to align the z-axis of the laboratory reference frame with the incidence direction and superpose the meridional plane corresponding to $\varphi = 0$ with the scattering plane (Fig. 15.1). Then the scattering matrix $\mathbf{F}$ can be defined as

$$\mathbf{F}(\theta^{\text{sca}}; \xi) = \mathbf{Z}(\theta^{\text{sca}}, \varphi^{\text{sca}} = 0; \theta^{\text{inc}} = 0, \varphi^{\text{inc}} = 0; \xi). \tag{15.6}$$

In general, all 16 elements of the scattering matrix are nonzero and depend on the particle's orientation with respect to the incidence and scattering directions.

This choice of the laboratory reference frame, with the z-axis along the incidence direction and the xz-half-plane, with $x \geq 0$, coinciding with the scattering plane, can often be inconvenient because any change in the incidence direction

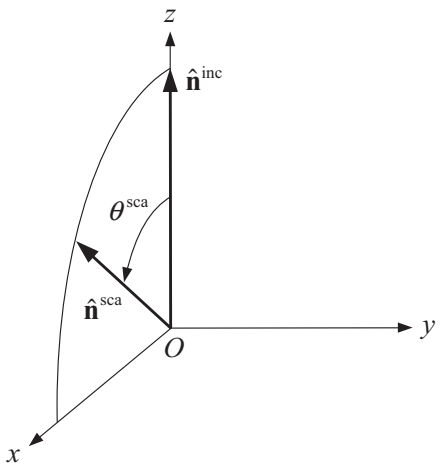

Fig. 15.1. Definition of the scattering matrix.

and/or orientation of the scattering plane also changes the particle orientation with respect to the reference frame. However, we will show in the following sections that the notion of the scattering matrix can be very useful in application to an ISRP because then the scattering matrix becomes independent of the incidence direction and orientation of the scattering plane, depends only on the angle $\Theta = \theta^{\text{sca}}$ between the incidence and scattering directions, and has a simple block-diagonal structure.

15.1 Symmetries of the Stokes scattering matrix

We begin by considering special symmetry properties of the amplitude scattering matrix that exist when the incidence and scattering directions both lie in the *xz*-plane (van de Hulst 1957). For the particle shown schematically in Fig. 15.2a, let

$$\begin{bmatrix} S_{11} & S_{12} \\ S_{21} & S_{22} \end{bmatrix} \tag{15.7a}$$

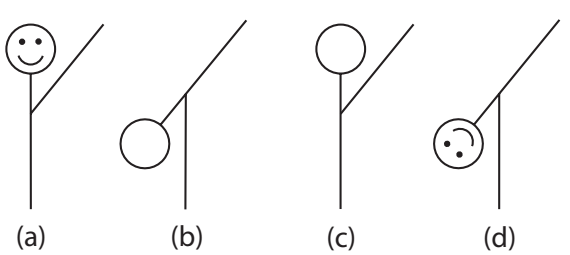

Fig. 15.2. Two orientations of an arbitrary particle and two orientations of its mirror counterpart that give rise to certain symmetries in scattering patterns.

be the amplitude scattering matrix that corresponds to the directions of incidence and scattering given by $\hat{\mathbf{n}}^{\text{inc}}$ and $\hat{\mathbf{n}}^{\text{sca}}$, respectively (Fig. 15.3). Rotating this particle by 180° about the bisectrix (i.e., the line in the scattering plane that bisects the angle $\pi - \Theta$ between the unit vectors $-\hat{\mathbf{n}}^{\text{inc}}$ and $\hat{\mathbf{n}}^{\text{sca}}$ in Fig. 15.3) puts it in the orientation shown schematically in Fig. 15.2b. It is clear that the amplitude scattering matrix (15.7a) is also the amplitude scattering matrix for this rotated particle when the directions of incidence and scattering are given by $-\hat{\mathbf{n}}^{\text{sca}}$ and $-\hat{\mathbf{n}}^{\text{inc}}$, respectively. Therefore, the reciprocity relation (5.31) implies that the amplitude scattering matrix of the particle shown in Fig. 15.2b that corresponds to the original directions of incidence and scattering, $\hat{\mathbf{n}}^{\text{inc}}$ and $\hat{\mathbf{n}}^{\text{sca}}$, is simply

$$\begin{bmatrix} S_{11} & -S_{21} \\ -S_{12} & S_{22} \end{bmatrix}. \tag{15.7b}$$

Mirroring the original particle, Fig. 15.2a, with respect to the scattering plane gives the particle shown in Fig. 15.2c. If we also reversed the direction of the unit vectors $\hat{\boldsymbol{\varphi}}^{\text{inc}}$ and $\hat{\boldsymbol{\varphi}}^{\text{sca}}$ in Fig. 15.3 then we would have the same scattering problem as for the particle shown in Fig. 15.2a. We may thus conclude that the amplitude scattering matrix for the particle shown in Fig. 15.2c that corresponds to the directions of incidence and scattering $\hat{\mathbf{n}}^{\text{inc}}$ and $\hat{\mathbf{n}}^{\text{sca}}$ is

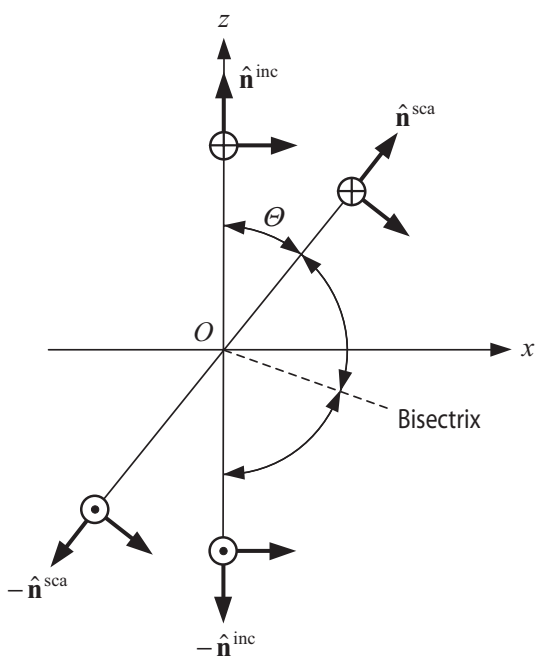

Fig. 15.3. The *xz*-plane of the laboratory reference frame acts as the scattering plane. The arrows perpendicular to the $\hat{\mathbf{n}}$-vectors show the corresponding $\hat{\boldsymbol{\theta}}$-vectors. The symbols $\oplus$ and $\odot$ indicate the corresponding $\hat{\boldsymbol{\varphi}}$-vectors directed into and out of the paper, respectively.

$$\begin{bmatrix} S_{11} & -S_{12} \\ -S_{21} & S_{22} \end{bmatrix}. \tag{15.7c}$$

Finally, mirroring the original particle with respect to the bisectrix plane (i.e., the plane through the bisectrix and the y-axis) gives the particle shown in Fig. 15.2d. Since this particle is the mirror counterpart of the particle shown in Fig. 15.2b, its amplitude scattering matrix corresponding to the directions of incidence and scattering $\hat{\mathbf{n}}^{\text{inc}}$ and $\hat{\mathbf{n}}^{\text{sca}}$ is given by

$$\begin{bmatrix} S_{11} & S_{21} \\ S_{12} & S_{22} \end{bmatrix}. \tag{15.7d}$$

It can be seen that any two of the three transformations shown in Figs. 15.2b–15.2d give the third one.

We will now discuss the implications of Eqs. (15.7a)–(15.7d) for average Stokes scattering matrices by considering the following four examples (van de Hulst 1957).

1. Let us first assume that there is only one kind of particle morphology ς and that any specific orientation, say Fig. 15.2a, is accompanied by the reciprocal orientation, Fig. 15.2b. It then follows from Eqs. (13.34)–(13.49), (15.6), (15.7a), and (15.7b) that the average scattering matrix has the following symmetry:

$$\begin{bmatrix} \langle F_{11}\rangle_\xi & \langle F_{12}\rangle_\xi & \langle F_{13}\rangle_\xi & \langle F_{14}\rangle_\xi \\ \langle F_{12}\rangle_\xi & \langle F_{22}\rangle_\xi & \langle F_{23}\rangle_\xi & \langle F_{24}\rangle_\xi \\ -\langle F_{13}\rangle_\xi & -\langle F_{23}\rangle_\xi & \langle F_{33}\rangle_\xi & \langle F_{34}\rangle_\xi \\ \langle F_{14}\rangle_\xi & \langle F_{24}\rangle_\xi & -\langle F_{34}\rangle_\xi & \langle F_{44}\rangle_\xi \end{bmatrix}. \tag{15.8}$$

The number of independent matrix elements is thus 10.

2. As a second example, let us assume that any morphology in orientation (a) is accompanied by a mirror morphology in orientation (c) (see Fig. 15.2). This excludes, for example, morphologies in the form of only right-handed or only left-handed helices. It is easy to verify that the resulting average scattering matrix involves eight independent elements and has the following structure:

$$\begin{bmatrix} \langle F_{11}\rangle_\xi & \langle F_{12}\rangle_\xi & 0 & 0 \\ \langle F_{21}\rangle_\xi & \langle F_{22}\rangle_\xi & 0 & 0 \\ 0 & 0 & \langle F_{33}\rangle_\xi & \langle F_{34}\rangle_\xi \\ 0 & 0 & \langle F_{43}\rangle_\xi & \langle F_{44}\rangle_\xi \end{bmatrix}. \tag{15.9}$$

3. As a third example, assume that any morphology in orientation (a) is accompanied by a mirror morphology in orientation (d). The average scattering matrix becomes

$$\begin{bmatrix} \langle F_{11}\rangle_\xi & \langle F_{12}\rangle_\xi & \langle F_{13}\rangle_\xi & \langle F_{14}\rangle_\xi \\ \langle F_{12}\rangle_\xi & \langle F_{22}\rangle_\xi & \langle F_{23}\rangle_\xi & \langle F_{24}\rangle_\xi \\ \langle F_{13}\rangle_\xi & \langle F_{23}\rangle_\xi & \langle F_{33}\rangle_\xi & \langle F_{34}\rangle_\xi \\ -\langle F_{14}\rangle_\xi & -\langle F_{24}\rangle_\xi & -\langle F_{34}\rangle_\xi & \langle F_{44}\rangle_\xi \end{bmatrix} \tag{15.10}$$

and has 10 independent elements.

4. Finally, let us make any two of the preceding assumptions. The third assumption follows automatically, so that there are equal numbers of morphologies in orientations (a), (b), (c), and (d). The resulting average scattering matrix is

$$\begin{bmatrix} \langle F_{11}\rangle_\xi & \langle F_{12}\rangle_\xi & 0 & 0 \\ \langle F_{12}\rangle_\xi & \langle F_{22}\rangle_\xi & 0 & 0 \\ 0 & 0 & \langle F_{33}\rangle_\xi & \langle F_{34}\rangle_\xi \\ 0 & 0 & -\langle F_{34}\rangle_\xi & \langle F_{44}\rangle_\xi \end{bmatrix} \tag{15.11}$$

and has eight nonzero elements, of which only six are independent.

15.2 Statistically isotropic and mirror-symmetric random particle

Now we are ready to consider the probability density function (15.1) with the uniform orientation distribution given by Eq. (15.5). In this case the assumptions of example 1 from the previous section are satisfied, and the average scattering matrix is given by Eq. (15.8). Furthermore, if each morphology is accompanied by its mirror counterpart then the assumptions of example 4 are satisfied, and the resulting average scattering matrix is given by Eq. (15.11).

As a consequence of the uniform orientation distribution, the random particle is statistically *isotropic* (i.e., there is no preferred propagation direction and no preferred plane through the incidence direction). Therefore, the average scattering matrix becomes independent of the incidence direction and the orientation of the scattering plane and depends only on the angle between the incidence and scattering directions, that is, the scattering angle

$$\Theta = \arccos(\hat{\mathbf{n}}^{\text{inc}} \cdot \hat{\mathbf{n}}^{\text{sca}}), \quad \Theta \in [0, \pi]. \tag{15.12}$$

Furthermore, the assumptions of example 4 ensure that the particle is statistically *mirror-symmetric* with respect to any plane and make the structure of the scattering matrix especially simple. We can thus rewrite Eq. (15.11) for the ISRP as

$$\langle \mathbf{F}(\Theta;\xi)\rangle_\xi = \begin{bmatrix} \langle F_{11}(\Theta;\xi)\rangle_\xi & \langle F_{12}(\Theta;\xi)\rangle_\xi & 0 & 0 \\ \langle F_{12}(\Theta;\xi)\rangle_\xi & \langle F_{22}(\Theta;\xi)\rangle_\xi & 0 & 0 \\ 0 & 0 & \langle F_{33}(\Theta;\xi)\rangle_\xi & \langle F_{34}(\Theta;\xi)\rangle_\xi \\ 0 & 0 & -\langle F_{34}(\Theta;\xi)\rangle_\xi & \langle F_{44}(\Theta;\xi)\rangle_\xi \end{bmatrix}. \tag{15.13}$$

As a direct consequence of Eqs. (13.50) and (13.51), we have the inequalities

$$\langle F_{11}\rangle_\xi \geq 0, \tag{15.14}$$

$$|\langle F_{ij}\rangle_\xi| \leq \langle F_{11}\rangle_\xi, \quad i, j = 1, \ldots, 4. \tag{15.15}$$

Additional general inequalities for the elements of the scattering matrix (15.13) are as follows:

$$[\langle F_{33}\rangle_\xi + \langle F_{44}\rangle_\xi]^2 + 4[\langle F_{34}\rangle_\xi]^2 \leq [\langle F_{11}\rangle_\xi + \langle F_{22}\rangle_\xi]^2 - 4[\langle F_{12}\rangle_\xi]^2, \tag{15.16}$$

$$|\langle F_{33}\rangle_\xi - \langle F_{44}\rangle_\xi| \leq \langle F_{11}\rangle_\xi - \langle F_{22}\rangle_\xi, \tag{15.17}$$

$$|\langle F_{22}\rangle_\xi - \langle F_{12}\rangle_\xi| \leq \langle F_{11}\rangle_\xi - \langle F_{12}\rangle_\xi, \tag{15.18}$$

$$|\langle F_{22}\rangle_\xi + \langle F_{12}\rangle_\xi| \leq \langle F_{11}\rangle_\xi + \langle F_{12}\rangle_\xi. \tag{15.19}$$

The proof of these and other useful inequalities is given in Hovenier *et al.* (1986).

15.3 Phase matrix

Knowledge of the matrix $\langle \mathbf{F}(\Theta;\xi)\rangle_\xi$ can be used to calculate the average Stokes phase matrix for an ISRP. Assume that $0 < \varphi^{\text{sca}} - \varphi^{\text{inc}} < \pi$ and consider the phase matrices $\langle \mathbf{Z}(\theta^{\text{sca}}, \varphi^{\text{sca}}; \theta^{\text{inc}}, \varphi^{\text{inc}}; \xi)\rangle_\xi$ and $\langle \mathbf{Z}(\theta^{\text{sca}}, \varphi^{\text{inc}}; \theta^{\text{inc}}, \varphi^{\text{sca}}; \xi)\rangle_\xi$. The second matrix involves the same polar angles of the incidence and scattering directions as the first, but the azimuth angles are switched, as indicated in their respective scattering geometries depicted in Figs. 15.4a and 15.4b. The phase matrix links the Stokes column vectors of the incident and scattered waves, specified relative to their respective meridional planes. Therefore, to compute the Stokes column vector of the scattered field with respect to the meridional plane of the scattering direction, we must:

- Calculate the Stokes column vector of the incident field with respect to the scattering plane.
- Multiply it by the scattering matrix, thereby obtaining the Stokes column vector of the scattered field with respect to the scattering plane.
- Compute the Stokes column vector of the scattered field with respect to the meridional plane of the scattering direction (Chandrasekhar 1950).

This procedure involves two rotations of the reference plane, as shown in Figs. 15.4a and 15.4b, and yields (Problem 15.1)

$$\langle \mathbf{Z}(\theta^{\text{sca}}, \varphi^{\text{sca}}; \theta^{\text{inc}}, \varphi^{\text{inc}}; \xi)\rangle_\xi = \mathbf{L}(-\sigma_2)\langle \mathbf{F}(\Theta;\xi)\rangle_\xi \mathbf{L}(\pi - \sigma_1)$$

$$= \begin{bmatrix} \langle F_{11}(\Theta;\xi)\rangle_\xi & C_1\langle F_{12}(\Theta;\xi)\rangle_\xi \\ C_2\langle F_{12}(\Theta;\xi)\rangle_\xi & C_1C_2\langle F_{22}(\Theta;\xi)\rangle_\xi - S_1S_2\langle F_{33}(\Theta;\xi)\rangle_\xi \\ -S_2\langle F_{12}(\Theta;\xi)\rangle_\xi & -C_1S_2\langle F_{22}(\Theta;\xi)\rangle_\xi - S_1C_2\langle F_{33}(\Theta;\xi)\rangle_\xi \\ 0 & S_1\langle F_{34}(\Theta;\xi)\rangle_\xi \end{bmatrix}$$

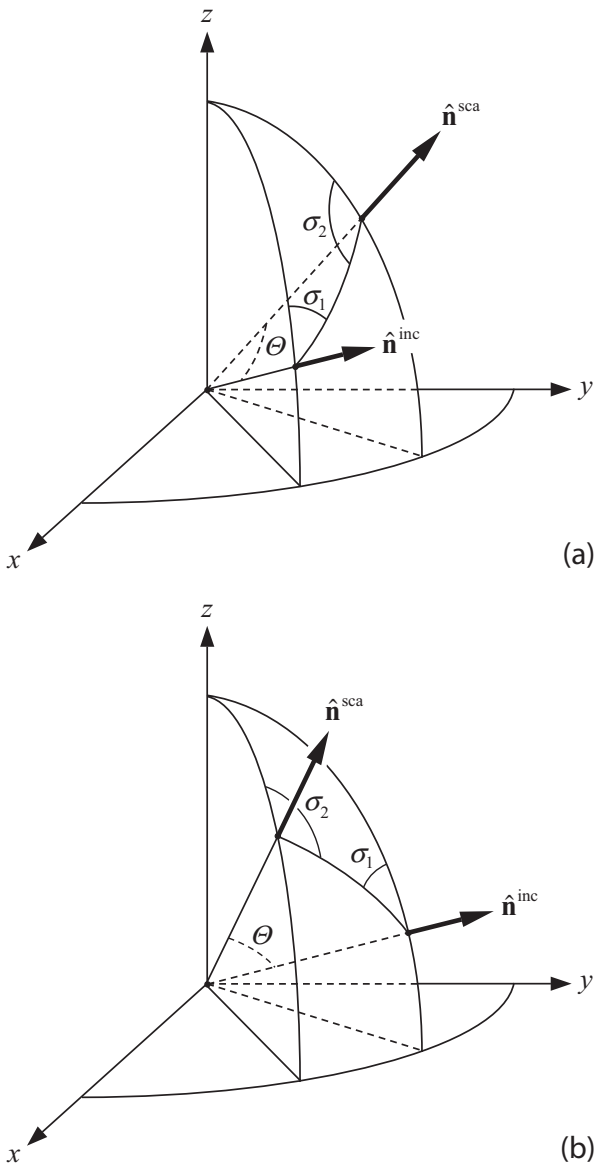

Fig. 15.4. Derivation of the relationship between the phase and scattering matrices.

$$\left.\begin{array}{cc} S_1\langle F_{12}(\Theta;\xi)\rangle_\xi & 0 \\ S_1C_2\langle F_{22}(\Theta;\xi)\rangle_\xi + C_1S_2\langle F_{33}(\Theta;\xi)\rangle_\xi & S_2\langle F_{34}(\Theta;\xi)\rangle_\xi \\ -S_1S_2\langle F_{22}(\Theta;\xi)\rangle_\xi + C_1C_2\langle F_{33}(\Theta;\xi)\rangle_\xi & C_2\langle F_{34}(\Theta;\xi)\rangle_\xi \\ -C_1\langle F_{34}(\Theta;\xi)\rangle_\xi & \langle F_{44}(\Theta;\xi)\rangle_\xi \end{array}\right], \quad (15.20)$$

$$\langle \mathbf{Z}(\theta^{\rm sca}, \varphi^{\rm inc}; \theta^{\rm inc}, \varphi^{\rm sca}; \xi)\rangle_\xi = \mathbf{L}(\sigma_2 - \pi)\langle \mathbf{F}(\Theta; \xi)\rangle_\xi \mathbf{L}(\sigma_1)$$

$$= \begin{bmatrix} \langle F_{11}(\Theta;\xi)\rangle_\xi & C_1\langle F_{12}(\Theta;\xi)\rangle_\xi & -S_1\langle F_{12}(\Theta;\xi)\rangle_\xi & 0 \\ C_2\langle F_{12}(\Theta;\xi)\rangle_\xi & C_1C_2\langle F_{22}(\Theta;\xi)\rangle_\xi - S_1S_2\langle F_{33}(\Theta;\xi)\rangle_\xi & -S_1C_2\langle F_{22}(\Theta;\xi)\rangle_\xi - C_1S_2\langle F_{33}(\Theta;\xi)\rangle_\xi & -S_2\langle F_{34}(\Theta;\xi)\rangle_\xi \\ S_2\langle F_{12}(\Theta;\xi)\rangle_\xi & C_1S_2\langle F_{22}(\Theta;\xi)\rangle_\xi + S_1C_2\langle F_{33}(\Theta;\xi)\rangle_\xi & -S_1S_2\langle F_{22}(\Theta;\xi)\rangle_\xi + C_1C_2\langle F_{33}(\Theta;\xi)\rangle_\xi & C_2\langle F_{34}(\Theta;\xi)\rangle_\xi \\ 0 & -S_1\langle F_{34}(\Theta;\xi)\rangle_\xi & -C_1\langle F_{34}(\Theta;\xi)\rangle_\xi & \langle F_{44}(\Theta;\xi)\rangle_\xi \end{bmatrix}, \quad (15.21)$$

where

$$C_i = \cos 2\sigma_i, \quad S_i = \sin 2\sigma_i, \quad i = 1, 2, \quad (15.22)$$

and the rotation matrix $\mathbf{L}$ is defined by Eq. (7.8).[1] The scattering angle Θ and the angles σ_1 and σ_2 can be calculated from $\theta^{\rm sca}$, $\theta^{\rm inc}$, $\varphi^{\rm sca}$, and $\varphi^{\rm inc}$ using spherical trigonometry:

$$\cos\Theta = \cos\theta^{\rm sca}\cos\theta^{\rm inc} + \sin\theta^{\rm sca}\sin\theta^{\rm inc}\cos(\varphi^{\rm sca} - \varphi^{\rm inc}), \quad (15.23)$$

$$\cos\sigma_1 = \frac{\cos\theta^{\rm sca} - \cos\theta^{\rm inc}\cos\Theta}{\sin\theta^{\rm inc}\sin\Theta}, \quad (15.24)$$

$$\cos\sigma_2 = \frac{\cos\theta^{\rm inc} - \cos\theta^{\rm sca}\cos\Theta}{\sin\theta^{\rm sca}\sin\Theta}. \quad (15.25)$$

Equations (15.20)–(15.25) demonstrate the obvious fact that the phase matrix of an ISRP depends only on the difference between the azimuthal angles of the scattering and incidence directions rather than on their specific values. In particular,

$$\langle \mathbf{Z}(\theta^{\rm sca}, 2\pi - \varphi^{\rm inc}; \theta^{\rm inc}, 2\pi - \varphi^{\rm sca}; \xi)\rangle_\xi = \langle \mathbf{Z}(\theta^{\rm sca}, \varphi^{\rm sca}; \theta^{\rm inc}, \varphi^{\rm inc}; \xi)\rangle_\xi \quad (15.26)$$

or, formally allowing negative azimuth-angle values,

$$\langle \mathbf{Z}(\theta^{\rm sca}, -\varphi^{\rm inc}; \theta^{\rm inc}, -\varphi^{\rm sca}; \xi)\rangle_\xi = \langle \mathbf{Z}(\theta^{\rm sca}, \varphi^{\rm sca}; \theta^{\rm inc}, \varphi^{\rm inc}; \xi)\rangle_\xi. \quad (15.27)$$

Comparison of Eqs. (15.20) and (15.21) yields the following symmetry relation (Hovenier 1969):

$$\begin{aligned}\langle \mathbf{Z}(\theta^{\rm sca}, \varphi^{\rm inc}; \theta^{\rm inc}, \varphi^{\rm sca}; \xi)\rangle_\xi &= \langle \mathbf{Z}(\theta^{\rm sca}, -\varphi^{\rm sca}; \theta^{\rm inc}, -\varphi^{\rm inc}; \xi)\rangle_\xi \\ &= \mathbf{\Delta}_{34}\langle \mathbf{Z}(\theta^{\rm sca}, \varphi^{\rm sca}; \theta^{\rm inc}, \varphi^{\rm inc}; \xi)\rangle_\xi \mathbf{\Delta}_{34}, \end{aligned} \quad (15.28)$$

where the 4×4 diagonal matrix $\mathbf{\Delta}_{34}$ is given by

[1] Recall that a rotation angle is positive if the rotation is performed in the clockwise direction when one is looking in the direction of propagation; see Section 7.2.

$$\mathbf{\Delta}_{34} = \mathbf{\Delta}_{34}^{\mathrm{T}} = \mathbf{\Delta}_{34}^{-1} = \mathrm{diag}[1, 1, -1, -1]. \tag{15.29}$$

Obviously, Eq. (15.28) is a manifestation of mirror symmetry with respect to the meridional plane of the incidence direction (cf. Fig. 15.4) or, equivalently, with respect to the *xz*-half-plane with $x \geq 0$. It is also easy to see from either Eq. (15.20) or Eq. (15.21) that

$$\langle \mathbf{Z}(\pi - \theta^{\mathrm{sca}}, \varphi^{\mathrm{sca}}; \pi - \theta^{\mathrm{inc}}, \varphi^{\mathrm{inc}}; \xi)\rangle_{\xi} = \mathbf{\Delta}_{34} \langle \mathbf{Z}(\theta^{\mathrm{sca}}, \varphi^{\mathrm{sca}}; \theta^{\mathrm{inc}}, \varphi^{\mathrm{inc}}; \xi)\rangle_{\xi} \mathbf{\Delta}_{34} \tag{15.30}$$

(Hovenier 1969), which is a manifestation of mirror symmetry with respect to the *xy*-plane. Finally, we can verify that

$$\begin{aligned} &\langle \mathbf{Z}(\pi - \theta^{\mathrm{inc}}, \varphi^{\mathrm{inc}} + \pi; \pi - \theta^{\mathrm{sca}}, \varphi^{\mathrm{sca}} + \pi; \xi)\rangle_{\xi} \\ &\quad = \langle \mathbf{Z}(\pi - \theta^{\mathrm{inc}}, \varphi^{\mathrm{inc}}; \pi - \theta^{\mathrm{sca}}, \varphi^{\mathrm{sca}}; \xi)\rangle_{\xi} \\ &\quad = \mathbf{\Delta}_3 [\langle \mathbf{Z}(\theta^{\mathrm{sca}}, \varphi^{\mathrm{sca}}; \theta^{\mathrm{inc}}, \varphi^{\mathrm{inc}}; \xi)\rangle_{\xi}]^{\mathrm{T}} \mathbf{\Delta}_3, \end{aligned} \tag{15.31}$$

where the matrix $\mathbf{\Delta}_3$ is given by Eq. (13.53). Obviously, this is the reciprocity relation (13.52). Other symmetry relations can be derived by forming combinations of Eqs. (15.28), (15.30), and (15.31). For example, combining Eqs. (15.28) and (15.30) yields

$$\langle \mathbf{Z}(\pi - \theta^{\mathrm{sca}}, \varphi^{\mathrm{inc}}; \pi - \theta^{\mathrm{inc}}, \varphi^{\mathrm{sca}}; \xi)\rangle_{\xi} = \langle \mathbf{Z}(\theta^{\mathrm{sca}}, \varphi^{\mathrm{sca}}; \theta^{\mathrm{inc}}, \varphi^{\mathrm{inc}}; \xi)\rangle_{\xi}. \tag{15.32}$$

Although Eq. (15.20) is valid only for $0 < \varphi^{\mathrm{sca}} - \varphi^{\mathrm{inc}} < \pi$, combining it with Eq. (15.28) yields the phase matrix for all possible incidence and scattering directions. The symmetry relations (15.30) and (15.31) further reduce the range of independent scattering geometries and can be very helpful in theoretical calculations or consistency checks on measurements.

15.4 Exact forward-scattering direction and extinction matrix

By virtue of spatial isotropy, the extinction matrix $\langle \mathbf{K}(\hat{\mathbf{n}}^{\mathrm{inc}}; \xi)\rangle_{\xi}$ characterizing an ISRP is independent of the direction of incidence and the orientation of the reference plane used to define the Stokes parameters. It also follows from Eqs. (13.64)–(13.67) and (15.7a)–(15.7d) that

$$\begin{aligned} &\langle K_{13}\rangle_{\xi} = \langle K_{14}\rangle_{\xi} = \langle K_{23}\rangle_{\xi} = \langle K_{24}\rangle_{\xi} \\ &\quad = \langle K_{31}\rangle_{\xi} = \langle K_{32}\rangle_{\xi} = \langle K_{41}\rangle_{\xi} = \langle K_{42}\rangle_{\xi} = 0 \end{aligned} \tag{15.33}$$

(Problem 15.2). Furthermore, we are about to show that the remaining off-diagonal elements of the average extinction matrix also vanish.

We will assume for simplicity that the incidence direction is parallel to the positive direction of the *z*-axis of the laboratory reference frame and will use the *xz*-half-plane with $x \geq 0$ as the meridional plane of the incident field. We will also assume that the initial orientation of the particle reference frame affixed to

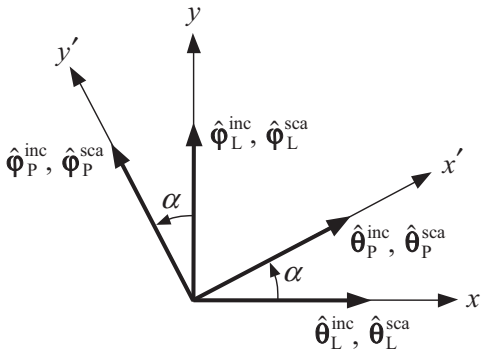

Fig. 15.5. Rotation of the laboratory reference frame L$\{x, y, z\}$ through an Euler angle α about the z-axis transforms it into the particle reference frame P$\{x', y', z'\}$. Since both the incident and the scattered waves propagate in the positive z-direction, their respective unit θ- and φ-vectors are the same.

the particle coincides with the laboratory reference frame. The forward-scattering amplitude matrix computed in the laboratory reference frame for this initial orientation is thus equal to the forward-scattering amplitude matrix computed in the particle reference frame. We will denote the latter as $\mathbf{S}_{\mathrm{P}}$.

Let us now rotate the particle reference frame through a Euler angle α about the z-axis in the clockwise direction, as viewed in the positive z-direction (Figs. C.1 and 15.5) and denote the new forward-scattering amplitude matrix with respect to the laboratory reference frame as $\mathbf{S}_{\mathrm{L}}^{\alpha}$. This matrix relates the column of the electric field vector components of the incident field to that of the field scattered in the exact forward direction:

$$\begin{bmatrix} E_{\theta\mathrm{L}}^{\mathrm{sca}} \\ E_{\varphi\mathrm{L}}^{\mathrm{sca}} \end{bmatrix} \propto \mathbf{S}_{\mathrm{L}}^{\alpha} \begin{bmatrix} E_{\theta\mathrm{L}}^{\mathrm{inc}} \\ E_{\varphi\mathrm{L}}^{\mathrm{inc}} \end{bmatrix}, \tag{15.34}$$

where the subscript L indicates that all field components are computed in the laboratory reference frame. Figure 15.5 shows the respective unit θ- and φ-vectors for the incidence and forward-scattering directions. Simple trigonometry allows us to express the column of the electric vector components in the particle reference frame in terms of that in the laboratory reference frame by means of a trivial matrix multiplication:

$$\begin{bmatrix} E_{\theta\mathrm{P}}^{\mathrm{inc}} \\ E_{\varphi\mathrm{P}}^{\mathrm{inc}} \end{bmatrix} = \begin{bmatrix} C & S \\ -S & C \end{bmatrix} \begin{bmatrix} E_{\theta\mathrm{L}}^{\mathrm{inc}} \\ E_{\varphi\mathrm{L}}^{\mathrm{inc}} \end{bmatrix}, \tag{15.35}$$

where $C = \cos\alpha$ and $S = \sin\alpha$. The reader can easily verify that the inverse relationship reads

$$\begin{bmatrix} E_{\theta\mathrm{L}}^{\mathrm{sca}} \\ E_{\varphi\mathrm{L}}^{\mathrm{sca}} \end{bmatrix} = \begin{bmatrix} C & -S \\ S & C \end{bmatrix} \begin{bmatrix} E_{\theta\mathrm{P}}^{\mathrm{sca}} \\ E_{\varphi\mathrm{P}}^{\mathrm{sca}} \end{bmatrix}. \tag{15.36}$$

Rewriting Eq. (15.34) in the particle reference frame,

$$\begin{bmatrix} E_{\theta\mathrm{P}}^{\mathrm{sca}} \\ E_{\varphi\mathrm{P}}^{\mathrm{sca}} \end{bmatrix} \propto \mathbf{S}_{\mathrm{P}} \begin{bmatrix} E_{\theta\mathrm{P}}^{\mathrm{inc}} \\ E_{\varphi\mathrm{P}}^{\mathrm{inc}} \end{bmatrix}, \tag{15.37}$$

and using Eqs. (15.35) and (15.36), we finally derive

$$\begin{aligned} \mathbf{S}_{\mathrm{L}}^{\alpha} &= \begin{bmatrix} C & -S \\ S & C \end{bmatrix} \mathbf{S}_{\mathrm{P}} \begin{bmatrix} C & S \\ -S & C \end{bmatrix} \\ &= \begin{bmatrix} C^2 S_{11\mathrm{P}} - SCS_{12\mathrm{P}} - SCS_{21\mathrm{P}} + S^2 S_{22\mathrm{P}} & SCS_{11\mathrm{P}} + C^2 S_{12\mathrm{P}} - S^2 S_{21\mathrm{P}} - SCS_{22\mathrm{P}} \\ SCS_{11\mathrm{P}} - S^2 S_{12\mathrm{P}} + C^2 S_{21\mathrm{P}} - SCS_{22\mathrm{P}} & S^2 S_{11\mathrm{P}} + SCS_{12\mathrm{P}} + SCS_{21\mathrm{P}} + C^2 S_{22\mathrm{P}} \end{bmatrix}. \end{aligned} \tag{15.38}$$

For $\alpha = 0$ and $\alpha = \pi/2$,

$$\mathbf{S}_{\mathrm{L}}^{0} = \begin{bmatrix} S_{11\mathrm{P}} & S_{12\mathrm{P}} \\ S_{21\mathrm{P}} & S_{22\mathrm{P}} \end{bmatrix}, \tag{15.39}$$

$$\mathbf{S}_{\mathrm{L}}^{\pi/2} = \begin{bmatrix} S_{22\mathrm{P}} & -S_{21\mathrm{P}} \\ -S_{12\mathrm{P}} & S_{11\mathrm{P}} \end{bmatrix}. \tag{15.40}$$

Because we are assuming random orientations of the particle reference frame, for each morphology in the initial orientation, $\alpha = 0$, there is always a morphology of the same type but in the orientation corresponding to $\alpha = \pi/2$. It therefore follows from Eqs. (13.63), (13.68), (15.39), and (15.40) that

$$\langle K_{12} \rangle_{\xi} = \langle K_{21} \rangle_{\xi} = \langle K_{34} \rangle_{\xi} = \langle K_{43} \rangle_{\xi} = 0 \tag{15.41}$$

(Problem 15.3). Finally, recalling Eq. (13.84), we conclude that the extinction matrix characterizing an ISRP is diagonal and has only one independent element:

$$\langle \mathbf{K}(\hat{\mathbf{n}}^{\mathrm{inc}}; \xi) \rangle_{\xi} \equiv \langle \mathbf{K}(\xi) \rangle_{\xi} = \langle C_{\mathrm{ext}}(\xi) \rangle_{\xi} \boldsymbol{\Delta}, \tag{15.42}$$

where

$$\boldsymbol{\Delta} = \mathrm{diag}[1, 1, 1, 1] \tag{15.43}$$

is the 4×4 unit matrix and $\langle C_{\mathrm{ext}}(\xi) \rangle_{\xi}$ is the average extinction cross section, which is now independent of the direction of incidence and the polarization state of the incident field. This dramatic simplification is useful in many practical circumstances.

The scattering matrix also becomes simpler when $\Theta = 0$. From Eqs. (13.35), (13.38), (13.45), (13.48), (15.39), and (15.40), we find that

$$\langle F_{12}(0; \xi) \rangle_{\xi} = \langle F_{21}(0; \xi) \rangle_{\xi} = \langle F_{34}(0; \xi) \rangle_{\xi} = \langle F_{43}(0; \xi) \rangle_{\xi} = 0. \tag{15.44}$$

Equation (15.38) gives for $\alpha = \pi/4$:

$$\mathbf{S}_{\mathrm{L}}^{\pi/4} = \frac{1}{2}\begin{bmatrix} S_{11\mathrm{P}} - S_{12\mathrm{P}} - S_{21\mathrm{P}} + S_{22\mathrm{P}} & S_{11\mathrm{P}} + S_{12\mathrm{P}} - S_{21\mathrm{P}} - S_{22\mathrm{P}} \\ S_{11\mathrm{P}} - S_{12\mathrm{P}} + S_{21\mathrm{P}} - S_{22\mathrm{P}} & S_{11\mathrm{P}} + S_{12\mathrm{P}} + S_{21\mathrm{P}} + S_{22\mathrm{P}} \end{bmatrix}. \quad (15.45)$$

Equations (13.39), (13.44), (15.39), and (15.45), as well as a considerable amount of algebra yield (Problem 15.5)

$$\langle F_{22}(0;\xi)\rangle_\xi = \langle F_{33}(0;\xi)\rangle_\xi. \quad (15.46)$$

Thus, recalling Eq. (15.13), we find that the Stokes forward-scattering matrix is diagonal and has only three independent elements:

$$\langle \mathbf{F}(0;\xi)\rangle_\xi = \begin{bmatrix} \langle F_{11}(0;\xi)\rangle_\xi & 0 & 0 & 0 \\ 0 & \langle F_{22}(0;\xi)\rangle_\xi & 0 & 0 \\ 0 & 0 & \langle F_{22}(0;\xi)\rangle_\xi & 0 \\ 0 & 0 & 0 & \langle F_{44}(0;\xi)\rangle_\xi \end{bmatrix} \quad (15.47)$$

(van de Hulst 1957).

A rotationally symmetric particle is obviously mirror-symmetric with respect to the plane through the direction of propagation and the axis of symmetry. Choosing this plane as the $x'z'$-plane of the particle reference frame, we see from Eqs. (15.7a) and (15.7c) that $S_{12\mathrm{P}} = S_{21\mathrm{P}} = 0$. This simplifies the amplitude scattering matrices (15.39) and (15.45) and ultimately yields

$$\langle F_{44}(0;\xi)\rangle_\xi = 2\langle F_{22}(0;\xi)\rangle_\xi - \langle F_{11}(0;\xi)\rangle_\xi, \quad (15.48)$$

$$0 \le \langle F_{22}(0;\xi)\rangle_\xi \le \langle F_{11}(0;\xi)\rangle_\xi. \quad (15.49)$$

15.5 Exact backward scattering

Equation (15.6) provides an unambiguous definition of the scattering matrix in terms of the phase matrix, except for the exact backscattering direction. Indeed, the backscattering direction for an incidence direction $\{\theta^{\mathrm{inc}}, \varphi^{\mathrm{inc}}\}$ is given by $\{\pi - \theta^{\mathrm{inc}}, \varphi^{\mathrm{inc}} + \pi\}$. Therefore, the complete definition of the scattering matrix should be as follows:

$$\mathbf{F}(\theta^{\mathrm{sca}};\xi) = \begin{cases} \mathbf{Z}(\theta^{\mathrm{sca}}, 0; 0, 0; \xi) & \text{for } \theta^{\mathrm{sca}} \in [0, \pi), \\ \mathbf{Z}(\pi, \pi; 0, 0; \xi) & \text{for } \theta^{\mathrm{sca}} = \pi, \end{cases}$$

which seems to be different from Eq. (15.6). It is easy to see, however, that

$$\mathbf{Z}(\pi, 0; 0, 0; \xi) = \mathbf{L}(\pi)\mathbf{Z}(\pi, \pi; 0, 0; \xi) \equiv \mathbf{Z}(\pi, \pi; 0, 0; \xi)$$

(cf. Eq. (7.7)), which demonstrates the equivalence of the two definitions.

We are ready now to consider the case of scattering in the exact backward direction, using the complete definition of the scattering matrix and the backscattering theorem derived in Section 5.4. Let us assume that the incidence direction is parallel to the positive z-axis of the laboratory coordinate system and use the

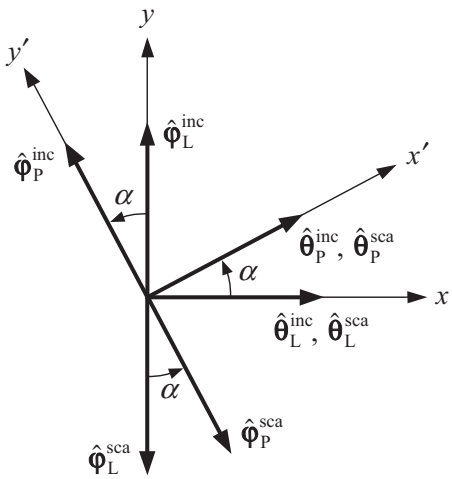

Fig. 15.6. As in Fig. 15.5, but for the case of scattering in the exact backward direction.

xz-half-plane with $x \geq 0$ as the meridional plane of the incidence direction. As in the previous section, we consider two orientations of the particle reference frame relative to the laboratory reference frame:

- the initial orientation, when $\mathrm{P}\{x', y', z\}$ coincides with $\mathrm{L}\{x, y, z\}$, and
- the orientation obtained by rotating $\mathrm{P}\{x', y', z\}$ about the z-axis through a positive Euler angle α.

Figure 15.6 shows the respective unit θ- and φ-vectors for the incidence and backscattering directions. Denote the backscattering amplitude matrix in the particle reference frame as $\mathbf{S}_{\mathrm{P}}$ and the backscattering amplitude matrix in the laboratory reference frame for the rotated particle reference frame as $\mathbf{S}_{\mathrm{L}}^{\alpha}$. A derivation similar to that in the previous section gives

$$\begin{aligned}\mathbf{S}_{\mathrm{L}}^{\alpha} &= \begin{bmatrix} C & S \\ -S & C \end{bmatrix} \mathbf{S}_{\mathrm{P}} \begin{bmatrix} C & S \\ -S & C \end{bmatrix} \\ &= \begin{bmatrix} C^2 S_{11\mathrm{P}} - SCS_{12\mathrm{P}} + SCS_{21\mathrm{P}} - S^2 S_{22\mathrm{P}} & SCS_{11\mathrm{P}} + C^2 S_{12\mathrm{P}} + S^2 S_{21\mathrm{P}} + SCS_{22\mathrm{P}} \\ -SCS_{11\mathrm{P}} + S^2 S_{12\mathrm{P}} + C^2 S_{21\mathrm{P}} - SCS_{22\mathrm{P}} & -S^2 S_{11\mathrm{P}} - SCS_{12\mathrm{P}} + SCS_{21\mathrm{P}} + C^2 S_{22\mathrm{P}} \end{bmatrix}. \end{aligned} \tag{15.50}$$

This formula can be simplified, because the backscattering theorem (5.32) yields $S_{21\mathrm{P}} = -S_{12\mathrm{P}}$. Assuming the random orientation distribution and considering the cases $\alpha = 0$ and $\alpha = \pi/2$, we find that

$$\langle F_{12}(\pi; \xi)\rangle_{\xi} = \langle F_{21}(\pi; \xi)\rangle_{\xi} = \langle F_{34}(\pi; \xi)\rangle_{\xi} = \langle F_{43}(\pi; \xi)\rangle_{\xi} = 0.$$

Similarly, considering the cases $\alpha = 0$ and $\alpha = \pi/4$ yields

$$\langle F_{33}(\pi;\xi)\rangle_\xi = -\langle F_{22}(\pi;\xi)\rangle_\xi.$$

Finally, recalling Eqs. (13.54) and (15.13), we conclude that the Stokes backscattering matrix is diagonal and has only two independent elements:

$$\langle \mathbf{F}(\pi;\xi)\rangle_\xi = \begin{bmatrix} \langle F_{11}(\pi;\xi)\rangle_\xi & 0 & 0 & 0 \\ 0 & \langle F_{22}(\pi;\xi)\rangle_\xi & 0 & 0 \\ 0 & 0 & -\langle F_{22}(\pi;\xi)\rangle_\xi & 0 \\ 0 & 0 & 0 & \langle F_{11}(\pi;\xi)\rangle_\xi - 2\langle F_{22}(\pi;\xi)\rangle_\xi \end{bmatrix} \tag{15.51}$$

(Mishchenko and Hovenier 1995). According to Eq. (15.15), $\langle F_{44}\rangle_\xi \le \langle F_{11}\rangle_\xi$, so we always have

$$\langle F_{22}(\pi;\xi)\rangle_\xi \ge 0. \tag{15.52}$$

15.6 Scattering cross section and asymmetry parameter

Like all other scattering characteristics, the average scattering cross section characterizing an ISRP is independent of the direction of incidence. Therefore, we will evaluate the integral on the right-hand side of Eq. (13.85), assuming that the incidence direction is parallel to the positive z-axis of the laboratory reference frame and that the xz-half-plane with $x \ge 0$ is the corresponding meridional plane. Figure 15.7 shows that in order to compute the Stokes column vector of the scattered field with respect to its own meridional plane, we must rotate the reference frame of the incidence direction by the angle φ, thereby modifying the Stokes column vector of the incident field according to Eq. (7.7), with $\eta = \varphi$, and then multiply the new Stokes column vector of the incident field by the scattering matrix. Therefore, the average phase matrix is simply

$$\langle \mathbf{Z}(\hat{\mathbf{n}}^{\rm sca}, \hat{\mathbf{n}}^{\rm inc};\xi)\rangle_\xi = \langle \mathbf{F}(\theta;\xi)\rangle_\xi \mathbf{L}(\varphi)$$
$$= \begin{bmatrix} \langle F_{11}(\theta;\xi)\rangle_\xi & \langle F_{12}(\theta;\xi)\rangle_\xi \cos 2\varphi & -\langle F_{12}(\theta;\xi)\rangle_\xi \sin 2\varphi & 0 \\ \langle F_{12}(\theta;\xi)\rangle_\xi & \langle F_{22}(\theta;\xi)\rangle_\xi \cos 2\varphi & -\langle F_{22}(\theta;\xi)\rangle_\xi \sin 2\varphi & 0 \\ 0 & \langle F_{33}(\theta;\xi)\rangle_\xi \sin 2\varphi & \langle F_{33}(\theta;\xi)\rangle_\xi \cos 2\varphi & \langle F_{34}(\theta;\xi)\rangle_\xi \\ 0 & -\langle F_{34}(\theta;\xi)\rangle_\xi \sin 2\varphi & -\langle F_{34}(\theta;\xi)\rangle_\xi \cos 2\varphi & \langle F_{44}(\theta;\xi)\rangle_\xi \end{bmatrix}. \tag{15.53}$$

Substituting this formula in Eq. (13.85), we find that the average scattering cross section is independent of the polarization state of the incident field and is given by

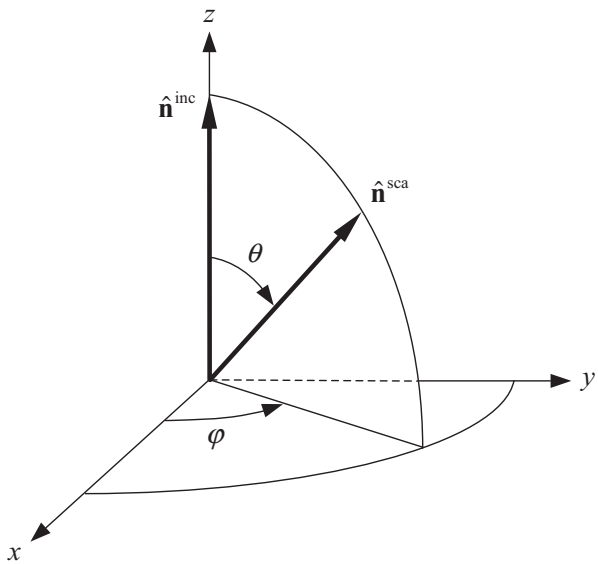

Fig. 15.7. Illustration of the relationship between the phase and scattering matrices when the incidence direction is along the positive z-axis.

$$\langle C_{\text{sca}}(\xi)\rangle_\xi = 2\pi \int_0^\pi \mathrm{d}\theta \sin\theta \, \langle F_{11}(\theta;\xi)\rangle_\xi. \tag{15.54}$$

The corresponding asymmetry parameter must also be independent of $\hat{\mathbf{n}}^{\text{inc}}$, and Eqs. (13.90), (13.94), and (15.53) yield

$$g = \frac{2\pi}{\langle C_{\text{sca}}(\xi)\rangle_\xi} \int_0^\pi \mathrm{d}\theta \sin\theta \cos\theta \, \langle F_{11}(\theta;\xi)\rangle_\xi. \tag{15.55}$$

Obviously, g is polarization-independent. The average absorption cross section,

$$\langle C_{\text{abs}}(\xi)\rangle_\xi = \langle C_{\text{ext}}(\xi)\rangle_\xi - \langle C_{\text{sca}}(\xi)\rangle_\xi, \tag{15.56}$$

and the single-scattering albedo,

$$\varpi = \frac{\langle C_{\text{sca}}(\xi)\rangle_\xi}{\langle C_{\text{ext}}(\xi)\rangle_\xi}, \tag{15.57}$$

are also independent of the direction and polarization state of the incident field. The same, of course, is true of the extinction, scattering, and absorption efficiency factors defined, respectively, as

$$Q_{\text{ext}} = \frac{\langle C_{\text{ext}}(\xi)\rangle_\xi}{\langle G(\xi)\rangle_\xi}, \quad Q_{\text{sca}} = \frac{\langle C_{\text{sca}}(\xi)\rangle_\xi}{\langle G(\xi)\rangle_\xi}, \quad Q_{\text{abs}} = \frac{\langle C_{\text{abs}}(\xi)\rangle_\xi}{\langle G(\xi)\rangle_\xi}, \tag{15.58}$$

where $\langle G(\xi)\rangle_\xi$ is the average area of the particle's geometrical projection.

15.7 Spherically symmetric particle

The structure of the scattering matrix simplifies further if the ISRP is spherically symmetric, i.e., is a homogeneous or radially inhomogeneous spherical particle composed of optically isotropic materials. Then the internal relative refractive index is a function of only the distance from the center of the particle. Irrespective of its "orientation" relative to the laboratory reference frame, the spherically symmetric particle is mirror-symmetric with respect to the *xz*-plane. Assuming that the incidence direction is parallel to the positive *z*-axis, restricting the scattering direction to the *xz*-half-plane with $x \geq 0$, and using this plane for reference, we find from Eqs. (15.7a) and (15.7c) that the amplitude scattering matrix is always diagonal: $S_{12} \equiv S_{21} \equiv 0$. Therefore, Eqs. (13.34), (13.39), (13.44), (13.49), and (15.13) yield

$$\langle \mathbf{F}(\Theta;\xi)\rangle_\xi = \begin{bmatrix} \langle F_{11}(\Theta;\xi)\rangle_\xi & \langle F_{12}(\Theta;\xi)\rangle_\xi & 0 & 0 \\ \langle F_{12}(\Theta;\xi)\rangle_\xi & \langle F_{11}(\Theta;\xi)\rangle_\xi & 0 & 0 \\ 0 & 0 & \langle F_{33}(\Theta;\xi)\rangle_\xi & \langle F_{34}(\Theta;\xi)\rangle_\xi \\ 0 & 0 & -\langle F_{34}(\Theta;\xi)\rangle_\xi & \langle F_{33}(\Theta;\xi)\rangle_\xi \end{bmatrix}. \quad (15.59)$$

A scattering matrix of this type appears in the Lorenz–Mie theory (LMT) of light scattering by a homogeneous isotropic sphere (Section 16.1.1). The results of the previous sections on forward and backward scattering further imply that

$$\langle F_{33}(0;\xi)\rangle_\xi = \langle F_{11}(0;\xi)\rangle_\xi, \quad \langle F_{33}(\pi;\xi)\rangle_\xi = -\langle F_{11}(\pi;\xi)\rangle_\xi, \quad (15.60)$$

$$\langle F_{12}(0;\xi)\rangle_\xi = \langle F_{12}(\pi;\xi)\rangle_\xi = 0. \quad (15.61)$$

15.8 Effects of morphology and orientation

The preceding discussion of symmetries enables us to summarize the most fundamental effects of morphology and orientation on the average optical characteristics of a random scattering particle. If the particle is not an ISRP then, in general:

- the average 4×4 extinction matrix does not degenerate to a direction- and polarization-independent scalar extinction cross section;
- the average extinction, scattering, and absorption cross sections, the single-scattering albedo, and the asymmetry parameter depend on the direction and polarization state of the incident field;
- the average scattering matrix $\langle \mathbf{F}\rangle_\xi$ does not have the simple block-diagonal structure of Eq. (15.13): all 16 elements of the scattering matrix can be nonzero as well as dependent on the incidence direction and the orientation of the scattering plane, rather than only on the scattering angle;
- the average phase matrix depends on the specific values of the azimuthal angles of the incidence and scattering directions, rather than on their differ-

ence; cannot be represented in the form of Eqs. (15.20) and (15.21); and does not obey the symmetry relations (15.26) and (15.28).

Any of these effects can directly indicate the presence of oriented particles lacking spherical symmetry.

If the random particle is an ISRP then:

- the average extinction matrix reduces to the scalar extinction cross section according to Eq. (15.42);
- all average optical cross sections, the single-scattering albedo, and the asymmetry parameter become orientation- and polarization-independent;
- the average scattering matrix becomes block-diagonal, Eq. (15.13), depends only on the scattering angle, and possesses almost the same structure as the Lorenz–Mie scattering matrix (15.59); and
- the average phase matrix depends only on the difference between the azimuthal angles of the incidence and scattering directions rather than on their specific values; has the structure specified by Eqs. (15.20) and (15.21); and obeys the symmetry relations (15.26) and (15.28).

Despite the similarity of the matrices (15.13) and (15.59), the Lorenz–Mie identities $\langle F_{22}(\Theta;\xi)\rangle_\xi \equiv \langle F_{11}(\Theta;\xi)\rangle_\xi$ and $\langle F_{44}(\Theta;\xi)\rangle_\xi \equiv \langle F_{33}(\Theta;\xi)\rangle_\xi$, as well as Eq. (15.60) do not hold, in general, for a nonspherical ISRP. As a consequence, measurements of the so-called linear backscattering depolarization ratio

$$\delta_{\mathrm{L}} = \frac{\langle F_{11}(\pi;\xi)\rangle_\xi - \langle F_{22}(\pi;\xi)\rangle_\xi}{\langle F_{11}(\pi;\xi)\rangle_\xi + \langle F_{22}(\pi;\xi)\rangle_\xi} \tag{15.62}$$

and the closely related (Problem 15.6) circular backscattering depolarization ratio

$$\delta_{\mathrm{C}} = \frac{\langle F_{11}(\pi;\xi)\rangle_\xi + \langle F_{44}(\pi;\xi)\rangle_\xi}{\langle F_{11}(\pi;\xi)\rangle_\xi - \langle F_{44}(\pi;\xi)\rangle_\xi} \tag{15.63}$$

are often used as a means of detecting nonsphericity.

15.9 Normalized scattering and phase matrices

It is often convenient to use the so-called normalized scattering matrix

$$\widetilde{\mathbf{F}}(\Theta) = \frac{4\pi}{\langle C_{\mathrm{sca}}(\xi)\rangle_\xi}\langle \mathbf{F}(\Theta;\xi)\rangle_\xi = \begin{bmatrix} a_1(\Theta) & b_1(\Theta) & 0 & 0 \\ b_1(\Theta) & a_2(\Theta) & 0 & 0 \\ 0 & 0 & a_3(\Theta) & b_2(\Theta) \\ 0 & 0 & -b_2(\Theta) & a_4(\Theta) \end{bmatrix} \tag{15.64}$$

with dimensionless elements. Similarly, the normalized phase matrix can be defined as

$$\widetilde{\mathbf{Z}}(\theta^{\text{sca}}, \varphi^{\text{sca}}; \theta^{\text{inc}}, \varphi^{\text{inc}}) = \frac{4\pi}{\langle C_{\text{sca}}(\xi)\rangle_\xi} \langle \mathbf{Z}(\theta^{\text{sca}}, \varphi^{\text{sca}}; \theta^{\text{inc}}, \varphi^{\text{inc}}; \xi)\rangle_\xi. \quad (15.65)$$

The $(1,1)$ element of the normalized scattering matrix, $a_1(\Theta)$, is traditionally called the phase function and, as follows from Eqs. (15.54) and (15.64), satisfies the following normalization condition:

$$\frac{1}{2}\int_0^\pi \mathrm{d}\Theta \sin\Theta\, a_1(\Theta) = 1. \quad (15.66)$$

Remember that we have already used the term "phase function" to name the quantity p defined by Eq. (13.92). It can be seen easily from Eqs. (13.90), (13.92), and (15.64) that the differential scattering cross section $\mathrm{d}C_{\text{sca}}/\mathrm{d}\Omega$ reduces to $\langle F_{11}\rangle_\xi$, and so p reduces to a_1, when unpolarized incident light propagates along the positive z-axis and is scattered in the xz-half-plane with $x \geq 0$. Equations (15.55) and (15.64) yield

$$g = \frac{1}{2}\int_0^\pi \mathrm{d}\Theta \sin\Theta\, a_1(\Theta) \cos\Theta. \quad (15.67)$$

The normalized scattering matrix possesses many properties of the regular scattering matrix, e.g.,

$$a_1 \geq 0, \quad (15.68)$$

$$|a_i| \leq a_1, \quad i = 2, 3, 4, \quad (15.69)$$

$$|b_i| \leq a_1, \quad i = 1, 2, \quad (15.70)$$

$$(a_3 + a_4)^2 + 4b_2^2 \leq (a_1 + a_2)^2 - 4b_1^2, \quad (15.71)$$

$$|a_3 - a_4| \leq a_1 - a_2, \quad (15.72)$$

$$|a_2 - b_1| \leq a_1 - b_1, \quad (15.73)$$

$$|a_2 + b_1| \leq a_1 + b_1, \quad (15.74)$$

$$\widetilde{\mathbf{F}}(0) = \begin{bmatrix} a_1(0) & 0 & 0 & 0 \\ 0 & a_2(0) & 0 & 0 \\ 0 & 0 & a_2(0) & 0 \\ 0 & 0 & 0 & a_4(0) \end{bmatrix}, \quad (15.75)$$

$$\widetilde{\mathbf{F}}(\pi) = \begin{bmatrix} a_1(\pi) & 0 & 0 & 0 \\ 0 & a_2(\pi) & 0 & 0 \\ 0 & 0 & -a_2(\pi) & 0 \\ 0 & 0 & 0 & a_4(\pi) \end{bmatrix}, \quad (15.76)$$

$$a_4(\pi) = a_1(\pi) - 2a_2(\pi), \quad a_2(\pi) \geq 0. \quad (15.77)$$

Also,

$$a_4(0) = 2a_2(0) - a_1(0), \quad a_2(0) \geq 0 \tag{15.78}$$

for a rotationally symmetric particle and

$$\widetilde{\mathbf{F}}(\Theta) = \begin{bmatrix} a_1(\Theta) & b_1(\Theta) & 0 & 0 \\ b_1(\Theta) & a_1(\Theta) & 0 & 0 \\ 0 & 0 & a_3(\Theta) & b_2(\Theta) \\ 0 & 0 & -b_2(\Theta) & a_3(\Theta) \end{bmatrix}, \tag{15.79}$$

$$a_3(0) = a_1(0), \quad a_3(\pi) = -a_1(\pi) \tag{15.80}$$

for a spherically symmetric particle. Similarly, for $0 < \varphi^{\text{sca}} - \varphi^{\text{inc}} < \pi$ the normalized phase matrix is given by

$$\widetilde{\mathbf{Z}}(\theta^{\text{sca}}, \varphi^{\text{sca}}; \theta^{\text{inc}}, \varphi^{\text{inc}}) = \begin{bmatrix} a_1(\Theta) & C_1 b_1(\Theta) & S_1 b_1(\Theta) & 0 \\ C_2 b_1(\Theta) & C_1 C_2 a_2(\Theta) - S_1 S_2 a_3(\Theta) & S_1 C_2 a_2(\Theta) + C_1 S_2 a_3(\Theta) & S_2 b_2(\Theta) \\ -S_2 b_1(\Theta) & -C_1 S_2 a_2(\Theta) - S_1 C_2 a_3(\Theta) & -S_1 S_2 a_2(\Theta) + C_1 C_2 a_3(\Theta) & C_2 b_2(\Theta) \\ 0 & S_1 b_2(\Theta) & -C_1 b_2(\Theta) & a_4(\Theta) \end{bmatrix} \tag{15.81}$$

(cf. Eq. (15.20)) and has the same symmetry properties as the regular phase matrix:

$$\widetilde{\mathbf{Z}}(\theta^{\text{sca}}, -\varphi^{\text{inc}}; \theta^{\text{inc}}, -\varphi^{\text{sca}}) = \widetilde{\mathbf{Z}}(\theta^{\text{sca}}, \varphi^{\text{sca}}; \theta^{\text{inc}}, \varphi^{\text{inc}}), \tag{15.82}$$

$$\widetilde{\mathbf{Z}}(\theta^{\text{sca}}, -\varphi^{\text{sca}}; \theta^{\text{inc}}, -\varphi^{\text{inc}}) = \mathbf{\Delta}_{34} \widetilde{\mathbf{Z}}(\theta^{\text{sca}}, \varphi^{\text{sca}}; \theta^{\text{inc}}, \varphi^{\text{inc}}) \mathbf{\Delta}_{34}, \tag{15.83}$$

$$\widetilde{\mathbf{Z}}(\pi - \theta^{\text{sca}}, \varphi^{\text{sca}}; \pi - \theta^{\text{inc}}, \varphi^{\text{inc}}) = \mathbf{\Delta}_{34} \widetilde{\mathbf{Z}}(\theta^{\text{sca}}, \varphi^{\text{sca}}; \theta^{\text{inc}}, \varphi^{\text{inc}}) \mathbf{\Delta}_{34}, \tag{15.84}$$

$$\widetilde{\mathbf{Z}}(\pi - \theta^{\text{inc}}, \varphi^{\text{inc}}; \pi - \theta^{\text{sca}}, \varphi^{\text{sca}}) = \mathbf{\Delta}_3 [\widetilde{\mathbf{Z}}(\theta^{\text{sca}}, \varphi^{\text{sca}}; \theta^{\text{inc}}, \varphi^{\text{inc}})]^{\text{T}} \mathbf{\Delta}_3. \tag{15.85}$$

15.10 Expansion in Wigner *d*-functions

A traditional way of specifying the elements of the normalized scattering matrix is to tabulate their numerical values for a representative grid of scattering angles (e.g., Deirmendjian 1969). However, a more mathematically appealing and practically efficient way is to expand the scattering matrix elements in so-called Wigner *d*-functions $d^s_{mn}(\Theta)$ or, equivalently, in generalized spherical functions $P^s_{mn}(\cos\Theta) = \mathrm{i}^{m-n} d^s_{mn}(\Theta)$ (see Appendix F):

$$a_1(\Theta) = \sum_{s=0}^{s_{\max}} \alpha_1^s P_{00}^s(\cos\Theta) = \sum_{s=0}^{s_{\max}} \alpha_1^s d_{00}^s(\Theta), \tag{15.86}$$

$$a_2(\Theta) + a_3(\Theta) = \sum_{s=0}^{s_{\max}} (\alpha_2^s + \alpha_3^s) P_{22}^s(\cos\Theta) = \sum_{s=0}^{s_{\max}} (\alpha_2^s + \alpha_3^s) d_{22}^s(\Theta), \tag{15.87}$$

$$a_2(\Theta) - a_3(\Theta) = \sum_{s=0}^{s_{\max}} (\alpha_2^s - \alpha_3^s) P_{2,-2}^s(\cos\Theta) = \sum_{s=0}^{s_{\max}} (\alpha_2^s - \alpha_3^s) d_{2,-2}^s(\Theta), \tag{15.88}$$

$$a_4(\Theta) = \sum_{s=0}^{s_{\max}} \alpha_4^s P_{00}^s(\cos\Theta) = \sum_{s=0}^{s_{\max}} \alpha_4^s d_{00}^s(\Theta), \tag{15.89}$$

$$b_1(\Theta) = \sum_{s=0}^{s_{\max}} \beta_1^s P_{02}^s(\cos\Theta) = -\sum_{s=0}^{s_{\max}} \beta_1^s d_{02}^s(\Theta), \tag{15.90}$$

$$b_2(\Theta) = \sum_{s=0}^{s_{\max}} \beta_2^s P_{02}^s(\cos\Theta) = -\sum_{s=0}^{s_{\max}} \beta_2^s d_{02}^s(\Theta) \tag{15.91}$$

(Hovenier *et al.* 2004). The angular behavior of several d-functions entering Eqs. (15.86)–(15.91) is illustrated in Fig. F.1. According to Appendix F, these expansions always exist in the sense of Eq. (F.16) provided that

$$\int_0^\pi \mathrm{d}\Theta \sin\Theta\, [a_i(\Theta)]^2 < \infty, \quad i = 1, 2, 3, 4, \tag{15.92}$$

$$\int_0^\pi \mathrm{d}\Theta \sin\Theta\, [b_i(\Theta)]^2 < \infty, \quad i = 1, 2. \tag{15.93}$$

In view of the inequalities (15.69) and (15.70), it is sufficient to require that

$$\int_0^\pi \mathrm{d}\Theta \sin\Theta\, [a_1(\Theta)]^2 < \infty. \tag{15.94}$$

There are no reasons to expect that the latter condition can be violated for real particles occurring in nature. According to Eqs. (F.5) and (F.7),

$$d_{2,-2}^s(0) = d_{02}^s(0) = 0, \tag{15.95}$$

$$d_{22}^s(\pi) = d_{02}^s(\pi) = 0. \tag{15.96}$$

Therefore, Eqs. (15.87), (15.88), (15.90), and (15.91) identically reproduce the specific structure of the normalized scattering matrix for the exact forward and backward directions, as given by Eqs. (15.75) and (15.76). The form of the expansions (15.86)–(15.89) also becomes simpler in the case of the exact forward or exact backward direction (Problem 15.8).

The number of nonzero terms in the expansions (15.86)–(15.91) is in principle infinite. In practice, however, the expansions are truncated at $s = s_{\max}$, the

upper summation limit $s_{\max}$ being chosen such that the corresponding finite sums differ from the respective scattering matrix elements on the entire interval $\Theta \in [0, \pi]$ of scattering angles within the requisite numerical accuracy. Since $d^s_{mn}(\Theta) \equiv 0$ for $s < \max(|m|, |n|)$, the coefficients α^0_2, α^1_2, α^0_3, α^1_3, β^0_1, β^1_1, β^0_2, and β^1_2 are not, strictly speaking, defined. However, it is often convenient to formally equate them to zero:

$$\alpha^0_2 = \alpha^1_2 = \alpha^0_3 = \alpha^1_3 = \beta^0_1 = \beta^1_1 = \beta^0_2 = \beta^1_2 = 0. \tag{15.97}$$

The analytical properties of the d-functions are summarized in Appendix F. For given m and n, the $d^s_{mn}(\Theta)$ with $s > \max(|m|, |n|)$, when multiplied by $\left(s + \frac{1}{2}\right)^{1/2}$, form a complete orthonormal set of functions of $\Theta \in [0, \pi]$. Therefore, using the orthogonality relation (F.13), we obtain from Eqs. (15.86)–(15.91):

$$\alpha^s_1 = \left(s + \tfrac{1}{2}\right) \int_0^\pi \mathrm{d}\Theta \sin\Theta \, a_1(\Theta) \, d^s_{00}(\Theta), \tag{15.98}$$

$$\alpha^s_2 + \alpha^s_3 = \left(s + \tfrac{1}{2}\right) \int_0^\pi \mathrm{d}\Theta \sin\Theta \, [a_2(\Theta) + a_3(\Theta)] \, d^s_{22}(\Theta), \tag{15.99}$$

$$\alpha^s_2 - \alpha^s_3 = \left(s + \tfrac{1}{2}\right) \int_0^\pi \mathrm{d}\Theta \sin\Theta \, [a_2(\Theta) - a_3(\Theta)] \, d^s_{2,-2}(\Theta), \tag{15.100}$$

$$\alpha^s_4 = \left(s + \tfrac{1}{2}\right) \int_0^\pi \mathrm{d}\Theta \sin\Theta \, a_4(\Theta) \, d^s_{00}(\Theta), \tag{15.101}$$

$$\beta^s_1 = -\left(s + \tfrac{1}{2}\right) \int_0^\pi \mathrm{d}\Theta \sin\Theta \, b_1(\Theta) \, d^s_{02}(\Theta), \tag{15.102}$$

$$\beta^s_2 = -\left(s + \tfrac{1}{2}\right) \int_0^\pi \mathrm{d}\Theta \sin\Theta \, b_2(\Theta) \, d^s_{02}(\Theta) \tag{15.103}$$

(cf. Eq. (F.17)). These formulas suggest a simple, albeit not always the most elegant and efficient way to compute the expansion coefficients by evaluating the integrals numerically using a suitable quadrature formula. Of course, this procedure assumes the knowledge of the normalized scattering matrix elements at the quadrature division points.

Because the d-functions possess well-known and convenient mathematical properties and can be efficiently computed by using the simple and numerically stable recurrence relation (F.8), the expansions (15.86)–(15.91) offer substantial practical advantages. For example, if the expansion coefficients appearing in these expansions are known, then the elements of the normalized scattering matrix can be calculated easily for essentially any number of scattering angles and with a minimal expenditure of computer time. Hence, instead of tabulating the elements of the scattering matrix for a large number of scattering angles (see, e.g., Deirmendjian 1969) and resorting to interpolation in order to find the scattering matrix at intermediate

points, one can provide a complete and accurate specification of the scattering matrix by tabulating a limited (and usually small) number of numerically significant expansion coefficients. This also explains why the expansion coefficients are especially convenient in averaging over orientations: instead of computing the scattering matrix elements for a large number of orientations, one can average a (much) smaller set of expansion coefficients.

Another advantage of expanding the scattering matrix elements in *d*-functions is that the latter obey an addition theorem and thereby provide an elegant analytical way of calculating the coefficients in a Fourier azimuthal decomposition of the normalized phase matrix (Kuščer and Ribarič 1959; Hovenier *et al.* 2004; MTL2).

An important additional advantage offered by the expansions (15.86)–(15.91) is that using the *T*-matrix or the superposition *T*-matrix method (see Section 16.1.8), the expansion coefficients for certain types of nonspherical particle can be calculated analytically without computing the normalized scattering matrix itself.

The expansion coefficients obey the general inequalities

$$|\alpha_i^s| \leq 2s+1, \quad i = 1, 2, 3, 4, \tag{15.104}$$

$$|\beta_i^s| < \frac{2s+1}{\sqrt{2}}, \quad i = 1, 2. \tag{15.105}$$

These and other useful inequalities were derived by van der Mee and Hovenier (1990). Since, for each s, $d_{00}^s(\Theta)$ is also a Legendre polynomial $P_s(\cos\Theta)$, Eq. (15.86) is the well-known expansion of the phase function in Legendre polynomials (Chandrasekhar 1950; Sobolev 1975; van de Hulst 1980). Equation (F.11) implies that $d_{00}^0(\Theta) \equiv 1$. Therefore, Eq. (15.98) and the normalization condition (15.66) yield the identity

$$\alpha_1^0 \equiv 1, \tag{15.106}$$

while the orthogonality property of the *d*-functions and Eq. (15.67) imply that

$$g = \tfrac{1}{3}\alpha_1^1. \tag{15.107}$$

To illustrate the typical traits of the expansion coefficients α_i^s and β_i^s, Fig. 15.8 depicts them as a function of s for two polydisperse models of a random homogeneous spherical particle, each described by a gamma distribution of radii given by

$$n(r) = \text{constant} \times r^{(1-3b)/b} \exp\left(-\frac{r}{ab}\right), \quad b \in \left(0, \tfrac{1}{2}\right). \tag{15.108}$$

The constant is chosen such that the size distribution satisfies the standard normalization (13.152). It is assumed for both models that the relative refractive index is $m = 1.5$, $r_{\min} = 0$, $r_{\max} = \infty$, and the so-called effective variance, defined by

$$v_{\text{eff}} = \frac{1}{\langle G \rangle r_{\text{eff}}^2} \int_{r_{\min}}^{r_{\max}} \mathrm{d}r\, n(r)(r - r_{\text{eff}})^2 \pi r^2, \tag{15.109}$$

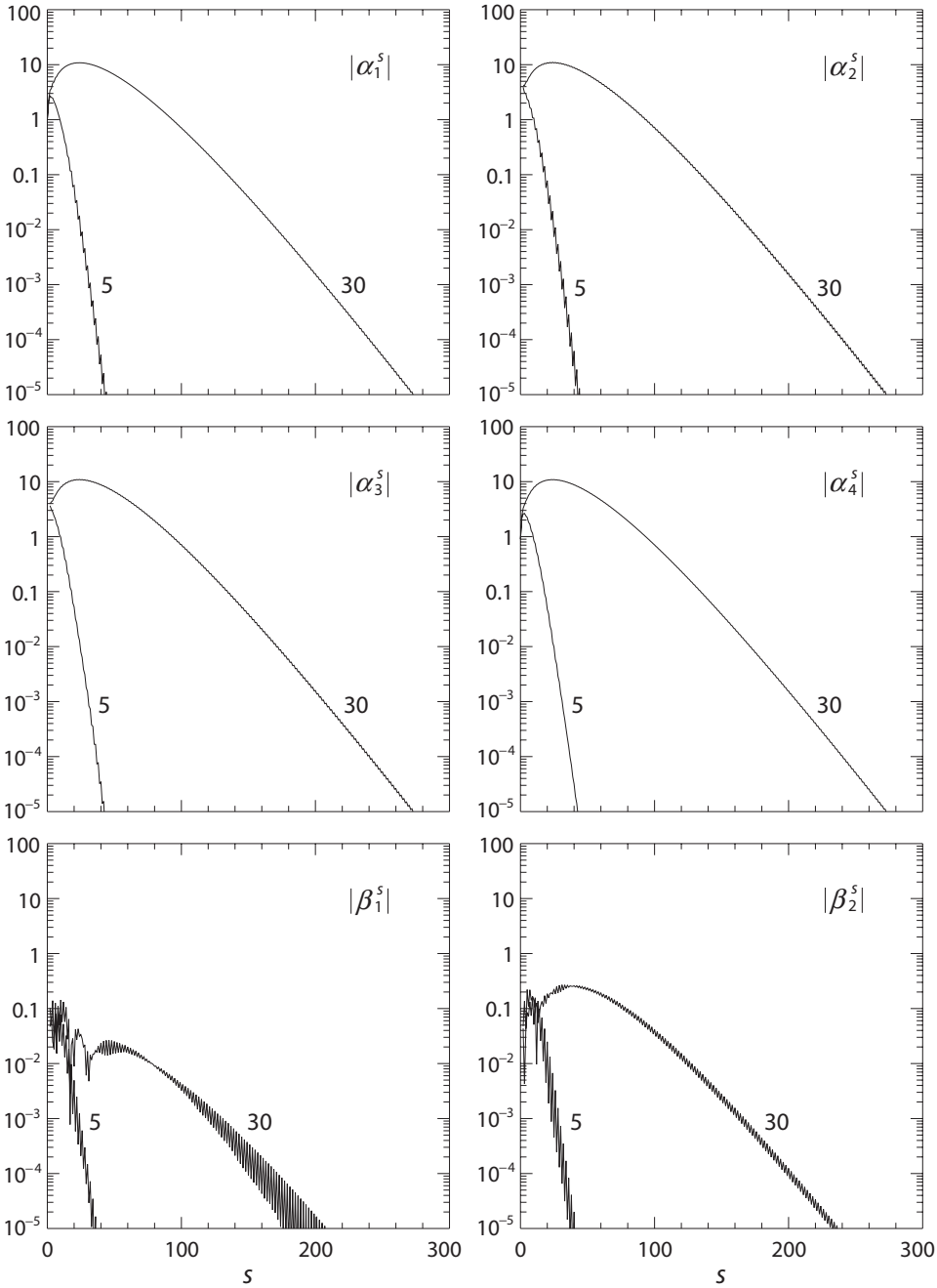

Fig. 15.8. Expansion coefficients for two models of a random homogeneous spherical particle characterized by effective size parameters $x_{\text{eff}} = 5$ and 30 (see text).

is equal to 0.2. In Eq. (15.109),

$$r_{\text{eff}} = \frac{1}{\langle G \rangle} \int_{r_{\min}}^{r_{\max}} \mathrm{d}r\, n(r)\, r \pi r^2 \tag{15.110}$$

is the so-called effective radius of the size distribution and

$$\langle G \rangle = \int_{r_{\min}}^{r_{\max}} \mathrm{d}r\, n(r) \pi r^2 \tag{15.111}$$

is the average area of the particle's geometrical projection. The effective size parameter $x_{\text{eff}} = k_1 r_{\text{eff}}$ is equal to 5 for the first model and to 30 for the second model. Figure 15.9 visualizes the four independent elements of the normalized Lorenz–Mie scattering matrix for both models. The computations were per-

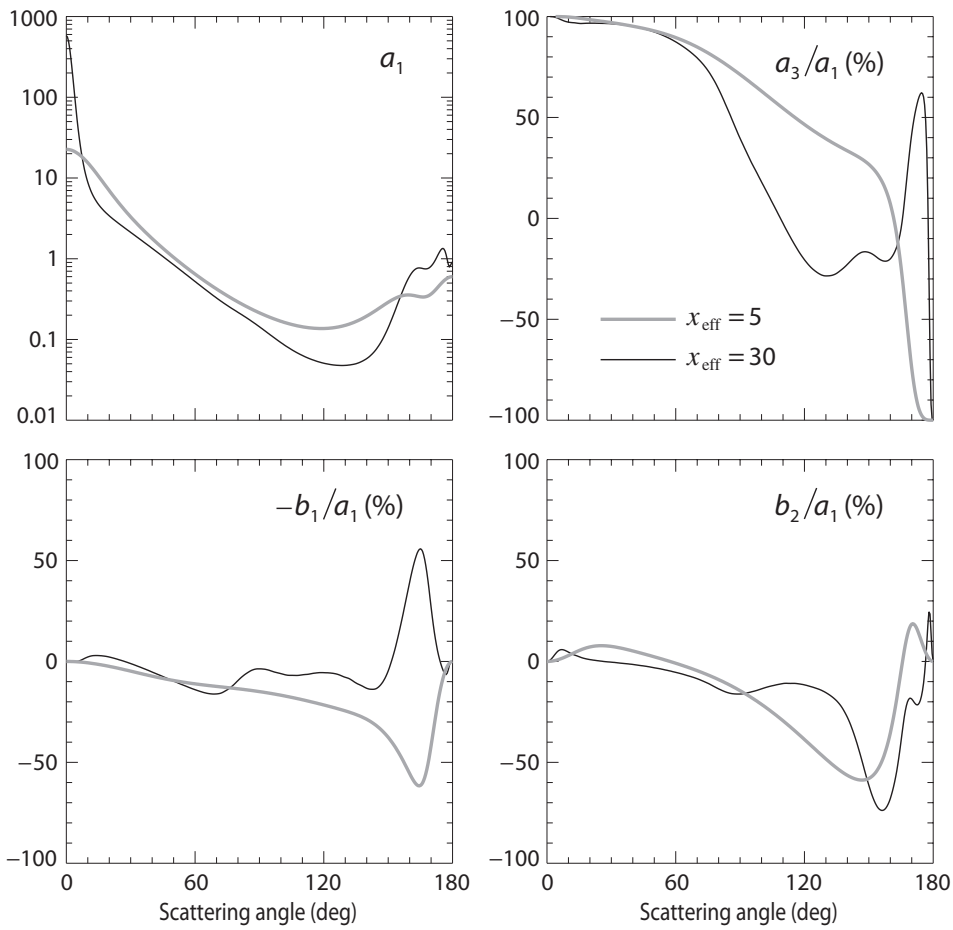

Fig. 15.9. Elements of the normalized scattering matrix for two models of a random homogeneous spherical particle characterized by effective size parameters $x_{\text{eff}} = 5$ and 30 (see text).

formed using the Lorenz–Mie computer code described in Section 5.10 of MTL1.

Figure 15.8 reveals the typical behavior of the expansion coefficients α_i^s with increasing index s: they first grow in magnitude and then decay to absolute values below a reasonable numerical threshold. The greater the effective size parameter, the larger the maximal absolute value of the expansion coefficients and the slower their decay. This trend is largely explained by the rapid growth of the height of the forward-scattering peak in the elements $a_1(\Theta)$ and $a_3(\Theta)$ with increasing size parameter (see Fig. 15.9 and Eqs. (H.41)–(H.43)). The $|\beta_i^s|$ remain significantly smaller than the $|\alpha_i^s|$ and exhibit more pronounced oscillations. The former trait is obviously explained by the fact that the elements $b_1(\Theta)$ and $b_2(\Theta)$ vanish at $\Theta = 0$ instead of having a strong peak typical of the elements $a_1(\Theta)$ and $a_3(\Theta)$.

Problems

15.1: Derive Eqs. (15.20) and (15.21).

15.2: Verify Eq. (15.33).

15.3: Verify Eq. (15.41).

15.4: What is the general structure of the extinction matrix for a statistically isotropic but not mirror-symmetric random particle?

15.5: Verify Eq. (15.46).

15.6: Derive the following relationship between the linear and circular backscattering depolarization ratios for an ISRP:

$$\delta_{\mathrm{C}} = \frac{2\delta_{\mathrm{L}}}{1 - \delta_{\mathrm{L}}} \tag{15.112}$$

(Mishchenko and Hovenier 1995). Prove that

$$0 \le \delta_{\mathrm{L}} \le 1, \quad \delta_{\mathrm{C}} \ge 0, \quad \text{and} \quad \delta_{\mathrm{C}} \ge \delta_{\mathrm{L}}. \tag{15.113}$$

15.7: Consider the case of an incident quasi-monochromatic beam of light polarized linearly in the scattering plane. The scattered intensity component polarized in the scattering plane is called the co-polarized intensity, whereas that polarized perpendicularly to the scattering plane is called the cross-polarized intensity. The linear polarization ratio (LPR) $\mu_{\mathrm{L}}(\Theta)$ is defined as the ratio of the cross-polarized and co-polarized scattered intensities as a function of the scattering angle Θ. Derive an explicit formula for $\mu_{\mathrm{L}}(\Theta)$ in terms of the elements of the normalized scattering matrix. Verify that

$$\delta_{\mathrm{L}} = \mu_{\mathrm{L}}(\pi). \tag{15.114}$$

Show that the LPR vanishes identically in the case of a spherically symmetric scatterer.

15.8: Simplify the expansions (15.86)–(15.89) in the cases of the exact forward and exact backward direction.

15.9: The term "Rayleigh scattering" traditionally refers to the case of FFS by an object with a size much smaller than the wavelength. For a nonspherical Rayleigh particle, the normalized scattering matrix obtained by averaging over the uniform orientation distribution (15.5) under the assumption (15.4) is given by

$$\widetilde{\mathbf{F}}_{\mathrm{R}}(\Theta) = \frac{3}{3y+1}\begin{bmatrix} y+\cos^2\Theta & -\sin^2\Theta & 0 & 0 \\ -\sin^2\Theta & 1+\cos^2\Theta & 0 & 0 \\ 0 & 0 & \frac{3}{2}\cos\Theta & 0 \\ 0 & 0 & 0 & \frac{3}{2}\cos\Theta \end{bmatrix} \tag{15.115}$$

(van de Hulst 1957; Bohren and Huffman 1983). Depending on the particle shape, the parameter y can range from 1 to 13, the former value corresponding to a spherically symmetric particle. Verify that the $(1,1)$ element of the Rayleigh scattering matrix is appropriately normalized. Derive the expansion coefficients entering the expansions (15.86)–(15.90) of the elements of the matrix $\widetilde{\mathbf{F}}_{\mathrm{R}}(\Theta)$ in Wigner d-functions.

15.10: Show that in the case of unpolarized incident light, the ratio $-b_1(\Theta)/a_1(\Theta)$ for an ISRP gives the signed degree of linear polarization P_Q of the scattered light.

15.11: Plot and discuss the phase function $a_1(\Theta)$, the signed degree of linear polarization for unpolarized incident light P_Q, and the ratio $a_3(\Theta)/a_1(\Theta)$ for a spherically symmetric Rayleigh particle.

15.12: Derive an explicit formula for the LPR $\mu_{\mathrm{LR}}(\Theta)$ in the Rayleigh limit. Plot this quantity for several values of the parameter y and discuss the evolution of its angular profile in the limit of vanishing particle nonsphericity.

15.13: The assumption $r_{\max} = \infty$ made in plotting Figs. 15.8 and 15.9 may seem to be unrealistic, since particles with infinite radii do not exist and actual scattering computations for such particles are impossible. Discuss the practical meaning of this assumption. Derive the normalization constant entering Eq. (15.108) by assuming that $r_{\min} = 0$ and $r_{\max} = \infty$; express r_{eff} and v_{eff} in terms of a and b.

15.14: In the old literature, the reader can encounter an artificial so-called Henyey–Greenstein phase function used as a simple "analytical" proxy to the $(1,1)$ element of the normalized scattering matrix of real spherical and nonspherical particles. This phase function is given by

$$a_{1,\mathrm{HG}}(\Theta) = \frac{1 - g^2}{(1 + g^2 - 2g\cos\Theta)^{3/2}} \tag{15.116}$$

and is conveniently characterized by only one free model parameter g such that $|g| < 1$. Verify that this phase function is properly normalized and plot it versus the scattering angle for several values of g. Show that $a_{1,\mathrm{HG}}$ has a backscattering peak for negative g, is isotropic for $g = 0$, and is forward-scattering for $g > 0$. Derive the corresponding expansion coefficients entering the expansion (15.86). Express the respective asymmetry parameter g_{HG} in terms of g.

16

Numerical computations and laboratory measurements of electromagnetic scattering

Solving the energy-budget and optical characterization problems formulated in Section 1.4 relies on one's ability to:

- compute the time-averaged Poynting vector and/or
- model theoretically the net signal recorded by a (polarimetric) WCR.

To accomplish either task one usually needs a direct computer solver of the MMEs. This solver may be required, for example, to calculate the spatial distribution of the Poynting vector inside a densely packed particulate medium, or to compute the extinction and phase matrices needed to analyze the reading of a far-field WCR.

Depending on the complexity and size of the scattering object (cf. Plate 1.1), direct computer solvers of the MMEs can become inefficient and may need to be replaced with a well-characterized and manageable approximate solution. For example, we will see in Chapter 19 that certain observable manifestations of scattering by a large random group of sparsely distributed particles, as well as its electromagnetic energy budget can be quantified by solving the so-called radiative transfer equation. However, two key quantities entering this equation, the single-particle extinction and phase matrices averaged over all particle microphysical states ξ, must still be calculated by using a numerical solver of the MMEs. We have seen that the same is true of the FOSA derived in Chapter 14 for a small group of randomly and sparsely distributed particles observed from a sufficiently large distance.

In some cases even the computation of the matrices $\langle \mathbf{K}(\hat{\mathbf{s}}; \xi) \rangle_\xi$ and $\langle \mathbf{Z}(\hat{\mathbf{q}}, \hat{\mathbf{q}}'; \xi) \rangle_\xi$ can become problematic. Then helpful quantitative information may be obtained by performing controlled laboratory measurements of electromagnetic scattering by well-characterized targets.

Given the vastness of the subject, the goal of this chapter is to provide only a brief summary of existing computer solvers of the MMEs, as well as advanced

laboratory techniques intended for measurements of electromagnetic scattering by individual particles and small groups of particles. We will primarily focus on numerically exact theoretical approaches (according to the definition given in the footnote on page 3) and on controlled laboratory methodologies based on measurements for scattering targets with fully (or almost fully) characterized microphysical characteristics. More detailed and systematic information, as well as numerous further references can be found in MTL1, in the book edited by Mishchenko *et al*. (2000), and in the review by Kahnert (2003).

16.1 Numerically exact theoretical techniques

The majority of existing numerically exact theoretical approaches belong to one of two broad categories. Differential equation methods yield the scattered field via the solution to the MMEs or the vector wave equation in the frequency or in the time domain, whereas integral equation methods are based on the volume or surface integral counterparts of the MMEs.

16.1.1 The Lorenz – Mie theory

The prime example of a differential equation method is the LMT derived for a homogeneous spherical object (van de Hulst 1957; Bohren and Huffman 1983; MTL1). This solution is based on the expansion of the incident, internal, and scattered fields in suitable sets of vector spherical wave functions (VSWFs). The expansion coefficients of the incident plane wave are given by closed-form analytical expressions, whereas those of the internal and scattered fields are determined by satisfying the boundary conditions (Section 2.2) on the sphere surface. Owing to the orthogonality of the VSWFs, each expansion coefficient of either the internal or the scattered field is determined separately. This makes the LMT numerically exact and extremely efficient.

Since detailed accounts of the LMT are available in several books, including MTL1, here we provide only a brief summary of the main results. The LMT amplitude scattering matrix for a homogeneous spherical object with a radius r and a relative refractive index m becomes especially simple when the incident plane electromagnetic wave propagates along the positive direction of the z-axis of the laboratory reference frame and $\varphi^{\mathrm{sca}} = \varphi^{\mathrm{inc}}$:

$$S_{11}(\theta^{\mathrm{sca}}, \varphi^{\mathrm{inc}}; 0, \varphi^{\mathrm{inc}}) = \frac{\mathrm{i}}{k_1} \sum_{n=1}^{\infty} \frac{2n+1}{n(n+1)} [b_n \pi_n(\theta^{\mathrm{sca}}) + a_n \tau_n(\theta^{\mathrm{sca}})], \quad (16.1)$$

$$S_{12}(\theta^{\mathrm{sca}}, \varphi^{\mathrm{inc}}; 0, \varphi^{\mathrm{inc}}) = S_{21}(\theta^{\mathrm{sca}}, \varphi^{\mathrm{inc}}; 0, \varphi^{\mathrm{inc}}) \equiv 0, \quad (16.2)$$

$$S_{22}(\theta^{\mathrm{sca}}, \varphi^{\mathrm{inc}}; 0, \varphi^{\mathrm{inc}}) = \frac{\mathrm{i}}{k_1} \sum_{n=1}^{\infty} \frac{2n+1}{n(n+1)} [b_n \tau_n(\theta^{\mathrm{sca}}) + a_n \pi_n(\theta^{\mathrm{sca}})]. \quad (16.3)$$

The angular functions π_n and τ_n are given by

$$\pi_n(\theta) = \frac{1}{2}n(n+1)[d_{11}^n(\theta) + d_{1,-1}^n(\theta)] = -\frac{1}{\sin\theta}P_n^1(\cos\theta), \tag{16.4}$$

$$\tau_n(\theta) = \frac{1}{2}n(n+1)[d_{11}^n(\theta) - d_{1,-1}^n(\theta)] = -\frac{\mathrm{d}}{\mathrm{d}\theta}P_n^1(\cos\theta), \tag{16.5}$$

while the Lorenz–Mie coefficients a_n and b_n are functions of the relative refractive index and size parameter $x = k_1 r$:

$$a_n = \frac{m\psi_n(mx)\psi_n'(x) - \psi_n(x)\psi_n'(mx)}{m\psi_n(mx)\xi_n'(x) - \xi_n(x)\psi_n'(mx)}, \tag{16.6}$$

$$b_n = \frac{m\psi_n(x)\psi_n'(mx) - \psi_n(mx)\psi_n'(x)}{m\xi_n(x)\psi_n'(mx) - \psi_n(mx)\xi_n'(x)}. \tag{16.7}$$

In Eqs. (16.6) and (16.7),

$$\psi_n(z) = z\,j_n(z), \quad \xi_n(z) = z h_n^{(1)}(z), \tag{16.8}$$

where j_n are spherical Bessel functions of the first kind and $h_n^{(1)}$ are spherical Hankel functions of the first kind.

Owing to Eq. (16.2), it can easily be shown that the normalized Stokes scattering matrix for a spherically symmetric object is given by Eq. (15.64) with

$$a_1(\Theta) \equiv a_2(\Theta) = \frac{2\pi}{C_{\mathrm{sca}}}\left[|S_{11}(\Theta, 0; 0, 0)|^2 + |S_{22}(\Theta, 0; 0, 0)|^2\right], \tag{16.9}$$

$$a_3(\Theta) \equiv a_4(\Theta) = \frac{4\pi}{C_{\mathrm{sca}}}\mathrm{Re}[S_{11}(\Theta, 0; 0, 0)S_{22}^*(\Theta, 0; 0, 0)], \tag{16.10}$$

$$b_1(\Theta) = \frac{2\pi}{C_{\mathrm{sca}}}\left[|S_{11}(\Theta, 0; 0, 0)|^2 - |S_{22}(\Theta, 0; 0, 0)|^2\right], \tag{16.11}$$

$$b_2(\Theta) = \frac{4\pi}{C_{\mathrm{sca}}}\mathrm{Im}[S_{11}(\Theta, 0; 0, 0)S_{22}^*(\Theta, 0; 0, 0)]. \tag{16.12}$$

The extinction and scattering cross sections are given by

$$C_{\mathrm{ext}} = \frac{2\pi}{k_1^2}\mathrm{Re}\sum_{n=1}^{\infty}(2n+1)(b_n + a_n), \tag{16.13}$$

$$C_{\mathrm{sca}} = \frac{2\pi}{k_1^2}\sum_{n=1}^{\infty}(2n+1)\left(|b_n|^2 + |a_n|^2\right). \tag{16.14}$$

All special functions entering the LMT can efficiently be computed using appropriate recurrence relations.

Several software implementations of the LMT are available on the World Wide Web. Section 5.10 of MTL1 is a user guide to the LMT program posted at http://www.giss.nasa.gov/staff/mmishchenko (assessed November 2013).

By implementing a recursive procedure, one can generalize the Lorenz–Mie solution and treat concentric multi-layer spheres. This procedure is summarized in the monograph by Babenko *et al*. (2003), which also describes the extension of the LMT to radially inhomogeneous and anisotropic spherical particles and provides further references.

16.1.2 Separation of variables method

The separation of variables method (SVM) for spheroids parallels the LMT in that is provides the solution of the electromagnetic scattering problem in the spheroidal coordinate system by means of expanding the incident, internal, and scattered fields in vector spheroidal wave functions (Oguchi 1973; Asano and Yamamoto 1975). The expansion coefficients of the incident field are computed analytically, whereas the unknown expansion coefficients of the internal and scattered fields are determined by applying the boundary conditions. Because the vector spheroidal wave functions are not orthogonal on the spheroid surface, this procedure yields an infinite set of linear algebraic equations for the unknown coefficients that must be truncated and solved numerically. The obvious limitation of the SVM is that it applies only to spheroidal scatterers, whereas its main advantages are the ability to yield very accurate results and the applicability to spheroids with extreme aspect ratios. This technique was significantly improved by Voshchinnikov and Farafonov (1993) and extended to core–mantle spheroids by Onaka (1980), Cooray and Ciric (1992), and Farafonov *et al*. (1996). Further references can be found in the review by Ciric and Cooray (2000) and the monograph by Li *et al*. (2002).

16.1.3 Multi-sphere and superposition *T*-matrix methods

The LMT can also be extended to a cluster of N spheres by using the translation addition theorem for the VSWFs (Fikioris and Waterman 1963; Bruning and Lo 1971a,b). The FEs allow one to express the total field scattered by a multi-sphere cluster as a superposition of N partial fields contributed by the N spheres. The external (incident) electric field and the partial fields generated by the component spheres are expanded in sets of VSWFs with origins at the individual sphere centers. The orthogonality of the VSWFs in the sphere boundary conditions is exploited by applying the translation addition theorem (Cruzan 1962), in which a VSWF centered at one sphere origin is re-expanded about another sphere origin. This procedure results in a cluster matrix equation for the scattered-field expansion coefficients of each sphere. Numerical solution of this equation for the specific incident field yields the partial scattered fields and thereby the total scattered field. This technique is called the multi-sphere method (MSM).

Alternatively, inversion of the cluster matrix equation gives sphere-centered transition matrices (or T matrices) that transform the expansion coefficients of the

incident field into the expansion coefficients of the individual scattered fields. In the far-field region, the individual scattered-field expansions can be transformed into a single expansion centered at a single origin inside the cluster. This procedure yields the T matrix that transforms the incident-field expansion coefficients into the single-origin expansion coefficients of the total scattered field (Mackowski 1994) and can be used in the analytical averaging of far-field observables over cluster orientations (Mackowski and Mishchenko 1996). This technique is known as the superposition T-matrix method (STMM).

Because of the analyticity of their mathematical formulation, the MSM and STMM are capable of producing very accurate numerical results. An efficient software implementation of the STMM was developed by Mackowski and Mishchenko (2011). The MSM has been extended to spheres with one or more eccentrically positioned spherical inclusions (Fuller 1995; Videen *et al*. 1995; Borghese *et al*. 2007) and to clusters of dielectric spheroids in an arbitrary configuration (Ciric and Cooray 2000). Mackowski *et al.* (2011) and Mackowski (2014) have extended the MSM and STMM to the general case of externally aggregated and/or nested spherical components potentially made of optically active materials.

Detailed reviews of the MSM and STMM can be found in Fuller and Mackowski (2000), Borghese *et al*. (2007), Quinten (2011), and Mackowski (2012).

16.1.4 Finite element method

The finite element method (FEM) is a differential equation technique that yields the scattered field by means of solving numerically the vector Helmholtz equations (4.8) and (4.9) subject to the standard boundary conditions. The particle is imbedded in a finite computational domain discretized into many cells, with about 10 to 20 cells per wavelength. The electric field values are specified at the nodes of the cells and are initially unknown. Using the boundary conditions, the differential equations are converted into matrix equations for the unknown node field values. The latter are solved using the standard Gaussian elimination or preconditioned iterative techniques such as the conjugate gradient method. Although scattering in the far zone is an open-space problem, the FEM is always implemented in a finite computational domain in order to limit the number of unknowns. Therefore, artificial absorbing boundary conditions must be imposed at the outer boundary of the computational domain in order to suppress wave reflections back into the domain and permit the numerical analogs of the outward-propagating wave to exit the domain, almost as if the latter were infinite.

The FEM can be applied to arbitrarily shaped and inhomogeneous particles, and is simple in concept and software implementation. However, FEM computations are spread over the entire computational domain rather than confined to the scatterer itself, thereby making the technique slow and limited to size parameters smaller than about 20. The finite spatial discretization and the artificial absorbing

boundary condition limit the accuracy of the method. Further information about the FEM can be found in the monographs by Silvester and Ferrari (1996), Volakis *et al.* (1998), and Jin (2002).

16.1.5 Finite difference time domain method

Unlike the FEM, the finite difference time domain method (FDTDM) yields the solution of the electromagnetic scattering problem in the time domain by directly solving the Maxwell time-dependent curl equations (2.2) and (2.4) (Yee 1966). The space and time derivatives of the electric and magnetic fields are approximated using a finite difference scheme with space and time discretizations selected so that they constrain computational errors and ensure numerical stability of the algorithm. Since the scattering object is imbedded in a finite computational domain, absorbing boundary conditions are employed to model scattering in the open space. Modeling scattering objects with curved boundaries using rectangular grid cells causes a staircasing effect and increases numerical errors, especially for objects with large relative refractive indices. Since FDTDM yields the near field in the time domain, a special near-zone to far-zone transformation must be invoked in order to compute the scattered far field in the frequency domain.

The FDTDM shares the advantages of the FEM, as well as its limitations in terms of accuracy and size parameter range. Additional information on the FDTDM and its applications can be found in the books by Kunz and Luebbers (1993), Taflove and Hagness (2005), and Inan and Marshall (2011), as well as in the review by Yang and Liou (2000). A promising variant of the FDTDM, called the pseudo-spectral time domain method, is described in Panetta *et al.* (2013) and references therein.

16.1.6 Point-matching method

The point-matching method (PMM) is a differential equation technique based on expanding the incident and internal fields in VSWFs regular at the origin of the object-centered coordinate system and expanding the scattered field outside the object in outgoing VSWFs. The expansion coefficients of the incident field are computed analytically, whereas the coefficients of the internal and scattered fields are found by truncating the expansions to a finite size and matching the fields at the surface of the object via the application of the boundary conditions. In the simple PMM, the fields are matched at as many points on the surface as there exist unknown expansion coefficients (Oguchi 1973). The simple PMM often produces poorly converging and unstable results, which some attribute to the fact that it explicitly relies on the so-called Rayleigh hypothesis. The latter states that the scattered field can be expanded in the outgoing VSWFs even in the volume bounded by the surface of the object and the smallest circumscribing sphere (Kahnert 2003; Rother and Kahnert 2014).

The convergence problem of the simple PMM appears to be partly ameliorated in the generalized PMM (GPMM) by creating an overdetermined system of equations for the unknown coefficients by means of matching the fields in the least squares sense at a number of surface points significantly greater than the number of unknowns (Morrison and Cross 1974). The performance of the GPMM is further improved by employing multiple spherical expansions to describe the fields both inside and outside the scattering object. This multiple-expansion GPMM (ME-GPMM) does not rely on the Rayleigh hypothesis and is otherwise known as the generalized multipole technique, discrete sources method, and Yasuura method (Wriedt 1999; Doicu *et al*. 2000).

16.1.7 Volume integral equation methods

As we have seen in Section 4.3, the interaction of the electromagnetic field with an object of volume V_{INT} is fully described by the VIE (4.23). The calculation of the total and scattered fields using Eqs. (4.22) and (4.23) would be straightforward except that the internal electric field is unknown. Therefore, this equation must first be solved for the internal field. The integral in Eq. (4.23) is approximated by discretizing the interior region into N cubic cells of a volume ΔV, with about 10 to 20 cells per wavelength and assuming that the electric field and the refractive index within each cell are constant:

$$\mathbf{E}(\mathbf{r}_i) = \mathbf{E}^{\mathrm{inc}}(\mathbf{r}_i) + k_1^2 \Delta V \sum_{j=1}^{N} [m^2(\mathbf{r}_j) - 1] \overleftrightarrow{G}(\mathbf{r}_i, \mathbf{r}_j) \cdot \mathbf{E}(\mathbf{r}_j), \quad i = 1, \ldots, N, \tag{16.15}$$

where $\mathbf{r}_i \in V_{\mathrm{INT}}$ is the central point of the ith cell. Equations (16.15) form a system of N linear algebraic equations for the N unknown internal fields $\mathbf{E}(\mathbf{r}_i)$ and are solved numerically. Once all internal fields $\mathbf{E}(\mathbf{r}_i)$ are found, the scattered field is determined from

$$\mathbf{E}^{\mathrm{sca}}(\mathbf{r}) = k_1^2 \Delta V \sum_{j=1}^{N} [m^2(\mathbf{r}_j) - 1] \overleftrightarrow{G}(\mathbf{r}, \mathbf{r}_j) \cdot \mathbf{E}(\mathbf{r}_j), \quad \mathbf{r} \in V_{\mathrm{EXT}}. \tag{16.16}$$

This version of the volume integral equation method (VIEM) is known as the method of moments (MOM). Since the free space dyadic Green's function becomes singular as $|\mathbf{r} - \mathbf{r}'| \to 0$, special techniques must be used to handle the self-interaction term ($j = i$) in the sum on the right-hand side of Eq. (16.15). The straightforward approach to solving the MOM matrix equation using the standard Gaussian elimination is not practical for size parameters exceeding unity. The conjugate gradient method, together with the fast Fourier transform (Peterson *et al*. 1998), can be applied to significantly larger size parameters and substantially reduces computer memory requirements. The standard drawback of using a preconditioned iterative technique is that computations must be fully repeated for each new incidence direction.

Another version of the VIEM is the so-called discrete dipole approximation (DDA). Whereas the MOM deals with the *actual* electric fields in the central points of the cells, the DDA exploits the concept of *exciting* fields and is based on partitioning the particle into a number N of elementary polarizable units called dipoles. The electromagnetic response of the dipoles to the local electric field is assumed to be known. The field exciting a dipole is a superposition of the external field and the fields scattered by all the other dipoles. This allows one to write a system of N linear equations for N fields exciting the N dipoles. The numerical solution of the DDA matrix equation is then used to compute the N partial fields scattered by the dipoles and thus the total scattered field. Although the original derivation of the DDA by Purcell and Pennypacker (1973) was heuristic, Lakhtakia and Mulholland (1993) showed that the DDA can be derived from Eq. (4.23) and is closely related to the MOM.

The major advantages of the MOM and the DDA are that they automatically satisfy the radiation condition (4.7) at infinity, are confined to the scatterer itself, thereby resulting in fewer unknowns than the differential equation methods, and can be applied to inhomogeneous, anisotropic, and optically active scatterers. However, the numerical accuracy of the methods is relatively low and improves slowly with increasing N, whereas the computer time grows rapidly with increasing particle size relative to the wavelength. Another disadvantage of these techniques is the need to repeat the entire calculation for each new direction of incidence. Further information on the MOM and DDA, as well as on their software implementations and applications, can be found in Miller *et al*. (1991), Draine and Flatau (1994, 2012), and Yurkin and Hoekstra (2007, 2011).

Equation (4.23) is a Fredholm-type integral equation with a singular kernel at $\mathbf{r}' = \mathbf{r}$. Holt *et al*. (1978) removed the singularity by applying the Fourier transform to the internal field and converting the volume integral into an integral in the wave number coordinate space. Discretization of the latter integral results in a matrix equation that is solved numerically and gives the scattered field. A limitation of this Fredholm integral equation method (FIEM) is that the matrix elements must be evaluated analytically, thereby requiring different programs for each shape and restricting computations to only a few models, such as spheroids, triaxial ellipsoids, and finite circular cylinders. The majority of reported FIEM computations pertain to size parameters smaller than five and tend to be rather time consuming (Holt 1982).

16.1.8 *T*-matrix method

The T-matrix method (TMM) was proposed by Waterman (1971) and in some sense is a direct generalization of the LMT. Consider the scattering of a plane electromagnetic wave

$$\mathbf{E}^{\text{inc}}(\mathbf{r}) = \mathbf{E}_0^{\text{inc}} \exp(\mathrm{i}k_1 \hat{\mathbf{n}}^{\text{inc}} \cdot \mathbf{r}), \quad \mathbf{E}_0^{\text{inc}} \cdot \hat{\mathbf{n}}^{\text{inc}} = 0 \tag{16.17}$$

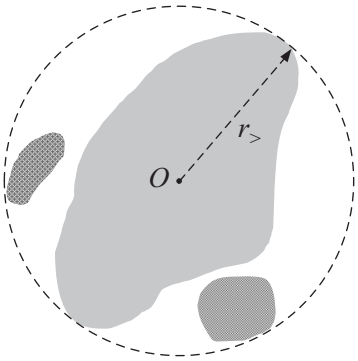

Fig. 16.1. Cross section of an arbitrarily shaped, finite scattering object. $r_>$ is the radius of the smallest circumscribing sphere centered at the origin O of the laboratory coordinate system.

by an arbitrary finite scattering object in the form of a single particle or a fixed aggregate. The incident and scattered fields are expanded in VSWFs as follows:

$$\mathbf{E}^{\text{inc}}(\mathbf{r}) = \sum_{n=1}^{\infty} \sum_{m=-n}^{n} [a_{mn} \operatorname{Rg} \mathbf{M}_{mn}(k_1 \mathbf{r}) + b_{mn} \operatorname{Rg} \mathbf{N}_{mn}(k_1 \mathbf{r})], \tag{16.18}$$

$$\mathbf{E}^{\text{sca}}(\mathbf{r}) = \sum_{n=1}^{\infty} \sum_{m=-n}^{n} [p_{mn} \mathbf{M}_{mn}(k_1 \mathbf{r}) + q_{mn} \mathbf{N}_{mn}(k_1 \mathbf{r})], \quad r > r_>, \tag{16.19}$$

where $r_>$ is the radius of the smallest circumscribing sphere of the scatterer, as shown in Fig. 16.1. The mathematical properties of the VSWFs appearing in Eqs. (16.18) and (16.19) are well known. The functions $\operatorname{Rg}\mathbf{M}_{mn}$ and $\operatorname{Rg}\mathbf{N}_{mn}$ are regular (finite) at the origin, while the use of the outgoing functions $\mathbf{M}_{mn}$ and $\mathbf{N}_{mn}$ in Eq. (16.19) is consistent with the radiation condition (4.7) in that it ensures that the transverse component of the scattered electric field decays as $1/r$, whereas the radial component decays faster than $1/r$, with $r \to \infty$.

The expansion coefficients of the incident plane wave are given by simple analytical expressions. Owing to the linearity of the MMEs and constitutive relations, the relation between the scattered-field expansion coefficients p_{mn} and q_{mn} on the one hand and the incident-field expansion coefficients a_{mn} and b_{mn} on the other hand must be linear and is given by the transition matrix $\mathbf{T}$ as follows:

$$p_{mn} = \sum_{n'=1}^{\infty} \sum_{m'=-n'}^{n'} (T^{11}_{mn\,m'n'}\, a_{m'n'} + T^{12}_{mn\,m'n'}\, b_{m'n'}), \tag{16.20}$$

$$q_{mn} = \sum_{n'=1}^{\infty} \sum_{m'=-n'}^{n'} (T^{21}_{mn\,m'n'}\, a_{m'n'} + T^{22}_{mn\,m'n'}\, b_{m'n'}). \tag{16.21}$$

In compact matrix notation,

$$\begin{bmatrix} \mathbf{p} \\ \mathbf{q} \end{bmatrix} = \mathbf{T} \begin{bmatrix} \mathbf{a} \\ \mathbf{b} \end{bmatrix} = \begin{bmatrix} \mathbf{T}^{11} & \mathbf{T}^{12} \\ \mathbf{T}^{21} & \mathbf{T}^{22} \end{bmatrix} \begin{bmatrix} \mathbf{a} \\ \mathbf{b} \end{bmatrix}, \tag{16.22}$$

which means that the column vector of the expansion coefficients of the scattered field is obtained by multiplying the T matrix and the column vector of the expansion coefficients of the incident field.

Equation (16.22) is the cornerstone of the TMM. Indeed, if the T matrix is known then one can find the scattered field everywhere outside the smallest circumscribing sphere of the object, including the far zone. A fundamental feature of the TMM is that the T matrix depends only on the physical and geometrical characteristics of the scattering particle (such as particle size relative to the wavelength, morphology, relative refractive index, and orientation with respect to the laboratory reference frame) and is completely independent of the propagation directions and polarization states of the incident and scattered fields. This means that the T matrix need be computed only once and then can be used in calculations for any directions of incidence and scattering and for any polarization state of the incident field.

The TMM was initially developed by Waterman (1971) for a single homogeneous object and was generalized to a multi-layered scatterer and an arbitrary cluster of nonspherical particles by Peterson and Ström (1973, 1974) and Litvinov and Ziegler (2008). For a spherically symmetric object, all TMM formulas reduce to those of the LMT owing to the fact that the T matrix becomes diagonal according to the identities

$$T^{12}_{mn\,m'n'} \equiv 0, \quad T^{21}_{mn\,m'n'} \equiv 0, \tag{16.23}$$

$$T^{11}_{mn\,m'n'} = -\delta_{mm'}\delta_{nn'}b_n, \tag{16.24}$$

$$T^{22}_{mn\,m'n'} = -\delta_{mm'}\delta_{nn'}a_n, \tag{16.25}$$

where δ_{mn} is the Kronecker delta (F.6). For a cluster composed of spherical components, the TMM reduces to the STMM described in Section 16.1.3.

The decisive advantage of the TMM is the use of special functions, with well known and convenient mathematical properties. As a consequence, the T matrix possesses a number of general analytical properties, the most important of which being the rotation and translation transformation rules.

Let us first consider a fixed laboratory coordinate system L and a coordinate system P affixed to the object. Both coordinate systems have a common origin inside the object. Let the Euler angles α, β, and γ (see Appendix C) transform the coordinate system L into the coordinate system P. Then it can be shown (Tsang *et al.* 1985) that

$$T^{kl}_{mn\,m'n'}(\mathrm{L};\alpha,\beta,\gamma) = \sum_{m_1 m_2} D^{n}_{m m_1}(\alpha,\beta,\gamma)\, T^{kl}_{m_1 n\, m_2 n'}(\mathrm{P})\, D^{n'}_{m_2 m'}(-\gamma,-\beta,-\alpha), \tag{16.26}$$

where $D^{n}_{mm'}(\alpha,\beta,\gamma) = \exp(-\mathrm{i}m\alpha)\, d^{n}_{mm'}(\beta)\exp(-\mathrm{i}m'\beta)$ are Wigner D functions.

Analogously, consider the same scattering problem in two coordinate systems that have identical spatial orientations but different origins. Let the vector $\mathbf{r}_{21}$ connect the origin of coordinate system 1 and that of coordinate system 2. Then the respective T matrices are expressed in terms of one another by the following linear relationship:

$$\begin{bmatrix} \mathbf{T}^{11}(2) & \mathbf{T}^{12}(2) \\ \mathbf{T}^{21}(2) & \mathbf{T}^{22}(2) \end{bmatrix} = \begin{bmatrix} \mathrm{Rg}\,\mathbf{A}(k_1\mathbf{r}_{21}) & \mathrm{Rg}\,\mathbf{B}(k_1\mathbf{r}_{21}) \\ \mathrm{Rg}\,\mathbf{B}(k_1\mathbf{r}_{21}) & \mathrm{Rg}\,\mathbf{A}(k_1\mathbf{r}_{21}) \end{bmatrix} \begin{bmatrix} \mathbf{T}^{11}(1) & \mathbf{T}^{12}(1) \\ \mathbf{T}^{21}(1) & \mathbf{T}^{22}(1) \end{bmatrix}$$
$$\times \begin{bmatrix} \mathrm{Rg}\,\mathbf{A}(-k_1\mathbf{r}_{21}) & \mathrm{Rg}\,\mathbf{B}(-k_1\mathbf{r}_{21}) \\ \mathrm{Rg}\,\mathbf{B}(-k_1\mathbf{r}_{21}) & \mathrm{Rg}\,\mathbf{A}(-k_1\mathbf{r}_{21}) \end{bmatrix} \tag{16.27}$$

(MTL1). The matrices on both sides of the T matrix on the right-hand side of Eq. (16.27) consist of coefficients that afford an efficient numerical computation.

The relation (16.26) allows one to drastically simplify the averaging of far-field observables over orientations of the scattering object (Section 13.9) by doing most of the work analytically (Mishchenko 1991a; Khlebtsov 1992). For example, the extinction cross section averaged over the uniform orientation distribution of a nonspherical particle having a plane of symmetry is given by the following remarkably simple formula (MTL1):

$$\langle C_{\mathrm{ext}}\rangle_{\mathrm{o}} = -\frac{2\pi}{k_1^2}\mathrm{Re}\sum_{nm}[T^{11}_{mn\,mn}(\mathrm{P}) + T^{22}_{mn\,mn}(\mathrm{P})]. \tag{16.28}$$

The corresponding formula for the orientation average of the scattering cross section is hardly more complicated:

$$\langle C_{\mathrm{sca}}\rangle_{\mathrm{o}} = \frac{2\pi}{k_1^2}\sum_{nmn'm'kl}|T^{kl}_{mn\,m'n'}(\mathrm{P})|^2, \tag{16.29}$$

where, again, the orientation distribution function is assumed to be given by Eq. (15.5). Analytical averaging of the phase matrix over orientations is also possible (MTL1, Mackowski and Mishchenko 1996). This approach has been found to be much more efficient than the direct numerical integration over the Euler angles according to Eq. (13.122), and helps reduce the requisite computer time by a factor of 50–200.

The computation of the T matrix for a scattering object in the form of a simple single-body particle is usually based on the so-called extended boundary condition method (EBCM) which was developed by Waterman (1971) and explicitly avoids the use of the Rayleigh hypothesis. The T matrix $\mathbf{T}(\mathrm{P})$ is expressed as $-(\mathrm{Rg}\mathbf{Q})\,\mathbf{Q}^{-1}$, where the elements of the matrices $\mathbf{Q}$ and $\mathrm{Rg}\mathbf{Q}$ are obtained numerically by integrating vector products of VSWFs over the object's surface using an appropriate quadrature formula (see Appendix E).

EBCM imposes no fundamental restrictions on particle shape, although computations become simpler and more efficient for bodies of revolution. Recent

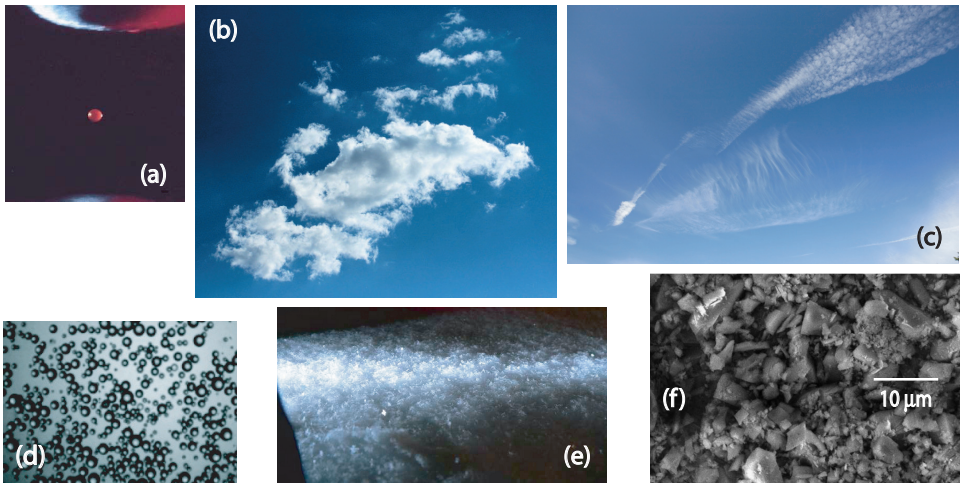

Plate 1.1. **(a)** A 60-µm-radius glycerol droplet levitated in a quadrupole meso-trap and illuminated by a 488-nm-wavelength laser beam (after Arnold *et al.* 1995). **(b)** A liquid-water cloud. **(c)** A jet-engine condensation trail cloud (after E. Wiebe, http://climate.uvic.ca, assessed November 2013). **(d)** A suspension of ~10-µm-radius polymethyl methacrylate spherical particles in a hydrophobic liquid (after Snabre and Pouligny 2008). **(e)** A fresh snow surface (after Peltoniemi *et al.* 2009). **(f)** A powder surface composed of feldspar particles (after Shkuratov *et al.* 2006).

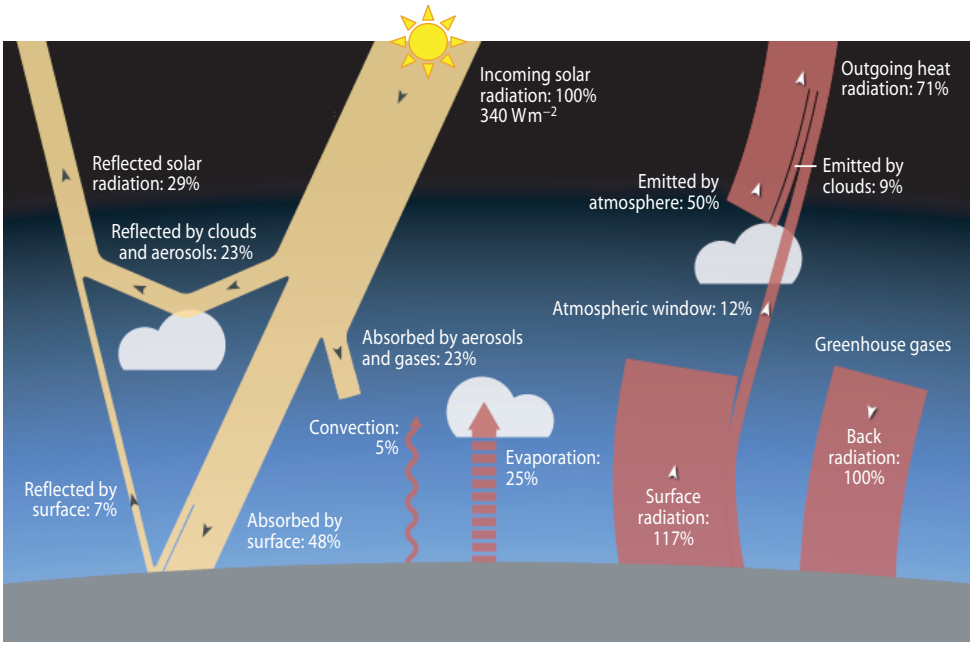

Plate 1.2. Current quantitative understanding of the energy budget of the terrestrial atmosphere–surface system.

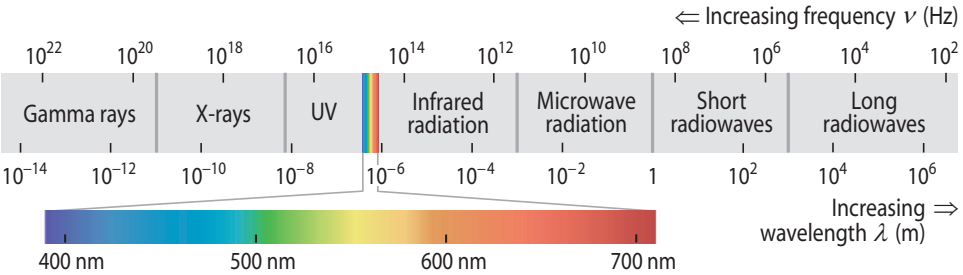

Plate 1.3. Electromagnetic spectrum in the order of increasing frequency $\nu = \omega/2\pi$ or increasing wavelength $\lambda = c/\nu$, where c is the speed of ligh in a vacuum.

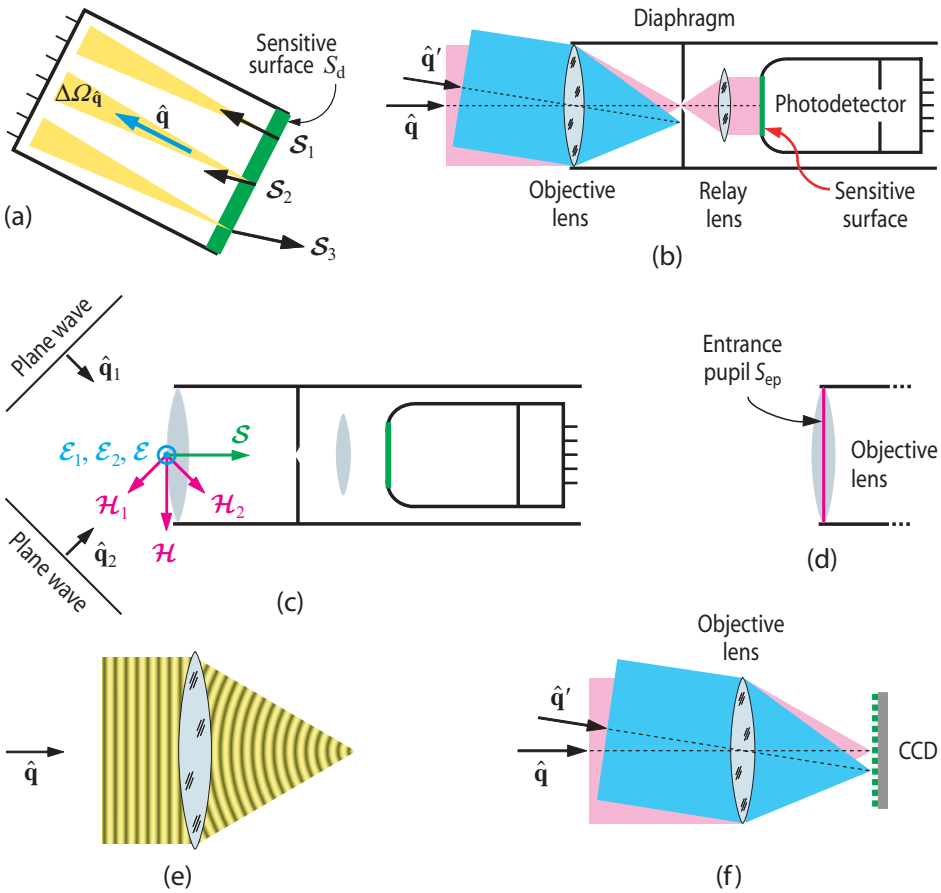

Plate 11.1. **(a)** Hypothetical directional meter of electromagnetic energy flow. **(b)** Basic optical scheme of a well-collimated radiometer. **(c)** The conventional WCR does not respond to the Poynting vector directed along the optical axis of the instrument. **(d)** Entrance pupil. **(e)** A lens focuses an incident plane wave by introducing a phase shift that varies quadratically with radial distance from the optical axis. **(f)** Basic optical scheme of a panoramic (imaging) radiometer.

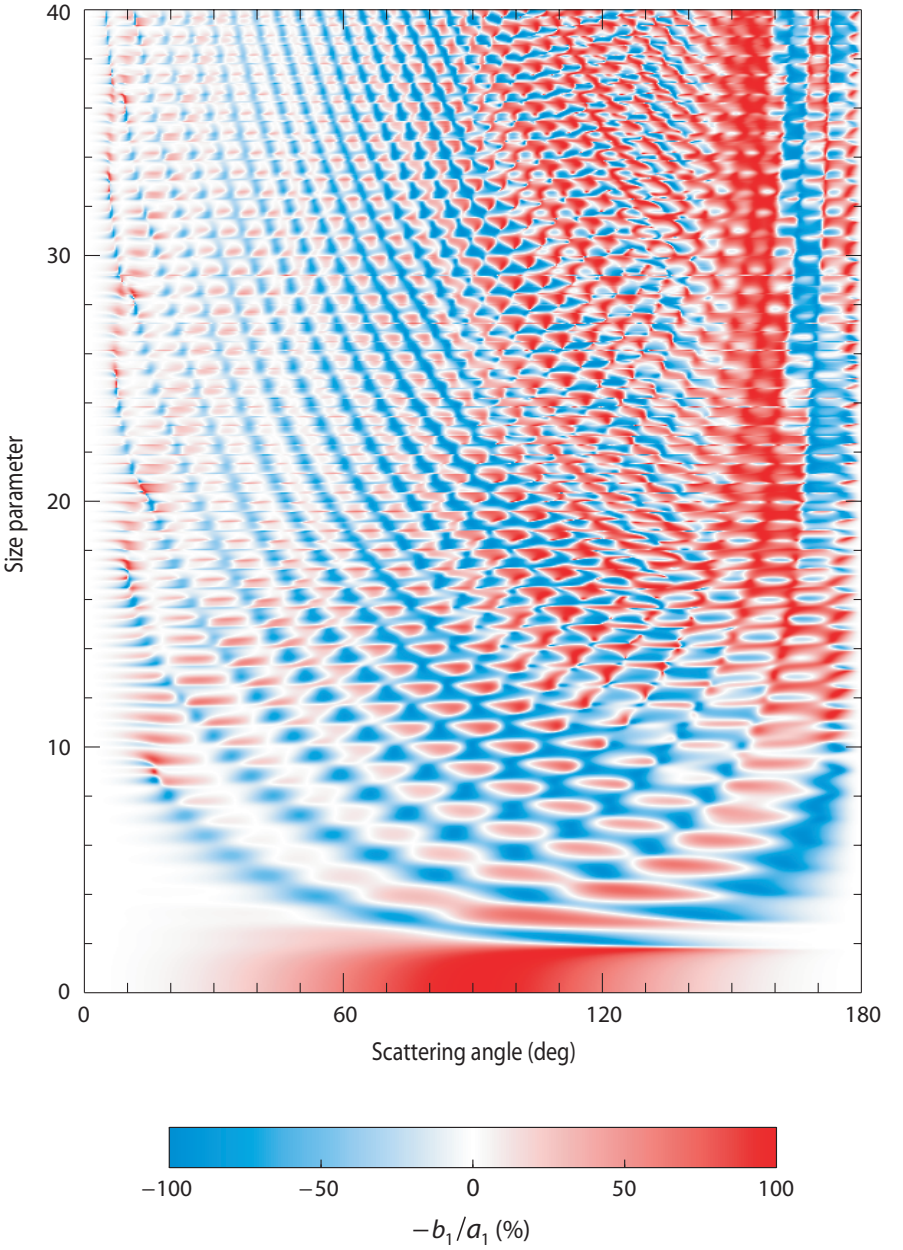

Plate 17.1. Low-resolution color image of the ratio $-b_1/a_1$ for a homogeneous spherical particle with a relative refractive index $m = 1.4$.

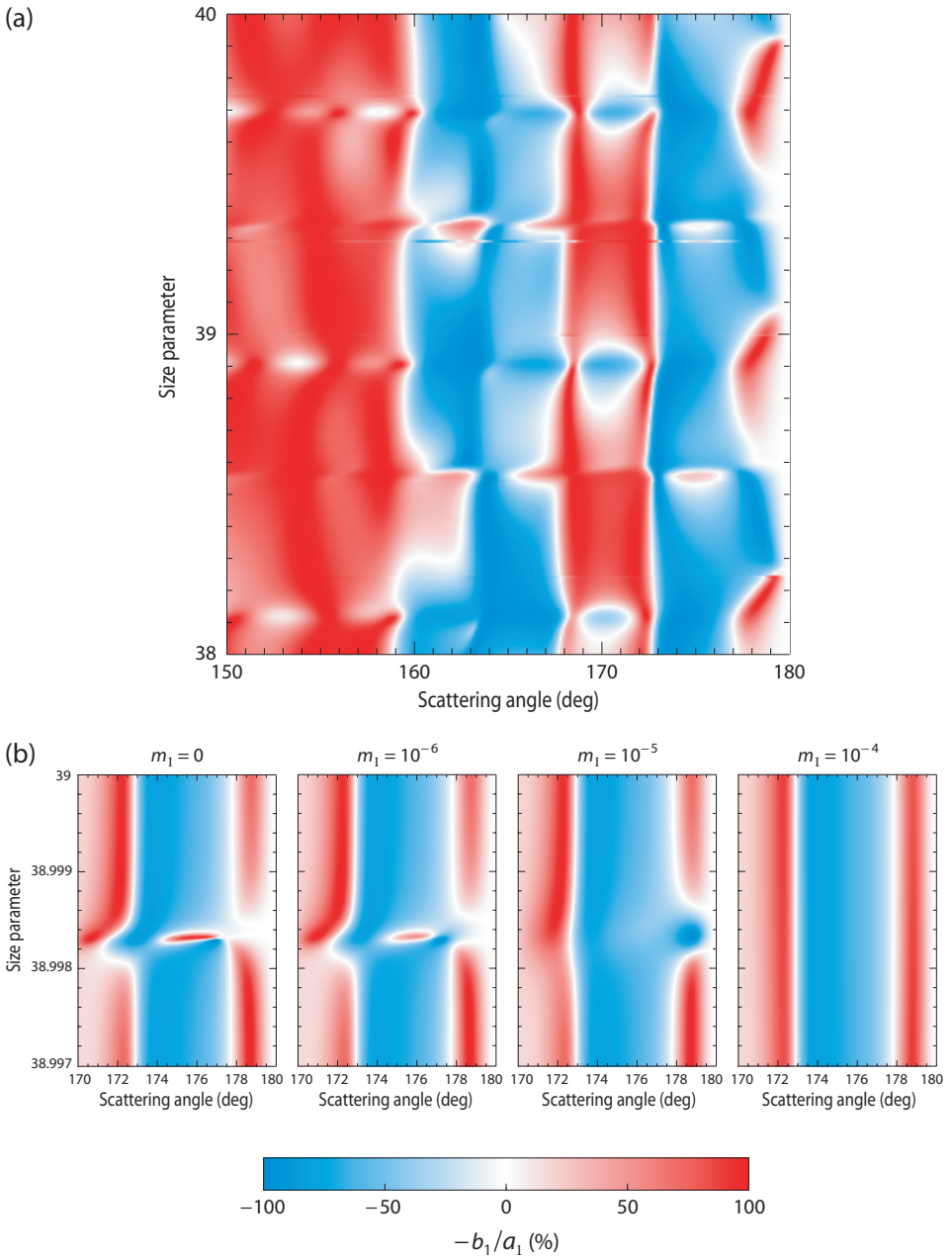

Plate 17.2. **(a)** As in Plate 17.1, but using a finer sampling resolution. **(b)** High-resolution color images of the ratio $-b_1/a_1$ in the neighborhood of the super-narrow resonance centered at $x \approx 38.9983$ for $m_R = 1.4$. The panels from left to right correspond to four increasing values of the imaginary part of the relative refractive index: $m_I = 0$, 10^{-6}, 10^{-5}, and 10^{-4}.

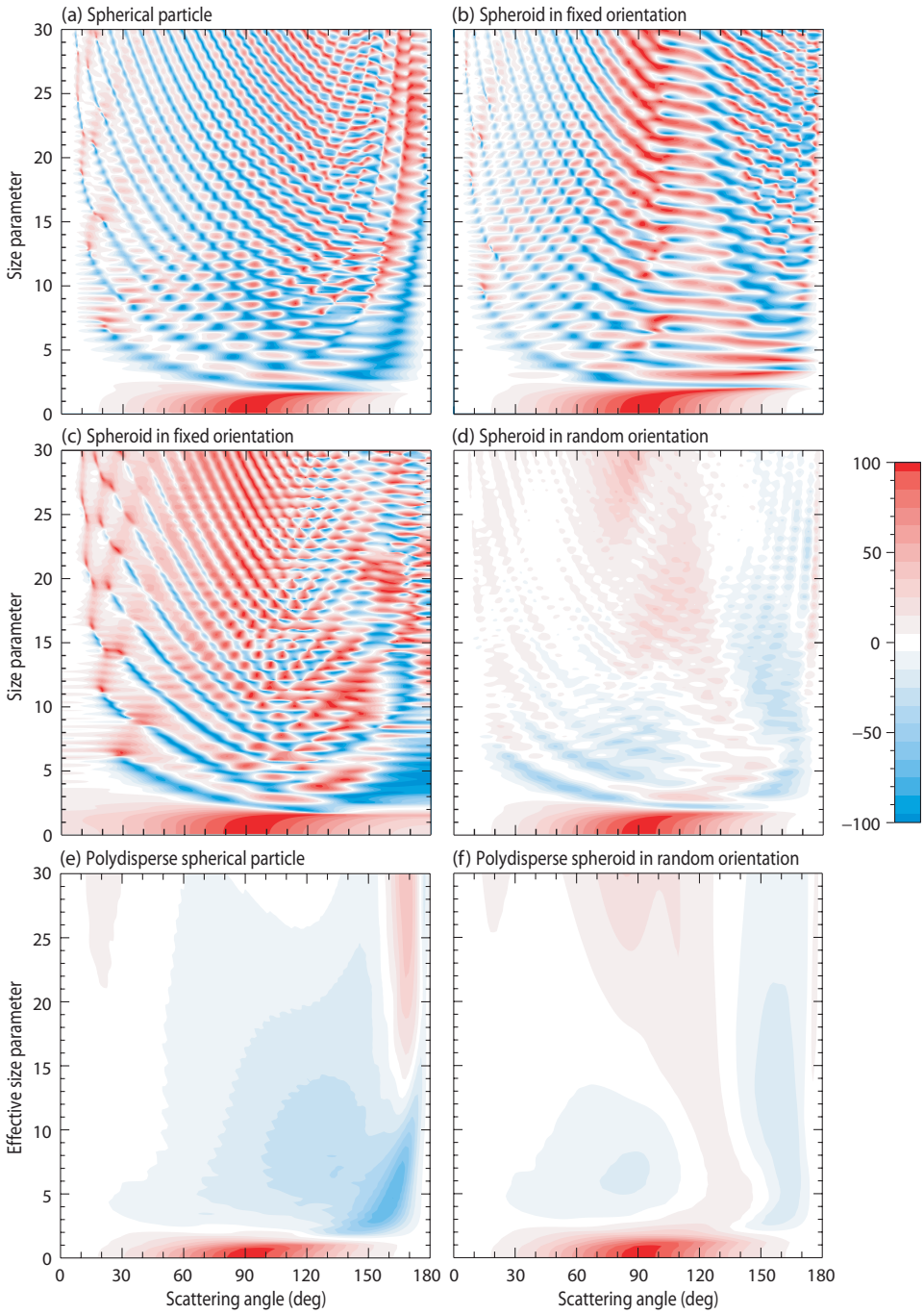

Plate 17.3. The signed degree of linear polarization P_Q of scattered light for unpolarized incident light computed for monodisperse and polydisperse spheres and spheroids in fixed and random orientations (see text).

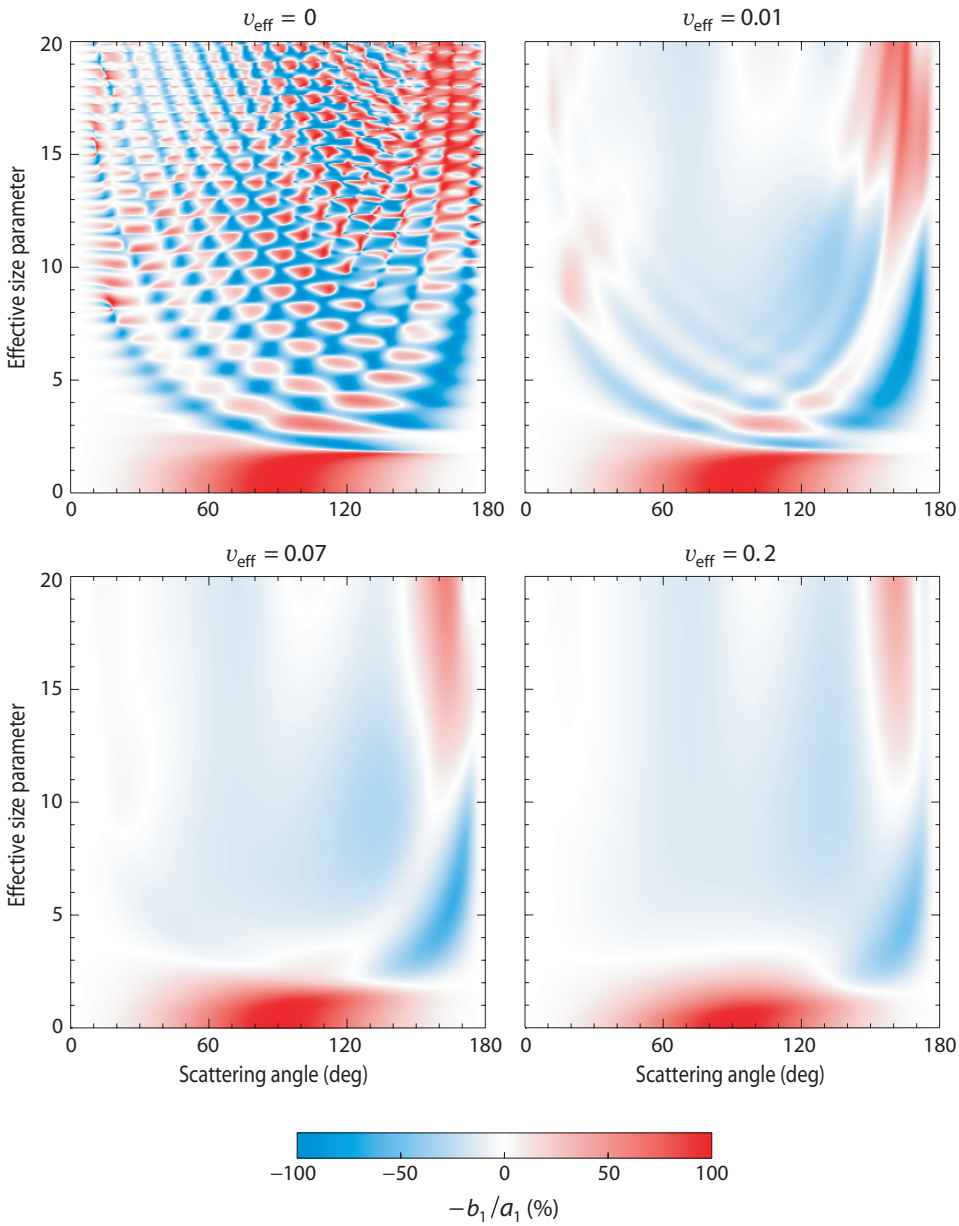

Plate 17.4. Color images of the ratio $-b_1/a_1$ for homogeneous spherical particles with $m = 1.44$ and $v_{eff} = 0$ (the value for a monodisperse sphere), 0.01, 0.7, and 0.02.

Plate 17.5. **(a)** Full-color numerical simulation for 400-μm-radius water drops superimposed on a photograph of the primary and secondary rainbows. **(b)** A beautiful glory photographed from San Francisco's Golden Gate Bridge and caused by swirling fog above cold water. **(c)** Full-color numerical simulation of scattering of sunlight by 4.8-μm-radius water drops superimposed on a photograph of a glory taken from a commercial aircraft. (After Mishchenko and Travis (2008); images courtesy of P. Laven (a,c) and L. Zinkova (b)).

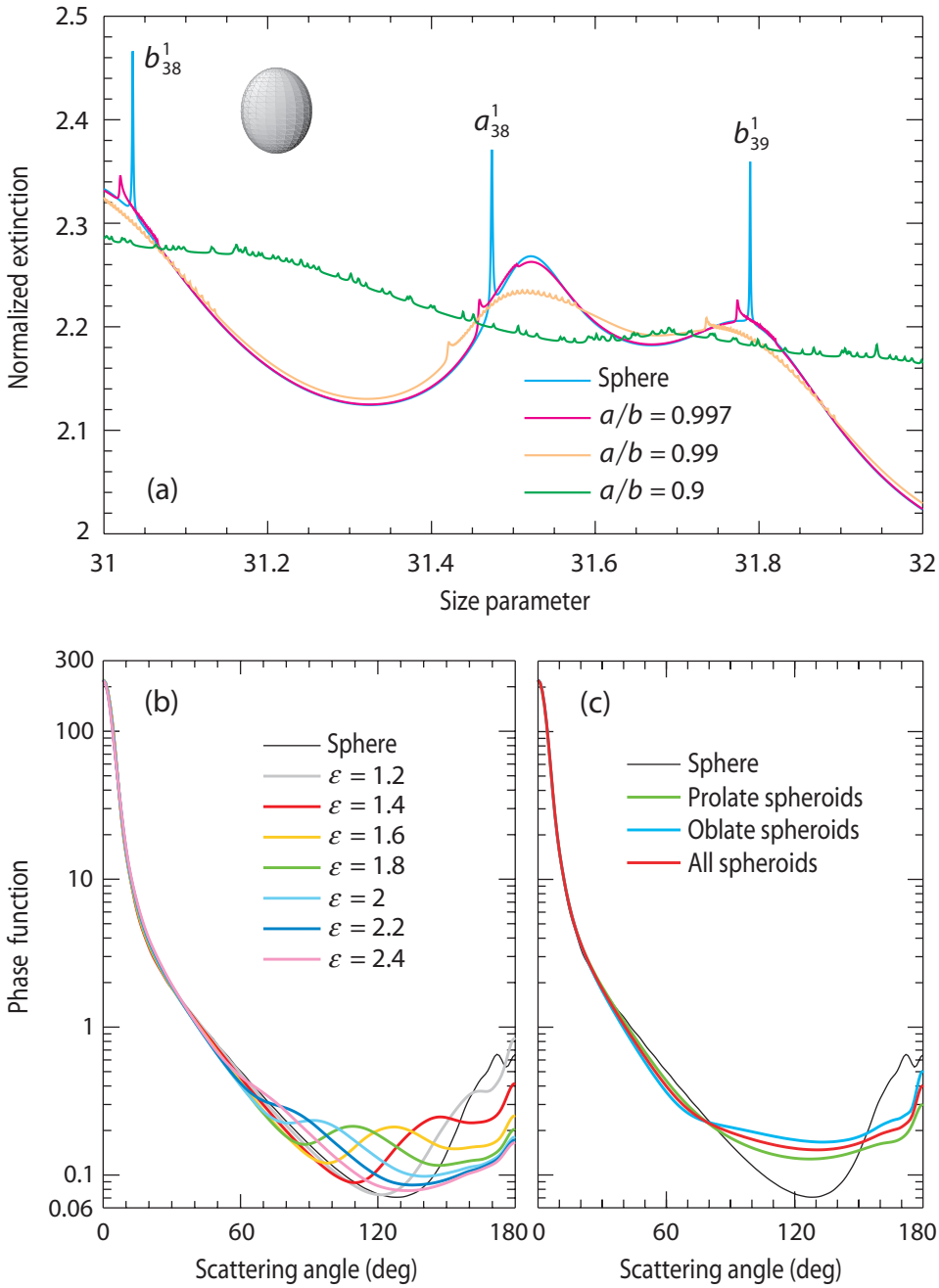

Plate 17.6. (a) Normalized extinction versus volume-equivalent-sphere size parameter for a monodisperse sphere and monodisperse randomly oriented prolate spheroids with different semi-axis ratios a/b and a fixed relative refractive index of 1.4. **(b, c)** Demonstration of the statistical approach (see text).

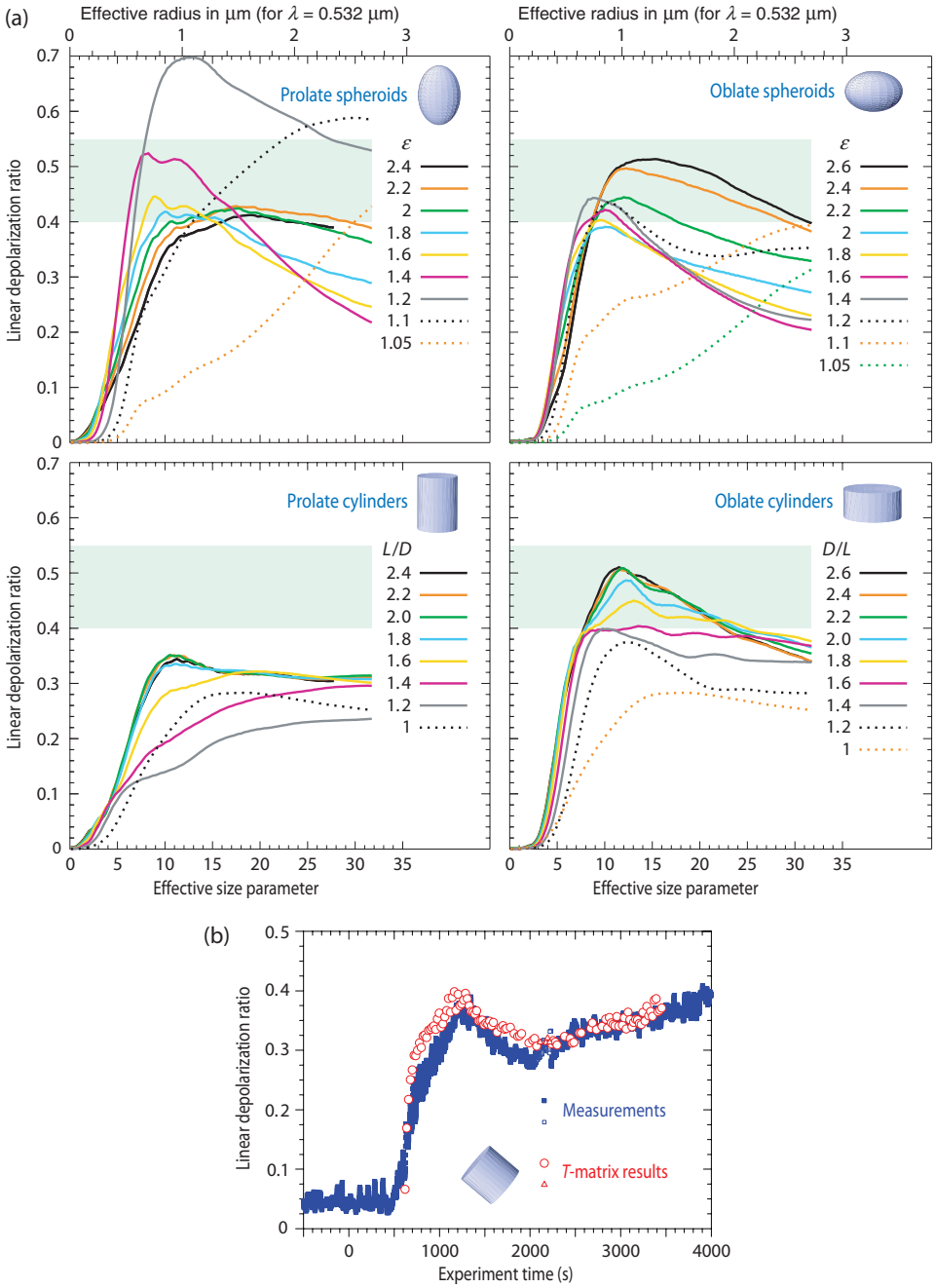

Plate 17.7. **(a)** Linear depolarization ratio versus effective surface-equivalent-sphere size parameter for polydisperse, randomly oriented ice spheroids with aspect ratios ranging from 1.05 to 2.6 and circular cylinders with various length-to-diameter (L/D) or diameter-to-length (D/L) ratios (see text). **(b)** Fit of theoretical computations to the results of laboratory measurements of the backscattering linear depolarization ratio (see text).

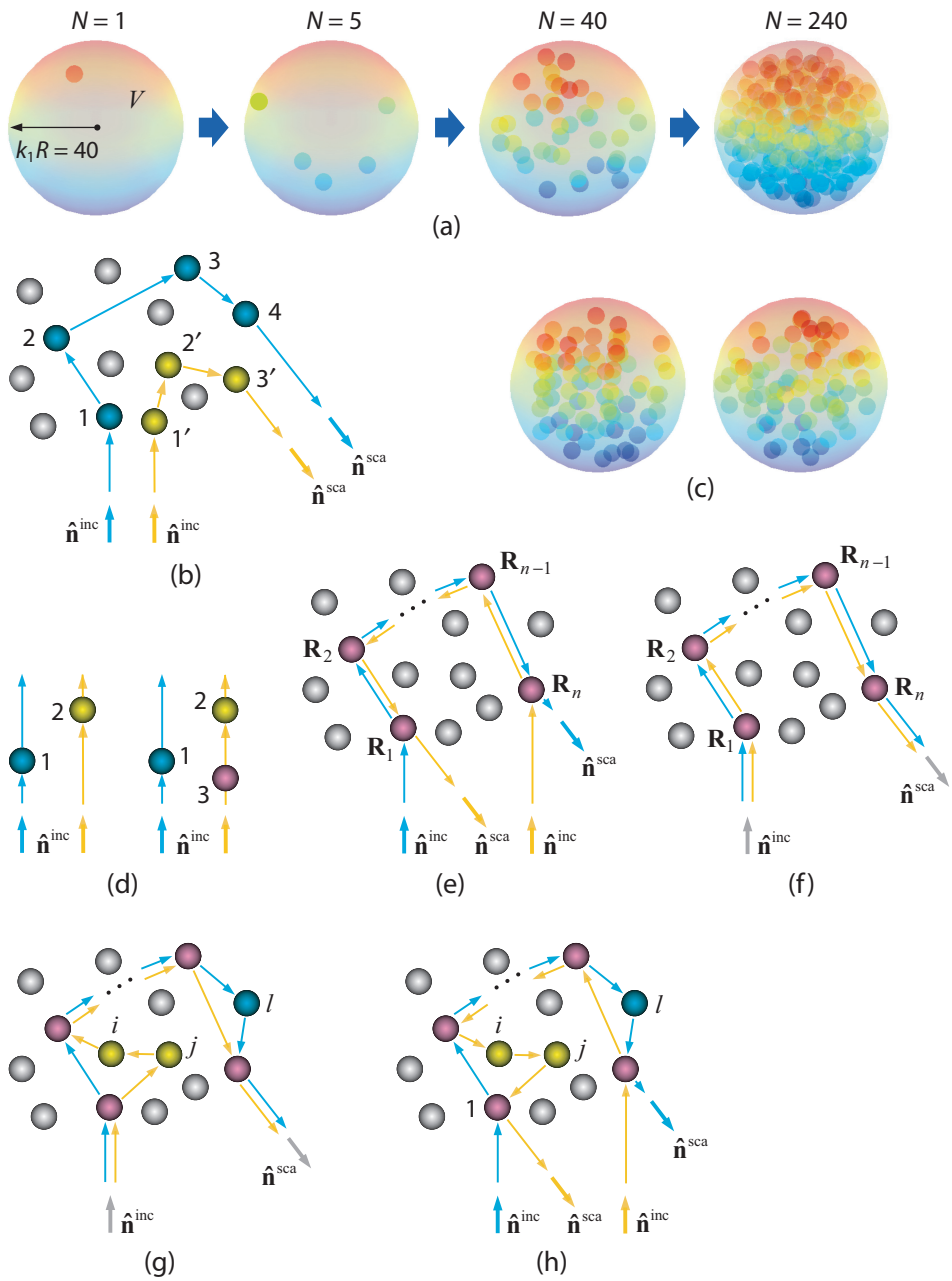

Plate 18.1. **(a)** Imaginary spherical scattering volume V filled with N randomly positioned particles. **(b)** Interference origin of speckle. **(c)** Two random realizations of the $N = 80$ particulate volume. **(d)** Forward-scattering interference. **(e)** Interference origin of weak localization. **(f)** Interference origin of the diffuse background. **(g)** A pair of particle sequences contributing to the time-averaged diffuse background. **(h)** A pair of particle sequences contributing to time-averaged weak localization.

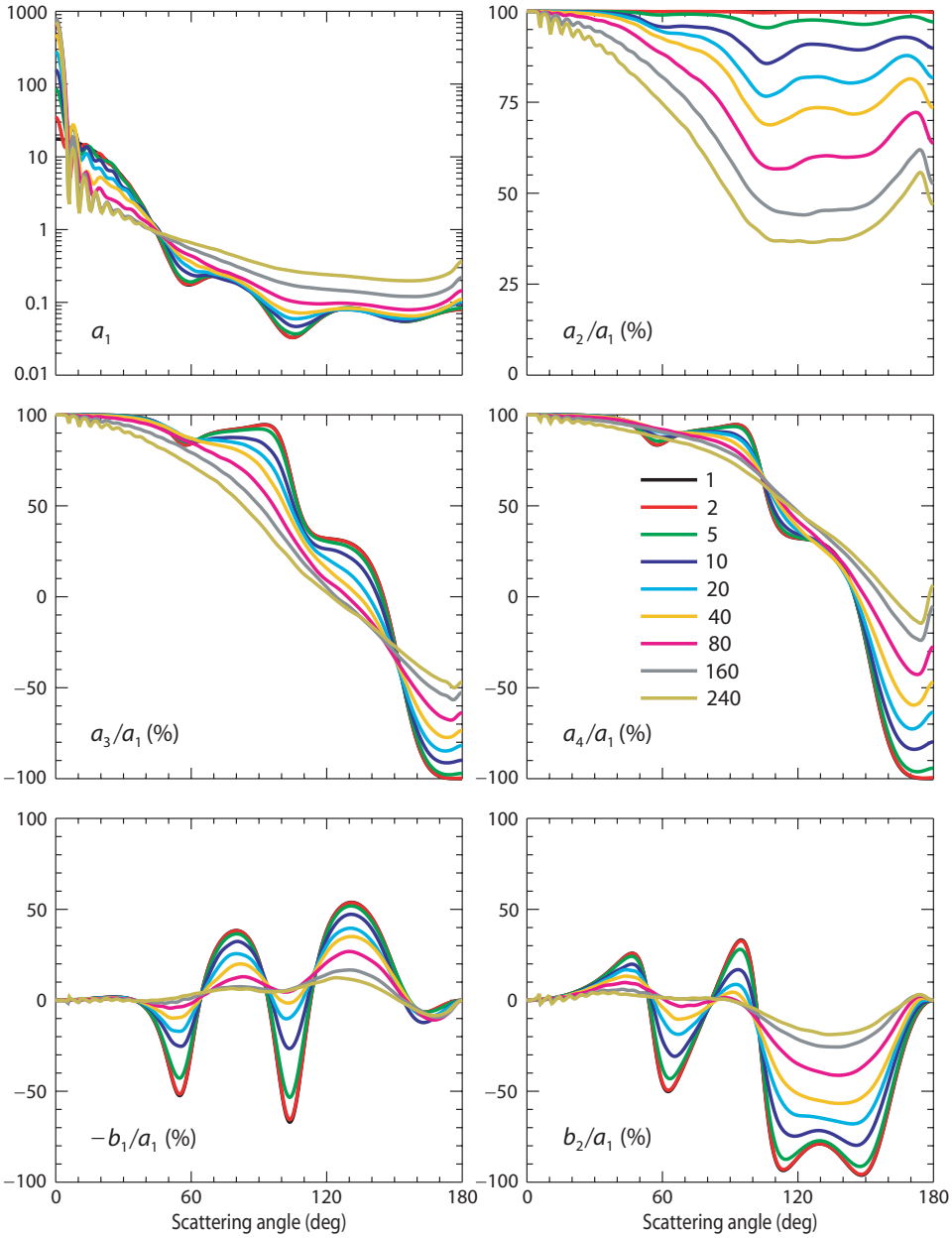

Plate 18.2. Elements of the normalized Stokes scattering matrix computed for a $k_1R = 40$ spherical volume of discrete random medium uniformly populated by $N = 1, \ldots, 240$ particles with $k_1r = 4$ and $m = 1.32$.

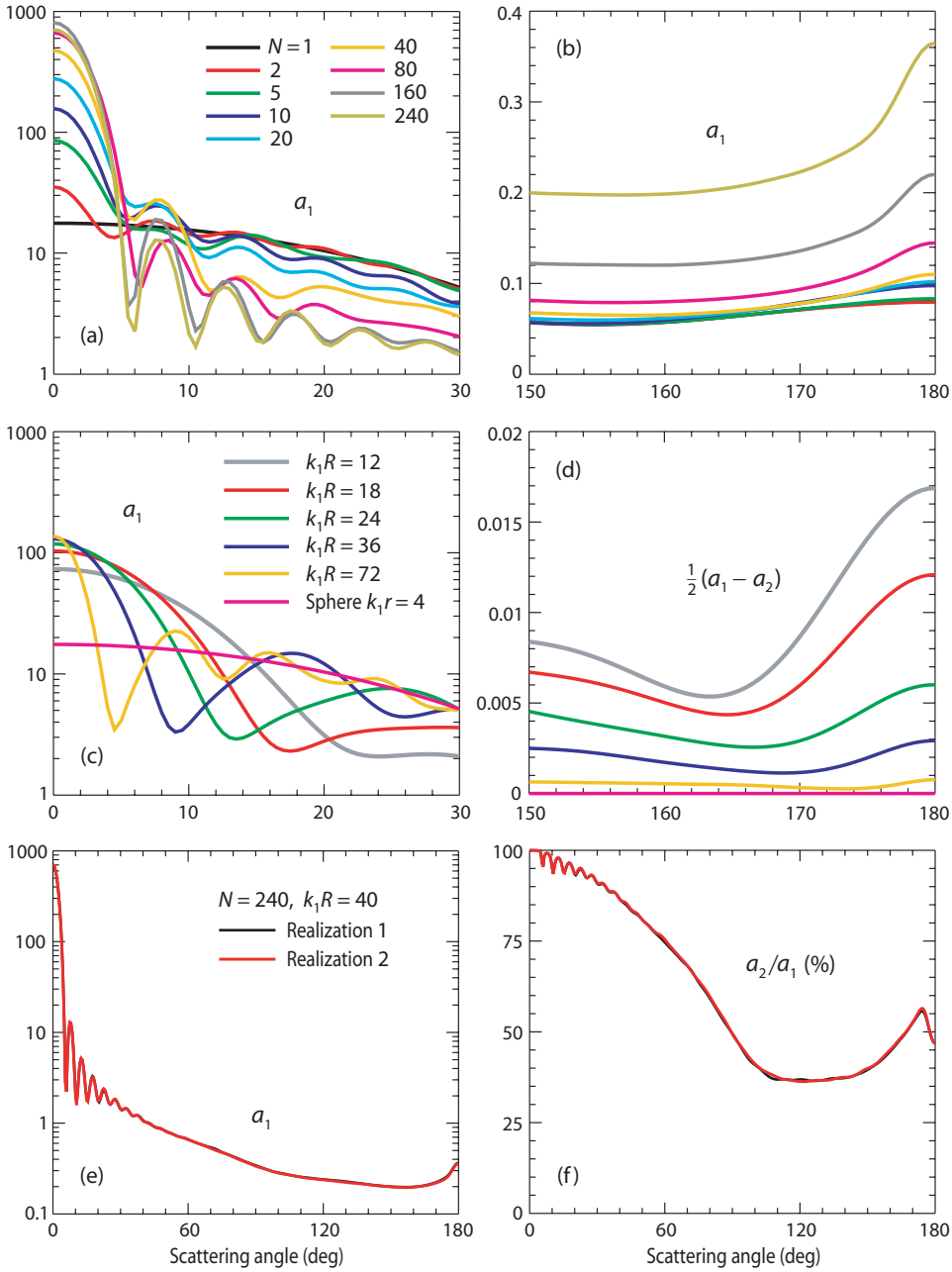

Plate 18.3. Scattering properties of a spherical volume of discrete random medium (see text). **(a, b)** $k_1R = 40$, $k_1r = 4$, and $m = 1.32$. N varies from 1 to 240. **(c, d)** $N = 8$, $k_1r = 4$, and $m = 1.32$. k_1R varies from 12 to 72. **(e, f)** $k_1R = 40$, $N = 240$, $k_1r = 4$, and $m = 1.32$.

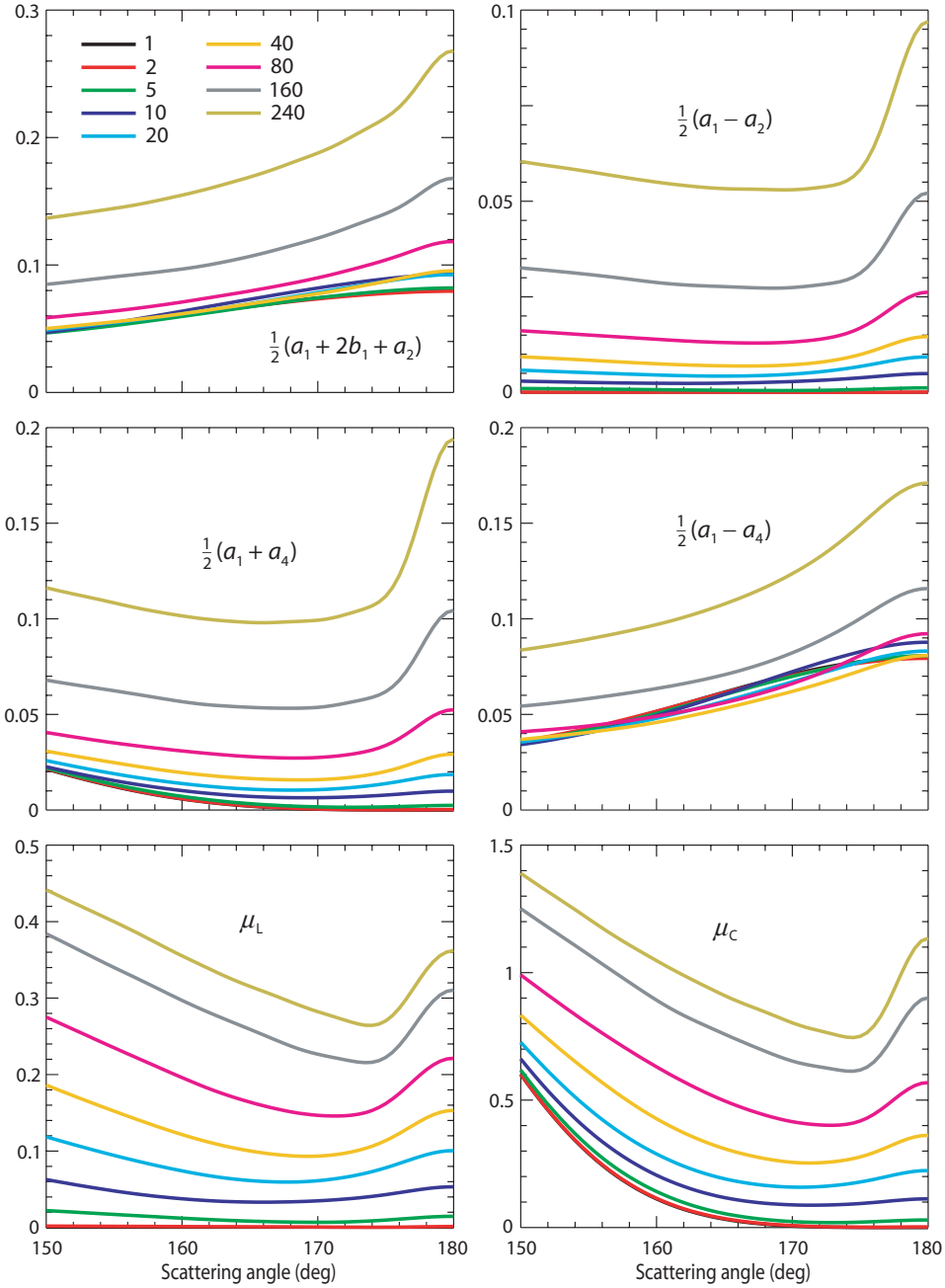

Plate 18.4. Polarization characteristics of backscattered light computed for a $k_1R = 40$ spherical volume of discrete random medium uniformly populated by $N = 1, \ldots, 240$ particles with $k_1r = 4$ and $m = 1.32$.

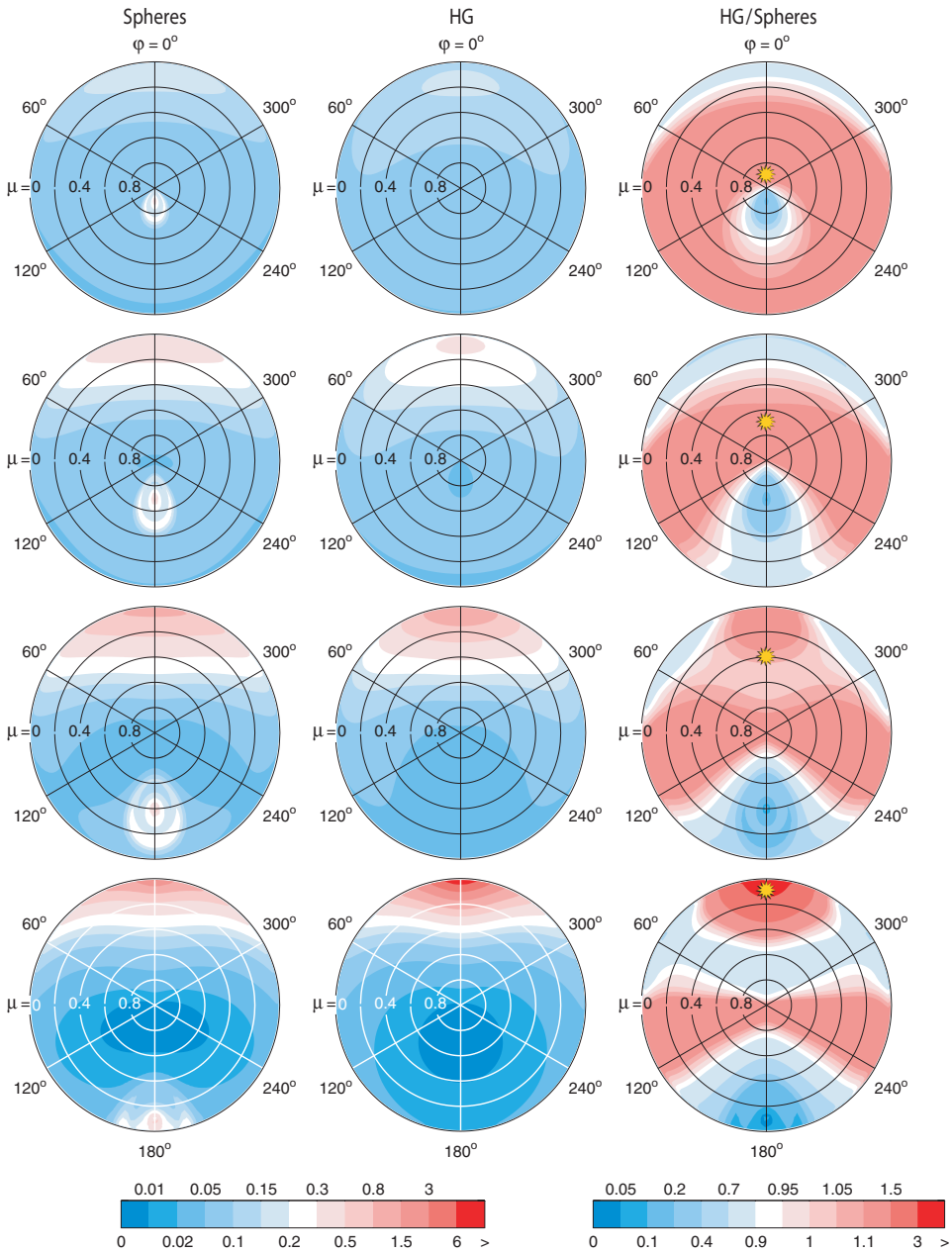

Plate 20.1. Left-hand column: reflected specific intensity (in $\mathrm{W\,m^{-2}\,sr^{-1}}$) versus μ and φ for a semi-infinite slab composed of model 1 spherical particles. The four values of minus the cosine of the illumination zenith angle $\mu_0 = 0.9$, 0.7, 0.4, and 0.1 are indicated by the yellow stars in the right-hand column. The azimuth angle of the unpolarized incident beam is zero and its intensity is $I_0 = \pi\ \mathrm{Wm^{-2}}$. Central column: as in the left-hand column, but for the asymmetry-parameter-equivalent HG phase function. Right-hand column: the ratio of the specific intensities shown in the central and left-hand columns.

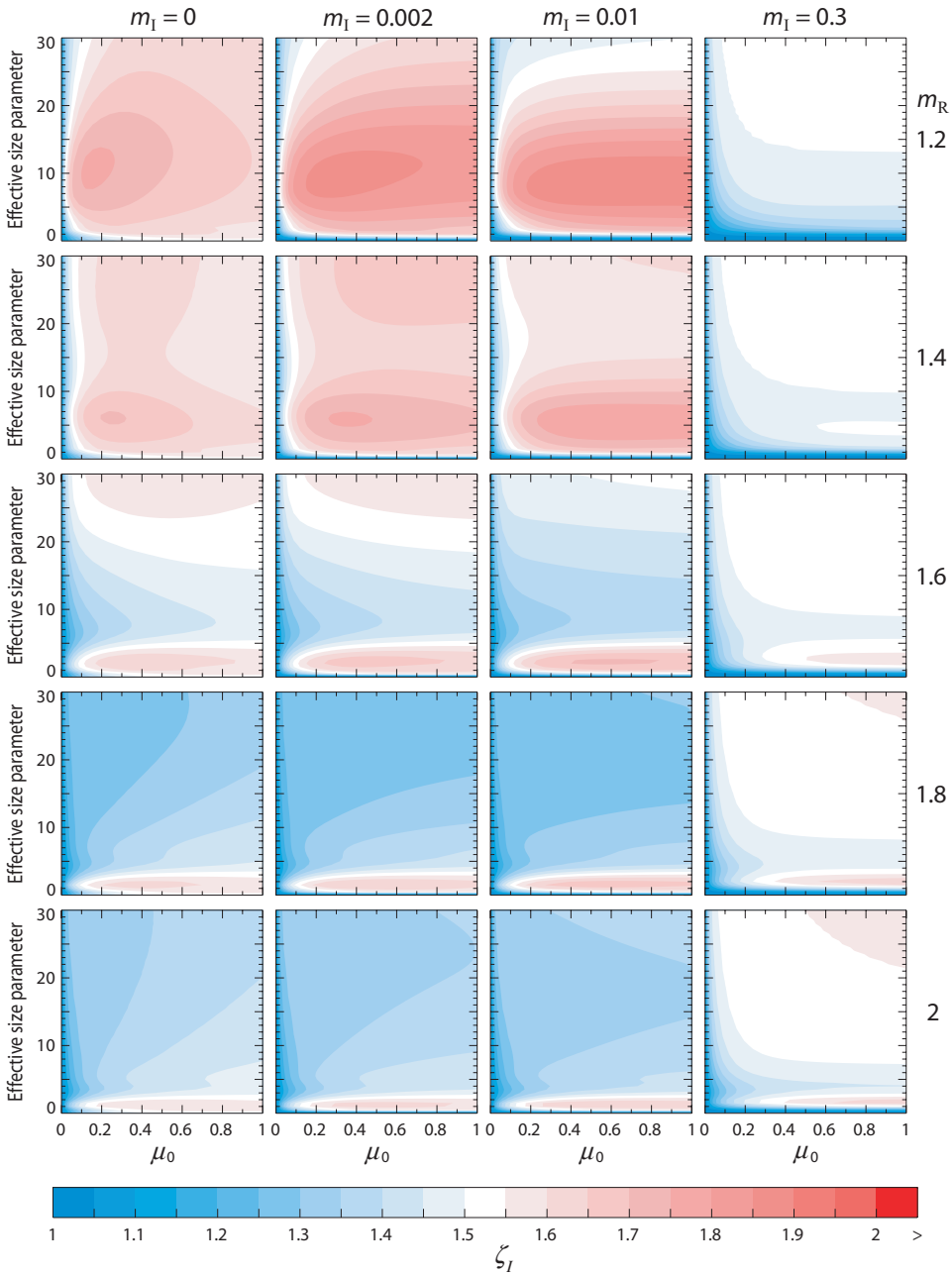

Plate 21.1. Backscattering enhancement factor ζ_I versus μ_0 and effective size parameter x_{eff} for a homogeneous semi-infinite slab populated by polydisperse spherical particles with $m_R = 1.2$, 1.4, 1.6, 1.8, and 2 and $m_I = 0$, 0.002, 0.01, and 0.3.

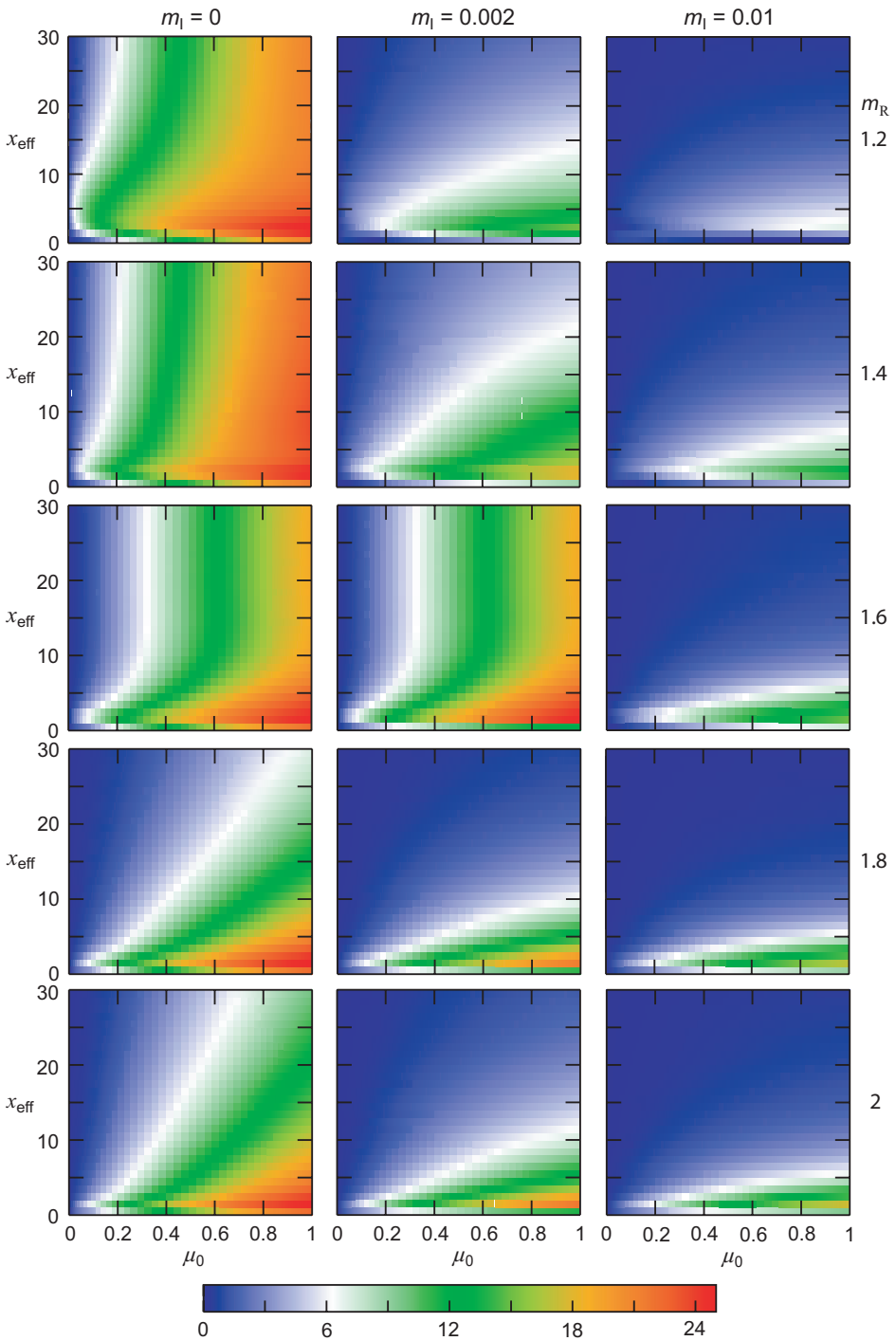

Plate 21.2. As in Plate 21.1, but for the percentage error δ_ζ. The values of δ_ζ for m_I = 0.3 (not shown) do not exceed 6%.

work has demonstrated the applicability of the EBCM to particles without axial symmetry (e.g., Kahnert 2013a,b). The computation of the *T* matrix for a cluster assumes that the *T* matrices of all components are known and is based on the use of the translation addition theorem for the VSWFs (Peterson and Ström 1973).

The numerical computation of the *T* matrix using the EBCM becomes problematic if the vector products of VSWFs vary over the particle surface by orders of magnitude, thereby resulting in loss of numerical accuracy. The numerical inversion of the matrix $\mathbf{Q}$ is an ill-posed problem and can also be unstable. However, as described in MTL1, efficient ways of improving the convergence of EBCM calculations are the following:

- the computation of the elements of the matrix $\mathbf{Q}$ and its inverse using extended-precision FORTRAN variables (real variables of the type `REAL*16` and complex variables of the type `COMPLEX*32`);
- the inversion of the matrix $\mathbf{Q}$ using a special version of the so-called LU factorization procedure.

Despite their simplicity, these recipes have helped increase the range of applications of the EBCM quite dramatically. Furthermore, a simple procedure described in MTL1 allows one to control automatically the convergence of computations upon increasing the size of the *T* matrix in unit steps, which makes EBCM computer calculations even more efficient. Other ways of improving the numerical stability of TMM computations have recently been proposed by Bi *et al.* (2013a), Somerville *et al.* (2013), and Volkov *et al.* (2013).

Figure 16.2 gives examples of particle morphologies that can be treated using various implementations of the TMM (including the STMM). The loss of efficiency for particles with large aspect ratios or with shapes lacking axial symmetry is the main drawback of the EBCM. The main advantages of the TMM are high accuracy and speed coupled with applicability to particles with equivalent-sphere size parameters exceeding 100 (see, e.g., MTL1 and Bi *et al.* (2013a,b)). Further information on the TMM, STMM, and EBCM, as well as on their modifications, generalizations, and applications can be found in the comprehensive *T*-matrix reference database maintained by the author and his colleagues (see Mishchenko *et al.* (2013a) and references therein).

A representative collection of public-domain *T*-matrix computer programs is available at http://www.giss.nasa.gov/staff/mmishchenko (assessed November 2013). These programs can be used in computations for axially symmetric objects and clusters of spherical monomers and have been thoroughly tested against SVM and independent MSM results. Very high numerical accuracy of the *T*-matrix codes has been used to generate benchmark results with five and more accurate decimals that can be used for testing other numerically exact and approximate approaches (MTL1). Extensive timing tests have shown that the numerical efficiency of these codes is unparalleled, especially in computations for randomly oriented particles.

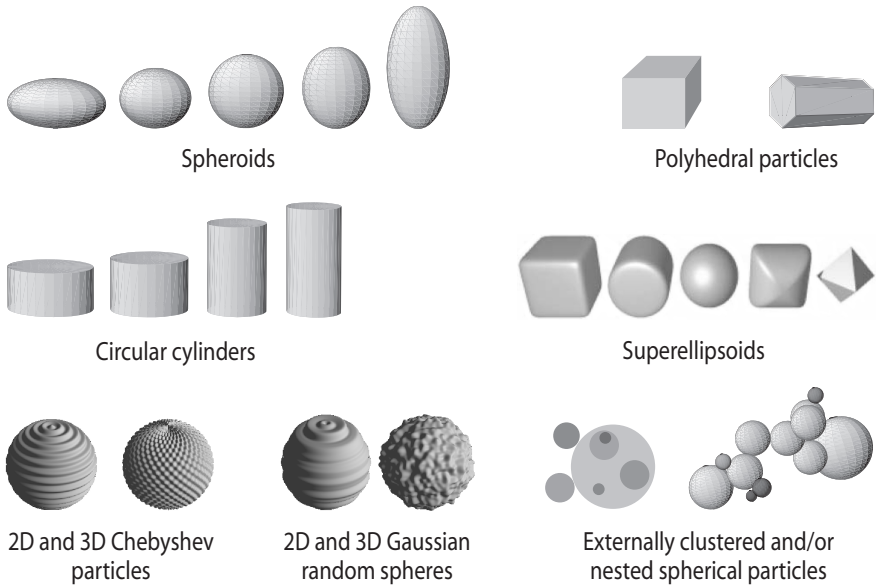

Fig. 16.2. Examples of object morphologies that can be treated with the TMM and the STMM (after Wriedt (2002), Penttilä and Lumme (2004), and Kahnert (2013a)).

16.1.9 Pros and cons of numerically exact computer solvers of the MMEs

The only methods yielding benchmark accuracy for objects comparable to and larger than a wavelength are the SVM, MSM, STMM, and TMM. The SVM, TMM, MSM, STMM, and ME-GPMM have been used extensively in computations for objects with size parameters exceeding ~50. The first four techniques appear to be the most efficient in application to bodies of revolution. The analytical averaging procedure makes the TMM the most efficient technique for nonspherical objects with a uniform distribution of orientations. Objects with extreme aspect ratios can be treated with the SVM, the so-called iterative EBCM, otherwise known as the null-field method with discrete sources (Doicu *et al.* 2006), the invariant-imbedding TMM (Bi *et al.* 2013a), and the ME-GPMM. Computations for anisotropic objects and homogeneous and inhomogeneous objects lacking rotational symmetry often have to rely on more flexible techniques, such as the FEM, FDTDM, MOM, and DDA. These techniques are simple in concept and computer implementation and have comparable performance characteristics, although their simplicity and flexibility are often accompanied by lower efficiency and accuracy and by stronger practical limitations on the maximal size parameter. A comprehensive collection of computer programs based on a variety of numerically exact computer solvers of the MMEs is posted at http://www.scattport.org (assessed December 2013).

16.2 Geometrical optics approximation

The practical importance of approximate approaches to electromagnetic scattering diminishes as various numerically exact techniques mature and become applicable to a wider range of problems, while computers become ever more powerful. However, it is likely that at least one approximation, the so-called geometrical optics method (GOM), will not become obsolete in the foreseeable future because in many cases its accuracy only improves as the object's size parameter grows, whereas all numerically exact techniques cease to be practical when the size parameter of a nonspherical object exceeds a certain threshold.

The GOM is a purely phenomenological methodology for computing far-field scattering by an arbitrarily shaped object with a size much larger than the wavelength (Liou *et al.* 2000; Yang and Liou 2006). The GOM is sometimes characterized as an asymptotic solution of the MMEs in the limit $k_1 D_{\min} \to \infty$, where $D_{\min}$ is the smallest dimension of the object, although this characterization is generally incorrect. In the case of scattering by a perfect homogeneous sphere, many features of the GOM can be justified, at least partially, by studying the behavior of the Lorenz–Mie solution in the limit $k_1 r \to \infty$, where r is the sphere radius (see, e.g., Grandy (2000), Adam (2002), and references therein). However, the availability and great numerical efficiency of the numerically exact LMT limit the practical usefulness of the GOM in the particular case of a spherically symmetric object, thereby making the GOM most useful in application to nonspherical objects. In this general case, however, the GOM has never been derived directly from the MMEs by evaluating the limit $k_1 D_{\min} \to \infty$. Instead, it remains a motley collection of intuitively appealing concepts, formulas, and recipes justified only by "simple physical considerations." Given the mathematical complexity of the general scattering problem, this situation is unlikely to change any time soon.

In the framework of the GOM, it is assumed that the incident plane electromagnetic wave can be represented as a "collection of independent parallel rays." The history of each ray impinging on the object's surface is traced separately using Snell's law and Fresnel's formulas (see Fig. 16.3). Each incident ray is partially reflected and partially refracted into the particle. The refracted ray may emerge after another refraction, possibly after one or more internal reflections, and may be attenuated by absorption inside the object. Each internal ray is traced until its intensity decreases below a prescribed cutoff value. Varying the polarization state of the incident rays, sampling all escaping rays into predefined narrow angular bins, and adding "incoherently" the respective Stokes parameters yields a quantitative representation of the object's scattering properties in terms of the ray-tracing phase matrix $\mathbf{Z}^{\mathrm{RT}}$. Because all rays impinging on the object's surface are either scattered or absorbed irrespective of their polarization state, the ray-tracing extinction matrix is always diagonal and is given by $\mathbf{K}^{\mathrm{RT}} = C_{\mathrm{ext}}^{\mathrm{RT}} \mathbf{\Delta}$, where, as before, $\mathbf{\Delta}$ is the 4×4 unit matrix. The corresponding ray-tracing ex-

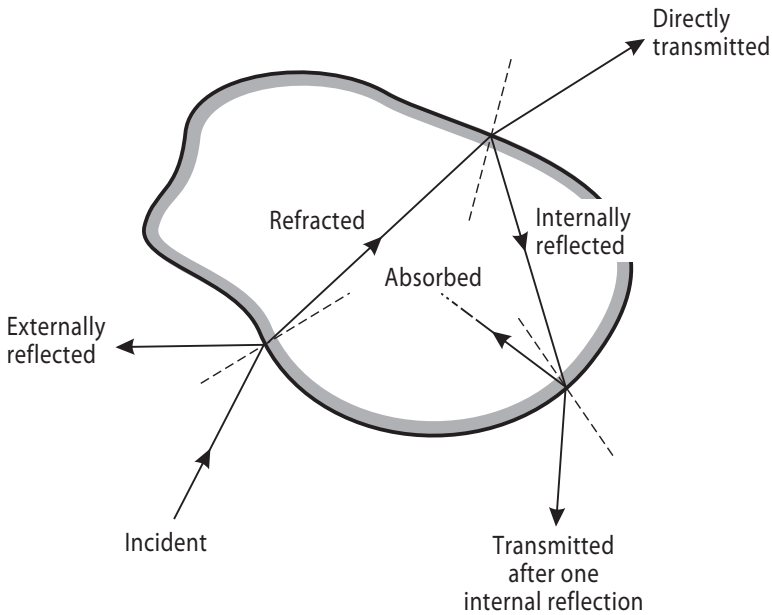

Fig. 16.3. Ray-tracing diagram.

tinction cross section $C_{\text{ext}}^{\text{RT}}$ does not depend on the polarization state of the incident wave and is equal to the geometrical area G of the object's projection on the plane perpendicular to the incidence direction. Since the presence of the object modifies the incident plane wave front by eliminating a part that has the shape and size of the geometrical projection of the object, the ray-tracing scattering pattern is supplemented by the computation of Fraunhofer diffraction of the incident wave on the object's projection. The diffraction component of the phase matrix $\mathbf{Z}^{\text{D}}$ is confined to a narrow angular cone centered at the exact forward-scattering direction and is usually computed in the Kirchhoff approximation (Jackson 1998), thereby contributing only to the diagonal elements of the total phase matrix. The diffraction component $\mathbf{K}^{\text{D}}$ of the total extinction matrix is equal to $\mathbf{K}^{\text{RT}}$. We thus have

$$\mathbf{Z}^{\text{GO}} = \mathbf{Z}^{\text{RT}} + \mathbf{Z}^{\text{D}} = \mathbf{Z}^{\text{RT}} + Z_{11}^{\text{D}}\mathbf{\Delta}, \tag{16.30}$$

$$\mathbf{K}^{\text{GO}} = \mathbf{K}^{\text{RT}} + \mathbf{K}^{\text{D}} = C_{\text{ext}}^{\text{GO}}\mathbf{\Delta}, \tag{16.31}$$

where

$$C_{\text{ext}}^{\text{GO}} = C_{\text{ext}}^{\text{RT}} + C_{\text{ext}}^{\text{D}} = 2G. \tag{16.32}$$

The total scattering cross section is the sum of the ray-tracing and diffraction components:

$$C_{\text{sca}}^{\text{GO}} = C_{\text{sca}}^{\text{RT}} + C_{\text{sca}}^{\text{D}}. \tag{16.33}$$

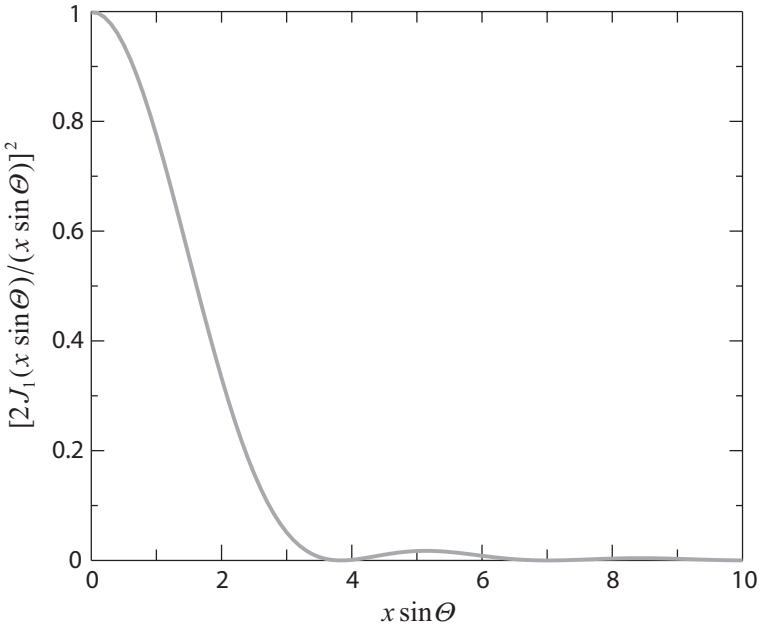

Fig. 16.4. Angular distribution of diffracted intensity.

Since the diffracted energy is not absorbed, the diffraction scattering cross section is equal to the diffraction extinction cross section:

$$C_{\text{sca}}^{\text{D}} = C_{\text{ext}}^{\text{D}} = G. \tag{16.34}$$

The ray-tracing scattering cross section $C_{\text{sca}}^{\text{RT}}$ is found from $\mathbf{Z}^{\text{RT}}$ and Eq. (13.85).

GOM calculations are particularly straightforward for spheres because the ray paths always remain in a plane, thereby simplifying the ray-tracing part of the computation, while the diffraction component of the phase matrix is given by a closed-form analytical formula

$$\mathbf{Z}^{\text{D}}(\hat{\mathbf{n}}^{\text{sca}}, \hat{\mathbf{n}}^{\text{inc}}) \underset{x\to\infty}{=} \frac{Gx^2}{16\pi}\left[\frac{2J_1(x\sin\Theta)}{x\sin\Theta}\right]^2 (1+\cos\Theta)^2\,\mathbf{\Delta}, \tag{16.35}$$

where $x = k_1 r$ is the size parameter, $\Theta = \arccos(\hat{\mathbf{n}}^{\text{sca}} \cdot \hat{\mathbf{n}}^{\text{inc}})$ is the scattering angle, and $J_1(z)$ is the Bessel function of order unity. Figure 16.4 shows the quantity $[2J_1(x\sin\Theta)/(x\sin\Theta)]^2$ as a function of $x\sin\Theta$. It is seen that for $x \gg 1$ essentially all the diffracted light is confined within an angular cone of half-width $\Theta \cong 7/x$.

The main advantage of the GOM is that it can be applied to essentially any shape. However, this technique is heuristic by design, and its range of applicability in terms of the smallest size parameter must be thoroughly checked by comparing GOM results with numerically exact solutions of the MMEs. As an example, Fig. 16.5 depicts the results of GOM and Lorenz–Mie computations of the

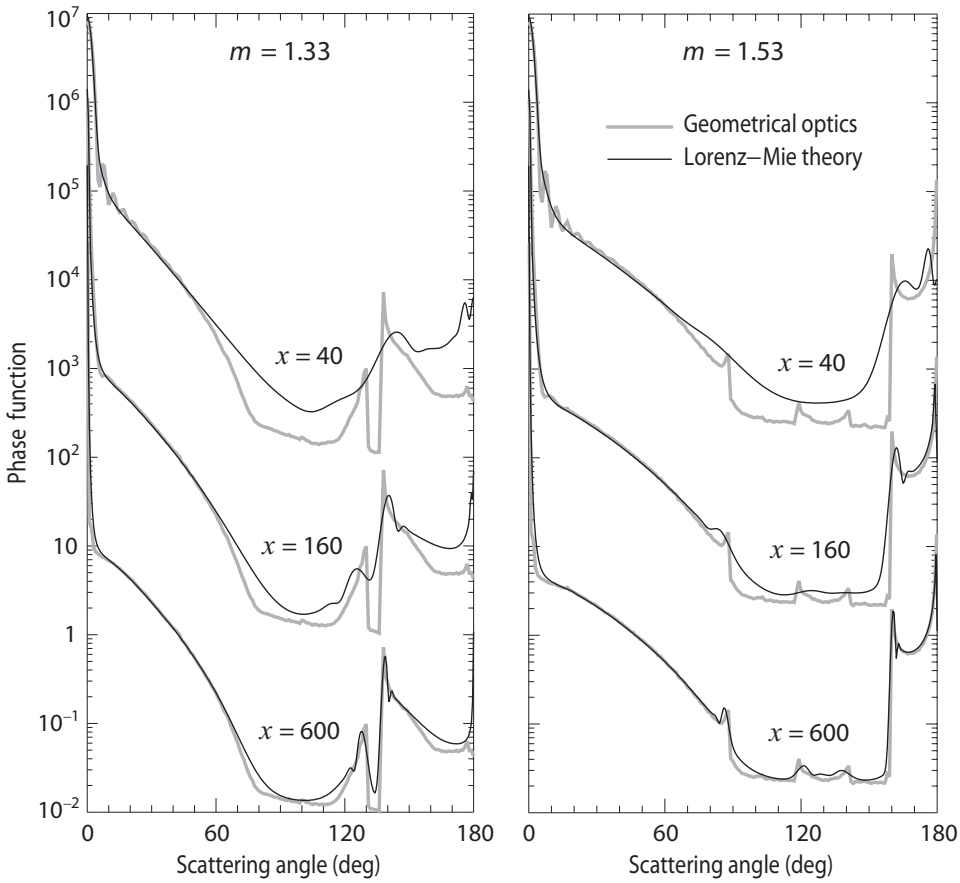

Fig. 16.5. Phase function $a_1(\Theta)$ versus scattering angle Θ computed with the GOM and the LMT for homogeneous spheres with relative refractive indices $m = 1.33$ and 1.53 and size parameters $x = 40$, 160, and 600. The vertical axis scale applies to the curves with $x = 600$, the other curves being successively displaced upward by a factor of 100. (After Hansen and Travis 1974.)

phase function $a_1(\Theta)$ for nonabsorbing homogeneous spheres with relative refractive indices $m = 1.33$ and 1.53 and size parameters $x = 40$, 160, and 600. The computations were performed using the ray-tracing code described by Macke and Mishchenko (1996) and the Lorenz–Mie code described in Section 5.10 of MTL1. The Lorenz–Mie results were averaged over a narrow size distribution given by Eq. (15.108), with $b = 0.07$, so that x represents the effective size parameter $k_1 r_{\text{eff}}$, where r_{eff} is the effective radius defined by Eq. (15.110). The ray-tracing and diffraction components of the GOM phase functions were averaged over 1°-wide angular bins. It is clear that the GOM phase-function results for spheres become reasonably accurate only at size parameters exceeding several hundred. Furthermore, the GOM fails to reproduce the strong backscattering peak

observed for spheres with $m = 1.33$ and usually associated with so-called "surface waves" (see Section 17.2).

Shown in Fig. 16.6 are the results of GOM and T-matrix computations of the phase function for monodisperse, randomly oriented circular cylinders with a diameter-to-length ratio of unity, relative refractive index $m = 1.311$, and surface-equivalent-sphere size parameters x_s varying from 40 to 180; Fig. 16.7 depicts all

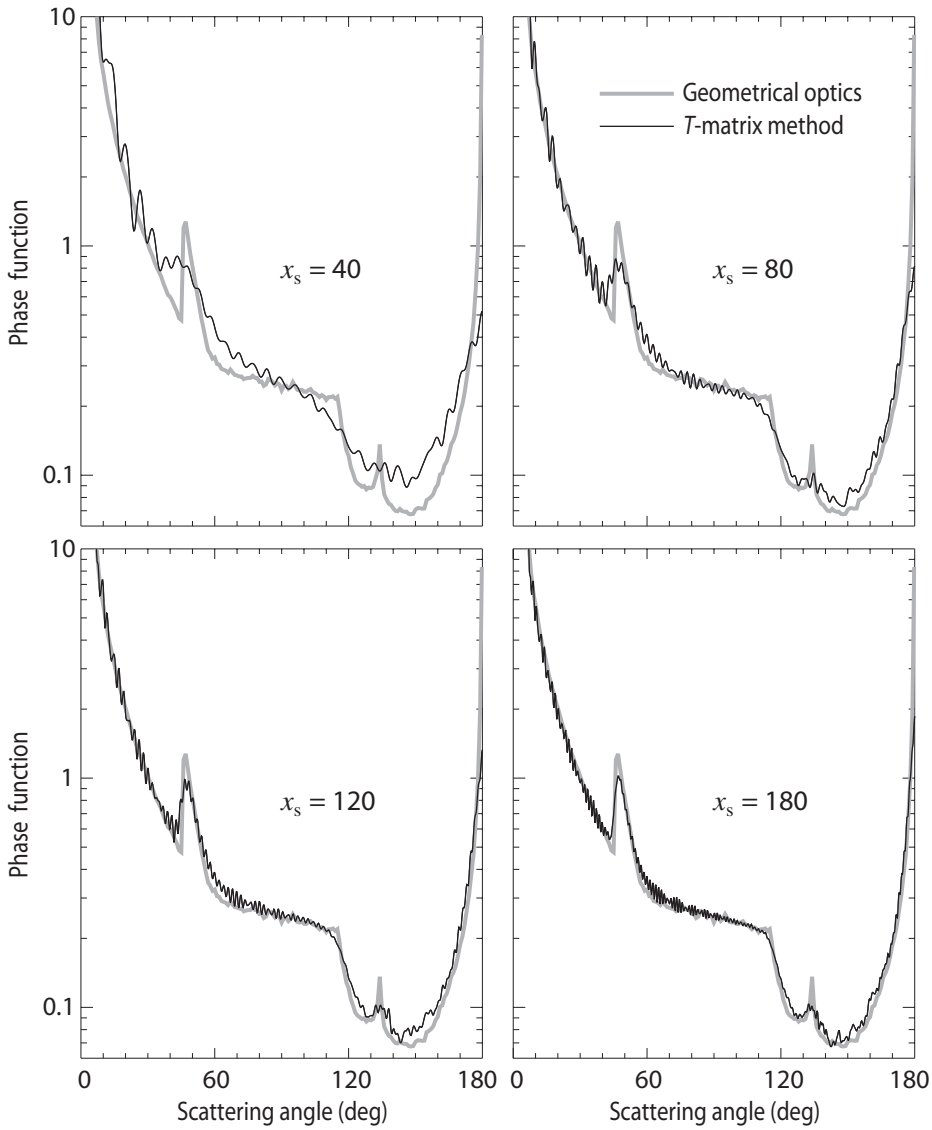

Fig. 16.6. GOM and T-matrix phase functions for monodisperse, randomly oriented circular cylinders with surface-equivalent-sphere size parameters x_s = 40, 80, 120, and 180.

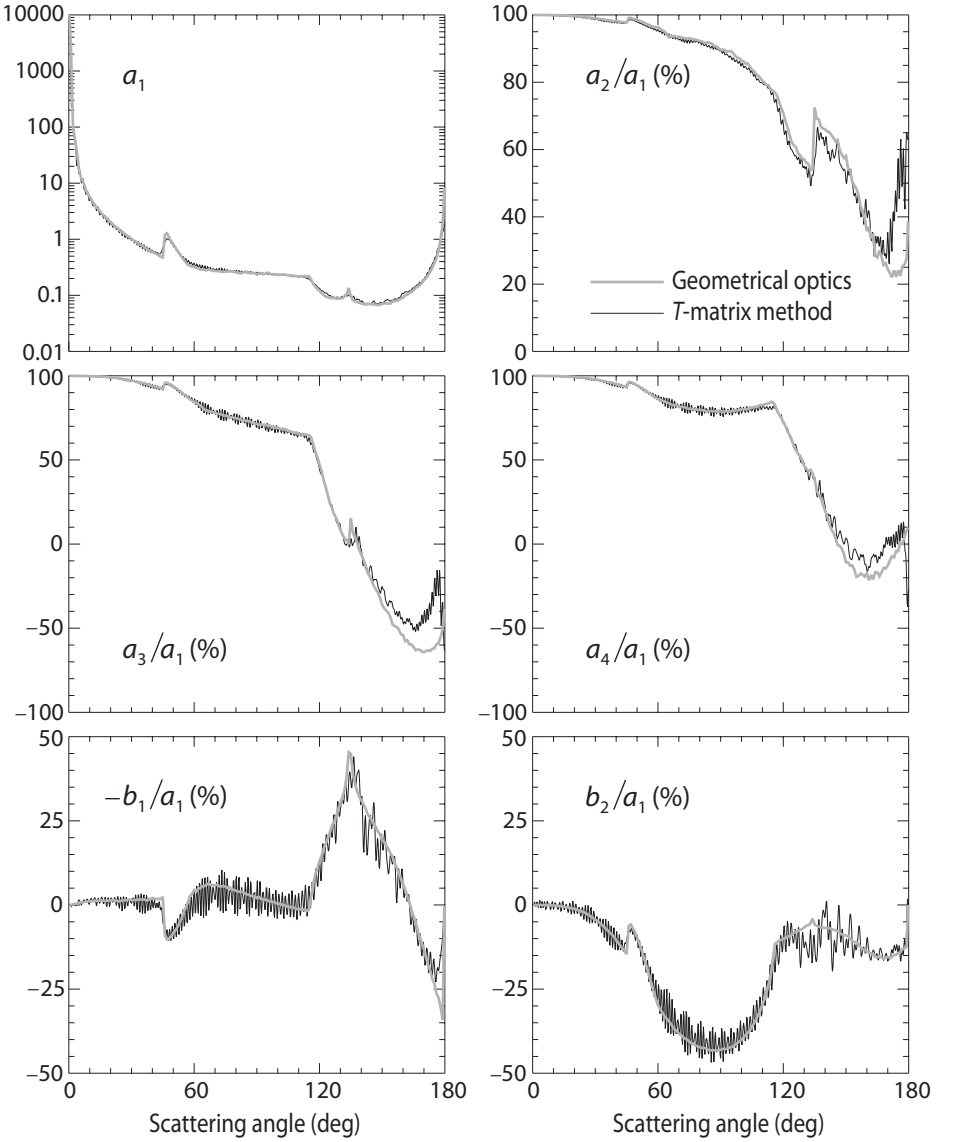

Fig. 16.7. Elements of the normalized Stokes scattering matrix for monodisperse, randomly oriented circular cylinders with a surface-equivalent-sphere size parameter $x_s = 180$.

elements of the normalized Stokes scattering matrix for $x_s = 180$. The small-amplitude ripple in the *T*-matrix curves is caused by interference effects characteristic of monodisperse particles and can be eliminated by averaging over a narrow size distribution (cf. Fig. 16.5). The curves in Figs. 16.6 and 16.7 seem to suggest that GOM results for a nonspherical particle in random orientation may

be somewhat more accurate for a given size parameter than those for a surface-equivalent sphere. However, it is clear that although the main geometrical optics features can be qualitatively reproduced by particles with size parameters less than 100, obtaining good quantitative accuracy in GOM computations of the scattering matrix for nonspherical particles still requires size parameters exceeding a few hundred.

Besides the simple version of the GOM based on the combination of the Snell–Fresnel ray tracing with diffraction on the object's projection, several more sophisticated versions of the GOM have been proposed, such as the geometrical theory of diffraction (e.g., Borovikov and Kinber 1994; James 2007) and the so-called physical optics approximation (e.g., Muinonen 1989; Mazeron and Muller 1996; Yang and Liou 1996, 2006; Borovoi 2013). In particular, the latter is based on expressing the far-zone scattered field in terms of the electric and magnetic fields on the exterior side of the object's surface, computed approximately using Fresnel's formulas and the standard ray-tracing procedure. Both approaches partially preserve the phase information and account for some physical optics effects completely ignored by the standard GOM. Like with any heuristic approach, the range of applicability of these and similar techniques is not well defined, and their accuracy should be thoroughly evaluated by comparing approximate results with those obtained by running numerically exact computer solvers of the MMEs. Further details can be found in the recent review by Bi and Yang (2013).

16.3 Controlled laboratory measurements

The majority of existing laboratory techniques are implementations of the general measurement strategy depicted in Figs. 13.1 and 14.3. Usually they fall into one of two broad categories:

- Scattering of visible or infrared light by particles with sizes ranging from tens of nanometers to several hundred micrometers. The particles can be electrostatically or optically levitated or are streaming through the measurement volume.
- Microwave scattering by fixed millimeter- and centimeter-sized objects.

Measurements in the visible and infrared spectral ranges benefit from the availability of sensitive detectors, intense sources of radiation, and high-quality optical elements. They involve cheaper and more portable instrumentation (e.g., Fig. 1.6c) and can be performed in the field, as well as in the laboratory. However, they become problematic when experimental data for a fixed scattering object are needed and may be difficult to interpret because of lack of independent information on sample microphysics and composition. Microwave scattering experiments require more cumbersome and expensive instrumentation and large measurement facilities (e.g., Fig. 1.6d), but allow full control over the scattering object.

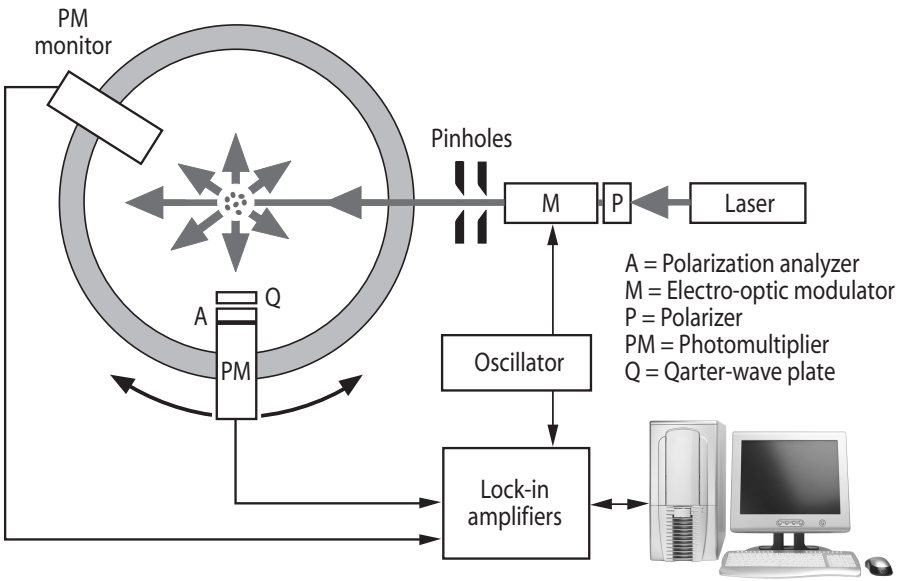

Fig. 16.8. Schematic view of a polarimetric nephelometer using visible light.

16.3.1 Measurements in the visible and infrared

In order to measure all 16 elements of the scattering matrix, one must use various optical elements that can alter the polarization state of light before and after scattering in a controllable way (see Chapter 12). Figure 16.8 (adapted from Hovenier (2000)) depicts the scheme of an advanced laboratory setup used to measure scattering matrix elements for small random groups of natural and artificial particles at visible or infrared wavelengths. The light beam generated by a laser passes through a linear polarizer and a polarization modulator and then illuminates particles contained in the scattering chamber. The modulator is intended to introduce a sinusoidal modulation in time of the polarization of light before scattering. Light scattered by the particles at an angle Θ relative to the incidence direction passes a quarter-wave plate (i.e., a retarder increasing the phase of one linear-polarization component by $\pi/2$ relative to the other) and another polarizer (called a polarization analyzer), after which its intensity is measured by a detector. Assuming that the scattering volume satisfies the criteria of applicability of the FOSA discussed in Chapter 14, we can write for the Stokes column vector of the beam reaching the detector the following expression:

$$\mathbf{I}' \propto \mathbf{A}\mathbf{Q}\, N\langle \mathbf{F}(\Theta;\xi)\rangle_{\xi}\, \mathbf{M}\mathbf{P}\mathbf{I}, \tag{16.36}$$

where $\mathbf{I}$ is the Stokes column vector of the beam leaving the light source, $\mathbf{A}$, $\mathbf{Q}$, $\mathbf{M}$, and $\mathbf{P}$ are 4×4 Mueller matrices of the analyzer, quarter-wave plate, modulator, and polarizer, respectively, N is the number of particles contributing to the

scattered field, and $\langle \mathbf{F}(\Theta;\xi)\rangle_\xi$ is the scattering matrix of the virtual FOSA particle averaged over particle microphysical states. It is assumed in Eq. (16.36) that the plane through the incidence and scattering directions serves as the reference plane for defining the Stokes parameters. The Mueller matrices of the polarizer, modulator, quarter-wave plate, and analyzer depend on their orientation with respect to the scattering plane and can be precisely varied. Because the detector measures only the first element of the Stokes column vector $\mathbf{I}'$, several measurements with different orientations of the optical components with respect to the scattering plane are required for the full determination of the scattering matrix. This procedure is repeated at different scattering angles to determine the angular profile of the scattering matrix.

The technique of the high-frequency sinusoidal modulation in time of the polarization of light before scattering, combined with intensity normalization, was developed by Hunt and Huffman (1973). When followed by lock-in detection, this technique can be used to increase the experimental accuracy by enabling direct measurements of the scattering matrix elements normalized by the (1, 1) element and provides the capability to determine several elements from only one detected signal.

A major advantage of measurements at visible and infrared wavelengths is that they can deal with real (natural or artificial) particle ensembles. However, they may suffer from the lack of detailed independent characterization of the particle size and shape distributions and relative refractive index, thereby potentially making comparisons of experimental and theoretical results problematic. The number of particles N contributing to the scattering signal is also seldom known and can, in fact, fluctuate, which precludes the absolute measurement of the (1, 1) element of the matrix $\langle \mathbf{F}(\Theta;\xi)\rangle_\xi$ (measurements of elements other than the (1, 1) element are usually reported in the form of N-independent ratios of the elements to the (1, 1) element).

Another drawback is that the arrangement of the source of light and the detector usually precludes measurements at scattering angles Θ close to 0° and 180°. For example, the setup described by Hovenier (2000) has the range of scattering angles [5°, 175°], while the angular range of the more recent instrument developed by Muñoz *et al.* (2010) is [3°, 177°]. As a consequence, experimental values of the (1, 1) element are often normalized to the value at a fixed scattering angle (e.g., 30°).

Muñoz *et al.* (2012) describe an extensive light scattering database created over the past two decades with similar polarimetric nephelometers built in Amsterdam and Granada.

16.3.2 Measurements at microwave frequencies

In accordance with the scale invariance rule discussed in Sections 5.5 and 13.2, the main idea of the microwave analog technique is to manufacture a centimeter-

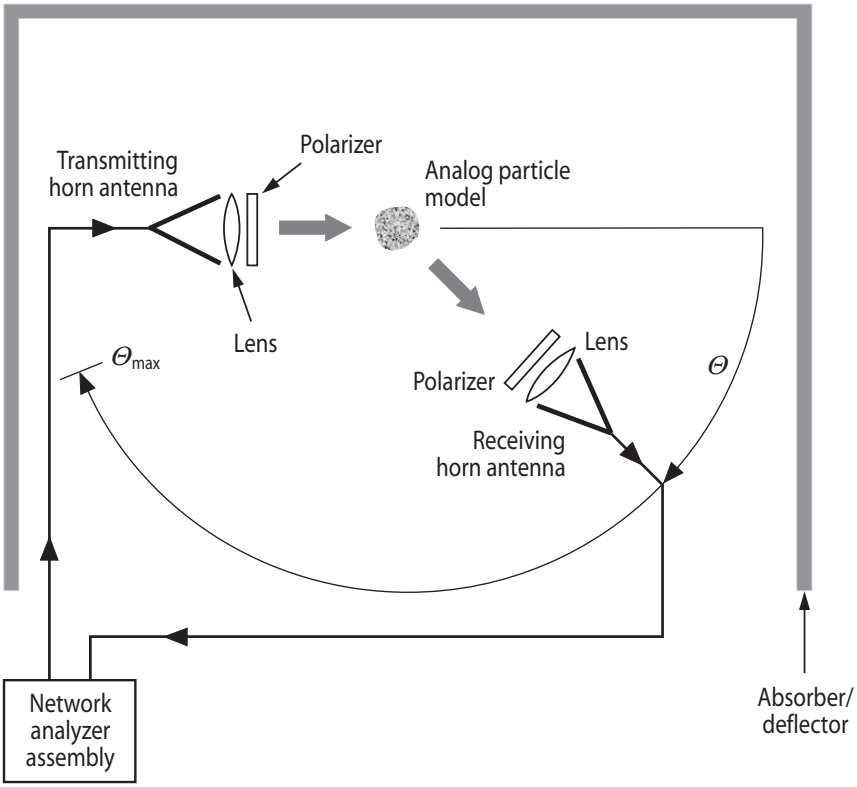

Fig. 16.9. Layout of a modern microwave analog scattering facility (after Gustafson 2000).

sized scattering object with desired shape and refractive index, measure the scattering of a microwave beam by this object, and finally extrapolate the measured phase matrix elements to other wavelengths (e.g., visible or infrared) by keeping the ratio size/wavelength fixed. In a modern microwave scattering setup (see Fig. 16.9), radiation from a transmitting conical horn antenna passes through a collimating lens and a polarizer. The lens produces a nearly flat wavefront, which is scattered by an analog particle model target. The scattered spherical wave passes through another polarizer and lens and is measured by a receiving horn antenna. The receiver end of the setup can be positioned at any scattering angle from 0° to $\Theta_{max} \cong 170°$, thereby providing measurements of the angular distribution of the scattered radiation. By varying the orientations of the two polarizers, one can measure all elements of the scattering matrix.

Microwave measurements allow coverage of a wide range of scattering angles, including the exact forward direction, and a much greater degree of control over the target size, shape, and orientation than measurements at visible or infrared wavelengths. Using special techniques, even the extinction matrix can be

measured. Measurements at angles close to the backscattering direction are usually problematic because the transmitting and receiving antennas would overlap. It is possible, however, to add a backscattering measurement capability ($\Theta = 180°$) by using the transmitting antenna as a receiver. Because the size of the scattering object is typically of the order of millimeters or centimeters, high-precision target manufacturing is easy and can involve computer-controlled milling or stereo lithography. Therefore, the results of controlled laboratory measurements of far-field electromagnetic scattering at microwave frequencies can readily be compared with theory.

A disadvantage of microwave measurements is that they can be performed only for one particle size, shape, and orientation at a time. As a consequence, averaging over particle states becomes a time-consuming procedure.

Updated overviews of the microwave analog technique and further references can be found in Gustafson (2009) and Vaillon *et al.* (2011).

Problem

16.1: Verify that the Lorenz–Mie formulas (16.13) and (16.14) follow from the TMM formulas (16.28) and (16.29), if the latter are applied to a spherically symmetric scattering object.

Notes and further reading

The theory of electromagnetic scattering by particles was pioneered by John William Strutt, Lord Rayleigh (1842–1919). He derived the so-called Rayleigh law describing the scattering of a plane electromagnetic wave by a spherical or ellipsoidal particle much smaller than the wavelength (Rayleigh 1871a,b, 1897) and developed a numerically exact theory of electromagnetic scattering by an infinite circular cylinder (Rayleigh 1881). He also introduced a conceptually important ansatz, called the Rayleigh hypothesis (Rayleigh 1907), which has found numerous applications, but still appears to cause controversy (see, e.g., Tishchenko (2010), Rother and Kahnert (2014), and references therein).

Arnold Sommerfeld (1868–1951) was the first to realize that the uniqueness of the solution of an open-space scattering problem depends on the explicit formulation of the radiation condition at infinity (Sommerfeld 1912). The history of Sommerfeld's radiation condition, as well as its extensions and modifications are described by Schot (1992). In the case of three-dimensional electromagnetic scattering by finite objects, the radiation condition takes the form of Eq. (4.7) and is traditionally called the Silver–Müller radiation condition.

The paper by Gustav Mie (1868–1957) on electromagnetic plane-wave scattering by a homogeneous spherical particle (Mie 1908) has become one of the most frequently cited papers in physics. The history of this publication in the general context of Mie's research is discussed by Mishchenko and Travis (2008)

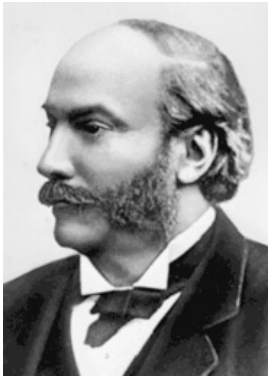
John William Strutt

Arnold Sommerfeld

Ludvig Valentin Lorenz

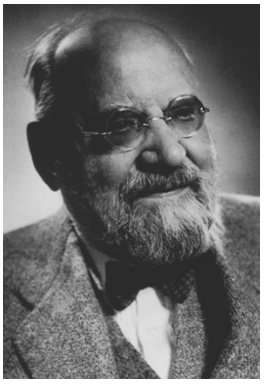
Gustav Mie

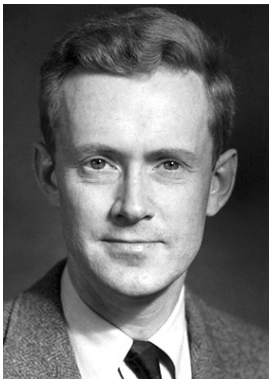
Edward Mills P r rcell

Peter Cary Waterman

and Hergert (2012). In its mathematical part, Mie's theory had largely been anticipated by Ludvig Valentin Lorenz (1829–91) in a 1890 paper written in Danish (Lorenz 1890). This paper appears to have been unknown to Mie, but has been acknowledged in the scientific literature in the recent decades by referring to the "Lorenz–Mie theory" (Logan 1965). A seminal theoretical development was the reformulation of the LMT by Stratton (1941) in terms of VSWFs introduced by the founder of microwave technology William Webster Hansen (1909–49) (Hansen 1935). An important role in the subsequent dissemination of the LMT has been played by the monographs by van de Hulst (1957), Born and Wolf (1999; first published in 1959), and Bohren and Huffman (1983).

Edward Mills Purcell (1912–97) (in co-authorship with C. R. Pennypacker) and Peter Cary Waterman (1928–2012) further advanced the theory of electromagnetic scattering by developing the widely used DDA and TMM. Waterman (in co-authorship with John Fikioris) pioneered the MSM in a report published in 1963 (Fikioris and Waterman 1963). The corresponding journal paper was finalized in 1964, but published nearly half a century later (Fikioris and Water-

man 2013). The history of this paper and its place in the general context of Waterman's contributions to the theory of wave scattering is summarized by Mishchenko and Martin (2013).

A plentiful source of information on advanced numerically exact computer solvers of the frequency- and time-domain MMEs and on modern controlled laboratory techniques is the growing collection of topical issues of the *Journal of Quantitative Spectroscopy and Radiative Transfer* (see Borghese *et al.* (2012) and references therein).

17

Far-field observables: qualitative and quantitative traits

In Chapters 13 and 15 we have introduced a number of important far-field characteristics and discussed their general mathematical properties. In Chapter 14, we have seen that the same quantities enter the FOSA for a small group of randomly and sparsely distributed particles observed from a sufficiently remote location. In Chapter 19, we will see that the same far-field characteristics enter the RTE for a very large random group of sparsely distributed particles observed from a point located in the near zone of the group. Given the ubiquity and great practical importance of these quantities, it would be essential to discuss their typical qualitative and quantitative traits. We will do this mostly with the help of the numerically exact LMT, TMM, and STMM described in the preceding chapter.

We have seen in Chapter 14 that, in the framework of the FOSA, the actual particles forming a random N-particle group are effectively replaced by N statistically identical copies of the virtual FOSA particle. We will see later that the same happens in the RTT. As a consequence, the far-field characteristics serve a triple purpose of representing: (i) the whole object in the framework of the FFS formalism, (ii) the virtual FOSA particle, and (iii) the virtual RTT particle. In this chapter we will not make a distinction between these three scenarios and will use the term "particle" in application to the whole FFS object, the virtual FOSA particle, or the virtual RTT particle.

17.1 Deterministic particle

We begin the discussion by considering far-field scattering by a "deterministic" particle, that is, a particle whose morphology and orientation do not change in time. The solid curve in Fig. 17.1 shows the extinction efficiency factor Q_{ext} as a function of the size parameter $x = k_1 r$ for a homogeneous spherical particle with a relative refractive index $m = 1.4$, while the dotted curve depicts the asymmetry

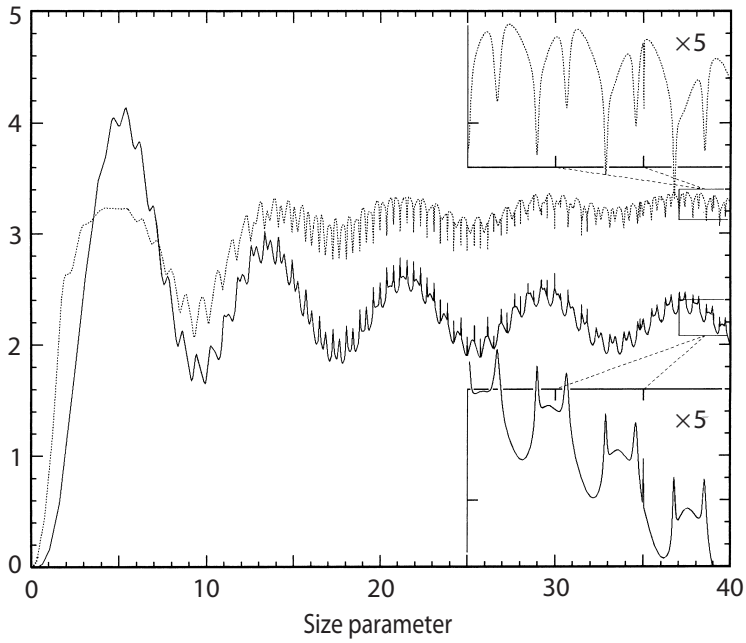

Fig. 17.1. Extinction efficiency factor Q_{ext} (solid curve) and asymmetry parameter g multiplied by a factor of 4 (dotted curve) versus size parameter x for a homogeneous spherical particle with a relative refractive index $m = 1.4$.

parameter g.[1] According to Section 15.6, both quantities are independent of the polarization state and propagation direction of the incident field. Since the imaginary part of the relative refractive index is here set at zero, the scattering efficiency factor is equal to the extinction efficiency factor, the absorption efficiency factor is equal to zero, and the single-scattering albedo is equal to unity. It is seen that both Q_{ext} and g rapidly vanish as x approaches zero (the so-called Rayleigh limit), while Q_{ext} tends to the asymptotic GOM value 2 as $x \to \infty$ (cf. Eq. (16.32)). In the intermediate (so-called resonance) region of size-parameter values, the extinction efficiency factor can significantly exceed the value 2, especially as the real part of the relative refractive index is increasing (cf. Fig. 17.2).

[1] The extinction efficiency factor is often used for demonstration purposes in lieu of the extinction cross section since the range of variability of the ratio C_{ext}/G is limited, whereas that of C_{ext} is not. It is important to remember, however, that only C_{ext} has physical significance. From reading some publications on electromagnetic scattering, the reader may get the wrong impression that Q_{ext} is a primordial quantity, whereas C_{ext} is a derivative one. However, it is easy to verify by inspecting those publications that Q_{ext} never appears in formulas describing actual optical observables or quantifying electromagnetic energy budget without being multiplied by the area of the particle's geometrical projection. This makes one to question the wisdom of using Q_{ext} in such formulas in the first place.

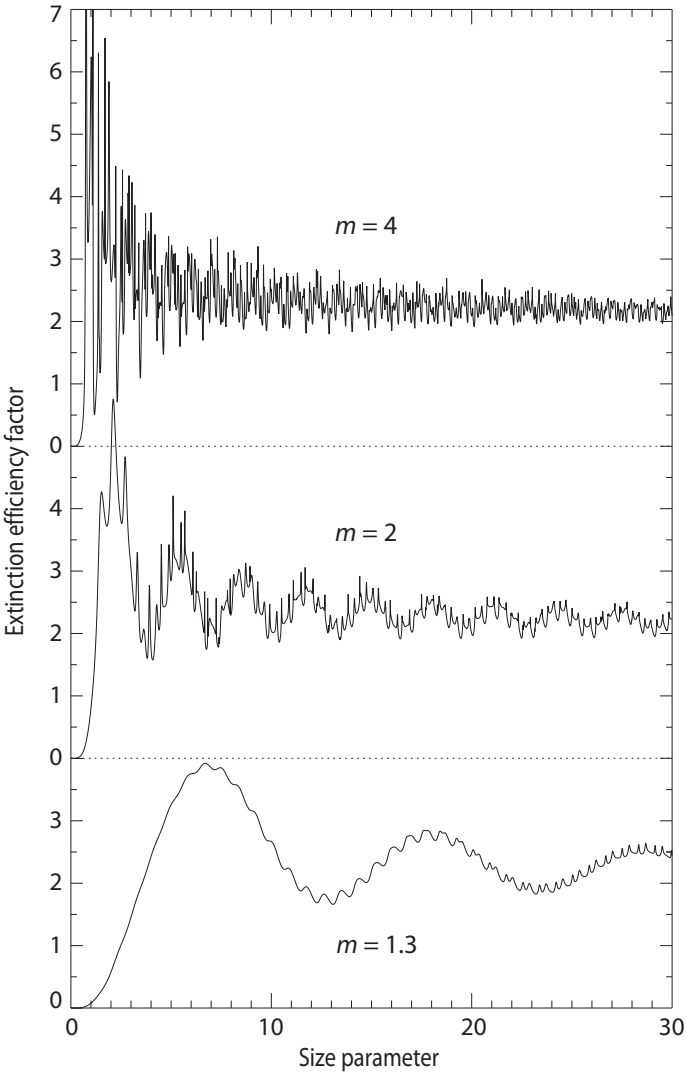

Fig. 17.2. Extinction efficiency factor Q_{ext} versus size parameter x for homogeneous spherical particles with relative refractive indices $m = 1.3$, 2, and 4.

Both curves in Fig. 17.1 are characterized by a succession of major low-frequency maxima and minima with superimposed high-frequency ripples composed of sharp, irregularly spaced extrema, some of which are super-narrow spike-like features. The major maxima and minima are called the "interference structure" since they are qualitatively attributed to the interference of the light diffracted and transmitted by the particle (van de Hulst 1957). A light ray passing through the center of a sphere acquires a phase shift $\rho = 2x(m_{\text{R}} - 1)$, where, as before, m_{R} is the real part of the relative refractive index. Therefore, constructive

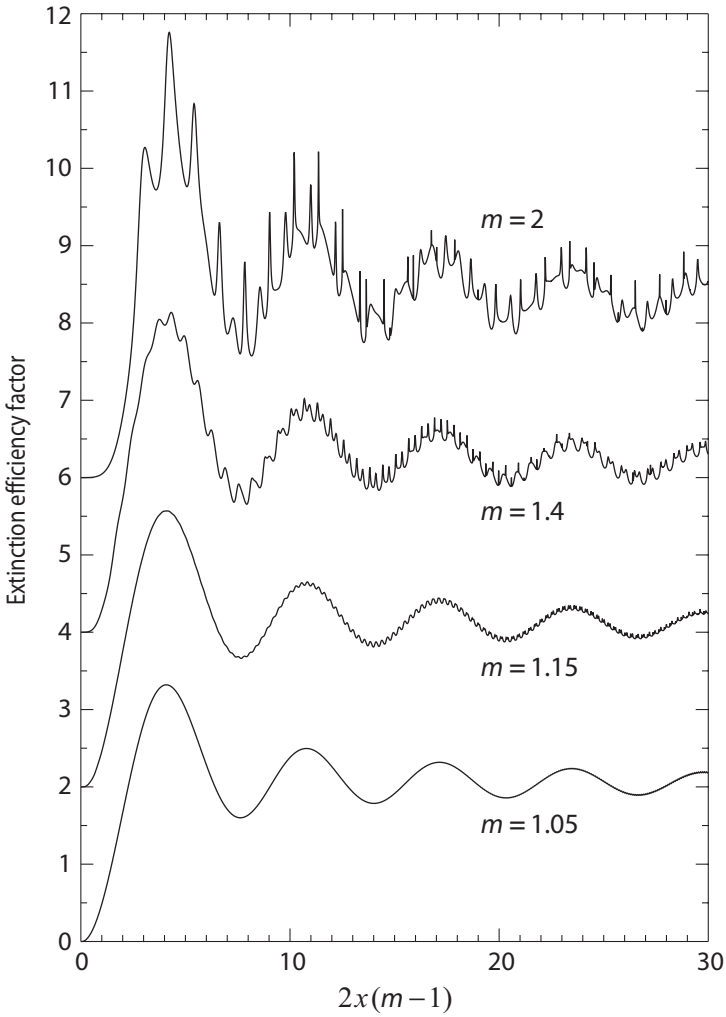

Fig. 17.3. Extinction efficiency factor versus phase shift for homogeneous spherical particles with relative refractive indices m = 1.05, 1.15, 1.4, and 2. The vertical scale applies to the curve for m = 1.05, the other curves being successively displaced upward by 2.

and destructive interference and, thus, maxima and minima in the extinction efficiency curve, occur successively at intervals $\approx 2\pi$ in ρ (see Fig. 17.3, which shows Q_{ext} as a function of ρ for monodisperse spheres with various real relative refractive indices). With $m_{\text{R}} \to \infty$, the central transmitted rays are increasingly attenuated by the external reflection, and the interference structure becomes less pronounced (cf. Fig. 17.2) and ultimately disappears (Chýlek and Zhan 1989).

Unlike the interference structure, the ripple is caused by the resonance behavior of the Lorenz–Mie coefficients a_n and b_n (see, e.g., the review by Hill and

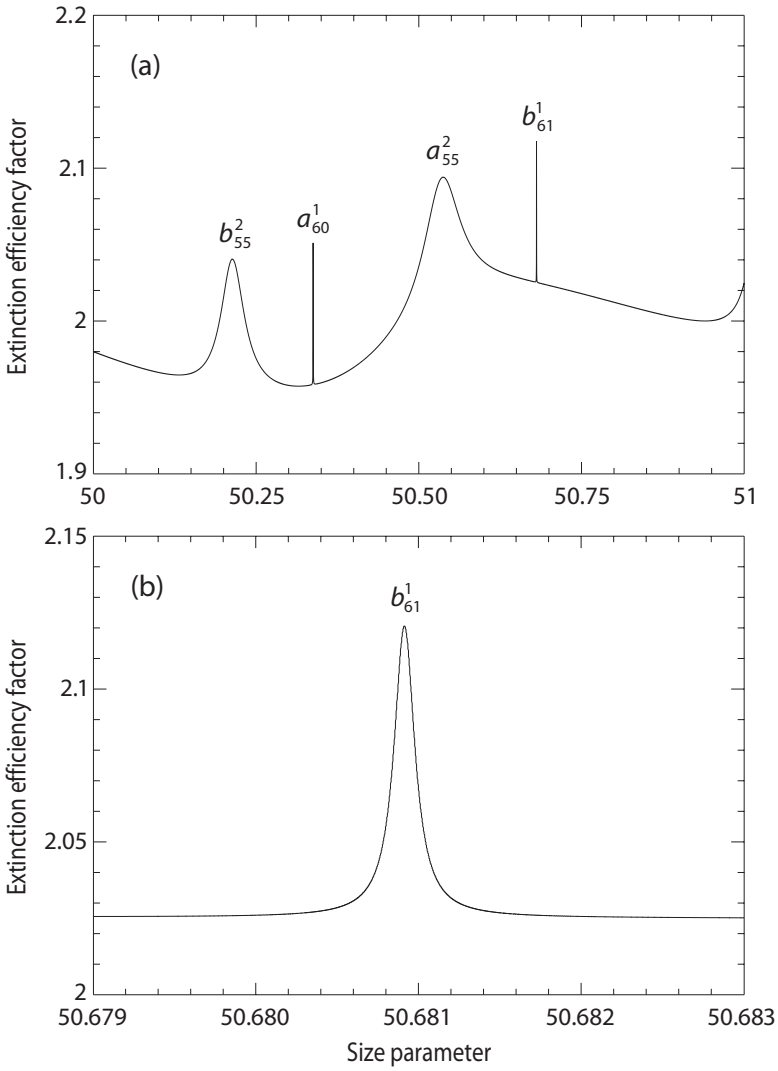

Fig. 17.4. **(a)** Ripple structure of the extinction efficiency factor for a spherical water droplet ($m = 1.33 + \mathrm{i} \times 10^{-8}$) on the interval [50, 51] of size parameters. **(b)** High-resolution profile of the resonance b_{61}^1.

Benner (1988) and references therein). The resonances in lower-order coefficients are rather broad and often overlap. As n increases, the resonance features become narrower, and starting with $n \sim 20$ (for $m = 1.4$) each feature in the ripple structure can be identified with an individual resonance in the corresponding partial coefficient a_n or b_n. As the size parameter approaches a resonant value, the denominator in Eq. (16.6) or (16.7) approaches a local minimum, thereby causing a local extremum (maximum or minimum) in the curve for a specific scattering characteristic. Accordingly, the numbers of spike-like extrema in the two curves

in Fig. 17.1 are identical, and a sharp local maximum in the extinction curve always corresponds to a sharp local minimum in the asymmetry parameter curve.

For a fixed m and each index n, there is a sequence of resonance x-values for either $a_n(x, m)$ or $b_n(x, m)$. Hence it is convenient to label each local extremum with the type of mode causing the resonance (a or b), the subscript n, and a superscript l indicating the sequential order of x (Chýlek 1976; Chýlek *et al.* 1978). This labeling convention is illustrated in Fig. 17.4a, which shows the resonance extinction features for a water droplet within the interval $x \in [50, 51]$. The main traits of the resonance features are that their width decreases as n increases for a given l and their width increases as l increases for a given n. For n greater than about 50, the $l = 1$ resonance can become extremely narrow, as demonstrated in Fig. 17.4b.

Figure 17.5 shows the behavior of the super-narrow resonance centered at $x \approx 38.9983$ (for $m_R = 1.4$) with increasing imaginary part of the relative refractive index m_I. It is seen that raising m_I from 0 to a very small value 10^{-5} almost completely destroys this spike-like feature, while causing no change whatsoever in the background Q_{ext} and g values. It takes significantly greater m_I values to eliminate the broader resonances and still greater values (of order 0.1) to eliminate the interference structure (Fig. 17.6). Therefore, measurements within super-narrow resonances can be far more sensitive to weak absorption than measurements in the "continuum" or within broader ripple features.

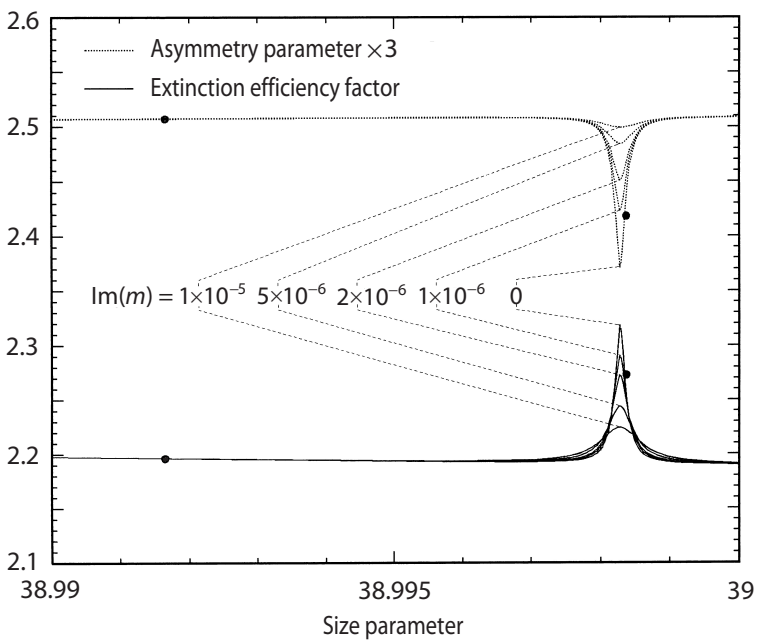

Fig. 17.5. Profile of the resonance centered at $x \approx 38.9983$ for $m_R = 1.4$ and five values of m_I. The dots show the sampling resolution used in Fig. 17.1.

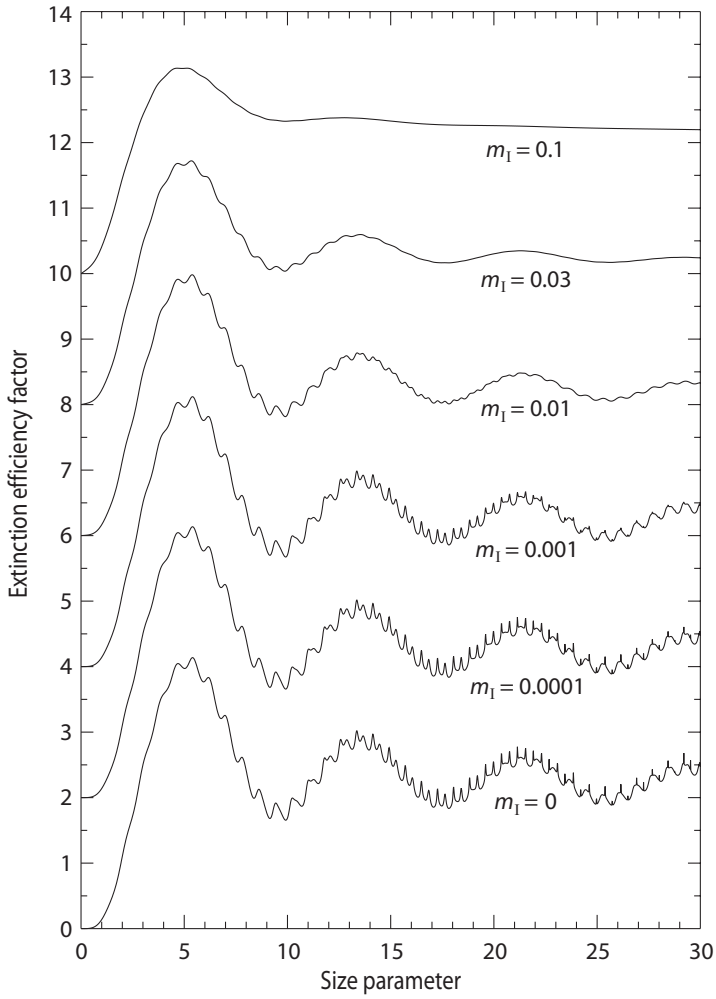

Fig. 17.6. The set of curves (bottom to top) shows the effect of increasing absorption on the interference and ripple structure of the extinction efficiency factor for a homogeneous spherical particle with the real part of the relative refractive index $m_R = 1.4$. The vertical axis scale applies to the curve with $m_I = 0$, the other curves being successively displaced upward by 2.

Manifestations of the ripple structure can be even more spectacular in the elements of the scattering matrix than in the optical cross sections and the asymmetry parameter. Since the normalized Stokes scattering matrix (15.79) for a fixed relative refractive index depends on two variables, i.e., the size parameter x and the scattering angle Θ, it is convenient to use two-dimensional color images plotted with fine angular and size-parameter sampling resolutions. Plate 17.1 shows the ratio $-b_1/a_1$ (in percent) as a function of Θ and x for a homogeneous sphere with a relative refractive index $m = 1.4$. This image was created using

sampling resolutions $\Delta\Theta = 1/3°$ and $\Delta x = 0.05$. With the exception of the region of Rayleigh scattering ($x \lesssim 2$; see Fig. H.2), the entire image is a field of sharp, alternating maxima and minima. The frequencies of the maxima and minima over both Θ and x increase with increasing size parameter. This very complex "butterfly" structure appears both to be chaotic and to reveal a slightly perceptible order.

Plate 17.2a provides a zoomed image of a small part of the field covered by Plate 17.1 and reveals with much greater detail the enormous complexity of the scattering pattern. Now the sampling resolution ($\Delta\Theta = 0.1°$ and $\Delta x = 0.007$) is fine enough to exhibit horizontal "dislocations" or "anomalous strips," which are first indicators of super-narrow resonances. One of these is centered at $x \approx 38.9983$ and is shown with even greater sampling resolution ($\Delta\Theta = 0.05°$ and $\Delta x = 0.00001$) in the left-hand panel of Plate 17.2b. This latter image demonstrates an immense degree of variability within the resonance, including drastic changes of sign and strong dependence on scattering angle.

The other three panels of Plate 17.2b are analogous to the left-hand panel, but show the results of computations for three increasing values of the imaginary part of the relative refractive index. Although many features within the resonance gradually weaken and ultimately disappear, the super-narrow minimum located at $\Theta \approx 177°$ and $x \approx 38.99828$ for $m_{\mathrm{I}} = 0$ becomes much more pronounced and shifts toward larger Θ and x before it finally disappears at $m_{\mathrm{I}} = 10^{-4}$. This behavior is quite different from that exhibited by Q_{ext} and g in Fig. 17.5.

The angular widths of the more prominent details of the "butterfly structure" in Plate 17.1 are consistent with the discussion preceding Eq. (13.22). It is obvious, however, that to fully resolve the super-narrow resonance features such as those seen in Plate 17.2, the distance from the particle to the WCR must be much greater than the criterion (13.22) suggests.

As discussed in Section 15.8, the extinction cross section for a nonspherical particle depends on the incidence direction. This is illustrated in Fig. 17.7 which depicts the results of TMM computations of the dimensionless normalized extinction $\widetilde{C}_{\mathrm{ext}} = C_{\mathrm{ext}}/(\pi r_{\mathrm{ev}}^2)$ for a prolate spheroid with a semi-axis ratio of $a/b = 0.9$, where r_{ev} is the radius of the equal-volume sphere, b is the spheroid semi-axis along the axis of revolution, and a is the semi-axis in the perpendicular direction. $\widetilde{C}_{\mathrm{ext}}$ is plotted as a function of the size parameter $x_{\mathrm{ev}} = k_1 r_{\mathrm{ev}}$ and the angle β between the spheroid axis of revolution and the incidence direction. The relative refractive index of the spheroid is 1.4, while the incident light is assumed to be unpolarized. The significant overall increase of the extinction cross section C_{ext} with increasing β can be explained qualitatively by the growing area of the spheroid geometrical projection on the plane perpendicular to the incidence direction. The numerous local maxima in the surface plot of the normalized extinction reveal the added complexity of the ripple structure caused by nonsphericity.

Panels (a)–(c) of Plate 17.3 illustrate the shape and orientation dependence of the ratio $-F_{12}/F_{11}$ of the elements of the scattering matrix (15.6). The

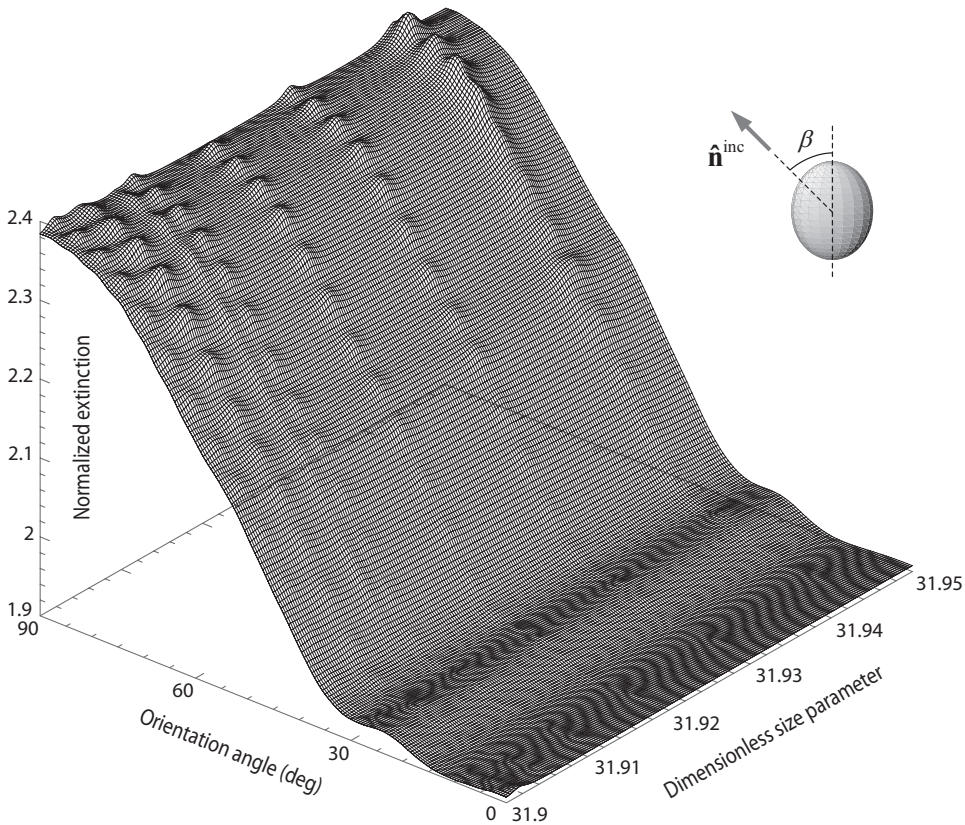

Fig. 17.7. Normalized extinction versus volume-equivalent-sphere size parameter and orientation angle β for a monodisperse prolate spheroid with a relative refractive index of 1.4 and a semi-axis ratio of $a/b = 0.9$ (after Mishchenko and Lacis 2003).

$-F_{12}/F_{11}$ for a sphere or a spheroids is plotted as a function of the scattering angle $\Theta = \theta^{\text{sca}}$ and the surface-equivalent-sphere size parameter $x_{\text{se}} = k_1 r_{\text{se}}$, where r_{se} is the radius of the surface-equivalent sphere. The rotation axis of the spheroids is oriented along the incidence direction (panel b) or perpendicularly to the scattering plane (panel c). With the exception of the region of Rayleigh scattering, the three panels are vastly different. In particular, the polarization patterns for the same spheroids, but in two different orientations, resemble each other no more than either pattern resembles that for the surface-equivalent spheres. The results shown in panel (c) obviously violate the equalities (15.61) and thus cannot be attributed mistakenly to spherically symmetric particles. However, the specific spheroid orientation used to create panel (b) does not cause a violation of Eq. (15.61), which shows that Eq. (15.61) alone may not be used to distinguish unambiguously between a spherically symmetric particle and a nonspherical particle in a fixed orientation.

17.2 Random spherical particle

The majority of natural and artificial ensembles of spherical particles do not exhibit the spike-like resonances described in the preceding section because even a narrow polydispersion washes out features that strongly depend on particle size. Figure 17.8 illustrates the effect of increasing width of the size distribution on the extinction efficiency factor for the gamma size distribution (15.108) of radii for a homogeneous spherical particle with a relative refractive index $m = 1.4$. The fig-

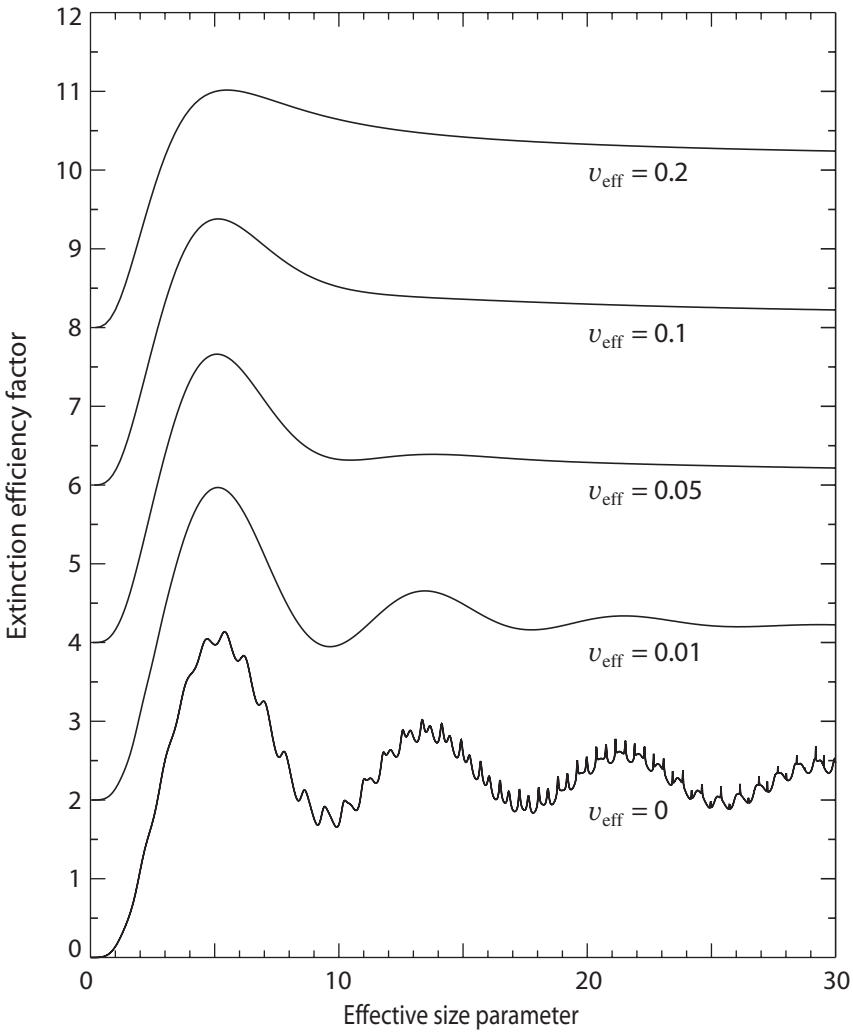

Fig. 17.8. The effect of increasing width of the size distribution on the interference and ripple structures in Q_{ext} for nonabsorbing spherical particles with relative refractive index 1.4. The vertical axis scale applies to the curve with $v_{\mathrm{eff}} = 0$, the other curves being successively displaced upward by 2.

ure depicts $Q_{\text{ext}} = \langle C_{\text{ext}} \rangle / \langle G \rangle$ versus effective size parameter $x_{\text{eff}} = k_1 r_{\text{eff}}$ for five increasing values of the effective variance v_{eff}, where $\langle C_{\text{ext}} \rangle$ and $\langle G \rangle$ are the size-averaged extinction and geometrical cross sections, respectively. The effective radius r_{eff} and the effective variance v_{eff} are defined by Eqs. (15.110) and (15.109) and, for the gamma distribution with $r_{\min} = 0$ and $r_{\max} = \infty$, coincide, respectively, with the parameters a and b of Eq. (15.108) (Problem 15.13). Figure 17.9 demonstrates the broadening of the size distribution with increasing v_{eff}, while the effective radius is kept constant. Note that the size distribution with $v_{\text{eff}} = 0$ corresponds to a monodisperse particle with the radius $r = r_{\text{eff}}$, while the effective variance values in the range [0.05, 0.1] are characteristic of sulfuric acid particles forming the clouds on Venus (Hansen and Hovenier 1974).

Similar to the case of increasing absorption, increasing the width of the size distribution first extinguishes the ripple and then eliminates the interference structure in Q_{ext}. It is in fact remarkable that as narrow a dispersion of sizes as that corresponding to $v_{\text{eff}} = 0.01$ completely washes out the ripple structure. The first major maximum of the interference structure persists to larger values of v_{eff}, but eventually fades away too. For distributions with $0.2 \lesssim v_{\text{eff}}$, the only surviving features are the typical behavior in the Rayleigh limit discussed in Section 17.1 and the asymptotic geometrical optics trend $Q_{\text{ext}} \to 2$ with $x \to \infty$, as discussed in Section 16.2.

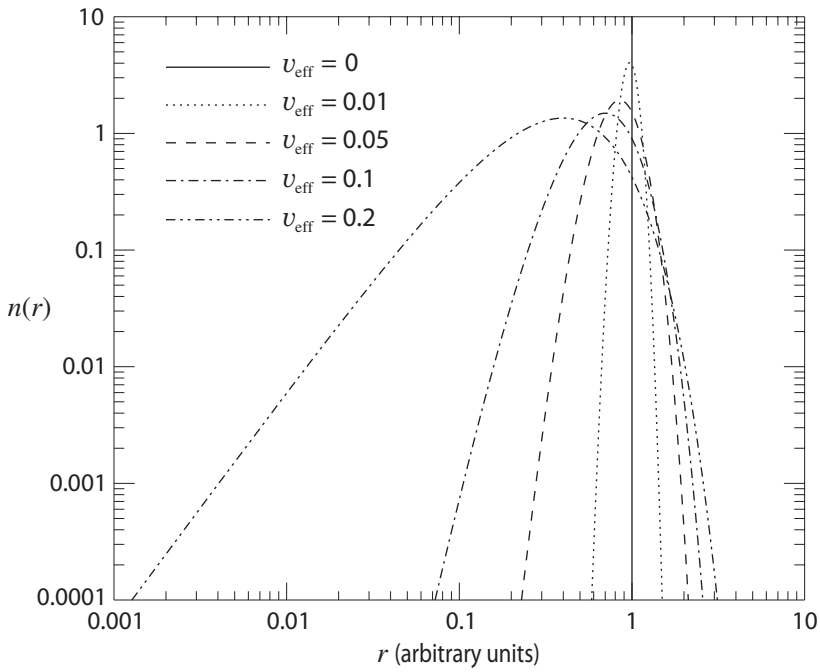

Fig. 17.9. Gamma distribution (15.108) with $r_{\min} = 0$, $r_{\max} = \infty$, $r_{\text{eff}} = 1$ (in arbitrary units of length), and $v_{\text{eff}} = 0$, 0.01, 0.05, 0.1, and 0.2.

The presence of the first maximum of the interference structure for relatively narrow size distributions creates the possibility of an infrequent phenomenon for which aerosol particles of just the right size have a lower extinction cross section in the blue than that at longer wavelengths in the red. Thus, in contrast to the familiar reddening of the setting sun owing to rapidly decreasing Rayleigh extinction with increasing wavelength, a sufficiently narrow size distribution of aerosol particles in the atmosphere, with an average size such that $4 \lesssim 2x_{\text{eff}}\,(m_{\text{R}} - 1) \lesssim 7$ for visible wavelengths (cf. Fig. 17.3), can produce a blue cast to the sun or moon and is perhaps responsible for the implied rarity associated with the phrase, "once in a blue moon" (cf. Chapter 4 of Bohren and Huffman (1983)).

Plate 17.4 shows the evolution of the ratio $-b_1/a_1$ with increasing width of the size distribution. The case $v_{\text{eff}} = 0.01$ demonstrates again that even a very narrow polydispersion is sufficient to extinguish most of the interference and resonance effects. With increasing v_{eff}, the maxima are smoothed out, the minima are filled in, and the polarization becomes more neutral. Additional effects of increasing v_{eff} are the depression to smaller size parameters of the region of maximal polarization corresponding to Rayleigh scattering and the erosion of the bridge of positive polarization connecting the Rayleigh region and the area of positive polarization at scattering angles around 160°. The island of positive polarization at $x_{\text{eff}} \sim 10$ and $\Theta \sim 25°$ for $v_{\text{eff}} = 0.01$ is usually explained as being an anomalous diffraction feature produced by the interference of diffracted light and light reflected and refracted by the particles in the near-forward direction (Hansen and Travis 1974). The magnitude of this feature strongly depends on the width of the size distribution: the feature significantly weakens as v_{eff} increases from 0.01 to 0.07 and has completely disappeared for $v_{\text{eff}} = 0.2$. All these effects of broadening the size distribution are easy to understand qualitatively in terms of taking weighted averages along vertical lines of increasing length in the polarization diagram for a monodisperse particle.

Some phase-function features for a spherical particle larger than the wavelength (Fig. 16.5) can be explained through the concepts of geometrical optics,

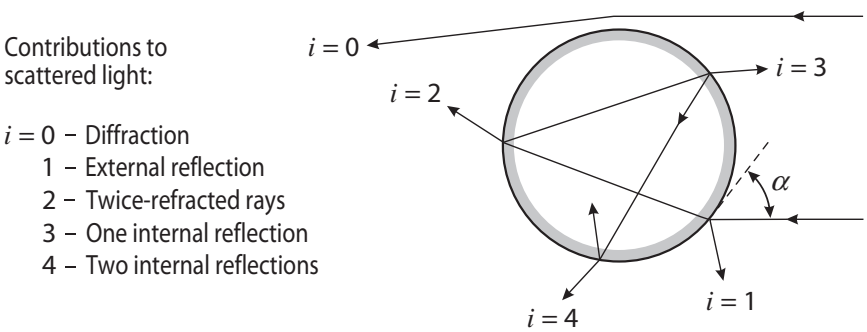

Fig. 17.10. Geometrical optics representation of scattering by a large sphere with $m_{\text{R}} > 1$ (after Hansen and Travis 1974).

using the terminology introduced in Fig. 17.10. Specifically, the concentration of light near $\Theta = 0°$ is caused by diffraction ($i = 0$ in Fig. 17.10). The external reflection ($i = 1$) does not generate any distinctive feature, whereas the twice-refracted rays ($i = 2$) cause a broad enhancement of the phase function in the forward-scattering hemisphere.

The features in Fig. 16.5 at $\Theta \approx 137°$ and 130° for $m = 1.33$ (160° and 88° for $m = 1.53$) are the primary and secondary rainbows generated by $i = 3$ and $i = 4$ rays, respectively. To explain the origin of the rainbows, one needs to express the scattering angle Θ of the emerging ray as a function of the local angle of incidence $\alpha \in [0°, 90°]$ (Fig. 17.10) for $i = 3, 4, \ldots$. This is always possible because the entire ray path remains in the plane containing the incident ray and the center of the sphere. When the derivative $\mathrm{d}\Theta_i(\alpha)/\mathrm{d}\alpha$ vanishes, the scattering angle becomes nearly constant for a range of incidence angles, thereby causing an increased concentration of emerging rays. The respective scattering angle is called the rainbow angle. The condition $\mathrm{d}\Theta_i(\alpha)/\mathrm{d}\alpha = 0$ implies that the rainbow angles correspond to *extrema* of the functions $\Theta_i(\alpha)$. Whether the extremum is a *minimum* or a *maximum* depends on i. The primary rainbow angle 137° for $m =$

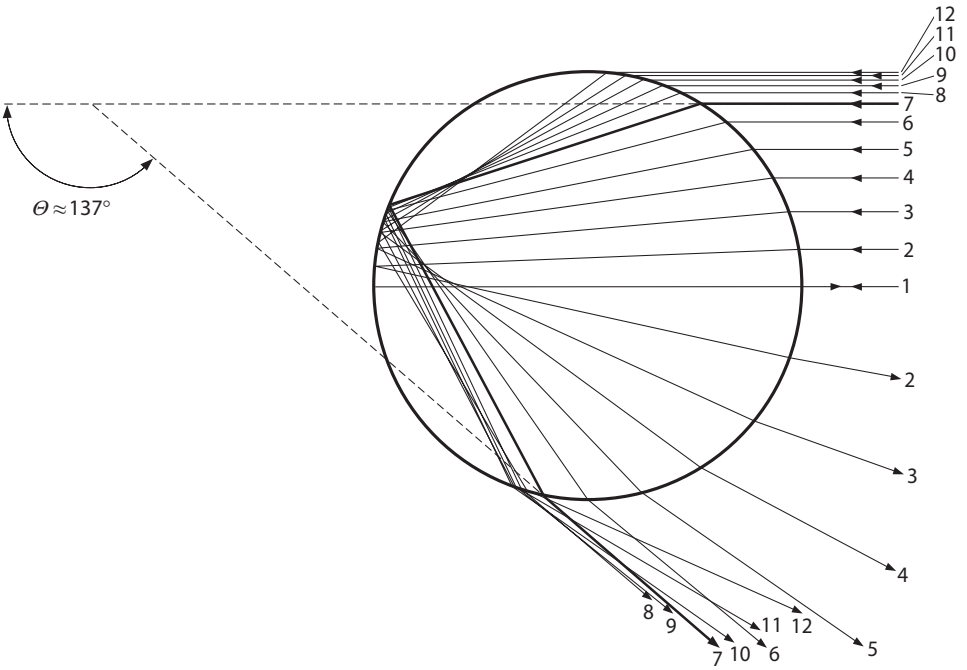

Fig. 17.11. Ray-tracing diagram explaining the origin of the primary rainbow for a large spherical particle with $m = 1.33$. The diagram shows that incident rays corresponding to a finite range of incidence angles α emerge at almost the same scattering angle, thereby creating a localized enhancement of intensity. The respective scattering angle $\Theta \approx 137°$ is the angle of minimum deviation for $i = 3$.

1.33 (160° for m = 1.53) corresponds to a minimum in $\Theta_3(\alpha)$ (ray 7 in Fig. 17.11), whereas the angle 130° for m = 1.33 (88° for m = 1.53) corresponds to a maximum of $\Theta_4(\alpha)$. As a consequence, there is a low-intensity zone (about 7° wide for m = 1.33 and 72° wide for m = 1.53) between the primary and secondary rainbows (the so-called Alexander's dark band), where the phase function is mostly determined by the externally reflected rays (i = 1). Note, however, that both rainbow angles correspond to rays that experience the least *cumulative* deviation from the initial incidence direction and hence are angles of *minimum deviation*. The maxima in Fig. 16.5 at $\Theta = 119°$ and 141° for m = 1.53 are the i = 6 and 7 rainbows, respectively.

The slight change of the rainbow angle with wavelength caused by dispersion (change of the relative refractive index with wavelength) gives rise to the spectacular colorful rainbows often observed during showers illuminated by the sun at an altitude lower than about 40°. Examples of beautiful rainbows are shown on the cover of this book as well as in Plate 17.5a. In the latter case, a full-color numerical Lorenz–Mie simulation (Laven 2003) is superimposed on a photograph of the primary and secondary rainbows, and illustrates the remarkable ability of the LMT to reproduce actual scattering phenomena.

The enhancement of intensity in the backscattering direction ($\Theta \approx 180°$) is called the "glory" and can be seen for objects such as fog (Plate 17.5b) or clouds (Plate 17.5c) as a series of colored rings around the shadow cast by the photographer or the airplane. Obvious but relatively weak contributors to the glory are the central rays ($\alpha = 90°$) externally (i = 1) and internally (i = 3, 5, …) reflected in the backscattering direction. Snell's law predicts that for real relative refractive indices in the range $2^{1/2} \le m \le 2$, a non-central incident ray ($0° < \alpha < 90°$ in Fig. 17.10) may emerge at $\Theta = 180°$ after just one internal reflection (i = 3). However, this ray-optics mechanism does not explain the equally pronounced glory generated by water droplets with $m = 1.33\,(< 2^{1/2})$ and x_{eff} = 600 in Fig. 16.5. Therefore, it is often claimed that a major contributor to the glory is that of the edge rays ($\alpha \approx 0°$), which set up so-called surface waves on the sphere. The latter are not included in the geometrical optics formulation and are discussed by van de Hulst (1957) and Nussenzveig (1992).

17.3 Random morphologically complex particle

In the case of a random nonspherical particle, far-field scattering patterns can be affected by averaging over particle orientations and/or morphologies, as well as sizes. We begin by discussing the effects of nonsphericity and random orientation on scattering resonances. Plate 17.6a summarizes the results of LMT and TMM computations for a monodisperse sphere and volume-equivalent, randomly oriented spheroids with a relative refractive index of 1.4 in the range of size parameters affected by three super-narrow Lorenz–Mie resonances b_{38}^1, a_{38}^1, and b_{39}^1, as well as three broader resonance features. Now the direction-independent

normalized extinction is defined as the ratio $\widetilde{C}_{\text{ext}} = \langle C_{\text{ext}}(\xi)\rangle_{\xi} / (\pi r_{\text{ev}}^2)$, where $\langle C_{\text{ext}}(\xi)\rangle_{\xi}$ is the orientation-averaged extinction cross section. It is seen that increasing the aspect ratio ε of the spheroids (i.e., the ratio of the largest to the smallest particle dimensions) drastically reduces the height of the normalized extinction peaks. It is in fact remarkable that the deformation of a sphere by as little as one hundredth of a wavelength essentially annihilates the super-narrow resonances. A secondary effect of increasing asphericity is to shift the resonances toward smaller size parameters. Obviously, it takes significantly larger asphericities to suppress the broader resonances. An interesting feature of the curve for $a/b = 0.9$ is the minute high-frequency ripple superposed on a slowly and weakly varying background. This ripple is absent in the curves for the nearly spherical spheroids and is the contribution of additional natural frequencies of oscillation of distinctly aspherical spheroids with specific orientations relative to the incident beam. This effect is well seen in Fig. 17.7.

The smoothing effect of averaging over orientations of a nonspherical particle on resonances is also well seen from the comparison of Plates 17.3b, 17.3c, and 17.3d. Averaging over sizes reinforces this effect. This is demonstrated by Plates 17.3e and 17.3f, which parallel plates 17.3a and 17.3d, respectively, and show the ratio $-\langle F_{12}(\Theta;\xi)\rangle_{\xi} / \langle F_{11}(\Theta;\xi)\rangle_{\xi}$ computed for a polydisperse sphere and a randomly oriented surface-equivalent spheroid, assuming a modified power-law size distribution defined by

$$n(r) = \begin{cases} \text{constant}, & 0 \le r \le r_1, \\ \text{constant} \times (r/r_1)^{\alpha}, & r_1 \le r \le r_2, \\ 0, & r_2 < r \end{cases} \tag{17.1}$$

with $\alpha = -3$ and $v_{\text{eff}} = 0.1$. The resulting polarization patterns are now smooth enough to derive conclusions regarding the likely qualitative and quantitative effects of nonsphericity of natural polydisperse particles. Among such effects are the bridge of positive polarization at side-scattering angles and a negative polarization branch at backscattering angles in Plate 17.3f, which are quite analogous to those measured previously for narrow size distributions of NaCl particles with mean size parameters ranging from 3.1 to 19.9 (Perry *et al.* 1978), as well as for other types of mineral particles (see Volten *et al.* (2001), Shkuratov *et al.* (2007), Muñoz and Hovenier (2011), Meland *et al.* (2012), and references therein).

Due to the unique properties of the super-narrow resonances, the measurement and analysis of their various manifestations turn out to be the most accurate means for the detection of even minute deviations of the particle shape from sphericity. The fact that even miniscule amounts of nonsphericity effectively extinguish the super-narrow resonances (Mishchenko and Lacis 2003) is likely to simplify numerical computations for polydisperse particle ensembles such as natural cloud droplets. Indeed, it has been hypothesized that not fully resolving the resonances owing to the use of a numerical size-integration quadrature form-

ula with insufficiently narrow separations between the quadrature nodes may result in significant errors in broadband absorption computations (Zender and Talamantes 2006). The analysis by Zender and Talamantes was based on the assumption that cloud droplets are perfect spheres and support even the narrowest resonances, thereby seemingly necessitating the use in Eq. (13.141) of quadrature formulas with extreme numbers of closely spaced quadrature nods and making computer calculations very time-consuming. However, real cloud droplets hardly have a perfectly spherical shape, given many ambient factors that are likely to cause significant distortions of the droplet shape and thereby suppress the super-narrow resonances.

Despite the significant progress in our ability to model scattering by nonspherical particles, accurate theoretical computations for many types of natural and artificial particles with sizes comparable to and greater than the wavelength (Fig. 1.1) remain problematic. Therefore, there have been several attempts to simulate the scattering and absorption properties of actual particles using simple model shapes. These attempts have been based on the realization that in addition to size and orientation averaging, as discussed above, averaging over shapes may also prove to be necessary in many cases. Indeed, quite often ensembles of natural and artificial particles exhibit a vast variety of shapes, which makes questionable the utility of a single model shape (however "irregular" it may look to the human eye) in the representation of scattering properties of an ensemble.

To illustrate this point, Plate 17.6b shows the results of TMM computations of the phase function $a_1(\Theta)$ versus scattering angle for a polydisperse sphere and seven polydisperse surface-equivalent prolate spheroids in random orientation (Mishchenko *et al.* 1997). The size distribution is described by a truncated log normal law and has an effective radius of 1.163 μm and an effective variance of 0.168. The relative refractive index is fixed at 1.53 + i0.008, assuming a visible wavelength of 443 nm; the former value is typical of terrestrial desert-dust aerosols at visible wavelengths. The spheroid aspect ratio varies from 1 (the value for the sphere) to 2.4. Plate 17.6b demonstrates that even after size and orientation averaging, each spheroidal shape produces a unique, shape-specific scattering pattern, whereas laboratory and *in situ* measurements for real nonspherical particles usually show rather featureless patterns. Indeed, although the individual phase functions in Plate 17.6b are rather smooth they still reveal a systematic change with increasing aspect ratio that renders each phase-function curve unique and dissimilar to all other curves. However, Plate 17.6c shows that this uniqueness is suppressed and ultimately removed by averaging over: (i) prolate spheroids with aspect ratios ranging from 1.2 to 2.4 in steps of 0.1; (ii) oblate spheroids with the same aspect ratios; and (iii) over all prolate and oblate spheroids. The final phase function (the red curve in Plate 17.6c) is very smooth and featureless and, in fact, almost perfectly coincides with the phase function experimentally measured by Jaggard *et al.* (1981) for micrometer-sized, irregularly shaped soil particles.

This example leads to two important conclusions. First of all, it provides evidence that the often observed smooth scattering-angle dependence of the elements of the scattering matrix for natural and artificial ensembles of nonspherical particles is largely caused by the diversity of particle shapes in the ensemble. Secondly, it suggests that at least some scattering properties of ensembles of irregular particles can be adequately modeled using polydisperse shape mixtures of simple particles such as spheroids. These two conclusions form the gist of the so-called statistical approach, according to which particles chosen for the purpose of ensemble averaging need not be in one-to-one morphological correspondence with the actual particle ensemble and may have relatively simple shapes (Hill *et al.* 1984; Mishchenko *et al.* 1997). Needless to say, forming representative mixtures of less regular particles than spheroids should be expected to eventually provide an even better model of electromagnetic scattering by many natural and artificial particle ensembles (see, e.g., the reviews by Nousiainen (2009) and Kahnert *et al.* (2014)).

The statistical approach is further illustrated in Fig. 17.12, in which the diamonds depict the results of laboratory measurements of the ensemble-averaged scattering matrix for micrometer-sized feldspar particles at a wavelength of 633 nm (Volten *et al.* 2001). The grey curves show that the measurement data can be accurately fitted with TMM results computed for a shape mixture of polydisperse, randomly oriented prolate and oblate spheroids (Dubovik *et al.* 2006). The real and model particle shapes are contrasted in the inset.

The black curves in Fig. 17.12 show the results of Lorenz–Mie computations for a volume-equivalent polydisperse spherical particle. Contrasting the grey and the corresponding black curves provides a good illustration of the typical nonspherical–spherical differences in the elements of the scattering matrix discussed in detail in MTL1. For example, several theoretical and laboratory analyses of the phase-function patterns for volume- or surface-equivalent spherical and nonspherical particles have revealed the following five distinct scattering-angle ranges:

$$\begin{array}{ll} \text{nonsphere} \approx \text{sphere} & \text{from } \Theta = 0^\circ \text{ to } \Theta \sim 15^\circ - 20^\circ; \\ \text{nonsphere} > \text{sphere} & \text{from } \Theta \sim 15^\circ - 20^\circ \text{ to } \Theta \sim 35^\circ; \\ \text{nonsphere} < \text{sphere} & \text{from } \Theta \sim 35^\circ \text{ to } \Theta \sim 85^\circ; \\ \text{nonsphere} \gg \text{sphere} & \text{from } \Theta \sim 85^\circ \text{ to } \Theta \sim 150^\circ; \\ \text{nonsphere} \ll \text{sphere} & \text{from } \Theta \sim 150^\circ \text{ to } \Theta = 180^\circ. \end{array} \tag{17.2}$$

Although the specific boundaries of these regions can shift with particle morphology and relative refractive index, the enhanced side-scattering and suppressed backscattering appear to be rather universal characteristics of nonspherical particles.

The ratio $-b_1(\Theta)/a_1(\Theta)$, which yields the signed degree of linear polarization for unpolarized incident light, tends to be positive at scattering angles around $100^\circ - 120^\circ$ for nonspherical particles. Equation (15.79) implies that $a_2(\Theta)/a_1(\Theta) \equiv 1$ for spherically symmetric scatterers, whereas the same ratio for nonspherical

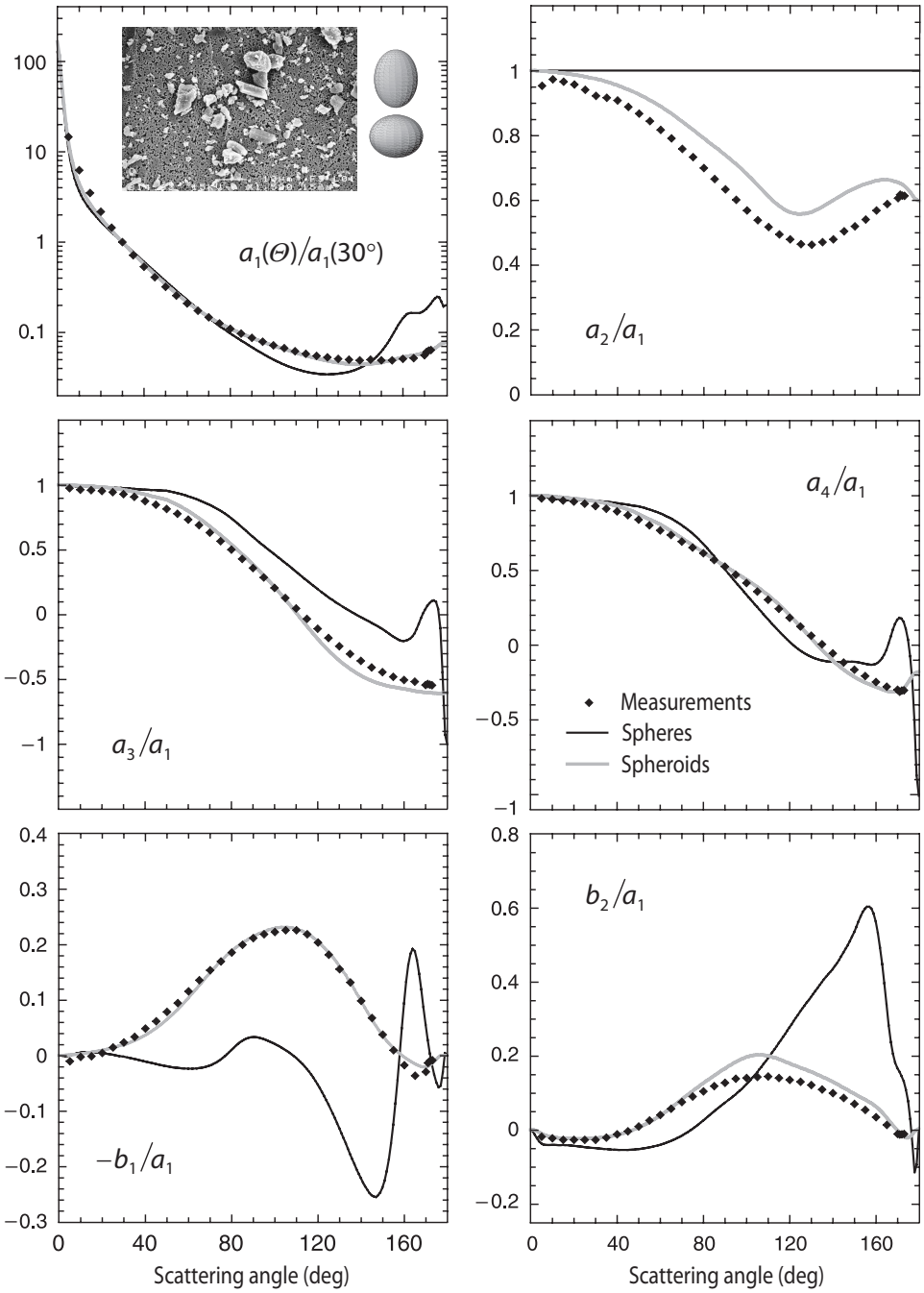

Fig. 17.12. Comparison of laboratory measurements and theoretical computations of the normalized scattering matrix obtained by averaging over particle states (see text).

particles deviates significantly from the value 1 and exhibits strong backscattering depolarization. Similarly, $a_3(\Theta)/a_1(\Theta) \equiv a_4(\Theta)/a_1(\Theta)$ for spherically symmetric particles, whereas the ratio $a_4(\Theta)/a_1(\Theta)$ for nonspherical particles tends to be greater than the ratio $a_3(\Theta)/a_1(\Theta)$ at most scattering angles and especially in the backscattering direction. The ratios $b_2(\Theta)/a_1(\Theta)$ for spherical and nonspherical particles also reveal significant quantitative differences, especially at large scattering angles.

Unlike a mixture of smooth-shaped spheroids with different aspect ratios, regular sharp-edged shapes may cause pronounced angular features in the elements of the scattering matrix, especially as the particle size starts to exceed the wavelength. This is well illustrated by Fig. 16.6, which shows the results of numerically exact TMM computations of the phase function for four randomly oriented compact circular cylinders with surface-equivalent-sphere size parameters ranging from 40 to 180. As the size parameter increases, the TMM phase function develops such typical geometrical-optics features – seen in the grey curves – as the 46° halo and the strong and narrow backscattering peak. The halo is produced by the same ray-tracing mechanism as the rainbows discussed in Section 17.2 and corresponds to a minimum angle of deviation for the 90° prisms formed by the side and end faces (Fig. 17.13a), whereas the backscattering peak is caused by rays twice internally reflected by mutually perpendicular faces (Fig. 17.13b). Such pronounced phase-function features caused by regular sharp-edged shapes are responsible for many spectacular atmospheric-optics displays (Lynch and Livingston 2001) and may affect the results of cirrus-cloud remote sensing (e.g., Mishchenko et al. 1996; Lynch et al. 2002). In many cases, however, various imperfections of the ice-crystal shape and/or multiple internal inclusions (e.g., in the form of air bubbles) destroy sharp geometrical-optics features and cause smooth and featureless phase functions similar to that depicted by diamonds in Fig. 17.12 (Macke 2000; Baran 2013).

We have already mentioned that backscattering depolarization measurements are widely used for detecting and characterizing nonspherical particles (Sassen

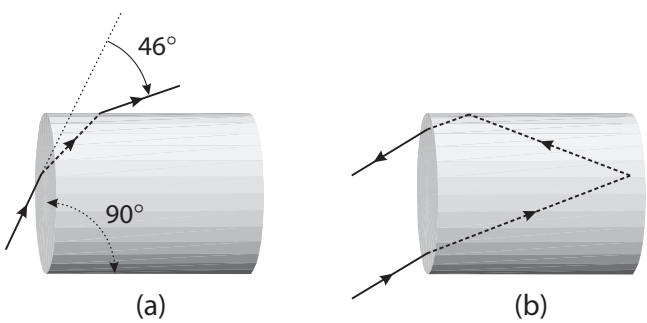

Fig. 17.13. **(a)** Refraction by a circular ice cylinder showing the rays associated with the 46° halo. **(b)** Double internal reflections causing the backscattering intensity peak.

2000). Plate 17.7a summarizes the results of TMM computations of the linear backscattering depolarization ratio (15.62) for polydisperse, randomly oriented ice spheroids with aspect ratios ranging from 1.05 to 2.6 and circular cylinders with various length-to-diameter or diameter-to-length ratios (after Mishchenko and Sassen 1998). The relative refractive index is fixed at 1.311, which is a value characteristic of water ice at visible wavelengths. The light-green bands show the range of highest depolarization ratios typically observed for anthropogenic cirrus clouds in the form of aircraft condensation trails (Freudenthaler *et al.* 1996). The size distribution is given by Eq. (17.1) with $\alpha = -3$ and a fixed effective variance of 0.1. The upper horizontal axes convert effective size parameters into effective radii assuming the 532-nm wavelength.

The results depicted in Plate 17.7a demonstrate indeed that wavelength-sized particles can produce large backscattering depolarization ratios approaching the theoretical upper limit of 1, Eq. (15.113). An interesting trait of essentially all the curves shown in this plate is a rapid increase in δ_{L} as the effective size parameter increases from 0 to about 10. Moreover, maximal δ_{L} values for most shapes are observed at size parameters close to and sometimes slightly smaller than 10. Unfortunately, the TMM results show no obvious relationship between δ_{L} and the particle aspect ratio. Even spheroids with aspect ratios as small as 1.05 (a 2.5% deviation from the perfect spherical shape) produce strong depolarization. In fact, the largest δ_{L} values are generated by prolate spheroids with aspect ratios as small as 1.2 (a 10% deviation from a sphere). Furthermore, the δ_{L} for spheroids and, especially, cylinders tends to saturate with increasing aspect ratio. These results suggest that although a nonzero δ_{L} value is an unequivocal indication of particle nonsphericity, it is not necessarily a measure of the degree of deviation of the particle shape from that of a perfect sphere.

TMM results plotted in Figs. 17.14 and 17.15 show that with increasing imaginary part of the relative refractive index, nonspherical–spherical differences weaken and ultimately disappear. For these particle polydispersions with an effective size parameter of $x_{\mathrm{eff}} = 15$, the scattering patterns corresponding to $m_{\mathrm{I}} = 0.5$ are dominated by diffraction and external reflections, and are essentially the same for a sphere and a surface-equivalent randomly oriented spheroid. This example illustrates the general GOM theorem formulated by van de Hulst (1957, Section 8.42): the scattering pattern caused by external reflection from a very large convex particle in random orientation is identical to that caused by external reflection from a very large sphere composed of the same material. Similarly, increasing m_{I} leads to reduced and ultimately vanishing backscattering depolarization ratios, as TMM results depicted in Fig. 17.16 illustrate. This factor limits the usefulness of depolarization observations of cirrus clouds and contrails at infrared wavelengths, where water ice is strongly absorbing. It is interesting, however, that the change of δ_{L} and δ_{C} with increasing absorption is not entirely monotonous and reveals a maximum at $m_{\mathrm{I}} \approx 2\times10^{-2}$, which illustrates again the intrinsic complexity of these far-field observables.

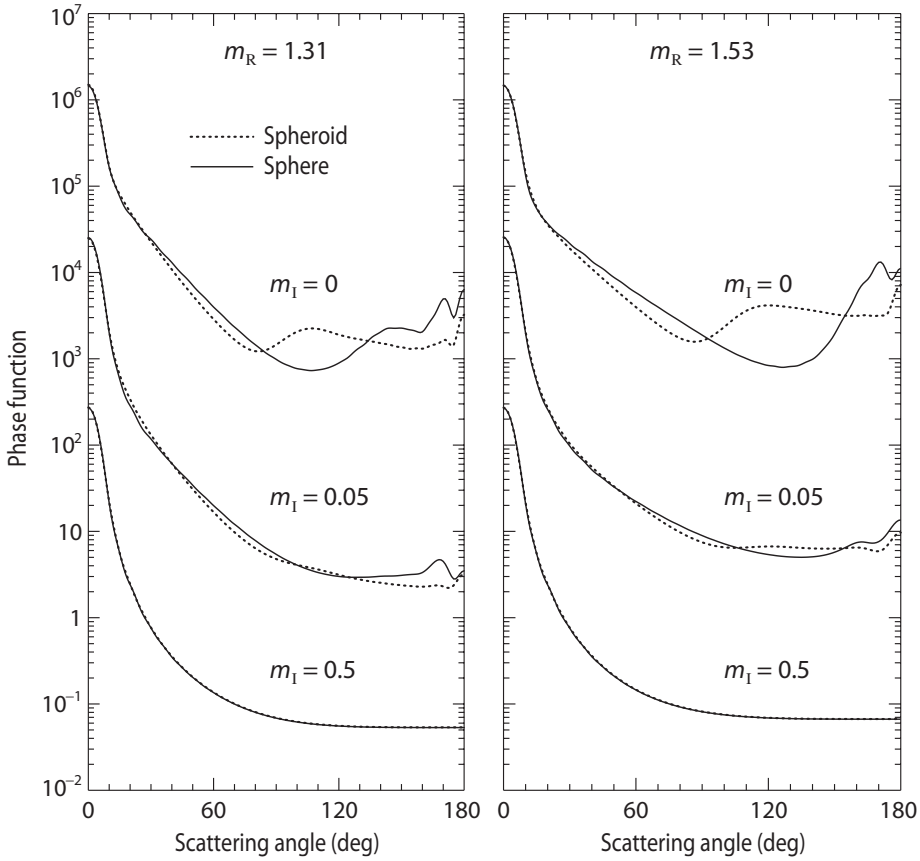

Fig. 17.14. Phase function a_1 versus scattering angle Θ for polydisperse, randomly oriented oblate spheroids with an aspect ratio of 1.7 and for surface-equivalent spheres. The results are shown for two values of the real part of the relative refractive index (m_R = 1.31 and 1.53) and three values of the imaginary part (m_I = 0, 0.05, and 0.5). The size distribution is given by Eq. (17.1) with $\alpha = -3$ and $v_{\text{eff}} = 0.1$. The effective size parameter is $x_{\text{eff}} = 15$. The vertical axis scale applies to the curves with m_I = 0.5, the other curves being successively displaced upward by a factor of 100.

In most cases nonspherical–spherical differences in the optical cross sections and the single-scattering albedo are not nearly as significant as those in the scattering matrix elements. The same is true of the asymmetry parameter (15.67). This does not mean, however, that the effects of nonsphericity on the integral scattering and absorption characteristics are always negligible or unimportant. An instructive example of particles characterized by integral radiometric properties vastly different from those of volume-equivalent spheres are clusters composed of large numbers of small monomers such as soot aggregates (see Fig. 1.1e). The overall morphology of a dry soot aerosol is usually parameterized by the following statistical scaling law (Sorensen 2001):

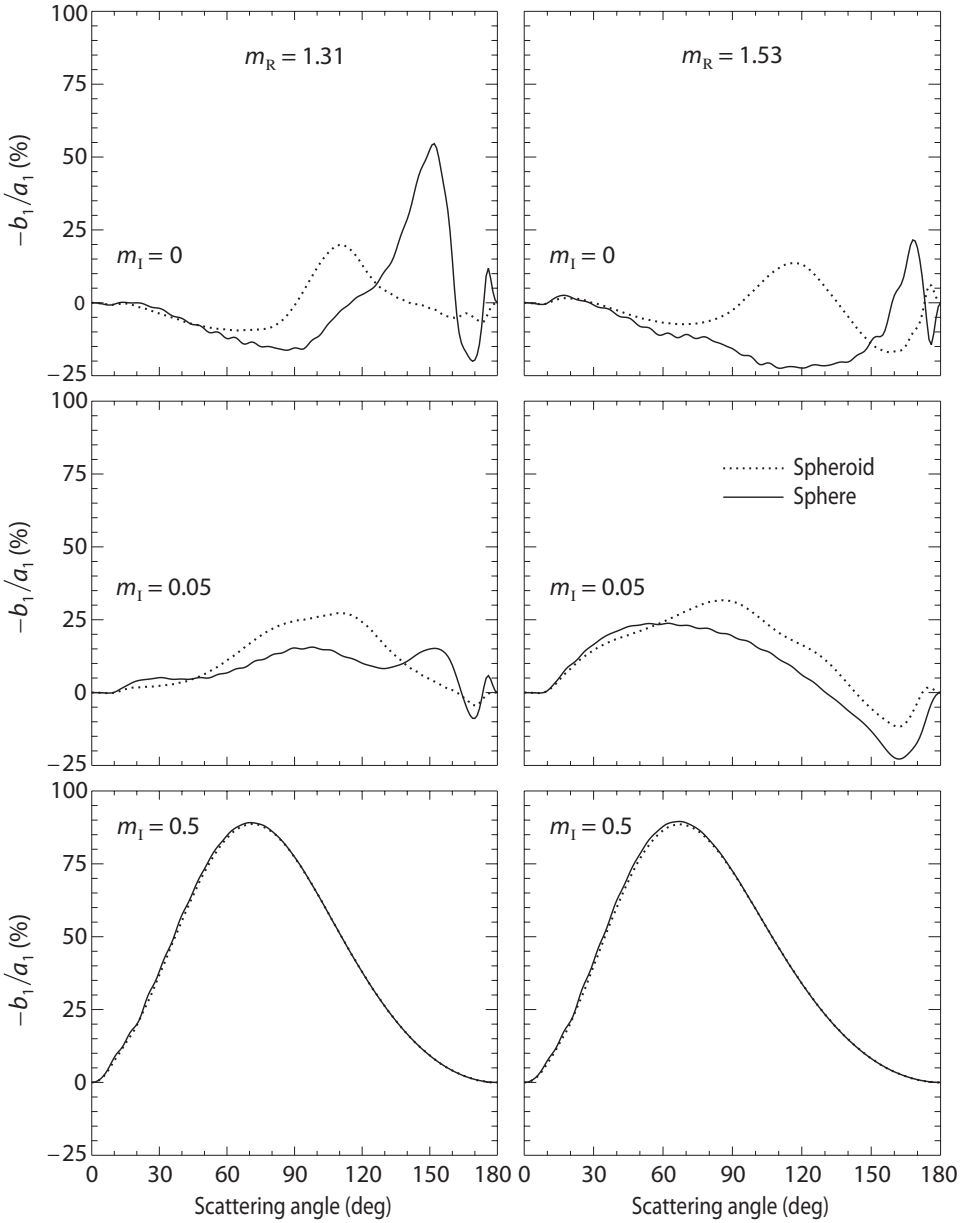

Fig. 17.15. As in Fig. 17.14, but for the ratio $-b_1/a_1$.

$$N_S = k_0(R_g/a)^{D_f}, \tag{17.3}$$

where N_S is the number of spherical monomers in the cluster, a is the monomer mean radius, k_0 is the prefactor, D_f is the fractal dimension, and R_g, called the radius of gyration, is a measure of the overall cluster radius. The fractal dimen-

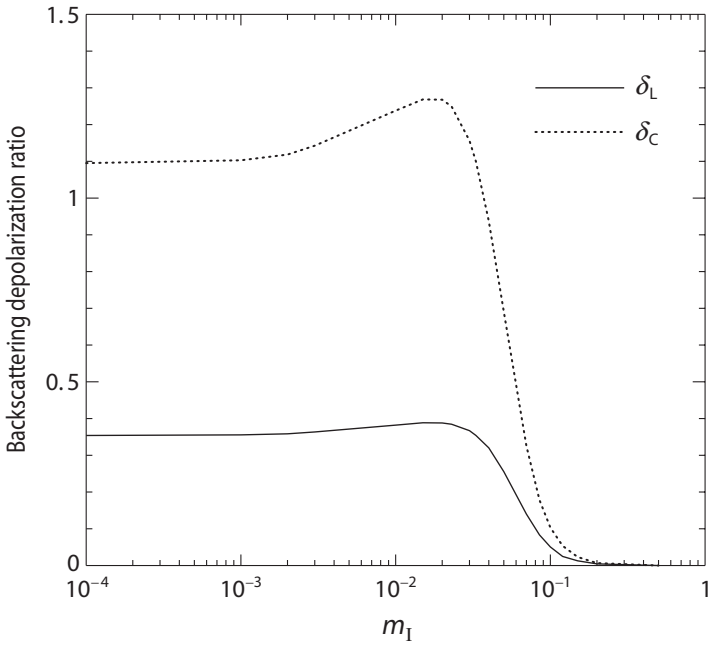

Fig. 17.16. Linear and circular backscattering depolarization ratios versus imaginary part of the relative refractive index for a polydisperse, randomly oriented oblate spheroid with an aspect ratio of 1.7. The size distribution is given by Eq. (17.1) with $\alpha = -3$ and $v_{\text{eff}} = 0.1$. The effective surface-equivalent-sphere size parameter is $x_{\text{eff}} = 15$ and the real part of the relative refractive index is 1.31.

sion is especially important for the quantitative characterization of the aggregate morphology. Compact densely packed aggregates have D_f values close to 3, whereas the fractal dimension of chain-like branched clusters can be significantly smaller. The other important structural coefficient, k_0, is also related to the state of compactness of a fractal aggregate. Examples of computer-generated fractal clusters are given in Fig. 17.17. Obviously, the aggregates become more compact as D_f increases.

Figure 17.18 depicts the ratios of $\langle C_{\text{ext}}(\xi)\rangle_\xi$, $\langle C_{\text{sca}}(\xi)\rangle_\xi$, $\langle C_{\text{abs}}(\xi)\rangle_\xi$, ϖ, and g computed, at a wavelength of 870 nm, for randomly oriented fractal soot aggregates with refractive indices 1.75 + i0.5 and 2 + i, monomer radii 15 and 25 nm, and numbers of monomers 200, 400, 600, and 800 to those for the corresponding volume-equivalent homogeneous spheres (Liu *et al.* 2008). These numerically exact STMM results demonstrate that the integral radiometric properties of the soot clusters are complex functions of the monomer size and refractive index and can often be profoundly different from those of the equal-volume spheres. The latter is especially true of the scattering cross section, single-scattering albedo, and asymmetry parameter. Not surprisingly, the overall differences in the integral

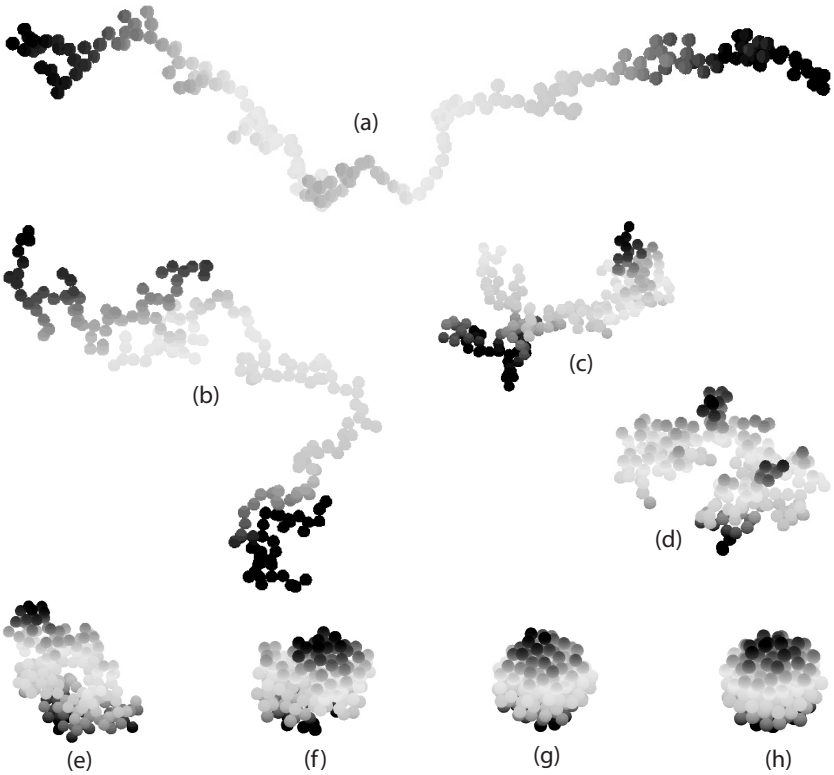

Fig. 17.17. Fractal aggregates composed of 200 monomers and characterized by different values of the fractal parameters D_f and k_0. **(a)–(g)** $D_f = 1.25$, 1.5, 1.75, 2, 2.25, 2.5, and 2.75, respectively; k_0 is fixed at 1.6. **(h)** $D_f = 3$ and $k_0 = 1.2$.

optical characteristics between an aggregate and the corresponding equal-volume sphere become smaller as the fractal dimension approaches the value 3 and the cluster becomes increasingly compact. The likely explanation of the residual differences between the STMM results for a cluster and the Lorenz–Mie results for the equivalent-volume sphere could be that the cluster still has empty spaces in it, even as $D_f \to 3$.

Figure 17.19 shows the results of STMM computations of the scattering matrix elements obtained by averaging over 20 soot-cluster realizations randomly computer-generated for the same values of the fractal parameters (Liu and Mishchenko 2007). In a rather peculiar way (West 1991), the angular scattering properties of the soot clusters appear to be a mix of those of wavelength-sized compact particles (the nearly isotropic Rayleigh phase function of the small individual spherules evolves into a forward-scattering phase function) and Rayleigh scatterers (i.e., $-b_1(\Theta)/a_1(\Theta)$ is zero at the exact forward- and backscattering directions and reaches a nearly 100% maximum at $\Theta \approx 90°$, while the ratio $b_2(\Theta)/a_1(\Theta)$ is very close to zero; see Fig. H.2). The deviation of the ratio

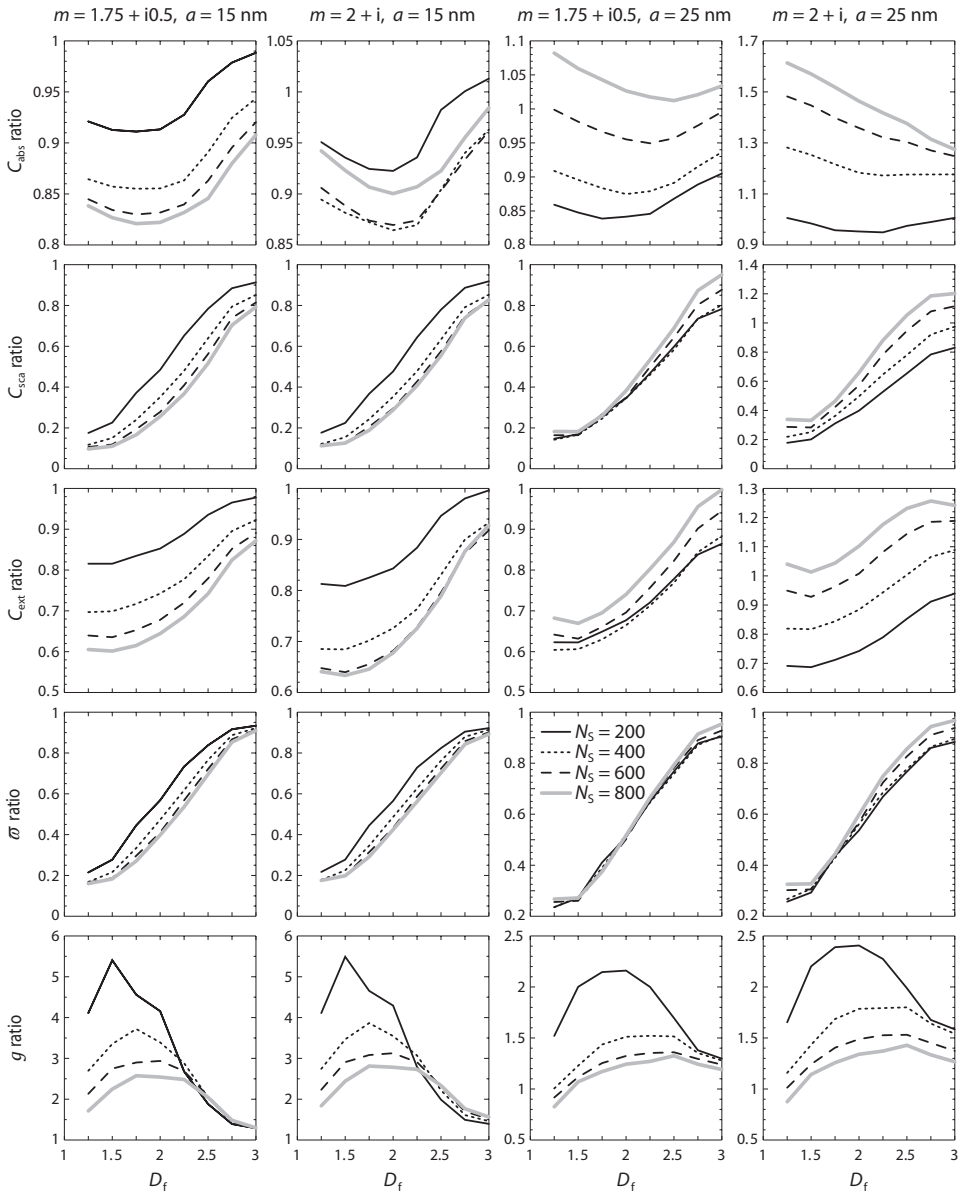

Fig. 17.18. Ratios of integral optical characteristics of soot fractals to those computed for the respective volume-equivalent spheres. The wavelength is fixed at 870 nm.

$a_2(\Theta)/a_1(\Theta)$ from unity is the only obvious manifestation of the overall non-sphericity of the soot clusters.

Also shown for comparison in Fig. 17.19 are two sets of approximate results. The first set includes the results obtained by applying the FOSA to the corres-

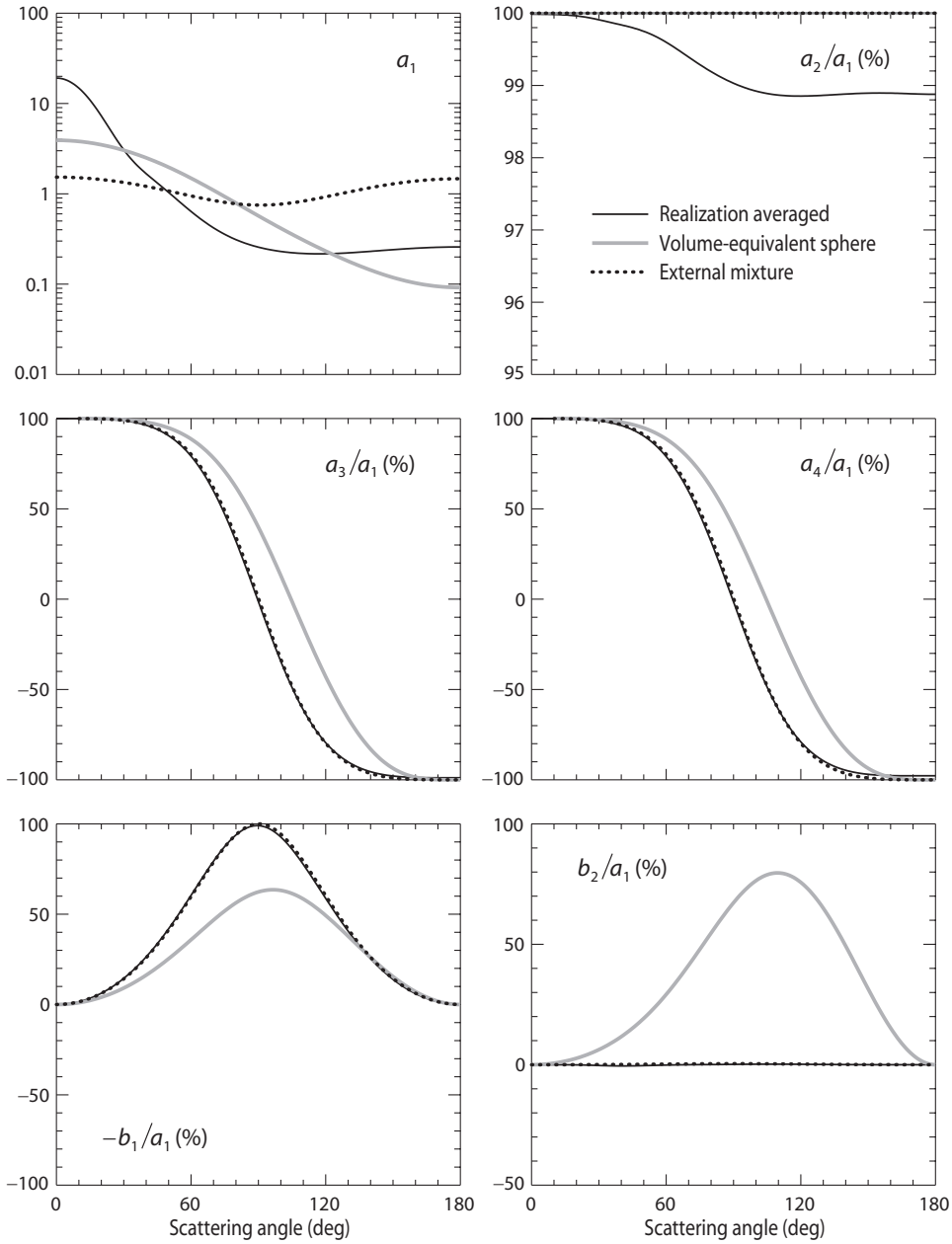

Fig. 17.19. Realization-averaged scattering matrix elements for randomly oriented fractal clusters with $D_f = 1.82$, $k_0 = 1.19$, $N_S = 400$, and $a = 0.02$ μm. The soot refractive index is 1.75 + i0.435 and the wavelength is 628 nm. Also shown are the results for the corresponding homogeneous volume-equivalent sphere and the "equivalent" external mixture of soot monomers.

ponding external mixture of the constituent monomers (i.e., by assuming that all monomers are widely separated and randomly positioned rather than form a cluster with touching components). The second set of results was computed by applying the Lorenz–Mie theory to a homogeneous sphere with a volume equal to the combined volume of the cluster monomers. Clearly, the external-mixture model provides a poor representation of the cluster phase function, whereas the performance of the equal-volume-sphere model is inadequate with respect to all scattering matrix elements.

A far-field characteristic that strongly depends on the particle morphology is the LPR defined by Eq. (H.40). This quantity is identically equal to zero for a spherically symmetric particle, but, according to Eq. (H.47) and Fig. H.3, can reach 100% for a nonspherical Rayleigh particle in random orientation. Figure 17.20 summarizes the results of STMM and TMM computations of $\mu_L(\Theta)$ for five nonspherical morphologies:

(i) a low-density fractal aggregate with a fractal dimension of $D_f = 1.82$ and a prefactor of $k_0 = 1.19$, composed of 422 identical soot spherules with a radius of 20 nm;

(ii) 422 soot spherules with the same radius densely and randomly compacted inside an imaginary circumscribing sphere with a radius of 225 nm;

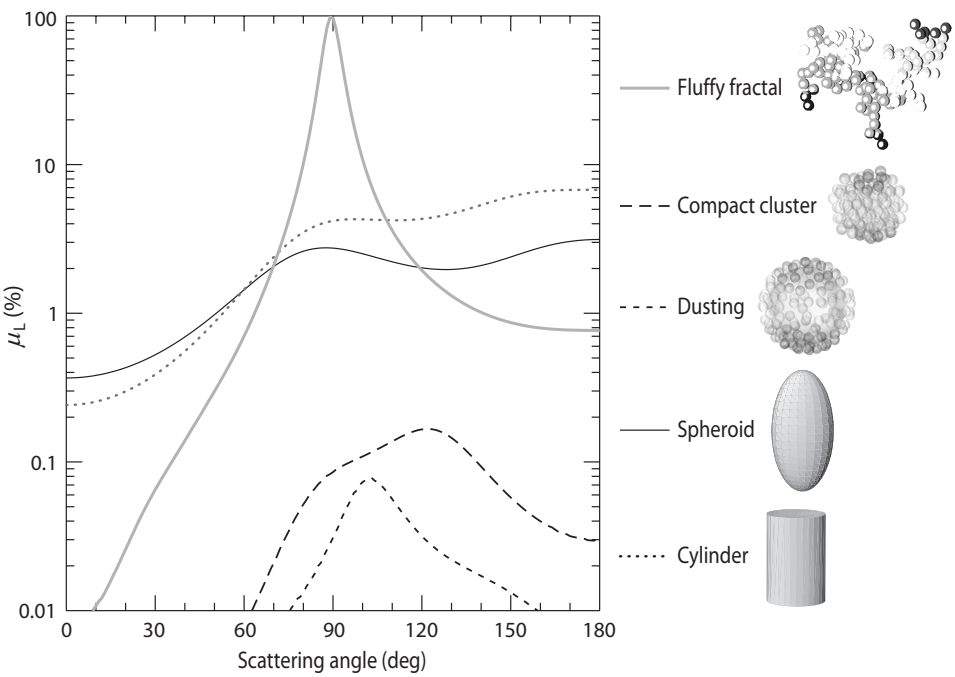

Fig. 17.20. Linear polarization ratio for five particle morphologies (see text).

(iii) 422 soot spherules with the same radius randomly covering a larger non-absorbing sulfate particle with a radius of 260 nm;

(iv) an equiprobable shape mixture of 10 prolate and oblate soot spheroids with aspect ratios 1.2, 1.4, 1.6 , 1.8, and 2; and

(v) an equiprobable shape mixture of 11 soot circular cylinders with diameter-to-length ratios 1/2, 1/1.8, 1/1.6, 1/1.4, 1/1.2, 1, 1.2, 1.4, 1.6 , 1.8, and 2

(Mishchenko *et al.* 2013b). The wavelength is fixed at 550 nm, the relative refractive indices of the soot and sulfate particles are assumed to be 1.75 + i0.435 and 1.44, respectively, and the equal-volume-sphere radius of the soot material in all five cases is 150 nm. The results for morphologies (i)–(iii) have been ensemble-averaged over 10 random computer realizations of each morphological type in order to provide a more realistic modeling of natural particle mixtures and ensure smooth LPR curves.

A remarkable feature of the grey curve in Fig. 17.20 is a sharp maximum at $\Theta \approx 90°$, which makes the central part of this curve very similar to that of the dashed curve in Fig. H.3 corresponding to the anisotropy parameter $y \sim 1.01$. We can thus conclude that, although the low-density soot fractal is not a Rayleigh scatterer, its LPR behaves analogously to that of a randomly oriented Rayleigh particle with a weakly anisotropic polarizability. This result is not surprising. In the framework of the FOSA, wherein each monomer is assumed to be excited only by the incident field, the LPR of a random soot cluster composed of spherical monomers would be exactly zero. This implies that a nonzero LPR must result from electromagnetic interactions between the monomers. However, the strongly absorbing nature of the soot material acts to suppress multi-monomer interactions, which makes it reasonable to assume that for a fluffy aggregate the nonzero LPR is caused primarily by double-scattering interactions between pairs of contacting monomers, the size parameter of such monomer doublets still being in the Rayleigh domain. It is thus the shape-induced anisotropic polarizability of these Rayleigh doublets that causes the sharp side-scattering peak in the angular profile of the LPR for fluffy soot fractals.

The multi-monomer interactions can be expected to be much stronger in the case of a densely packed soot aggregate, owing to the fact that almost every monomer is now surrounded by many closely positioned monomers rather than being quasi-isolated. As a consequence, the resulting LPR must be affected by the overall shape of the cluster. It is seen indeed from Fig. 17.20 that densely packing the same number of soot monomers into a compact, nearly spherical cluster reduces the magnitude of the LPR maximum by almost two orders of magnitude. The maximum LPR value for habit (iii) is even smaller, owing to the scattering dominance of the large spherical host. The LPR curves for the ensemble-averaged spheroid and cylinder are rather close to each other, exhibit a near-monotonous increase with scattering angle by about an order of magnitude, and show the highest δ_{L} values.

17.4 Optical characterization

As we have mentioned in Section 1.4, there are two general classes of problems involving electromagnetic scattering by particles: the direct problem and the inverse problem. Thus far, we have dealt primarily with the direct problem of calculating or measuring the scattering by a known, well-defined object. By solving the inverse problem, one can attempt to characterize an object of interest using scattering data collected from laboratory or *in situ* measurements or remote-sensing observations.

The potentially strong dependence of the scattering properties of particles on their size parameter, morphology, and relative refractive index makes measurements of electromagnetic scattering a powerful noninvasive means of particle characterization. In fact, there are so many applications of optical particle characterization in laboratory and remote-sensing research that even listing them is impracticable. Therefore, we will describe only three selected examples, directing the reader to the literature cited at the end of this chapter for more details.

The bottom curve in Fig. 17.21 depicts measurements of the intensity of the light scattered by a slowly evaporating glycerol droplet at a scattering angle of approximately 90°. The droplet was illuminated by a linearly polarized laser beam at a wavelength of $\lambda_1 = 0.5145$ μm, the same beam being used to levitate the particle. The upper curve shows the results of Lorenz–Mie computations for a spherical droplet with a radius ranging from 4.38 to 4.67 μm and a relative re-

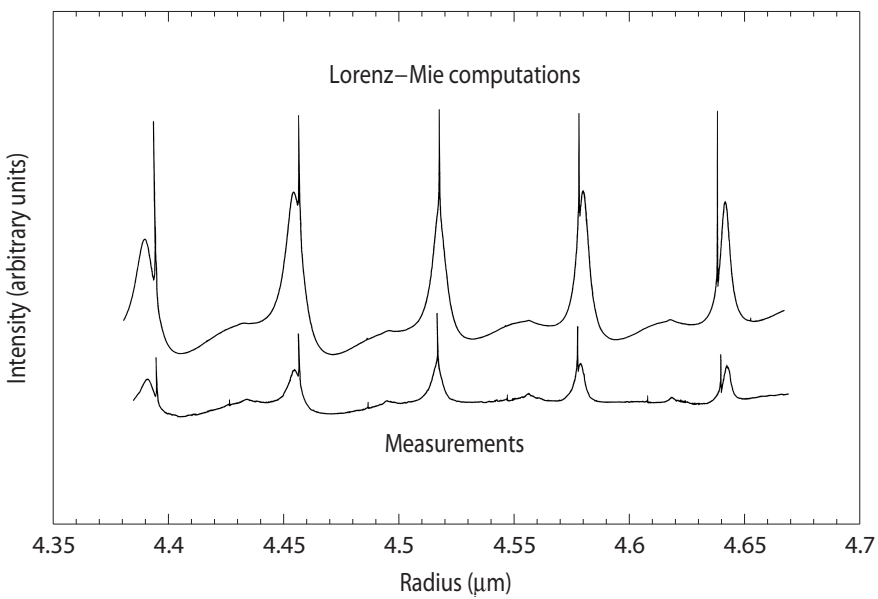

Fig. 17.21. Measurements and computations of the intensity (in arbitrary units) scattered by a glycerol droplet at a scattering angle of approximately 90° versus droplet radius (after Chýlek *et al.* 1992).

fractive index of 1.4746, corresponding to that of glycerol at the visible wavelength. Comparison of the two curves demonstrates that by identifying the locations of the narrow resonance features in the experimental data, the radii of spherical droplets can be determined with extreme precision. Chýlek *et al.* (1983) developed a technique for determining the relative refractive index as well as the size of an optically levitated spherical particle illuminated by a tunable dye laser. The technique is based on analyzing both the wavelengths of the resonance peaks and the line profiles in the curve of the backscattered intensity as a function of laser wavelength. More recent developments have been described by Huckaby *et al.* (1994), Ray and Nandakumar (1995), and Tu and Ray (2001).

Muñoz *et al.* (2010) described the use of the polarimetric nephelometer shown in Fig. 1.6c for the characterization of polydisperse microscopic water droplets generated by a nebulizer. The specific conditions of the experiment justified the use of the simple FOSA to simulate theoretically the measurement results. Muñoz *et al.* measured the entire normalized scattering matrix and verified experimentally its expected block diagonal structure summarized by Eq. (15.79). The measurements were performed at wavelengths 488, 520, and 647 nm. Some of the data at the 488- and 647-nm wavelengths are depicted in Fig. 17.22. As the first step, Muñoz *et al.* fitted the measured values of the ratios $a_1(\Theta)/a_1(30°)$ and $-b_1(\Theta)/a_1(\Theta)$ at each wavelength by assuming a wavelength-independent relative refractive index of 1.33 and by parameterizing the polydispersion of droplet radii in terms of the following log-normal distribution:

$$n(r) = \frac{1}{(2\pi)^{1/2}\ln\sigma_g}\frac{1}{r}\exp\left[-\frac{(\ln r - \ln r_g)^2}{2\ln^2\sigma_g}\right], \quad r \in [0,\infty), \tag{17.4}$$

where

$$\ln r_g = \int_0^\infty \mathrm{d}r \ln r\, n(r), \tag{17.5}$$

$$\ln^2\sigma_g = \int_0^\infty \mathrm{d}r (\ln r - \ln r_g)^2\, n(r). \tag{17.6}$$

The method to find the best-fit values of r_g and $\ln\sigma_g$ was based on the so-called downhill simplex method and yielded the following average results: $r_g = 0.80 \pm 0.07$ μm and $\ln\sigma_g = 1.50 \pm 0.04$. These values were then used to calculate all elements of the Lorenz–Mie scattering matrix. The resulting curves showed an excellent quantitative agreement with the experimental data over the entire scattering-angle range and at all three wavelengths, as exemplified by Fig. 17.22. This result confirmed the high fidelity of laboratory measurements as well as demonstrated the power of polarimetric nephelometry as a particle characterization tool.

Finally, Plate 17.7b illustrates the use of laboratory measurements of the backscattering linear depolarization ratio δ_{L} for characterization of nonspherical

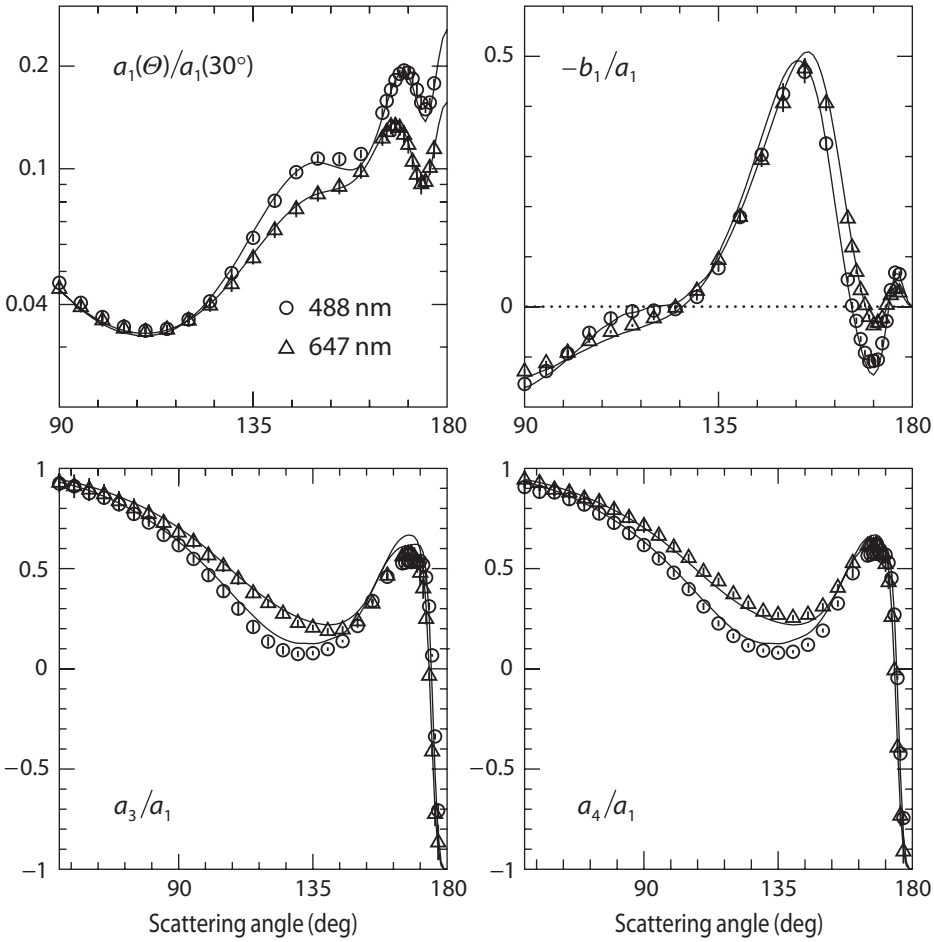

Fig. 17.22. The results of laboratory measurements (symbols) and theoretical Lorenz–Mie computations (curves) of scattering matrix elements for polydisperse microscopic water droplets at 488- and 647-nm wavelengths (see text). The vertical bars indicate estimated measurement uncertainties.

particles (after Schnaiter *et al.* 2012). The blue symbols show the results of measurements performed at the Aerosol Interactions and Dynamics in the Atmosphere facility of the Forschungszentrum Karlsruhe (Wagner *et al.* 2009) at the laser wavelength 488 nm. This ice cloud experiment was started at an initial temperature of 192 K and in ice saturated conditions. Nano-sized meteoric smoke analog particles were used as ice seeds. Expansion cooling of the chamber gas was initiated at $t = 0$ and resulted in a gradual increase of the ice saturation ratio. After the ice supersaturation ratio was increased to about 35% (at $t = 500$ s), ice crystals started to nucleate heterogeneously on the surfaces of the aerosol particles, as indicated by the steep increase of the measured depolarization ratio. The

expansion cooling lasted until $t = 2000$ s, resulting in the growth of the ice crystals to a median equal-volume diameter of about 3 μm. The time-dependent ice crystal size distribution was retrieved from simultaneous infrared extinction measurements using theoretical computations based on the TMM. After the expansion cooling was stopped, the ice cloud started to evaporate due to the heat flux from the warmer chamber walls. The best theoretical fit to the measured infrared extinction spectra was achieved by assuming oblate ice cylinders with a diameter-to-length ratio of 1.25. The use of this aspect ratio and the retrieved temporal evolution of the size distribution in subsequent TMM calculations of the backscattering linear depolarization ratio resulted in a close quantitative agreement with the corresponding laboratory data, as Plate 17.7b beautifully demonstrates.

Problems

17.1: Use the Lorenz–Mie program described in Section 5.10 of MTL1 and available at http://www.giss.nasa.gov/staff/mmishchenko/ftpcode/spher.f (assessed November 2013) to compute the extinction cross section and asymmetry parameter for polydisperse spheres with real-valued relative refractive indices varying from 1.3 to 1.7 in steps of 0.05 and effective size parameters varying from 0.2 to 15 in steps of 0.2. Use the gamma distribution (15.108) with $r_{\min} = 0$, $r_{\max} = \infty$ (in the sense of Problem 5.13), and a fixed effective variance of 0.2. Normalize the results by those for the central refractive index 1.45 and plot them as functions of the effective size parameter. Analyze the variability of $\langle C_{\text{ext}} \rangle$ and g with wavelength for the various effective size parameters.

17.2: Use the same computer program to calculate the elements of the normalized scattering matrix for monodisperse spherical particles with relative refractive indices 1.05, 1.1, 1.3, and 1.8 and size parameters 0.5, 1, 1.5, 2, 3, 4, and 5. Plot the results in the format similar to that of Fig. H.2. Analyze the size-parameter extent of the Rayleigh domain as a function of relative refractive index.

Further reading

An extensive source of specific information on far-field observable properties of spherical and nonspherical particles and on optical particle characterization are MTL1, the collective monograph edited by Mishchenko *et al.* (2000), and the expanding collection of special issues of the *Journal of Quantitative Spectroscopy and Radiative Transfer* (see Borghese *et al.* (2012) and references therein). A comprehensive review of applications of the TMM in plasmonics was recently published by Khlebtsov (2013).

18

Electromagnetic scattering by discrete random media: far field

By definition, a discrete random medium (DRM) is a scattering object in the form of an imaginary volume V populated by a large number N of particles in such a way that the spatial distribution of the particles throughout the volume is statistically uniform or quasi-uniform. Over time, particle positions and states change randomly, thereby resulting in random changes of the state ψ of the entire object (Section 10.4). Classical examples of a DRM are clouds and particle suspensions (Plates 1.1b–1.1d). In many cases a particulate surface (Plates 1.1e and 1.1f) can also be modeled as a DRM, since even minute changes of the source-of-light → object → detector configuration during the measurement are equivalent to multi-wavelength shifts in particle positions and, in essence, result in a stochastic scattering object. The volume packing density of a DRM can vary from almost zero for a cloud to more than 50% for a particulate surface.

Given their specific morphological traits and ubiquitous presence, scattering objects in the form of a DRM deserve a detailed study. As always, the desirable way to model electromagnetic scattering by an ergodic DRM is to solve the MMEs numerically for a representative set of realizable states ψ of the object and then average the relevant optical observables or energy-budget characteristics using an appropriate probability density function $p(\psi)$ (Section 10.4). This approach has no restrictions on the volume packing density of a DRM and has been gaining popularity over the past several years, although it remains quite limited in terms of the number of constituent particles N and the overall size of the object relative to the wavelength. The case of a very large number of particles coupled with a large overall size of a DRM can be handled analytically by using the far-field FEs (Section 6.3), but this approach implies that the packing density is extremely small.

In this chapter we will exploit the availability of the highly efficient STMM solver of the MMEs to compute and analyze far-zone scattering characteristics of

ergodic random particulate volumes with moderate numbers of constituent particles and with volume packing densities ranging from essentially zero to several dozen percent. The main purpose of this analysis is to illustrate speckle patterns caused by a fixed scattering object and demonstrate the main effects of averaging over varying states of a stochastic object.

18.1 Is there multiple scattering?

It is instructive to begin this chapter by dispelling one more time the intuitively appealing, but inherently deceptive, notion of multiple scattering. Throughout scientific literature, one can encounter various definitions of "multiple scattering," all of them stemming from a heuristic idea of successive scattering events caused by a sequence of particles in a multi-particle group. However, the characterization of a morphologically complex object, such as a cloud, as being composed of separate particles is based solely on the human visual perception and is immaterial in the framework of the frequency-domain MMEs. Indeed, the same VIE (4.23) describes electromagnetic scattering by a "multi-particle system" shown in Fig. 1.2 as well as by a "single isolated particle," even though the interior volume V_{INT} in the former case is the union of the nonoverlapping "constituent-particle volumes" rather than one connected volume. In other words, an object remains a single, unified scatterer irrespective of the complexity of its morphology.

To illustrate this point, let us consider FFS of a parallel quasi-monochromatic beam of light by three fixed objects shown in Fig. 18.1: an oblate spheroid with an aspect ratio of two, a circular cylinder with a diameter-to-length ratio of one, and a cluster of 80 identical small spherical particles distributed throughout an imaginary spherical volume V with a radius R. The volume-equivalent-sphere size parameters of the spheroid and the cylinder are the same and are equal to that of the imaginary spherical volume: $k_1R = 40$. The size parameter of the constituent spherical particles is $k_1r = 4$. The relative refractive indices of the spheroid, the cylinder, and the constituent spherical particles are the same and are equal to 1.32. The coordinates of the constituent spheres populating the volume V were selected using a random number generator, but otherwise they are fixed.

The laboratory spherical coordinate system used to describe far-field electromagnetic scattering by each object is shown in Fig. 18.2, in which the unit vectors $\hat{\mathbf{n}}^{\mathrm{inc}}$ and $\hat{\mathbf{n}}^{\mathrm{sca}}$ specify the directions of incidence and scattering, respectively.

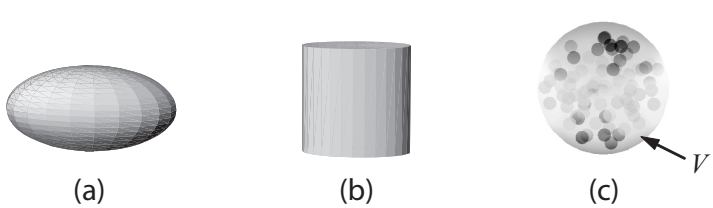

Fig. 18.1. Three scattering objects.

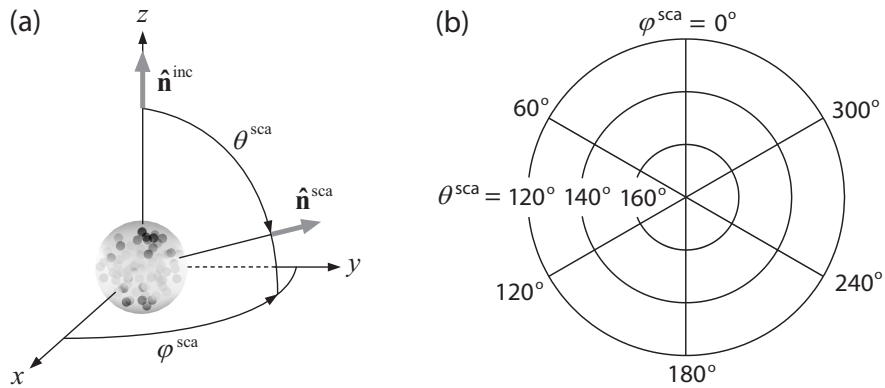

Fig. 18.2. (a) Explanation of the scattering geometry. **(b)** Angular coordinates used in Figs. 18.3 and 18.4.

The orientation of a scattering object with respect to the laboratory frame is specified by the Euler angles of rotation, as described in Section 13.9 and Appendix C, assuming that the z-axis of the particle reference frame is directed along the symmetry axis of the spheroids or the cylinder. The corresponding sets of the Euler angles $\{\alpha, \beta, \gamma\}$ are given by $\{145°, 52°, 0°\}$ for the spheroid and the cylinder and by $\{0°, 0°, 0°\}$ for the spherical particulate volume.

The zenith and azimuth angles of the incidence direction are assumed to be $\theta^{\text{inc}} = 0°$ and $\varphi^{\text{inc}} = 0°$, respectively. The incident beam is taken to be circularly polarized in the counter-clockwise sense when looking in the direction of propagation, which implies that $\langle\langle V^{\text{inc}}\rangle\rangle = \langle\langle I^{\text{inc}}\rangle\rangle$ and $\langle\langle Q^{\text{inc}}\rangle\rangle = \langle\langle U^{\text{inc}}\rangle\rangle = 0$.

The left-hand panels of Fig. 18.3 show the far-field angular distributions of the intensity $\langle\langle I^{\text{sca}}\rangle\rangle$ scattered in the backward hemisphere by the three fixed objects. These intensity distributions were calculated using numerically exact TMM and STMM computer programs and demonstrate typical speckle patterns of comparable complexity. The speckle patterns in Figs. 18.3a and 18.3b appear to be somewhat less irregular than that in Fig. 18.3c. This can be explained qualitatively by the greater morphological complexity of the random multi-sphere group, the less regular spatial distribution of the elementary volume elements contributing to the integral on the right-hand side of Eq. (5.9), and the fact that empty spaces between the constituent spheres do not contribute to the scattered field.

The right-hand panels of Fig. 18.3 show the results obtained by averaging the scattered intensity over the uniform orientation distribution of the respective objects. Not surprisingly, the average intensity distributions are rotationally symmetric with respect to the incidence direction. The scattering patterns for the randomly oriented spheroid and cylinder show residual interference effects, whereas that for the randomly oriented multi-particle group is rather featureless, the strong and narrow backscattering peak being the only notable exception.

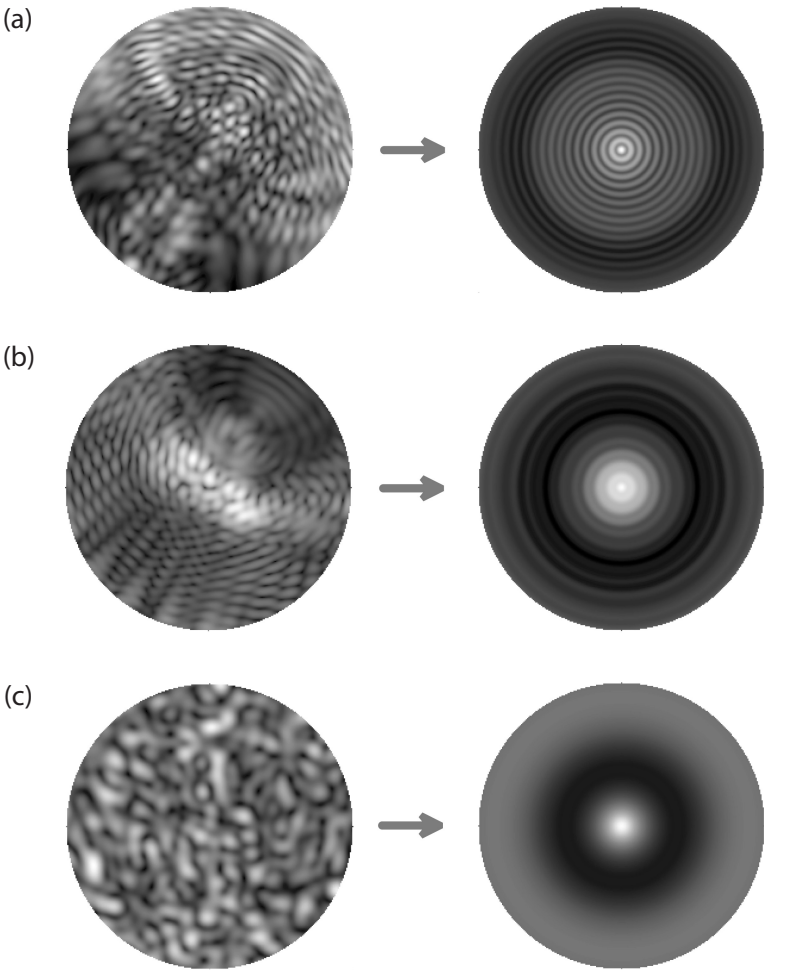

Fig. 18.3. Scattered intensity for the spheroid **(a)**, the cylinder **(b)**, and the spherical particulate volume **(c)** in fixed (left-hand panels) and random (right-hand panels) orientations. The grey scale is individually adjusted in order to maximally reveal the fine structure of each scattering pattern. Fig. 18.2b shows the angular coordinates used for all six panels.

Figure 18.3 demonstrates that there can be vast differences between instantaneous or statistically averaged scattering patterns generated by different objects. However, these differences result from differences in the objects' characteristics (such as the overall size relative to the wavelength, morphology, and relative refractive index) rather than from differences in fundamental physical laws describing electromagnetic scattering. The physics of electromagnetic scattering, as embodied by the frequency-domain MMEs or the mathematically equivalent VIE, remains the same, irrespective of the nature of the scattering object. To the extent that analytical or numerically exact solutions of these primordial equations are

possible in practice, they incorporate and represent all the physics of the scattering problem.

Despite this irrefutable fact, there has been a tendency to believe that the "multi-particle" morphology shown in Fig. 18.1c somehow results in a multiple-scattering object, whereas the "single-particle" morphologies shown in Figs. 18.1a and 18.1b result in single-scattering objects. However, as we have mentioned in Section 6.2, multiple frequency-domain electromagnetic scattering is not a real physical phenomenon, albeit it can be a useful mathematical abstraction. Indeed, all three left-hand panels in Fig. 18.3 are the result of solving the same MMEs and describe single electromagnetic scattering by three morphologically different objects. In particular, the computation of the left-hand panel in Fig. 18.3c did not involve any new fundamental equations and, thus, any new physical phenomena.

18.2 Speckle

Let us discuss in more detail the properties of the far-field speckle generated by a random particulate volume. As before, we assume that N identical spherical particles are distributed randomly and quasi-uniformly throughout an imaginary spherical volume V with a radius R much greater than the particle radius r, as shown in Plate 18.1a. The size parameters of the particles and the spherical volume are fixed at $k_1 r = 4$ and $k_1 R = 40$, respectively. The refractive index of the particles relative to that of the homogeneous surrounding medium is 1.32. The spherical volume V is illuminated by a parallel quasi-monochromatic beam of light propagating in the positive direction of the z-axis of the laboratory reference frame, according to Fig. 18.2a. The beam is circularly polarized such that $\langle\langle V^{\text{inc}}\rangle\rangle = \langle\langle I^{\text{inc}}\rangle\rangle$ and $\langle\langle Q^{\text{inc}}\rangle\rangle = \langle\langle U^{\text{inc}}\rangle\rangle = 0$. Figures 18.4a–18.4e show the far-field angular distributions of the intensity $\langle\langle I^{\text{sca}}\rangle\rangle$ scattered in the backward hemisphere by the spherical volumes filled with $N = 1$, 5, 20, 40, and 80 particles. The individual particle positions within V were again chosen using a random coordinate generator, but otherwise they are fixed. The scattering pattern for $N = 1$ is rather smooth and perfectly azimuthally symmetric, as it should be for a single wavelength-sized spherical particle. However, Figs. 18.4b–18.4e demonstrate typical speckle patterns of increasing complexity.

To discuss and interpret the results of these and forthcoming STMM computations, we will extensively use the mathematical concept of ordered multi-particle sequences representing the various terms on the right-hand side of Eq. (6.20). Plate 18.1b shows schematically two such sequences depicted using the blue and yellow colors. To make the interpretation even more specific, we will assign a cumulative phase to each multi-particle sequence by assuming that each subsequent particle is in the far zone of the preceding particle. For example, particle 4 of the blue sequence in Plate 18.1b is assumed to be in the far zone of particle 3, particle 3 is assumed to be in the far zone of particle 2, etc. This implies

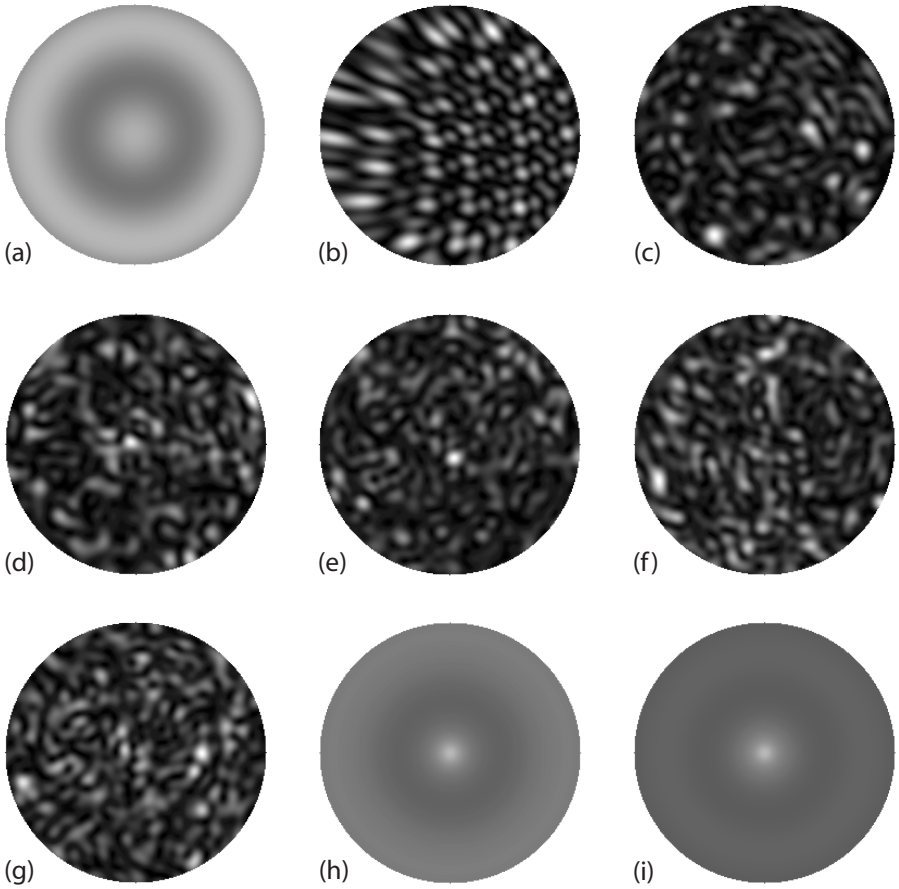

Fig. 18.4. Angular distribution of scattered intensity in the far zone of the imaginary spherical volume V filled with N particles. **(a)** $N = 1$ and $m = 1.32$. **(b)** $N = 5$ and $m = 1.32$. **(c)** $N = 20$ and $m = 1.32$. **(d)** $N = 40$ and $m = 1.32$. **(e)** $N = 80$ and $m = 1.32$. **(f)** $N = 80$ and $m = 1.32$. **(g)** $N = 80$ and $m = 1.5$. **(h)** $N = 80$ and $m = 1.32$, random orientation. **(i)** $N = 80$ and $m = 1.5$, random orientation. The gray scale is individually adjusted in order to maximally reveal the details of each scattering pattern. Figure 18.2b shows the angular coordinates used for all panels.

that now we are dealing with the approximate Neumann expansion (6.48) in lieu of the exact expansion (6.20), and so the expression for the partial electric field contributed by this four-particle sequence at the observation point includes the complex exponential factor

$$\exp\left[\mathrm{i}k_1(r_4 + R_{43} + R_{32} + R_{21} + \hat{\mathbf{n}}^{\mathrm{inc}} \cdot \mathbf{R}_1)\right], \tag{18.1}$$

where we use the notation of Fig. 6.1. Thus the corresponding cumulative phase of the blue four-particle sequence is

$$\delta_{\text{blue}} = k_1(r_4 + R_{43} + R_{32} + R_{21} + \hat{\mathbf{n}}^{\text{inc}} \cdot \mathbf{R}_1). \tag{18.2}$$

The cumulative phases of other multi-particle sequences are determined similarly. For example, for the yellow three-particle sequence it is given by

$$\delta_{\text{yellow}} = k_1(r_{3'} + R_{3'2'} + R_{2'1'} + \hat{\mathbf{n}}^{\text{inc}} \cdot \mathbf{R}_{1'}). \tag{18.3}$$

It should be kept in mind that the very notion of the cumulative phase becomes questionable if at least one particle of a sequence is located in the near zone of the preceding particle. This often happens in a densely packed particulate volume, thereby making the expansion (6.48) inapplicable in the strict mathematical sense. We will see later, however, that qualitative interpretations of STMM results using the concept of the cumulative phase may remain meaningful, even in the case of random particulate volumes with relatively large packing densities.

Now the origin of the far-field speckle can be explained as follows. Equation (6.48) suggests that at a distant observation point, the partial field due to any particle sequence is an outgoing transverse spherical wavelet centered at the origin of the last particle of the sequence.[1] Since the distance to the far-field observation point is much greater than the radius R of the volume V, all such partial wavelets at the observation point propagate in essentially the same direction given by the unit vector $\hat{\mathbf{n}}^{\text{sca}}$ (Plate 18.1b). The Stokes parameters of the scattered field at the observation point (Eq. (13.25)) can be directly expressed in terms of the elements of the scattering coherency dyad $\langle\langle \vec{\rho}^{\text{sca}} \rangle\rangle = \langle\langle \mathbf{E}^{\text{sca}} \otimes (\mathbf{E}^{\text{sca}})^* \rangle\rangle$ according to

$$\langle\langle \mathbf{I}^{\text{sca}} \rangle\rangle = \frac{1}{2}\sqrt{\frac{\epsilon_1}{\mu_0}} \begin{bmatrix} \hat{\boldsymbol{\theta}}^{\text{sca}} \cdot \langle\langle \vec{\rho}^{\text{sca}} \rangle\rangle \cdot \hat{\boldsymbol{\theta}}^{\text{sca}} + \hat{\boldsymbol{\varphi}}^{\text{sca}} \cdot \langle\langle \vec{\rho}^{\text{sca}} \rangle\rangle \cdot \hat{\boldsymbol{\varphi}}^{\text{sca}} \\ \hat{\boldsymbol{\theta}}^{\text{sca}} \cdot \langle\langle \vec{\rho}^{\text{sca}} \rangle\rangle \cdot \hat{\boldsymbol{\theta}}^{\text{sca}} - \hat{\boldsymbol{\varphi}}^{\text{sca}} \cdot \langle\langle \vec{\rho}^{\text{sca}} \rangle\rangle \cdot \hat{\boldsymbol{\varphi}}^{\text{sca}} \\ -\hat{\boldsymbol{\theta}}^{\text{sca}} \cdot \langle\langle \vec{\rho}^{\text{sca}} \rangle\rangle \cdot \hat{\boldsymbol{\varphi}}^{\text{sca}} - \hat{\boldsymbol{\varphi}}^{\text{sca}} \cdot \langle\langle \vec{\rho}^{\text{sca}} \rangle\rangle \cdot \hat{\boldsymbol{\theta}}^{\text{sca}} \\ \mathrm{i}(\hat{\boldsymbol{\varphi}}^{\text{sca}} \cdot \langle\langle \vec{\rho}^{\text{sca}} \rangle\rangle \cdot \hat{\boldsymbol{\theta}}^{\text{sca}} - \hat{\boldsymbol{\theta}}^{\text{sca}} \cdot \langle\langle \vec{\rho}^{\text{sca}} \rangle\rangle \cdot \hat{\boldsymbol{\varphi}}^{\text{sca}}) \end{bmatrix} \tag{18.4}$$

(Problem 18.2), where $\hat{\boldsymbol{\theta}}^{\text{sca}}$ and $\hat{\boldsymbol{\varphi}}^{\text{sca}}$ are the polar-angle and azimuth-angle unit vectors of the scattering direction such that $\hat{\mathbf{n}}^{\text{sca}} = \hat{\boldsymbol{\theta}}^{\text{sca}} \times \hat{\boldsymbol{\varphi}}^{\text{sca}}$. It can be easily seen that the dyadic product of the right-hand side of Eq. (6.48) and its complex-conjugate counterpart is the sum of an infinite number of terms, each describing the result of interference of two spherical wavelets centered at the end particles of a pair of particle sequences.

One such pair is exemplified by the blue and yellow sequences shown in Plate 18.1b. If the interference of the corresponding pair of spherical wavelets at the observation point is constructive (destructive) then it serves to increase (decrease) the total intensity scattered in the direction $\hat{\mathbf{n}}^{\text{sca}}$. According to Eqs. (18.2) and (18.3), the result of the interference depends largely on the phase difference $\Delta = \delta_{\text{blue}} - \delta_{\text{yellow}}$ given by

[1] This, in fact, is true, irrespective of whether the particles in the sequence are densely packed or sparsely distributed (Problem 18.1).

$$\Delta = k_1(r_4 + R_{43} + R_{32} + R_{21} + \hat{\mathbf{n}}^{\text{inc}} \cdot \mathbf{R}_1 - r_{3'} - R_{3'2'} - R_{2'1'} - \hat{\mathbf{n}}^{\text{inc}} \cdot \mathbf{R}_{1'}). \qquad (18.5)$$

The total scattered intensity is the sum of the interference results contributed by all possible pairs of particle sequences. The minimal angular width of such interference maxima and minima is proportional to $1/k_1R$, whereas their number grows swiftly with increasing N. These two factors explain the increasingly spotty appearance of the scattering patterns in Figs. 18.4b–18.4e.

Equation (18.5) suggests that the speckle pattern must depend not only on the number of particles N, but also on the specific way they are arranged with respect to the laboratory coordinate system. This is illustrated indeed by Figs. 18.4e and 18.4f computed for two different random 80-particle configurations shown in Plate 18.1c. Owing to the refractive-index dependence of the scattering dyadics $\vec{A}_i$ entering the expansion (6.48), the speckle pattern must also depend on the particle refractive index. This is exemplified by Figs. 18.4e and 18.4g computed for the same 80-particle configuration – shown in the left-hand panel of Plate 18.1c – but for different relative refractive indices 1.32 and 1.5, respectively.

Sometimes it is claimed in the scientific literature that a speckle pattern can only be caused by monochromatic incident light such a continuous laser beam. Our STMM results and discussion show that all one needs to observe a speckle is a fixed object illuminated by a parallel quasi-monochromatic beam of light.

18.3 Dynamic and static scattering

Figures 18.4e and 18.4f are indicative of the range of variability of the speckle pattern that can be expected upon temporal changes in a multi-particle configuration. After such patterns have been computed or measured for a representative set of states of a random particulate volume, one has a choice of:

- analyzing the statistical information content of differences in the individual speckle patterns; or
- assuming ergodicity and applying an averaging procedure, thereby isolating the static component of the speckle patterns.

These two approaches are known as *dynamic* and *static* light scattering (Berne and Pecora 1976; Brown 1993; MTL2). In what follows, we will discuss only static scattering. In particular, we will demonstrate in the subsequent chapters that the classical theories of radiative transfer and WL fall in the realm of static scattering and describe the result of averaging the relevant optical observables and energy-budget characteristics over a significant period of time or, equivalently, over a significant range of random particle positions.

18.4 Static scattering by a random particulate volume

To compute and analyze the static far-field scattering pattern, one needs an efficient way of averaging relevant optical observables over very many random re-

alizations of an N-particle group. A brute-force solution would be to use a random coordinate generator repeatedly to create a large number of different N-particle configurations and then average numerically over the corresponding individual results. The more effective approach used here is to create only one random N-particle configuration and then average over all possible orientations of this configuration with respect to the laboratory coordinate system. This procedure yields an infinite continuous set of random realizations of the N-particle group and takes full advantage of the highly efficient orientation averaging procedure afforded by the STMM. The robustness of this approach will be discussed at the end of this section.

Figures 18.4h and 18.4i show the result of averaging the speckle pattern over the uniform orientation distribution of the 80-particle configuration shown in the left-hand panel of Plate 18.1c for $m = 1.32$ and 1.5, respectively. One can see that with the exception of notable backscattering peaks, the speckle structure is essentially gone. This is not surprising. Indeed, according to the above discussion, each far-field speckle element can be thought of as being the result of constructive or destructive interference of two wavelets contributed by specific multi-particle sequences, such as those shown in Plate 18.1b. The difference (18.5) between the cumulative phases of the wavelets at the observation point changes randomly as the particles move, so that the average result of the interference is zero. However, there are certain pairs of wavelets that interfere constructively, irrespective of particle positions, and thereby are responsible for the residual static scattering pattern. We will demonstrate below that the backscattering intensity peaks seen in Figures 18.4h and 18.4i, as well as the smooth intensity backgrounds are in fact caused by special classes of pairs of multi-particle sequences.

In what follows, we employ the concept of the cumulative phase of a multi-particle sequence to interpret various effects of increasing the number of particles filling the scattering volume on the static scattering patterns obtained by averaging over all orientations of a random N-particle configuration with respect to the laboratory reference frame. We make a simplifying assumption that $\varphi^{\text{sca}} = 0$ and define the scattering direction in terms of the scattering angle $\Theta = \theta^{\text{sca}}$. Then the far-field scattering pattern can be conveniently described in terms of the normalized Stokes scattering matrix (15.64). The block-diagonal structure of this matrix was confirmed by the numerically exact STMM results and is largely caused by averaging over the uniform orientation distribution of a multi-particle group coupled with sufficient uniformity of particle positions throughout the scattering volume. Each scattering matrix element denoted in Eq. (15.64) by a zero has been found to be at least an order of magnitude smaller than the smallest nonzero element (in the absolute-value sense).

The upper left-hand panel of Plate 18.2 vividly demonstrates several fundamental consequences of increasing the number of particles in the scattering volume. First, the constructive interference of light singly scattered by the component particles in the exact forward direction causes a strong and narrow forward-

scattering enhancement discussed in Section 14.6. This feature is further detailed in Plate 18.3a and explained in Plate 18.1d. It can be called forward-scattering localization of electromagnetic waves. Indeed, the exact forward-scattering direction is unique in that the phases of the wavelets forward-scattered by all the individual particles in the volume are exactly the same, irrespective of the specific particle positions (see the left-hand panel of Plate 18.1d). In the absence of multi-particle sequences, the constructive interference of these single-particle wavelets would lead to an increase of the forward-scattering phase function $a_1(0°)$ by a factor of N. Indeed, the forward-scattering value of the (1,1) element of the matrix $\langle \mathbf{F} \rangle_{\mathbf{R}}$ in Eq. (15.64) would grow by a factor of N^2, while the scattering cross section $\langle C_{\text{sca}} \rangle_{\mathbf{R}}$ would grow by a factor of N, thereby implying an N-fold increase in $a_1(0°)$. This increase does occur for $N = 2$ and 5 (Plate 18.3a), but then it slows down, and by the time N reaches the value 160 the $a_1(0°)$ value saturates. This behavior can be interpreted qualitatively in terms of a multi-particle interaction effect whereby particle 3 (see the right-hand panel of Plate 18.1d) "shades" particle 2 by attenuating the incident field exciting particle 2. In fact, we will see in the following chapter that it is this multi-particle interaction effect that leads to the exponential extinction law in the framework of the RTT.

Second, the phase functions at scattering angles $\Theta > 170°$ start to develop a backscattering maximum which becomes quite pronounced for $N \geq 160$ (see Plate 18.3b). This feature is a typical manifestation of WL of electromagnetic waves in the backscattering direction (also known as coherent backscattering).[2] The qualitative explanation of WL is illustrated in Plate 18.1e. The conjugate wavelets caused by the same chain of n particles but sequenced in opposite order interfere in the far zone, the interference being constructive or destructive, depending on the respective phase difference between the blue and yellow sequences,

$$\Delta = k_1 (\mathbf{R}_1 - \mathbf{R}_n) \cdot (\hat{\mathbf{n}}^{\text{inc}} + \hat{\mathbf{n}}^{\text{sca}}) \tag{18.6}$$

(Problem 18.3). If the observation direction $\hat{\mathbf{n}}^{\text{sca}}$ is far from the exact backscattering direction given by $-\hat{\mathbf{n}}^{\text{inc}}$ then the average effect of interference of the conjugate wavelets caused by any chain of particles is zero, owing to randomness of particle positions. But at exactly the backscattering direction, $\hat{\mathbf{n}}^{\text{sca}} = -\hat{\mathbf{n}}^{\text{inc}}$, the phase difference between the conjugate wavelets caused by *any* chain of particles is identically equal to zero. Therefore, the interference is always constructive and causes an intensity peak.

The third consequence of increasing N is that the phase functions at scattering angles $30° \leq \Theta \leq 170°$ become progressively smooth and featureless, thereby causing the "diffuse" intensity background clearly identifiable in Fig. 18.4h. The major contributor to the background intensity is another class of wavelet pairs, as

[2] The term "weak localization of electromagnetic waves" was introduced by solid-state physicists in order to draw an analogy with the effect of weak localization of electrons in dirty metals (Sheng 2006; Akkermans and Montambaux 2007).

illustrated in Plate 18.1f. Now the wavelet caused by the blue sequence of n particles is the same as that caused by the yellow sequence and thus "interferes with itself." Since the corresponding phase difference is exactly equal to zero irrespective of particle positions, the self-interference is always constructive for any chain of particles. Therefore, the contribution of this class of wavelet pairs survives the ensemble averaging for any $\hat{\mathbf{n}}^{\text{inc}}$ and $\hat{\mathbf{n}}^{\text{sca}}$. The progressive smoothness of the background intensity with growing N in the upper left-hand panel of Plate 18.2 can be explained by the effect of averaging over the contributions from the rapidly increasing number of multi-particle chains.

As we have already mentioned, the degree of linear polarization of the scattered light for unpolarized incident light is given by the ratio $-b_1/a_1$. The bottom left-hand panel of Plate 18.2 shows that the most obvious effect of increasing N is to smooth out the low-frequency oscillations in the polarization curve for the single wavelength-sized sphere and, on average, to make polarization more neutral. This implies that the main contribution to the second Stokes parameter, $\langle\langle Q^{\text{sca}}\rangle\rangle$, comes from single-particle chains, whereas the contributions from many-particle chains are largely unpolarized.

We have seen before that the ratio a_2/a_1 is identically equal to unity for scattering by a single sphere. Therefore, the rapidly growing deviation of this ratio from 100% for $N \geq 5$ in Plate 18.2 should again be attributed to multi-particle chains. Similarly, $a_3(\Theta) \equiv a_4(\Theta)$ and $a_3(180°)/a_1(180°) = -1$ for scattering by a spherically symmetric particle, but contributions from multi-particle chains in particulate volumes with $N \geq 5$ cause an increasingly significant violation of these equalities.

If the incident light is polarized linearly in the xz-plane then, according to Eqs. (H.38) and (H.39), the angular distributions of the corresponding co-polarized and cross-polarized scattered intensities are defined by the quantities $\frac{1}{2}[a_1(\Theta)+2b_1(\Theta)+a_2(\Theta)]$ and $\frac{1}{2}[a_1(\Theta)-a_2(\Theta)]$. These are plotted in Plate 18.4. Also depicted are the quantities $\frac{1}{2}[a_1(\Theta)+a_4(\Theta)]$ and $\frac{1}{2}[a_1(\Theta)-a_4(\Theta)]$ that define the same-helicity and opposite-helicity scattered intensities for the case of incident light polarized circularly in the counterclockwise direction when looking in the direction of propagation (Problem 18.4). All of these quantities exhibit WL in the form of backscattering peaks growing in amplitude with N.

By far the most definitive demonstration of the onset of WL is provided by the $(a_1-a_2)/2$ and $(a_1+a_4)/2$ curves in Plate 18.4. Indeed, the corresponding single-particle curves show no backscattering enhancement whatsoever, so the backscattering peaks that develop with increasing N (and thus with increasing contributions from multi-particle chains) can be attributed unequivocally to WL. Plate 18.4 also depicts the angular profiles of the LPR and CPR given by Eqs. (H.40) and (H.54). Our results demonstrate that the contribution from multi-particle chains causes an increasingly significant deviation of $\mu_{\text{L}}(180°)$ and $\mu_{\text{C}}(180°)$ from zero, while WL causes pronounced backscattering peaks in the LPR and CPR angular profiles.

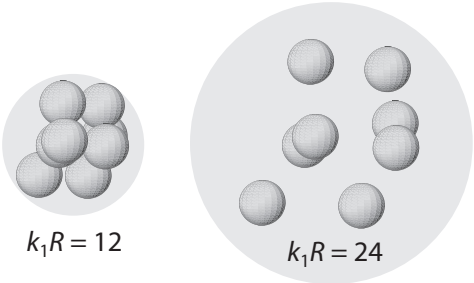

Fig. 18.5. Imaginary spherical volumes populated by eight identical particles.

The interference mechanism illustrated by Plates 18.1d and 18.1e implies that the angular widths of the forward-scattering and WL peaks must be proportional to $1/k_1R$. To verify this, we have performed computations assuming that the number of $k_1r = 4$ particles is fixed at $N = 8$, while the size parameter of the volume is varied from $k_1R = 12$ to 72 in steps of 6. The arrangement of the eight particles inside the $k_1R = 12$ volume is random, but such that each particle is in contact with at least one other particle. The other ten particulate volumes with $k_1R = 18, 24, \ldots, 72$ are obtained by uniformly scaling all particle coordinates of the $k_1R = 12$ volume, while keeping the particle size fixed. This procedure is illustrated in Fig. 18.5, showing the original $k_1R = 12$ volume and the derivative $k_1R = 24$ volume. The corresponding STMM results are depicted in Plates 18.3c and 18.3d and demonstrate indeed that the widths of both peaks decrease with increasing inter-particle separation, thus corroborating their interference nature. The nearly constant amplitude of the forward-scattering peak and the rapidly decreasing amplitude of the backscattering peak testify again that these features are caused by pairs of single-particle and multi-particle sequences, respectively. Indeed, the single-particle term does not and the multi-particle terms do contain $1/(\text{inter-particle distance})$ factors in the far-field Neumann expansion (6.48).

A more subtle manifestation of WL can be observed in the case of a random particulate volume populated by particles with sizes significantly smaller than the wavelength (Mishchenko *et al.* 2009b). Figure 18.6 depicts the ratio $-b_1/a_1$ for a particulate volume with $k_1R = 31$ populated by $N = 1, \ldots, 1875$ identical spherical particles with $k_1r = 2$ and $m = 1.31$ (Mackowski and Mishchenko 2011). The reader can see that, unlike the $-b_1/a_1$ trend seen in Plate 18.2, the increase in the particle number first to 75 and then to 750 causes the onset and rapid growth of a new feature not exhibited by the $N = 1$ curve. It is this narrow asymmetric minimum of polarization at backscattering angles that was called the polarization opposition effect (Mishchenko 1993). Like other manifestations of WL, it is caused by pairs of multi-particle sequences exemplified by Plate 18.1e. A qualitative interpretation of this WL feature can be found in the review by Shkuratov *et al.* (1994) as well as in Mishchenko *et al.* (2009b).

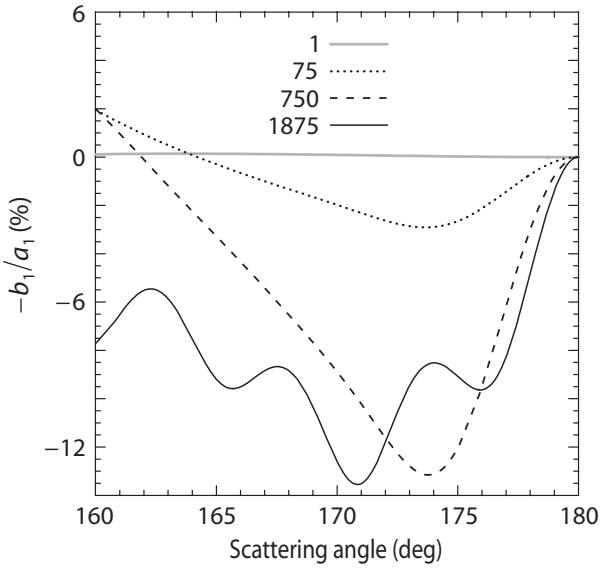

Fig. 18.6. Polarization opposition effect.

The effect of increasing the number of particles N in a random particulate volume can be expected to be twofold. On one hand, it serves to increase the number of multi-particle chains and thereby enhances such corollaries of the expansion (6.48) as the smoothness of the scattered intensity at side-scattering angles and the various WL features at backscattering angles. On the other hand, it leads to increased packing density and can eventually cause features in the scattering patterns not implied by the far-field Neumann expansion. One should, therefore, expect that the above interpretation of numerically exact STMM results must ultimately become inadequate when the particle packing density becomes exceedingly large (Dlugach *et al.* 2011; Tishkovets *et al.* 2011). Figure 18.6 shows that this is indeed the case: unlike the other curves, the black solid curve exhibits a high-frequency ripple reminiscent of a homogeneous spherical particle with a size parameter of $k_1R = 31$. Obviously, the corresponding packing density of 50% is so high that the expansion (6.48), as well as the assumption of randomness and uniformity of the particles' spatial distribution become inapplicable.

Nevertheless, the direct solutions of the MMEs discussed above do demonstrate that the classical consequences of the low-density assumption can survive – at least in a semi-quantitative sense – volume packing densities reaching 24% (see the curves in Plates 18.2–18.4 corresponding to $N = 240$). Such values are typical of particle suspensions and even of some particulate surfaces.

To conclude this section, let us examine whether it was appropriate to calculate each curve in Plates 18.2–18.4 and Fig. 18.6 by averaging over orientations of only one N-particle configuration. In the beginning of this section, we made a

bold assumption that the results thus obtained would be statistically representative of all possible realizations of the N-particle group, at least for large N. The correctness of this assumption is well illustrated by Plates 18.3e and 18.3f computed for two different realizations of a random 240-particle group populating a $k_1R = 40$ spherical volume. Even though the two sets of initial coordinates of the 240 particles were quite different, averaging over all orientations of each configuration yielded virtually indistinguishable results.

18.5 Conditions of applicability of the single-scattering approximation

Numerically exact STMM computations of far-field scattering by a random particulate volume can be used to quantify the range of applicability of one of the main assumptions of the FOSA, i.e., the SSA (14.1)–(14.3). We have seen in the preceding section that if all multi-particle sequences in the far-field Neumann expansion (6.48) are neglected then the constructive forward-scattering interference of all partial wavelets at the far-zone observation point makes the total amplitude scattering matrix for $\Theta = 0$ equal to N times the corresponding single-particle amplitude scattering matrix. As a consequence,

$$\langle C_{\text{ext}}(\text{particulate volume})\rangle_{\mathbf{R}} = NC_{\text{ext}}(\text{one particle}). \tag{18.7}$$

Another corollary of the neglect of all multi-particle sequences is

$$a_1(\Theta = 0°; \text{particulate volume}) = Na_1(\Theta = 0°; \text{one particle}). \tag{18.8}$$

Finally, all manifestations of WL must also disappear. Therefore, a significant violation of the equalities (18.7) and (18.8) and/or a pronounced WL feature in the backscattered light indicate that the SSA does not hold.

Figure 18.7 parallels Plates 18.3c and 18.3d, discussed in the preceding section, and depicts the ratios

$$\frac{\langle C_{\text{ext}}(\text{particulate volume})\rangle_{\mathbf{R}}}{8C_{\text{ext}}(\text{one particle})} \tag{18.9}$$

and

$$\frac{a_1(\Theta = 0°; \text{particulate volume})}{8a_1(\Theta = 0°; \text{one particle})} \tag{18.10}$$

as functions of the size parameter k_1R of the random particulate volume populated by eight identical spherical particles with $k_1r = 4$ and $m = 1.32$. The upper horizontal axis translates the volume size parameter into the particle packing density ρ and the quantity $k_1\langle d\rangle_{\mathbf{R}}$, where $\langle d\rangle_{\mathbf{R}}$ is the average distance between the sphere centers.

The SSA implies that both ratios (18.9) and (18.10) must be equal to unity and $\frac{1}{2}[a_1(\Theta) - a_2(\Theta)]$ must be equal to zero. However, Fig. 18.7 and Plate 18.3d demonstrate that as small a packing density as 1% already leads to significant de-

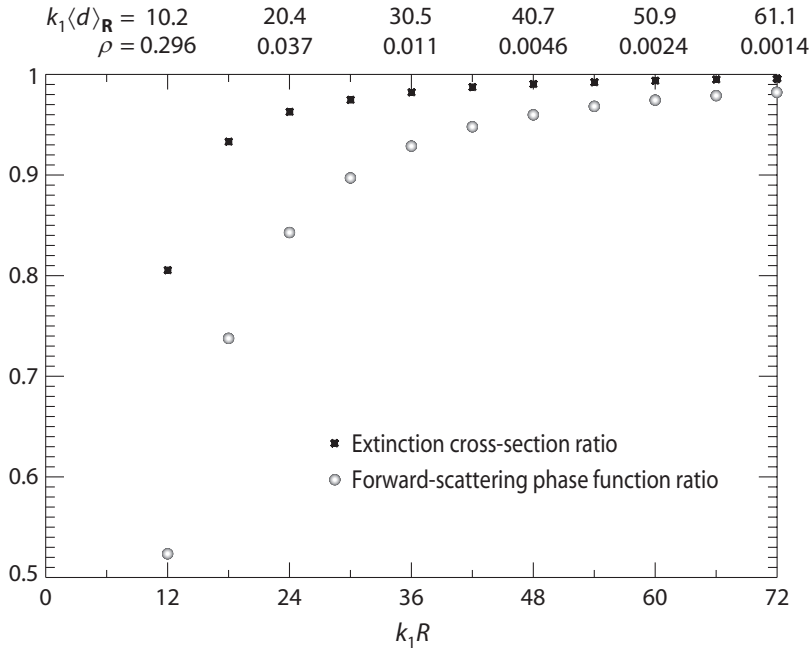

Fig. 18.7. Ratios defined by Eqs. (18.9) and (18.10) versus k_1R. Also shown are the ρ and $k_1\langle d\rangle_{\mathbf{R}}$ values corresponding to $k_1R = 12$, 24, 36, 48, 60, and 72.

viations from the SSA predictions. They obviously indicate that one needs large inter-particle distances and very low packing densities in order to make the SSA sufficiently accurate.

Problems

18.1: Show that at a sufficiently distant observation point, the partial electromagnetic field due to any particle sequence contributing to the right-hand side of Eq. (6.20) is an outgoing transverse spherical wavelet centered at the origin of the last particle of the sequence.

18.2: Derive Eq. (18.4).

18.3: Derive Eq. (18.6).

18.4: Consider the case of an incident quasi-monochromatic beam of light polarized circularly in the counter-clockwise direction when looking in the direction of propagation. The scattered intensity component circularly polarized in the same sense is called the same-helicity intensity, whereas that polarized in the opposite sense is called the opposite-helicity intensity. The circular polarization ratio (CPR) $\mu_{\mathrm{C}}(\Theta)$ is defined as the ratio of the same-helicity and opposite-helicity scattered intensities as a function of the scat-

tering angle Θ. Derive an explicit formula for $\mu_C(\Theta)$ in terms of the elements of the normalized scattering matrix. Show that

$$\delta_C = \mu_C(\pi). \tag{18.11}$$

Notes and further reading

One can often encounter in the literature the notion of multiple electromagnetic scattering as a "random walk of photons" inside a particulate volume. However, this notion is never introduced in the proper QED framework and as such is thoroughly fallacious and misleading (Mishchenko 2009).

Apparently, the first laboratory observation of WL, in the form of the polarization opposition effect, was reported by a pioneer of polarimetric remote sensing Bernard Lyot (1897–1952) (see Lyot 1929). Oetking (1966) observed WL in the form of a narrow intensity peak centered at the exact backscattering direction. However, neither Lyot nor Oetking offered a correct theoretical explanation of their experimental results. The first theoretical prediction of WL was made by K. M. Watson with a reference to a private communication from R. Ruffine (Watson 1969). The first true laboratory demonstrations of WL accompanied by a correct theoretical interpretation should be credited to Kuga and Ishimaru (1984), Tsang and Ishimaru (1984), Van Albada and Lagendijk (1985), and Wolf and Maret (1985).

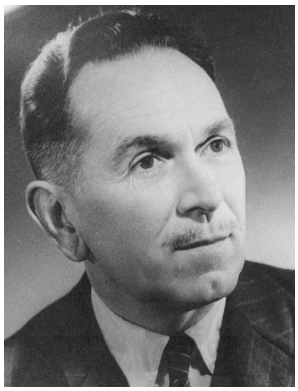

Bernard Lyot

A thorough discussion of speckle phenomena in optics can be found in the monograph by Goodman (2007). Speckle patterns such as those shown in the left-hand column of Fig. 18.3 are also called two-dimensional angle-resolved optical scattering (TAOS) patterns. Analyzing instantaneous TAOS patterns measured for individual aerosol particles is increasingly used as a tool by which the particles can be characterized, classified, and, in some cases, identified (see, e.g., the reviews by Kaye *et al.* (2007), Aptowicz *et al.* (2013), and Crosta *et al.* (2013)).

19

Near-field scattering by a sparse discrete random medium: microphysical radiative transfer theory

The discussion in the preceding chapter was limited to the far field of a random particulate volume comprising a moderate number of particles. However, one is often interested in the near field in order to compute the energy budget of a volume element of a DRM rather than of the entire DRM. Furthermore, in the majority of actual applications the detector of light is located in the near zone of the entire DRM, including the cases of being inside the particulate volume. Although numerically exact solvers of the MMEs such as the MSM (Section 16.1.3) can be used to compute the near field of a DRM (see, e.g., Mackowski and Mishchenko 2013), the applicability of this direct approach is still limited in terms of the number of constituent particles and the overall size of the particulate volume relative to the wavelength.

This implies that the near-field solution of the MMEs for stochastic multiparticle objects such as those shown in Plates 1.1b–1.1f has to be based on a number of simplifying assumptions such as ergodicity, the sparsity and statistical uniformity of the particles' spatial distribution, and the asymptotic limit $N \to \infty$, where N is the number of particles in a DRM. The main objective of the following analysis is to show that this methodology can indeed be used to derive analytically a set of closed-form equations that can be solved numerically with relative ease. As a result, it becomes possible to address the energy-budget problem and quantify the response of near-field WCRs for a representative range of models of a DRM.

Following the discussion in Chapter 8, the solution of the energy-budget problem will be based on the computation of the ensemble-averaged PST of the total field via Eqs. (8.4) and (8.5). The quantification of the reading of a near-field WCR will require ensemble averaging of a "partial" PST contributed by particles residing in the conical acceptance volume $\Delta V_{\hat{\mathbf{q}}}$ of the instrument (Fig. 11.8). We will see that addressing both problems can be reduced to solving the

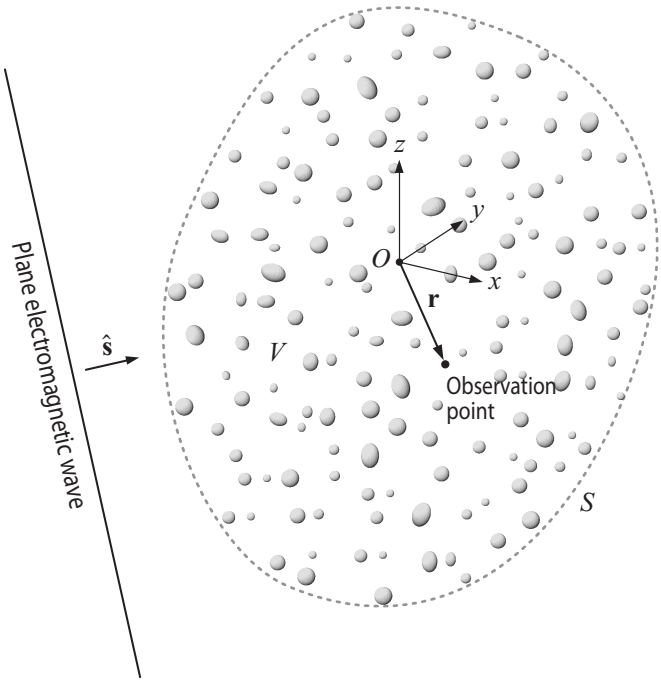

Fig. 19.1. Electromagnetic scattering by a large number of discrete particles sparsely distributed throughout an imaginary macroscopic volume V.

same intermediate equation traditionally called the radiative transfer equation (RTE). As usual, we will first consider the case of purely monochromatic radiation and then discuss the more general case of polychromatic scattering.

19.1 The Twersky approximation

Let us consider electromagnetic scattering by a large group of N particles imbedded in an infinite, homogeneous, isotropic, and nonabsorbing medium. The particles are sparsely distributed throughout a macroscopic volume V and are illuminated by a plane electromagnetic wave propagating in the direction of the unit vector $\hat{\mathbf{s}}$ according to Eq. (6.27) (see Fig. 19.1). We will assume that:

- the particles are separated widely enough that each of them is located in the far zones of all the other particles; and
- the observation point is also located in the far zones of all the particles, although in general it can be located in the near zone of the entire particulate volume V.

These assumptions make applicable the far-field Neumann expansion of the total electric field (6.47)–(6.48). Each term on the right-hand side of Eq. (6.48) can be

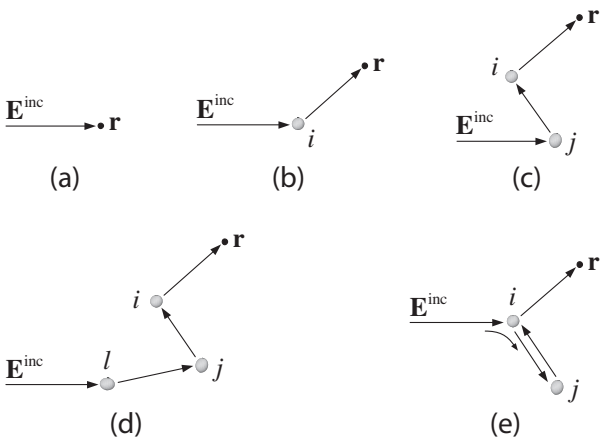

Fig. 19.2. **(a)** Incident field, **(b)** a one-particle sequence, **(c)** a two-particle sequence, **(d)** a self-avoiding three-particle sequence, and **(e)** a three-particle sequence involving particle i twice.

said to be contributed by a one- or multi-particle sequence. Figure 19.2 shows examples of one-, two-, and three-particle sequences.

The terms with $j = i$ and $l = j$ in the triple summation on the right-hand side of Eq. (6.48) are excluded, but the terms with $l = i$ are not. Therefore, we can decompose this summation as follows:

$$\sum_{i=1}^{N}\sum_{\substack{j=1\\ j\neq i}}^{N}\sum_{\substack{l=1\\ l\neq j}}^{N}\vec{B}_{rij}\cdot\vec{B}_{ijl}\cdot\vec{B}_{jl0}\cdot\mathbf{E}_l^{\text{inc}} = \sum_{i=1}^{N}\sum_{\substack{j=1\\ j\neq i}}^{N}\sum_{\substack{l=1\\ l\neq i\\ l\neq j}}^{N}\vec{B}_{rij}\cdot\vec{B}_{ijl}\cdot\vec{B}_{jl0}\cdot\mathbf{E}_l^{\text{inc}} + \sum_{i=1}^{N}\sum_{\substack{j=1\\ j\neq i}}^{N}\vec{B}_{rij}\cdot\vec{B}_{iji}\cdot\vec{B}_{ji0}\cdot\mathbf{E}_i^{\text{inc}}. \tag{19.1}$$

The triple summation on the right-hand side of Eq. (19.1) is illustrated in Fig. 19.2d and includes multi-particle sequences involving a particle only once (so-called self-avoiding sequences), whereas the double summation includes sequences involving a particle more than once, as shown schematically in Fig. 19.2e. Higher-order summations in Eq. (6.48) can be decomposed similarly.

Thus, the total field at an observation point **r** is composed of the incident field, one-particle contributions, and multi-particle contributions that can be divided into two groups. The first one includes all the terms contributed by self-avoiding multi-particle sequences (Fig. 19.3a), whereas the second group includes all the terms corresponding to multi-particle sequences that involve a particle more than once (Figs. 19.3b–19.3e).

The so-called Twersky approximation (Twersky 1964) neglects the terms belonging to the second group and retains only the terms from the first group:

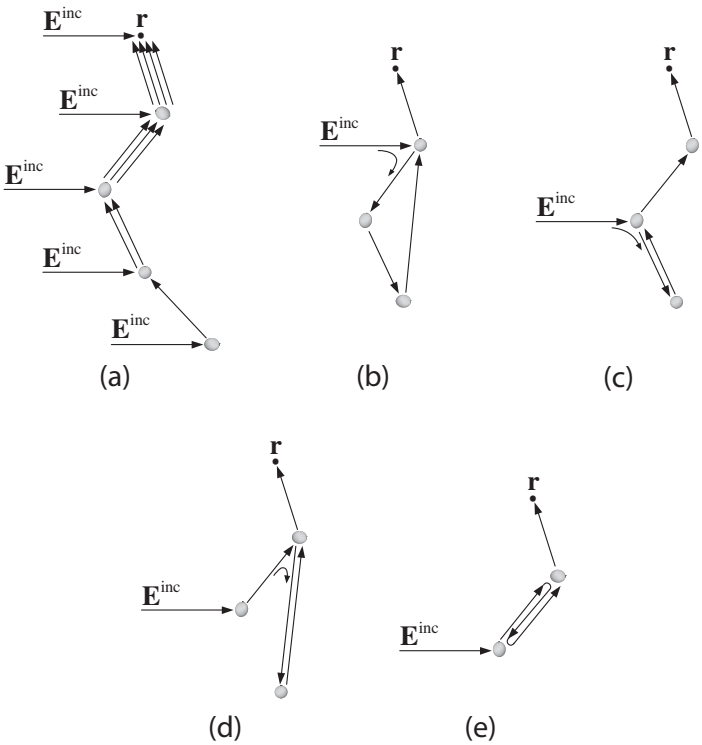

Fig. 19.3. (a) Self-avoiding sequences and **(b)–(e)** four-particle sequences involving a particle more than once.

$$\mathbf{E} \approx \mathbf{E}^{\mathrm{inc}} + \sum_{i=1}^{N} \overleftrightarrow{B}_{ri0} \cdot \mathbf{E}_i^{\mathrm{inc}} + \sum_{i=1}^{N} \sum_{\substack{j=1 \\ j \neq i}}^{N} \overleftrightarrow{B}_{rij} \cdot \overleftrightarrow{B}_{ij0} \cdot \mathbf{E}_j^{\mathrm{inc}} + \sum_{i=1}^{N} \sum_{\substack{j=1 \\ j \neq i}}^{N} \sum_{\substack{l=1 \\ l \neq i \\ l \neq j}}^{N} \overleftrightarrow{B}_{rij} \cdot \overleftrightarrow{B}_{ijl} \cdot \overleftrightarrow{B}_{jl0} \cdot \mathbf{E}_l^{\mathrm{inc}}$$

$$+ \sum_{i=1}^{N} \sum_{\substack{j=1 \\ j \neq i}}^{N} \sum_{\substack{l=1 \\ l \neq i \\ l \neq j}}^{N} \sum_{\substack{m=1 \\ m \neq i \\ m \neq j \\ m \neq l}}^{N} \overleftrightarrow{B}_{rij} \cdot \overleftrightarrow{B}_{ijl} \cdot \overleftrightarrow{B}_{jlm} \cdot \overleftrightarrow{B}_{lm0} \cdot \mathbf{E}_m^{\mathrm{inc}} + \cdots. \tag{19.2}$$

It is straightforward to show that for a large N, the Twersky approximation accounts for the majority of multi-particle sequences. Specifically, an L-fold summation with $L > 2$ on the right-hand side of the full expansion (6.48) contains $N(N-1)^{L-1}$ terms, whereas that in the truncated expansion (19.2) contains $N!/(N-L)!$ terms. The ratio of these two numbers indeed tends to unity as $N \to \infty$, which suggests that one can expect the Twersky approximation to yield rather accurate results, provided that the number of particles is sufficiently large.

It is convenient to represent Neumann expansions of the electric field using the diagram method. Figure 19.4a visualizes the full expansion (6.48), whereas

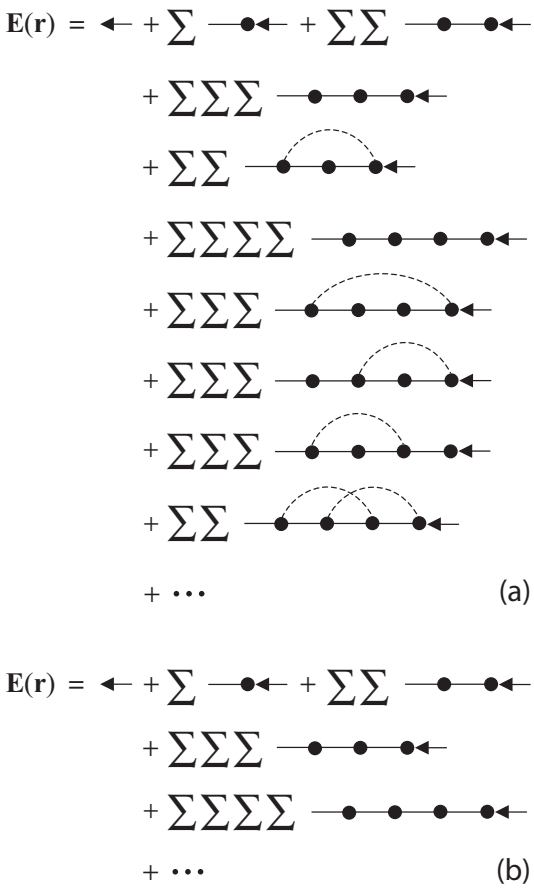

Fig. 19.4. Diagrammatic representations of **(a)** Eqs. (6.47)–(6.48) and **(b)** Eq. (19.2).

Fig. 19.4b illustrates the Twersky approximation (19.2). The arrows in these diagrams represent the incident field, the symbol —● denotes the outcome of multiplying an "incoming" field by a $\vec{B}$ dyadic, and a dashed curve indicates the repeated occurrence of the same particle in a multi-particle sequence.

19.2 The Twersky expansion of the coherent field

Let us now assume that the N particles filling the volume V are randomly moving and consider the total field $\mathbf{E}(\mathbf{r})$ at an internal point $\mathbf{r} \in V$. In general, $\mathbf{E}(\mathbf{r})$ varies (fluctuates) in time because of the random temporal variations of the particle coordinates and states, albeit at a much slower rate than the time-harmonic factor $\exp(-\mathrm{i}\omega t)$. Since one is typically interested in time-averaged characteristics of the total electromagnetic field, it is convenient to decompose $\mathbf{E}(\mathbf{r})$ into the aver-

age (or coherent) part $\mathbf{E}_{\mathrm{c}}(\mathbf{r})$ and the fluctuating part $\mathbf{E}_{\mathrm{f}}(\mathbf{r})$:

$$\mathbf{E}(\mathbf{r}) = \mathbf{E}_{\mathrm{c}}(\mathbf{r}) + \mathbf{E}_{\mathrm{f}}(\mathbf{r}), \tag{19.3}$$

where, upon assuming that the particle ensemble is fully ergodic (see Section 10.4),

$$\mathbf{E}_{\mathrm{c}}(\mathbf{r}) = \langle\langle \mathbf{E}(\mathbf{r}) \rangle\rangle = \langle \mathbf{E}(\mathbf{r}) \rangle_{\mathbf{R},\xi}, \tag{19.4}$$

$$\langle\langle \mathbf{E}_{\mathrm{f}}(\mathbf{r}) \rangle\rangle = \langle \mathbf{E}_{\mathrm{f}}(\mathbf{r}) \rangle_{\mathbf{R},\xi} = \mathbf{0}. \tag{19.5}$$

The ensemble averaging is performed over a statistically representative set of coordinates and states of all the N particles.

It is imperative to recognize that the coherent field $\mathbf{E}_{\mathrm{c}}(\mathbf{r})$ thus defined is not a real physical field, but rather is a purely mathematical construction. Indeed, if we restore the time-harmonic factor $\exp(-\mathrm{i}\omega t)$, which we have been omitting so far for the sake of brevity, then we must conclude that the time average of the actual electric field is equal to zero, according to Eq. (7.1). In contrast, the coherent field does not vanish because it is defined as the time average of the part of the electric field that does not include the factor $\exp(-\mathrm{i}\omega t)$. The only reason to introduce the coherent field in the first place is that it will eventually appear in formulas for quantities that determine the time-averaged energy budget of the scattering medium and/or can actually be measured with a suitable optical device. As we have seen before, these quantities are always defined in such a way that the factor $\exp(-\mathrm{i}\omega t)$ naturally disappears upon multiplication by its complex-conjugate counterpart.

Let us now assume that:

- all particle positions $\mathbf{R}_i$ as well as all particle microphysical states ξ_i (and thus the corresponding particle-centered scattering dyadics $\vec{A}_i(\hat{\mathbf{n}}', \hat{\mathbf{n}})$) as functions of time are independent random processes;
- all particles have the same statistical characteristics; and
- the individual spatial distributions of all the N particles throughout the entire volume V are statistically uniform.

This implies that averaging over all the individual-particle coordinates and all the individual-particle microphysical states can be performed independently and that all individual-particle coordinate probability density functions are given by Eq. (14.16). We then have from Eq. (19.2):

$$\begin{aligned}\mathbf{E}_{\mathrm{c}} = \mathbf{E}^{\mathrm{inc}} &+ \sum_{i=1}^{N} \langle \vec{B}_{ri0} \cdot \mathbf{E}_i^{\mathrm{inc}} \rangle_{\mathbf{R},\xi} + \sum_{i=1}^{N} \sum_{\substack{j=1 \\ j \neq i}}^{N} \langle \vec{B}_{rij} \cdot \vec{B}_{ij0} \cdot \mathbf{E}_j^{\mathrm{inc}} \rangle_{\mathbf{R},\xi} \\ &+ \sum_{i=1}^{N} \sum_{\substack{j=1 \\ j \neq i}}^{N} \sum_{\substack{l=1 \\ l \neq i \\ l \neq j}}^{N} \langle \vec{B}_{rij} \cdot \vec{B}_{ijl} \cdot \vec{B}_{jl0} \cdot \mathbf{E}_l^{\mathrm{inc}} \rangle_{\mathbf{R},\xi} + \cdots\end{aligned}$$

$$
\begin{aligned}
&= \mathbf{E}^{\text{inc}} + \frac{1}{V}\sum_{i=1}^{N}\int \mathrm{d}^3\mathbf{R}_i\,\mathrm{d}\xi_i\, p_\xi(\xi_i)\,\vec{\vec{B}}_{ri0}\cdot\mathbf{E}_i^{\text{inc}} \\
&\quad + \frac{1}{V^2}\sum_{i=1}^{N}\sum_{\substack{j=1\\ j\neq i}}^{N}\int \mathrm{d}^3\mathbf{R}_i\,\mathrm{d}\xi_i\,\mathrm{d}^3\mathbf{R}_j\,\mathrm{d}\xi_j\, p_\xi(\xi_i)\,p_\xi(\xi_j)\,\vec{\vec{B}}_{rij}\cdot\vec{\vec{B}}_{ij0}\cdot\mathbf{E}_j^{\text{inc}} \\
&\quad + \frac{1}{V^3}\sum_{i=1}^{N}\sum_{\substack{j=1\\ j\neq i}}^{N}\sum_{\substack{l=1\\ l\neq i\\ l\neq j}}^{N}\int \mathrm{d}^3\mathbf{R}_i\,\mathrm{d}\xi_i\,\mathrm{d}^3\mathbf{R}_j\,\mathrm{d}\xi_j\,\mathrm{d}^3\mathbf{R}_l\,\mathrm{d}\xi_l\, p_\xi(\xi_i)\,p_\xi(\xi_j)\,p_\xi(\xi_l) \\
&\qquad\qquad \times\vec{\vec{B}}_{rij}\cdot\vec{\vec{B}}_{ijl}\cdot\vec{\vec{B}}_{jl0}\cdot\mathbf{E}_l^{\text{inc}} \\
&\quad + \cdots. \qquad (19.6)
\end{aligned}
$$

The spatial integrations are performed over the entire volume V.

Note that since the far-field FEs are valid only in the far zones of all the N particles, each volume integration on the right-hand side of Eq. (19.6) should not, in principle, include a spherical volume element centered at the observation point $\mathbf{r}$ or at a particle origin $\mathbf{R}_i$ $(i = 1, \ldots, N)$ and having a radius defined by the inequalities (5.12)–(5.14). Typically, however, this volume element is much smaller than V, and its relative contribution to the respective volume integral can be expected to be negligible.

Equations (6.42)–(6.45) imply that

$$
\begin{aligned}
\mathbf{E}_{\text{c}} &= \mathbf{E}^{\text{inc}} + \frac{1}{V}\sum_{i=1}^{N}\int_V \mathrm{d}^3\mathbf{R}_i\, G(r_i)\langle\vec{\vec{A}}(\hat{\mathbf{r}}_i,\hat{\mathbf{s}})\rangle_\xi\cdot\mathbf{E}_i^{\text{inc}} \\
&\quad + \frac{1}{V^2}\sum_{i=1}^{N}\sum_{\substack{j=1\\ j\neq i}}^{N}\int_V \mathrm{d}^3\mathbf{R}_i\,\mathrm{d}^3\mathbf{R}_j\, G(r_i)\,G(R_{ij})\langle\vec{\vec{A}}(\hat{\mathbf{r}}_i,\hat{\mathbf{R}}_{ij})\rangle_\xi\cdot\langle\vec{\vec{A}}(\hat{\mathbf{R}}_{ij},\hat{\mathbf{s}})\rangle_\xi\cdot\mathbf{E}_j^{\text{inc}} \\
&\quad + \frac{1}{V^3}\sum_{i=1}^{N}\sum_{\substack{j=1\\ j\neq i}}^{N}\sum_{\substack{l=1\\ l\neq i\\ l\neq j}}^{N}\int_V \mathrm{d}^3\mathbf{R}_i\,\mathrm{d}^3\mathbf{R}_j\,\mathrm{d}^3\mathbf{R}_l\, G(r_i)\,G(R_{ij})\,G(R_{jl})\langle\vec{\vec{A}}(\hat{\mathbf{r}}_i,\hat{\mathbf{R}}_{ij})\rangle_\xi \\
&\qquad\qquad \cdot\langle\vec{\vec{A}}(\hat{\mathbf{R}}_{ij},\hat{\mathbf{R}}_{jl})\rangle_\xi\cdot\langle\vec{\vec{A}}(\hat{\mathbf{R}}_{jl},\hat{\mathbf{s}})\rangle_\xi\cdot\mathbf{E}_l^{\text{inc}} \\
&\quad + \cdots, \qquad (19.7)
\end{aligned}
$$

where $\langle\vec{\vec{A}}(\hat{\mathbf{n}}',\hat{\mathbf{n}})\rangle_\xi$ is the average of the single-particle scattering dyadic over the particle states. Finally, taking the limit $N\to\infty$, we obtain (Problem 19.1)

$$
\begin{aligned}
\mathbf{E}_{\text{c}} &\underset{N\to\infty}{=} \mathbf{E}^{\text{inc}} + n_0\int_V \mathrm{d}^3\mathbf{R}_1\, G(r_1)\langle\vec{\vec{A}}(\hat{\mathbf{r}}_1,\hat{\mathbf{s}})\rangle_\xi\cdot\mathbf{E}_1^{\text{inc}} \\
&\quad + n_0^2\int_V \mathrm{d}^3\mathbf{R}_1\,\mathrm{d}^3\mathbf{R}_2\, G(r_1)\,G(R_{12})\langle\vec{\vec{A}}(\hat{\mathbf{r}}_1,\hat{\mathbf{R}}_{12})\rangle_\xi\cdot\langle\vec{\vec{A}}(\hat{\mathbf{R}}_{12},\hat{\mathbf{s}})\rangle_\xi\cdot\mathbf{E}_2^{\text{inc}}
\end{aligned}
$$

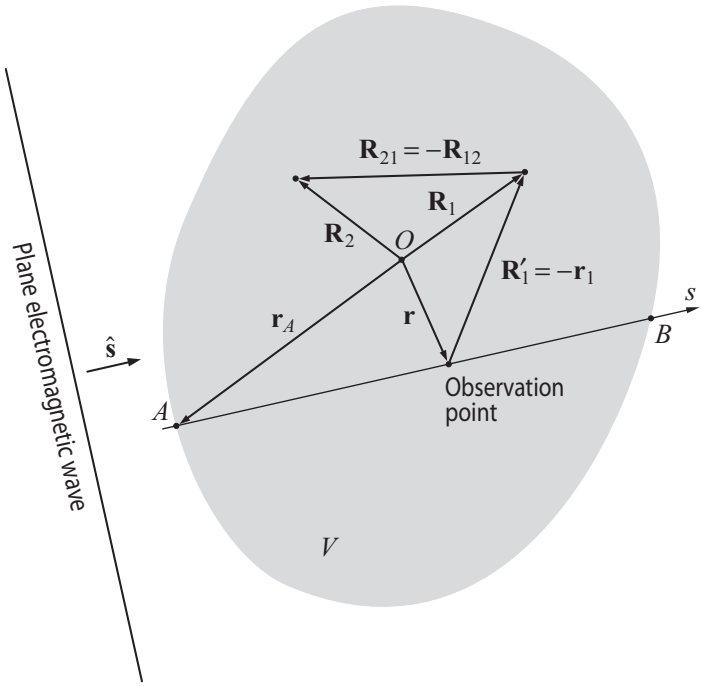

Fig. 19.5. Geometry showing the quantities used in the derivation of Eq. (19.16).

$$
\begin{aligned}
&+ n_0^3 \int_V \mathrm{d}^3\mathbf{R}_1 \mathrm{d}^3\mathbf{R}_2 \mathrm{d}^3\mathbf{R}_3 G(r_1) G(R_{12}) G(R_{23}) \langle \overleftrightarrow{A}(\hat{\mathbf{r}}_1, \hat{\mathbf{R}}_{12}) \rangle_\xi \\
&\qquad \cdot \langle \overleftrightarrow{A}(\hat{\mathbf{R}}_{12}, \hat{\mathbf{R}}_{23}) \rangle_\xi \cdot \langle \overleftrightarrow{A}(\hat{\mathbf{R}}_{23}, \hat{\mathbf{s}}) \rangle_\xi \cdot \mathbf{E}_3^{\mathrm{inc}} \\
&+ \cdots,
\end{aligned}
\tag{19.8}
$$

where $n_0 = N/V$ is the average particle number density. Note that the subscripts 1, 2, … are now used to label different integration variables rather than to number the actual particles. Equation (19.8) is the full vector version of the expansion derived by Twersky (1964) for scalar waves.

19.3 Coherent field

Let us now assume for the sake of simplicity that the volume V is uniformly convex. This assumption ensures that all points of a straight line connecting any two points of the medium lie inside the medium. It is convenient for our purposes to introduce an s-axis parallel to the incidence direction and going through the observation point. This axis enters the volume V at the point A such that $s(A) = 0$ and exits it at point B (Fig. 19.5). Let us consider the first integral on the right-hand side of Eq. (19.8) and denote it $\mathbf{I}_1$. From $\mathbf{R}_1 = \mathbf{r} + \mathbf{R}_1'$, we have

$$\mathbf{I}_1 = n_0 \int_V \mathrm{d}^3\mathbf{R}_1 G(r_1) \langle \overleftrightarrow{A}(\hat{\mathbf{r}}_1, \hat{\mathbf{s}}) \rangle_\xi \cdot \mathbf{E}_1^{\mathrm{inc}}$$
$$= n_0 \int_V \mathrm{d}^3\mathbf{R}_1' \exp(\mathrm{i}k_1 \hat{\mathbf{s}} \cdot \mathbf{R}_1') \frac{\exp(\mathrm{i}k_1 R_1')}{R_1'} \langle \overleftrightarrow{A}(-\hat{\mathbf{R}}_1', \hat{\mathbf{s}}) \rangle_\xi \cdot \mathbf{E}^{\mathrm{inc}}(\mathbf{r}). \tag{19.9}$$

The observation point is assumed to be in the far zone of any particle, which means that $k_1 R_1' \gg 1$. We may, therefore, use in Eq. (19.9) the Saxon's asymptotic expansion of a plane wave in spherical waves (see Appendix D):

$$\exp(\mathrm{i}k_1 \hat{\mathbf{s}} \cdot \mathbf{R}_1') \underset{k_1 R_1' \to \infty}{=} \frac{\mathrm{i}2\pi}{k_1 R_1'} [\delta(\hat{\mathbf{s}} + \hat{\mathbf{R}}_1') \exp(-\mathrm{i}k_1 R_1') - \delta(\hat{\mathbf{s}} - \hat{\mathbf{R}}_1') \exp(\mathrm{i}k_1 R_1')]. \tag{19.10}$$

In order to evaluate the integral (19.9), we use a spherical polar coordinate system with origin at the observation point and with the z-axis directed along the s-axis. We thus have

$$\mathbf{I}_1 = \frac{\mathrm{i}2\pi n_0}{k_1} \int_{4\pi} \mathrm{d}\hat{\mathbf{R}}_1' \int \mathrm{d}R_1' \langle \overleftrightarrow{A}(-\hat{\mathbf{R}}_1', \hat{\mathbf{s}}) \rangle_\xi \cdot \mathbf{E}^{\mathrm{inc}}(\mathbf{r}) [\delta(\hat{\mathbf{s}} + \hat{\mathbf{R}}_1') - \delta(\hat{\mathbf{s}} - \hat{\mathbf{R}}_1') \exp(2\mathrm{i}k_1 R_1')]$$
$$= \frac{\mathrm{i}2\pi n_0}{k_1} s(\mathbf{r}) \langle \overleftrightarrow{A}(\hat{\mathbf{s}}, \hat{\mathbf{s}}) \rangle_\xi \cdot \mathbf{E}^{\mathrm{inc}}(\mathbf{r})$$
$$- \frac{\pi n_0}{k_1^2} \exp\{\mathrm{i}2k_1[s(B) - s(\mathbf{r})]\} \langle \overleftrightarrow{A}(-\hat{\mathbf{s}}, \hat{\mathbf{s}}) \rangle_\xi \cdot \mathbf{E}^{\mathrm{inc}}(\mathbf{r}). \tag{19.11}$$

Let us now recall that the number of particles filling the volume V is assumed to be very large, and the particles are assumed to be separated by distances greatly exceeding the wavelength (Eq. (H.7)). As a consequence, $s(\mathbf{r}) \gg 1/k_1$ (except for points in the immediate vicinity of the boundary), which suggests that the second term on the right-hand side of Eq. (19.11) must be much smaller than the first term. Also, for objects like clouds, the imaginary boundaries of the scattering volume V are not perfectly fixed and can be expected to fluctuate during the time interval necessary to compute the coherent field. Averaging over these fluctuations does not affect the first term on the right-hand side of Eq. (19.11), but effectively extinguishes the second term proportional to the rapidly oscillating exponential $\exp\{\mathrm{i}2k_1[s(B) - s(\mathbf{r})]\}$. Thus,

$$\mathbf{I}_1 = \frac{\mathrm{i}2\pi n_0}{k_1} s(\mathbf{r}) \langle \overleftrightarrow{A}(\hat{\mathbf{s}}, \hat{\mathbf{s}}) \rangle_\xi \cdot \mathbf{E}^{\mathrm{inc}}(\mathbf{r}). \tag{19.12}$$

Consider now the second integral on the right-hand side of Eq. (19.8) and denote it $\mathbf{I}_2$. Since $\mathbf{R}_2 = \mathbf{r} + \mathbf{R}_1' + \mathbf{R}_{21}$, we have

$$\mathbf{I}_2 = n_0^2 \int \mathrm{d}R_1' R_1'^2 G(R_1') \int_{4\pi} \mathrm{d}\hat{\mathbf{R}}_1' \int \mathrm{d}R_{21} R_{21}^2 G(R_{21}) \int_{4\pi} \mathrm{d}\hat{\mathbf{R}}_{21}$$
$$\times \langle \overleftrightarrow{A}(-\hat{\mathbf{R}}_1', -\hat{\mathbf{R}}_{21}) \rangle_\xi \cdot \langle \overleftrightarrow{A}(-\hat{\mathbf{R}}_{21}, \hat{\mathbf{s}}) \rangle_\xi \cdot \mathbf{E}_2^{\mathrm{inc}}, \tag{19.13}$$

where

$$\begin{aligned}\mathbf{E}_2^{\text{inc}} &= \exp(\mathrm{i}k_1\hat{\mathbf{s}}\cdot\mathbf{R}_2)\mathbf{E}_0^{\text{inc}}\\ &= \exp(\mathrm{i}k_1\hat{\mathbf{s}}\cdot\mathbf{R}_1')\exp(\mathrm{i}k_1\hat{\mathbf{s}}\cdot\mathbf{R}_{21})\mathbf{E}^{\text{inc}}(\mathbf{r})\\ &= \left(\frac{\mathrm{i}2\pi}{k_1}\right)^2\frac{1}{R_1'}[\delta(\hat{\mathbf{s}}+\hat{\mathbf{R}}_1')\exp(-\mathrm{i}k_1R_1') - \delta(\hat{\mathbf{s}}-\hat{\mathbf{R}}_1')\exp(\mathrm{i}k_1R_1')]\\ &\quad\times\frac{1}{R_{21}}[\delta(\hat{\mathbf{s}}+\hat{\mathbf{R}}_{21})\exp(-\mathrm{i}k_1R_{21}) - \delta(\hat{\mathbf{s}}-\hat{\mathbf{R}}_{21})\exp(\mathrm{i}k_1R_{21})]\mathbf{E}^{\text{inc}}(\mathbf{r}).\end{aligned} \tag{19.14}$$

It is thus clear that only particles with origins on the s-axis contribute to $\mathbf{I}_2$. Substituting Eq. (19.14) in Eq. (19.13) yields

$$\mathbf{I}_2 = \frac{1}{2}\left[\frac{\mathrm{i}2\pi n_0}{k_1}s(\mathbf{r})\right]^2\langle\overleftrightarrow{A}(\hat{\mathbf{s}},\hat{\mathbf{s}})\rangle_\xi\cdot\langle\overleftrightarrow{A}(\hat{\mathbf{s}},\hat{\mathbf{s}})\rangle_\xi\cdot\mathbf{E}^{\text{inc}}(\mathbf{r}). \tag{19.15}$$

The remaining integrals in Eq. (19.8) are evaluated analogously. The final result is as follows:

$$\mathbf{E}_{\text{c}}(\mathbf{r}) = \exp\left[\frac{\mathrm{i}2\pi n_0}{k_1}s(\mathbf{r})\langle\overleftrightarrow{A}(\hat{\mathbf{s}},\hat{\mathbf{s}})\rangle_\xi\right]\cdot\mathbf{E}^{\text{inc}}(\mathbf{r}), \tag{19.16}$$

where the dyadic exponential is defined as

$$\exp\overleftrightarrow{B} = \overleftrightarrow{I} + \overleftrightarrow{B} + \frac{1}{2!}\overleftrightarrow{B}\cdot\overleftrightarrow{B} + \frac{1}{3!}\overleftrightarrow{B}\cdot\overleftrightarrow{B}\cdot\overleftrightarrow{B} + \cdots. \tag{19.17}$$

It is clear from the derivation of Eq. (19.16) that all single- and multi-particle paths that contribute to the coherent field at an internal observation point lie on the straight line parallel to the incidence direction and going through the observation point. Furthermore, all particles that contribute to the coherent field lie between the source of illumination and the observation point. Since the products

$$\langle\overleftrightarrow{A}(\hat{\mathbf{s}},\hat{\mathbf{s}})\rangle_\xi\cdot\mathbf{E}_0^{\text{inc}},\ \ \langle\overleftrightarrow{A}(\hat{\mathbf{s}},\hat{\mathbf{s}})\rangle_\xi\cdot\langle\overleftrightarrow{A}(\hat{\mathbf{s}},\hat{\mathbf{s}})\rangle_\xi\cdot\mathbf{E}_0^{\text{inc}},\ \text{etc.}$$

always yield electric vectors perpendicular to $\hat{\mathbf{s}}$, the coherent field satisfies the transversality condition

$$\mathbf{E}_{\text{c}}(\mathbf{r})\cdot\hat{\mathbf{s}} = 0. \tag{19.18}$$

The fact that the coherent field is controlled by the forward-scattering dyadic is not surprising. Indeed, the fluctuating component of the total field is the vector sum of the partial fields generated by different particles. Random movements of the particles involve large phase shifts in the partial fields, thereby causing the fluctuating field to vanish when it is averaged over particle positions. The exact forward-scattering direction is different because the phase of the partial wave forward-scattered by a particle towards the observation point in response to the incident wave does not depend on the particle position along the line connecting the source of illumination and the observation point (see Fig. 19.6). Therefore,

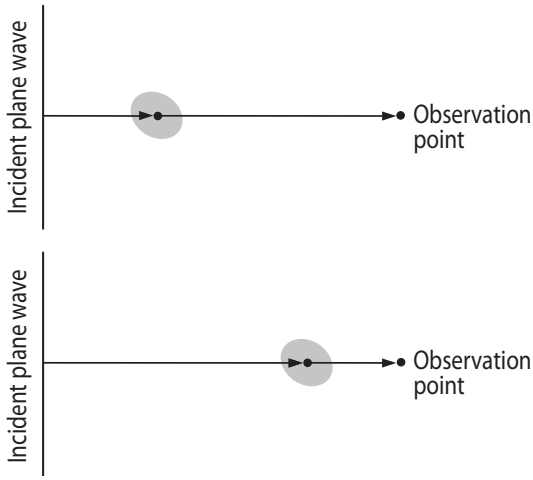

Fig. 19.6. The phase of the wave forward-scattered by a particle in response to the incident plane wave is the same, irrespective of the exact position of the particle on the line connecting the source of illumination and the observation point.

the interference of the incident wave and the forward-scattered partial wave is always the same, irrespective of the precise position of the particle, and the result of the interference does not vanish upon statistical averaging over particle positions. The same is true of the interference of the incident field and a wave forward scattered along a multi-particle sequence of any order as well as of the mutual interference of different forward-scattered waves.

Since $\mathbf{r} = \mathbf{r}_A + s(\mathbf{r})\hat{\mathbf{s}}$ (Fig. 19.5), we have from Eq. (19.16):

$$\begin{aligned}\mathbf{E}_{\mathrm{c}}(\mathbf{r}) &= \exp(\mathrm{i}k_1\hat{\mathbf{s}}\cdot\mathbf{r}_A)\exp[\mathrm{i}k_1 s(\mathbf{r})]\exp\left[\frac{\mathrm{i}2\pi n_0}{k_1}s(\mathbf{r})\langle\overleftrightarrow{A}(\hat{\mathbf{s}},\hat{\mathbf{s}})\rangle_\xi\right]\cdot\mathbf{E}_0^{\mathrm{inc}}\\ &= \exp[\mathrm{i}\overleftrightarrow{\varkappa}(\hat{\mathbf{s}})s(\mathbf{r})]\cdot\mathbf{E}^{\mathrm{inc}}(\mathbf{r}_A)\end{aligned} \tag{19.19}$$

or

$$\mathbf{E}_{\mathrm{c}}(s) = \overleftrightarrow{\eta}(\hat{\mathbf{s}}, s)\cdot\mathbf{E}_{\mathrm{c}}(s=0), \tag{19.20}$$

where

$$\overleftrightarrow{\varkappa}(\hat{\mathbf{s}}) = k_1\overleftrightarrow{I} + \frac{2\pi n_0}{k_1}\langle\overleftrightarrow{A}(\hat{\mathbf{s}},\hat{\mathbf{s}})\rangle_\xi \tag{19.21}$$

is the dyadic propagation constant for the propagation direction $\hat{\mathbf{s}}$,

$$\overleftrightarrow{\eta}(\hat{\mathbf{s}}, s) = \exp[\mathrm{i}\overleftrightarrow{\varkappa}(\hat{\mathbf{s}})s] \tag{19.22}$$

is the coherent transmission dyadic, and

$$\mathbf{E}_{\mathrm{c}}(s=0) = \mathbf{E}^{\mathrm{inc}}(\mathbf{r}_A) \tag{19.23}$$

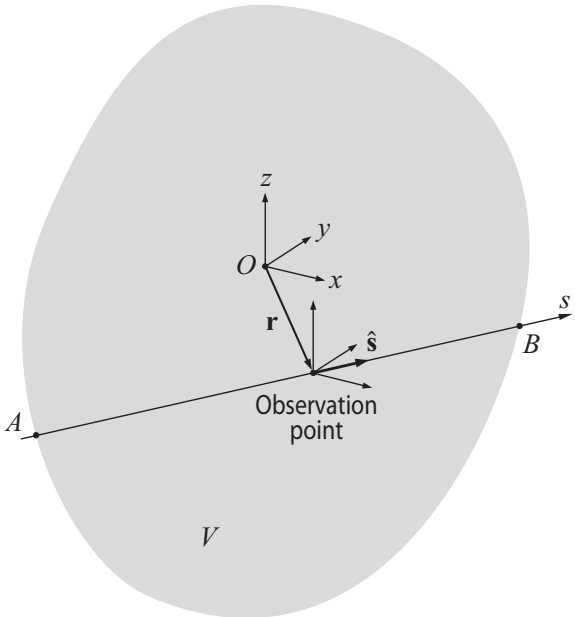

Fig. 19.7. The direction of propagation and the electric field vector components of the coherent field at an observation point **r** are specified using a local coordinate system with the same orientation as the laboratory coordinate system centered at O.

is the boundary value of the coherent field. This is the general vector form of the Foldy approximation for the coherent field (cf. Foldy 1945). Another form of Eq. (19.19) is

$$\frac{\mathrm{d}\mathbf{E}_{\mathrm{c}}(\mathbf{r})}{\mathrm{d}s} = \mathrm{i}\vec{\varkappa}(\hat{\mathbf{s}}) \cdot \mathbf{E}_{\mathrm{c}}(\mathbf{r}), \quad \mathbf{E}_{\mathrm{c}}(\mathbf{r}_A) = \mathbf{E}^{\mathrm{inc}}(\mathbf{r}_A). \tag{19.24}$$

Although Eqs. (19.18) and (19.19) may appear to describe a transverse electromagnetic wave, the reader should not forget that $\mathbf{E}_{\mathrm{c}}(\mathbf{r})$ is not a real physical field. Furthermore, the coherent field was computed by taking an average over a uniform distribution of particle positions, as well as over all physically realizable particle states. Therefore, it is not defined at any given moment in time.

We can exploit the transversality of the coherent field to rewrite the above equations in a simpler matrix form. As in Section 7.1, we characterize the direction of propagation $\hat{\mathbf{s}}$ at the observation point **r** using the corresponding polar and azimuth angles in the local coordinate system, which is centered at the observation point and has the same spatial orientation as the laboratory coordinate system (see Fig. 19.7). Then the electric vector of the coherent field can be written as the vector sum of the corresponding θ- and φ-components:

$$\mathbf{E}_{\mathrm{c}}(\mathbf{r}) = E_{\mathrm{c}\theta}(\mathbf{r})\hat{\boldsymbol{\theta}}(\hat{\mathbf{s}}) + E_{\mathrm{c}\varphi}(\mathbf{r})\hat{\boldsymbol{\varphi}}(\hat{\mathbf{s}}). \tag{19.25}$$

Defining the two-component electric column vector of the coherent field according to

$$\mathbf{E}_{\mathrm{c}}(\mathbf{r}) = \begin{bmatrix} E_{\mathrm{c}\theta}(\mathbf{r}) \\ E_{\mathrm{c}\varphi}(\mathbf{r}) \end{bmatrix}, \tag{19.26}$$

we have instead of Eq. (19.24)

$$\frac{\mathrm{d}\mathbf{E}_{\mathrm{c}}(\mathbf{r})}{\mathrm{d}s} = \mathrm{i}\mathbf{k}(\hat{\mathbf{s}})\mathbf{E}_{\mathrm{c}}(\mathbf{r}), \quad \mathbf{E}_{\mathrm{c}}(\mathbf{r}_A) = \mathbf{E}^{\mathrm{inc}}(\mathbf{r}_A), \tag{19.27}$$

where $\mathbf{k}(\hat{\mathbf{s}})$ is the 2×2 matrix propagation constant with elements

$$k_{11}(\hat{\mathbf{s}}) = \hat{\boldsymbol{\theta}}(\hat{\mathbf{s}}) \cdot \ddot{\varkappa}(\hat{\mathbf{s}}) \cdot \hat{\boldsymbol{\theta}}(\hat{\mathbf{s}}), \tag{19.28}$$

$$k_{12}(\hat{\mathbf{s}}) = \hat{\boldsymbol{\theta}}(\hat{\mathbf{s}}) \cdot \ddot{\varkappa}(\hat{\mathbf{s}}) \cdot \hat{\boldsymbol{\varphi}}(\hat{\mathbf{s}}), \tag{19.29}$$

$$k_{21}(\hat{\mathbf{s}}) = \hat{\boldsymbol{\varphi}}(\hat{\mathbf{s}}) \cdot \ddot{\varkappa}(\hat{\mathbf{s}}) \cdot \hat{\boldsymbol{\theta}}(\hat{\mathbf{s}}), \tag{19.30}$$

$$k_{22}(\hat{\mathbf{s}}) = \hat{\boldsymbol{\varphi}}(\hat{\mathbf{s}}) \cdot \ddot{\varkappa}(\hat{\mathbf{s}}) \cdot \hat{\boldsymbol{\varphi}}(\hat{\mathbf{s}}). \tag{19.31}$$

Obviously,

$$\mathbf{k}(\hat{\mathbf{s}}) = k_1 \begin{bmatrix} 1 & 0 \\ 0 & 1 \end{bmatrix} + \frac{2\pi n_0}{k_1} \langle \mathbf{S}(\hat{\mathbf{s}}, \hat{\mathbf{s}}) \rangle_{\xi}, \tag{19.32}$$

where $\langle \mathbf{S}(\hat{\mathbf{s}}, \hat{\mathbf{s}}) \rangle_{\xi}$ is the forward-scattering amplitude matrix averaged over the particle states (cf. Eqs. (5.26)–(5.29)).

It is often convenient to rewrite Eq. (19.27) in the form

$$\mathbf{E}_{\mathrm{c}}(s) = \mathbf{h}(\hat{\mathbf{s}}, s)\mathbf{E}_{\mathrm{c}}(s = 0), \tag{19.33}$$

where

$$\mathbf{h}(\hat{\mathbf{s}}, s) = \exp[\mathrm{i}s\mathbf{k}(\hat{\mathbf{s}})] \tag{19.34}$$

is the coherent transmission amplitude matrix and the 2×2 matrix exponential is defined as follows:

$$\exp\mathbf{B} = \begin{bmatrix} 1 & 0 \\ 0 & 1 \end{bmatrix} + \mathbf{B} + \frac{1}{2!}\mathbf{BB} + \frac{1}{3!}\mathbf{BBB} + \cdots. \tag{19.35}$$

19.4 Transfer equation for the coherent field

We will now describe the coherent field in terms of quantities having the dimension of monochromatic energy flux. We first define the coherency column vector of the coherent field according to

$$\mathbf{J}_{\mathrm{c}} = \frac{1}{2}\sqrt{\frac{\epsilon_1}{\mu_0}} \begin{bmatrix} E_{\mathrm{c}\theta} E_{\mathrm{c}\theta}^* \\ E_{\mathrm{c}\theta} E_{\mathrm{c}\varphi}^* \\ E_{\mathrm{c}\varphi} E_{\mathrm{c}\theta}^* \\ E_{\mathrm{c}\varphi} E_{\mathrm{c}\varphi}^* \end{bmatrix} \tag{19.36}$$

(cf. Eq. (7.40)) and easily derive from Eqs. (19.27) and (19.32) the following transfer equation:

$$\frac{\mathrm{d}\mathbf{J}_{\mathrm{c}}(\mathbf{r})}{\mathrm{d}s} = -n_0\langle \mathbf{K}^J(\hat{\mathbf{s}})\rangle_\xi \mathbf{J}_{\mathrm{c}}(\mathbf{r}), \quad \mathbf{J}_{\mathrm{c}}(\mathbf{r}_A) = \mathbf{J}^{\mathrm{inc}}, \tag{19.37}$$

where $\mathbf{K}^J$ is the coherency extinction matrix given by Eq. (13.58). The Stokes-vector representation of this equation is obtained by using the definition

$$\mathbf{I}_{\mathrm{c}} = \mathbf{D}\mathbf{J}_{\mathrm{c}} = \frac{1}{2}\sqrt{\frac{\epsilon_1}{\mu_0}}\begin{bmatrix} E_{\mathrm{c}\theta}E_{\mathrm{c}\theta}^* + E_{\mathrm{c}\varphi}E_{\mathrm{c}\varphi}^* \\ E_{\mathrm{c}\theta}E_{\mathrm{c}\theta}^* - E_{\mathrm{c}\varphi}E_{\mathrm{c}\varphi}^* \\ -2\,\mathrm{Re}(E_{\mathrm{c}\theta}E_{\mathrm{c}\varphi}^*) \\ 2\,\mathrm{Im}(E_{\mathrm{c}\theta}E_{\mathrm{c}\varphi}^*) \end{bmatrix} \tag{19.38}$$

and Eq. (13.61) (Problem 19.3):

$$\frac{\mathrm{d}\mathbf{I}_{\mathrm{c}}(\mathbf{r})}{\mathrm{d}s} = -n_0\langle \mathbf{K}(\hat{\mathbf{s}})\rangle_\xi \mathbf{I}_{\mathrm{c}}(\mathbf{r}), \quad \mathbf{I}_{\mathrm{c}}(\mathbf{r}_A) = \mathbf{I}^{\mathrm{inc}}, \tag{19.39}$$

where $\mathbf{K}$ is the Stokes extinction matrix with elements given by Eqs. (13.62)–(13.68).

The formal solution of Eq. (19.39) can be written in the form

$$\begin{aligned} \mathbf{I}_{\mathrm{c}}(\mathbf{r}) &= \mathbf{H}[\hat{\mathbf{s}}, s(\mathbf{r})]\mathbf{I}_{\mathrm{c}}(\mathbf{r}_A) \\ &= \mathbf{H}[\hat{\mathbf{s}}, s(\mathbf{r})]\mathbf{I}^{\mathrm{inc}}, \end{aligned} \tag{19.40}$$

where $\mathbf{I}^{\mathrm{inc}}$ is the Stokes column vector of the incident plane wave and

$$\mathbf{H}(\hat{\mathbf{s}}, s) = \exp[-n_0 s\langle \mathbf{K}(\hat{\mathbf{s}})\rangle_\xi] \tag{19.41}$$

is the coherent transmission Stokes matrix. As usual, the 4×4 matrix exponential is defined by

$$\exp\mathbf{B} = \mathbf{\Delta} + \mathbf{B} + \frac{1}{2!}\mathbf{B}\mathbf{B} + \frac{1}{3!}\mathbf{B}\mathbf{B}\mathbf{B} + \cdots, \tag{19.42}$$

where $\mathbf{\Delta}$ is the 4×4 unit matrix.

19.5 Ladder approximation for the dyadic correlation function

We are now well prepared to start the derivation of the ensemble-averaged dyadic correlation function of the total field for two internal observation points. Recalling Eq. (8.5), we have

$$\langle \ddot{C}(\mathbf{r}, \mathbf{r}')\rangle_{\xi,\mathbf{R}} = \langle \mathbf{E}(\mathbf{r}) \otimes [\mathbf{E}(\mathbf{r}')]^*\rangle_{\xi,\mathbf{R}}, \quad \mathbf{r}, \mathbf{r}' \in V. \tag{19.43}$$

The Twersky approximation defined by Eq. (19.2) and Fig. 19.4b implies that the dyadic correlation function is given by the expression shown diagrammatically in Fig. 19.8. To classify the different terms entering the expanded expression inside

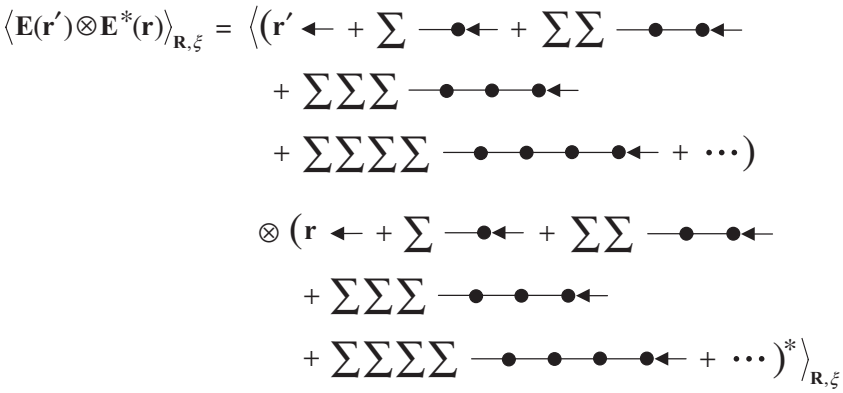

Fig. 19.8. The Twersky expansion of the dyadic correlation function.

the angular brackets on the right-hand side of this equation, we will use the notation illustrated in Fig. 19.9a. In this particular case, the upper and lower sequences involve different particles. However, the two sequences can involve one or more common particles, as shown in Figs. 19.9c–19.9f by using the dashed connectors. Furthermore, if the number of common particles is two or more, they can enter the upper and lower sequences in the same order, as in Fig. 19.9d, or in the reverse order, as in Fig. 19.9e. Figure 19.9f shows a mixed diagram in which two common particles appear in the same order and two other common particles appear in the reverse order. The contribution of this diagram to the dyadic correlation function is simply

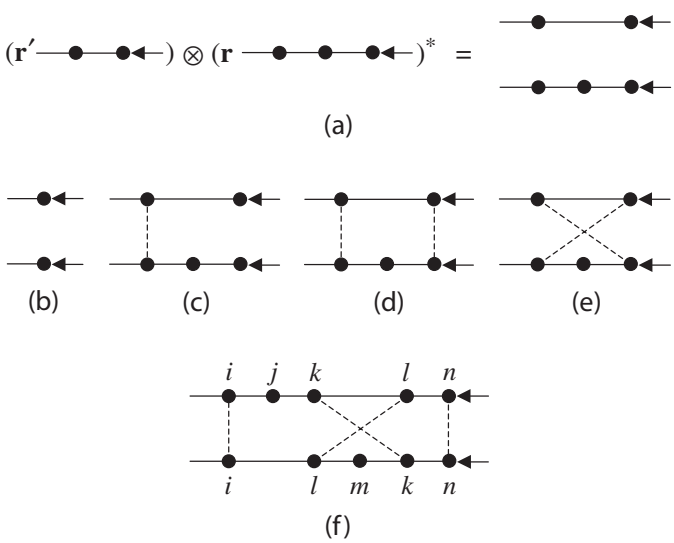

Fig. 19.9. Classification of terms entering the Twersky expansion of the dyadic correlation function.

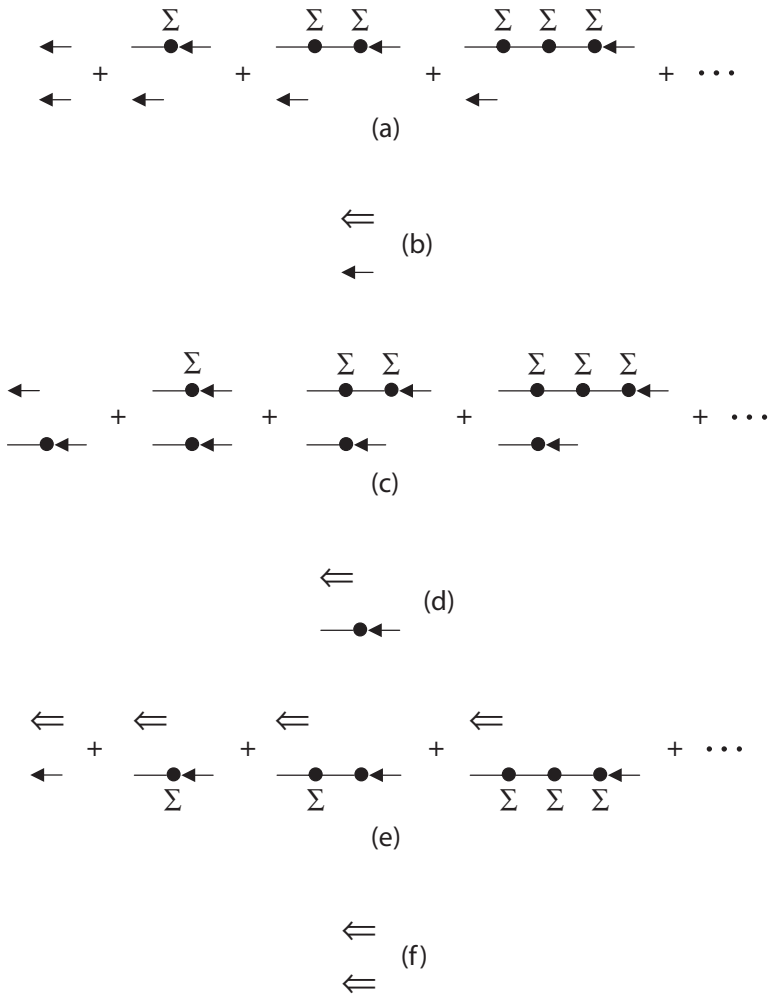

Fig. 19.10. Calculation of the cumulative contribution of the diagrams with no connectors.

$$[\ddot{B}_{r'ij} \cdot \ddot{B}_{ijk} \cdot \ddot{B}_{jkl} \cdot \ddot{B}_{kln} \cdot \ddot{B}_{ln0} \cdot \mathbf{E}_n^{\text{inc}}] \otimes [\ddot{B}_{ril} \cdot \ddot{B}_{ilm} \cdot \ddot{B}_{lmk} \cdot \ddot{B}_{mkn} \cdot \ddot{B}_{kn0} \cdot \mathbf{E}_n^{\text{inc}}]^*.$$

By the very nature of the Twersky approximation, neither the upper sequence nor the lower sequence can involve a particle more than once. Therefore, no particle can be the origin of more than one connector.

To sum and average all the diagrams entering the expanded expression for the dyadic correlation function in Fig. 19.8 is a very difficult problem that we will not try to address fully. Instead, in this chapter we will neglect all diagrams with crossing connectors and will work with a truncated expansion that includes only the diagrams with vertical or no connectors. This approximation will allow us to sum and average large groups of diagrams independently. The con-

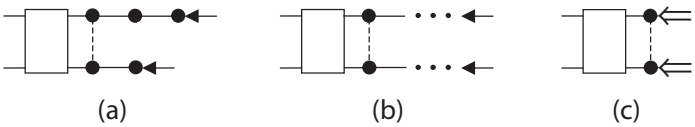

Fig. 19.11. Diagrams with one or more vertical connectors.

sequences of neglecting the diagrams with crossing connectors will be discussed in Section 19.13.

Let us begin with diagrams that have no connectors. Since these diagrams do not involve common particles, the ensemble averaging of the upper and lower particle sequences can be performed independently. Consider first the sum of the diagrams shown in Fig. 19.10a, in which the symbol Σ indicates both the summation over all appropriate particles and the statistical averaging over the particle states and positions. According to the results of Section 19.3, summing the upper sequences yields the coherent field at the point $\mathbf{r}$. This result can be represented by the diagram shown in Fig. 19.10b, in which the symbol $\Leftarrow$ denotes the coherent field.

Similarly, summing the upper sequences of the diagram shown in Fig. 19.10c yields, in the limit $N \to \infty$, the diagram shown in Fig. 19.10d. Indeed, since one particle is already "reserved" for the lower sequence, the number of particles contributing to the upper sequences in panel Fig. 19.10c is $N-1$. However, the difference between the sum of the upper sequences in panel Fig. 19.10c and the coherent field at $\mathbf{r}$ vanishes as N tends to infinity. We can continue this process and eventually conclude that the total contribution of the diagrams with no connectors is given by the sum of the diagrams shown in Fig. 19.10e.

It is now clear that the final result can be represented by the diagram in Fig. 19.10f, which means that the contribution of all the diagrams with no connectors to the dyadic correlation function is simply the dyadic product of the coherent fields at the points $\mathbf{r}'$ and $\mathbf{r}$: $\mathbf{E}_c(\mathbf{r}') \otimes [\mathbf{E}_c(\mathbf{r})]^*$. This result explains the usefulness of introducing the concept of the coherent field in Section 19.2, despite the fact that $\mathbf{E}_c(\mathbf{r})$ does not represent the actual time (or, equivalently, ensemble) average of the electric field.

All other diagrams contributing to the dyadic correlation function have at least one vertical connector, as shown in Fig. 19.11a. The part of the diagram on the right-hand side of the right-most connector will be called the tail, whereas the box represents collectively the part of the diagram on the left-hand side of the right-most connector and can, in principle, be empty. The right-most common particle and the box form the body of the diagram.

Let us first consider the group of diagrams with the same body, but with different tails, as shown in Fig. 19.11b. We can repeat the derivation of Section 19.3 and verify that in the limit $N \to \infty$, the sum of all diagrams in Fig. 19.12a gives the diagram shown in Fig. 19.12c. Indeed, let particle q be the right-most con-

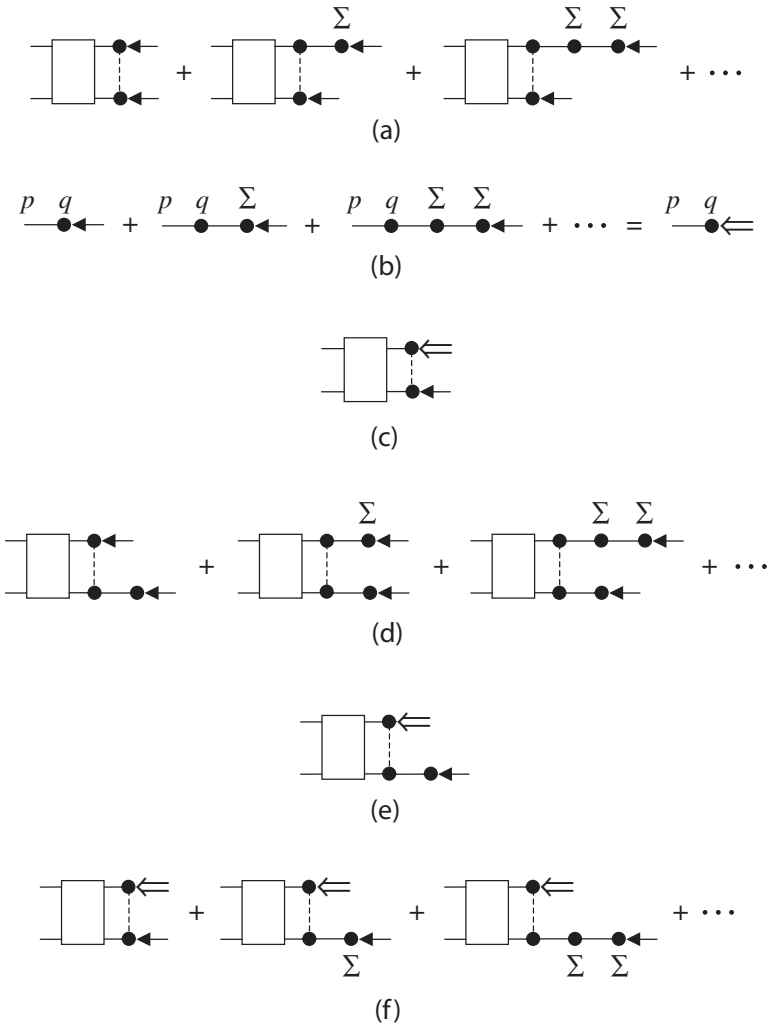

Fig. 19.12. Summation of the tails.

nected particle and particle p be the right-most particle on the left-hand side of particle q in the upper sequence of the diagrams shown in Fig. 19.12a. Consider the cumulative contribution of all the diagrams on the left-hand side of Fig. 19.12b to the total electric field created at the origin of particle p. Writing this contribution in the expanded form and then taking the limit $N \to \infty$ yields (Problem 19.5)

$$G(R_{pq})\,\overleftrightarrow{A}(\hat{\mathbf{R}}_{pq}, \hat{\mathbf{s}}) \cdot \mathbf{E}_q^{\text{inc}}$$
$$+ \frac{N-n}{N} n_0 G(R_{pq}) \int_V \mathrm{d}^3\mathbf{R}_i\, G(R_{qi})\,\overleftrightarrow{A}(\hat{\mathbf{R}}_{pq}, \hat{\mathbf{R}}_{qi}) \cdot \langle \overleftrightarrow{A}(\hat{\mathbf{R}}_{qi}, \hat{\mathbf{s}}) \rangle_\xi \cdot \mathbf{E}_i^{\text{inc}}$$

$$+\frac{(N-n)(N-n-1)}{N^2}n_0^2\,G(R_{pq})\int_V \mathrm{d}^3\mathbf{R}_i\,\mathrm{d}^3\mathbf{R}_j\,G(R_{qi})\,G(R_{ij})\,\vec{A}(\hat{\mathbf{R}}_{pq},\hat{\mathbf{R}}_{qi})$$
$$\cdot\langle\vec{A}(\hat{\mathbf{R}}_{qi},\hat{\mathbf{R}}_{ij})\rangle_\xi\cdot\langle\vec{A}(\hat{\mathbf{R}}_{ij},\hat{\mathbf{s}})\rangle_\xi\cdot\mathbf{E}_j^{\mathrm{inc}}$$
$$+\cdots\underset{N\to\infty}{=}G(R_{pq})\,\vec{A}(\hat{\mathbf{R}}_{pq},\hat{\mathbf{s}})\cdot\mathbf{E}_{\mathrm{c}}(\mathbf{R}_q),\tag{19.44}$$

where n is the number of particles in the common body of the diagrams. This result is summarized by the right-hand side of Fig. 19.12b.

Analogously, the sum of the diagrams in Fig. 19.12d is given by the diagram in Fig. 19.12e, and so on. We can now sum up all diagrams in Fig. 19.12f and obtain the diagram shown in Fig. 19.11c.

Thus the collective contribution to the dyadic correlation function of all the diagrams with the same body and all possible tails is equivalent to the contribution of a single diagram formed by the body alone, provided that the right-most common particle is "excited" by the coherent field rather than by the external incident field. This represents a radical difference from the initial expansion (19.2), in which the "source of multiple scattering" is the incident field. This important result allows us to cut off all tails and consider only truncated diagrams of the type shown in Fig. 19.11c.

Thus, the dyadic correlation function is equal to $\mathbf{E}_{\mathrm{c}}(\mathbf{r}')\otimes[\mathbf{E}_{\mathrm{c}}(\mathbf{r})]^*$ plus the statistical average of the sum of all connected diagrams of the type illustrated by Figs. 19.13a–19.13c. The symbols $\cdots$ in these diagrams denote all possible combinations of unconnected particles. Let us, for example, consider the statistical average of the sum of all diagrams of the kind shown in Fig. 19.13d with the same fixed shaded part. We thus must evaluate the left-hand side of the equation shown in Fig. 19.13f, where, as before, the symbol Σ indicates both the summation over all appropriate particles and the statistical averaging over the particle states and positions. Let particle w be the right-most particle on the left-hand side of particle p in the upper sequences of the diagrams on the left-hand side of Fig. 19.13f and u be the left-most particle on the right-hand side of particle q. The electric field created by particle p at the origin of particle w via the upper sequences of all the diagrams shown on the left-hand side of Fig. 19.13f is given by the left-hand side of the equation shown diagrammatically in Fig. 19.13g and can be written in expanded form as

$$\mathbf{E}_w = G(R_{wp})G(R_{pq})\,\vec{A}_p(\hat{\mathbf{R}}_{wp},\hat{\mathbf{R}}_{pq})\cdot\vec{A}_q(\hat{\mathbf{R}}_{pq},\hat{\mathbf{R}}_{qu})\cdot\mathbf{E}_q$$
$$+\sum_i G(R_{wp})\langle G(R_{pi})G(R_{iq})\,\vec{A}_p(\hat{\mathbf{R}}_{wp},\hat{\mathbf{R}}_{pi})\cdot\vec{A}_i(\hat{\mathbf{R}}_{pi},\hat{\mathbf{R}}_{iq})$$
$$\cdot\vec{A}_q(\hat{\mathbf{R}}_{iq},\hat{\mathbf{R}}_{qu})\rangle_{\mathbf{R},\xi}\cdot\mathbf{E}_q$$
$$+\sum_{ij} G(R_{wp})\langle G(R_{pi})G(R_{ij})G(R_{jq})\,\vec{A}_p(\hat{\mathbf{R}}_{wp},\hat{\mathbf{R}}_{pi})\cdot\vec{A}_i(\hat{\mathbf{R}}_{pi},\hat{\mathbf{R}}_{ij})\cdot\vec{A}_j(\hat{\mathbf{R}}_{ij},\hat{\mathbf{R}}_{jq})$$
$$\cdot\vec{A}_q(\hat{\mathbf{R}}_{jq},\hat{\mathbf{R}}_{qu})\rangle_{\mathbf{R},\xi}\cdot\mathbf{E}_q$$

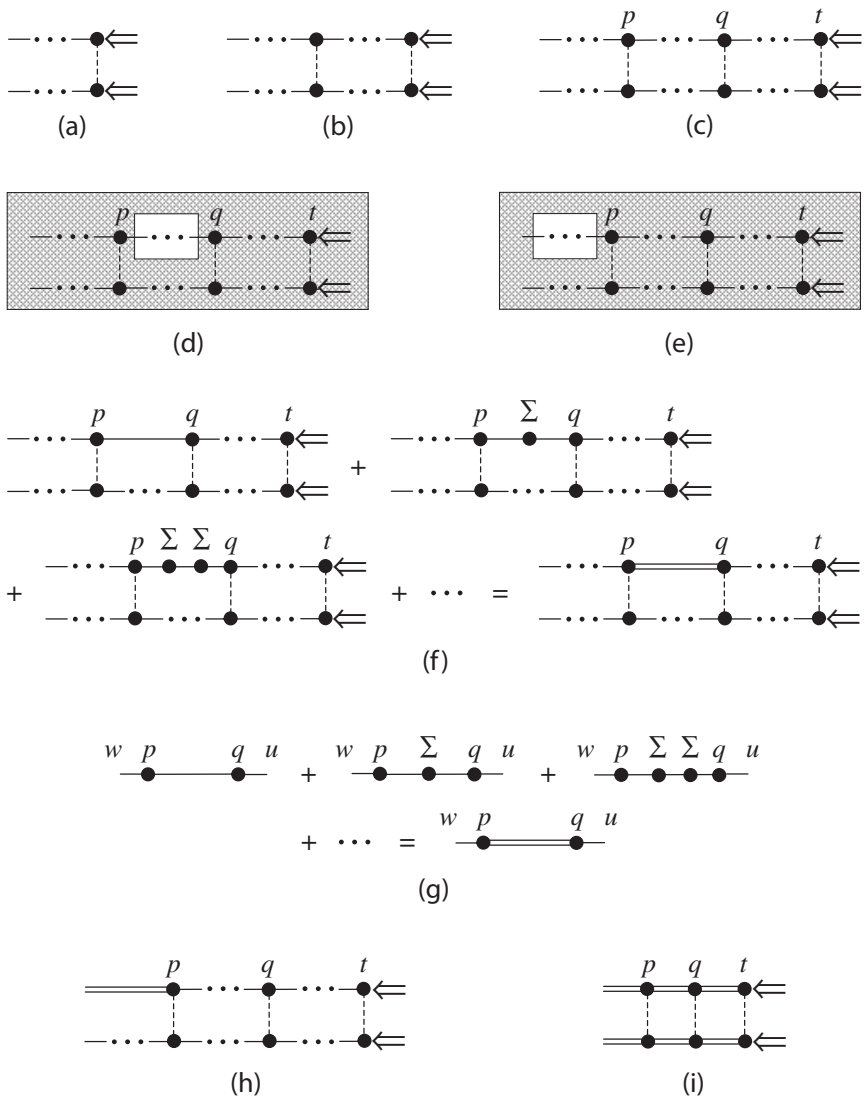

Fig. 19.13. Derivation of the ladder approximation for the dyadic correlation function.

$$+ \cdots, \tag{19.45}$$

where $\mathbf{E}_q$ is the electric field "coming" to the origin of particle q via particle u, while the summations and statistical averaging are performed over all appropriate unconnected particles (see Fig. 19.14). In the limit $N \to \infty$, Eq. (19.45) takes the form

$$\mathbf{E}_w = G(R_{wp})G(R_{pq})\,\overleftrightarrow{A}_p(\hat{\mathbf{R}}_{wp}, \hat{\mathbf{R}}_{pq}) \cdot \overleftrightarrow{A}_q(\hat{\mathbf{R}}_{pq}, \hat{\mathbf{R}}_{qu}) \cdot \mathbf{E}_q$$

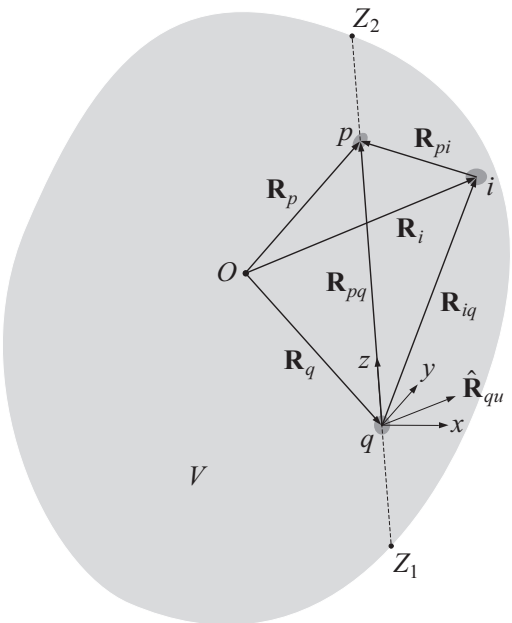

Fig. 19.14. Calculation of the integrals entering Eq. (19.46).

$$
\begin{aligned}
&+ n_0 G(R_{wp}) \int_V \mathrm{d}^3\mathbf{R}_i\, G(R_{pi}) G(R_{iq})\, \overleftrightarrow{A}_p(\hat{\mathbf{R}}_{wp}, \hat{\mathbf{R}}_{pi}) \cdot \langle \overleftrightarrow{A}(\hat{\mathbf{R}}_{pi}, \hat{\mathbf{R}}_{iq}) \rangle_\xi \\
&\qquad \cdot \overleftrightarrow{A}_q(\hat{\mathbf{R}}_{iq}, \hat{\mathbf{R}}_{qu}) \cdot \mathbf{E}_q \\
&+ n_0^2 G(R_{wp}) \int_V \mathrm{d}^3\mathbf{R}_i\, \mathrm{d}^3\mathbf{R}_j\, G(R_{pi}) G(R_{ij}) G(R_{jq})\, \overleftrightarrow{A}_p(\hat{\mathbf{R}}_{wp}, \hat{\mathbf{R}}_{pi}) \\
&\qquad \cdot \langle \overleftrightarrow{A}(\hat{\mathbf{R}}_{pi}, \hat{\mathbf{R}}_{ij}) \rangle_\xi \cdot \langle \overleftrightarrow{A}(\hat{\mathbf{R}}_{ij}, \hat{\mathbf{R}}_{jq}) \rangle_\xi \cdot \overleftrightarrow{A}_q(\hat{\mathbf{R}}_{jq}, \hat{\mathbf{R}}_{qu}) \cdot \mathbf{E}_q \\
&+ \cdots, \qquad (19.46)
\end{aligned}
$$

where the angular brackets now denote scattering dyadics averaged over the particle states.

Let us consider the first integral on the right-hand side of Eq. (19.46):

$$
\begin{aligned}
\mathbf{I}_1 = n_0 G(R_{wp}) \int_V \mathrm{d}^3\mathbf{R}_i\, \frac{\exp[\mathrm{i}k_1(R_{pi} + R_{iq})]}{R_{pi} R_{iq}}\, \overleftrightarrow{A}_p(\hat{\mathbf{R}}_{wp}, \hat{\mathbf{R}}_{pi}) \\
\cdot \langle \overleftrightarrow{A}(\hat{\mathbf{R}}_{pi}, \hat{\mathbf{R}}_{iq}) \rangle_\xi \cdot \overleftrightarrow{A}_q(\hat{\mathbf{R}}_{iq}, \hat{\mathbf{R}}_{qu}) \cdot \mathbf{E}_q. \qquad (19.47)
\end{aligned}
$$

Since the factor $\exp[\mathrm{i}k_1(R_{pi} + R_{iq})]$ is a rapidly oscillating function of $\mathbf{R}_i$, the contribution of a major part of V to $\mathbf{I}_1$ can be expected to zero out. The only exception is the small region around the straight line connecting particles q and p, where the phase $k_1(R_{pi} + R_{iq})$ is almost constant. Therefore, we can evaluate the integral (19.47) using the method of stationary phase (see Appendix G).

Using the Cartesian coordinate system with origin inside particle q and the z-axis along the vector $\mathbf{R}_{pq}$, as shown in Fig. 19.14, Eq. (19.47) can be rewritten in the form

$$\mathbf{I}_1 = n_0 G(R_{wp}) \int_{-\infty}^{+\infty} \mathrm{d}x_i \int_{-\infty}^{+\infty} \mathrm{d}y_i \int \mathrm{d}z_i \frac{\exp[\mathrm{i}k_1(R_{pi} + R_{iq})]}{R_{pi} R_{iq}} \times \ddot{A}_p(\hat{\mathbf{R}}_{wp}, \hat{\mathbf{R}}_{pi}) \cdot \langle \ddot{A}(\hat{\mathbf{R}}_{pi}, \hat{\mathbf{R}}_{iq}) \rangle_\xi \cdot \ddot{A}_q(\hat{\mathbf{R}}_{iq}, \hat{\mathbf{R}}_{qu}) \cdot \mathbf{E}_q, \tag{19.48}$$

where x_i, y_i, and z_i are the coordinates of particle i and the integration limits for x_i and y_i are set to infinity owing to the fact that only a small part of V along the z-axis contributes to $\mathbf{I}_1$. According to Eq. (G.10), the integral over z_i can be subdivided into three integrals covering the regions with $Z_1 < z_i < 0$, $0 < z_i < R_{pq}$, and $R_{pq} < z_i < Z_2$ (Fig. 19.14). The first and third integrals involve rapidly oscillating functions of z_i and vanish. Indeed,

$$\begin{aligned}\int_{Z_1}^{0} \mathrm{d}z_i \frac{\exp[\mathrm{i}k_1(R_{pq} - 2z_i)]}{R_{pq} - 2z_i} &= \frac{1}{2}\int_{k_1 R_{pq}}^{\infty} \mathrm{d}t \frac{\exp(\mathrm{i}t)}{t} - \frac{1}{2}\int_{k_1(R_{pq}+2|Z_1|)}^{\infty} \mathrm{d}t \frac{\exp(\mathrm{i}t)}{t} \\ &= \frac{1}{2}\{-\mathrm{Ci}(k_1 R_{pq}) - \mathrm{i}\,\mathrm{si}(k_1 R_{pq}) \\ &\quad + \mathrm{Ci}[k_1(R_{pq} + 2|Z_1|)] + \mathrm{i}\,\mathrm{si}[k_1(R_{pq} + 2|Z_1|)]\} \\ &= O\left(\frac{1}{k_1 R_{pq}}\right),\end{aligned} \tag{19.49}$$

where $t = k_1(R_{pq} - 2z_i)$,

$$\mathrm{si}(y) = -\int_y^{\infty} \mathrm{d}t \frac{\sin t}{t} \tag{19.50}$$

is the sine integral, and

$$\mathrm{Ci}(y) = -\int_y^{\infty} \mathrm{d}t \frac{\cos t}{t} \tag{19.51}$$

is the cosine integral (see Section 5.2 of Abramowitz and Stegun (1964) or Section 5.10 of Arfken and Weber (2005)). Similarly,

$$\begin{aligned}\int_{R_{pq}}^{Z_2} \mathrm{d}z_i \frac{\exp[\mathrm{i}k_1(R_{pq} + 2z_i)]}{R_{pq} + 2z_i} &= \frac{1}{2}\int_{3k_1 R_{pq}}^{\infty} \mathrm{d}t \frac{\exp(\mathrm{i}t)}{t} - \frac{1}{2}\int_{k_1(R_{pq}+2Z_2)}^{\infty} \mathrm{d}t \frac{\exp(\mathrm{i}t)}{t} \\ &= \frac{1}{2}\{-\mathrm{Ci}(3k_1 R_{pq}) - \mathrm{i}\,\mathrm{si}(3k_1 R_{pq}) \\ &\quad + \mathrm{Ci}[k_1(R_{pq} + 2Z_2)] + \mathrm{i}\,\mathrm{si}[k_1(R_{pq} + 2Z_2)]\} \\ &= O\left(\frac{1}{k_1 R_{pq}}\right),\end{aligned} \tag{19.52}$$

where $t = k_1(R_{pq} + 2z_i)$. Thus only the interval $0 < z_i < R_{pq}$ gives a nonzero contribution. We can now use Eq. (G.10),

$$\int_{-\infty}^{+\infty} \mathrm{d}x_i \int_{-\infty}^{+\infty} \mathrm{d}y_i \frac{\exp[\mathrm{i}k_1(R_{pi} + R_{iq})]}{R_{pi} R_{iq}} \overleftrightarrow{A}_p(\hat{\mathbf{R}}_{wp}, \hat{\mathbf{R}}_{pi}) \cdot \langle \overleftrightarrow{A}(\hat{\mathbf{R}}_{pi}, \hat{\mathbf{R}}_{iq}) \rangle_\xi \cdot \overleftrightarrow{A}_q(\hat{\mathbf{R}}_{iq}, \hat{\mathbf{R}}_{qu}) \cdot \mathbf{E}_q$$

$$\approx \frac{\mathrm{i}2\pi}{k_1} \frac{\exp(\mathrm{i}k_1 R_{pq})}{R_{pq}} \overleftrightarrow{A}_p(\hat{\mathbf{R}}_{wp}, \hat{\mathbf{R}}_{pq}) \cdot \langle \overleftrightarrow{A}(\hat{\mathbf{R}}_{pq}, \hat{\mathbf{R}}_{pq}) \rangle_\xi \cdot \overleftrightarrow{A}_q(\hat{\mathbf{R}}_{pq}, \hat{\mathbf{R}}_{qu}) \cdot \mathbf{E}_q \tag{19.53}$$

to derive

$$\mathbf{I}_1 = G(R_{wp}) \frac{\exp(\mathrm{i}k_1 R_{pq})}{R_{pq}} \frac{\mathrm{i}2\pi n_0 R_{pq}}{k_1} \overleftrightarrow{A}_p(\hat{\mathbf{R}}_{wp}, \hat{\mathbf{R}}_{pq}) \cdot \langle \overleftrightarrow{A}(\hat{\mathbf{R}}_{pq}, \hat{\mathbf{R}}_{pq}) \rangle_\xi$$
$$\cdot \overleftrightarrow{A}_q(\hat{\mathbf{R}}_{pq}, \hat{\mathbf{R}}_{qu}) \cdot \mathbf{E}_q. \tag{19.54}$$

The other integrals on the right-hand side of Eq. (19.46) are computed analogously. The final result is

$$\mathbf{E}_w = G(R_{wp}) \overleftrightarrow{A}_p(\hat{\mathbf{R}}_{wp}, \hat{\mathbf{R}}_{pq}) \cdot \frac{\exp[\mathrm{i}\overleftrightarrow{\varkappa}(\hat{\mathbf{R}}_{pq}) R_{pq}]}{R_{pq}} \cdot \overleftrightarrow{A}_q(\hat{\mathbf{R}}_{pq}, \hat{\mathbf{R}}_{qu}) \cdot \mathbf{E}_q \tag{19.55a}$$

$$= G(R_{wp}) \overleftrightarrow{A}_p(\hat{\mathbf{R}}_{wp}, \hat{\mathbf{R}}_{pq}) \cdot \frac{\overleftrightarrow{\eta}(\hat{\mathbf{R}}_{pq}, R_{pq})}{R_{pq}} \cdot \overleftrightarrow{A}_q(\hat{\mathbf{R}}_{pq}, \hat{\mathbf{R}}_{qu}) \cdot \mathbf{E}_q, \tag{19.55b}$$

where the dyadic propagation constant $\overleftrightarrow{\varkappa}$ and the coherent transmission dyadic $\overleftrightarrow{\eta}$ are given by Eqs. (19.21) and (19.22), respectively. These equations are similar to Eqs. (19.19) and (19.20) for the coherent field, a notable difference being the extra factor $1/R_{pq}$.

Equation (19.55a) can be summarized by the diagram on the right-hand side of Fig. 19.13g, thereby yielding the right-hand side of the equation in Fig. 19.13f. The double rather than a single line indicates that the scalar factor $\exp(\mathrm{i}k_1 R_{pq})/R_{pq}$ has been replaced by the dyadic factor $\exp[\mathrm{i}\overleftrightarrow{\varkappa}(\hat{\mathbf{R}}_{pq}) R_{pq}]/R_{pq}$.

In a quite similar way one can show that the sum of all diagrams of the kind shown in Fig. 19.13e with the same fixed shaded part is given by the diagram shown in Fig. 19.13h.

It is now clear that the total contribution of all diagrams with three fixed common particles t, q, and p to the dyadic correlation function can be represented by the diagram in Fig. 19.13i or, in expanded form, by the statistical average of the following product:

$$\left[\frac{\overleftrightarrow{\eta}(\hat{\mathbf{R}}_{r'p}, R_{r'p})}{R_{r'p}} \cdot \overleftrightarrow{A}_p(\hat{\mathbf{R}}_{r'p}, \hat{\mathbf{R}}_{pq}) \cdot \frac{\overleftrightarrow{\eta}(\hat{\mathbf{R}}_{pq}, R_{pq})}{R_{pq}} \cdot \overleftrightarrow{A}_q(\hat{\mathbf{R}}_{pq}, \hat{\mathbf{R}}_{qt}) \right.$$
$$\left. \cdot \frac{\overleftrightarrow{\eta}(\hat{\mathbf{R}}_{qt}, R_{qt})}{R_{qt}} \cdot \overleftrightarrow{A}_t(\hat{\mathbf{R}}_{qt}, \hat{\mathbf{s}}) \cdot \mathbf{E}_\mathrm{c}(\mathbf{R}_t) \right]$$

$$\langle \mathbf{E}(\mathbf{r}') \otimes [\mathbf{E}(\mathbf{r})]^* \rangle_{\mathbf{R},\xi} \approx$$

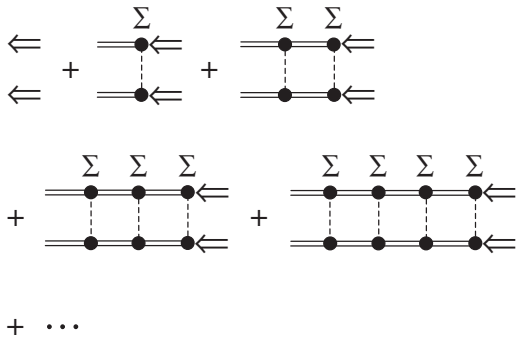

Fig. 19.15. Ladder approximation for the dyadic correlation function.

$$\otimes \left[\frac{\overleftrightarrow{\eta}(\hat{\mathbf{R}}_{rp}, R_{rp})}{R_{rp}} \cdot \overleftrightarrow{A}_p(\hat{\mathbf{R}}_{rp}, \hat{\mathbf{R}}_{pq}) \cdot \frac{\overleftrightarrow{\eta}(\hat{\mathbf{R}}_{pq}, R_{pq})}{R_{pq}} \cdot \overleftrightarrow{A}_q(\hat{\mathbf{R}}_{pq}, \hat{\mathbf{R}}_{qt}) \cdot \frac{\overleftrightarrow{\eta}(\hat{\mathbf{R}}_{qt}, R_{qt})}{R_{qt}} \cdot \overleftrightarrow{A}_t(\hat{\mathbf{R}}_{qt}, \hat{\mathbf{s}}) \cdot \mathbf{E}_{\mathrm{c}}(\mathbf{R}_t) \right]^*, \tag{19.56}$$

where the subscripts r and r' refer to the observation points $\mathbf{r}$ and $\mathbf{r}'$, respectively.

After we have neglected all the diagrams with crossing connectors, computed the contribution of all the diagrams with no connectors, and figured out how to calculate the contributions from various diagrams with one or more vertical connectors, we are perfectly positioned to complete the derivation of the dyadic correlation function. The final result is shown in Fig. 19.15, in which the symbols Σ have the usual meaning. Owing to their appearance, the diagrams on the right-hand side of this symbolic equation are called ladder diagrams. Therefore, this entire diagrammatic formula can be called the ladder approximation for the dyadic correlation function.

19.6 Integral equation for the ladder specific coherency dyadic

The explicit expanded form of the ladder approximation for the dyadic correlation function is as follows (Problem 19.6):

$$\langle \overleftrightarrow{C}(\mathbf{r}', \mathbf{r}) \rangle_{\mathbf{R},\xi} \approx \mathbf{E}_{\mathrm{c}}(\mathbf{r}') \otimes [\mathbf{E}_{\mathrm{c}}(\mathbf{r})]^* + n_0 \int \mathrm{d}^3\mathbf{R}_1 \, \mathrm{d}\xi_1 \, p_\xi(\xi_1) \frac{\overleftrightarrow{\eta}(\hat{\mathbf{r}}_1', r_1')}{r_1'} \cdot \overleftrightarrow{A}_1(\hat{\mathbf{r}}_1', \hat{\mathbf{s}}) \cdot \overleftrightarrow{C}_{\mathrm{c}}(\mathbf{R}_1) \cdot [\overleftrightarrow{A}_1(\hat{\mathbf{r}}_1, \hat{\mathbf{s}})]^{\mathrm{T}*} \cdot \frac{[\overleftrightarrow{\eta}(\hat{\mathbf{r}}_1, r_1)]^{\mathrm{T}*}}{r_1}$$

$$
\begin{aligned}
&+ n_0^2 \int \mathrm{d}^3\mathbf{R}_1 \mathrm{d}\xi_1 \int \mathrm{d}^3\mathbf{R}_2 \mathrm{d}\xi_2\, p_\xi(\xi_1) p_\xi(\xi_2) \frac{\overleftrightarrow{\eta}(\hat{\mathbf{r}}_1', r_1')}{r_1'} \cdot \overleftrightarrow{A}_1(\hat{\mathbf{r}}_1', \hat{\mathbf{R}}_{12}) \\
&\qquad \cdot \frac{\overleftrightarrow{\eta}(\hat{\mathbf{R}}_{12}, R_{12})}{R_{12}} \cdot \overleftrightarrow{A}_2(\hat{\mathbf{R}}_{12}, \hat{\mathbf{s}}) \cdot \overleftrightarrow{C}_{\mathrm{c}}(\mathbf{R}_2) \cdot [\overleftrightarrow{A}_2(\hat{\mathbf{R}}_{12}, \hat{\mathbf{s}})]^{\mathrm{T}*} \\
&\qquad \cdot \frac{[\overleftrightarrow{\eta}(\hat{\mathbf{R}}_{12}, R_{12})]^{\mathrm{T}*}}{R_{12}} \cdot [\overleftrightarrow{A}_1(\hat{\mathbf{r}}_1, \hat{\mathbf{R}}_{12})]^{\mathrm{T}*} \cdot \frac{[\overleftrightarrow{\eta}(\hat{\mathbf{r}}_1, r_1)]^{\mathrm{T}*}}{r_1} \\
&+ n_0^3 \int \mathrm{d}^3\mathbf{R}_1 \mathrm{d}\xi_1 \int \mathrm{d}^3\mathbf{R}_2 \mathrm{d}\xi_2 \int \mathrm{d}^3\mathbf{R}_3 \mathrm{d}\xi_3\, p_\xi(\xi_1) p_\xi(\xi_2) p_\xi(\xi_3) \\
&\qquad \times \frac{\overleftrightarrow{\eta}(\hat{\mathbf{r}}_1', r_1')}{r_1'} \cdot \overleftrightarrow{A}_1(\hat{\mathbf{r}}_1', \hat{\mathbf{R}}_{12}) \cdot \frac{\overleftrightarrow{\eta}(\hat{\mathbf{R}}_{12}, R_{12})}{R_{12}} \cdot \overleftrightarrow{A}_2(\hat{\mathbf{R}}_{12}, \hat{\mathbf{R}}_{23}) \\
&\qquad \cdot \frac{\overleftrightarrow{\eta}(\hat{\mathbf{R}}_{23}, R_{23})}{R_{23}} \cdot \overleftrightarrow{A}_3(\hat{\mathbf{R}}_{23}, \hat{\mathbf{s}}) \cdot \overleftrightarrow{C}_{\mathrm{c}}(\mathbf{R}_3) \cdot [\overleftrightarrow{A}_3(\hat{\mathbf{R}}_{23}, \hat{\mathbf{s}})]^{\mathrm{T}*} \\
&\qquad \cdot \frac{[\overleftrightarrow{\eta}(\hat{\mathbf{R}}_{23}, R_{23})]^{\mathrm{T}*}}{R_{23}} \cdot [\overleftrightarrow{A}_2(\hat{\mathbf{R}}_{12}, \hat{\mathbf{R}}_{23})]^{\mathrm{T}*} \cdot \frac{[\overleftrightarrow{\eta}(\hat{\mathbf{R}}_{12}, R_{12})]^{\mathrm{T}*}}{R_{12}} \\
&\qquad \cdot [\overleftrightarrow{A}_1(\hat{\mathbf{r}}_1, \hat{\mathbf{R}}_{12})]^{\mathrm{T}*} \cdot \frac{[\overleftrightarrow{\eta}(\hat{\mathbf{r}}_1, r_1)]^{\mathrm{T}*}}{r_1} \\
&+ \cdots,
\end{aligned}
\tag{19.57}
$$

where we use the notation of Fig. 19.16 and

$$
\overleftrightarrow{C}_{\mathrm{c}}(\mathbf{r}) = \mathbf{E}_{\mathrm{c}}(\mathbf{r}) \otimes [\mathbf{E}_{\mathrm{c}}(\mathbf{r})]^*. \tag{19.58}
$$

Let us now take into account the far-field condition $k_1 r_1' \gg 1$, as well as assume that $\overleftrightarrow{A}_1(\hat{\mathbf{r}}_1', \hat{\mathbf{q}})$ is a rather slowly varying function of $\hat{\mathbf{r}}_1'$ and all elements of the dyadic $2\pi n_0 k_1^{-1} \langle \overleftrightarrow{A}(\hat{\mathbf{q}}, \hat{\mathbf{q}}) \rangle_\xi$ are much smaller (in the absolute-value sense) than the wave number k_1. Then (Problem 19.7)

$$
\nabla_{\mathbf{r}_1'} \times \frac{\overleftrightarrow{\eta}(\hat{\mathbf{r}}_1', r_1')}{r_1'} \cdot \overleftrightarrow{A}_1(\hat{\mathbf{r}}_1', \hat{\mathbf{q}}) \approx \mathrm{i} k_1 \hat{\mathbf{r}}_1' \times \frac{\overleftrightarrow{\eta}(\hat{\mathbf{r}}_1', r_1')}{r_1'} \cdot \overleftrightarrow{A}_1(\hat{\mathbf{r}}_1', \hat{\mathbf{q}}). \tag{19.59}
$$

Let us also integrate over all positions of particle 1 using a local coordinate system with origin at the observation point $\mathbf{r}$, integrate over all positions of particle 2 using a local coordinate system with origin at the origin of particle 1, integrate over all positions of particle 3 using a local coordinate system with origin at the origin of particle 2, etc. Using the notation introduced in Fig. 19.16 and taking into account that $\mathrm{d}^3\mathbf{p} = r_1^2 \mathrm{d}p \mathrm{d}\hat{\mathbf{p}}$, $\mathrm{d}^3\mathbf{R}_{21} = R_{21}^2 \mathrm{d}R_{21} \mathrm{d}\hat{\mathbf{R}}_{21}$, and so on, we get from Eqs. (8.4), (19.57), and (19.59):

$$
\langle\langle \overleftrightarrow{P}(\mathbf{r}) \rangle\rangle = \langle \overleftrightarrow{P}(\mathbf{r}) \rangle_{\mathbf{R},\xi} \approx -\frac{1}{2} \sqrt{\frac{\epsilon_1}{\mu_0}} \int_{4\pi} \mathrm{d}\hat{\mathbf{p}}\, \hat{\mathbf{p}} \times \overleftrightarrow{\Sigma}_{\mathrm{L}}(\mathbf{r}, -\hat{\mathbf{p}}), \tag{19.60}
$$

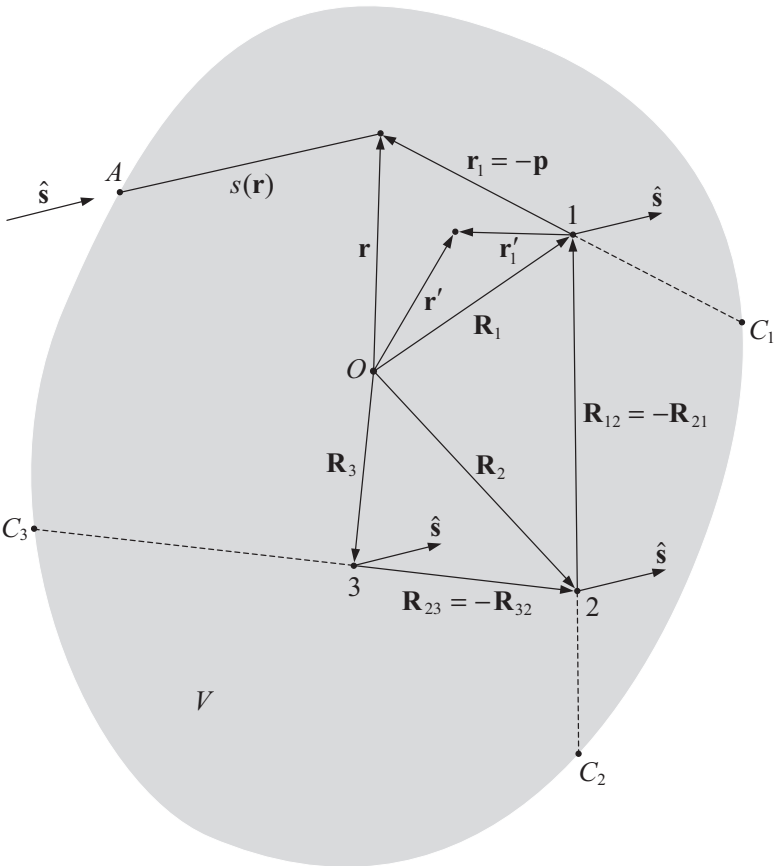

Fig. 19.16. Geometry showing the quantities appearing in Eq. (19.57).

where $\overleftrightarrow{\Sigma}_{\mathrm{L}}(\mathbf{r}, -\hat{\mathbf{p}})$ is the ladder specific coherency dyadic defined by

$$
\begin{aligned}
\overleftrightarrow{\Sigma}_{\mathrm{L}}(\mathbf{r}, -\hat{\mathbf{p}}) = {} & \delta(\hat{\mathbf{p}} + \hat{\mathbf{s}})\overleftrightarrow{C}_{\mathrm{c}}(\mathbf{r}) \\
& + n_0 \int \mathrm{d}p\, \mathrm{d}\xi_1\, p_\xi(\xi_1)\, \overleftrightarrow{\eta}(-\hat{\mathbf{p}}, p) \cdot \overleftrightarrow{A}_1(-\hat{\mathbf{p}}, \hat{\mathbf{s}}) \cdot \overleftrightarrow{C}_{\mathrm{c}}(\mathbf{r} + \mathbf{p}) \\
& \qquad \cdot [\overleftrightarrow{A}_1(-\hat{\mathbf{p}}, \hat{\mathbf{s}})]^{\mathrm{T}*} \cdot [\overleftrightarrow{\eta}(-\hat{\mathbf{p}}, p)]^{\mathrm{T}*} \\
& + n_0^2 \int \mathrm{d}p\, \mathrm{d}\xi_1 \int \mathrm{d}R_{21}\, \mathrm{d}\hat{\mathbf{R}}_{21}\, \mathrm{d}\xi_2\, p_\xi(\xi_1)\, p_\xi(\xi_2)\, \overleftrightarrow{\eta}(-\hat{\mathbf{p}}, p) \cdot \overleftrightarrow{A}_1(-\hat{\mathbf{p}}, -\hat{\mathbf{R}}_{21}) \\
& \qquad \cdot \overleftrightarrow{\eta}(-\hat{\mathbf{R}}_{21}, R_{21}) \cdot \overleftrightarrow{A}_2(-\hat{\mathbf{R}}_{21}, \hat{\mathbf{s}}) \cdot \overleftrightarrow{C}_{\mathrm{c}}(\mathbf{r} + \mathbf{p} + \mathbf{R}_{21}) \\
& \qquad \cdot [\overleftrightarrow{A}_2(-\hat{\mathbf{R}}_{21}, \hat{\mathbf{s}})]^{\mathrm{T}*} \cdot [\overleftrightarrow{\eta}(-\hat{\mathbf{R}}_{21}, R_{21})]^{\mathrm{T}*} \cdot [\overleftrightarrow{A}_1(-\hat{\mathbf{p}}, -\hat{\mathbf{R}}_{21})]^{\mathrm{T}*} \\
& \qquad \cdot [\overleftrightarrow{\eta}(-\hat{\mathbf{p}}, p)]^{\mathrm{T}*}
\end{aligned}
$$

$$
\begin{aligned}
&+ n_0^3 \int \mathrm{d}p\,\mathrm{d}\xi_1 \int \mathrm{d}R_{21}\,\mathrm{d}\hat{\mathbf{R}}_{21}\,\mathrm{d}\xi_2 \int \mathrm{d}R_{32}\,\mathrm{d}\hat{\mathbf{R}}_{32}\,\mathrm{d}\xi_3\, p_\xi(\xi_1)\, p_\xi(\xi_2)\, p_\xi(\xi_3) \\
&\qquad \times \overleftrightarrow{\eta}(-\hat{\mathbf{p}}, p)\cdot \overleftrightarrow{A}_1(-\hat{\mathbf{p}}, -\hat{\mathbf{R}}_{21})\cdot \overleftrightarrow{\eta}(-\hat{\mathbf{R}}_{21}, R_{21})\cdot \overleftrightarrow{A}_2(-\hat{\mathbf{R}}_{21}, -\hat{\mathbf{R}}_{32}) \\
&\qquad \cdot \overleftrightarrow{\eta}(-\hat{\mathbf{R}}_{32}, R_{32})\cdot \overleftrightarrow{A}_3(-\hat{\mathbf{R}}_{32}, \hat{\mathbf{s}})\cdot \overleftrightarrow{C}_{\mathrm{c}}(\mathbf{r}+\mathbf{p}+\mathbf{R}_{21}+\mathbf{R}_{32}) \\
&\qquad \cdot [\overleftrightarrow{A}_3(-\hat{\mathbf{R}}_{32}, \hat{\mathbf{s}})]^{\mathrm{T}*}\cdot [\overleftrightarrow{\eta}(-\hat{\mathbf{R}}_{32}, R_{32})]^{\mathrm{T}*}\cdot [\overleftrightarrow{A}_2(-\hat{\mathbf{R}}_{21}, -\hat{\mathbf{R}}_{32})]^{\mathrm{T}*} \\
&\qquad \cdot [\overleftrightarrow{\eta}(-\hat{\mathbf{R}}_{21}, R_{21})]^{\mathrm{T}*}\cdot [\overleftrightarrow{A}_1(-\hat{\mathbf{p}}, -\hat{\mathbf{R}}_{21})]^{\mathrm{T}*}\cdot [\overleftrightarrow{\eta}(-\hat{\mathbf{p}}, p)]^{\mathrm{T}*} \\
&+ \cdots. \qquad (19.61)
\end{aligned}
$$

Note that p ranges from zero at the observation point $\mathbf{r}$ to the corresponding value at the point where the straight line in the $\hat{\mathbf{p}}$ direction crosses the boundary of the medium (point C_1 in Fig. 19.16), R_{21} ranges from zero at the origin of particle 1 to the corresponding value at point C_2, etc. Importantly, the ladder specific coherency dyadic has the dimension of specific intensity or radiance ($\mathrm{W\,m^{-2}\,sr^{-1}}$) rather than that of intensity ($\mathrm{W\,m^{-2}}$).

It can be readily verified that the ladder specific coherency dyadic satisfies the following closed-form integral equation:

$$
\begin{aligned}
\overleftrightarrow{\Sigma}_{\mathrm{L}}(\mathbf{r}, -\hat{\mathbf{p}}) &= \delta(\hat{\mathbf{p}}+\hat{\mathbf{s}})\,\overleftrightarrow{C}_{\mathrm{c}}(\mathbf{r}) \\
&\quad + n_0 \int \mathrm{d}p\,\mathrm{d}\hat{\mathbf{p}}'\,\mathrm{d}\xi\, p_\xi(\xi)\,\overleftrightarrow{\eta}(-\hat{\mathbf{p}}, p)\cdot \overleftrightarrow{A}(\xi; -\hat{\mathbf{p}}, -\hat{\mathbf{p}}')\cdot \overleftrightarrow{\Sigma}_{\mathrm{L}}(\mathbf{r}+\mathbf{p}, -\hat{\mathbf{p}}') \\
&\qquad \cdot [\overleftrightarrow{A}(\xi; -\hat{\mathbf{p}}, -\hat{\mathbf{p}}')]^{\mathrm{T}*}\cdot [\overleftrightarrow{\eta}(-\hat{\mathbf{p}}, p)]^{\mathrm{T}*}. \qquad (19.62)
\end{aligned}
$$

Indeed, using $\delta(\hat{\mathbf{p}}+\hat{\mathbf{s}})\,\overleftrightarrow{C}_{\mathrm{c}}(\mathbf{r})$ as an initial approximation for $\overleftrightarrow{\Sigma}_{\mathrm{L}}(\mathbf{r}, -\hat{\mathbf{p}})$, we can substitute it in the integral on the right-hand side of Eq. (19.62) and obtain an improved approximation. By continuing this iterative process, we arrive at Eq. (19.61), which is simply the Neumann expansion of the ladder specific coherency dyadic.

19.7 Integro-differential equation for the diffuse specific coherency dyadic

To derive the integro-differential form of Eq. (19.62), we introduce a q-axis, as shown in Fig. 19.17. This axis originates at point C and goes through the observation point in the direction of the unit vector $\hat{\mathbf{q}} = -\hat{\mathbf{p}}$ (see Fig. 19.16). We can now rewrite Eq. (19.62) as

$$
\begin{aligned}
\overleftrightarrow{\Sigma}_{\mathrm{L}}(Q, \hat{\mathbf{q}}) &= \delta(\hat{\mathbf{q}}-\hat{\mathbf{s}})\,\overleftrightarrow{C}_{\mathrm{c}}(Q) \\
&\quad + n_0 \int_0^Q \mathrm{d}q \int \mathrm{d}\xi \int_{4\pi} \mathrm{d}\hat{\mathbf{q}}'\, p_\xi(\xi)\,\overleftrightarrow{\eta}(\hat{\mathbf{q}}, Q-q)\cdot \overleftrightarrow{A}(\xi; \hat{\mathbf{q}}, \hat{\mathbf{q}}') \\
&\qquad \cdot \overleftrightarrow{\Sigma}_{\mathrm{L}}(q, \hat{\mathbf{q}}')\cdot [\overleftrightarrow{A}(\xi; \hat{\mathbf{q}}, \hat{\mathbf{q}}')]^{\mathrm{T}*}\cdot [\overleftrightarrow{\eta}(\hat{\mathbf{q}}, Q-q)]^{\mathrm{T}*}. \qquad (19.63)
\end{aligned}
$$

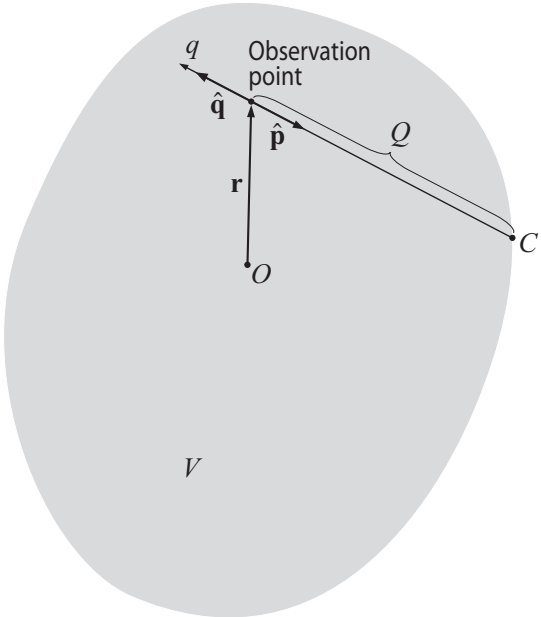

Fig. 19.17. Geometry showing the quantities appearing in the derivation of the integro-differential form of Eq. (19.62).

The diffuse specific coherency dyadic is defined as the difference between the full ladder specific coherency dyadic and its coherent component:

$$\overleftrightarrow{\Sigma}_{\mathrm{d}}(Q,\hat{\mathbf{q}}) = \overleftrightarrow{\Sigma}_{\mathrm{L}}(Q,\hat{\mathbf{q}}) - \delta(\hat{\mathbf{q}}-\hat{\mathbf{s}})\overleftrightarrow{C}_{\mathrm{c}}(Q). \tag{19.64}$$

It is easily seen that the integral equation for $\overleftrightarrow{\Sigma}_{\mathrm{d}}(Q,\hat{\mathbf{q}})$ is as follows:

$$\begin{aligned}\overleftrightarrow{\Sigma}_{\mathrm{d}}(Q,\hat{\mathbf{q}}) = {} & n_0\int_0^Q \mathrm{d}q \int \mathrm{d}\xi\, p_\xi(\xi)\,\overleftrightarrow{\eta}(\hat{\mathbf{q}},Q-q)\cdot\overleftrightarrow{A}(\xi;\hat{\mathbf{q}},\hat{\mathbf{s}})\cdot\overleftrightarrow{C}_{\mathrm{c}}(q)\\ & \cdot[\overleftrightarrow{A}(\xi;\hat{\mathbf{q}},\hat{\mathbf{s}})]^{\mathrm{T}*}\cdot[\overleftrightarrow{\eta}(\hat{\mathbf{q}},Q-q)]^{\mathrm{T}*}\\ & + n_0\int_0^Q \mathrm{d}q \int \mathrm{d}\xi \int_{4\pi} \mathrm{d}\hat{\mathbf{q}}'\, p_\xi(\xi)\,\overleftrightarrow{\eta}(\hat{\mathbf{q}},Q-q)\cdot\overleftrightarrow{A}(\xi;\hat{\mathbf{q}},\hat{\mathbf{q}}')\cdot\overleftrightarrow{\Sigma}_{\mathrm{d}}(q,\hat{\mathbf{q}}')\\ & \cdot[\overleftrightarrow{A}(\xi;\hat{\mathbf{q}},\hat{\mathbf{q}}')]^{\mathrm{T}*}\cdot[\overleftrightarrow{\eta}(\hat{\mathbf{q}},Q-q)]^{\mathrm{T}*}.\end{aligned} \tag{19.65}$$

Differentiating both sides of Eq. (19.65) finally yields (Problem 19.8)

$$\begin{aligned}\frac{\mathrm{d}\overleftrightarrow{\Sigma}_{\mathrm{d}}(Q,\hat{\mathbf{q}})}{\mathrm{d}Q} = {} & \mathrm{i}\overleftrightarrow{\varkappa}(\hat{\mathbf{q}})\cdot\overleftrightarrow{\Sigma}_{\mathrm{d}}(Q,\hat{\mathbf{q}}) - \mathrm{i}\overleftrightarrow{\Sigma}_{\mathrm{d}}(Q,\hat{\mathbf{q}})\cdot[\overleftrightarrow{\varkappa}(\hat{\mathbf{q}})]^{\mathrm{T}*}\\ & + n_0\int \mathrm{d}\xi \int_{4\pi} \mathrm{d}\hat{\mathbf{q}}'\, p_\xi(\xi)\,\overleftrightarrow{A}(\xi;\hat{\mathbf{q}},\hat{\mathbf{q}}')\cdot\overleftrightarrow{\Sigma}_{\mathrm{d}}(Q,\hat{\mathbf{q}}')\cdot[\overleftrightarrow{A}(\xi;\hat{\mathbf{q}},\hat{\mathbf{q}}')]^{\mathrm{T}*}\end{aligned}$$

$$+\, n_0 \int \mathrm{d}\xi\, p_\xi(\xi)\, \vec{A}(\xi;\hat{\mathbf{q}},\hat{\mathbf{s}}) \cdot \overleftrightarrow{C}_{\mathrm{c}}(Q) \cdot [\vec{A}(\xi;\hat{\mathbf{q}},\hat{\mathbf{s}})]^{\mathrm{T}*}. \tag{19.66}$$

For further use, it is more convenient to rewrite Eqs. (19.64) and (19.66) in the following form:

$$\overleftrightarrow{\Sigma}_{\mathrm{L}}(\mathbf{r},\hat{\mathbf{q}}) = \delta(\hat{\mathbf{q}}-\hat{\mathbf{s}})\overleftrightarrow{C}_{\mathrm{c}}(\mathbf{r}) + \overleftrightarrow{\Sigma}_{\mathrm{d}}(\mathbf{r},\hat{\mathbf{q}}), \tag{19.67}$$

$$\begin{aligned}\frac{\mathrm{d}\overleftrightarrow{\Sigma}_{\mathrm{d}}(\mathbf{r},\hat{\mathbf{q}})}{\mathrm{d}q} &= \mathrm{i}\vec{\varkappa}(\hat{\mathbf{q}}) \cdot \overleftrightarrow{\Sigma}_{\mathrm{d}}(\mathbf{r},\hat{\mathbf{q}}) - \mathrm{i}\overleftrightarrow{\Sigma}_{\mathrm{d}}(\mathbf{r},\hat{\mathbf{q}}) \cdot [\vec{\varkappa}(\hat{\mathbf{q}})]^{\mathrm{T}*} \\ &\quad + n_0 \int \mathrm{d}\xi \int_{4\pi} \mathrm{d}\hat{\mathbf{q}}'\, p_\xi(\xi)\, \vec{A}(\xi;\hat{\mathbf{q}},\hat{\mathbf{q}}') \cdot \overleftrightarrow{\Sigma}_{\mathrm{d}}(\mathbf{r},\hat{\mathbf{q}}') \cdot [\vec{A}(\xi;\hat{\mathbf{q}},\hat{\mathbf{q}}')]^{\mathrm{T}*} \\ &\quad + n_0 \int \mathrm{d}\xi\, p_\xi(\xi)\, \vec{A}(\xi;\hat{\mathbf{q}},\hat{\mathbf{s}}) \cdot \overleftrightarrow{C}_{\mathrm{c}}(\mathbf{r}) \cdot [\vec{A}(\xi;\hat{\mathbf{q}},\hat{\mathbf{s}})]^{\mathrm{T}*},\end{aligned} \tag{19.68}$$

where the path-length element $\mathrm{d}q$ is measured along the unit vector $\hat{\mathbf{q}}$. The latter formula is the integro-differential equation for the diffuse specific coherency dyadic. Equation (19.60) then becomes

$$\langle\langle \vec{P}(\mathbf{r}) \rangle\rangle \approx \frac{1}{2}\sqrt{\frac{\epsilon_1}{\mu_0}} \int_{4\pi} \mathrm{d}\hat{\mathbf{q}}\, \hat{\mathbf{q}} \times \overleftrightarrow{\Sigma}_{\mathrm{L}}(\mathbf{r},\hat{\mathbf{q}}). \tag{19.69}$$

19.8 Radiative transfer equation

After the dyad $\overleftrightarrow{C}_{\mathrm{c}}(\mathbf{r})$ is calculated according to Eqs. (19.58) and (19.19), the diffuse specific coherency dyadic can be found by solving Eq. (19.68). The energy-budget problem can then be addressed by calculating the ensemble-averaged Poynting vector at an internal point $\mathbf{r} \in V$ from Eqs. (H.14), (19.69), and (19.67). However, it is imperative first to convert all these dyadic equations into equivalent matrix equations suitable for actual numerical computations. To do that, we will exploit the transversality of the dyad $\overleftrightarrow{C}_{\mathrm{c}}(\mathbf{r})$ and the dyadic $\overleftrightarrow{\Sigma}_{\mathrm{d}}(\mathbf{r},\hat{\mathbf{q}})$ (Problem 19.9):

$$\hat{\mathbf{s}} \cdot \overleftrightarrow{C}_{\mathrm{c}}(\mathbf{r}) = \overleftrightarrow{C}_{\mathrm{c}}(\mathbf{r}) \cdot \hat{\mathbf{s}} = \mathbf{0}, \tag{19.70}$$

$$\hat{\mathbf{q}} \cdot \overleftrightarrow{\Sigma}_{\mathrm{d}}(\mathbf{r},\hat{\mathbf{q}}) = \overleftrightarrow{\Sigma}_{\mathrm{d}}(\mathbf{r},\hat{\mathbf{q}}) \cdot \hat{\mathbf{q}} = \mathbf{0}. \tag{19.71}$$

Thus only four out of nine components of either $\overleftrightarrow{C}_{\mathrm{c}}(\mathbf{r})$ or $\overleftrightarrow{\Sigma}_{\mathrm{d}}(\mathbf{r},\hat{\mathbf{q}})$ are nonzero, which allows us to define the corresponding coherency matrix and diffuse specific coherency matrix using the local coordinate system with origin at the observation point and orientation identical to that of the laboratory reference frame:

$$\boldsymbol{\rho}_{\mathrm{c}}(\mathbf{r}) = \frac{1}{2}\sqrt{\frac{\epsilon_1}{\mu_0}} \begin{bmatrix} \hat{\boldsymbol{\theta}}(\hat{\mathbf{s}}) \cdot \overleftrightarrow{C}_{\mathrm{c}}(\mathbf{r}) \cdot \hat{\boldsymbol{\theta}}(\hat{\mathbf{s}}) & \hat{\boldsymbol{\theta}}(\hat{\mathbf{s}}) \cdot \overleftrightarrow{C}_{\mathrm{c}}(\mathbf{r}) \cdot \hat{\boldsymbol{\varphi}}(\hat{\mathbf{s}}) \\ \hat{\boldsymbol{\varphi}}(\hat{\mathbf{s}}) \cdot \overleftrightarrow{C}_{\mathrm{c}}(\mathbf{r}) \cdot \hat{\boldsymbol{\theta}}(\hat{\mathbf{s}}) & \hat{\boldsymbol{\varphi}}(\hat{\mathbf{s}}) \cdot \overleftrightarrow{C}_{\mathrm{c}}(\mathbf{r}) \cdot \hat{\boldsymbol{\varphi}}(\hat{\mathbf{s}}) \end{bmatrix}, \tag{19.72}$$

$$\widetilde{\boldsymbol{\rho}}_{\mathrm{d}}(\mathbf{r},\hat{\mathbf{q}}) = \frac{1}{2}\sqrt{\frac{\epsilon_1}{\mu_0}}\begin{bmatrix}\hat{\boldsymbol{\theta}}(\hat{\mathbf{q}})\cdot\ddot{\Sigma}_{\mathrm{d}}(\mathbf{r},\hat{\mathbf{q}})\cdot\hat{\boldsymbol{\theta}}(\hat{\mathbf{q}}) & \hat{\boldsymbol{\theta}}(\hat{\mathbf{q}})\cdot\ddot{\Sigma}_{\mathrm{d}}(\mathbf{r},\hat{\mathbf{q}})\cdot\hat{\boldsymbol{\varphi}}(\hat{\mathbf{q}})\\ \hat{\boldsymbol{\varphi}}(\hat{\mathbf{q}})\cdot\ddot{\Sigma}_{\mathrm{d}}(\mathbf{r},\hat{\mathbf{q}})\cdot\hat{\boldsymbol{\theta}}(\hat{\mathbf{q}}) & \hat{\boldsymbol{\varphi}}(\hat{\mathbf{q}})\cdot\ddot{\Sigma}_{\mathrm{d}}(\mathbf{r},\hat{\mathbf{q}})\cdot\hat{\boldsymbol{\varphi}}(\hat{\mathbf{q}})\end{bmatrix}. \tag{19.73}$$

Note that hereinafter a tilde is used to label a quantity having the dimension of radiance rather than that of intensity. We can then rewrite Eqs. (19.65) and (19.68) in the form of the integral and integro-differential equations for the diffuse specific coherency matrix:

$$\begin{aligned}\widetilde{\boldsymbol{\rho}}_{\mathrm{d}}(Q,\hat{\mathbf{q}}) = {} & n_0\int_0^Q \mathrm{d}q\int \mathrm{d}\xi\, p_\xi(\xi)\mathbf{h}(\hat{\mathbf{q}},Q-q)\mathbf{S}(\xi;\hat{\mathbf{q}},\hat{\mathbf{s}})\boldsymbol{\rho}_{\mathrm{c}}(q)\\ & \times[\mathbf{S}(\xi;\hat{\mathbf{q}},\hat{\mathbf{s}})]^{\mathrm{T}*}[\mathbf{h}(\hat{\mathbf{q}},Q-q)]^{\mathrm{T}*}\\ & + n_0\int_0^Q \mathrm{d}q\int \mathrm{d}\xi\int_{4\pi}\mathrm{d}\hat{\mathbf{q}}'\, p_\xi(\xi)\mathbf{h}(\hat{\mathbf{q}},Q-q)\mathbf{S}(\xi;\hat{\mathbf{q}},\hat{\mathbf{q}}')\widetilde{\boldsymbol{\rho}}_{\mathrm{d}}(q,\hat{\mathbf{q}}')\\ & \times[\mathbf{S}(\xi;\hat{\mathbf{q}},\hat{\mathbf{q}}')]^{\mathrm{T}*}[\mathbf{h}(\hat{\mathbf{q}},Q-q)]^{\mathrm{T}*},\end{aligned} \tag{19.74}$$

$$\begin{aligned}\frac{\mathrm{d}\widetilde{\boldsymbol{\rho}}_{\mathrm{d}}(\mathbf{r},\hat{\mathbf{q}})}{\mathrm{d}q} = {} & \mathrm{i}\mathbf{k}(\hat{\mathbf{q}})\widetilde{\boldsymbol{\rho}}_{\mathrm{d}}(\mathbf{r},\hat{\mathbf{q}}) - \mathrm{i}\widetilde{\boldsymbol{\rho}}_{\mathrm{d}}(\mathbf{r},\hat{\mathbf{q}})[\mathbf{k}(\hat{\mathbf{q}})]^{\mathrm{T}*}\\ & + n_0\int \mathrm{d}\xi\int_{4\pi}\mathrm{d}\hat{\mathbf{q}}'\, p_\xi(\xi)\mathbf{S}(\xi;\hat{\mathbf{q}},\hat{\mathbf{q}}')\widetilde{\boldsymbol{\rho}}_{\mathrm{d}}(\mathbf{r},\hat{\mathbf{q}}')[\mathbf{S}(\xi;\hat{\mathbf{q}},\hat{\mathbf{q}}')]^{\mathrm{T}*}\\ & + n_0\int \mathrm{d}\xi\, p_\xi(\xi)\mathbf{S}(\xi;\hat{\mathbf{q}},\hat{\mathbf{s}})\boldsymbol{\rho}_{\mathrm{c}}(\mathbf{r})[\mathbf{S}(\xi;\hat{\mathbf{q}},\hat{\mathbf{s}})]^{\mathrm{T}*},\end{aligned} \tag{19.75}$$

where $\mathbf{S}$ is the amplitude scattering matrix, $\mathbf{h}$ is the coherent transmission amplitude matrix given by Eq. (19.34), and $\mathbf{k}$ is the matrix propagation constant given by Eqs. (19.32).

The next obvious step is to introduce the corresponding four-element coherency column vectors $\mathbf{J}_{\mathrm{c}}$ and $\widetilde{\mathbf{J}}_{\mathrm{d}}$ composed of the elements of the matrices $\boldsymbol{\rho}_{\mathrm{c}}$ and $\widetilde{\boldsymbol{\rho}}_{\mathrm{d}}$:

$$\mathbf{J}_{\mathrm{c}}(\mathbf{r}) = \begin{bmatrix}\rho_{\mathrm{c}11}(\mathbf{r})\\ \rho_{\mathrm{c}12}(\mathbf{r})\\ \rho_{\mathrm{c}21}(\mathbf{r})\\ \rho_{\mathrm{c}22}(\mathbf{r})\end{bmatrix}, \tag{19.76}$$

$$\widetilde{\mathbf{J}}_{\mathrm{d}}(\mathbf{r},\hat{\mathbf{q}}) = \begin{bmatrix}\widetilde{\rho}_{\mathrm{d}11}(\mathbf{r},\hat{\mathbf{q}})\\ \widetilde{\rho}_{\mathrm{d}12}(\mathbf{r},\hat{\mathbf{q}})\\ \widetilde{\rho}_{\mathrm{d}21}(\mathbf{r},\hat{\mathbf{q}})\\ \widetilde{\rho}_{\mathrm{d}22}(\mathbf{r},\hat{\mathbf{q}})\end{bmatrix} \tag{19.77}$$

(cf. Eq. (7.40)). After lengthy, but straightforward algebraic manipulations, we derive (Problem 19.10)

$$\widetilde{\mathbf{J}}_{\mathrm{d}}(Q,\hat{\mathbf{q}}) = n_0\int_0^Q \mathrm{d}q\,\mathbf{H}^J(\hat{\mathbf{q}},Q-q)\langle\mathbf{Z}^J(\hat{\mathbf{q}},\hat{\mathbf{s}})\rangle_\xi\mathbf{J}_{\mathrm{c}}(q)$$
$$+\,n_0\int_0^Q \mathrm{d}q\int_{4\pi}\mathrm{d}\hat{\mathbf{q}}'\,\mathbf{H}^J(\hat{\mathbf{q}},Q-q)\langle\mathbf{Z}^J(\hat{\mathbf{q}},\hat{\mathbf{q}}')\rangle_\xi\widetilde{\mathbf{J}}_{\mathrm{d}}(q,\hat{\mathbf{q}}'), \quad (19.78)$$

$$\frac{\mathrm{d}\widetilde{\mathbf{J}}_{\mathrm{d}}(\mathbf{r},\hat{\mathbf{q}})}{\mathrm{d}q} = -n_0\langle\mathbf{K}^J(\hat{\mathbf{q}})\rangle_\xi\widetilde{\mathbf{J}}_{\mathrm{d}}(\mathbf{r},\hat{\mathbf{q}}) + n_0\int_{4\pi}\mathrm{d}\hat{\mathbf{q}}'\langle\mathbf{Z}^J(\hat{\mathbf{q}},\hat{\mathbf{q}}')\rangle_\xi\widetilde{\mathbf{J}}_{\mathrm{d}}(\mathbf{r},\hat{\mathbf{q}}')$$
$$+\,n_0\langle\mathbf{Z}^J(\hat{\mathbf{q}},\hat{\mathbf{s}})\rangle_\xi\mathbf{J}_{\mathrm{c}}(\mathbf{r}), \quad (19.79)$$

where

$$\mathbf{H}^J(\hat{\mathbf{s}},s) = \exp\{-n_0 s\langle\mathbf{K}^J(\hat{\mathbf{s}})\rangle_\xi\} \quad (19.80)$$

and $\langle\mathbf{K}^J(\hat{\mathbf{q}})\rangle_\xi$ and $\langle\mathbf{Z}^J(\hat{\mathbf{q}},\hat{\mathbf{q}}')\rangle_\xi$ are the coherency extinction and phase matrices averaged over the particle states (see Eqs. (13.58) and (13.30)). The column vector $\mathbf{J}_{\mathrm{c}}(\mathbf{r})$ satisfies the transfer equation (19.37).

Our final step is to define the coherent Stokes column vector and the diffuse specific intensity column vector according to Eq. (7.43),

$$\mathbf{I}_{\mathrm{c}}(\mathbf{r}) = \begin{bmatrix} I_{\mathrm{c}}(\mathbf{r}) \\ Q_{\mathrm{c}}(\mathbf{r}) \\ U_{\mathrm{c}}(\mathbf{r}) \\ V_{\mathrm{c}}(\mathbf{r}) \end{bmatrix} = \mathbf{D}\mathbf{J}_{\mathrm{c}}(\mathbf{r}), \quad (19.81)$$

$$\widetilde{\mathbf{I}}_{\mathrm{d}}(\mathbf{r},\hat{\mathbf{q}}) = \begin{bmatrix} \widetilde{I}_{\mathrm{d}}(\mathbf{r},\hat{\mathbf{q}}) \\ \widetilde{Q}_{\mathrm{d}}(\mathbf{r},\hat{\mathbf{q}}) \\ \widetilde{U}_{\mathrm{d}}(\mathbf{r},\hat{\mathbf{q}}) \\ \widetilde{V}_{\mathrm{d}}(\mathbf{r},\hat{\mathbf{q}}) \end{bmatrix} = \mathbf{D}\widetilde{\mathbf{J}}_{\mathrm{d}}(\mathbf{r},\hat{\mathbf{q}}), \quad (19.82)$$

and rewrite Eqs. (19.78) and (19.79) in the form

$$\widetilde{\mathbf{I}}_{\mathrm{d}}(Q,\hat{\mathbf{q}}) = n_0\int_0^Q \mathrm{d}q\,\mathbf{H}(\hat{\mathbf{q}},Q-q)\langle\mathbf{Z}(\hat{\mathbf{q}},\hat{\mathbf{s}})\rangle_\xi\mathbf{I}_{\mathrm{c}}(q)$$
$$+\,n_0\int_0^Q \mathrm{d}q\int_{4\pi}\mathrm{d}\hat{\mathbf{q}}'\,\mathbf{H}(\hat{\mathbf{q}},Q-q)\langle\mathbf{Z}(\hat{\mathbf{q}},\hat{\mathbf{q}}')\rangle_\xi\widetilde{\mathbf{I}}_{\mathrm{d}}(q,\hat{\mathbf{q}}'), \quad (19.83)$$

$$\frac{\mathrm{d}\widetilde{\mathbf{I}}_{\mathrm{d}}(\mathbf{r},\hat{\mathbf{q}})}{\mathrm{d}q} = -n_0\langle\mathbf{K}(\hat{\mathbf{q}})\rangle_\xi\widetilde{\mathbf{I}}_{\mathrm{d}}(\mathbf{r},\hat{\mathbf{q}}) + n_0\int_{4\pi}\mathrm{d}\hat{\mathbf{q}}'\langle\mathbf{Z}(\hat{\mathbf{q}},\hat{\mathbf{q}}')\rangle_\xi\widetilde{\mathbf{I}}_{\mathrm{d}}(\mathbf{r},\hat{\mathbf{q}}')$$
$$+\,n_0\langle\mathbf{Z}(\hat{\mathbf{q}},\hat{\mathbf{s}})\rangle_\xi\mathbf{I}_{\mathrm{c}}(\mathbf{r}), \quad (19.84)$$

where $\langle\mathbf{K}(\hat{\mathbf{q}})\rangle_\xi$ is the average of the Stokes extinction matrix given by Eq. (13.61) over the particle states and $\langle\mathbf{Z}(\hat{\mathbf{q}},\hat{\mathbf{q}}')\rangle_\xi$ is the analogous average of the Stokes phase matrix given by Eq. (13.33). The coherent Stokes column vector $\mathbf{I}_{\mathrm{c}}(\mathbf{r})$ satisfies the transfer equation (19.39) and is given by Eq. (19.40).

Unlike the closed-form integral RTE (19.83), the integro-differential RTE (19.84) requires the specification of an appropriate boundary condition. This condition follows from Eq. (19.83) and reads

$$\widetilde{\mathbf{I}}_{\mathrm{d}}(\mathbf{r}, \hat{\mathbf{q}}_{\leftarrow})|_{\mathbf{r}\in S} = \mathbf{0}, \tag{19.85}$$

where S is the boundary of the particulate volume V (Fig. 19.1), $\hat{\mathbf{q}}_{\leftarrow}$ is any unit vector directed *into* the volume, and $\mathbf{0}$ is a four-element column with zero components.

Equations (19.39) and (19.84) can also be written as

$$\hat{\mathbf{s}} \cdot \nabla \mathbf{I}_{\mathrm{c}}(\mathbf{r}) = -n_0 \langle \mathbf{K}(\hat{\mathbf{s}}) \rangle_{\xi} \mathbf{I}_{\mathrm{c}}(\mathbf{r}), \quad \mathbf{I}_{\mathrm{c}}(\mathbf{r}_A) = \mathbf{I}^{\mathrm{inc}}, \tag{19.86}$$

$$\begin{aligned} \hat{\mathbf{q}} \cdot \nabla \widetilde{\mathbf{I}}_{\mathrm{d}}(\mathbf{r}, \hat{\mathbf{q}}) = {} & -n_0 \langle \mathbf{K}(\hat{\mathbf{q}}) \rangle_{\xi} \widetilde{\mathbf{I}}_{\mathrm{d}}(\mathbf{r}, \hat{\mathbf{q}}) + n_0 \int_{4\pi} \mathrm{d}\hat{\mathbf{q}}' \langle \mathbf{Z}(\hat{\mathbf{q}}, \hat{\mathbf{q}}') \rangle_{\xi} \widetilde{\mathbf{I}}_{\mathrm{d}}(\mathbf{r}, \hat{\mathbf{q}}') \\ & + n_0 \langle \mathbf{Z}(\hat{\mathbf{q}}, \hat{\mathbf{s}}) \rangle_{\xi} \mathbf{I}_{\mathrm{c}}(\mathbf{r}). \end{aligned} \tag{19.87}$$

These equations represent the conventional integro-differential form of the RTE applicable to arbitrarily sized, shaped, and oriented particles.

It is often convenient to introduce the full specific intensity column vector according to

$$\widetilde{\mathbf{I}}(\mathbf{r}, \hat{\mathbf{q}}) = \begin{bmatrix} \widetilde{I}(\mathbf{r}, \hat{\mathbf{q}}) \\ \widetilde{Q}(\mathbf{r}, \hat{\mathbf{q}}) \\ \widetilde{U}(\mathbf{r}, \hat{\mathbf{q}}) \\ \widetilde{V}(\mathbf{r}, \hat{\mathbf{q}}) \end{bmatrix} = \delta(\hat{\mathbf{q}} - \hat{\mathbf{s}}) \mathbf{I}_{\mathrm{c}}(\mathbf{r}) + \widetilde{\mathbf{I}}_{\mathrm{d}}(\mathbf{r}, \hat{\mathbf{q}}) \tag{19.88}$$

and rewrite Eqs. (19.86) and (19.87) as a single integro-differential RTE:

$$\hat{\mathbf{q}} \cdot \nabla \widetilde{\mathbf{I}}(\mathbf{r}, \hat{\mathbf{q}}) = -n_0 \langle \mathbf{K}(\hat{\mathbf{q}}) \rangle_{\xi} \widetilde{\mathbf{I}}(\mathbf{r}, \hat{\mathbf{q}}) + n_0 \int_{4\pi} \mathrm{d}\hat{\mathbf{q}}' \langle \mathbf{Z}(\hat{\mathbf{q}}, \hat{\mathbf{q}}') \rangle_{\xi} \widetilde{\mathbf{I}}(\mathbf{r}, \hat{\mathbf{q}}'). \tag{19.89}$$

Accordingly, the integral RTE (19.83) takes the form

$$\widetilde{\mathbf{I}}(Q, \hat{\mathbf{q}}) = \delta(\hat{\mathbf{q}} - \hat{\mathbf{s}}) \mathbf{I}_{\mathrm{c}}(Q) + n_0 \int_0^Q \mathrm{d}q \int_{4\pi} \mathrm{d}\hat{\mathbf{q}}' \mathbf{H}(\hat{\mathbf{q}}, Q - q) \langle \mathbf{Z}(\hat{\mathbf{q}}, \hat{\mathbf{q}}') \rangle_{\xi} \widetilde{\mathbf{I}}(q, \hat{\mathbf{q}}'), \tag{19.90}$$

while the boundary condition (19.85) becomes

$$\widetilde{\mathbf{I}}(\mathbf{r}, \hat{\mathbf{q}}_{\leftarrow})|_{\mathbf{r}\in S} = \delta(\hat{\mathbf{s}} - \hat{\mathbf{q}}_{\leftarrow}) \mathbf{I}^{\mathrm{inc}}. \tag{19.91}$$

It is straightforward to show that both $\mathbf{I}_{\mathrm{c}}(\mathbf{r})$, $\widetilde{\mathbf{I}}_{\mathrm{d}}(\mathbf{r}, \hat{\mathbf{q}})$, and $\widetilde{\mathbf{I}}(\mathbf{r}, \hat{\mathbf{q}})$ have real-valued components (Problem 19.11).

In the absence of particles, the coherent Stokes column vector, the diffuse specific intensity column vector, and the full specific intensity column vector become independent of the spatial coordinates. This property follows directly from Eqs. (19.86)–(19.88) in the limit $n_0 \to 0$.

19.9 Statistically isotropic and mirror-symmetric random particles

One can expect significant simplifications in cases when the ensemble-averaged extinction matrix is diagonal and given by Eq. (15.42). Indeed, then Eqs. (19.41) and (19.40) become

$$\mathbf{H}(\hat{\mathbf{s}}, s) = \exp[-n_0 s \langle C_{\text{ext}} \rangle_\xi] \mathbf{\Delta}, \tag{19.92}$$

$$\begin{aligned} \mathbf{I}_{\text{c}}(\mathbf{r}) &= \exp[-n_0 \langle C_{\text{ext}} \rangle_\xi s(\mathbf{r})] \mathbf{I}^{\text{inc}} \\ &= \exp[-\alpha_{\text{ext}} s(\mathbf{r})] \mathbf{I}^{\text{inc}}, \end{aligned} \tag{19.93}$$

which means that the elements of the Stokes column vector of the coherent field are exponentially attenuated with increasing s. The attenuation rates for all four components are the same, which means that the polarization state of the coherent field does not change with s. Equation (19.93) is the standard Bouguer (or Bouguer–Beer) law with

$$\alpha_{\text{ext}} = n_0 \langle C_{\text{ext}} \rangle_\xi = n_0 [\langle C_{\text{sca}} \rangle_\xi + \langle C_{\text{abs}} \rangle_\xi] \tag{19.94}$$

being the attenuation (or extinction) coefficient. Equations (19.83) and (19.84) become

$$\begin{aligned} \widetilde{\mathbf{I}}_{\text{d}}(Q, \hat{\mathbf{q}}) &= n_0 \int_0^Q \mathrm{d}q \exp[-n_0 (Q-q) \langle C_{\text{ext}} \rangle_\xi] \langle \mathbf{Z}(\hat{\mathbf{q}}, \hat{\mathbf{s}}) \rangle_\xi \mathbf{I}_{\text{c}}(q) \\ &\quad + n_0 \int_0^Q \mathrm{d}q \int_{4\pi} \mathrm{d}\hat{\mathbf{q}}' \exp[-n_0 (Q-q) \langle C_{\text{ext}} \rangle_\xi] \langle \mathbf{Z}(\hat{\mathbf{q}}, \hat{\mathbf{q}}') \rangle_\xi \widetilde{\mathbf{I}}_{\text{d}}(q, \hat{\mathbf{q}}'), \end{aligned} \tag{19.95}$$

$$\begin{aligned} \frac{\mathrm{d}\widetilde{\mathbf{I}}_{\text{d}}(\mathbf{r}, \hat{\mathbf{q}})}{\mathrm{d}q} &= -n_0 \langle C_{\text{ext}} \rangle_\xi \widetilde{\mathbf{I}}_{\text{d}}(\mathbf{r}, \hat{\mathbf{q}}) + n_0 \int_{4\pi} \mathrm{d}\hat{\mathbf{q}}' \langle \mathbf{Z}(\hat{\mathbf{q}}, \hat{\mathbf{q}}') \rangle_\xi \widetilde{\mathbf{I}}_{\text{d}}(\mathbf{r}, \hat{\mathbf{q}}') \\ &\quad + n_0 \langle \mathbf{Z}(\hat{\mathbf{q}}, \hat{\mathbf{s}}) \rangle_\xi \mathbf{I}_{\text{c}}(\mathbf{r}). \end{aligned} \tag{19.96}$$

19.10 Energy-budget problem

We are now perfectly positioned to finalize the solution of the energy-budget problem. Indeed, it is straightforward to show (Problem 19.12) that the ensemble-averaged Poynting vector at an internal observation point $\mathbf{r} \in V$ is given by

$$\begin{aligned} \langle\langle \boldsymbol{\mathcal{S}}(\mathbf{r}, t) \rangle\rangle = \text{Re} \langle\langle \mathbf{S}(\mathbf{r}) \rangle\rangle &\approx \int_{4\pi} \mathrm{d}\hat{\mathbf{q}}\, \hat{\mathbf{q}}\, \widetilde{I}(\mathbf{r}, \hat{\mathbf{q}}) \\ &= \hat{\mathbf{s}} I_{\text{c}}(\mathbf{r}) + \int_{4\pi} \mathrm{d}\hat{\mathbf{q}}\, \hat{\mathbf{q}}\, \widetilde{I}_{\text{d}}(\mathbf{r}, \hat{\mathbf{q}}), \quad \mathbf{r} \in V, \end{aligned} \tag{19.97}$$

where $\widetilde{I}(\mathbf{r}, \hat{\mathbf{q}})$ is the first element of the specific intensity column vector (19.88) and is traditionally called the specific intensity. The importance of this direct

corollary of the frequency-domain MMEs is hard to overstate. Indeed, it implies that to compute the local Poynting vector averaged over a sufficiently long period of time, one can solve the RTE for the direction-dependent specific intensity column vector and then integrate the direction-weighted first element of $\widetilde{\mathbf{I}}(\mathbf{r}, \hat{\mathbf{q}})$ over all directions. This approach is far more practicable than solving the primordial frequency-domain MMEs or the equivalent FEs written for the entire multi-particle object.

A fundamental and practically important property of the RTE is that it satisfies precisely the energy conservation law. Indeed, using the vector identity (H.1) and taking into account that $\hat{\mathbf{q}}$ is a constant vector, we can rewrite Eq. (19.89) as

$$\nabla \cdot [\hat{\mathbf{q}}\, \widetilde{\mathbf{I}}(\mathbf{r}, \hat{\mathbf{q}})] = -n_0 \langle \mathbf{K}(\mathbf{r}, \hat{\mathbf{q}}) \rangle_\xi \widetilde{\mathbf{I}}(\mathbf{r}, \hat{\mathbf{q}}) + n_0 \int_{4\pi} \mathrm{d}\hat{\mathbf{q}}' \langle \mathbf{Z}(\mathbf{r}, \hat{\mathbf{q}}, \hat{\mathbf{q}}') \rangle_\xi \widetilde{\mathbf{I}}(\mathbf{r}, \hat{\mathbf{q}}'). \quad (19.98)$$

Integrating both sides of this equation over all directions $\hat{\mathbf{q}}$ and recalling Eqs. (13.84)–(13.86) yields

$$-\nabla \cdot \langle\langle \mathbf{S}(\mathbf{r}) \rangle\rangle = n_0 \int_{4\pi} \mathrm{d}\hat{\mathbf{q}} \langle C_{\mathrm{abs}}(\mathbf{r}, \hat{\mathbf{q}}) \rangle_\xi \widetilde{I}(\mathbf{r}, \mathbf{q}), \quad (19.99)$$

where $\widetilde{I}(\mathbf{r}, \mathbf{q})$ is the first element of the column (19.88) traditionally called the specific intensity. The physical meaning of this formula is very transparent: the net inflow of electromagnetic power per unit volume is equal to the total power absorbed per unit volume. If the particles forming the scattering medium are nonabsorbing, so that $\langle C_{\mathrm{abs}}(\mathbf{r}, \hat{\mathbf{q}}) \rangle_\xi = 0$, then the time-averaged Poynting vector becomes divergence free:

$$\nabla \cdot \langle\langle \mathbf{S}(\mathbf{r}) \rangle\rangle = 0. \quad (19.100)$$

This means that the time-averaged amount of electromagnetic energy entering a differential volume element per unit time is equal to the time-averaged amount of electromagnetic energy leaving the differential volume element per unit time. This important result can be used for testing various numerical techniques for solving the RTE and is a particularly attractive feature of the RTT.

The previous discussion clearly shows that the RTE follows from the frequency-domain MMEs only upon making several well-defined assumptions, including the consideration of only the ladder diagrams. Still, it is very rewarding to see that these assumptions are sufficiently consistent with each other in that the final result fully complies with the energy conservation law. This also implies, of course, that the contribution of all the other types of diagram to the time-averaged Poynting vector must be identically equal to zero.

19.11 Reading of a well-collimated radiometer

Consider WCR 1 placed inside the random particulate volume V and oriented such that its small acceptance solid angle $\Delta\Omega_{\hat{\mathbf{q}}}$ does not subtend the incidence

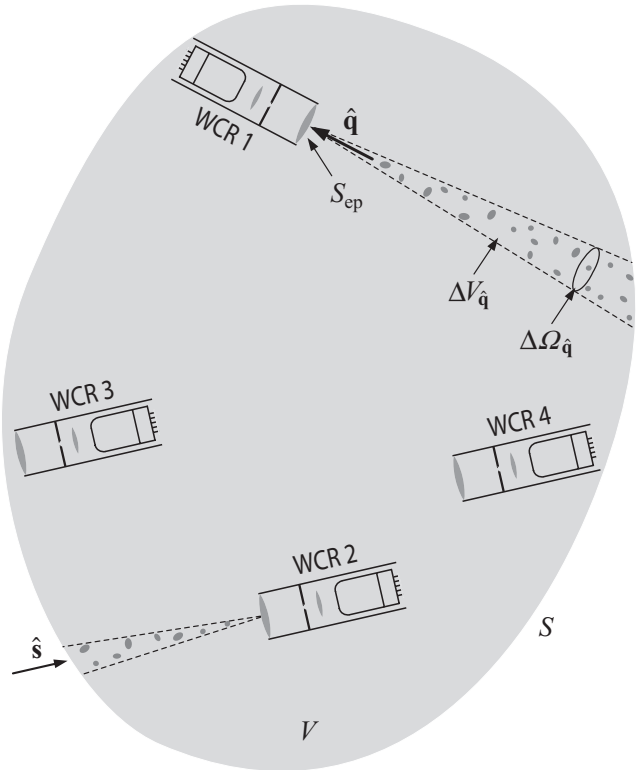

Fig. 19.18. WCRs placed inside the random particulate volume. The sizes of the instruments and the particles relative to that of the medium are exaggerated for demonstration purposes.

direction $\hat{\mathbf{s}}$ (Fig. 19.18). The discussion in Section 11.4 implies that in the framework of the far-field Neumann expansion (6.48), this instrument reacts only to partial wavelets generated by multi-particle sequences having their end particles located within the corresponding conical acceptance volume $\Delta V_{\hat{\mathbf{q}}}$. Thus, the reading of the instrument is defined not by the full PST (19.60), but rather by the corresponding partial PST $\langle \ddot{P}(\mathbf{r}; \Delta V_{\hat{\mathbf{q}}})\rangle_{\mathbf{R},\xi}$, where the subscripts $\mathbf{R}$ and ξ denote averaging over coordinates and states of all the N particles constituting the scattering medium and not just those located inside $\Delta V_{\hat{\mathbf{q}}}$. $\langle \ddot{P}(\mathbf{r}; \Delta V_{\hat{\mathbf{q}}})\rangle_{\mathbf{R},\xi}$ can be computed by making the standard assumptions invoked previously to calculate $\langle \ddot{P}(\mathbf{r})\rangle_{\mathbf{R},\xi}$, but also requiring that the end particle of any multi-particle sequence be located inside the acceptance volume $\Delta V_{\hat{\mathbf{q}}}$. According to the discussion in Section 19.5, the latter is equivalent to requiring that the left-most common particle of any ladder diagram in Fig. 19.15 be located inside $\Delta V_{\hat{\mathbf{q}}}$.

The outcome of this lengthy yet straightforward computation is as follows (Problem 19.13):

$$\langle\langle \vec{P}(\mathbf{r}; \Delta V_{\hat{\mathbf{q}}}) \rangle\rangle = \langle \vec{P}(\mathbf{r}; \Delta V_{\hat{\mathbf{q}}}) \rangle_{\mathbf{R},\xi} \approx \Delta\Omega \frac{1}{2}\sqrt{\frac{\epsilon_1}{\mu_0}}\, \hat{\mathbf{q}} \times \vec{\Sigma}_{\mathrm{L}}(\mathbf{r}, \hat{\mathbf{q}}), \quad \mathbf{r} \in V, \quad (19.101)$$

where the unit vector $\hat{\mathbf{q}}$ is directed along the optical axis of WCR 1. It can be verified (Problem 19.14) that Eq. (19.101) remains valid if $\hat{\mathbf{q}} = \hat{\mathbf{s}}$, which implies that $\Delta\Omega_{\hat{\mathbf{q}}}$ subtends the incidence direction (WCR 2 in Fig. 19.18). Finally, by analogy with Eq. (19.97), we have for the net time-averaged electromagnetic energy recorded by a WCR per unit time:

$$\langle\langle \text{EM power}(\mathbf{r}, \hat{\mathbf{q}}) \rangle\rangle \approx \chi[\Delta\Omega_{\hat{\mathbf{q}}}, \hat{\mathbf{s}}] S_{\mathrm{ep}} I_{\mathrm{c}}(\mathbf{r}) + S_{\mathrm{ep}} \Delta\Omega\, \widetilde{I}_{\mathrm{d}}(\mathbf{r}, \hat{\mathbf{q}}), \quad \mathbf{r} \in V, \quad (19.102)$$

where the step function $\chi[\Delta\Omega_{\hat{\mathbf{q}}}, \hat{\mathbf{s}}]$ is defined by Eq. (11.10). More generally, the net signal recorded by a polarization-sensitive WCR per unit time is given by the following four-component column:

$$\langle\langle \mathbf{Signal}(\mathbf{r}, \hat{\mathbf{q}}) \rangle\rangle \approx \chi[\Delta\Omega_{\hat{\mathbf{q}}}, \hat{\mathbf{s}}] S_{\mathrm{ep}} \mathbf{I}_{\mathrm{c}}(\mathbf{r}) + S_{\mathrm{ep}} \Delta\Omega\, \widetilde{\mathbf{I}}_{\mathrm{d}}(\mathbf{r}, \hat{\mathbf{q}}), \quad \mathbf{r} \in V. \quad (19.103)$$

The fact that the signal recorded by the WCR can be modeled theoretically by solving the RTE often makes the {WCR, RTE} combination a potent optical-characterization tool. Furthermore, comparison of Eqs. (19.97) and (19.102) shows that a WCR can be used to solve the energy-budget problem experimentally by scanning over the entire range of directions $\hat{\mathbf{q}} \in 4\pi$. Of course, such optical-characterization and energy-budget applications of WCRs are only possible if the random particulate medium possesses specific macro- and microphysical properties, as discussed earlier in this chapter.

Equation (19.103) together with Eq. (19.93) clarifies the practical meaning of the coherent Stokes column vector. Indeed, if the acceptance solid angle $\Delta\Omega$ of a WCR were infinitely small and the optical axis of the instrument were perfectly parallel to the incidence direction $(\hat{\mathbf{q}} = \hat{\mathbf{s}})$, then the response of the WCR would be equal to $S_{\mathrm{ep}}\mathbf{I}_{\mathrm{c}}(\mathbf{r})$. In other words, the WCR would record only the Stokes column vector of the coherent field. In reality, $\Delta\Omega$ is never equal to zero, and the WCR always picks up some of the diffuse signal. Still, if both $\Delta\Omega$ and $\widetilde{\mathbf{I}}_{\mathrm{d}}(\mathbf{r}, \hat{\mathbf{s}})$ are sufficiently small and $\mathbf{I}_{\mathrm{c}}(\mathbf{r})$ is sufficiently large, then the response of the WCR facing the incident wave is mostly determined by the first term on the right-hand side of Eq. (19.103). It is reasonable to expect that this happens when the WCR is located close to the part of the volume's boundary S directly illuminated by the incident wave (WCR 3 in Fig. 19.18), so that $\mathbf{I}_{\mathrm{c}}(\mathbf{r})$ is still weakly attenuated and there is not much diffuse signal corresponding to directions close to $\hat{\mathbf{s}}$. As the WCR is moved farther from the illuminated boundary (WCR 2), $\mathbf{I}_{\mathrm{c}}(\mathbf{r})$ is progressively attenuated and the diffuse component corresponding to directions close to $\hat{\mathbf{s}}$ increases, thereby making the second term on the right-hand side of Eq. (19.103) comparable to the first term. Ultimately, when the WCR is placed deeply inside an optically thick medium (WCR 4), its reading is heavily dominated by the diffuse component and is given by the second term on the right-hand side of Eq. (19.103).

19.12 External observation point

The case of an external observation point $\mathbf{r} \notin V$ located in the near zone of the entire particulate volume can be treated analogously to that of an internal observation point. Therefore, below we give only a summary of the corresponding results and refer the reader to Section 8.14 of MTL2 for specific details.

First, we introduce the direct internal pathlength $\Delta s(\mathbf{r})$ for an external observation point $\mathbf{r}$ as follows. Let us draw a straight line from the observation point in the direction of the unit vector $-\hat{\mathbf{s}}$, i.e., opposite to the incidence direction (Fig. 19.19). Then $\Delta s(\mathbf{r})$ is defined as the length of the segment of this line embedded in the particulate volume V. The reader can see that for observation points 1 and 2 not "shadowed" by the volume, $\Delta s(\mathbf{r}_1) = \Delta s(\mathbf{r}_2) = 0$, whereas for observation point 3 "shadowed" by the volume, $\Delta s(\mathbf{r}_3) > 0$. Another two quantities are introduced in Fig. 19.20. Specifically, $\Omega_V(\mathbf{r})$ is the solid angle subtended by the particulate volume as viewed from an external observation point $\mathbf{r}$, while $\mathbf{r}_S(\mathbf{r}, \hat{\mathbf{q}})$ is the boundary point at which the straight line drawn through the observation point in the direction $-\hat{\mathbf{q}}$ enters the volume.

Using this notation, we can write the "external" counterparts of Eqs. (19.97), (19.102), and (19.103) (Problem 19.15):

$$\langle\langle \boldsymbol{\mathcal{S}}(\mathbf{r}, t)\rangle\rangle = \mathrm{Re}\langle\langle \mathbf{S}(\mathbf{r})\rangle\rangle \approx \hat{\mathbf{s}} I_{\mathrm{c}}^{\mathrm{ex}}(\mathbf{r}) + \int_{\Omega_V(\mathbf{r})} \mathrm{d}\hat{\mathbf{q}}\, \hat{\mathbf{q}}\, \widetilde{I}_{\mathrm{d}}[\mathbf{r}_S(\mathbf{r}, \hat{\mathbf{q}}), \hat{\mathbf{q}}], \quad \mathbf{r} \notin V, \qquad (19.104)$$

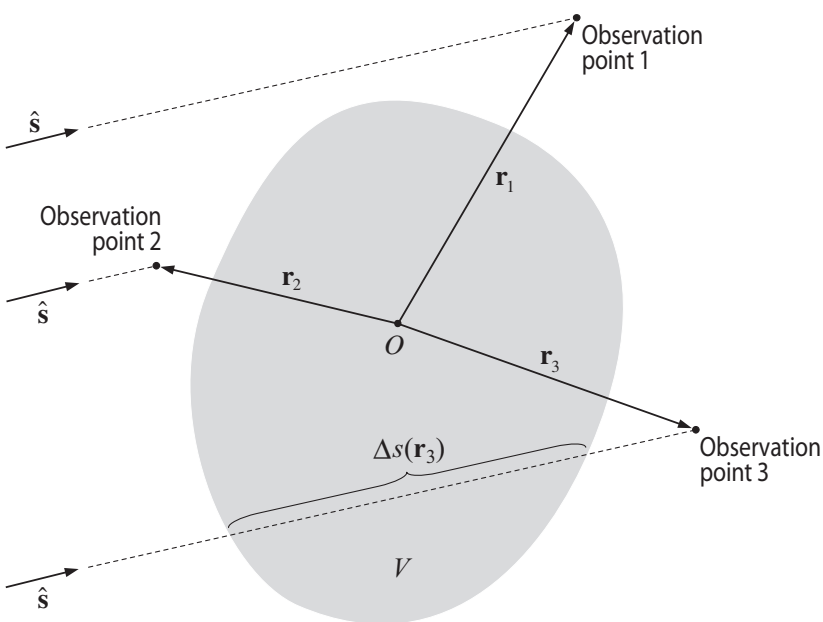

Fig. 19.19. Definition of $\Delta s(\mathbf{r})$ for $\mathbf{r} \notin V$.

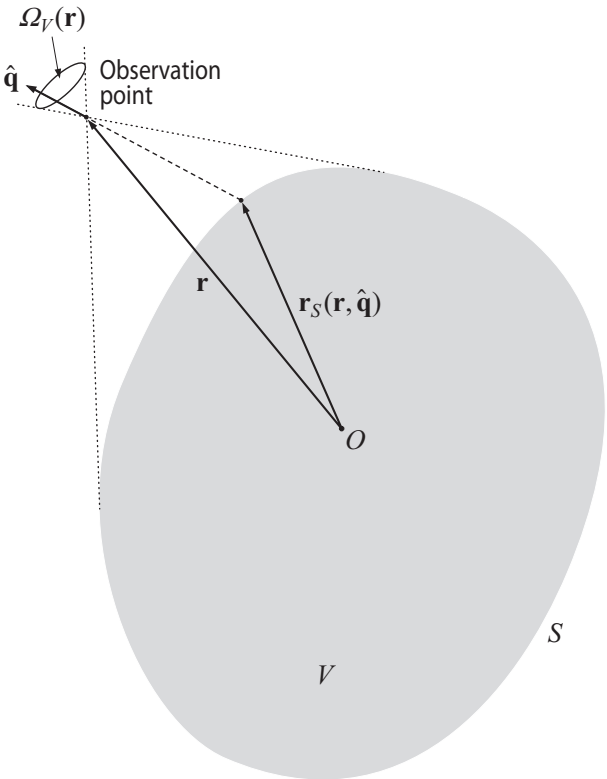

Fig. 19.20. Definitions of $\Omega_V(\mathbf{r})$ and $\mathbf{r}_S(\mathbf{r}, \hat{\mathbf{q}})$ for $\mathbf{r} \notin V$.

$$\langle\langle \text{EM power}(\mathbf{r}, \hat{\mathbf{q}})\rangle\rangle \approx \chi[\Delta\Omega_{\hat{\mathbf{q}}}, \hat{\mathbf{s}}] S_{\text{ep}} I_{\text{c}}^{\text{ex}}(\mathbf{r}) + S_{\text{ep}} \int_{\Delta\Omega_{\hat{\mathbf{q}}}} \mathrm{d}\hat{\mathbf{q}}' \chi[\Omega_V(\mathbf{r}), \hat{\mathbf{q}}'] \widetilde{I}_{\text{d}}[\mathbf{r}_S(\mathbf{r}, \hat{\mathbf{q}}'), \hat{\mathbf{q}}'], \quad \mathbf{r} \notin V, \tag{19.105}$$

$$\langle\langle \textbf{Signal}(\mathbf{r}, \hat{\mathbf{q}})\rangle\rangle \approx \chi[\Delta\Omega_{\hat{\mathbf{q}}}, \hat{\mathbf{s}}] S_{\text{ep}} \mathbf{I}_{\text{c}}^{\text{ex}}(\mathbf{r}) + S_{\text{ep}} \int_{\Delta\Omega_{\hat{\mathbf{q}}}} \mathrm{d}\hat{\mathbf{q}}' \chi[\Omega_V(\mathbf{r}), \hat{\mathbf{q}}'] \widetilde{\mathbf{I}}_{\text{d}}[\mathbf{r}_S(\mathbf{r}, \hat{\mathbf{q}}'), \hat{\mathbf{q}}'], \quad \mathbf{r} \notin V, \tag{19.106}$$

where

$$\mathbf{I}_{\text{c}}^{\text{ex}}(\mathbf{r}) = \mathbf{H}[\hat{\mathbf{s}}, \Delta s(\mathbf{r})] \mathbf{I}^{\text{inc}} \tag{19.107}$$

and $I_{\text{c}}^{\text{ex}}(\mathbf{r})$ is the first element of this four-element column. Again, $\Delta s(\mathbf{r})$ vanishes for observation points not shadowed by the particulate volume, in which case $\mathbf{H}[\hat{\mathbf{s}}, \Delta s(\mathbf{r})]$ becomes a unit matrix and $\mathbf{I}_{\text{c}}^{\text{ex}}(\mathbf{r})$ reduces to the Stokes column vector of the incident plane wave. Note that, unlike Eqs. (19.102) and (19.103), Eqs. (19.105) and (19.106) are not based on the assumption that the diffuse component $\widetilde{\mathbf{I}}_{\text{d}}[\mathbf{r}_S(\mathbf{r}, \hat{\mathbf{q}}')$ is nearly constant for all $\hat{\mathbf{q}}' \in \Delta\Omega_{\hat{\mathbf{q}}}$. As a consequence, the latter formulas can be used in cases when the distance from the particulate vol-

ume to the observation point is so large that $\Delta\Omega$ is comparable to or exceeds $\Omega_V(\mathbf{r})$.

The reader can see that Eqs. (19.104)–(19.106) again involve the solution of the RTE (19.84) supplemented by the boundary condition (19.85). This time, however, the diffuse component of the Stokes specific intensity column vector is evaluated not at the external observation point $\mathbf{r}$, but rather at the corresponding point $\mathbf{r}_S(\mathbf{r}, \hat{\mathbf{q}}')$ on the boundary S of the particulate volume.

If the particles populating the volume V are ISRPs then Eq. (19.107) becomes

$$\mathbf{I}_{\mathrm{c}}^{\mathrm{ex}}(\mathbf{r}) = \exp[-n_0\langle C_{\mathrm{ext}}\rangle_\xi \Delta s(\mathbf{r})]\mathbf{I}^{\mathrm{inc}}. \tag{19.108}$$

19.13 Summary of assumptions and approximations

Since the microphysical derivation of the final formulas of Sections 19.08–19.12 is rather lengthy and technical, it is instructive to recapitulate and further discuss the specific assumptions and approximations that had to be made at the various stages. They can be summarized as follows:

1. We have assumed that the particulate volume is illuminated by a monochromatic plane electromagnetic wave. However, the results of Section 10.3 imply that all results of this chapter are also applicable to the case of an incident field in the form of a polychromatic parallel beam with N quasi-monochromatic components. Specifically, let $\widetilde{\mathbf{I}}(\mathbf{r}, \hat{\mathbf{q}}, \omega_n) = \delta(\hat{\mathbf{q}} - \hat{\mathbf{s}})\mathbf{I}_{\mathrm{c}}(\mathbf{r}, \omega_n) + \widetilde{\mathbf{I}}_{\mathrm{d}}(\mathbf{r}, \hat{\mathbf{q}}, \omega_n)$ be the "partial" solution of the RTT obtained by replacing $\mathbf{I}^{\mathrm{inc}}$ with $\langle\langle \mathbf{I}_n^{\mathrm{inc}} \rangle\rangle$, the latter being the time-averaged Stokes column vector of the nth quasi-monochromatic component of the incident beam. Then the total specific intensity column vector is given by

$$\widetilde{\mathbf{I}}^{\mathrm{tot}}(\mathbf{r}, \hat{\mathbf{q}}, \hat{\mathbf{s}}) = \sum_{n=1}^{N} \widetilde{\mathbf{I}}(\mathbf{r}, \hat{\mathbf{q}}, \omega_n). \tag{19.109}$$

As usual, the applicability of the formulas quantifying the reading of a WCR rests on the assumption that the detection efficiency of the instrument is frequency independent. Furthermore, all formulas of the RTT can be generalized to the case of illumination by several polychromatic beams having different propagation directions (Problem 19.17).

2. We have assumed that each particle is located in the far zones of all the other particles and that the observation point is also located in the far zones of all the particles forming the scattering medium. This allowed us to use the far-field Neumann expansion (6.48).

3. We have assumed that the observation point is located in the near zone of the entire particulate volume.

4. We have neglected all multi-particle sequences involving a particle two or more times (the Twersky approximation). As we have seen in Section 19.1, doing this is justified when the total number of particles in the medium is very large.

5. We have assumed that the scattering system is fully ergodic and that averaging over time can be replaced by averaging over particle positions and states (Section 10.4).

6. We have assumed that: (i) the position and state of each particle are statistically independent of each other and of those of all the other particles; (ii) all particles are characterized by the same probability density function $p_\xi(\xi)$; and (iii) the spatial distribution of the particles throughout the medium is random and statistically uniform (Section 19.2).

7. We have assumed that the scattering medium is convex, which assured that a wave exiting the medium cannot re-enter it (Section 19.3).

8. We have assumed that the number of particles N forming the scattering medium is very large and replaced all factors of the type $(N-n)!/(N-n-k)!$ by N^k (Sections 19.2 and 19.5).

9. We have ignored all diagrams with crossing connectors in the diagrammatic expansion of the dyadic correlation function (Section 19.5).

Assumptions 2 and 8 imply that the overall size of the scattering medium must be much greater than the wavelength, average particle size, and average distance between two neighboring particles. They ensure, in particular, that the exponential factors of the type $\exp(\mathrm{i}k_1 r)$ oscillate many times over the distances traveled by the particles during the measurement, thereby leading to Eqs. (19.12), (19.15), and (19.54) and, ultimately, to Eqs. (19.16) and (19.55).

Another consequence of assumptions 2 and 6 is that the average particle number density in the scattering medium must be rather small. Therefore, the microphysical RTT may not be expected to perform well for densely packed media (see Chapter 22).

The meaning of assumptions 5 and 6 is illustrated in Fig. 19.21. The acceptance solid angle of the WCR $\Delta\Omega$ is small enough to resolve the angular variability of the diffuse component in Eq. (19.103) (e.g., $\sim 1°$). The entrance pupil S_{ep} of the WCR along with $\Delta\Omega$ defines the part of the particulate volume V bounded schematically by the dotted lines in Fig. 19.21; this part will be called the acceptance volume. We have seen that the signal recorded by the WCR is caused only by the particles residing in the acceptance volume.

Let us assume that the WCR accumulates the signal over a time interval T and subdivide the acceptance volume into a number of sampling volumes such that their optical thickness $n_0\langle C_{\mathrm{ext}}\rangle_\xi \Delta q$ along the line of sight of the detector is very small (~ 0.01). One of these sampling volumes is shown schematically in Fig. 19.21. Then it follows from the RTE (19.95) that the contribution of a particle to the WCR signal is essentially independent of the specific particle position

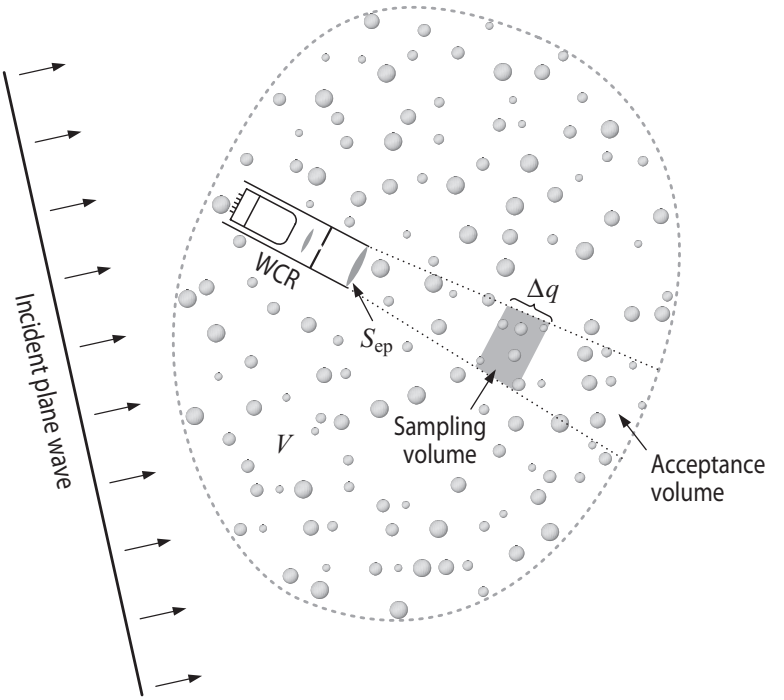

Fig. 19.21. Practical meaning of the assumptions of ergodicity and spatial uniformity. The sizes of the WCR and the particles are exaggerated relative to that of the particulate volume for demonstration purposes.

in the sampling volume. Therefore, the *strict* meaning of the assumptions of ergodicity and statistical uniformity of particle positions within the volume V is that each particle visits each sampling volume during the measurement time interval T.

In reality, however, the particulate volume V can be expected to contain many particles of the same type. Therefore, the *practical* meaning of ergodicity and uniformity is that particles of each type visit each sampling volume during the measurement interval T a number of times statistically representative of the total number of such particles in the entire volume. Obviously, this requirement is significantly softer and can be expected to be met in many actual circumstances.

Although Eqs. (19.105) and (19.106) have been derived while assuming that the observation point is located in the near zone of the particulate volume, the reader can easily verify that in the limit $r \to \infty$ the entire volume starts to behave like a single far-field scatterer. Indeed, the diffuse terms on the right-hand side of these formulas become the products of r^{-2} and r-independent yet $\hat{\mathbf{q}}$-dependent integrals over the part of the boundary S visible from the observation point. This is a very important result. Indeed, the reader should recall that in Section 18.4,

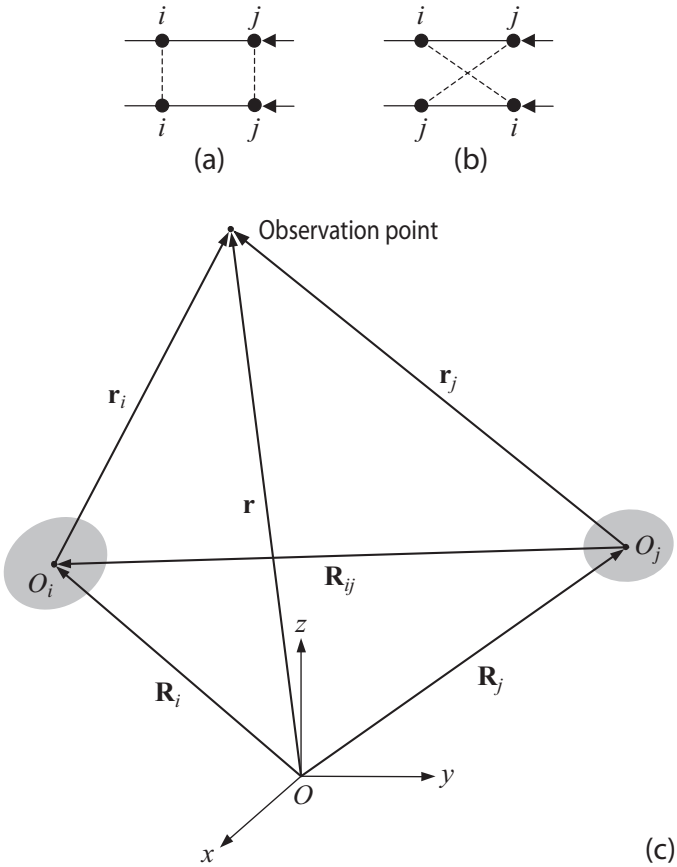

Fig. 19.22. Practical meaning of the assumptions of ergodicity and uniformity. The sizes of the detector and the particles are exaggerated relative to that of the particulate volume for demonstration purposes.

we attributed the diffuse background seen in Fig. 18.4h to the class of wavelet pairs depicted in Plate 18.1f. It is obvious that such wavelet pairs correspond to diagrams contributing to the ladder approximation of the time-averaged PST, as discussed in Sections 19.5 and 19.6. This implies that the diffuse background in Fig. 18.4h can be associated with the diffuse RTT regime. In fact, we can now broaden the class of wavelet pairs contributing to the diffuse background by including pairs of the type shown in Plate 18.1g. As we have seen before, the coordinate-averaged effect of the unconnected particles i, j, and l is reduced to exponential attenuation and, possibly, dichroism.

To justify approximation 9, let us consider, for example, the contributions of two simple two-particle diagrams, shown in Figs. 19.22a and 19.22b, to the time-averaged PST of the total field. According to Eqs. (8.3), (3.36), and (6.48), these contributions are given by

$$\frac{1}{2}\sqrt{\frac{\epsilon_1}{\mu_0}}\langle r_i^{-2}R_{ij}^{-2}\hat{\mathbf{r}}_i\times[\overleftrightarrow{A}_i(\hat{\mathbf{r}}_i,\hat{\mathbf{R}}_{ij})\cdot\overleftrightarrow{A}_j(\hat{\mathbf{R}}_{ij},\hat{\mathbf{s}})\cdot\mathbf{E}_0^{\text{inc}}]$$
$$\otimes[\overleftrightarrow{A}_i(\hat{\mathbf{r}}_i,\hat{\mathbf{R}}_{ij})\cdot\overleftrightarrow{A}_j(\hat{\mathbf{R}}_{ij},\hat{\mathbf{s}})\cdot\mathbf{E}_0^{\text{inc}}]^*\rangle_{\mathbf{R},\xi} \tag{19.110}$$

and

$$\frac{1}{2}\sqrt{\frac{\epsilon_1}{\mu_0}}\langle(r_ir_jR_{ij}^2)^{-1}\exp[\mathrm{i}k_1(r_i-r_j-\hat{\mathbf{s}}\cdot\hat{\mathbf{R}}_{ij})]\hat{\mathbf{r}}_i\times[\overleftrightarrow{A}_i(\hat{\mathbf{r}}_i,\hat{\mathbf{R}}_{ij})\cdot\overleftrightarrow{A}_j(\hat{\mathbf{R}}_{ij},\hat{\mathbf{s}})\cdot\mathbf{E}_0^{\text{inc}}]$$
$$\otimes[\overleftrightarrow{A}_j(\hat{\mathbf{r}}_j,-\hat{\mathbf{R}}_{ij})\cdot\overleftrightarrow{A}_i(-\hat{\mathbf{R}}_{ij},\hat{\mathbf{s}})\cdot\mathbf{E}_0^{\text{inc}}]^*\rangle_{\mathbf{R},\xi}, \tag{19.111}$$

respectively, where the notation follows that in Fig. 19.22c. The main difference between the expressions inside the angular brackets in these formulas is that the latter contains the rapidly oscillating complex exponential factor $\exp[\mathrm{i}k_1(r_i-r_j-\hat{\mathbf{s}}\cdot\hat{\mathbf{R}}_{ij})]$, which changes with $\mathbf{r}_i$ and $\mathbf{r}_j$ much faster than all the other participating factors. The presence of this exponential factor causes the contribution given by Eq. (19.111) to vanish upon the configurational averaging. The reader can verify that this is true of any diagram with crossing connectors and explains why their cumulative contribution to the time-averaged PST is negligible relative to the contribution of the diagrams with vertical connectors.

An important exception is the situation where the observation point is located in the far zone of the entire particulate volume in the direction opposite to the direction of incidence. Then the phase difference $\Delta = k_1(r_i - r_j - \hat{\mathbf{s}}\cdot\hat{\mathbf{R}}_{ij})$ vanishes, the exponential factor becomes identically equal to unity, and the contribution of the diagrams with crossing connectors becomes comparable to the contribution of the ladder diagrams. Again, the reader should recognize that we have attributed the backscattering peak seen in Fig. 18.4h to the class of wavelet pairs depicted in Plate 18.1e and that such wavelet pairs correspond to the diagrams of the type shown in Fig. 19.22b. This implies that the microphysical RTT does not describe the far-zone WL effect.

Similarly to WL, the forward-scattering localization of electromagnetic waves discussed in Section 18.4 and illustrated in Plate 18.1d is an expressly far-field scattering effect and as such is not accounted for by the microphysical RTT. Indeed, it can be readily demonstrated that the contribution of the diagrams of the type shown in Fig. 19.9b evaluated at a near-field observation point does not vanish only when both particles are positioned along the same straight line parallel to the incidence direction and going through the observation point. This non-vanishing contribution is ultimately included in the exponentially attenuated coherent Stokes column vector $\mathbf{I}_{\text{c}}$. In order to observe the forward-scattering interference effect directly, the observation point must be located in the far zone of the entire particulate volume, i.e., at a distance r from the scattering volume satisfying the inequalities (5.12)–(5.14). For most particulate volumes encountered in practice, this distance is unrealistically large, which makes the microphysical RTT a rather robust modeling tool.

The assumption that the particulate volume is statistically uniform simplified greatly the derivation of the microphysical RTT. It has been shown by the author (Mishchenko 2006) that all results of the RTT remain unchanged for a random particulate medium with small-scale random spatial inhomogeneities. Although a similar derivation for a general statistically inhomogeneous DRM is absent, it is very tempting to assume that the RTT remains valid, provided that the scale of inhomogeneities greatly exceeds the average distance between the particles. In this case the extinction and phase matrices averaged over particle states and the particle number density become functions of spatial coordinates, and so Eqs. (19.86), (19.87), and (19.89) take the form

$$\hat{\mathbf{s}} \cdot \nabla \mathbf{I}_{\mathrm{c}}(\mathbf{r}) = -n_0(\mathbf{r}) \langle \mathbf{K}(\mathbf{r}, \hat{\mathbf{s}}) \rangle_\xi \mathbf{I}_{\mathrm{c}}(\mathbf{r}), \quad \mathbf{I}_{\mathrm{c}}(\mathbf{r}_A) = \mathbf{I}^{\mathrm{inc}}, \tag{19.112}$$

$$\begin{aligned} \hat{\mathbf{q}} \cdot \nabla \widetilde{\mathbf{I}}_{\mathrm{d}}(\mathbf{r}, \hat{\mathbf{q}}) = {} & -n_0(\mathbf{r}) \langle \mathbf{K}(\mathbf{r}, \hat{\mathbf{q}}) \rangle_\xi \widetilde{\mathbf{I}}_{\mathrm{d}}(\mathbf{r}, \hat{\mathbf{q}}) + n_0(\mathbf{r}) \int_{4\pi} \mathrm{d}\hat{\mathbf{q}}' \langle \mathbf{Z}(\mathbf{r}, \hat{\mathbf{q}}, \hat{\mathbf{q}}') \rangle_\xi \widetilde{\mathbf{I}}_{\mathrm{d}}(\mathbf{r}, \hat{\mathbf{q}}') \\ & + n_0(\mathbf{r}) \langle \mathbf{Z}(\mathbf{r}, \hat{\mathbf{q}}, \hat{\mathbf{s}}) \rangle_\xi \mathbf{I}_{\mathrm{c}}(\mathbf{r}), \end{aligned} \tag{19.113}$$

$$\hat{\mathbf{q}} \cdot \nabla \widetilde{\mathbf{I}}(\mathbf{r}, \hat{\mathbf{q}}) = -n_0(\mathbf{r}) \langle \mathbf{K}(\mathbf{r}, \hat{\mathbf{q}}) \rangle_\xi \widetilde{\mathbf{I}}(\mathbf{r}, \hat{\mathbf{q}}) + n_0(\mathbf{r}) \int_{4\pi} \mathrm{d}\hat{\mathbf{q}}' \langle \mathbf{Z}(\mathbf{r}, \hat{\mathbf{q}}, \hat{\mathbf{q}}') \rangle_\xi \widetilde{\mathbf{I}}(\mathbf{r}, \hat{\mathbf{q}}'). \tag{19.114}$$

19.14 Corollaries of the microphysical radiative transfer theory

Important corollaries of the microphysical RTT are the following:

1. The derivation of the RTT does not need fundamental physical laws other than those already contained in the classical frequency-domain macroscopic electromagnetics. In particular, the ill-defined concepts of collective effects, elementary volume elements, incoherent light rays, and photons as localized particles of light have no relevance whatsoever to the transport of electromagnetic radiation in elastically scattering DRMs. It is, in fact, remarkable that although the RTE (19.87) has the formal mathematical structure of a kinetic equation describing particle transport, it follows directly from the electromagnetic *wave* theory.

2. Neither the coherent Stokes column vector nor the diffuse specific intensity column vector characterize the instantaneous distribution of the radiation field inside the scattering medium. Instead, both are averages over a sufficiently long period of time. The minimal averaging time necessary to ensure ergodicity may be different for different scattering systems, but the following is always true: the longer the averaging time the more accurate the theoretical prediction based on the RTT. Accumulating a signal over an extended period of time is often used to improve the accuracy of a measurement by reducing the effect of random noise. However, the situation with the RTT is fundamentally different since averaging the signal over an extended period of time is necessary to ensure the very applicability of the RTE.

3. Averaging over all particle positions makes both $\mathbf{I}_c$ and $\widetilde{\mathbf{I}}_d$ continuous functions of the position vector of the observation point $\mathbf{r}$ and also makes $\widetilde{\mathbf{I}}_d$ a continuous function of the "propagation" direction $\hat{\mathbf{q}}$. For the same reason, $\widetilde{\mathbf{I}}$ differs from the Stokes column vector of a transverse electromagnetic wave, $\mathbf{I}$, in that it has the dimension of monochromatic radiance, $\mathrm{Wm^{-2}sr^{-1}}$, rather than the dimension of monochromatic energy flux, $\mathrm{Wm^{-2}}$.

4. In the context of the RTT, the scattering properties of particles are specified in terms of the extinction and phase matrices rather than in terms of the scattering dyadic or the scattering amplitude matrix. Each particle with its individual extinction and phase matrices is effectively replaced with a virtual random particle characterized by the extinction and phase matrices obtained by averaging over the states of all the particles.

5. The RTE is an inherently vector equation. The frequently used scalar version of the RTE is obtained by artificially replacing the specific intensity column vector by its first element (i.e., the specific intensity) and the extinction and phase matrices by their respective $(1,1)$ elements. As such, the scalar approximation has no compelling physical justification besides being easier to solve and yielding sufficiently accurate values of the specific intensity in some (but not all!) cases. Section 13.1 of MTL2 contains an extensive discussion of the numerical accuracy of the scalar approximation.

6. The specific intensity is a nonnegative quantity (Problem 19.18). This corollary ensures that Eqs. (19.102), (19.103), (19.105), and (19.106) are physically meaningful.

7. If the incident field is a plane electromagnetic wave then the elements of the coherent Stokes column vector (19.38) (or (19.81)) satisfy the Stokes identity (7.4), while the elements of the diffuse specific intensity column vector $\widetilde{\mathbf{I}}_d(\mathbf{r},\hat{\mathbf{q}})$ satisfy the Stokes–Verdet inequality (9.34). If the incident field is a polychromatic parallel beam with quasi-monochromatic components then the elements of either the total coherent Stokes column vector or the total diffuse specific intensity column vector satisfy the Stokes–Verdet inequality (9.34) (Problem 19.19).

8. Although Eqs. (11.12) and (19.97) have the same mathematical structure, it can be shown that $\widetilde{N}(\mathbf{r},\hat{\mathbf{q}}) \neq \widetilde{I}(\mathbf{r},\hat{\mathbf{q}})$. Specifically, let us recall that the microphysical derivation of the time-averaged Poynting vector is based on the complex-vector frequency-domain formalism. This approach allows one to conveniently factor out the time-harmonic dependence of the electric and magnetic fields, but necessitates the initial definition of the Poynting vector and the PST as averages over a sufficiently large number of time-harmonic oscillations captured by a time interval $T \gg 2\pi/\omega$ (Section 2.3). This means that the frequency-domain formalism cannot be used to evaluate the integrals in Eq. (11.11). Indeed, time-harmonic oscillations of the electric and magnetic vectors cause a rapidly oscillating Poynting vector at the observation point. At certain moments $\boldsymbol{\mathcal{S}}(\mathbf{r},t)$ can be directed along $\hat{\mathbf{q}}$ and thereby contribute to $\widetilde{N}(\mathbf{r},\hat{\mathbf{q}})$, while at other mo-

ments it can be directed along $-\hat{\mathbf{q}}$ and contribute to $\widetilde{N}(\mathbf{r}, -\hat{\mathbf{q}})$. While these "opposing" contributions are accounted for and accumulated in the computation of $\widetilde{N}(\mathbf{r}, \hat{\mathbf{q}})$ and $\widetilde{N}(\mathbf{r}, -\hat{\mathbf{q}})$, they substantially (but, of course, not completely) cancel each other in the frequency-domain computation of $\widetilde{I}(\mathbf{r}, \hat{\mathbf{q}})$ and $\widetilde{I}(\mathbf{r}, -\hat{\mathbf{q}})$, owing to the initial averaging over a large number of time-harmonic oscillations. This implies that $\widetilde{I}(\mathbf{r}, \hat{\mathbf{q}})$ would not be measured by the hypothetical directional detector discussed in Section 11.3, even if it could be built.

Of course, the inequality $\widetilde{N}(\mathbf{r}, \hat{\mathbf{q}}) \neq \widetilde{I}(\mathbf{r}, \hat{\mathbf{q}})$ coupled with the mathematical uniqueness of solution of Eq. (19.89) supplemented by the boundary condition (19.91) implies that $\widetilde{N}(\mathbf{r}, \hat{\mathbf{q}})$ cannot be the first element of a four-element column satisfying the standard RTE. It remains unknown whether a closed-form analytical equation for $\widetilde{N}(\mathbf{r}, \hat{\mathbf{q}})$ exists, but if it were derived then it would offer an alternative way of solving the time-averaged radiation-budget problem via Eq. (11.12).

This discussion implies that the specific intensity $\widetilde{I}(\mathbf{r}, \hat{\mathbf{q}})$ cannot be interpreted as describing the directional distribution of electromagnetic energy flow at the point $\mathbf{r}$. Actual physical significance can be attributed only to the integral of $\hat{\mathbf{q}}\widetilde{I}(\mathbf{r}, \hat{\mathbf{q}})$ over all directions $\hat{\mathbf{q}}$, rather than to the particular values of $\widetilde{I}(\mathbf{r}, \hat{\mathbf{q}})$ corresponding to individual directions. Indeed, adding to $\widetilde{I}(\mathbf{r}, \hat{\mathbf{q}})$ any function $f(\mathbf{r}, \hat{\mathbf{q}})$ such that

$$\int_{4\pi} \mathrm{d}\hat{\mathbf{q}}\, \hat{\mathbf{q}}\, f(\mathbf{r}, \hat{\mathbf{q}}) = \mathbf{0}$$

yields another "specific intensity" causing the same $\langle\langle \boldsymbol{\mathcal{S}}(\mathbf{r}, t)\rangle\rangle$. A simple example would be any symmetric function such that $f(\mathbf{r}, -\hat{\mathbf{q}}) = f(\mathbf{r}, \hat{\mathbf{q}})$. We have seen in Section 2.4 that even the Poynting vector cannot be legitimately claimed to specify the direction of time-averaged electromagnetic energy flow, and so there is even less justification for ascribing any "directional energy" content to the specific intensity. The quantity $\widetilde{I}(\mathbf{r}, \hat{\mathbf{q}})$ is nothing but a formal solution of the intermediate equation (19.89) and appears merely as a byproduct of the mathematical derivation of Eqs. (19.97) and (19.102) from the frequency-domain MMEs.

19.15 "Independent" scattering

We have seen before that at any moment in time, the incident electromagnetic wave perceives the entire multi-particle group as a unified, albeit morphologically complex, scatterer. We have also witnessed how the RTE emerges from the MMEs as a consequence of several specific assumptions and, in the final analysis, contains single-particle extinction and phase matrices averaged over the particle states. However, the traditional phenomenological way of addressing electromagnetic energy transport in particulate media has been to proceed in exactly the opposite direction:

- by first considering the scattering properties of each particle in total isolation from all the other particles by solving individually the MMEs (e.g., by using the LMT);
- then considering widely separated, randomly positioned particles forming a particle group as "independent scatterers" characterized individually by the previously determined extinction and phase matrices;
- then considering "incoherent single scattering" by the "independently scattering particles" occupying an imaginary "elementary volume element";
- then considering "incoherent multiple scattering" by the "elementary volume elements"; and finally
- by speculating how the "single-scattering properties" of the individual particles and of the "elementary volume elements" can change as a consequence of hypothetical "packing density" effects.

It is thus clear that the notion of "independent scattering" has been very important to the phenomenological RTT. Several definitions of "independently scattering particles" have been given in the literature over the years, most of them being rather vague. The common intent of those definitions has been to ensure that observable consequences of scattering by a disperse medium are described in terms of the extinction and phase matrices of the individual particles, i.e., the *quantities describing single-particle transformations of Stokes parameters rather than electromagnetic fields*.

The microphysical RTT outlined above makes it quite clear that a particle is an independent scatterer only when it is completely alone. Particles forming a group cannot be independent scatterers, irrespective of how widely they are separated and how randomly they are distributed since the forward-scattering interference and WL effects are ubiquitous and cannot be described in terms of individual-particle extinction and phase matrices. In the case of large rarified objects such as terrestrial water clouds, the forward-scattering and WL intensity peaks are extremely narrow, contain a negligible fraction of the total scattered energy, and are hardly observable, thereby making the RTT a very good quantitative descriptor of many actual observables. We have seen, however, that even in the limited context of the RTT, particles are not characterized by their individual extinction and phase matrices. Instead, each actual particle is replaced by an imaginary "average particle" characterized by the ensemble-averaged extinction and phase matrices. We must, therefore, conclude that the term "independent scattering" has little heuristic value and can, in fact, be quite misleading.

19.16 Gaseous media

It is well known that electromagnetic scattering can be caused not only by particles with distinct boundaries, but also by density and anisotropy fluctuations in

rarified molecular media such as gases (Smoluchowski 1908). This type of scattering is traditionally called Rayleigh scattering and is thoroughly reviewed by Fabelinskii (1968), Crosignani *et al.* (1975), and Kuz'min *et al.* (1994). Each density and/or anisotropy fluctuation can be considered a particle in the sense of causing the electric permittivity (or, in general, the electric permittivity tensor) in a small volume element to be different from that of the surrounding medium. As long as such volume elements are located in the far zones of each other, the far-field Neumann expansion (6.48), as well as the microphysical RTT outlined above remain applicable. The specific form of the corresponding extinction and phase matrices entering the RTE depends on the type of gas (or gas mixture) and on factors such as gaseous pressure and temperature.

It is sometimes claimed that the actual cause of Rayleigh scattering in an optically thick gaseous medium are randomly positioned and randomly moving individual molecules rather than electric permittivity fluctuations. However, molecules can often be separated by distances much smaller than the wavelength, thereby grossly violating the far-field assumption used to derive the RTE. Of course, one cannot exclude completely the possibility that the RTE can be derived without the far-field assumption, but until and unless this has been done, it is more prudent to attribute Rayleigh scattering in optically thick gaseous media to molecular fluctuations rather than to the individual molecules.

Quite often a gaseous medium contains randomly distributed macroscopic particles. Typical examples are aerosols and cloud particles suspended in the atmospheres of the Earth and other planets. Obviously, the RTE still remains applicable, provided that the particles and the density/anisotropy fluctuations are located in the far zones of each other. The phase and extinction matrices entering the RTE are obtained by straightforward averaging over the gas–particle mixture.

Problems

19.1: Derive Eq. (19.8).

19.2: Derive the reciprocity relations for the coherent transmission dyadic and the coherent transmission amplitude matrix.

19.3: Derive Eq. (19.39).

19.4: Derive the reciprocity relation for the coherent transmission Stokes matrix.

19.5: Derive Eq. (19.44).

19.6: Derive Eq. (19.57).

19.7: Derive Eq. (19.59).

19.8: Derive Eq. (19.66).

19.9: Verify the transversality properties (19.70) and (19.71).

19.10: Derive Eqs. (19.78) and (19.79).

19.11: Prove that all elements of the columns $\mathbf{I}_c(\mathbf{r})$, $\widetilde{\mathbf{I}}_d(\mathbf{r}, \hat{\mathbf{q}})$, and $\widetilde{\mathbf{I}}(\mathbf{r}, \hat{\mathbf{q}})$ are real valued.

19.12: Derive Eq. (19.97).

19.13: Derive Eq. (19.101).

19.14: Verify that Eq. (19.101) also applies to the case of $\hat{\mathbf{s}} \in \Delta\Omega_{\hat{\mathbf{q}}}$.

19.15: Derive Eqs. (19.104)–(19.107) by following the approach outlined in Section 8.14 of MTL2.

19.16: Consider the scattering problem sketched in Fig. 14.3 and recover Eqs. (14.47) and (14.48) from Eqs. (19.106) and (19.107).

19.17: Generalize Eq. (19.109) to the case of an incident field in the form of a superposition of several polychromatic parallel beams with quasi-monochromatic components and different propagation directions. Discuss the implications of this result assuming that the cloud is illuminated by the sun. Take into account that the thermally emitted solar light is a superposition of statistically independent quasi-monochromatic waves with propagation directions confined to the solid angle subtended by the solar disk. At a large distance from the sun each such wave becomes locally plane.

19.18: Prove that the specific intensity is a nonnegative quantity.

19.19: Prove corollary 7 of Section 19.14.

Notes and further reading

The RTT was originally developed by using the old conceptual framework of phenomenological photometry. A thorough account of the early history of photometry was provided by D. L. DiLaura in Lambert (2001). He attributes the culmination of medieval optics to *Ad Vitellionem Paralipomena* by Johannes Kepler (1571–1630) (Kepler 1604), which contains one of the most fundamental elements of photometry: the attenuation of light as the inverse square of distance from a point-like source. However, establishing photometry as a scientific discipline was the result of systematic studies by Pierre Bouguer (1698–1758) followed by those of Johann Lambert (1728–77). Bouguer's *Essai d'Optique* was published in 1729 (Bouguer 1729), while its thorough augmentation, *Traité d'Optique*, appeared posthumously in 1760 (Bouguer 1760). Bouguer's research was mostly experimental and based on several ingeniously designed photometric instruments. In particular, in *Essai d'Optique* he describes the use of the inverse-square law to derive the ratio of luminous intensities of two light sources and

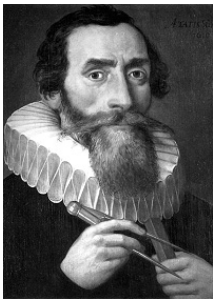
Johannes Kepler

Pierre Bouguer

Johann Lambert

Eugen von Lommel

Orest Khvolson

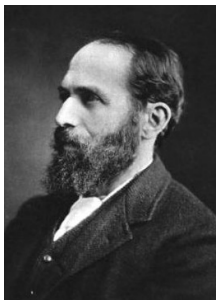
Arthur Schuster

Viktor Sobolev

Hendrik van de Hulst

Viktor Ambartsumian and S. Chandrasekhar

discovers the famous exponential attenuation law (sometimes incorrectly attributed to Lambert) by studying the diminution of light as it passes through translucent media. In his *Photometria*, Lambert (1760) was the first to extensively use contemporary mathematics, including calculus, to interpret experimental results and developed the mathematical foundation of radiometry by introducing specific definitions of photometric quantities and a unified set of photometric principles and laws.

The impact of Bouguer's and Lambert's work was so profound that even now much of illumination engineering is based on their treatises. Perhaps the only notable augmentation was the incorporation of the solution concentration

into the Bouguer's exponential attenuation law by August Beer (Beer 1854). All in all, phenomenological photometry, as summarized eloquently by Gershun (1936) in terms of the so-called "light field," has been one of the oldest surviving paradigms in contemporary science despite its whopping disconnect from the "mainland" of modern physics (in the words of Preisendorfer (1965)).

The main contribution by Eugen von Lommel (1837–99) was to introduce the notion of the amount of radiant energy crossing an imaginary geometrical rather than an actual physical surface element. This allowed him to conceptualize the directional flow of radiant energy through space and introduce the integral form of the RTE as a way of solving the problem of diffusion of light through a turbid medium composed of isotropically scattering centers (Lommel 1887). Virtually identical results were published independently by Orest Khvolson (1852–1934) two years later (Chwolson 1889) (see also the instructive historical account of the early history of the phenomenological RTT by Ivanov 1994). The work by Lommel and Khvolson has remained largely unnoticed. The first introduction of the RTE has traditionally been attributed to Arthur Schuster (1851–1934) who, in fact, proposed what is now known as the two-stream approximation rather than the integral or integro-differential form of the RTE (Schuster 1905). The work by Viktor A. Ambartsumian (1908–96), Subrahmanyan Chandrasekhar (1910–95), Viktor V. Sobolev (1915–99), and Hendrik C. van de Hulst (1918–2000), among others, had served to transform the phenomenological RTT into a branch of mathematical physics.

François Arago was among the first to criticize phenomenological photometry for complete neglect of polarization state of light. This criticism was nominally addressed by replacing the specific intensity $\widetilde{I}(\mathbf{r}, \hat{\mathbf{q}})$ with the four-element specific intensity column vector $\widetilde{\mathbf{I}}(\mathbf{r}, \hat{\mathbf{q}})$. Richard Gans (1880–1954) was the first to consider the transfer of polarized light in a plane-parallel Rayleigh-scattering atmosphere (Gans 1924); however, he analyzed only the special case of perpendicularly incident light and considered only the first two components of the specific intensity column vector. The case of arbitrary illumination and arbitrary polarization was studied by Chandrasekhar (1950). In a paper never translated into English, Georgi Rozenberg (1914–82) introduced the most general form of the vector RTE (Eqs. (19.86) and (19.87)) for sparse scattering media composed of arbitrarily shaped and arbitrarily oriented particles (Rozenberg 1955).

Whether spelled out explicitly or not, the key premise of phenomenological photometry, as well as of the phenomenological RTT, is that matter interacts with the energy of the electromagnetic field rather than with the electromagnetic field itself. This profoundly false assumption explains the deceitful simplicity of the phenomenological concepts, as well as their ultimate failure. Indeed, the very outset of both phenomenological disciplines is the postulation of the existence of specific intensity as the primordial physical quantity describing the "directional distribution of the radiant energy flow" at a point in space. This is followed by a back-of-an-envelope "derivation" of the scalar RTE on the basis of "simple

physical considerations." The often uncontrollable use of the word "photon" taken out of its proper QED framework is another manifestation of the implicit desire to bypass the complexities of dealing with the electromagnetic field. The inevitable outcome of such verbal speculations has been the notorious "photonic confusion."

In the paper titled "Anti-photon", Willis Lamb Jr. famously stated: "There is no such thing as a photon. Only a comedy of errors and historical accidents led to its popularity among physicists and optical scientists" (Lamb 1995). What Lamb meant is that in most cases the word "photon" is used without clear understanding of what a QED photon actually is and, in particular, without recognizing that it is not a localized particle of light. The QED photon represented a new profound paradigm brought about by the work of Paul Dirac, Werner Heisenberg, and Pascual Jordan in the late 1920s–early 1930s, and the consequences of this major conceptual shift are still being evaluated (Roychoudhury *et al.* 2008).

Paraphrasing Lamb, it can be said that "there is no such thing as phenomenological specific intensity." Indeed, the very notion of polydirectional propagation of electromagnetic energy at a point in space contradicts basic laws of classical electromagnetics and does not follow from QED. Furthermore, there is no practical need whatsoever to postulate specific intensity as a primordial physical quantity with its *a priori* defined properties. As this chapter demonstrates, all one needs to do is clearly formulate specific problems of actual practical significance and solve them using the MMEs as the starting point. It then becomes obvious that the specific intensity is just the formal solution of an auxiliary mathematical equation rather than a primordial physical quantity. One can say figuratively that the specific intensity is what a WCR measures, but only on condition that the parameters of the particulate medium in question are consistent with the set of assumptions summarized in Section 19.13.

The fundamental weaknesses of the phenomenological approach to directional photometry and radiative transfer have been thoroughly exposed in the literature (e.g., Preisendorfer 1965; Wolf 1978; Apresyan and Kravtsov 1996; Mishchenko 2009, 2011, 2013; Mishchenko *et al.* 2011b). As a result of recent research, there has been a paradigm-changing shift in the physical foundation of these disciplines that has finally brought them into the realm of physical optics. From allegedly describing the "directional flow of radiant energy," directional photometry and the RTT have been transformed into the discipline of performing measurements with WCRs and modeling these measurements theoretically on the basis of fundamental physical laws.

The development of the microphysical RTT in this chapter largely follows that in MTL2 and Mishchenko (2010). Important early contributions to the microphysical approach had been made by Borovoy (1966), Dolginov *et al.* (1970), Barabanenkov (1975), and Tsang *et al.* (1985). The case of an absorbing host medium was addressed by Mishchenko (2008a,b).

20

Radiative transfer in plane-parallel particulate media

In order to use the results of Sections 19.10–19.12 in various practical applications, one needs efficient techniques for solving the RTE in either the integral or the integro-differential form. Unfortunately, like many other integral and integro-differential equations, the RTE is difficult to solve analytically or numerically. In order to facilitate the solution, it is customary to make several simplifying assumptions. The most typical of them, which will be used throughout this chapter, are the assumptions that the particulate medium:

- is plane parallel;
- has an infinite horizontal extent; and
- is illuminated from above by a plane electromagnetic wave or a parallel polychromatic beam with quasi-monochromatic components.

These assumptions mean that all statistically averaged optical properties of the medium and all observable characteristics of the radiation field may vary only in the vertical direction and are independent of the horizontal coordinates. Taken together, these assumptions specify the so-called *standard one-dimensional problem* of the RTT and provide a model relevant to a great variety of applications in diverse fields of science and engineering.

To simplify the standard problem even further, we will also assume that the particulate medium is populated by statistically isotropic and mirror-symmetric random particles and use the extinction matrix given by Eq. (15.42) and the phase matrix given by Eqs. (15.20) and (15.21).

In this chapter we will derive several general equations describing the radiation field in the particular case of plane-parallel scattering geometry. Also we will describe several selected illustrative examples which demonstrate typical qualitative and quantitative predictions of the RTE and are expected to be of interest to a broad range of customers of the RTT.

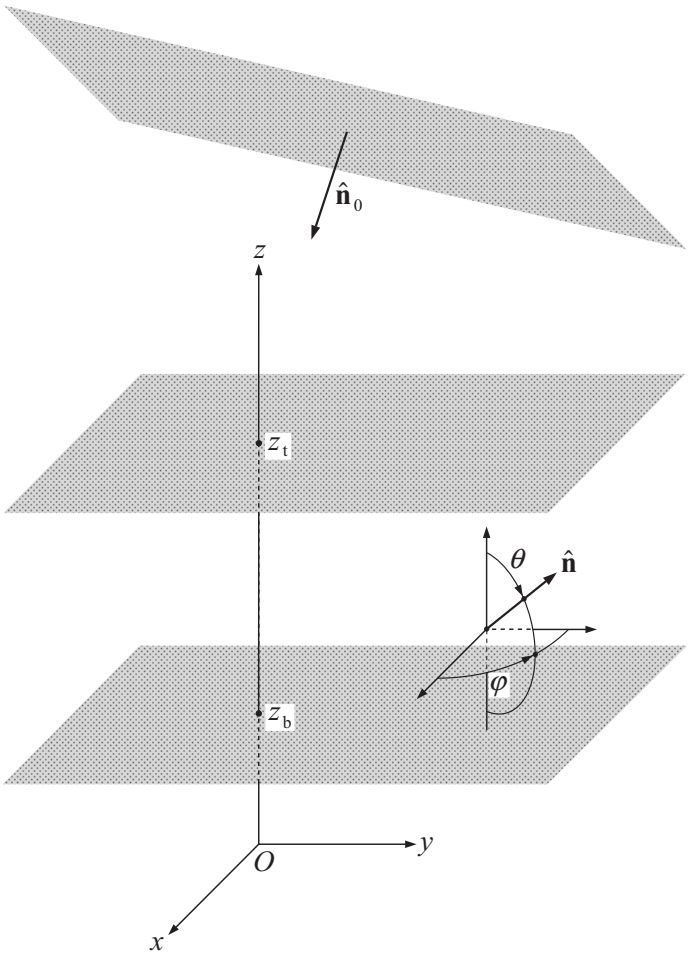

Fig. 20.1. Plane-parallel particulate medium illuminated from above by a parallel polychromatic beam with quasi-monochromatic components.

20.1 The standard problem

Let us consider a plane-parallel particulate layer extending in the vertical direction from $z = z_b$ to $z = z_t$, where the z-axis of the laboratory right-handed coordinate system is perpendicular to the boundaries of the medium and is directed upwards, while "b" and "t" stand for "bottom" and "top", respectively (Fig. 20.1). A propagation direction $\hat{\mathbf{n}}$ at a point in space will be specified by a couplet $\{u, \varphi\}$, where $u = -\cos\theta \in [-1, +1]$ is the direction cosine, while θ and φ are the corresponding polar and azimuth angles with respect to the local coordinate system having the same spatial orientation as the laboratory coordinate system. A positive u always corresponds to a downward direction, whereas a negative u

always corresponds to an upward direction. It is also convenient to introduce a nonnegative quantity $\mu = |u| \in [0,1]$.

Let us assume that the particulate layer is illuminated from above by a plane electromagnetic wave or a parallel quasi-monochromatic beam of light propagating in the direction $\hat{\mathbf{n}}_0 = \{u_0, \varphi_0\}$. The uniformity and the infinite transverse extent of the wave or the beam ensure that all parameters of the internal radiation field (including that at the boundaries of the particulate layer) are independent of the coordinates x and y. Therefore, Eqs. (19.112) and (19.113) can be rewritten in a simplified form:

$$-u\,\frac{\mathrm{d}\mathbf{I}_{\mathrm{c}}(z)}{\mathrm{d}z} = -n_0(z)\mathbf{K}(z,\hat{\mathbf{n}})\mathbf{I}_{\mathrm{c}}(z), \quad \mathbf{I}_{\mathrm{c}}(z_{\mathrm{t}}) = \mathbf{I}_0, \tag{20.1}$$

$$\begin{aligned} -u\,\frac{\mathrm{d}\widetilde{\mathbf{I}}_{\mathrm{d}}(z,\hat{\mathbf{n}})}{\mathrm{d}z} &= -n_0(z)\mathbf{K}(z,\hat{\mathbf{n}})\widetilde{\mathbf{I}}_{\mathrm{d}}(z,\hat{\mathbf{n}}) + n_0(z)\int_{4\pi}\mathrm{d}\hat{\mathbf{n}}'\,\mathbf{Z}(z,\hat{\mathbf{n}},\hat{\mathbf{n}}')\,\widetilde{\mathbf{I}}_{\mathrm{d}}(z,\hat{\mathbf{n}}') \\ &\quad + n_0(z)\mathbf{Z}(z,\hat{\mathbf{n}},\hat{\mathbf{n}}_0)\mathbf{I}_{\mathrm{c}}(z), \end{aligned} \tag{20.2}$$

where $\mathbf{I}_0$ is the Stokes column vector of the incident radiation, while $\mathbf{K}$ and $\mathbf{Z}$ are the extinction and phase matrices, respectively, averaged over particle states (note that henceforth we omit the angular brackets $\langle\cdots\rangle_\xi$ for the sake of brevity). As before, the tilde distinguishes specific intensity column vectors from Stokes column vectors. Equation (20.2) must be supplemented by the boundary conditions

$$\widetilde{\mathbf{I}}_{\mathrm{d}}(z_{\mathrm{t}},\mu,\varphi) = \widetilde{\mathbf{I}}_{\mathrm{d}}(z_{\mathrm{b}},-\mu,\varphi) = \mathbf{0}, \tag{20.3}$$

where, as before, $\mathbf{0}$ is a zero four-element column. These boundary conditions follow directly from Eq. (19.85) and mean that there is no "downwelling" diffuse radiation at the upper boundary of the layer and no "upwelling" diffuse radiation at the lower boundary. Equations (19.109) and (20.1)–(20.3) collectively represent what we have called the *standard problem*.

Let us further assume that the particles populating the plane-parallel medium are ISRPs as defined in Chapter 15. Then Eqs. (20.1)–(20.3) become (Problem 20.1)

$$\mathbf{I}_{\mathrm{c}}(\tau) = \exp(-\tau/\mu_0)\mathbf{I}_0, \tag{20.4}$$

$$\begin{aligned} u\,\frac{\mathrm{d}\widetilde{\mathbf{I}}_{\mathrm{d}}(\tau,u,\varphi)}{\mathrm{d}\tau} &= -\widetilde{\mathbf{I}}_{\mathrm{d}}(\tau,u,\varphi) \\ &\quad + \frac{1}{C_{\mathrm{ext}}(\tau)}\int_0^{2\pi}\mathrm{d}\varphi'\int_{-1}^{+1}\mathrm{d}u'\,\mathbf{Z}(\tau;u,\varphi;u',\varphi')\widetilde{\mathbf{I}}_{\mathrm{d}}(\tau,u',\varphi') \\ &\quad + \frac{1}{C_{\mathrm{ext}}(\tau)}\mathbf{Z}(\tau;u,\varphi;\mu_0,\varphi_0)\exp(-\tau/\mu_0)\mathbf{I}_0, \end{aligned} \tag{20.5}$$

where

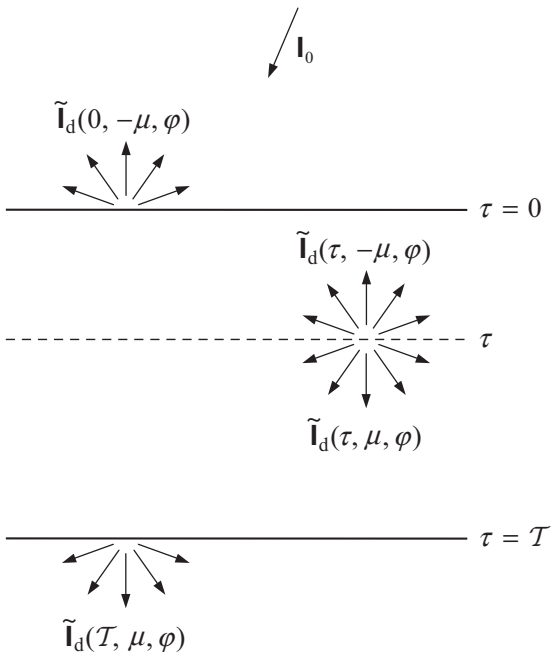

Fig. 20.2. The standard problem.

$$\tau(z) = \int_z^\infty \mathrm{d}z' n_0(z') C_\mathrm{ext}(z') \tag{20.6}$$

is the so-called *optical depth* and C_ext is the depth-dependent average extinction cross section (see Fig. 20.2). Unlike the geometrical height z, the optical depth is dimensionless. Replacing the phase matrix in Eq. (20.5) by the normalized phase matrix according to Eq. (15.65) finally yields

$$\begin{aligned} u\frac{\mathrm{d}\tilde{\mathbf{I}}_\mathrm{d}(\tau,u,\varphi)}{\mathrm{d}\tau} &= -\tilde{\mathbf{I}}_\mathrm{d}(\tau,u,\varphi) + \frac{\varpi(\tau)}{4\pi}\int_0^{2\pi}\mathrm{d}\varphi'\int_{-1}^{+1}\mathrm{d}u'\tilde{\mathbf{Z}}(\tau;u,\varphi;u',\varphi')\tilde{\mathbf{I}}_\mathrm{d}(\tau,u',\varphi') \\ &\quad + \frac{\varpi(\tau)}{4\pi}\tilde{\mathbf{Z}}(\tau;u,\varphi;\mu_0,\varphi_0)\exp(-\tau/\mu_0)\mathbf{I}_0, \end{aligned} \tag{20.7}$$

where

$$\varpi(\tau) = \frac{C_\mathrm{sca}(\tau)}{C_\mathrm{ext}(\tau)} \tag{20.8}$$

is the optical-depth-dependent single-scattering albedo. The standard problem is now reformulated by supplementing Eqs. (20.4) and (20.7) with the boundary conditions

$$\tilde{\mathbf{I}}_\mathrm{d}(0,\mu,\varphi) = \tilde{\mathbf{I}}_\mathrm{d}(\mathcal{T},-\mu,\varphi) = \mathbf{0}, \tag{20.9}$$

where $\mathcal{T} = \tau(z_\mathrm{b})$ is the *optical thickness* of the layer (Fig. 20.2).

20.2 Integral equation

Let us define the so-called matrix source function as a four-element column

$$\mathbf{J}(\tau, u, \varphi) = \frac{\varpi(\tau)}{4\pi}\int_0^{2\pi} \mathrm{d}\varphi' \int_{-1}^{+1} \mathrm{d}u' \widetilde{\mathbf{Z}}(\tau; u, \varphi; u', \varphi')\widetilde{\mathbf{I}}_{\mathrm{d}}(\tau, u', \varphi') + \frac{\varpi(\tau)}{4\pi}\widetilde{\mathbf{Z}}(\tau; u, \varphi; \mu_0, \varphi_0)\exp(-\tau/\mu_0)\mathbf{I}_0. \tag{20.10}$$

Then (Problem 20.2)

$$\widetilde{\mathbf{I}}_{\mathrm{d}}(\tau, \mu, \varphi) = \int_0^{\tau} \frac{\mathrm{d}\tau'}{\mu}\mathbf{J}(\tau', \mu, \varphi)\exp[-(\tau - \tau')/\mu], \tag{20.11}$$

$$\widetilde{\mathbf{I}}_{\mathrm{d}}(\tau, -\mu, \varphi) = \int_{\tau}^{\mathcal{T}} \frac{\mathrm{d}\tau'}{\mu}\mathbf{J}(\tau', -\mu, \varphi)\exp[-(\tau' - \tau)/\mu]. \tag{20.12}$$

The reader can verify (Problem 20.3) that the substitution of Eq. (20.10) in Eqs. (20.11) and (20.12) yields the "plane-parallel" version of the integral RTE (19.83).

Iteration of Eqs. (20.10)–(2.12) using $\frac{\varpi(\tau)}{4\pi}\widetilde{\mathbf{Z}}(\tau; u, \varphi; \mu_0, \varphi_0)\exp(-\tau/\mu_0)\mathbf{I}_0$ as the initial approximation for $\mathbf{J}(\tau, u, \varphi)$ shows that the diffuse specific intensity column vector $\widetilde{\mathbf{I}}_{\mathrm{d}}(\tau, u, \varphi)$ is linearly expressed in the Stokes column vector of the incident field $\mathbf{I}_0$. This expression is usually formulated in terms of 4×4 Green's matrices $\mathbf{U}$ and $\mathbf{D}$ as follows:

$$\widetilde{\mathbf{I}}_{\mathrm{d}}(\tau, -\mu, \varphi) = \frac{1}{\pi}\mu_0\mathbf{U}(\tau; \mu, \varphi; \mu_0, \varphi_0)\mathbf{I}_0, \tag{20.13}$$

$$\widetilde{\mathbf{I}}_{\mathrm{d}}(\tau, \mu, \varphi) = \frac{1}{\pi}\mu_0\mathbf{D}(\tau; \mu, \varphi; \mu_0, \varphi_0)\mathbf{I}_0. \tag{20.14}$$

At the upper and lower boundaries,

$$\widetilde{\mathbf{I}}_{\mathrm{d}}(0, -\mu, \varphi) = \frac{1}{\pi}\mu_0\mathbf{R}(\mu, \varphi; \mu_0, \varphi_0)\mathbf{I}_0, \tag{20.15}$$

$$\widetilde{\mathbf{I}}_{\mathrm{d}}(\mathcal{T}, \mu, \varphi) = \frac{1}{\pi}\mu_0\mathbf{T}(\mu, \varphi; \mu_0, \varphi_0)\mathbf{I}_0, \tag{20.16}$$

respectively, where $\mathbf{R}(\mu, \varphi; \mu_0, \varphi_0) = \mathbf{U}(0; \mu, \varphi; \mu_0, \varphi_0)$ is the so-called reflection matrix and $\mathbf{T}(\mu, \varphi; \mu_0, \varphi_0) = \mathbf{D}(\mathcal{T}; \mu, \varphi; \mu_0, \varphi_0)$ is the transmission matrix.

There are several efficient, numerically exact computer techniques for solving the RTEs (20.7) or (20.10)–(20.12) and calculating the matrices $\mathbf{U}$, $\mathbf{D}$, $\mathbf{R}$, and $\mathbf{T}$. Detailed discussions can be found in Hansen and Travis (1974), Marchuk *et al.* (1980), Lenoble (1985), Hovenier *et al.* (2004), and Chapter 12 of MTL2. Using these techniques, one can calculate all quantities necessary to solve the radiation-budget problem via Eqs. (19.97) and (19.104) as well as to quantify the read-

ing of a WCR via Eqs. (19.103) and (19.106). It is straightforward to show that the time-averaged Poynting vector at an external observation point and the reading of an external WCR are independent of the distance from the particulate layer (Problem 20.4).

Note that analogously to the case for the phase matrix (Section 15.3), the azimuthal symmetry of the particulate medium causes the matrices $\mathbf{U}$, $\mathbf{D}$, $\mathbf{R}$, and $\mathbf{T}$ to depend on the difference $\varphi-\varphi'$ rather than on φ and φ' separately. In other words, if $\varphi-\varphi'=\varphi_1-\varphi_1'$ then $\mathbf{D}(\tau;\mu,\varphi_1;\mu',\varphi_1')=\mathbf{D}(\tau;\mu,\varphi;\mu',\varphi')$, and analogously for the other matrices. This is equivalent to the statement that for any φ, φ', and $\Delta\varphi$,

$$\mathbf{Y}(\mu,\varphi+\Delta\varphi;\mu',\varphi'+\Delta\varphi) = \mathbf{Y}(\mu,\varphi;\mu',\varphi'), \tag{20.17}$$

where $\mathbf{Y}$ stands for $\mathbf{U}$, $\mathbf{D}$, $\mathbf{R}$, or $\mathbf{T}$ (see Section 12.2 of MTL2).

20.3 Scalar approximation

Equations (20.7) and (20.9) can be further simplified by artificially neglecting polarization and so replacing the specific intensity column vector by its first element (i.e., the specific intensity) and the normalized phase matrix by its (1, 1) element (i.e., the phase function):

$$\begin{aligned} u\frac{\mathrm{d}\widetilde{I}_{\mathrm{d}}(\tau,u,\varphi)}{\mathrm{d}\tau} &= -\widetilde{I}_{\mathrm{d}}(\tau,u,\varphi)+\frac{\varpi(\tau)}{4\pi}\int_0^{2\pi}\mathrm{d}\varphi'\int_{-1}^{+1}\mathrm{d}u'\widetilde{Z}_{11}(\tau;u,\varphi;u',\varphi')\widetilde{I}_{\mathrm{d}}(\tau,u',\varphi') \\ &\quad+\frac{\varpi(\tau)}{4\pi}\widetilde{Z}_{11}(\tau;u,\varphi;\mu_0,\varphi_0)\exp(-\tau/\mu_0)I_0 \qquad (20.18)\\ &= -\widetilde{I}_{\mathrm{d}}(\tau,u,\varphi)+\frac{\varpi(\tau)}{4\pi}\int_0^{2\pi}\mathrm{d}\varphi'\int_{-1}^{+1}\mathrm{d}u'a_1(\tau;\Theta')\widetilde{I}_{\mathrm{d}}(\tau,u',\varphi') \\ &\quad+\frac{\varpi(\tau)}{4\pi}a_1(\tau;\Theta_0)\exp(-\tau/\mu_0)I_0, \qquad (20.19)\end{aligned}$$

$$\widetilde{I}_{\mathrm{d}}(0,\mu,\varphi) = \widetilde{I}_{\mathrm{d}}(\mathcal{T},-\mu,\varphi) = 0, \tag{20.20}$$

where I_0 is the first element of the column $\mathbf{I}_0$, while

$$\Theta' = \arccos[uu'+(1-u^2)^{1/2}(1-u'^2)^{1/2}\cos(\varphi-\varphi')] \tag{20.21}$$

and

$$\Theta_0 = \arccos[u\mu_0+(1-u^2)^{1/2}(1-\mu_0^2)^{1/2}\cos(\varphi-\varphi_0)] \tag{20.22}$$

are the corresponding scattering angles (see Eqs. (15.23) and (15.81)). We have already mentioned that ignoring the vector nature of light and replacing the exact RTE by its approximate scalar counterpart has no rigorous physical justification. Nevertheless, this simplification is widely used when the medium is illuminated by unpolarized light and only the specific intensity of multiply-scattered light needs to be computed. The main (and probably outdated) reason for doing that is

saving computer resources. It should be kept in mind, however, that the errors of the scalar approximation can exceed 12% (see Section 13.1 of MTL2).

20.4 Directional reflectance and spherical and plane albedos

In this section we will use numerically exact computer solutions of the standard problem summarized by Eqs. (20.7) and (20.9) to analyze how the various parameters of a particulate slab affect the angular dependence of the reflected specific intensity and its integral characteristics. It will be assumed for simplicity that the plane-parallel particulate medium is homogeneous and that the particles populating the medium are homogeneous spheres. All numerical data in this and the following section have been obtained with the so-called fast invariant-imbedding technique described in Mishchenko (1991b).

We have seen in the preceding chapter that the total diffuse specific intensity column vector is the result of summing all ladder diagrams with varying numbers of connected particles. In other words, we can write the Neumann expansion

$$\widetilde{\mathbf{I}}_{\mathrm{d}}(\tau, \hat{\mathbf{n}}) = \sum_{n=1}^{\infty} \widetilde{\mathbf{I}}_{\mathrm{d}}^{n}(\tau, \hat{\mathbf{n}}), \tag{20.23}$$

where $\widetilde{\mathbf{I}}_{\mathrm{d}}^{n}(\tau, \hat{\mathbf{n}})$ is the cumulative contribution of all ladder diagrams with n connected particles. An analytical expression for $\widetilde{\mathbf{I}}_{\mathrm{d}}^{n}(\tau, \hat{\mathbf{n}})$ can be derived by iterating the integral RTE (20.10)–(2.12) and will not be given here explicitly (Problem 20.5). However, the reader can verify that besides angular and τ-integrations, the nth order Neumann term involves:

- n multiplications by the single-scattering albedo ϖ;
- n left multiplications by the normalized phase matrix $\widetilde{\mathbf{Z}}$; and
- n multipliers of the type $\exp(\pm(\tau'' - \tau')/\mu')$.

The combined effect of these operations can be quite convoluted. However, in some cases the contributing factors listed above can be used to give a simple qualitative interpretation of computer solutions of the plane-parallel version of the RTE.

Figure 20.3 shows the phase function and other elements of the normalized Stokes scattering matrix for a gamma size distribution of spherical particles given by Eq. (15.108) with $r_{\min} = 0$ and $r_{\max} = \infty$. The effective radius and the effective variance of the size distribution are $r_{\mathrm{eff}} = 1.05\ \mu\mathrm{m}$ and $v_{\mathrm{eff}} = 0.07$, respectively, the particle relative refractive index is $m = 1.44$, and the wavelength of the quasi-monochromatic incident field is $\lambda_1 = 550$ nm. Note that owing to $m_{\mathrm{I}} = 0$, these particles are nonabsorbing (i.e., $\varpi = 1$).

Let us consider a homogeneous slab populated by such particles and assume that it is illuminated by an unpolarized parallel quasi-monochromatic beam of light incident perpendicularly to the upper boundary of the slab. The intensity of

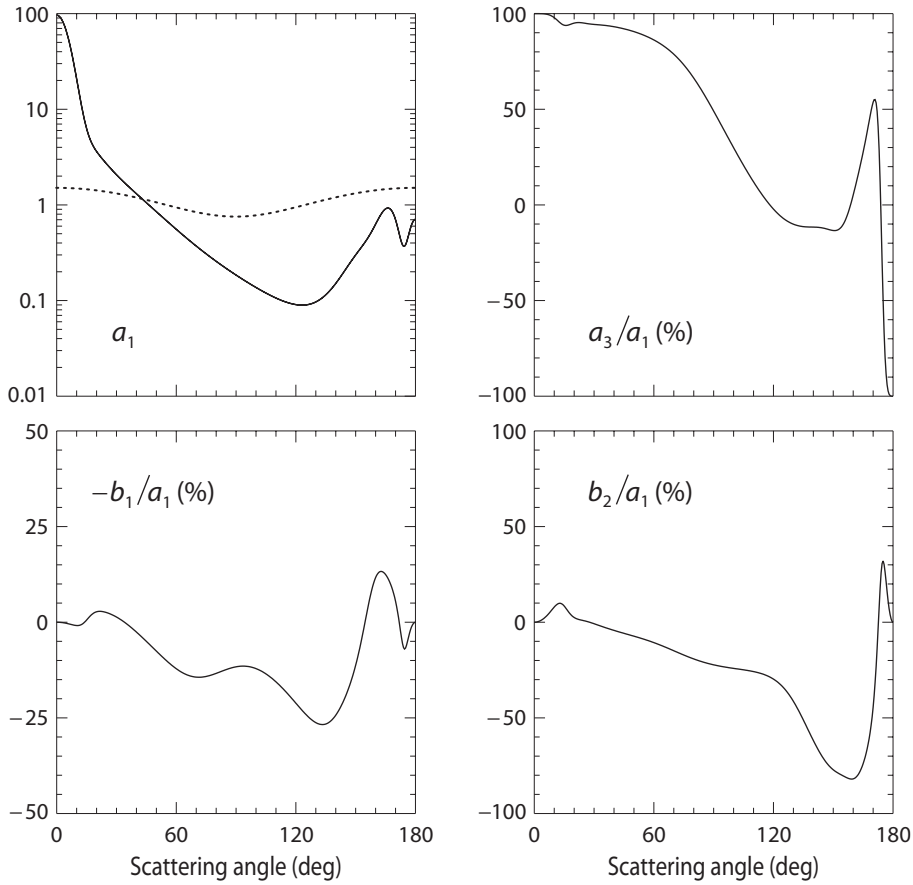

Fig. 20.3. Elements of the normalized scattering matrix for polydisperse spherical particles (see text). The dotted curve depicts the Rayleigh phase function.

this beam is $I_0 = \pi$ Wm^{-2}. Owing to the azimuthal symmetry of the illumination–reflection geometry, the reflected specific intensity, given by

$$\widetilde{I}(0, -\mu, \varphi) = R_{11}(\mathcal{T}; \mu, \varphi; 1, \varphi_0) \quad (\mathrm{Wm^{-2}sr^{-1}}) \tag{20.24}$$

(see Eq. (20.15)), is independent of the azimuth angles of the incidence and reflection directions, φ_0 and φ, and depends only on the polar angle of the reflection direction, θ. Figure 20.4 shows the reflected specific intensity versus $180° - \theta$ for five optical thickness values increasing from 0.01 to 100. Note that the angle $180° - \theta$ is equal to the scattering angle for the contribution from the first-order Neumann term (H.63).

The comparison of the bottom curve in Fig. 20.4 and the solid curve in the upper left diagram of Fig. 20.3 reveals that the angular distribution of the specific intensity reflected by an optically thin layer closely follows that of single-particle scattering. This is consistent with the formula (Problem 20.6)

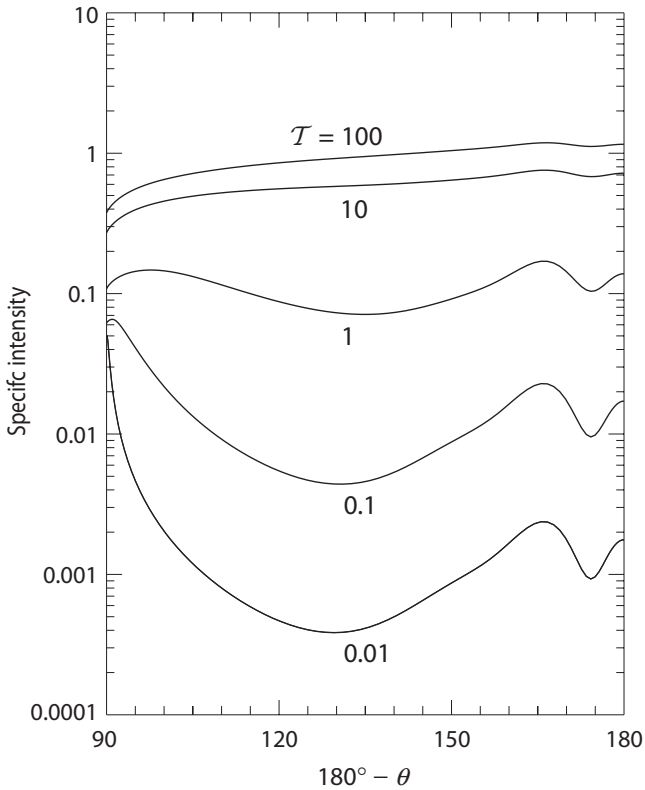

Fig. 20.4. Angular dependence of the reflected specific intensity (in $\mathrm{Wm^{-2}sr^{-1}}$) for a homogeneous slab populated by polydisperse spherical particles (see text). The optical thickness of the slab varies from $\mathcal{T} = 0.01$ to 100.

$$\lim_{\mathcal{T} \to 0} \mathbf{R}(\mathcal{T}; \mu, \varphi; \mu_0, \varphi_0) = \frac{\varpi \mathcal{T}}{4\mu\mu_0} \widetilde{\mathbf{Z}}(-\mu, \varphi; \mu_0, \varphi_0). \tag{20.25}$$

In particular, such phase-function features as the glory centered at $\Theta = 180°$ and the primary rainbow centered at $\Theta \sim 163°$ clearly show up in the reflected light. As the optical thickness of the slab grows from 0.01 to 100, the specific intensity increases by three orders of magnitude, the characteristic phase-function features become less pronounced, and the angular profile of the reflected specific intensity becomes very smooth. This behavior is quite similar to that of the curves in the upper left diagram of Plate 18.2.

All these effects are easy to understand qualitatively. Indeed, let us consider three particulate slabs with optical thicknesses $\mathcal{T}_1 < \mathcal{T}_2 < \mathcal{T}_3$, as shown in Fig. 20.5. The single-particle sequence 1 contributes to the specific intensity reflected by all three slabs. The multi-particle sequence 2 contributes to the specific intensity reflected by layers 2 and 3, but not by layer 1. Finally, the multi-particle sequence 3 contributes only to the specific intensity reflected by layer 3. Thus,

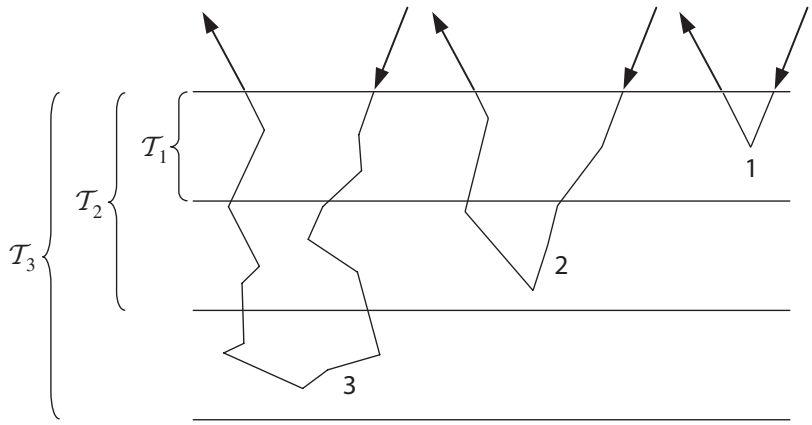

Fig. 20.5. Various sequences of connected particles contributing to the specific intensity of reflected light.

increasing optical thickness accommodates more multi-particle sequences contributing to the reflected light, which explains the increase of the reflected specific intensity in Fig. 20.4.

However, the multi-particle sequences reaching large optical depths, such as the multi-particle sequences 2 and 3 in Fig. 20.5, are longer than those controlling the reflectivity of optically thin layers, such as the sequence 1, and involve many more multiplications by normalized phase matrices. As such, they are less dependent on the original incidence direction and are likely to contribute more evenly to all reflection directions, thereby creating a more isotropic angular distribution of the reflected specific intensity than that typical of optically thin slabs. The latter is dominated by the first-order Neumann contribution and preserves pronounced single-particle features such as the glory and the rainbow.

It is instructive to visualize the overall increase of the reflected specific intensity with growing optical thickness by plotting the so-called spherical albedo

$$A_{\mathrm{S}}(\mathcal{T}) = \frac{2}{\pi}\int_0^{2\pi} \mathrm{d}\varphi \int_0^1 \mathrm{d}\mu\,\mu \int_0^1 \mathrm{d}\mu_0\,\mu_0\,R_{11}(\mathcal{T};\mu,\varphi;\mu_0,\varphi_0) \tag{20.26}$$

as a function of $\mathcal{T}$. The term "spherical albedo" comes from planetary astrophysics, wherein A_{S} represents the ratio of the electromagnetic energy reflected by the whole planet covered with a uniform cloud layer to the total (unpolarized) solar energy falling on the planet (Sobolev 1975). The solid curve in the upper left panel of Fig. 20.6 depicts A_{S} versus $\mathcal{T}$ for a slab composed of the micrometer-sized spherical particles. Taking into account that the $\mathcal{T}$ scale in Fig. 20.6 is logarithmic, one can clearly identify the following three regimes:

- a nearly linear growth of A_{S} on the interval $0 \lesssim \mathcal{T} \lesssim 1$;
- a nearly logarithmic growth of A_{S} on the interval $1 \lesssim \mathcal{T} \lesssim 20$; and
- the regime of slow saturation at $\mathcal{T} > 20$.

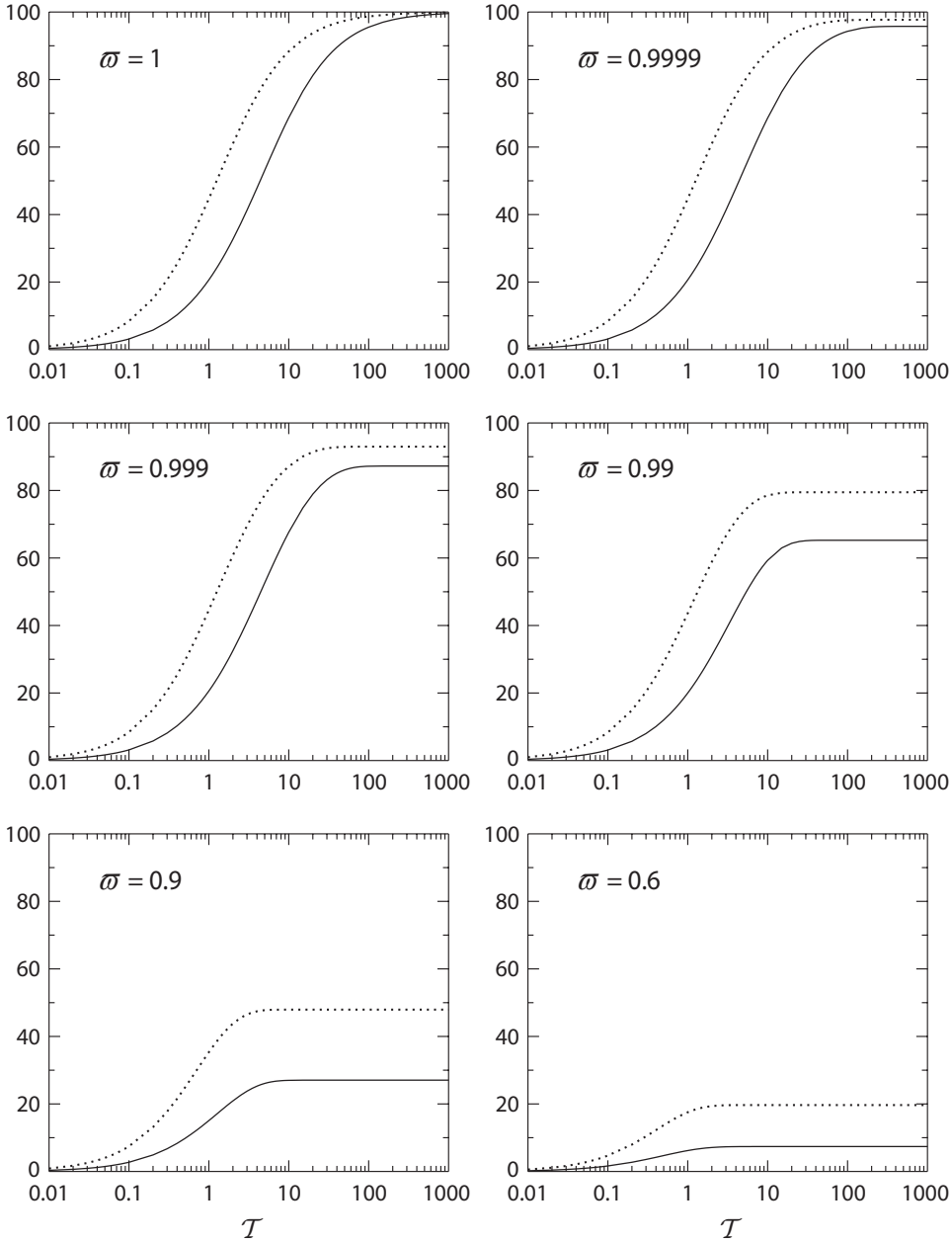

Fig. 20.6. Solid curves depict the spherical albedo (in percent) of a homogeneous slab composed of polydisperse spherical particles. Dotted curves show the results for Rayleigh-scattering slabs.

It is also seen that

$$\lim_{\mathcal{T} \to \infty} A_{\mathrm{S}}(\mathcal{T})\Big|_{\varpi = 1} = 1. \tag{20.27}$$

The above limit is an obvious manifestation of the energy conservation law: all light incident from above on a semi-infinite nonabsorbing scattering slab must eventually exit the slab through its only boundary.

The linear regime at small $\mathcal{T}$ is consistent with Eq. (20.25). The existence of the slow saturation regime for a slab composed of nonabsorbing particles is also easy to understand. Indeed, the particle phase function, Fig. 20.3, has a pronounced forward-scattering peak, which implies that ladder diagrams involving multiplications by forward-scattering phase matrices $\widetilde{\mathbf{Z}}(\hat{\mathbf{n}};\hat{\mathbf{n}}')$ with $\hat{\mathbf{n}} \approx \hat{\mathbf{n}}'$ carry a much larger contribution than those involving multiplications by side- and backscattering phase matrices. It is obvious that a sequence involving only near-forward-scattering phase matrices must consist of very many particles in order to contribute to the diffusely reflected specific intensity. Some of such sequences are so long and extend so deeply into the slab that they still contribute significantly to the diffusely transmitted light even for very large $\mathcal{T}$, thereby causing the spherical albedo to be smaller than one. Therefore, it takes exceedingly large optical thicknesses to prevent the loss of a few percent of the incident energy through the lower boundary of the slab.

The dotted curve in the upper left panel of Fig. 20.6 is computed for a Rayleigh-scattering slab and reveals spherical albedo values always exceeding those for optical-thickness-equivalent slabs populated by the micrometer-sized spherical particles. This overestimation is especially large at small optical thicknesses, where it exceeds a factor of two. The obvious reason for this overestimation is that the Rayleigh phase function, shown by the dotted curve in the upper left panel of Fig. 20.3, is nearly isotropic, lacks a forward-scattering peak, and has significantly larger side- and back-scattering values than the phase function shown by the solid curve. As a consequence, low-order sequences of Rayleigh particles provide a significantly stronger contribution to the reflected light than low-order sequences of forward-scattering micrometer-sized particles.

The presence of a lower boundary is not the only factor reducing the spherical albedo. Another factor is a nonzero m_{I} causing a single-scattering albedo value smaller than one. Although a non-zero m_{I} can also modify the elements of the normalized Stokes scattering matrix and, thus, the elements of the normalized phase matrix, it is instructive to examine the "pure" effect of absorption on RTT computations by simply varying the single-scattering albedo and keeping the normalized phase matrix fixed. The corresponding numerical results are shown in the remaining panels of Fig. 20.6. Not surprisingly, decreasing ϖ causes progressively reduced spherical albedo values. This effect is much more pronounced at larger optical thicknesses, where it causes an early saturation of A_{S} at values progressively smaller than unity. To explain this result, let us recall that the con-

tribution of an n-particle sequence to the reflected specific intensity is proportional to the nth power of the single-scattering albedo. Therefore, although optically thick slabs can accommodate very long sequences, the contribution of these sequences rapidly vanishes with growing n because the factor ϖ^n becomes negligibly small. It is in fact remarkable that as small a deviation of the single-scattering albedo from the value one as 0.0001 (see the top right-hand panel of Fig. 20.6) already causes the loss of several percent of the incident energy in a slab with infinite optical thickness. The effect of absorption on the spherical albedo is noticeably weaker for Rayleigh-scattering slabs, which can be explained by a larger contribution of low-order sequences to the reflected specific intensity and the fact that these sequences are less affected by absorption.

We have mentioned in Chapter 15 that a widespread practice in many applied science and engineering disciplines had been to replace the actual phase function by an asymmetry-parameter-equivalent Henyey–Greenstein (HG) phase function (15.116). Although not a solution of the MMEs, this "unphysical" phase function has several attractive properties discussed in Problem 15.14. Figure 20.7 compares Lorenz–Mie phase functions computed for two models of polydisperse spherical particles with their g-equivalent HG counterparts. For both models we assumed the gamma size distribution (15.108) with $r_{\min} = 0$, $r_{\max} = \infty$, an effective radius $r_{\text{eff}} = 10$ μm, and an effective variance $v_{\text{eff}} = 0.1$. The model 1 and 2 values of the relative refractive index were 1.55 + i0.001 and 1.55 + i0.004, respectively, whereas the incident wavelength was fixed at 0.63 μm. The corresponding values of the asymmetry parameter g were 0.838 and 0.901.

Plate 20.1 shows the angular distribution of the reflected specific intensity for a semi-infinite homogeneous slab composed of model 1 particles, as well as for

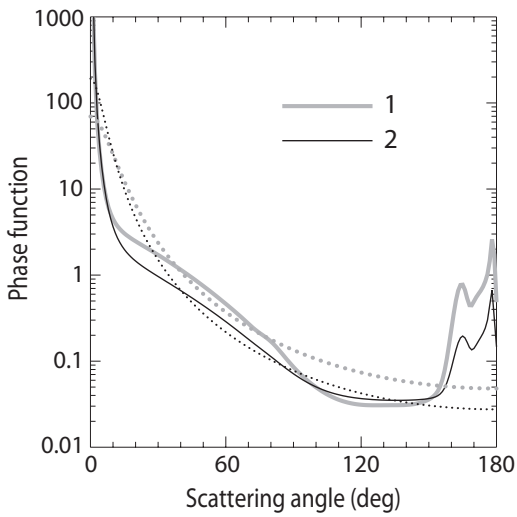

Fig. 20.7. Phase functions for model 1 and 2 polydisperse spherical particles (solid curves) and their HG counterparts (dotted curves).

its HG counterpart. Two obvious features of the reflected specific intensity distributions in the left-hand column are the backscattering enhancement caused by the glory and the primary rainbow in the Lorenz–Mie phase function (see the gray solid curve in Fig. 20.7) as well as the strong near-forward scattering for the cases of grazing and near-grazing incidence (μ_0 equal or close to zero). The reflectance patterns for the asymmetry-parameter-equivalent HG phase function lack the first feature, which is explained by the absence of backscattering phase function maxima. The right-hand column of Plate 20.1 shows that errors in the reflected specific intensity caused by the use of the approximate HG phase function can be very large and can, in fact, exceed a factor of 20 at backscattering geometries and a factor of 3 at near-forward-scattering geometries. These errors can be unequivocally attributed to the large phase-function differences in Fig. 20.7. Thus, Plate 20.1 makes a compelling case against the use of the HG phase function in directional reflectance computations, even for semi-infinite slabs.

The upper panel of Fig. 20.8 depicts the so-called plane albedo

$$A_{\mathrm{P}}(\mathcal{T}, \mu_0) = \frac{1}{\pi}\int_0^{2\pi} \mathrm{d}\varphi \int_0^1 \mathrm{d}\mu\, \mu\, R_{11}(\mathcal{T}; \mu, \varphi; \mu_0, \varphi_0) \tag{20.28}$$

as a function of μ_0 for two semi-infinite homogeneous slabs composed of the model 1 and 2 particles, respectively. In general, the plane albedo characterizes situations when a slab is illuminated by an unpolarized parallel beam of light, and is defined as the ratio of the radiant energy reflected by the slab per unit area of the upper boundary per unit time to the incident energy per unit area of the upper boundary per unit time (Sobolev 1975). Comparison of Eqs. (20.26) and (20.28) reveals a close connection between the spherical and plane albedos. Specifically,

$$A_{\mathrm{S}}(\mathcal{T}) = 2\int_0^1 \mathrm{d}\mu_0\, \mu_0\, A_{\mathrm{P}}(\mathcal{T}, \mu_0). \tag{20.29}$$

We also computed the plane albedo using the asymmetry-parameter-equivalent HG phase functions. The ratios of these approximate plane-albedo values to the respective exact ones are shown in the bottom panel of Fig. 20.8.

Not surprisingly, the plane albedos shown in the upper panel of Fig. 20.8 decrease with increasing m_{I} and, thus, with decreasing single-scattering albedo. The g-equivalent HG phase functions cause significant plane-albedo errors, especially for grazing illumination. The use of the HG phase functions overestimates $A_{\mathrm{P}}(\mathcal{T}, \mu_0)$ for small μ_0 and underestimates it for μ_0 close to unity, which is naturally explained by the angular pattern of the phase-function differences seen in Fig. 20.7. The plane-albedo errors increase significantly with increasing absorption. This trend is caused by the increasing relative contribution of the first-order ladder diagrams coupled with the large phase-function differences.

The respective spherical albedo ratios (0.99 for model 1 and 0.98 for model 2) are much closer to unity. This significantly better accuracy of the HG estimate

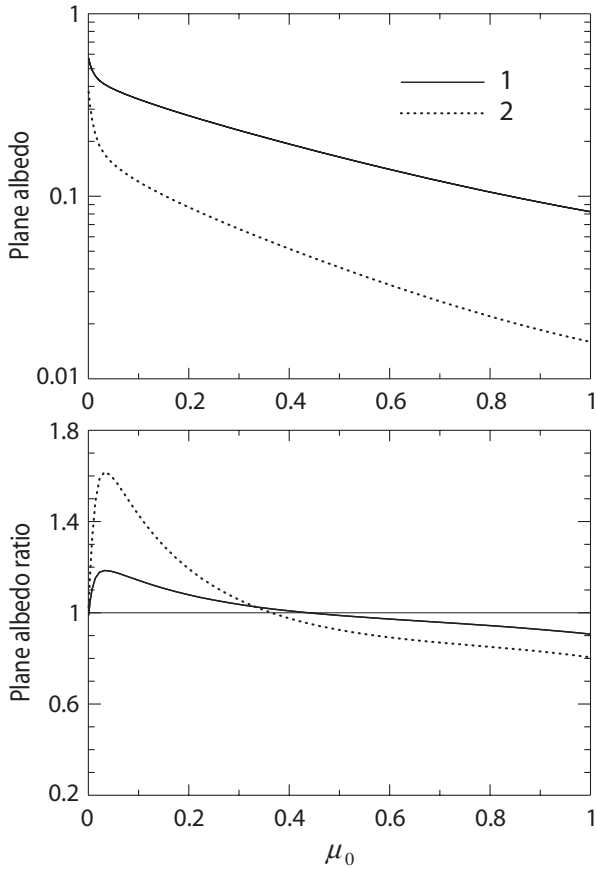

Fig. 20.8. Top panel: plane albedo versus μ_0 for two homogeneous semi-infinite slabs composed of model 1 and 2 spherical particles, respectively. Bottom panel: plane albedos computed for HG phase functions relative to their g-equivalent Lorenz–Mie counterparts.

of the spherical albedo can be explained in terms of cancellation of the plane-albedo errors upon integration over μ_0 in Eq. (20.29).

20.5 Polarization as an effect and as a characterization tool

The widespread use of the approximate scalar RTE has caused an equally widespread ignorance of an important scattering effect called polarization. This term refers to the situation when an initially unpolarized incident light becomes polarized upon scattering. This means that at least one of the elements of the specific intensity column vector other than the specific intensity acquires a nonzero value.

This effect is illustrated in Fig. 20.9, which parallels Fig. 20.4, but shows the absolute value of the second element of the specific intensity column vector of the reflected light. Owing to the particular illumination geometry and to the inci-

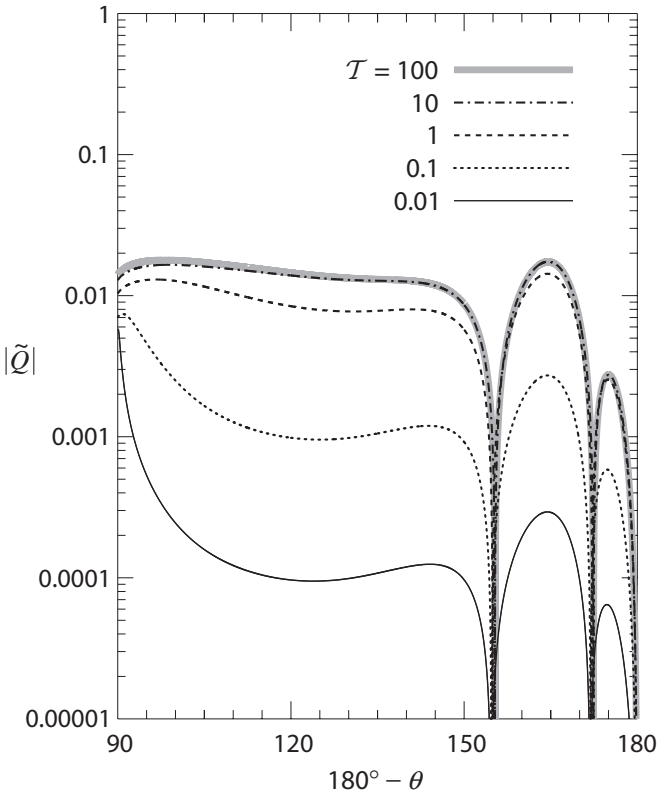

Fig. 20.9. As in Fig. 20.4, but for $|\widetilde{Q}(0, -\mu, \varphi)|$ (in $\mathrm{W\,m^{-2}\,sr^{-1}}$).

dent beam being unpolarized, the third and fourth elements of the specific intensity column vector are equal to zero, whereas the second one is independent of the azimuth angle of the reflection direction.

There are two striking differences between the results shown in Fig. 20.9 and in Fig. 20.4. First, the overall growth of $|\widetilde{Q}|$ as $\mathcal{T}$ increases from 0.01 to 100 is more than an order of magnitude smaller than that of $\widetilde{I}$. Second, the saturation of $|\widetilde{Q}|$ occurs at smaller values of the optical thickness than that of the specific intensity. In particular, the $|\widetilde{Q}|$ curves for $\mathcal{T} = 10$ and $\mathcal{T} = 100$ are hardly distinguishable, while the overall growth of $|\widetilde{Q}|$ as $\mathcal{T}$ increases from 1 to 100 is less than a factor of 2. These results suggest unequivocally that the main contribution to $\widetilde{Q}$ is carried by low-order Neumann terms in Eq. (20.23), the first-order term being the prime contributor, whereas the contribution of higher-order terms becomes largely unpolarized.

These conclusions are corroborated by Fig. 20.10 which shows the corresponding signed degree of linear polarization of the reflected light (cf. Eq. (9.40)). One can see indeed that the ratio $-\widetilde{Q}/\widetilde{I}$ for small $\mathcal{T}$ essentially replicates the ratio $-b_1/a_1$ of the elements of the normalized Stokes scattering matrix (see the

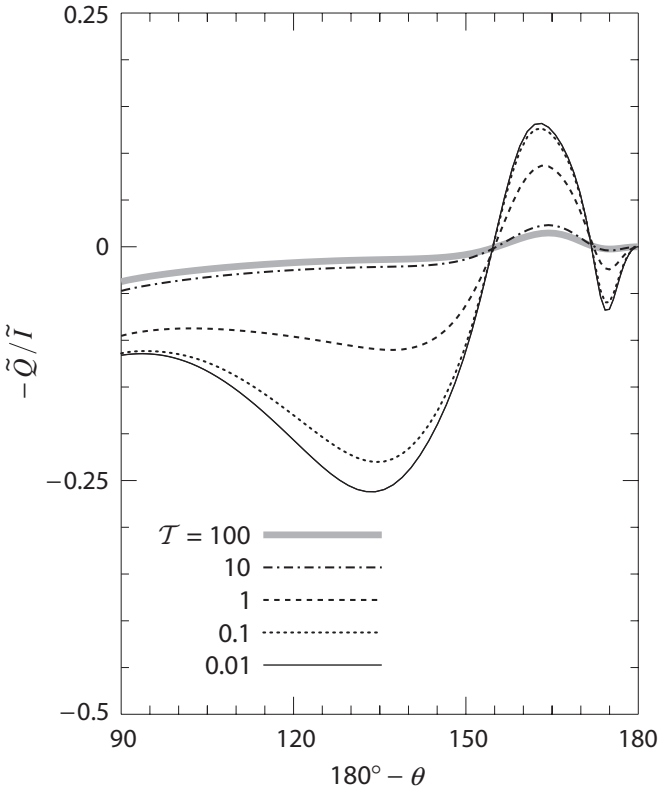

Fig. 20.10. As in Fig. 20.9, but for $-\widetilde{Q}(0, -\mu, \varphi)/\widetilde{I}(0, -\mu, \varphi)$.

bottom left-hand panel in Fig. 20.3), whereas the growth of $\mathcal{T}$ only serves to make the polarization more neutral.

Note that the deep spikes in the curves shown in Fig. 20.9 correspond to so-called inversion (or neutral) points of polarization, i.e., the scattering angles at which the signed degree of linear polarization switches sign. The remarkable constancy of both inversion angles with increasing $\mathcal{T}$ in Fig. 20.9 indicates too that the main contribution to the second element of the specific intensity column vector comes from the first-order Neumann term.

The majority of particle characterization techniques in disciplines such as terrestrial and planetary remote sensing, astrophysics, and biomedicine are based on intensity measurements. However, there are two major factors that can make polarimetry a much more sensitive particle characterization tool. First, the absolute accuracy of intensity measurements is typically of order $0.05I$ and can become significantly worse for weak signals, whereas the absolute accuracy of measurements of the ratios Q/I, U/I, and V/I can be as good as 0.001 and sometimes is much better (see, e.g., Table 1.3 of Tinbergen (1996), which lists the best accuracies obtained in various types of astrophysical polarimetric observations). Ow-

ing to the Stokes–Verdet inequality, these ratios can vary between –1 and +1. However, the 0.001 absolute accuracy makes informative even data spanning a significantly narrower range, as, for example, in Fig. 20.10. Second, a major contribution to $\widetilde{Q}$ and $\widetilde{U}$ comes from the first-order Neumann term, which causes these quantities to preserve more information content of the Stokes scattering matrix than the specific intensity. Furthermore, the degree of the "first-order" polarization given by $-b_1(\Theta)/a_1(\Theta)$ exhibits a much stronger variability with particle size, shape, and relative refractive index than the phase function $a_1(\Theta)$, which makes the former a more sensitive indicator of particle microphysical characteristics (see Chapters 9 and 10 of MTL1 and references therein).

Problems

20.1: Derive Eqs. (20.4) and (20.5).

20.2: Show that Eqs. (20.10)–(20.12) give the solution of the boundary-value problem specified by Eqs. (20.7) and (20.9).

20.3: Show that Eqs. (20.11) and (20.12) represent the specific version of the integral RTE (19.83) applicable to a plane-parallel particulate slab.

20.4: Verify that in the case of a plane-parallel particulate layer, the left-hand sides of Eqs. (19.104) and (19.106) are independent of the distance from the upper or lower boundary of the medium.

20.5: Derive explicit analytical expressions for the first-order terms in the Neumann expansions of the reflection and transmission matrices of a homogeneous plane-parallel particulate medium.

20.6: Derive Eq. (20.25) from the RTE (20.7). Show that the result is consistent with taking the limit $\mathcal{T} \to 0$ in Eq. (H.63).

Notes and further reading

Diverse applications of the RTT in atmospheric radiation and terrestrial remote sensing are discussed in the textbooks and monographs by Goody and Yung (1989), Liou (1992, 2002), Lenoble (1993), Stephens (1994), Yanovitskij (1997), Thomas and Stamnes (1999), Zdunkowski *et al.* (2007), and Wendisch and Yang (2012). The subject of ocean optics is covered in the books by Shifrin (1988), Mobley (1994), and Spinrad *et al.* (1994). Planetary remote sensing and various applications of the RTT in astrophysics are described in Dolginov *et al.* (1995), Hanel *et al.* (2003), Videen *et al.* (2004), and Mishchenko *et al.* (2010, 2011a). Applications in biomedicine and engineering are discussed thoroughly in the monographs by Tuchin (2002, 2007), Tuchin *et al.* (2006), Howell *et al.* (2011), and Modest (2013). Marshak and Davis (2005) and Davis and Marshak (2010)

reviewed the application of the RTT to particulate media other than plane-parallel slabs.

The word "photon" is frequently used in descriptions of the Monte Carlo solution of the integral RTT (20.10)–(20.12) (e.g., Welch and van Gemert 2011). It is imperative to recognize, however, that the RTT is derived from classical Maxwell's electromagnetics and as such does not involve quantization of the electromagnetic field. Therefore, the imaginary "Monte Carlo photons" have nothing to do with the real QED photons. The following quote from Wiscombe (2005, p. 36) is quite instructive:

> Monte Carlo is just a way of solving the integral form of the radiative transfer equation. At root… Monte Carlo has nothing to do with "photons" propagating from one "point scatter" to the next; these are merely convenient (but potentially misleading) fictions for algorithmically calculating the Monte Carlo solution. Expressing the radiative transfer equation with scattering in integral form leads to a sum of integrals of increasing dimensionality, corresponding to higher and higher numbers of scatters (sometimes called the Neumann series). There are no good quadrature methods for such N-dimensional integrals except Monte Carlo and, for small N, a generalization of Trapezoidal Rule… All the elegant Gaussian quadrature methods for one-dimensional integrals are useless for N-dimensional integrals. So… "[Monte Carlo] photons" are merely drunken census takers, careening around the medium to get a decent-enough sample to do the N-dimensional integrals.

Similarly, it is incorrect to characterize the Monte Carlo solution of the integral RTT as beam or ray tracing.

21

Weak localization

The main advantage of the microphysical approach to radiative transfer is that it establishes a direct link between the MMEs and the RTE via a sequence of nine unambiguously defined and physically realizable assumptions and approximations summarized in Section 19.13. By keeping assumptions 1, 2, and 4–8 from Section 19.13, but relaxing approximations 3 and 9, one can extend the microphysical approach and establish a similar direct link between the MMEs and the effect of WL of electromagnetic waves by a sparse DRM. Specifically, one can supplement the computation of the ladder component of the dyadic correlation function with the computation of the so-called "cyclical" component. The latter is caused by pairs of multi-particle sequences exemplified by Plates 18.1e and 18.1h. As we have seen in Section 18.4, the sum of the ladder and cyclical components can be expected to provide a better representation of optical observables at certain points located in the far zone of the particulate medium.

It is important to recognize that WL is not an independent physical phenomenon. It is implicitly contained in the exact solution of the MMEs (Section 18.4) but "falls through the cracks" when one resorts to the ladder approximation in order to simplify the computation. Therefore, one may characterize WL as the difference between the exact solution of the MMEs for a sparse DRM and the ladder approximation, although this characterization may still not be fully accurate since it neglects the existence of multi-particle sequences that go through a particle more than once.

Given the complexity of the subject, this chapter provides only a brief introduction to the theory of WL and a few numerical examples. Further details and references can be found in Chapter 14 of MTL2.

21.1 Weak localization by a sparse discrete random medium

Consider again a scattering object in the form of a large group of discrete, randomly and sparsely distributed particles, as shown schematically in Fig. 21.1.

Fig. 21.1. Scattering of a plane electromagnetic wave by a volume of discrete random medium populated by sparsely distributed particles. The size of the particulate volume is exaggerated relative to its distance from observation point 3 for demonstration purposes.

The object is illuminated by a plane electromagnetic wave. The reader should recall that the final formulas of the RTT have been derived by neglecting all diagrams with crossing connectors in the diagrammatic representation of the dyadic correlation function. Following the line of reasoning outlined in Section 19.13, one may indeed conclude that upon statistical averaging, the contribution to the total PST of all the diagrams of the type illustrated in Fig. 21.2 must vanish at near-field observation points located either inside (observation point 1) or outside (observation point 2) the object.

However, we have already discussed in Section 19.13 that there is an exception corresponding to the situation when the observation point is in the far zone of the entire particulate volume and resides within its "back-shadow" (observation point 3 in Fig. 21.1). Then the class of diagrams illustrated by Plates 18.1e and 18.1h and Figs. 21.2c–21.2e gives a nonzero contribution that causes the

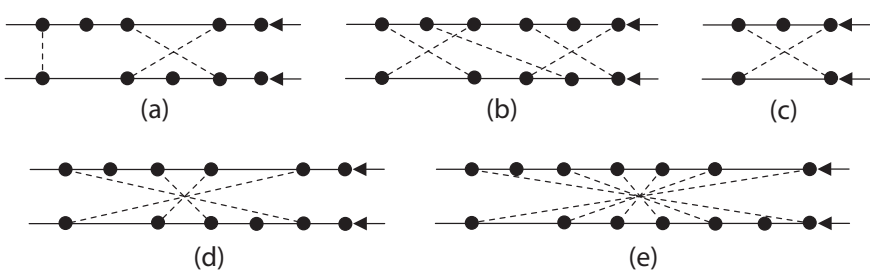

Fig. 21.2. Diagrams with crossing connectors.

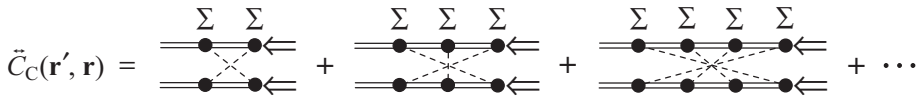

Fig. 21.3. The cyclical part of the far-field dyadic correlation function.

WL effect. These diagrams were called by Barabanenkov (1973) cyclical or maximally crossed, since they can be drawn in such a way that all connectors cross at one point.

The expression for the cumulative contribution of all cyclical diagrams to the far-field dyadic correlation function, $\ddot{C}_{\mathrm{C}}(\mathbf{r}', \mathbf{r})$, can be derived using the diagrammatic technique introduced in Chapter 19. The final result can be summarized by the diagrammatic expression shown in Fig. 21.3. As before, the symbol Σ denotes both the summation over all appropriate particles and the statistical averaging over the particle states and positions, whereas the double lines account for the effect of exponential attenuation and, possibly, dichroism. It is very instructive to compare Fig. 21.3 with Fig. 19.15, since this comparison reveals quite vividly the morphological difference between the participating diagrams. The total far-field dyadic correlation function is now approximated by the following expression:

$$\langle \ddot{C}(\mathbf{r}', \mathbf{r}) \rangle_{\mathbf{R},\xi} \approx \ddot{C}_{\mathrm{L}}(\mathbf{r}', \mathbf{r}) + \ddot{C}_{\mathrm{C}}(\mathbf{r}', \mathbf{r}), \tag{21.1}$$

where, as before, the ladder component $\ddot{C}_{\mathrm{L}}(\mathbf{r}', \mathbf{r})$ is given by the right-hand side of the equation shown in Fig. 19.15. Accordingly,

$$\langle\langle \ddot{P}(\mathbf{r}) \rangle\rangle = \langle \ddot{P}(\mathbf{r}) \rangle_{\mathbf{R},\xi} \approx \langle \ddot{P}_{\mathrm{L}}(\mathbf{r}) \rangle_{\mathbf{R},\xi} + \langle \ddot{P}_{\mathrm{C}}(\mathbf{r}) \rangle_{\mathbf{R},\xi}, \tag{21.2}$$

where $\langle \ddot{P}_{\mathrm{L}}(\mathbf{r}) \rangle_{\mathbf{R},\xi}$ and $\langle \ddot{P}_{\mathrm{C}}(\mathbf{r}) \rangle_{\mathbf{R},\xi}$ are the ladder and cyclical components, respectively, of the total time-averaged PST at the far-field observation point $\mathbf{r}$. The ladder component is given by an appropriate modification of Eq. (19.69).

The inclusion of the cyclical diagrams makes the computation of the total PST much more involved and limits the range of problems that can be solved accurately. In particular, no closed-form analytical equation similar to the RTE (19.62) has been derived for the computation of $\langle \ddot{P}_{\mathrm{C}}(\mathbf{r}) \rangle_{\mathbf{R},\xi}$. As a consequence, the cyclical component is often computed using the brute-force Monte Carlo summation of the cyclical diagrams (e.g., Muinonen 2004; Muinonen *et al.* 2012).

It follows from Eq. (18.6) that the range of scattering directions affected by WL is inversely proportional to $k_1 \langle l \rangle$, where $\langle l \rangle$ is the average distance between the end particles of the various multi-particle sequences such as those shown in Plates 18.1e and 18.1h. Factors limiting $\langle l \rangle$ and thereby increasing the angular width of various manifestations of WL are absorption by particles and a finite size of the scattering medium. The finite-size effect is well illustrated by Plate 18.3d which reveals that the angular widths of the backscattering WL maxima decrease as the size parameter $k_1 R$ of the particulate volume increases. For an

optically thick, plane-parallel, nonabsorbing DRM, a good proxy for $\langle l \rangle$ is the so-called transport mean free path given by

$$l_{\rm tr} = \frac{1}{n_0 \langle C_{\rm ext} \rangle_\xi (1-g)} \tag{21.3}$$

(Ishimaru 1978).

The interference origin of WL implies that in the case of plane-wave illumination, the observer must be located in the far zone of the entire scattering medium. In reality, various manifestations of WL can be observed at distances much shorter than those dictated by Eq. (5.14). Specifically, the distance D from the particulate medium to the observation point must satisfy the following inequality (Problem 21.1):

$$D \gg \frac{1}{2} k_1 \langle l \rangle^2. \tag{21.4}$$

This requirement ensures that the observation point is in the far zones of the majority of individual multi-particle sequences contributing significantly to the right-hand side of the Neumann expansion (6.48). However, the inequality (21.4) can still be rather demanding if the scattering medium is composed of sparsely distributed, nonabsorbing, wavelength-sized or larger particles with asymmetry parameters approaching the value one and if the minimal dimension of the medium is comparable to or greater than $l_{\rm tr}$.

The transport mean free path for sparsely populated objects such as liquid-water clouds is many orders of magnitude greater than the wavelength. Therefore, the angular width of various WL features for such particulate media can be expected to be extremely small, thus making them hardly observable with passive instruments measuring the scattered sunlight. However, WL can affect the results of active observations of clouds with lidars and radars designed to observe electromagnetic radiation scattered in exactly the backscattering direction (e.g., Kobayashi *et al.* 2007).

The situation is different for densely packed particulate media, in which case $l_{\rm tr}$ can be comparable to the wavelength of the incident wave. As a consequence, WL can be detectable not only with active instruments or specially designed laboratory equipment (e.g., Gross *et al.* 2007; Psarev *et al*. 2007), but even in telescopic observations of sunlight scattered by particulate surfaces of high-albedo solar system bodies (see, e.g., Mishchenko *et al.* (2010), Rosenbush and Mishchenko (2011), and references therein).

Monostatic radars use the same antenna to transmit and receive electromagnetic waves. Therefore, radar observations of particulate surfaces are inevitably affected by WL. Several solar system objects have been found to generate radar returns quite uncharacteristic of bare solid surfaces. For example, the icy Galilean satellites of Jupiter exhibit both strong radar reflectivities and $\delta_{\rm C}$ values exceeding one (Ostro 1993). Similar radar echoes have been detected in observations of the poles of Mercury (Harmon *et al.* 1994). These measurements have

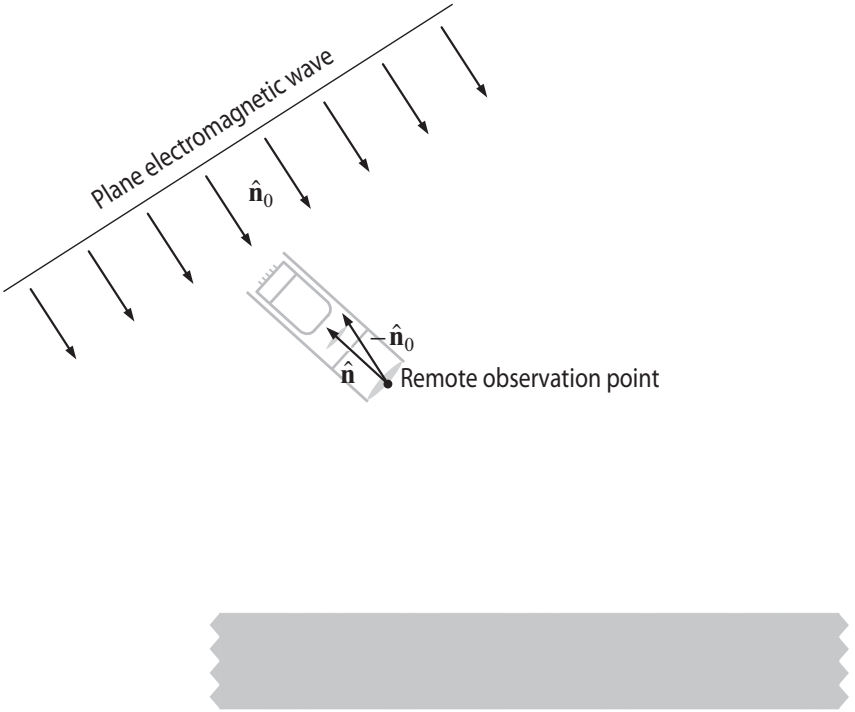

Fig. 21.4. Electromagnetic scattering by a plane-parallel sparse DRM of infinite lateral extent.

been interpreted in terms of electromagnetic scattering by voids and/or rocks imbedded in a transparent layer of ice (Hapke 1990; Mishchenko 1992a).

Although it is straightforward to derive a general analytical expression for the cyclical dyadic correlation function supplementing Eq. (19.57), the use of this expression in practical computations, either analytical or numerical, still remains highly problematic. Nevertheless, there are two rigorous particular solutions of the problem that have already found extensive applications. The aim of the following section is to briefly discuss these solutions and their consequences.

21.2 Weak localization by a plane-parallel discrete random medium

Being a far-field phenomenon, WL should ideally be observed with a WCR located in the far zone of the entire scattering medium (Chapter 18). Since in the majority of practical situations this is virtually impossible, in what follows we will assume that a WCR is located in the near zone of the particulate volume yet far enough to satisfy the inequality (21.4).

Consider the scattering of a plane electromagnetic wave $\mathbf{E}_0^{\rm inc}\exp(\mathrm{i}k_1\hat{\mathbf{n}}_0\cdot\mathbf{r})$ by a plane-parallel layer of sparse DRM populated by ISRPs (Fig. 21.4). A remote WCR scans a range of upward directions $\hat{\mathbf{n}}$, including the exact backscattering

direction given by $\hat{\mathbf{n}} = -\hat{\mathbf{n}}_0$. Since the scattering slab is assumed to have infinite lateral extent, the reading of the WCR is independent of the distance to the upper boundary of the slab, as long as it satisfies the inequality (21.4).

It follows from Eq. (19.106) that in the absence of WL, the polarized reading of the WCR would be given by the product $\Delta\Omega S_{\rm ep}\widetilde{\mathbf{I}}_{\rm d}(0,\hat{\mathbf{n}})$, where, as before, $\Delta\Omega$ is the acceptance solid angle of the WCR and $S_{\rm ep}$ is the area of its entrance pupil, while $\widetilde{\mathbf{I}}_{\rm d}(0,\hat{\mathbf{n}})$ is the diffuse specific intensity column vector at the upper boundary of the slab expressed in terms of the RTT reflection matrix $\mathbf{R}$, according to Eq. (20.15). To take account of WL, the polarized signal recorded by the WCR must be written as $\Delta\Omega S_{\rm ep}\widetilde{\boldsymbol{\mathcal{I}}}(\hat{\mathbf{n}})$, where the four-element specific intensity column vector $\widetilde{\boldsymbol{\mathcal{I}}}(\hat{\mathbf{n}})$ is the sum of the ladder (diffuse) and cyclical components:

$$\widetilde{\boldsymbol{\mathcal{I}}}(\hat{\mathbf{n}}) = [\widetilde{\mathcal{I}}(\hat{\mathbf{n}}),\widetilde{\mathcal{Q}}(\hat{\mathbf{n}}),\widetilde{\mathcal{U}}(\hat{\mathbf{n}}),\widetilde{\mathcal{V}}(\hat{\mathbf{n}})]^{\rm T} = \widetilde{\boldsymbol{\mathcal{I}}}^{\rm L}(\hat{\mathbf{n}}) + \widetilde{\boldsymbol{\mathcal{I}}}^{\rm C}(\hat{\mathbf{n}}) \equiv \widetilde{\mathbf{I}}_{\rm d}(0,\hat{\mathbf{n}}) + \widetilde{\boldsymbol{\mathcal{I}}}^{\rm C}(\hat{\mathbf{n}}). \quad (21.5)$$

By analogy with Eq. (20.15),

$$\widetilde{\boldsymbol{\mathcal{I}}}(\hat{\mathbf{n}}) = \frac{1}{\pi}\mu_0\boldsymbol{\mathcal{R}}(\hat{\mathbf{n}},\hat{\mathbf{n}}_0)\mathbf{I}_0, \quad (21.6)$$

where the "full" 4×4 reflection matrix $\boldsymbol{\mathcal{R}}$ is also given by the sum of the ladder (RTT) and cyclical components:

$$\boldsymbol{\mathcal{R}}(\hat{\mathbf{n}},\hat{\mathbf{n}}_0) = \boldsymbol{\mathcal{R}}^{\rm L}(\hat{\mathbf{n}},\hat{\mathbf{n}}_0) + \boldsymbol{\mathcal{R}}^{\rm C}(\hat{\mathbf{n}},\hat{\mathbf{n}}_0) \equiv \mathbf{R}(\hat{\mathbf{n}},\hat{\mathbf{n}}_0) + \boldsymbol{\mathcal{R}}^{\rm C}(\hat{\mathbf{n}},\hat{\mathbf{n}}_0). \quad (21.7)$$

In accordance with the previous discussion of WL, it is useful to consider the following three scenarios:

1. The direction $\hat{\mathbf{n}}$ is relatively far from the exact backscattering direction $-\hat{\mathbf{n}}_0$. Then the cyclical component of the full specific intensity column vector $\widetilde{\boldsymbol{\mathcal{I}}}(\hat{\mathbf{n}})$ vanishes, and the response of the WCR is fully defined by the slowly changing ladder component (Fig. 21.5):

$$\widetilde{\boldsymbol{\mathcal{I}}}(\hat{\mathbf{n}}) \approx \widetilde{\boldsymbol{\mathcal{I}}}^{\rm L}(\hat{\mathbf{n}}) \equiv \widetilde{\mathbf{I}}_{\rm d}(0,\hat{\mathbf{n}}) \approx \widetilde{\mathbf{I}}_{\rm d}(0,-\hat{\mathbf{n}}_0). \quad (21.8)$$

This implies that the response of the polarization-sensitive WCR can be quantified in terms of the ladder reflection matrix $\boldsymbol{\mathcal{R}}^{\rm L}(\hat{\mathbf{n}},\hat{\mathbf{n}}_0)$ obtained by solving the RTE with one of the available numerically exact computer techniques mentioned in Chapter 20:

$$\boldsymbol{\mathcal{R}}(\hat{\mathbf{n}},\hat{\mathbf{n}}_0) \approx \boldsymbol{\mathcal{R}}^{\rm L}(\hat{\mathbf{n}},\hat{\mathbf{n}}_0) \equiv \mathbf{R}(\hat{\mathbf{n}},\hat{\mathbf{n}}_0) \approx \mathbf{R}(-\hat{\mathbf{n}}_0,\hat{\mathbf{n}}_0). \quad (21.9)$$

2. The WCR is aligned along the exact backscattering direction. Then the effects of WL can be expected to be maximal and must be taken into account by computing the respective full reflection matrix $\boldsymbol{\mathcal{R}}(-\hat{\mathbf{n}}_0,\hat{\mathbf{n}}_0)$ and the full column vector $\widetilde{\boldsymbol{\mathcal{I}}}(-\hat{\mathbf{n}}_0)$ (see Fig. 21.5). We will explain in Section 21.2.1 that, somewhat unexpectedly, this can also be done in terms of the solution of the standard RTE.

3. As the axis of the WCR deviates more and more from the exact backscattering direction, the effects of WL can be expected to weaken and gradually

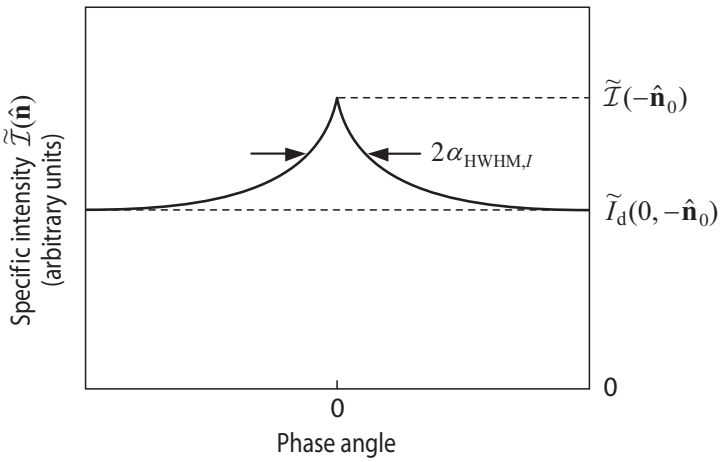

Fig. 21.5. Backscattering enhancement caused by weak localization. The phase angle is defined as the angle between the unit vectors $\hat{\mathbf{n}}$ and $-\hat{\mathbf{n}}_0$.

disappear (see Fig. 21.5). The quantification of the angular profile of the WCR response in this transition region of scattering directions requites the knowledge of the full specific intensity column vector $\widetilde{\boldsymbol{\mathcal{I}}}(\hat{\mathbf{n}})$ and thus the full reflection matrix $\boldsymbol{\mathcal{R}}(\hat{\mathbf{n}}, \hat{\mathbf{n}}_0)$. The calculation of $\boldsymbol{\mathcal{R}}(\hat{\mathbf{n}}, \hat{\mathbf{n}}_0)$ is a very complex problem that has been solved analytically only in a few particular cases. We will discuss the consequences of one such solution in Section 21.2.2.

21.2.1 Exact backscattering direction

Let us expand the ladder component of the reflection matrix into the first-order (superscript 1) and cumulative higher-order (or "multiple-order," superscript M) contributions:

$$\boldsymbol{\mathcal{R}}(\hat{\mathbf{n}}, \hat{\mathbf{n}}_0) = \mathbf{R}^{1}(\hat{\mathbf{n}}, \hat{\mathbf{n}}_0) + \mathbf{R}^{\mathrm{M}}(\hat{\mathbf{n}}, \hat{\mathbf{n}}_0) + \boldsymbol{\mathcal{R}}^{\mathrm{C}}(\hat{\mathbf{n}}, \hat{\mathbf{n}}_0). \tag{21.10}$$

The first-order component $\mathbf{R}^{1}(\hat{\mathbf{n}}, \hat{\mathbf{n}}_0)$ is given by Eq. (H.63), while $\mathbf{R}^{\mathrm{M}}(\hat{\mathbf{n}}, \hat{\mathbf{n}}_0)$ is obtained by subtracting $\mathbf{R}^{1}(\hat{\mathbf{n}}, \hat{\mathbf{n}}_0)$ from $\mathbf{R}(\hat{\mathbf{n}}, \hat{\mathbf{n}}_0)$ after the latter has been calculated by solving the RTE. Analogously,

$$\widetilde{\boldsymbol{\mathcal{I}}}(\hat{\mathbf{n}}) = \widetilde{\mathbf{I}}^{1}(0, \hat{\mathbf{n}}) + \widetilde{\mathbf{I}}^{\mathrm{M}}(0, \hat{\mathbf{n}}) + \widetilde{\boldsymbol{\mathcal{I}}}^{\mathrm{C}}(\hat{\mathbf{n}}), \tag{21.11}$$

where

$$\widetilde{\mathbf{I}}^{1}(0, \hat{\mathbf{n}}) + \widetilde{\mathbf{I}}^{\mathrm{M}}(0, \hat{\mathbf{n}}) = \widetilde{\mathbf{I}}_{\mathrm{d}}(0, \hat{\mathbf{n}}). \tag{21.12}$$

One of the few rigorous results of the analytical theory of WL has been derived by applying the Saxon's reciprocity relation for the scattering dyadic (5.30) to the expressions for the ladder and cyclical components of the specific coherency dyadic corresponding to the case of the exact backscattering direction (see

Section 14.3 of MTL2 for details). The final result is a remarkably simple relation between the corresponding matrices $\mathbf{R}^{\mathrm{M}}(-\hat{\mathbf{n}}_0, \hat{\mathbf{n}}_0)$ and $\boldsymbol{\mathcal{R}}^{\mathrm{C}}(-\hat{\mathbf{n}}_0, \hat{\mathbf{n}}_0)$ (Mishchenko 1992b):

$$\boldsymbol{\mathcal{R}}^{\mathrm{C}} = \begin{bmatrix} \mathcal{R}_{11}^{\mathrm{C}} & R_{12}^{\mathrm{M}} & 0 & 0 \\ R_{12}^{\mathrm{M}} & \mathcal{R}_{22}^{\mathrm{C}} & 0 & 0 \\ 0 & 0 & \mathcal{R}_{33}^{\mathrm{C}} & R_{34}^{\mathrm{M}} \\ 0 & 0 & -R_{34}^{\mathrm{M}} & \mathcal{R}_{44}^{\mathrm{C}} \end{bmatrix}, \tag{21.13}$$

where

$$\mathcal{R}_{11}^{\mathrm{C}} = \frac{1}{2}[R_{11}^{\mathrm{M}} + R_{22}^{\mathrm{M}} - R_{33}^{\mathrm{M}} + R_{44}^{\mathrm{M}}], \tag{21.14}$$

$$\mathcal{R}_{22}^{\mathrm{C}} = \frac{1}{2}[R_{11}^{\mathrm{M}} + R_{22}^{\mathrm{M}} + R_{33}^{\mathrm{M}} - R_{44}^{\mathrm{M}}], \tag{21.15}$$

$$\mathcal{R}_{33}^{\mathrm{C}} = \frac{1}{2}[-R_{11}^{\mathrm{M}} + R_{22}^{\mathrm{M}} + R_{33}^{\mathrm{M}} + R_{44}^{\mathrm{M}}], \tag{21.16}$$

$$\mathcal{R}_{44}^{\mathrm{C}} = \frac{1}{2}[R_{11}^{\mathrm{M}} - R_{22}^{\mathrm{M}} + R_{33}^{\mathrm{M}} + R_{44}^{\mathrm{M}}]. \tag{21.17}$$

The arguments $(-\hat{\mathbf{n}}_0, \hat{\mathbf{n}}_0)$ in Eqs. (21.13)–(21.17) are omitted for the sake of compactness. The importance of this rigorous result is hard to overstate. Indeed, it demonstrates that although the RTT is based on the neglect of all cyclical diagrams, all observable characteristics of WL at the *exact backscattering direction* can still be calculated by solving the RTE. Furthermore, this can be done by characterizing the scattering medium in terms of actual physical parameters, such as the optical thickness of the slab and the size, shape, and refractive index of the constituent particles. Equations (21.13)–(21.17) apply to quasi-monochromatic as well as to monochromatic scattering.

Let us consider one instructive application of Eqs. (21.10) and (21.13). In the case of an unpolarized quasi-monochromatic incident beam the specific intensity of light reflected in exactly the backscattering direction is given by

$$\widetilde{\mathcal{I}}(-\hat{\mathbf{n}}_0) = \frac{1}{\pi}\mu_0 \mathcal{R}_{11}(-\hat{\mathbf{n}}_0, \hat{\mathbf{n}}_0) I_0,$$

where I_0 is the intensity of the incident beam. On the other hand, the diffuse background is given by

$$\widetilde{I}_{\mathrm{d}}(0, -\hat{\mathbf{n}}_0) = \frac{1}{\pi}\mu_0[R_{11}^{1}(-\hat{\mathbf{n}}_0, \hat{\mathbf{n}}_0) + R_{11}^{\mathrm{M}}(-\hat{\mathbf{n}}_0, \hat{\mathbf{n}}_0)] I_0$$

(see Fig. 21.5). Therefore, we can define the corresponding WL enhancement factor as

$$\zeta_I(\hat{\mathbf{n}}_0) = \frac{\widetilde{\mathcal{I}}(-\hat{\mathbf{n}}_0)}{\widetilde{I}_{\mathrm{d}}(0, -\hat{\mathbf{n}}_0)} = 1 + \frac{R_{11}^{\mathrm{M}} + R_{22}^{\mathrm{M}} - R_{33}^{\mathrm{M}} + R_{44}^{\mathrm{M}}}{2(R_{11}^{1} + R_{11}^{\mathrm{M}})}, \tag{21.18}$$

where the angular arguments $(-\hat{\mathbf{n}}_0, \hat{\mathbf{n}}_0)$ on the right-hand side are again omitted for brevity. We have already mentioned that the enhancement factor is a quantity that can be measured for particle suspensions and particulate surfaces using specialized laboratory equipment, as well as for atmosphereless solar-system objects using ground-based or spaceborne telescopes. As such, ζ_I may be useful in retrieving macro- and microphysical characteristics of various particulate media.

Plate 21.1 shows the results of numerically exact computer calculations of ζ_I for a homogeneous semi-infinite layer populated by polydisperse spherical particles. The enhancement factor is depicted as a function of the particle effective size parameter $x_{\text{eff}} = k_1 r_{\text{eff}}$ and μ_0 for several values of the real and imaginary parts of the relative refractive index. The particle size distribution is given by the gamma law (15.108) with $r_{\min} = 0$, $r_{\max} = \infty$, and a fixed effective variance $v_{\text{eff}} = 0.1$. The reflection matrix $\mathbf{R}(\hat{\mathbf{n}}, \hat{\mathbf{n}}_0)$ was found by solving numerically the Ambartsumian nonlinear integral equation (see Section 12.4 of MTL2).

Plate 21.1 reveals a surprisingly complex dependence of the enhancement factor on the particle microphysical properties. For example, we have seen in Section 20.4 that increasing absorption can be expected to suppress higher-order terms in the ladder expansion of the reflection matrix $\mathbf{R}(\hat{\mathbf{n}}, \hat{\mathbf{n}}_0)$ and thus reduce the enhancement factor. Yet ζ_I can be seen to grow as the imaginary part of the relative refractive index increases and can reach maximal values for moderately absorbing particles. A more detailed discussion of these computational results, as well as of other analytical and numerical implications of Eqs. (21.10) and (21.13) can be found in Sections 14.5 and 14.6 of MTL2.

Similarly to the scalar version of the RTT discussed in Section 20.3, the scalar treatment of WL is based on the assumption that all elements of the reflection matrix $\mathcal{R}(\hat{\mathbf{n}}, \hat{\mathbf{n}}_0)$ other than the $(1,1)$ element can be ignored if the incident light is unpolarized and one is interested in the computation of only the specific intensity $\widetilde{\mathcal{I}}(\hat{\mathbf{n}})$. It is important to emphasize, however, that the rigorous formula (21.18) derived for the case of unpolarized incident light involves all the diagonal elements of the matrix $\mathbf{R}^{\mathrm{M}}(\hat{\mathbf{n}}_0, \hat{\mathbf{n}}_0)$ rather than only its $(1,1)$ element. One may therefore expect substantial differences between numerical predictions of the enhancement factor ζ_I based on the scalar approximation and the corresponding exact results.

Plate 21.2 (adapted from Mishchenko and Dlugach (2008)) complements Plate 21.1 by showing the percentage error of the scalar approximation in the enhancement factor defined as

$$\delta_\zeta = \frac{|\zeta_I - \zeta|}{\zeta_I} \times 100\%, \tag{21.19}$$

where ζ is the "scalar" analog of ζ_I. It is seen indeed that the errors of the scalar approximation in the WL enhancement factor can often exceed 20%. The errors are especially large for nonabsorbing particles (the left-hand column of Plate 21.2) and can reach 25%. In the limit $\mu_0 \to 0$, both ζ_I and ζ tend to unity,

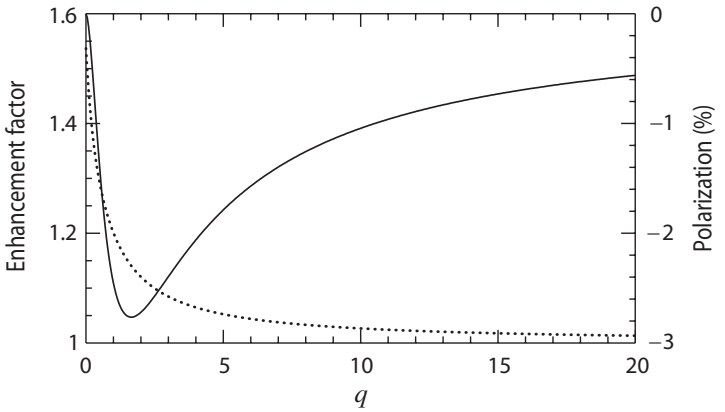

Fig. 21.6. Angular profiles of the enhancement factor (dotted curve) and the degree of linear polarization for unpolarized incident light (solid curve).

thereby resulting in smaller δ_ζ. Large nonabsorbing spherical particles with $m_{\mathrm{R}} = 1.8$ and 2 develop a strong backscattering peak in the phase function. As a consequence, R_{11}^{1} strongly increases (see Eq. (H.63)), whereas ζ_I, ζ, and δ_ζ decrease.

It is obvious that the percentage errors δ_ζ in the WL enhancement factor ζ_I corresponding to the case of unpolarized incident light can be so large that one should exercise extreme caution when using the scalar approximation. Perhaps it would be wise to avoid the use of this approximation altogether.

21.2.2 Angular dependence of weak localization: Rayleigh scattering

In this section we use an exact solution of the WL problem obtained by Amic *et al.* (1997) in order to illustrate the angular distribution of the reflected intensity and polarization in the vicinity of the exact backscattering direction. Specifically, let us assume that a homogeneous semi-infinite slab is populated by nonabsorbing particles with sizes much smaller than the wavelength. The slab is illuminated by an unpolarized quasi-monochromatic beam incident perpendicularly to the slab boundary.

Figure 21.6 depicts the corresponding enhancement factor $\zeta_I(q)$ as a function of the dimensionless so-called angular parameter $q = k_1 l_{\mathrm{tr}} \alpha$, where α is the phase angle. The dotted curve exhibits a typical WL peak centered at exactly the backscattering direction. The amplitude of the peak is $\zeta_I(0) \approx 1.537$ and its half-width at half-maximum is $q_{\mathrm{HWHM},I} = k_1 l_{\mathrm{tr}} \alpha_{\mathrm{HWHM},I} \approx 0.597$ (see Fig. 21.5). Thus the relationship between the half-width at half-maximum of the backscattering intensity peak and the transport mean free path for the particular case of conservative Rayleigh scattering and unpolarized normal illumination is given by

$$\alpha_{\mathrm{HWHM},I} \approx \frac{0.597}{k_1 l_{\mathrm{tr}}}. \tag{21.20}$$

The degree of linear polarization of the reflected light for unpolarized incident light is equal to minus the ratio of the second element of the total specific intensity column vector to the total specific intensity:

$$P(q) = -\frac{\widetilde{\mathcal{Q}}(q)}{\widetilde{\mathcal{I}}(q)} = -\frac{R^{\mathrm{I}}_{21}(q) + R^{\mathrm{M}}_{21}(q) + \mathcal{R}^{\mathrm{C}}_{21}(q)}{R^{\mathrm{I}}_{11}(q) + R^{\mathrm{M}}_{11}(q) + \mathcal{R}^{\mathrm{C}}_{11}(q)}. \tag{21.21}$$

Both $R^{\mathrm{I}}_{21}(0)$, $R^{\mathrm{M}}_{21}(0)$, and $\mathcal{R}^{\mathrm{C}}_{21}(0)$ vanish, the latter two quantities as a consequence of azimuthal symmetry in the case of normal illumination and unpolarized incident light. Furthermore, both $R^{\mathrm{I}}_{11}(q)$, $R^{\mathrm{M}}_{11}(q)$, $R^{\mathrm{I}}_{21}(q)$, and $R^{\mathrm{M}}_{21}(q)$ change with reflection direction much more slowly than $\mathcal{R}^{\mathrm{C}}_{11}(q)$ and $\mathcal{R}^{\mathrm{C}}_{21}(q)$ within the range of reflection directions affected by WL. As a result,

$$P(q) \approx -\frac{\mathcal{R}^{\mathrm{C}}_{21}(q)}{R^{\mathrm{I}}_{11}(0) + R^{\mathrm{M}}_{11}(0) + \mathcal{R}^{\mathrm{C}}_{11}(q)}. \tag{21.22}$$

This quantity is shown in Fig. 21.6 by the solid curve. It is seen indeed that polarization is zero at the exact backscattering direction. However, with increasing q, polarization becomes negative, rapidly grows in absolute value, and reaches its minimal value $P_{\min} \approx -2.765\%$ at a reflection direction very close to opposition ($q_P \approx 1.68$). This depression is highly asymmetric, so that the half-minimal value –1.383% is first reached at $q_{P,1} \approx 0.498$, which is even smaller than the value $q_{\mathrm{HWHM},I} \approx 0.597$ corresponding to the half-width at half-maximum of the backscattering intensity peak, and then at a much larger $q_{P,2} \approx 7.10$. This unusual behavior of polarization at near-backscattering angles is the polarization opposition effect discussed in Section 18.4 (see Fig. 18.6). Astrophysical observations of this effect have played an important role in remote characterization of regolith particles covering the surfaces of high-albedo atmosphereless solar-system bodies (Mishchenko *et al.* 2010; Rosenbush and Mishchenko 2011).

Problems

21.1: Derive the requirement (21.4).

21.2: Discuss what happens if the requirement (21.4) is not satisfied.

21.3: The angular resolution of the WCR shown in Plate 11.1b is defined by the diameter of the pinhole d and the focal length of the objective lens f (Section 11.4). What must be the distance D from the particulate layer to the WCR in Fig. 21.4 and the WCR's d and f in order to fully resolve the backscattering peak in Fig. 21.5 and accurately determine its amplitude?

22

Epilogue

The diagram in Fig. 22.1 provides a schematic summary of this textbook and serves to classify the place of the microphysical theories of radiative transfer and WL within the broader context of Maxwell's electromagnetics. Although we have been using the adjective "microphysical" in order to emphasize the back-traceability of both theories to the MMEs, it can also be said that these theories have a mesoscopic origin. Indeed, the term "mesoscopic physics" refers to a size regime that is intermediate between the microscopic and macroscopic and is characteristic of a region where a large number of particles can interact in a correlated fashion. The direct computer solutions of the Maxwell equations described in Chapter 18 demonstrate indeed how the "macroscopic" regime of radiative transfer and WL emerges from the "microscopic" particle-level regime of Maxwell's electromagnetics upon averaging over random realizations of a multiparticle group. Extensive discussions of mesoscopic optical phenomena can be found in the monographs by Sheng (2006) and Akkermans and Montambaux (2007).

Besides being a one-page summary of the book, Fig. 22.1 also helps identify problems that still await solution. First of all, by using the frequency-domain MMEs as the point of departure, we have completely excluded from consideration such phenomena as emission of electromagnetic waves and frequency redistribution, as well as situations involving pulsed illumination. These areas of electromagnetic energy transfer remain purely phenomenological (e.g., Oxenius 1986; Hanel *et al.* 2003; Mätzler 2006; Wehrse and Kalkofen 2006; Ito *et al.* 2007) and invoke modified versions of the RTE without strict derivation from first physical principles.

Another challenging subject is electromagnetic scattering by stochastic heterogeneous media composed of widely separated yet spatially correlated particles. For example, it has been suggested by Knyazikhin *et al.* (2005) and Marshak *et al.* (2005) that cloud droplets belonging to a particular size range may tend to form relatively small groups imbedded in an otherwise homogeneous

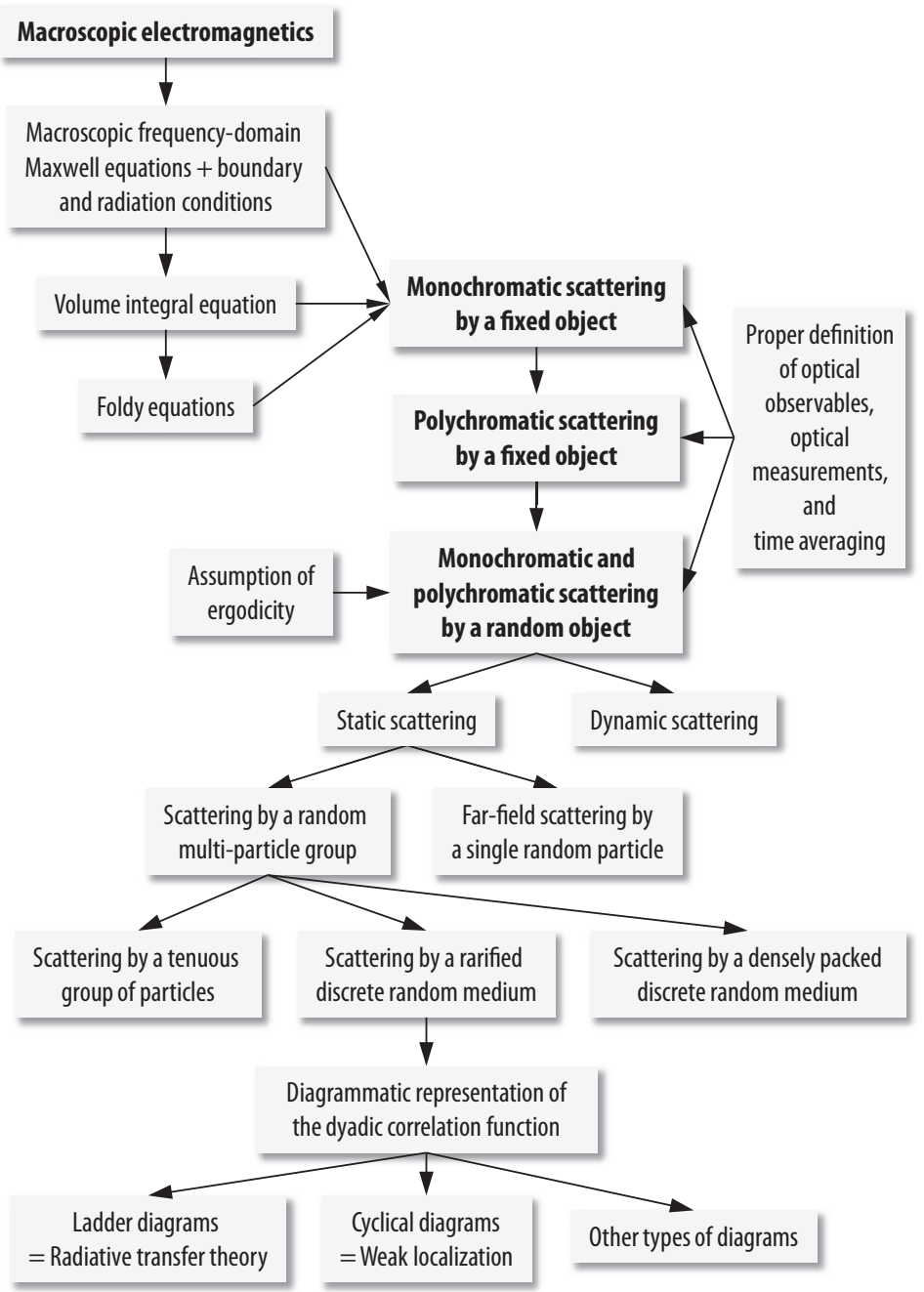

Fig. 22.1. Classification of electromagnetic scattering problems.

cloud. It was shown by Mishchenko (2006) on the basis of the microphysical approach that as long as such inclusions are sufficiently small and specific assumptions of ergodicity and spatial uniformity hold, one can still apply the conventional RTE, in which the participating extinction and phase matrices are obtained by averaging the respective single-particle matrices over all the particles constituting the entire cloud. However, this result may not necessarily apply to clouds with larger inhomogeneities.

Apart from Mishchenko (2006), the problem of electromagnetic scattering by stochastic media composed of widely separated yet correlated particles has been analyzed so far by using the motley concepts of the phenomenological RTT, including the fictitious "photons" (e.g., Pomraning (1991), Borovoi (2006), Davis and Marshak (2010), and references therein). We have seen in Chapter 19 that the extinction and phase matrices appear in the standard RTE as a consequence of well-defined assumptions and approximations and only as ensemble-averaged quantities. In the phenomenological stochastic RTT, the extinction and phase matrices are taken for granted and are postulated to be the primary optical attributes of the individual particles. Clearly, a self-consistent application of the microphysical approach is necessary to determine whether and to what extent the concepts of extinction and phase matrices can be applied to correlated particles.

Many geophysical scattering media consist of densely packed and strongly correlated particles. Typical examples are snow, soil and regolith surfaces, as well as vegetation. There is a rapidly growing number of publications in which numerical solutions of the RTE are used to model optical characteristics of the various densely packed particulate media. The reader can recall that the formal applicability of the RTT rests on the assumption that scattering particles are located in each-other's far zones and are uncorrelated. The obvious violation of this assumption in the case of densely packed particles can lead to significant deviations from the numerical predictions based on the RTE. Therefore, it is important to analyze, both theoretically and experimentally, to what extent the RTT – as well as the theory of WL – can be applied to densely packed particulate media. Recent progress in this direction has been reported by Voit *et al.* (2009), Muinonen *et al.* (2012), Mackowski and Mishchenko (2013), and Mishchenko *et al.* (2013c) based on numerically exact solutions of the MMEs and results of controlled laboratory experiments.

The rigorous *analytical* theory of electromagnetic energy transport in densely packed particulate media directly back-traceable to the MMEs is still in progress (e.g., Tishkovets *et al.* (2011) and references therein). There are several heuristic approaches to this problem that start with the notion of "independent scattering" and attempt to predict the modification of the phase and extinction matrices by effects of packing density (e.g., Hapke 2012), but the conceptual value of such approximations is limited and their range of validity is unknown, if not quite questionable. Fortunately, the ever-increasing power of scientific workstations coupled with the availability of efficient numerical techniques has led to the

emergence of an accurate quantitative approach to this complex problem based on direct computer solutions of the MMEs (see Chapter 18, Dlugach *et al.* (2011), Mackowski and Mishchenko (2013), and references therein).

Another important problem is electromagnetic scattering by an infinite random rough surface separating two half-spaces with different refractive indices. Although some rough surfaces, such as the ocean surface, indeed change randomly in time, many rough interfaces do not change and are deterministic rather than random. However, quite often their position relative to the source of light and/or the detector is not fixed during the measurement and their vertical profile is described by a highly irregular function of lateral coordinates. Even minute displacements of the source of light and/or the detector change phase differences entirely, thereby destroying the speckle pattern. Furthermore, the detector may view different parts of the surface at different moments in time, thereby in effect recording an average over a temporally varying surface profile. These two factors make the concept of a random rough surface a good model for describing the results of many actual static measurements. Further information on this subject can be found in the review by Shchegrov *et al*. (2004) and numerous publications cited therein.

One can also think of more complex problems involving different types of volume and/or surface scattering. A good example is electromagnetic scattering by a layer of continuous fluctuating medium comprising randomly positioned discrete particles and bounded by random rough interfaces. Although problems like this one are important in practice and have been treated using various phenomenological approaches, microphysical treatments based on consistent application of the Maxwell equations have been extremely scarce (e.g., Mudaliar 2013).

Problems

22.1: Discuss the main results of this textbook by following the flow of the diagram in Fig. 22.1.

22.2: The essays by Mishchenko (2009) and Mishchenko *et al.* (2011b) dispel numerous profound and long-lasting misconceptions encountered in the theory of electromagnetic scattering by particles, as well as in the phenomenological disciplines of directional radiometry and radiative transfer. Discuss the issues raised in those essays in the context of the diagram in Fig. 22.1.

Appendix A

Dyads and dyadics

Considered as mathematical entities, dyads and dyadics share with vectors the property of being independent of any coordinate system, although they possess representations in each of the reference frames appropriate for representations of vectors. This trait makes dyads and dyadics useful as mathematical measures of certain types of physical quantities that, like the directional quantities represented by vectors, can be visualized and manipulated without specifying beforehand a particular coordinate system.

From this coordinate-free standpoint, a *dyad* is defined as the result of a dyadic product of two vectors $\mathbf{a} \otimes \mathbf{b}$ such that the operation $(\mathbf{a} \otimes \mathbf{b}) \cdot \mathbf{c}$ yields the vector $\mathbf{a}(\mathbf{b} \cdot \mathbf{c})$ and the operation $\mathbf{c} \cdot (\mathbf{a} \otimes \mathbf{b})$ yields the vector $(\mathbf{c} \cdot \mathbf{a})\mathbf{b}$. The vector product $(\mathbf{a} \otimes \mathbf{b}) \times \mathbf{c}$ is defined as a dyad $\mathbf{a} \otimes (\mathbf{b} \times \mathbf{c})$, and $\mathbf{c} \times (\mathbf{a} \otimes \mathbf{b})$ yields $(\mathbf{c} \times \mathbf{a}) \otimes \mathbf{b}$. The dot product of two dyads $\mathbf{a} \otimes \mathbf{b}$ and $\mathbf{c} \otimes \mathbf{d}$ yields the dyad $(\mathbf{b} \cdot \mathbf{c})(\mathbf{a} \otimes \mathbf{d})$.

The sum of two dyads $\overleftrightarrow{A} = \mathbf{a} \otimes \mathbf{b} + \mathbf{c} \otimes \mathbf{d}$ is not necessarily a dyad in that there may not exist two vectors $\mathbf{e}$ and $\mathbf{f}$ such that $\overleftrightarrow{A} = \mathbf{e} \otimes \mathbf{f}$. Therefore, the sum of two or more dyads is called a *dyadic*. The result of a dyadic operating on a vector is another vector:

$$\overleftrightarrow{A} \cdot \mathbf{e} = \mathbf{a}(\mathbf{b} \cdot \mathbf{e}) + \mathbf{c}(\mathbf{d} \cdot \mathbf{e}), \tag{A.1}$$

$$\mathbf{e} \cdot \overleftrightarrow{A} = (\mathbf{e} \cdot \mathbf{a})\mathbf{b} + (\mathbf{e} \cdot \mathbf{c})\mathbf{d}. \tag{A.2}$$

The vector products $\overleftrightarrow{A} \times \mathbf{e}$ and $\mathbf{e} \times \overleftrightarrow{A}$ are defined analogously.

From the coordinate standpoint, the operation (A.1) may be thought of as a 3×3 matrix representing the dyadic multiplying a column matrix consisting of the initial vector components, thereby producing another column matrix consisting of the resulting vector components. The components of both vectors must be specified in the same coordinate system.

Any dyadic can be represented as a sum of at most nine dyads. For example, in Cartesian coordinates any dyadic $\overleftrightarrow{A}$ can be expressed as

$$\begin{aligned}\overleftrightarrow{A} = \; & A_{xx}\,\hat{\mathbf{x}}\otimes\hat{\mathbf{x}} + A_{xy}\,\hat{\mathbf{x}}\otimes\hat{\mathbf{y}} + A_{xz}\,\hat{\mathbf{x}}\otimes\hat{\mathbf{z}} \\ & + A_{yx}\,\hat{\mathbf{y}}\otimes\hat{\mathbf{x}} + A_{yy}\,\hat{\mathbf{y}}\otimes\hat{\mathbf{y}} + A_{yz}\,\hat{\mathbf{y}}\otimes\hat{\mathbf{z}} \\ & + A_{zx}\,\hat{\mathbf{z}}\otimes\hat{\mathbf{x}} + A_{zy}\,\hat{\mathbf{z}}\otimes\hat{\mathbf{y}} + A_{zz}\,\hat{\mathbf{z}}\otimes\hat{\mathbf{z}},\end{aligned} \tag{A.3}$$

where $\hat{\mathbf{x}}$, $\hat{\mathbf{y}}$, and $\hat{\mathbf{z}}$ are the unit vectors along the x-, y-, and z-axis, respectively, and the coefficients A_{ij} can be thought of as elements of the matrix representing the dyadic. It can be shown that dyadics are Cartesian tensors of rank two.

The transpose of a dyadic $\overleftrightarrow{A}$ is a dyadic $\overleftrightarrow{A}^{\mathrm{T}}$ such that

$$\overleftrightarrow{A}\cdot\mathbf{a} = \mathbf{a}\cdot\overleftrightarrow{A}^{\mathrm{T}} \tag{A.4}$$

for any $\mathbf{a}$. One may easily verify that transposing a dyadic is equivalent to transposing the matrix representing the dyadic in a coordinate system. Obviously,

$$(\overleftrightarrow{A}^{\mathrm{T}})^{\mathrm{T}} = \overleftrightarrow{A} \tag{A.5}$$

and

$$\mathbf{a}\cdot\overleftrightarrow{A} = \overleftrightarrow{A}^{\mathrm{T}}\cdot\mathbf{a}. \tag{A.6}$$

A dyadic $\overleftrightarrow{A}$ is symmetric if

$$\overleftrightarrow{A}^{\mathrm{T}} = \overleftrightarrow{A} \tag{A.7}$$

and is Hermitian if

$$\overleftrightarrow{A}^{\mathrm{T}} = \overleftrightarrow{A}^{*}. \tag{A.8}$$

The identity dyadic $\overleftrightarrow{I}$ is defined by the relations

$$\overleftrightarrow{I}\cdot\mathbf{a} = \mathbf{a}\cdot\overleftrightarrow{I} = \mathbf{a} \tag{A.9}$$

for any $\mathbf{a}$. As a consequence, we have for any $\overleftrightarrow{A}$:

$$\overleftrightarrow{I}\cdot\overleftrightarrow{A} = \overleftrightarrow{A}\cdot\overleftrightarrow{I} = \overleftrightarrow{A}. \tag{A.10}$$

Problems

A.1: Show that

$$(\mathbf{a}\cdot\overleftrightarrow{A})\cdot\mathbf{b} = \mathbf{a}\cdot(\overleftrightarrow{A}\cdot\mathbf{b}) = \mathbf{a}\cdot\overleftrightarrow{A}\cdot\mathbf{b}, \tag{A.11}$$

$$(\mathbf{a}\cdot\overleftrightarrow{A})\cdot\overleftrightarrow{B} = \mathbf{a}\cdot(\overleftrightarrow{A}\cdot\overleftrightarrow{B}) = \mathbf{a}\cdot\overleftrightarrow{A}\cdot\overleftrightarrow{B}, \tag{A.12}$$

$$\overleftrightarrow{A}\cdot(\overleftrightarrow{B}\cdot\mathbf{a}) = (\overleftrightarrow{A}\cdot\overleftrightarrow{B})\cdot\mathbf{a} = \overleftrightarrow{A}\cdot\overleftrightarrow{B}\cdot\mathbf{a}, \tag{A.13}$$

$$(\overleftrightarrow{A}\cdot\overleftrightarrow{B})\cdot\overleftrightarrow{C} = \overleftrightarrow{A}\cdot(\overleftrightarrow{B}\cdot\overleftrightarrow{C}) = \overleftrightarrow{A}\cdot\overleftrightarrow{B}\cdot\overleftrightarrow{C}, \tag{A.14}$$

$$\mathbf{a}\cdot\overleftrightarrow{A}\cdot\mathbf{b} = \mathbf{b}\cdot\overleftrightarrow{A}^{\mathrm{T}}\cdot\mathbf{a}, \tag{A.15}$$

$$(\overleftrightarrow{A}\cdot\overleftrightarrow{B})^{\mathrm{T}} = \overleftrightarrow{B}^{\mathrm{T}}\cdot\overleftrightarrow{A}^{\mathrm{T}}, \tag{A.16}$$

$$(\overleftrightarrow{A}\cdot\mathbf{a})\otimes(\overleftrightarrow{B}\cdot\mathbf{b}) = \overleftrightarrow{A}\cdot(\mathbf{a}\otimes\mathbf{b})\cdot\overleftrightarrow{B}^{\mathrm{T}}, \tag{A.17}$$

$$(\mathbf{a}\times\mathbf{b})\cdot\overleftrightarrow{A} = \mathbf{a}\cdot(\mathbf{b}\times\overleftrightarrow{A}). \tag{A.18}$$

A.2: Show that

$$\overleftrightarrow{I} = \hat{\mathbf{x}}\otimes\hat{\mathbf{x}} + \hat{\mathbf{y}}\otimes\hat{\mathbf{y}} + \hat{\mathbf{z}}\otimes\hat{\mathbf{z}} \tag{A.19}$$

in Cartesian coordinates and

$$\overleftrightarrow{I} = \hat{\mathbf{r}}\otimes\hat{\mathbf{r}} + \hat{\boldsymbol{\theta}}\otimes\hat{\boldsymbol{\theta}} + \hat{\boldsymbol{\varphi}}\otimes\hat{\boldsymbol{\varphi}} \tag{A.20}$$

in spherical polar coordinates, where $\hat{\mathbf{r}}$, $\hat{\boldsymbol{\theta}}$, and $\hat{\boldsymbol{\varphi}}$ are the corresponding unit vectors.

Notes and further reading

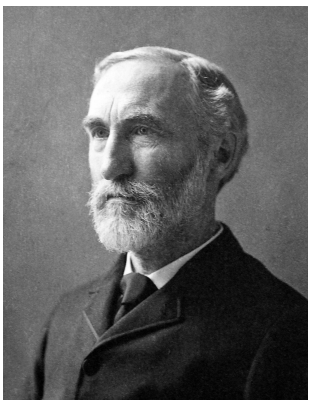
Josiah Willard Gibbs

The profound concept of dyads and dyadics was pioneered by the great American physicist and mathematician J. Willard Gibbs (1839–1903) (see, in particular, the famous textbook by Gibbs and Wilson 1909). Among his other supreme contributions to physics, mathematics, and physical chemistry are the foundation of classical statistical physics, the development (independently of Oliver Heaviside) of vector calculus, and the formulation of the phase rule for a heterogeneous system in thermodynamic equilibrium. Although Gibbs' dyadic calculus has eventually become part of the more general tensor calculus, it remains an extremely useful mathematical tool in electromagnetics and optics.

A comprehensive introduction to dyadic calculus can be found in Drew (1961). A useful compendium of formulas from dyadic algebra and dyadic analysis is given in Appendix 4 of Van Bladel (2007).

Appendix B

Free-space dyadic Green's function

The free-space dyadic Green's function is defined as

$$\overleftrightarrow{G}(\mathbf{r},\mathbf{r}') = \left(\overleftrightarrow{I} + \frac{1}{k^2}\nabla\otimes\nabla\right)g(\mathbf{r},\mathbf{r}'), \tag{B.1}$$

where $\mathbf{r},\mathbf{r}'\in\Re^3$, k is a positive real number, and

$$g(\mathbf{r},\mathbf{r}') = \frac{\exp(\mathrm{i}k|\mathbf{r}-\mathbf{r}'|)}{4\pi|\mathbf{r}-\mathbf{r}'|} \tag{B.2}$$

is the real-valued scalar Green's function. The latter satisfies the three-dimensional Helmholtz equation

$$(\nabla^2 + k^2)g(\mathbf{r},\mathbf{r}') = -\delta(\mathbf{r}-\mathbf{r}') \tag{B.3}$$

(see, e.g., p. 598 of Arfken and Weber (2005)), where $\delta(\mathbf{r}-\mathbf{r}')$ is the three-dimensional delta function defined by

$$\delta(\mathbf{r}-\mathbf{r}') = \begin{cases} \delta(x-x')\delta(y-y')\delta(z-z') & \text{(Cartesian coordinates)}, \\ \dfrac{1}{r^2}\delta(r-r')\delta(\cos\theta-\cos\theta')\delta(\varphi-\varphi') & \text{(spherical polar coordinates)}. \end{cases} \tag{B.4}$$

Furthermore, it obeys the obvious symmetry relation

$$g(\mathbf{r}',\mathbf{r}) = g(\mathbf{r},\mathbf{r}') \tag{B.5}$$

and the asymptotic limit

$$\lim_{|\mathbf{r}-\mathbf{r}'|\to\infty} g(\mathbf{r},\mathbf{r}') = 0. \tag{B.6}$$

Let us now invoke the dyadic identities

$$\nabla\times(\nabla\otimes\nabla) = (\nabla\times\nabla)\otimes\nabla = \overleftrightarrow{0}, \tag{B.7}$$

$$\nabla \times \nabla \times (\overleftrightarrow{I} g) = \nabla \otimes \nabla g - \overleftrightarrow{I}\, \nabla^2 g \tag{B.8}$$

(Van Bladel 2007), where $\overleftrightarrow{0}$ is a zero dyad. By applying these to Eq. (B.1) and taking into account Eq. (B.3), we easily verify that $\overleftrightarrow{G}(\mathbf{r}, \mathbf{r}')$ satisfies the following differential equation:

$$\nabla \times \nabla \times \overleftrightarrow{G}(\mathbf{r}, \mathbf{r}') - k^2 \overleftrightarrow{G}(\mathbf{r}, \mathbf{r}') = \overleftrightarrow{I}\, \delta(\mathbf{r} - \mathbf{r}'). \tag{B.9}$$

If we recall that in Cartesian coordinates

$$\nabla = \hat{\mathbf{x}} \frac{\partial}{\partial x} + \hat{\mathbf{y}} \frac{\partial}{\partial y} + \hat{\mathbf{z}} \frac{\partial}{\partial z} \tag{B.10}$$

and denote the gradient operator in the primed Cartesian coordinates by ∇' then $\nabla' g(\mathbf{r}, \mathbf{r}') = -\nabla g(\mathbf{r}, \mathbf{r}')$ and $\nabla' \otimes \nabla' g(\mathbf{r}, \mathbf{r}') = \nabla \otimes \nabla g(\mathbf{r}, \mathbf{r}')$. By interchanging $\mathbf{r}$ and $\mathbf{r}'$ in Eq. (B.1) and recalling Eq. (B.2), we obtain

$$\begin{aligned}
\overleftrightarrow{G}(\mathbf{r}', \mathbf{r}) &= \left(\overleftrightarrow{I} + \frac{1}{k^2} \nabla' \otimes \nabla' \right) g(\mathbf{r}', \mathbf{r}) \\
&= \left(\overleftrightarrow{I} + \frac{1}{k^2} \nabla \otimes \nabla \right) g(\mathbf{r}', \mathbf{r}) \\
&= \left(\overleftrightarrow{I} + \frac{1}{k^2} \nabla \otimes \nabla \right) g(\mathbf{r}, \mathbf{r}'),
\end{aligned}$$

which yields the symmetry property

$$\overleftrightarrow{G}(\mathbf{r}', \mathbf{r}) = \overleftrightarrow{G}(\mathbf{r}, \mathbf{r}'). \tag{B.11}$$

Furthermore, Eqs. (B.1) and (B.10) imply that $\overleftrightarrow{G}(\mathbf{r}, \mathbf{r}')$ is a symmetric dyad:

$$\overleftrightarrow{G}(\mathbf{r}, \mathbf{r}') = [\overleftrightarrow{G}(\mathbf{r}, \mathbf{r}')]^{\mathrm{T}}. \tag{B.12}$$

Hence

$$\overleftrightarrow{G}(\mathbf{r}', \mathbf{r}) = [\overleftrightarrow{G}(\mathbf{r}, \mathbf{r}')]^{\mathrm{T}}. \tag{B.13}$$

Equation (B.10) also implies the property of translational invariance:

$$\overleftrightarrow{G}(\mathbf{r} + \mathbf{R}, \mathbf{r}' + \mathbf{R}) = \overleftrightarrow{G}(\mathbf{r}, \mathbf{r}'). \tag{B.14}$$

Let us now take into account that in spherical coordinates,

$$\nabla = \hat{\mathbf{r}} \frac{\partial}{\partial r} + \hat{\boldsymbol{\theta}} \frac{1}{r} \frac{\partial}{\partial \theta} + \hat{\boldsymbol{\varphi}} \frac{1}{r \sin\theta} \frac{\partial}{\partial \varphi}, \tag{B.15}$$

$$\frac{\partial}{\partial r} \hat{\mathbf{r}} = 0, \quad \frac{\partial}{\partial \theta} \hat{\mathbf{r}} = \hat{\boldsymbol{\theta}}, \quad \frac{\partial}{\partial \varphi} \hat{\mathbf{r}} = \hat{\boldsymbol{\varphi}} \sin\theta, \tag{B.16}$$

the order of operator components relative to $\hat{\mathbf{r}}$, $\hat{\boldsymbol{\theta}}$, and $\hat{\boldsymbol{\varphi}}$ in Eq. (B.15) being essential because the unit basis vectors depend on θ and φ. Assuming that

$kr \gg 1$, we derive from Eqs. (B.1) and (B.2):

$$\overleftrightarrow{G}(\mathbf{r}, \mathbf{0}) \underset{kr \gg 1}{=} (\overleftrightarrow{I} - \hat{\mathbf{r}} \otimes \hat{\mathbf{r}}) \frac{\exp(\mathrm{i}kr)}{4\pi r} \tag{B.17}$$

(Problem B.1). Furthermore, since

$$\nabla \times (\overleftrightarrow{I} g) = (\nabla g) \times \overleftrightarrow{I} \tag{B.18}$$

(Van Bladel 2007), we can use Eqs. (B.1), (B.7), and (B.17) to derive the following radiation condition for the dyadic Green's function:

$$\mathbf{r} \times [\nabla \times \overleftrightarrow{G}(\mathbf{r}, \mathbf{0})] + \mathrm{i}kr \overleftrightarrow{G}(\mathbf{r}, \mathbf{0}) \underset{kr \gg 1}{=} \overleftrightarrow{0} \tag{B.19}$$

(Problem B.2). Taking into account that

$$|\mathbf{r} - \mathbf{r}'| = r \sqrt{1 - 2\frac{\hat{\mathbf{r}} \cdot \mathbf{r}'}{r} + \frac{r'^2}{r^2}} \underset{r \gg r'}{=} r - \hat{\mathbf{r}} \cdot \mathbf{r}' + \frac{r'^2}{2r}, \tag{B.20}$$

we derive from Eqs. (B.14) and (B.17):

$$\overleftrightarrow{G}(\mathbf{r}, \mathbf{r}') \underset{\substack{kr \gg 1 \\ r \gg r' \\ kr'^2/2r \ll 1}}{=} (\overleftrightarrow{I} - \hat{\mathbf{r}} \otimes \hat{\mathbf{r}}) \frac{\exp(\mathrm{i}kr)}{4\pi r} \exp(-\mathrm{i}k\hat{\mathbf{r}} \cdot \mathbf{r}'). \tag{B.21}$$

Finally, Eqs. (B.10), (B.14), and (B.19) imply that

$$\mathbf{r} \times [\nabla \times \overleftrightarrow{G}(\mathbf{r}, \mathbf{r}')] + \mathrm{i}kr \overleftrightarrow{G}(\mathbf{r}, \mathbf{r}') \underset{\substack{kr \gg 1 \\ r \gg r'}}{=} \overleftrightarrow{0}. \tag{B.22}$$

Problems

B.1: Derive Eq. (B.17).

B.2: Derive Eq. (B.19).

Notes and further reading

The dyadic Green's function was introduced by Levine and Schwinger (1950). It belongs to the general class of functions first studied by the self-taught English mathematician (and professional miller) George Green (1793–1841) in his initially obscure, but now famous *Essay* (Green 1828). Typically a Green's function is an integral kernel that can be used to solve an inhomogeneous differential equation defined on a domain, with specified boundary (or initial) conditions (see, e.g., Barton (1989)). Green's approach was popularized by W. Thomson, Lord Kelvin and further developed into an efficient mathematical tool by O. Heaviside. For a scientific biography of George Green see Cannell (2001).

Appendix C

Euler rotation angles

Consider right-handed Cartesian coordinate systems $\{x, y, z\}$ and $\{x', y', z'\}$ having a common origin. It is often convenient to specify the orientation of the coordinate system $\{x', y', z'\}$ relative to the coordinate system $\{x, y, z\}$ in terms of three Euler rotation angles α, β, and γ which transform the coordinate system $\{x, y, z\}$ into the coordinate system $\{x', y', z'\}$, as shown in Fig. C.1. Specifically, the three consecutive Euler rotations are performed as follows:

- Rotation of the coordinate system $\{x, y, z\}$ about the z-axis through an angle $\alpha \in [0, 2\pi)$, reorienting the y-axis in such a way that it coincides with the line of nodes (i.e., the line formed by the intersection of the xy- and the $x'y'$-planes).

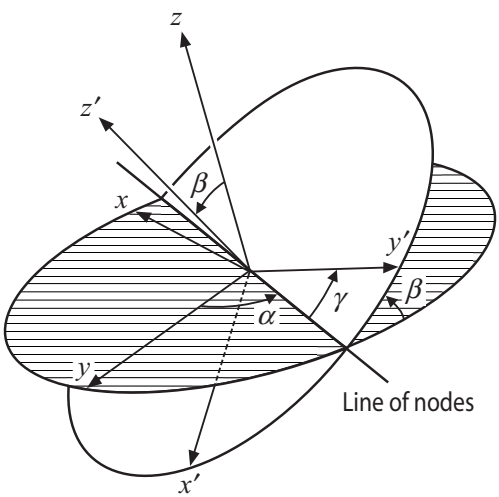

Fig. C.1. Euler angles of rotation α, β, and γ transforming the coordinate system $\{x, y, z\}$ into the coordinate system $\{x', y', z'\}$.

- Rotation about the new y-axis through an angle $\beta \in [0, \pi]$.
- Rotation about the z'-axis through an angle $\gamma \in [0, 2\pi)$.

An angle of rotation is positive if the rotation is performed in the *clockwise* direction when one is looking in the positive direction of the rotation axis.

Appendix D

Spherical-wave decomposition of a plane wave in the far zone

In this appendix we derive Eq. (13.14) following the approach described by Saxon (1955b). We begin with the well-known expansion of a plane wave in scalar spherical harmonics (see p. 471 of Jackson (1998)):

$$\exp(\mathrm{i}\mathbf{r}\cdot\mathbf{r}') = 4\pi \sum_{l=0}^{\infty} \mathrm{i}^l j_l(rr') \sum_{m=-l}^{l} Y_{lm}^*(\hat{\mathbf{r}}) Y_{lm}(\hat{\mathbf{r}}'), \tag{D.1}$$

where $\hat{\mathbf{r}} = \mathbf{r}/r$, $\hat{\mathbf{r}}' = \mathbf{r}'/r'$,

$$j_l(y) = y^l \left(-\frac{1}{y}\frac{\mathrm{d}}{\mathrm{d}y}\right)^l \left(\frac{\sin y}{y}\right) \tag{D.2}$$

are spherical Bessel functions of the first kind, and $Y_{lm}(\hat{\mathbf{r}})$ are scalar spherical harmonics. The latter are defined as

$$Y_{lm}(\hat{\mathbf{r}}) = \sqrt{\frac{(2l+1)(l-m)!}{4\pi(l+m)!}}\, P_l^m(\cos\theta)\exp(\mathrm{i}m\varphi), \tag{D.3}$$

where θ and φ are spherical angular coordinates of the unit vector $\hat{\mathbf{r}}$ and the P_l^m are associated Legendre functions defined in terms of Legendre polynomials P_l as follows:

$$P_l^m(x) = (-1)^m (1-x^2)^{m/2} \frac{\mathrm{d}^m}{\mathrm{d}x^m} P_l(x), \tag{D.4}$$

$$P_l(x) = \frac{1}{2^l l!}\frac{\mathrm{d}^l}{\mathrm{d}x^l}(x^2-1)^l \tag{D.5}$$

with $x \in [-1, 1]$. Using the asymptotic form (see p. 729 of Arfken and Weber (2005)),

$$j_l(y) \underset{y\to\infty}{=} \frac{1}{y}\sin\left(y - \frac{l\pi}{2}\right), \tag{D.6}$$

we have

$$j_l(rr') \underset{rr'\to\infty}{=} \frac{\mathrm{i}}{2rr'}\left[\exp\left(-\mathrm{i}rr' + \frac{\mathrm{i}l\pi}{2}\right) - \exp\left(\mathrm{i}rr' - \frac{\mathrm{i}l\pi}{2}\right)\right]. \tag{D.7}$$

Substituting this expression in Eq. (D.1) and making use of the completeness relation for the spherical harmonics (see p. 108 of Jackson (1998))

$$\sum_{l=0}^{\infty}\sum_{m=-l}^{l} Y_{lm}^*(\hat{\mathbf{r}})Y_{lm}(\hat{\mathbf{r}}') = \delta(\hat{\mathbf{r}} - \hat{\mathbf{r}}') \tag{D.8}$$

and the symmetry relation

$$Y_{lm}(-\hat{\mathbf{r}}') = (-1)^l Y_{lm}(\hat{\mathbf{r}}'), \tag{D.9}$$

we finally derive after simple algebra:

$$\exp(\mathrm{i}rr'\hat{\mathbf{r}}\cdot\hat{\mathbf{r}}') \underset{rr'\to\infty}{=} \frac{\mathrm{i}2\pi}{r'}\left[\delta(\hat{\mathbf{r}} + \hat{\mathbf{r}}')\frac{\exp(-\mathrm{i}rr')}{r} - \delta(\hat{\mathbf{r}} - \hat{\mathbf{r}}')\frac{\exp(\mathrm{i}rr')}{r}\right], \tag{D.10}$$

where $\delta(\hat{\mathbf{r}} - \hat{\mathbf{r}}')$ is the solid-angle delta function given by Eq. (13.15).

A direct consequence of Eq. (D.10) is the so-called Jones' lemma (see, e.g., Appendix XII of Born and Wolf (1999)), which states the following:

$$\frac{1}{R}\oint_S \mathrm{d}^2\mathbf{r}\, f(\mathbf{r})\exp(\mathrm{i}k\hat{\mathbf{n}}\cdot\mathbf{r}) \underset{kR\to\infty}{=} \frac{\mathrm{i}2\pi}{k}[f(-R\hat{\mathbf{n}})\exp(-\mathrm{i}kR) - f(R\hat{\mathbf{n}})\exp(\mathrm{i}kR)], \tag{D.11}$$

where S is the surface of a sphere centered at the origin, R is the sphere radius, the position vector $\mathbf{r}$ connects the origin and a point on the surface, $f(\mathbf{r})$ is a "well-behaved" function of the position vector, and $\hat{\mathbf{n}}$ is a constant unit vector.

Appendix E

Integration quadrature formulas

Practical numerical evaluation of definite integrals is often based on using one of the so-called quadrature formulas. Assume, for example, that one needs to compute numerically the integral

$$I = \int_a^b \mathrm{d}x\, f(x), \tag{E.1}$$

where $f(x)$ is a real-valued function. The simplest approach is to use the (extended) trapezoidal rule

$$I \approx \frac{b-a}{N-1}\left[\frac{f(x_1)+f(x_N)}{2} + \sum_{n=2}^{N-1} f(x_n)\right], \tag{E.2}$$

where

$$x_n = a + \frac{(n-1)(b-a)}{N-1} \tag{E.3}$$

are equidistant so-called division points such that $x_1 = a$ and $x_N = b$. By increasing the number of division points N, the result can usually be made arbitrarily accurate. However, this simplistic approach often leads to a rapid increase in computer time.

In many cases a much more accurate and faster result can be achieved by using so-called quadrature formulas of the highest algebraic degree of precision (Krylov 1962; Press *et al.* 1992). Perhaps the most important example is the Gaussian quadrature formula, which reads

$$\int_{-1}^{1} \mathrm{d}x\, f(x) \approx \sum_{n=1}^{N} w_n f(x_n), \tag{E.4}$$

where the nth quadrature division point x_n is the nth zero of the Nth degree Legendre polynomial $P_N(x)$ defined by Eq. (D.5), while the quadrature weights w_n are given by

Table E.1. Gaussian division points and weights for $N = 9$.

n	x_n	w_n
1	–0.968160239507626	0.081274388361574
2	–0.836031107326636	0.180648160694857
3	–0.613371432700590	0.260610696402935
4	–0.324253423403809	0.312347077040003
5	0.000000000000000	0.330239355001260
6	0.324253423403809	0.312347077040003
7	0.613371432700590	0.260610696402935
8	0.836031107326636	0.180648160694857
9	0.968160239507626	0.081274388361574

$$w_n = \frac{2}{(1-x_n^2)[P_N'(x_n)]^2}. \tag{E.5}$$

The Gaussian quadrature formula is exact for all functions that can be represented by a polynomial of degree smaller than or equal to $2N-1$. Substituting $f(x) \equiv 1$ yields a useful numerical check on the quadrature weights:

$$\sum_{n=1}^{N} w_n \equiv 2. \tag{E.6}$$

As an illustration, Table E.1 lists the Gaussian division points and weights for $N = 9$. Notice that $x_n = -x_{N-n+1}$ and $w_n = w_{N-n+1}$ so that the middle division point of the Gauss quadrature of any odd order is always zero.

The Gaussian formula for an arbitrary integration interval $[a, b]$ follows from Eq. (E.4):

$$\int_a^b \mathrm{d}y\, f(y) \approx \sum_{n=1}^{N} u_n f(y_n), \tag{E.7}$$

where the corresponding division points and weights are now given by

$$y_n = \frac{b-a}{2} x_n + \frac{b+a}{2}, \tag{E.8}$$

$$u_n = \frac{b-a}{2} w_n. \tag{E.9}$$

For given a, b, and N, the division points of the Gaussian quadrature formula are chosen automatically so that the formula is exact for polynomials of the high-

Table E.2. Division points and weights of the Markov quadrature formula on the interval [–1, 1] with $N = 9$ and one prescribed division point $x_9 = 1$.

n	x_n	w_n
1	–0.964440169705273	0.090714504923282
2	–0.817352784200412	0.200553298024552
3	–0.571383041208738	0.286386696357232
4	–0.256135670833455	0.337693966975930
5	0.090373369606853	0.348273002772967
6	0.426350485711139	0.316843775670438
7	0.711267485915709	0.247189378204593
8	0.910732089420060	0.147654019046315
9	1.000000000000000	0.024691358024692

est possible degree. As a consequence, one has no direct control over the exact location of the division points, the middle division point $(b + a)/2$ for an odd N being the only exception. However, it is often convenient to have an integration formula that has one or more prescribed division points and still provides the highest possible degree of precision. If the number of prescribed division points is M and the total number of points is N then this so-called Markov quadrature formula (Krylov 1962) is exact for all polynomials of degree smaller than or equal to $2N - M - 1$. The Markov quadrature with $M = 1$ and $x_1 = a$ is often called the Radau formula, whereas that with $M = 2$, $x_1 = a$, and $x_N = b$ is called the Lobatto formula. As an example, Table E.2 lists the division points and weights for the Markov quadrature formula on the interval [–1, 1] with $N = 9$ and one prescribed division point $x_9 = 1$.

Tables E.1 and E.2 were computed using FORTRAN subroutines GAUSS and MARK included in the code refl.f available at http://www.giss.nasa.gov/staff/mmishchenko/brf (assessed November 2013).

Appendix F

Wigner *d*-functions

Wigner *d*-functions are defined as

$$d^s_{mn}(\theta) = \sqrt{(s+m)!\,(s-m)!\,(s+n)!\,(s-n)!}$$
$$\times \sum_k (-1)^k \frac{\left(\cos\frac{1}{2}\theta\right)^{2s-2k+m-n}\left(\sin\frac{1}{2}\theta\right)^{2k-m+n}}{k!\,(s+m-k)!\,(s-n-k)!\,(n-m+k)!}, \tag{F.1}$$

where s, m, and n are integers, $0 \le \theta \le \pi$, and the sum is taken over all integer values of k that lead to nonnegative factorials. Thus the summation index runs from $k_{\min} = \max(0, m-n)$ to $k_{\max} = \min(s+m, s-n)$. Therefore, $d^s_{mn}(\theta) = 0$ unless $k_{\max} \ge k_{\min}$ or, equivalently, $s \ge 0$ and $-s \le m, n \le s$. As follows from their definition, the *d*-functions are real-valued.

The *d*-functions possess the following symmetry properties:

$$d^s_{mn}(\theta) = (-1)^{m-n} d^s_{-m,-n}(\theta) = (-1)^{m-n} d^s_{nm}(\theta) = d^s_{-n,-m}(\theta), \tag{F.2}$$

$$d^s_{mn}(-\theta) = (-1)^{m-n} d^s_{mn}(\theta) = d^s_{nm}(\theta), \tag{F.3}$$

$$d^s_{mn}(\pi-\theta) = (-1)^{s-n} d^s_{-mn}(\theta) = (-1)^{s+m} d^s_{m,-n}(\theta). \tag{F.4}$$

Furthermore,

$$d^s_{mn}(0) = \delta_{mn}, \tag{F.5}$$

where δ_{mn} is the Kronecker delta:

$$\delta_{mn} = \begin{cases} 1 & \text{if } m = n, \\ 0 & \text{if } m \ne n. \end{cases} \tag{F.6}$$

Equations (F.4) and (F.5) imply that

$$d^s_{mn}(\pi) = (-1)^{s-n}\delta_{-mn}. \tag{F.7}$$

A convenient and efficient way to compute the *d*-functions is to use the following recurrence relation:

$$d_{mn}^{s+1}(\theta) = \frac{1}{s\sqrt{(s+1)^2-m^2}\sqrt{(s+1)^2-n^2}}\{(2s+1)[s(s+1)x-mn]d_{mn}^{s}(\theta)$$
$$-(s+1)\sqrt{s^2-m^2}\sqrt{s^2-n^2}\,d_{mn}^{s-1}(\theta)\}, \quad s \geq s_{\min}, \tag{F.8}$$

where

$$s_{\min} = \max(|m|,|n|). \tag{F.9}$$

The initial values are given by

$$d_{mn}^{s_{\min}-1}(\theta) = 0, \tag{F.10}$$

$$d_{mn}^{s_{\min}}(\theta) = \xi_{mn}\,2^{-s_{\min}}\left[\frac{(2s_{\min})!}{(|m-n|)!\,(|m+n|)!}\right]^{1/2}(1-x)^{|m-n|/2}(1+x)^{|m+n|/2}, \tag{F.11}$$

where

$$\xi_{mn} = \begin{cases} 1 & \text{for } n \geq m, \\ (-1)^{m-n} & \text{for } n < m. \end{cases} \tag{F.12}$$

The d-functions are orthogonal on the interval $[0,\pi]$:

$$\int_0^\pi \mathrm{d}\theta \sin\theta\, d_{mn}^{s}(\theta)\, d_{mn}^{s'}(\theta) = \frac{2}{2s+1}\,\delta_{ss'}. \tag{F.13}$$

Furthermore, functions $\sqrt{s+\frac{1}{2}}\,d_{mn}^{s}(\theta)$ with $s = s_{\min}, s_{\min}+1, \ldots$ form a complete orthonormal system of functions on $[0,\pi]$. This means that if a real-valued function $f(\theta)$ defined on the closed interval $[0,\pi]$ is square integrable on this interval, i.e., if

$$\int_0^\pi \mathrm{d}\theta \sin\theta\,[f(\theta)]^2 < \infty, \tag{F.14}$$

then there exists a unique set of coefficients η_s with $s \geq s_{\min}$ such that the series expansion

$$f(\theta) = \sum_{s=s_{\min}}^{\infty} \eta_s\, d_{mn}^{s}(\theta), \quad \theta \in [0,\pi] \tag{F.15}$$

holds in the following sense:

$$\lim_{S\to\infty}\int_0^\pi \mathrm{d}\theta \sin\theta \left| f(\theta) - \sum_{s=s_{\min}}^{S} \eta_s\, d_{mn}^{s}(\theta)\right|^2 = 0. \tag{F.16}$$

Conversely, if a real-valued function $f(\theta)$ on $[0,\pi]$ admits the expansion (F.15) in the sense of Eq. (F.16), then it is square integrable on $[0,\pi]$ and the expansion coefficients are given by

$$\eta_s = \left(s+\tfrac{1}{2}\right)\int_0^\pi \mathrm{d}\theta \sin\theta\, f(\theta)\, d_{mn}^{s}(\theta). \tag{F.17}$$

The latter formula follows directly from Eqs. (F.15) and (F.13).

The Wigner *d*-functions with $m = n = 0$ are equivalent to the usual Legendre polynomials defined by Eq. (D.5):

$$d^s_{00}(\theta) = P_s(x). \tag{F.18}$$

For $n = 0$, we obtain

$$d^s_{m0}(\theta) = \sqrt{\frac{(s-m)!}{(s+m)!}}\, P^m_s(x), \tag{F.19}$$

where $P^m_s(x)$ are associated Legendre functions defined by Eq. (D.4). Equations (F.8) and (F.19) yield a simple recurrence relation for the associated Legendre functions:

$$(s-m+1)\,P^m_{s+1}(x) = (2s+1)\,x\,P^m_s(x) - (s+m)\,P^m_{s-1}(x). \tag{F.20}$$

Despite its simplicity, the use of this relation in computer calculations for large s and $|m|$ results in overflows, whereas the original recurrence relation for the functions $d^s_{m0}(\theta)$ remains stable and accurate. Furthermore, the Wigner functions $d^s_{m0}(\theta)$ have simpler symmetry properties than the $P^m_s(x)$. It is, therefore, advisable to use the *d*-functions instead of the associated Legendre functions from both the analytical and the numerical standpoint.

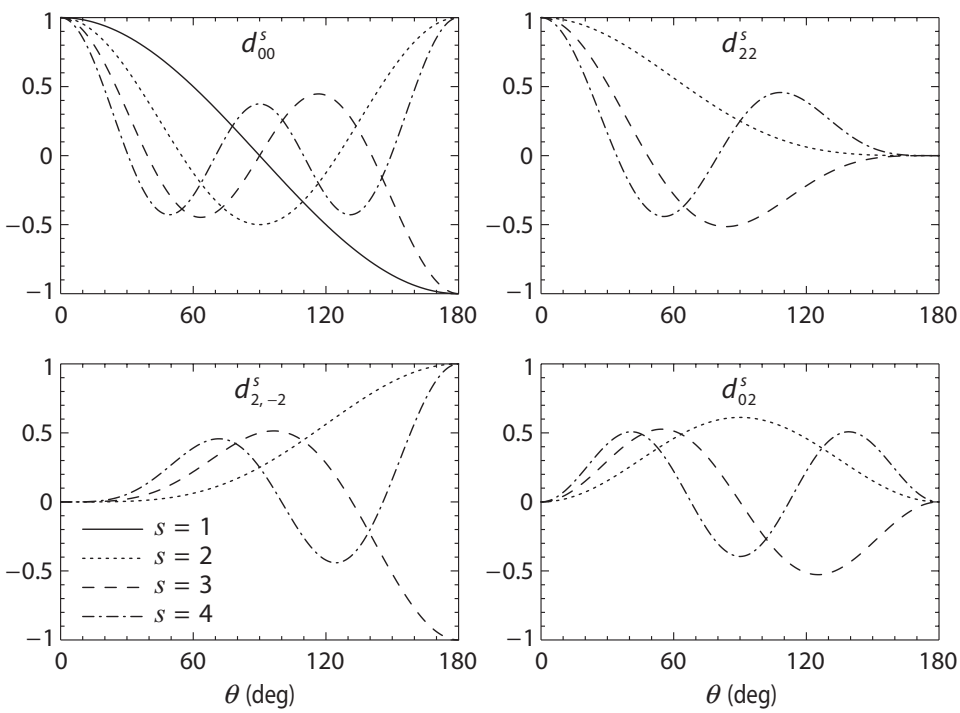

Fig. F.1. Wigner *d*-functions.

Table F.1. Wigner d-functions appearing in the expansions (15.86)–(15.91).

s	$d^s_{00}(\theta)$	$d^s_{22}(\theta)$	$d^s_{2,-2}(\theta)$	$d^s_{02}(\theta)$
0	1	0	0	0
1	$\cos\theta$	0	0	0
2	$\frac{1}{2}(3\cos^2\theta - 1)$	$\frac{1}{4}(1 + \cos\theta)^2$	$\frac{1}{4}(1 - \cos\theta)^2$	$\frac{1}{2}\sqrt{\frac{3}{2}}\sin^2\theta$
3	$-\frac{1}{2}\cos\theta(3 - 5\cos^2\theta)$	$-\frac{1}{4}(1 + \cos\theta)^2(2 - 3\cos\theta)$	$\frac{1}{4}(1 - \cos\theta)^2(2 + 3\cos\theta)$	$\sqrt{\frac{15}{8}}\sin^2\theta\cos\theta$
4	$\frac{1}{8}(3 - 30\cos^2\theta + 35\cos^4\theta)$	$\frac{1}{4}(1 + \cos\theta)^2(1 - 7\cos\theta + 7\cos^2\theta)$	$\frac{1}{4}(1 - \cos\theta)^2(1 + 7\cos\theta + 7\cos^2\theta)$	$-\sqrt{\frac{5}{32}}\sin^2\theta(1 - 7\cos^2\theta)$

Figure F.1 and Table F.1 illustrate the *d*-functions used in the expansions (15.86)–(15.91).

Further reading

Detailed accounts of the Wigner *d*-functions, as well as of the closely related Jacobi polynomials and generalized spherical functions are given in Rose (1957), Szegő (1959), Gelfand *et al.* (1963), Varshalovich *et al.* (1988), and Edmonds (1996). Our definition of the *d*-functions is consistent with that of Rose (1957), Varshalovich *et al.* (1988), and Hovenier *et al.* (2004). Edmonds (1996) uses functions $d_{mn}^{(s)}(\theta) = (-1)^{m+n} d_{mn}^{s}(\theta)$.

Appendix G

Stationary phase evaluation of a double integral

Consider the double integral

$$I = \int_{-\infty}^{+\infty} \mathrm{d}x \int_{-\infty}^{+\infty} \mathrm{d}y\, A(x, y) \frac{\exp[\mathrm{i} f(x, y)]}{r_1 r_2}, \tag{G.1}$$

where

$$f(x, y) = k(r_1 + r_2), \tag{G.2}$$

$$r_1 = \sqrt{x^2 + y^2 + z^2}, \tag{G.3}$$

$$r_2 = \sqrt{x^2 + y^2 + (Z - z)^2}, \tag{G.4}$$

and k is real. The exponential $\exp[\mathrm{i} f(x, y)]$ is a rapidly oscillating function everywhere except in the region in which $f(x, y) \approx$ constant. Therefore, if $A(x, y)$ is a slowly varying function of x and y then the only significant contribution to I arises from the nearest vicinity of the stationary phase point determined from

$$\frac{\partial f(x, y)}{\partial x} = 0 \quad \text{and} \quad \frac{\partial f(x, y)}{\partial y} = 0 \tag{G.5}$$

and given by $x = 0$ and $y = 0$. Expanding $f(x, y)$ in a Taylor series about this point, we have

$$\begin{aligned} f(x, y) \approx\ & f(0, 0) + x \left.\frac{\partial f(x, y)}{\partial x}\right|_{x=0,\, y=0} + y \left.\frac{\partial f(x, y)}{\partial y}\right|_{x=0,\, y=0} \\ & + \frac{1}{2} x^2 \left.\frac{\partial^2 f(x, y)}{\partial x^2}\right|_{x=0,\, y=0} + \frac{1}{2} y^2 \left.\frac{\partial^2 f(x, y)}{\partial y^2}\right|_{x=0,\, y=0} \\ & + xy \left.\frac{\partial^2 f(x, y)}{\partial x \partial y}\right|_{x=0,\, y=0} \end{aligned}$$

$$= k(|z|+|Z-z|) + \frac{k}{2}\left(\frac{1}{|z|} + \frac{1}{|Z-z|}\right)(x^2+y^2). \tag{G.6}$$

Finally, approximating

$$A(x, y) \approx A(0, 0), \tag{G.7}$$

$$\frac{1}{r_1 r_2} \approx \frac{1}{|z||Z-z|}, \tag{G.8}$$

substituting Eq. (G.6) in Eq. (G.1), and taking into account that

$$\int_{-\infty}^{+\infty} \mathrm{d}x \int_{-\infty}^{+\infty} \mathrm{d}y \exp[\mathrm{i}a(x^2+y^2)] = \frac{\mathrm{i}\pi}{a}, \quad a > 0 \tag{G.9}$$

yields

$$I = \frac{\mathrm{i}2\pi}{k} \frac{\exp[\mathrm{i}k(|z|+|Z-z|)]}{|z|+|Z-z|} A(0, 0). \tag{G.10}$$

Appendix H

Hints and answers to selected problems

2.1: $\epsilon(\mathbf{r}, t-t') = \epsilon(\mathbf{r})\delta(t-t')$, $\mu(\mathbf{r}, t-t') = \mu(\mathbf{r})\delta(t-t')$, and $\sigma(\mathbf{r}, t-t') = \sigma(\mathbf{r})\delta(t-t')$, where $\delta(t-t')$ is the delta function. It is easy to verify that the substitution of these formulas into Eqs. (2.13)–(2.15) indeed yields Eqs. (2.9)–(2.11).

2.3: Equations (2.1) and (2.21) yield:

$$\nabla \cdot \mathbf{D}(\mathbf{r})\exp(-\mathrm{i}2\omega t) + \nabla \cdot \mathbf{D}^*(\mathbf{r}) = \rho(\mathbf{r})\exp(-\mathrm{i}2\omega t) + \rho^*(\mathbf{r}).$$

This formula must be valid for any t, which implies Eq. (2.22). Equations (2.23)–(2.26) are derived similarly.

2.7: Use Eq. (2.60) along with the constitutive relations (2.30)–(2.32).

3.1: Take into account the following well-known formulas of vector calculus:

$$\nabla \cdot (f\mathbf{a}) = f\nabla \cdot \mathbf{a} + \mathbf{a} \cdot \nabla f, \tag{H.1}$$

$$\nabla \times (f\mathbf{a}) = f\nabla \times \mathbf{a} + (\nabla f) \times \mathbf{a}, \tag{H.2}$$

$$\nabla \exp(\mathrm{i}\mathbf{k} \cdot \mathbf{r}) = \mathrm{i}\mathbf{k}\exp(\mathrm{i}\mathbf{k} \cdot \mathbf{r}). \tag{H.3}$$

3.2: Take the vector product of $\mathbf{k}$ with both sides of Eq. (3.5) and use Eq. (3.6) and the vector identity (3.18) together with Eq. (3.3).

3.4: Use Eqs. (2.27), (2.28), (2.41), and (2.51).

3.5: Recall Eqs. (3.3), (3.5), and (3.10) and apply the well-known vector identity

$$(\mathbf{a} \times \mathbf{b}) \cdot (\mathbf{c} \times \mathbf{d}) = (\mathbf{a} \cdot \mathbf{c})(\mathbf{b} \cdot \mathbf{d}) - (\mathbf{a} \cdot \mathbf{d})(\mathbf{b} \cdot \mathbf{c}). \tag{H.4}$$

4.1: Taking the divergence of both sides of Eq. (2.23) and accounting for the vector identity $\nabla \cdot (\nabla \times \mathbf{a}) = 0$ yields Eq. (2.24). Similarly, taking the divergence of both sides of Eq. (2.25) and accounting for Eq. (2.26) yields Eq. (2.22).

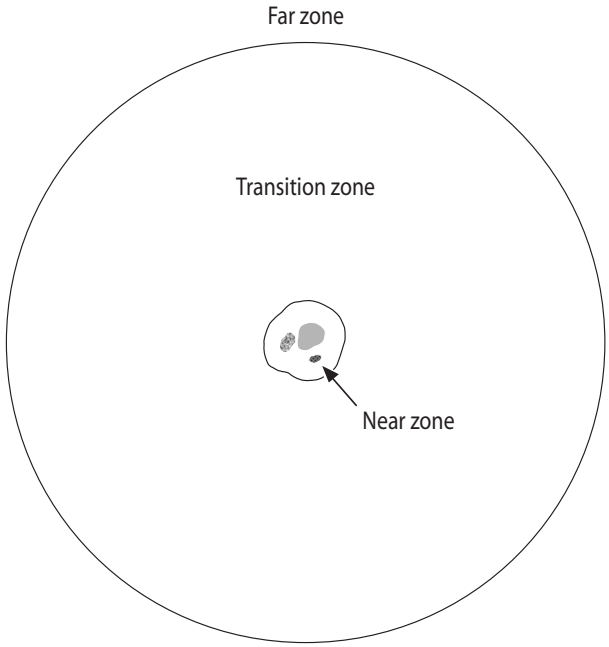

Fig. H.1. Near, transition, and far zones.

5.1: According to Eq. (B.14), $\overleftrightarrow{G}(\mathbf{r},\mathbf{r}') = \overleftrightarrow{G}(\mathbf{r}-\mathbf{r}',\mathbf{0})$. Then use Eq. (B.17).

5.2: For particles comparable to and greater than the incident wavelength, there exist three distinct zones (Fig. H.1). In the far zone, all three criteria (5.12)–(5.14) are satisfied and the total scattered field is a unified outgoing spherical wave. Each point of the transition zone satisfies the inequality (5.12), but not the inequalities (5.13) and (5.14). Therefore, although the total scattered field is not a unified spherical wave, it can still be represented as a superposition of outgoing spherical wavelets generated by the elementary volume elements of the object. In the near zone, all three criteria (5.12)–(5.14) are violated, and the total scattered field does not have a simple representation.

5.3: Use the unit-vector identities

$$\hat{\boldsymbol{\theta}}(-\hat{\mathbf{n}}) = \hat{\boldsymbol{\theta}}(\hat{\mathbf{n}}), \quad \hat{\boldsymbol{\varphi}}(-\hat{\mathbf{n}}) = -\hat{\boldsymbol{\varphi}}(\hat{\mathbf{n}}). \tag{H.5}$$

6.1: According to the results of Section 5.2, Eq. (6.21a) is valid provided that any point inside particle i is located in the far zone of particle j:

$$k_1(R_{ij} - a_i - a_j) \gg 1, \quad R_{ij} - a_i \gg a_j, \quad R_{ij} - a_i \gg k_1 a_j^2/2, \tag{H.6}$$

where a_i and a_j are the radii of the smallest circumscribing spheres of particles i and j, respectively. Similarly, Eq. (6.21b) follows from

$$k_1 R_{ij} \gg 1, \quad R_{ij} \gg |\mathbf{r} - \mathbf{R}_i|, \quad R_{ij} \gg \frac{k_1 |\mathbf{r} - \mathbf{R}_i|^2}{2}. \tag{H.7}$$

6.2:

$$k_1(r_i - a_i) \gg 1, \quad r_i \gg a_i, \quad r_i \gg k_1 a_i^2/2 \quad \text{for any } i. \tag{H.8}$$

7.2:

$$\mathbf{D} = \begin{bmatrix} 1 & 0 & 0 & 1 \\ 1 & 0 & 0 & -1 \\ 0 & -1 & -1 & 0 \\ 0 & -\mathrm{i} & \mathrm{i} & 0 \end{bmatrix}, \qquad \mathbf{D}^{-1} = \frac{1}{2}\begin{bmatrix} 1 & 1 & 0 & 0 \\ 0 & 0 & -1 & \mathrm{i} \\ 0 & 0 & -1 & -\mathrm{i} \\ 1 & -1 & 0 & 0 \end{bmatrix}, \tag{H.9}$$

$$\mathbf{B} = \begin{bmatrix} \frac{1}{2} & \frac{1}{2} & 0 & 0 \\ \frac{1}{2} & -\frac{1}{2} & 0 & 0 \\ 0 & 0 & 1 & 0 \\ 0 & 0 & 0 & 1 \end{bmatrix}, \qquad \mathbf{B}^{-1} = \begin{bmatrix} 1 & 1 & 0 & 0 \\ 1 & -1 & 0 & 0 \\ 0 & 0 & 1 & 0 \\ 0 & 0 & 0 & 1 \end{bmatrix}, \tag{H.10}$$

$$\mathbf{A} = \frac{1}{2}\begin{bmatrix} 0 & 1 & \mathrm{i} & 0 \\ 1 & 0 & 0 & 1 \\ 1 & 0 & 0 & -1 \\ 0 & 1 & -\mathrm{i} & 0 \end{bmatrix}, \qquad \mathbf{A}^{-1} = \begin{bmatrix} 0 & 1 & 1 & 0 \\ 1 & 0 & 0 & 1 \\ -\mathrm{i} & 0 & 0 & \mathrm{i} \\ 0 & 1 & -1 & 0 \end{bmatrix}. \tag{H.11}$$

7.3: The modified Stokes column vector has only one nonzero element and is equal to $[I\ 0\ 0\ 0]^{\mathrm{T}}$ if $\zeta = \pi/2$ (the electric field vector vibrates along the θ-axis, i.e., in the meridional plane) or $[0\ I\ 0\ 0]^{\mathrm{T}}$ if $\zeta = 0$ (the electric field vector vibrates along the φ-axis, i.e., in the plane perpendicular to the meridional plane) (see Fig. 7.3c).

7.4: The circular-polarization column vector $\mathbf{I}^{\mathrm{CP}}$ has only one nonzero element and takes the values $[0\ 0\ I\ 0]^{\mathrm{T}}$ and $[0\ I\ 0\ 0]^{\mathrm{T}}$ for right- and left-handed circular polarization, respectively.

7.5:

$$\mathbf{L}^{\mathrm{MS}}(\eta) = \mathbf{B}\mathbf{L}(\eta)\mathbf{B}^{-1} = \begin{bmatrix} \cos^2\eta & \sin^2\eta & -\frac{1}{2}\sin 2\eta & 0 \\ \sin^2\eta & \cos^2\eta & \frac{1}{2}\sin 2\eta & 0 \\ \sin 2\eta & -\sin 2\eta & \cos 2\eta & 0 \\ 0 & 0 & 0 & 1 \end{bmatrix}, \tag{H.12}$$

$$\mathbf{L}^{\mathrm{CP}}(\eta) = \mathbf{A}\mathbf{L}(\eta)\mathbf{A}^{-1} = \begin{bmatrix} \exp(\mathrm{i}2\eta) & 0 & 0 & 0 \\ 0 & 1 & 0 & 0 \\ 0 & 0 & 1 & 0 \\ 0 & 0 & 0 & \exp(-\mathrm{i}2\eta) \end{bmatrix}. \tag{H.13}$$

7.7: Use the formula $\mathbf{L}(\eta) = \mathbf{A}^{-1}\mathbf{L}^{\mathrm{CP}}(\eta)\mathbf{A}$ and the matrix identity $(\mathbf{GH})^{-1} = \mathbf{H}^{-1}$

$\times \mathbf{G}^{-1}$ along with Eqs. (7.49)–(7.50).

8.1:
$$\mathbf{S} = (P^*_{zy} - P^*_{yz})\hat{\mathbf{x}} + (P^*_{xz} - P^*_{zx})\hat{\mathbf{y}} + (P^*_{yx} - P^*_{xy})\hat{\mathbf{z}}. \tag{H.14}$$

8.2: In this case, $\mathbf{H}(\mathbf{r}) = (\epsilon/\mu)^{1/2}\,\hat{\mathbf{n}} \times \mathbf{E}(\mathbf{r})$, where the unit vector $\hat{\mathbf{n}}$ specifies the local propagation direction. Therefore, one has in local spherical coordinates (Fig. 7.1):

$$\mathbf{S} = (P^*_{\varphi\theta} - P^*_{\theta\varphi})\hat{\mathbf{n}}, \tag{H.15}$$

$$\mathbf{I} = \begin{bmatrix} P^*_{\varphi\theta} - P^*_{\theta\varphi} \\ P^*_{\varphi\theta} + P^*_{\theta\varphi} \\ P^*_{\theta\theta} - P^*_{\varphi\varphi} \\ \mathrm{i}(P^*_{\theta\theta} + P^*_{\varphi\varphi}) \end{bmatrix}. \tag{H.16}$$

8.3: Use the first equalities of Eqs. (4.2) and (4.3).

9.1: Let us first consider the superposition of two monochromatic plane waves with different angular frequencies. We have

$$I_1^2 = Q_1^2 + U_1^2 + V_1^2, \quad I_2^2 = Q_2^2 + U_2^2 + V_2^2, \tag{H.17}$$

from which we need to prove that

$$(I_1 + I_2)^2 \geq (Q_1 + Q_2)^2 + (U_1 + U_2)^2 + (V_1 + V_2)^2. \tag{H.18}$$

In view of Eq. (H.17), proving the inequality (H.18) is equivalent to proving that

$$I_1 I_2 \geq Q_1 Q_2 + U_1 U_2 + V_1 V_2. \tag{H.19}$$

This latter inequality follows from the positivity of the intensities I_1 and I_2 combined with the Cauchy–Schwartz inequality

$$\left(\sum_{n=1}^{N} a_n b_n\right)^2 \leq \left(\sum_{n=1}^{N} a_n^2\right)\left(\sum_{n=1}^{N} b_n^2\right), \tag{H.20}$$

where a_n and b_n are real numbers. Indeed,

$$(Q_1 Q_2 + U_1 U_2 + V_1 V_2)^2 \leq (Q_1^2 + U_1^2 + V_1^2)(Q_2^2 + U_2^2 + V_2^2) = I_1^2 I_2^2. \tag{H.21}$$

Let us now denote $I_{12} = I_1 + I_2$, $Q_{12} = Q_1 + Q_2$, $U_{12} = U_1 + U_2$, $V_{12} = V_1 + V_2$ and add a third monochromatic plane wave to the mix. In this case

$$I_{12}^2 \geq Q_{12}^2 + U_{12}^2 + V_{12}^2, \quad I_3^2 = Q_3^2 + U_3^2 + V_3^2, \tag{H.22}$$

and we have again

$$(I_{12} + I_3)^2 \geq (Q_{12} + Q_3)^2 + (U_{12} + U_3)^2 + (V_{12} + V_3)^2. \tag{H.23}$$

The general case of an arbitrary number of monochromatic plane waves is then handled by induction.

9.2: Let us first consider the superposition of two monochromatic plane waves with different angular frequencies. For Eq. (H.17) to imply

$$(I_1 + I_2)^2 = (Q_1 + Q_2)^2 + (U_1 + U_2)^2 + (V_1 + V_2)^2, \tag{H.24}$$

the following equality must hold:

$$I_1 I_2 = Q_1 Q_2 + U_1 U_2 + V_1 V_2. \tag{H.25}$$

The equality in Eq. (H.20) holds only if $a_n = \alpha b_n$ for any n, where α is a real-valued constant. Therefore,

$$(Q_1 Q_2 + U_1 U_2 + V_1 V_2)^2 = (Q_1^2 + U_1^2 + V_1^2)(Q_2^2 + U_2^2 + V_2^2) = I_1^2 I_2^2 \tag{H.26}$$

only if $Q_1 = \alpha Q_2$, $U_1 = \alpha U_2$, and $V_1 = \alpha V_2$, which implies that $I_1 = |\alpha| I_2$. For $(Q_1 Q_2 + U_1 U_2 + V_1 V_2)^2 = I_1^2 I_2^2$ to yield Eq. (H.25), α must be positive. This proves Eq. (9.19) for the case $N = 2$. The general case of an arbitrary number of monochromatic plane waves is handled by induction.

9.3: Let us first consider the case of two quasi-monochromatic waves, of which the first is partially polarized. Omitting for the sake of brevity the angular brackets $\langle\langle\cdots\rangle\rangle$, we have for the respective time-averaged Stokes parameters:

$$I_1^2 > Q_1^2 + U_1^2 + V_1^2, \qquad I_2^2 \geq Q_2^2 + U_2^2 + V_2^2, \tag{H.27}$$

from which we need to prove that

$$(I_1 + I_2)^2 > (Q_1 + Q_2)^2 + (U_1 + U_2)^2 + (V_1 + V_2)^2. \tag{H.28}$$

In view of Eq. (H.27), proving the inequality (H.28) is equivalent to proving that

$$I_1 I_2 \geq Q_1 Q_2 + U_1 U_2 + V_1 V_2. \tag{H.29}$$

This latter inequality follows from the positivity of the intensities I_1 and I_2 combined with the Cauchy–Schwartz inequality. Indeed,

$$(Q_1 Q_2 + U_1 U_2 + V_1 V_2)^2 \leq (Q_1^2 + U_1^2 + V_1^2)(Q_2^2 + U_2^2 + V_2^2) < I_1^2 I_2^2. \tag{H.30}$$

The general case of an arbitrary number of quasi-monochromatic waves is handled by induction.

9.4: Take into account the definitions (9.37)–(9.39) and Eqs. (7.7)–(7.8).

10.1: Use the dyadic identity (A.17).

10.2: Write Eq. (10.7) in Cartesian coordinates and use Eq. (H.14).

10.3: Equations (10.16) (10.23), and (10.38) become, respectively,

$$\ddot{P}(\mathbf{r}) = \sum_{n=1}^{N} \hat{\mathcal{T}}(\mathbf{r}, \hat{\mathbf{n}}_n^{\text{inc}}, \omega_n)\, \ddot{P}_n^{\text{inc}}, \tag{H.31}$$

$$\langle\langle \ddot{P}(\mathbf{r}, t)\rangle\rangle = \sum_{n=1}^{N} \hat{\mathcal{T}}(\mathbf{r}, \hat{\mathbf{n}}_n^{\text{inc}}, \omega_n) \langle\langle \ddot{P}_n^{\text{inc}}(t)\rangle\rangle. \tag{H.32}$$

$$\langle\langle \ddot{P}(\mathbf{r}, t)\rangle\rangle = \sum_{n=1}^{N} \langle\langle \hat{\mathcal{T}}(\mathbf{r}, \hat{\mathbf{n}}_n^{\text{inc}}, \omega_n, t)\rangle\rangle \langle\langle \ddot{P}_n^{\text{inc}}(t)\rangle\rangle, \tag{H.33}$$

where $\hat{\mathbf{n}}_n^{\text{inc}}$ is the incidence direction of the nth monochromatic or quasi-monochromatic component.

11.1: From $\mathcal{H}_i = (\epsilon_1/\mu_0)^{1/2}\, \hat{\mathbf{n}} \times \mathcal{E}_i$ for any i and the vector identity (3.18), we derive:

$$\sum_{i=1}^{N} \mathcal{E}_i \times \sum_{j=1}^{N} \mathcal{H}_j = \hat{\mathbf{n}} \sqrt{\frac{\epsilon_1}{\mu_0}} \left| \sum_{i=1}^{N} \mathcal{E}_i \right|^2. \tag{H.34}$$

13.2:

$$\begin{aligned}
\langle W_2 \rangle &= \int_{S_{\text{ep}2}} \mathrm{d}^2\mathbf{r}'\, \hat{\mathbf{r}}' \cdot \langle \mathcal{S}(\mathbf{r}', t)\rangle \\
&\approx S_{\text{ep}} \frac{1}{2} \sqrt{\frac{\epsilon_1}{\mu_0}}\, |\mathbf{E}_0^{\text{inc}}|^2 + \int_{S_{\text{ep}2}} \mathrm{d}^2\mathbf{r}'\, \hat{\mathbf{n}}^{\text{inc}} \cdot [\langle \mathcal{S}^{\text{sca}}(\mathbf{r}', t)\rangle + \langle \mathcal{S}^{\text{ext}}(\mathbf{r}', t)\rangle] \\
&\approx S_{\text{ep}} \frac{1}{2} \sqrt{\frac{\epsilon_1}{\mu_0}} \left[|\mathbf{E}_0^{\text{inc}}|^2 + \frac{1}{r^2} |\mathbf{E}_1^{\text{sca}}(\hat{\mathbf{n}}^{\text{inc}})|^2 \right] \\
&\quad + r^2 \int_{\Omega_{\text{ep}2}} \mathrm{d}\hat{\mathbf{r}}'\, \hat{\mathbf{n}}^{\text{inc}} \cdot \langle \mathcal{S}^{\text{ext}}(r'\hat{\mathbf{r}}', t)\rangle \\
&\approx S_{\text{ep}} \frac{1}{2} \sqrt{\frac{\epsilon_1}{\mu_0}} \left[|\mathbf{E}_0^{\text{inc}}|^2 + \frac{1}{r^2} |\mathbf{E}_1^{\text{sca}}(\hat{\mathbf{n}}^{\text{inc}})|^2 \right] \\
&\quad - \frac{2\pi}{k_1} \sqrt{\frac{\epsilon_1}{\mu_0}}\, \mathrm{Im}[\mathbf{E}_1^{\text{sca}}(\hat{\mathbf{n}}^{\text{inc}}) \cdot (\mathbf{E}_0^{\text{inc}})^*],
\end{aligned}$$

where $\Omega_{\text{ep}2} = S_{\text{ep}2}/r^2$ is the solid angle centered around the direction $\hat{\mathbf{n}}^{\text{inc}}$ and subtended by the entrance pupil of WCR 2 at the distance r from the origin.

13.3: Use Eqs. (7.43) and (7.46).

13.5: $\mathsf{Z}^J(-\hat{\mathbf{n}}^{\text{inc}}, -\hat{\mathbf{n}}^{\text{sca}}) = \mathsf{D}^{-1}\mathsf{Z}(-\hat{\mathbf{n}}^{\text{inc}}, -\hat{\mathbf{n}}^{\text{sca}})\mathsf{D}$

$$
\begin{aligned}
&= \mathbf{D}^{-1}\mathbf{\Delta}_3[\mathbf{Z}(\hat{\mathbf{n}}^{\text{sca}}, \hat{\mathbf{n}}^{\text{inc}})]^{\text{T}}\mathbf{\Delta}_3\mathbf{D} \\
&= \mathbf{D}^{-1}\mathbf{\Delta}_3[\mathbf{D}\,\mathbf{Z}^J(\hat{\mathbf{n}}^{\text{sca}}, \hat{\mathbf{n}}^{\text{inc}})\mathbf{D}^{-1}]^{\text{T}}\mathbf{\Delta}_3\mathbf{D} \\
&= \mathbf{D}^{-1}\mathbf{\Delta}_3[\mathbf{D}^{-1}]^{\text{T}}[\mathbf{Z}^J(\hat{\mathbf{n}}^{\text{sca}}, \hat{\mathbf{n}}^{\text{inc}})]^{\text{T}}\mathbf{D}^{\text{T}}\mathbf{\Delta}_3\mathbf{D} \\
&= \mathbf{\Delta}_{23}[\mathbf{Z}^J(\hat{\mathbf{n}}^{\text{sca}}, \hat{\mathbf{n}}^{\text{inc}})]^{\text{T}}\mathbf{\Delta}_{23},
\end{aligned}
\tag{H.35}
$$

where

$$
\mathbf{\Delta}_{23} = \mathbf{\Delta}_{23}^{\text{T}} = \mathbf{\Delta}_{23}^{-1} = \text{diag}[1, -1, -1, 1]. \tag{H.36}
$$

14.3: Make use of Eq. (5.35).

15.4: In this case, Eq. (15.5) holds whereas Eq. (15.4) does not. Therefore, Eqs, (13.62)–(13.68), (15.39), and (15.40) yield

$$
\begin{aligned}
&\langle \mathbf{K}(\hat{\mathbf{n}}^{\text{inc}}; \xi)\rangle_\xi \equiv \langle \mathbf{K}(\xi)\rangle_\xi \\
&= \begin{bmatrix} \langle K_{11}(\xi)\rangle_\xi & 0 & 0 & \langle K_{14}(\xi)\rangle_\xi \\ 0 & \langle K_{11}(\xi)\rangle_\xi & \langle K_{23}(\xi)\rangle_\xi & 0 \\ 0 & -\langle K_{23}(\xi)\rangle_\xi & \langle K_{11}(\xi)\rangle_\xi & 0 \\ \langle K_{14}(\xi)\rangle_\xi & 0 & 0 & \langle K_{11}(\xi)\rangle_\xi \end{bmatrix}.
\end{aligned}
\tag{H.37}
$$

15.7: If the incident quasi-monochromatic beam of light is polarized linearly in the scattering plane then $\langle\langle Q^{\text{inc}}\rangle\rangle = \langle\langle I^{\text{inc}}\rangle\rangle$, whereas $\langle\langle U^{\text{inc}}\rangle\rangle = \langle\langle V^{\text{inc}}\rangle\rangle = 0$. It is easily seen that the corresponding angular distributions of the co-polarized and cross-polarized scattered intensities are given by

$$
\frac{1}{2}[\langle\langle I^{\text{sca}}(\Theta)\rangle\rangle + \langle\langle Q^{\text{sca}}(\Theta)\rangle\rangle] \propto \frac{1}{2}[a_1(\Theta) + 2b_1(\Theta) + a_2(\Theta)]\langle\langle I^{\text{inc}}\rangle\rangle, \tag{H.38}
$$

$$
\frac{1}{2}[\langle\langle I^{\text{sca}}(\Theta)\rangle\rangle - \langle\langle Q^{\text{sca}}(\Theta)\rangle\rangle] \propto \frac{1}{2}[a_1(\Theta) - a_2(\Theta)]\langle\langle I^{\text{inc}}\rangle\rangle. \tag{H.39}
$$

Therefore, the LPR is given by

$$
\mu_{\text{L}}(\Theta) = \frac{a_1(\Theta) - a_2(\Theta)}{a_1(\Theta) + 2b_1(\Theta) + a_2(\Theta)}. \tag{H.40}
$$

15.8: Equations (F.5), (F.7), (15.75), and (15.76) yield for the exact forward and exact backward directions:

$$
a_1(0) = \sum_{s=0}^{s_{\max}} \alpha_1^s, \tag{H.41}
$$

$$
2a_2(0) = \sum_{s=0}^{s_{\max}} (\alpha_2^s + \alpha_3^s), \tag{H.42}
$$

$$a_4(0) = \sum_{s=0}^{s_{\max}} \alpha_4^s, \tag{H.43}$$

$$a_1(\pi) = \sum_{s=0}^{s_{\max}} (-1)^s \alpha_1^s, \tag{H.44}$$

$$2a_2(\pi) = \sum_{s=0}^{s_{\max}} (-1)^s (\alpha_2^s - \alpha_3^s), \tag{H.45}$$

$$a_4(\pi) = \sum_{s=0}^{s_{\max}} (-1)^s \alpha_4^s. \tag{H.46}$$

15.9: Make use of Table F.1.

15.11: See Fig. H.2.

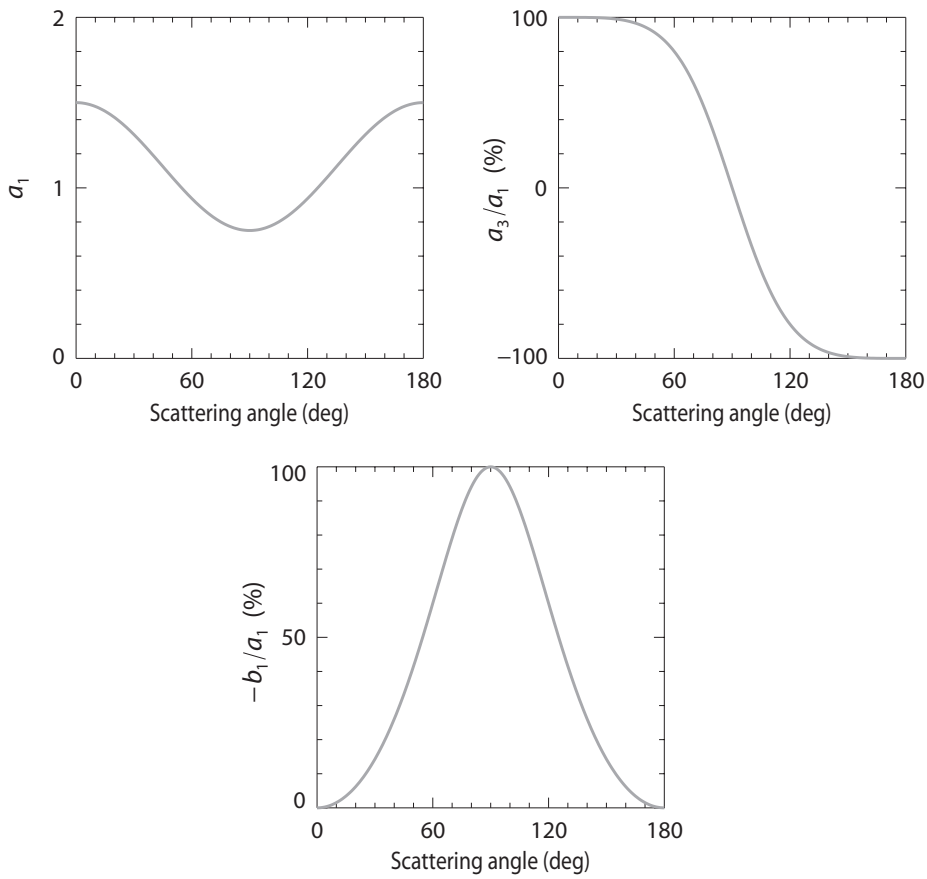

Fig. H.2. Elements of the normalized scattering matrix for a spherically symmetric Rayleigh particle.

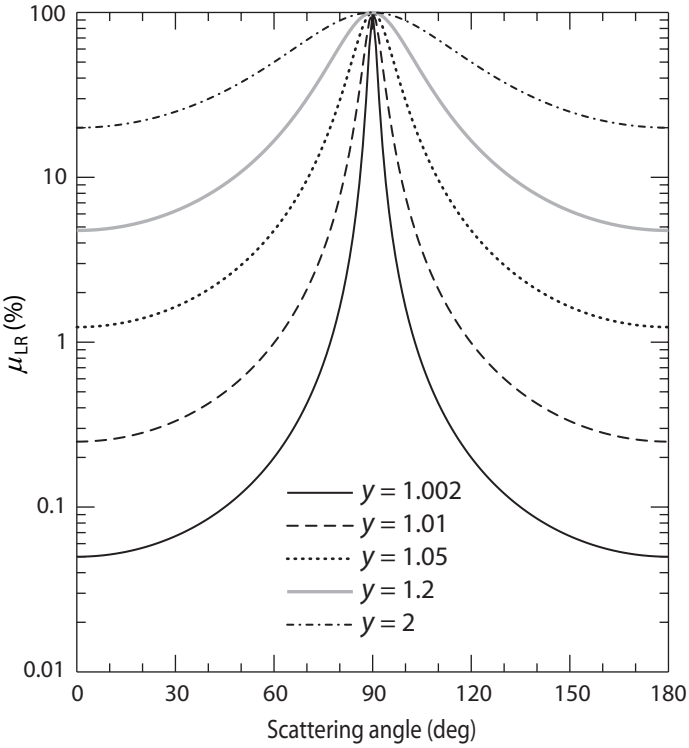

Fig. H.3. Linear polarization ratio for a nonspherical Rayleigh particle in random orientation.

15.12:

$$\mu_{LR}(\Theta) = \frac{y-1}{y+2\cos 2\Theta+1}. \tag{H.47}$$

This quantity is plotted in Fig. H.3 for $1 \le y \le 2$. Please note the logarithmic vertical scale.

15.13: Let us assume that r_{max} remains finite while being increased in small steps until the average scattering and absorption characteristics of the size distribution, as well as its effective radius and effective variance computed according to Eqs. (15.109)–(15.111) converge within a prescribed numerical accuracy. Then the truncated size distribution with the "converged" finite r_{max} is numerically equivalent to the distribution with $r_{max} = \infty$. Assuming that $r_{min} = 0$ and $r_{max} = \infty$ in Eq. (15.108) implies that

$$\text{constant} = \frac{1}{\Gamma[(1-2b)/b](ab)^{(1-2b)/b}}, \tag{H.48}$$

$$r_{eff} = a, \quad v_{eff} = b, \tag{H.49}$$

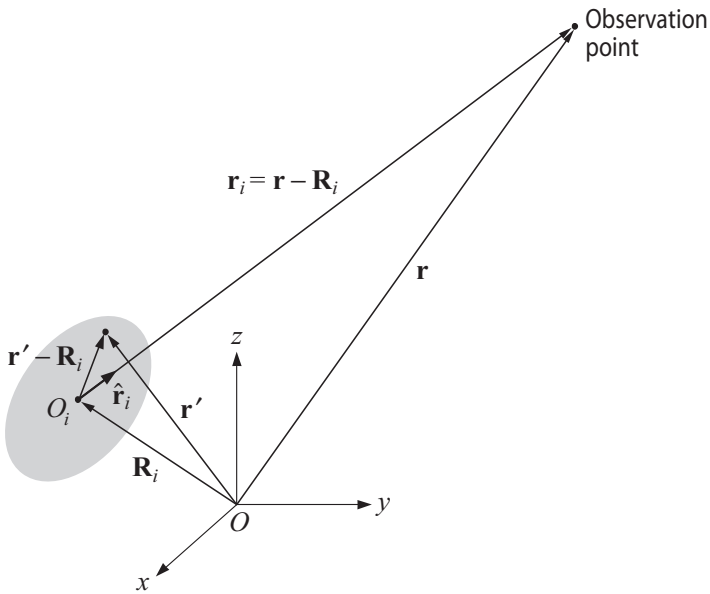

Fig. H.4. Notation used in Eq. (H.51).

where $\Gamma(x)$ is the gamma function (see Chapter 8 of Arfken and Weber (2005)).

15.14:

$$\alpha^s_{1,\mathrm{HG}} = (2s+1)g^s, \quad g_{\mathrm{HG}} = g. \tag{H.50}$$

16.1: Make use of Eqs. (16.23)–(16.25) and keep in mind that m ranges from $-n$ to $+n$ according to Eqs. (16.18)–(16.21).

17.1: Use the following input parameters for each effective size parameter and relative refractive index: NDISTR = 4, AA = x_{eff}, BB = 0.2, R1 = 0, R2 = $8x_{\mathrm{eff}}$, LAM = 2π, MRR = m, MRI = 0, N = 10, NK = 100, NPNA = 19, DDELT = 0.0001 (the parameters GAM and NP are ignored). Compare the resulting plots with Plate 1 in Mishchenko and Travis (1997).

18.1: Consider, for example, the term $\hat{G}\hat{T}_i\hat{G}\hat{T}_j\hat{G}\hat{T}_l E^{\mathrm{inc}}$ on the right-hand side of Eq. (6.20), assuming that the observation point is located in the far zone of the ith particle. Using the translational invariance property (B.14) and the asymptotic relation (B.21), we have

$$\vec{G}(\mathbf{r},\mathbf{r}') = \vec{G}(\mathbf{r}-\mathbf{R}_i,\mathbf{r}'-\mathbf{R}_i) = \vec{G}(\mathbf{r}_i,\mathbf{r}'-\mathbf{R}_i)$$
$$\underset{r_i\to\infty}{\to} (\vec{I} - \hat{\mathbf{r}}_i\otimes\hat{\mathbf{r}}_i)\frac{\exp(\mathrm{i}k_1 r_i)}{4\pi r_i}\exp[-\mathrm{i}k_1\hat{\mathbf{r}}_i\cdot(\mathbf{r}'-\mathbf{R}_i)], \quad \mathbf{r}'\in V_i, \tag{H.51}$$

the notation being explained in Fig. H.4. After the requisite $\mathbf{r}'$-integration

over the volume V_i, the constant factor $(\vec{I} - \hat{\mathbf{r}}_i \otimes \hat{\mathbf{r}}_i)\exp(\mathrm{i}k_1 r_i)(4\pi r_i)^{-1}$ defines an outgoing transverse spherical wave centered at O_i.

18.4: If the incident quasi-monochromatic beam of light is polarized circularly in the counter-clockwise direction when looking in the direction of propagation then $\langle\langle V^{\mathrm{inc}}\rangle\rangle = \langle\langle I^{\mathrm{inc}}\rangle\rangle$, whereas $\langle\langle Q^{\mathrm{inc}}\rangle\rangle = \langle\langle U^{\mathrm{inc}}\rangle\rangle = 0$. It is easily seen that the corresponding angular distributions of the same-helicity and opposite-helicity scattered intensities are given by

$$\frac{1}{2}[\langle\langle I^{\mathrm{sca}}(\Theta)\rangle\rangle + \langle\langle V^{\mathrm{sca}}(\Theta)\rangle\rangle] \propto \frac{1}{2}[a_1(\Theta) + a_4(\Theta)]\langle\langle I^{\mathrm{inc}}\rangle\rangle, \tag{H.52}$$

$$\frac{1}{2}[\langle\langle I^{\mathrm{sca}}(\Theta)\rangle\rangle - \langle\langle V^{\mathrm{sca}}(\Theta)\rangle\rangle] \propto \frac{1}{2}[a_1(\Theta) - a_4(\Theta)]\langle\langle I^{\mathrm{inc}}\rangle\rangle. \tag{H.53}$$

Therefore, the CPR is given by

$$\mu_{\mathrm{C}}(\Theta) = \frac{a_1(\Theta) + a_4(\Theta)}{a_1(\Theta) - a_4(\Theta)}. \tag{H.54}$$

19.2: Equation (A.16), the matrix identity $(\mathbf{AB})^{\mathrm{T}} = \mathbf{B}^{\mathrm{T}}\mathbf{A}^{\mathrm{T}}$, and the reciprocity relations (5.30) and (5.31) imply that

$$\vec{\eta}(-\hat{\mathbf{s}}, s) = [\vec{\eta}(\hat{\mathbf{s}}, s)]^{\mathrm{T}}, \tag{H.55}$$

$$\mathbf{h}(-\hat{\mathbf{s}}, s) = \begin{bmatrix} 1 & 0 \\ 0 & -1 \end{bmatrix}[\mathbf{h}(\hat{\mathbf{s}}, s)]^{\mathrm{T}}\begin{bmatrix} 1 & 0 \\ 0 & -1 \end{bmatrix}. \tag{H.56}$$

19.4: Equation (13.70) implies that

$$\mathbf{H}(-\hat{\mathbf{s}}, s) = \mathbf{\Delta}_3[\mathbf{H}(\hat{\mathbf{s}}, s)]^{\mathrm{T}}\mathbf{\Delta}_3. \tag{H.57}$$

19.6: Use Eqs. (A.16) and (A.17).

19.7: Use Eq. (B.15) and the formulas

$$\nabla\times(f\vec{C}) = (\nabla f)\times\vec{C} + f\nabla\times\vec{C}, \tag{H.58}$$

$$\nabla[r^{-1}\exp(\mathrm{i}kr)] = (\mathrm{i}k - r^{-1})r^{-1}\exp(\mathrm{i}kr)\hat{\mathbf{r}} \underset{kr\gg 1}{\rightarrow} \mathrm{i}kr^{-1}\exp(\mathrm{i}kr)\hat{\mathbf{r}}. \tag{H.59}$$

19.8: Use the Leibniz rule

$$\frac{\partial}{\partial b}\int_a^b \mathrm{d}x\, f(x, b) = f(b, b) + \int_a^b \mathrm{d}x\, \frac{\partial f(x, b)}{\partial b}. \tag{H.60}$$

19.9: Use Eqs. (19.18) and (19.65) as well as the transversality of the scattering dyadic.

19.11: Since all elements of the extinction matrix and the column $\mathbf{I}^{\mathrm{inc}}$ are real valued, Eqs. (19.40) and (19.41) imply that the column $\mathbf{I}_{\mathrm{c}}(\mathbf{r})$ is also real val-

ued. All elements of the phase matrix are real valued as well. Therefore, iterating Eq. (19.83) and using the first term on the right-hand side as the initial approximation proves that $\widetilde{\mathbf{I}}_{\mathrm{d}}(Q, \hat{\mathbf{q}})$ is real valued too.

19.12: Use Eq. (19.69), the formulas $\hat{\mathbf{q}} \times \hat{\boldsymbol{\theta}}(\hat{\mathbf{q}}) = \hat{\boldsymbol{\varphi}}(\hat{\mathbf{q}})$ and $\hat{\mathbf{q}} \times \hat{\boldsymbol{\varphi}}(\hat{\mathbf{q}}) = -\hat{\boldsymbol{\theta}}(\hat{\mathbf{q}})$, and the definitions (19.88), (19.81), and (19.82).

19.16: First, solve Eq. (19.83) by iteration, using the first term on the right-hand side as the initial approximation. Second, assume that the number of particles in the scattering volume is sufficiently small that $|n_0 L[\langle \mathbf{K}(\hat{\mathbf{q}})\rangle_\xi]_{pq}| \ll 1$ and $|n_0 L[\langle \mathbf{Z}(\hat{\mathbf{q}}, \hat{\mathbf{q}}')\rangle_\xi]_{pq}| \ll 1$ for p, q = 1, …, 4 and for any $\hat{\mathbf{q}}$ and $\hat{\mathbf{q}}'$, where L is the largest linear dimension of the particulate volume. As a consequence, all terms proportional to powers of n_0 higher than the first can be neglected.

19.17: Let $\widetilde{\mathbf{I}}^{\mathrm{tot}}(\mathbf{r}, \hat{\mathbf{q}}, \hat{\mathbf{s}})$ be the specific intensity column vector corresponding to the case of the incident field represented by a parallel polychromatic beam with quasi-monochromatic components propagating in the direction of the unit vector $\hat{\mathbf{s}}$ (see Eq. (19.109)). If the incident field is a superposition of M polychromatic beams with propagation directions $\hat{\mathbf{s}}_i$, i = 1, 2, …, M, then the resulting specific intensity column vector is given by

$$\widetilde{\mathbf{I}}^{\mathrm{tot}}(\mathbf{r}, \hat{\mathbf{q}}) = \sum_{i=1}^{M} \widetilde{\mathbf{I}}^{\mathrm{tot}}(\mathbf{r}, \hat{\mathbf{q}}, \hat{\mathbf{s}}_i). \tag{H.61}$$

19.18: Note that $I_{\mathrm{c}}(\mathbf{r}) = \rho_{\mathrm{c}\theta\theta}(\mathbf{r}) + \rho_{\mathrm{c}\varphi\varphi}(\mathbf{r})$ and $\widetilde{I}_{\mathrm{d}}(\mathbf{r}, \hat{\mathbf{q}}) = \widetilde{\rho}_{\mathrm{d}\theta\theta}(\mathbf{r}, \hat{\mathbf{q}}) + \widetilde{\rho}_{\mathrm{d}\varphi\varphi}(\mathbf{r}, \hat{\mathbf{q}})$, where $\boldsymbol{\rho}_{\mathrm{c}}(\mathbf{r})$ and $\widetilde{\boldsymbol{\rho}}_{\mathrm{d}}(\mathbf{r}, \hat{\mathbf{q}})$ are given by Eqs. (19.72) and (19.73), respectively. The nonnegativity of $I_{\mathrm{c}}(\mathbf{r})$ follows from Eq. (19.58). The nonnegativity of $\widetilde{I}_{\mathrm{d}}(\mathbf{r}, \hat{\mathbf{q}})$ can be shown by solving Eq. (19.74) iteratively. The initial approximation is the first term on the right-hand side of this equation. It is easily seen that the integrand can be represented by a matrix product of the type

$$\begin{bmatrix} a \\ b \end{bmatrix} [a^* \;\; b^*], \tag{H.62}$$

which implies the nonnegativity of the initial approximation for $\widetilde{I}_{\mathrm{d}}(\mathbf{r}, \hat{\mathbf{q}})$. The substitution of this initial approximation in the second integral on the right-hand side of Eq. (19.74) also leads to an integrand of the type (H.62), and so on. This implies the nonnegativity of each iterative approximation for $\widetilde{I}_{\mathrm{d}}(\mathbf{r}, \hat{\mathbf{q}})$ and, by induction, the nonnegativity of $\widetilde{I}_{\mathrm{d}}(\mathbf{r}, \hat{\mathbf{q}})$.

19.19: Recall the solution of Problem 19.18 and take into account that the integrand of the type (H.62) yields a differential contribution to $\widetilde{\mathbf{I}}_{\mathrm{d}}(\mathbf{r}, \hat{\mathbf{q}})$ satisfying the Stokes identity (7.4). Subsequent integration over coordinates and states coupled with the Cauchy–Schwartz inequality implies that the

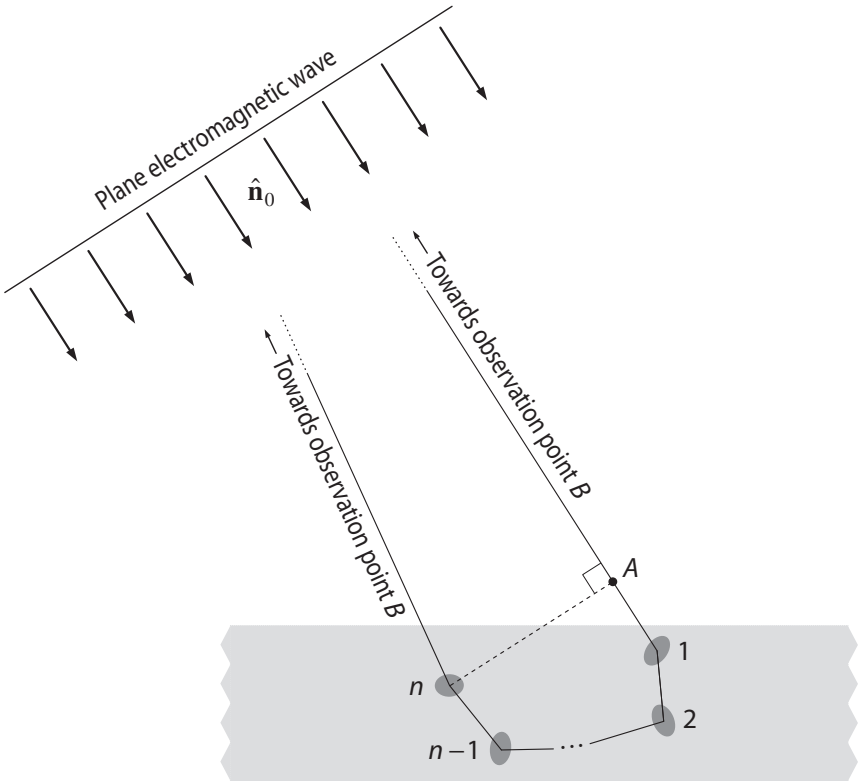

Fig. H.5. Derivation of Eq. (H.66).

elements of $\widetilde{\mathbf{I}}_{\mathrm{d}}(\mathbf{r}, \hat{\mathbf{q}})$ satisfy the Stokes–Verdet inequality (9.34) (see the solution of Problem 9.1).

20.2: Differentiate Eqs. (20.11) and (20.12) with respect to τ.

20.5:

$$\mathbf{R}^1(\mu, \varphi; \mu_0, \varphi_0) = \frac{\varpi}{4} \frac{1 - \exp\left[-\mathcal{T}\left(\frac{1}{\mu} + \frac{1}{\mu_0}\right)\right]}{\mu + \mu_0} \widetilde{\mathbf{Z}}(-\mu, \varphi; \mu_0, \varphi_0), \quad \text{(H.63)}$$

$$\mathbf{T}^1(\mu, \varphi; \mu_0, \varphi_0) = \frac{\varpi}{4} \frac{\mathrm{e}^{-\mathcal{T}/\mu_0} - \mathrm{e}^{-\mathcal{T}/\mu}}{\mu_0 - \mu} \widetilde{\mathbf{Z}}(\mu, \varphi; \mu_0, \varphi_0) \text{ if } \mu \neq \mu_0, \quad \text{(H.64)}$$

$$\mathbf{T}^1(\mu_0, \varphi; \mu_0, \varphi_0) = \frac{\varpi}{4} \frac{\mathcal{T}\,\mathrm{e}^{-\mathcal{T}/\mu_0}}{\mu_0^2} \widetilde{\mathbf{Z}}(\mu_0, \varphi; \mu_0, \varphi_0). \quad \text{(H.65)}$$

21.1: To estimate how far the observation point should be from a particulate slab, let us assume that it lies on the straight line originating at particle 1 and drawn in the exact backscattering direction $-\hat{\mathbf{n}}_0$ (see Fig. H.5). Then the requirement that the phase difference between the two reciprocal paths

going through particles $1 \to 2 \to \ldots \to n-1 \to n$ and $n \to n-1 \to \ldots \to 2 \to 1$ and arriving at the observation point B be much smaller than one implies that

$$\frac{k_1(\overline{nA})^2}{2\,\overline{AB}} \ll 1, \tag{H.66}$$

where $\overline{AB}$ is the distance between points A and B. Thus, in general, the distance D from the scattering medium to the observation point must satisfy the inequality (21.4).

21.2: The phase difference between very long multi-particle sequences becomes randomized. As a consequence, the angular widths of various manifestations of WL can increase, while the WL intensity peaks can become rounded and their amplitudes can decrease.

21.3: The following inequalities must be satisfied: $\langle l \rangle / D \ll d/f \ll 2\alpha_{\mathrm{HWHM},I}$. The first inequality ensures that for the majority of multi-particle sequences, the WCR captures the backscattering interference of the wavelets coming from both end particles (see Fig. H.5).

B.1: Use Eq. (3.27).

B.2: Recall Eq. (A.20) and the vector identities $\hat{\mathbf{r}} \times \hat{\boldsymbol{\theta}} = \hat{\boldsymbol{\varphi}}$ and $\hat{\mathbf{r}} \times \hat{\boldsymbol{\varphi}} = -\hat{\boldsymbol{\theta}}$.

References

Abramowitz, M. and Stegun, I. A., eds. (1964). *Handbook of Mathematical Functions with Formulas, Graphs and Mathematical Tables* (National Bureau of Standards, Washington, DC).

Adam, J. A. (2002). The mathematical physics of rainbows and glories. *Phys. Rep.* **356**, 229–365.

Akhiezer, A. I. and Berestetskii, V. B. (1965). *Quantum Electrodynamics* (Wiley Interscience, New York).

Akhiezer, A. I. and Peletminskii, S. V. (1981). *Methods of Statistical Physics* (Pergamon Press, Oxford). (original Russian edition: Nauka, Moscow, 1977.)

Akkermans, E. and Montambaux, G. (2007). *Mesoscopic Physics of Electrons and Photons* (Cambridge University Press, Cambridge, UK).

Amic, E., Luck, J. M., and Nieuwenhuizen, Th. M. (1997). Multiple Rayleigh scattering of electromagnetic waves. *J. Phys. I (France)* **7**, 445–483.

Apresyan, L. A. and Kravtsov, Yu. A. (1996). *Radiation Transfer. Statistical and Wave Aspects* (Gordon and Breach, Basel).

Aptowicz, K. B., Pan, Y.-L., Martin, S. D., *et al.* (2013). Decomposition of atmospheric aerosol phase function by particle size and asphericity from measurements of single particle optical scattering patterns. *J. Quant. Spectrosc. Radiat. Transfer* **131**, 13–23.

Arfken, G. B. and Weber, H. J. (2005). *Mathematical Methods for Physicists* (Elsevier, Amsterdam).

Arnold, S., Holler, S., Li, J. H., *et al.* (1995). Aerosol particle microphotography and glare-spot absorption spectroscopy. *Opt. Lett.* **20**, 773–775.

Arnott, W. P., Dong, Y. Y., Hallett, J., and Poellot, M. R. (1994). Role of small ice crystals in radiative properties of cirrus: a case study, FIRE II, November 22, 1991. *J. Geophys. Res*. **99**, 1371–1381.

Arons, A. B. and Peppard, M. B. (1965). Einstein's proposal of the photon concept – a translation of the *Annalen der Physik* paper of 1905. *Am. J. Phys.* **33**, 367–374.

Asano, S. and Yamamoto, G. (1975). Light scattering by a spheroidal particle. *Appl. Opt.* **14**, 29–49.

Azzam, R. M. A. and Bashara, N. M. (1977). *Ellipsometry and Polarized Light* (North Holland, Amsterdam).

Babenko, V. A., Astafyeva, L. G., and Kuzmin, V. N. (2003). *Electromagnetic Scattering in Disperse Media: Inhomogeneous and Anisotropic Particles* (Praxis Publishing, Chichester, UK).

Barabanenkov, Yu. N. (1973). Wave corrections to the transfer equation for "back" scattering. *Radiophys. Quantum Electron*. **16**, 65–71.

Barabanenkov, Yu. N. (1975). Multiple scattering of waves by ensembles of particles and the theory of radiation transport. *Sov. Phys.–Usp.* **18**, 673–689.

Baran, A. J. (2013). Light scattering by irregular particles in the Earth's atmosphere. *Light Scattering Rev.* **8**, 3–68.

Barber, P. W. and Hill, S. C. (1990). *Light Scattering by Particles: Computational Methods* (World Scientific, Singapore).

Barton, G. (1989). *Elements of Green's Functions and Propagation. Potentials, Diffusion and Waves* (Oxford University Press, Oxford).

Beer, A. (1854). *Grundriss des Photometrischen Calcüles* (Friedrich Vieweg und Sohn, Braunschweig).

Berg, M. J., Sorensen, C. M., and Chakrabarti, A. (2008). Extinction and the optical theorem. Part I. Single particles. *J. Opt. Soc. Am. A* **25**, 1504–1513.

Berglund, C. N. and Spicer, W. E. (1964). Photoemission studies of copper and silver: theory. *Phys. Rev.* **136**, A1030–A1044.

Berne, B. J. and Pecora, R. (1976). *Dynamic Light Scattering with Applications to Chemistry, Biology, and Physics* (Wiley, New York). (Also: Dover, Mineola, NY, 2000.)

Bi, L. and Yang, P. (2013). Physical-geometric optics hybrid methods for computing the scattering and absorption properties of ice crystals and dust aerosols. *Light Scattering Rev.* **8**, 69–114.

Bi, L., Yang, P., Kattawar, G. W., and Mishchenko, M. I. (2013a). Efficient implementation of the invariant imbedding T-matrix method and the separation of variables method applied to large nonspherical inhomogeneous particles. *J. Quant. Spectrosc. Radiat. Transfer* **116**, 169–183.

Bi, L., Yang, P., Kattawar, G. W., and Mishchenko, M. I. (2013b). A numerical combination of extended boundary condition method and invariant imbedding method applied to light scattering by large spheroids and cylinders. *J. Quant. Spectrosc. Radiat. Transfer* **123**, 17–22.

Bohm, D. (1951). *Quantum Theory* (Prentice-Hall, Englewood Cliffs, NJ).

Bohren, C. F. and Huffman, D. R. (1983). *Absorption and Scattering of Light by Small Particles* (Wiley, New York).

Boltzmann, L. (1893). *Vorlesungen über Maxwells Theorie der Elektricität und des Lichtes*, Vol. II (J. A. Barth, Leipzig).

Borghese, F., Denti, P., and Saija, R. (2007). *Scattering from Model Nonspherical Particles: Theory and Applications to Environmental Physics* (Springer, Berlin).

Borghese, F., Saija, R., Gucciardi, P. G., *et al.*, eds. (2012). Electromagnetic and light scattering XIII. *J. Quant. Spectrosc. Radiat. Transfer* **113**, 2277–2279.

Born, M. and Wolf, E. (1999). *Principles of Optics* (Cambridge University Press, Cambridge, UK).

Borovikov, V. A. and Kinber, B. Y. (1994). *Geometrical Theory of Diffraction* (IEE Press, Herts, UK).

Borovoi, A. G. (2006). Multiple scattering of short waves by uncorrelated and correlated scatterers. *Light Scattering Rev.* **1**, 181–252.

Borovoi, A. G. (2013). Light scattering by large particles: physical optics and shadow-forming field. *Light Scattering Rev.* **8**, 115–138.

Borovoy, A. G. (1966). Method of iterations in multiple scattering: the transfer equation. *Izv. Vuzov Fizika*, No. 6, 50–54 (in Russian).

Bouguer, P. (1729). *Essai d'Optique sur la Gradation de la Lumiere* (Claude Jombert, Paris).

Bouguer, P. (1760). *Traité d'Optique sur la Gradation de la Lumiere* (Académie Royale des Sciences, Paris). English translation by W. E. K. Middleton: *Pierre Bouguer's Optical Treatise on the Gradation of Light* (University of Toronto Press, Toronto, 1961).

Brosseau, C. (1998). *Polarized Light: A Statistical Optics Approach* (Wiley, New York).

Brown, W., ed. (1993). *Dynamic Light Scattering: The Method and Some Applications* (Oxford University Press, Oxford).

Bruning, J. H. and Lo, Y. T. (1971a). Multiple scattering of EM waves by spheres. I. Multipole expansion and ray-optical solutions. *IEEE Trans. Antennas Propag.* **19**, 378–390.

Bruning, J. H. and Lo, Y. T. (1971b). Multiple scattering of EM waves by spheres. II. Numerical and experimental results. *IEEE Trans. Antennas Propag.* **19**, 391–400.

Bukshtab, M. (2012). *Applied Photometry, Radiometry, and Measurements of Optical Lossess* (Springer, Dordrecht, The Netherlands).

Burr, D. W., Daun, K. J., Thomson, K. A., and Smallwood, G. J. (2012). Optimization of measurement angles for soot aggregate sizing by elastic light scattering, through design-of-experiment theory. *J. Quant. Spectrosc. Radiat. Transfer* **113**, 355–365.

Campbell, L. and Garnett, W. (1884). *The Life of James Clerk Maxwell* (Macmillan, London) (also Elibron Classics, New York, 2005).

Cannell, D. M. (2001). *George Green: Mathematician and Physicist 1793–1841: The Background to His Life and Work* (SIAM, Philadelphia).

Chamaillard, K., Jennings, S. G., Kleefeld, C., *et al.* (2003). Light backscattering and scattering by nonspherical sea-salt aerosols. *J. Quant. Spectrosc. Radiat. Transfer* **79–80**, 577–597.

Chandrasekhar, S. (1950). *Radiative Transfer* (Oxford University Press, Oxford). (Also: Dover, New York, 1960.)

Chwolson, O. (1889). Grundzüge einer mathematischen Theorie der inneren Diffusion des Lichtes. *Bull. l'Acad. Impériale Sci. St. Pétersbourg* **33**, 221–256.

Chyba, T. H. and Mandel, L. (1988). Angular sensitivity of a vacuum photodiode, or does a photodetector always count absorbed photons? *J. Opt. Soc. Am. B* **5**, 1305–1311.

Chýlek, P. (1976). Partial-wave resonances and the ripple structure in the Mie normalized extinction cross section. *J. Opt. Soc. Am.* **66**, 285–287.

Chýlek, P. and Zhan, J. (1989). Interference structure of the Mie extinction cross section. *J. Opt. Soc. Am. A* **6**, 1846–1851.

Chýlek, P., Kiehl, J. T., and Ko, M. K. W. (1978). Narrow resonance structure in the Mie scattering characteristics. *Appl. Opt.* **17**, 3019–3021.

Chýlek, P., Ramaswamy, V., Ashkin, A., and Dziedzic, J. M. (1983). Simultaneous determination of refractive index and size of spherical dielectric particles from light scattering data. *Appl. Opt.* **22**, 2302–2307.

Chýlek, P., Ngo, D., and Pinnick, R. G. (1992). Resonance structure of composite and slightly absorbing spheres. *J. Opt. Soc. Am. A* **9**, 775–780.

Ciric, I. R. and Cooray, F. R. (2000). Separation of variables for electromagnetic scattering by spheroidal particles. In *Light Scattering by Nonspherical Particles: Theory, Measurements, and Applications*, ed. M. I. Mishchenko, J. W. Hovenier, and L. D. Travis, pp. 89–130 (Academic Press, San Diego).

Clarke, D. (2010). *Stellar Polarimetry* (Wiley-VCH, Weinheim, Germany).

Clarke, D. and Grainger, J. F. (1971). *Polarized Light and Optical Measurement* (Pergamon Press, Oxford).

Cloude, S. (2010). *Polarisation: Applications in Remote Sensing* (Oxford University Press, Oxford).

Cohen-Tannoudji, C., Dupont-Roc, J., and Grynberg, G. (1989). *Photons and Atoms: Introduction to Quantum Electrodynamics* (Wiley, New York).

Cohen-Tannoudji, C., Dupont-Roc, J., and Grynberg, G. (1992). *Atom–Photon Interactions: Basic Processes and Applications* (Wiley, New York).

Collett, E. (1992). *Polarized Light: Fundamentals and Applications* (Marcel Dekker, New York).

Cooray, M. F. R. and Ciric, I. R. (1992). Scattering of electromagnetic waves by a coated dielectric spheroid. *J. Electromagn. Waves Appl.* **6**, 1491–1507.

Coulson, K. L. (1988). *Polarization and Intensity of Light in the Atmosphere* (A. Deepak Publishing, Hampton, VA).

Craig, D. P. and Thirunamachandran, T. (1984). *Molecular Quantum Electrodynamics: An Introduction to Radiation–Molecule Interactions* (Academic Press, London).

Crease, R. P. (2004). The greatest equations ever. *Phys. World* **17**(10), 14–15.

Crosignani, B., Di Porto, P., and Bertolotti, M. (1975). *Statistical Properties of Scattered Light* (Academic Press, New York).

Crosta, G. F., Pan, Y.-L., Aptowicz, K. B., *et al.* (2013). Automated classification of single airborne particles from two-dimensional angle-resolved optical scattering (*TAOS*) patterns by non-linear filtering. *J. Quant. Spectrosc. Radiat. Transfer* **131**, 215–233.

Cruzan, O. R. (1962). Translational addition theorems for spherical vector wave functions. *Quart. Appl. Math.* **20**, 33–40.

Davis, A. B. and Marshak, A. (2010). Solar radiation transport in the cloudy atmosphere: a 3D perspective on observations and climate impacts. *Rep. Prog. Phys.* **73**, 026801.

de Groot, S. R. (1969). *The Maxwell Equations* (North-Holland, Amsterdam).

de Groot, S. R. and Suttorp, L. G. (1972). *Foundations of Electrodynamics* (North-Holland, Amsterdam).

Deirmendjian, D. (1969). *Electromagnetic Scattering on Spherical Polydispersions* (Elsevier, New York).

Dlugach, J. M., Mishchenko, M. I., Liu, L., and Mackowski, D. W. (2011). Numerically exact computer simulations of light scattering by densely packed, random particulate media. *J. Quant. Spectrosc. Radiat. Transfer* **112**, 2068–2078.

Dodd, J. N. (1991). *Atoms and Light: Interactions* (Plenum Press, New York).

Doicu, A., Eremin, Yu., and Wriedt, T. (2000). *Acoustic and Electromagnetic Scattering Analysis Using Discrete Sources* (Academic Press, San Diego).

Doicu, A., Wriedt, T., and Eremin, Y. A. (2006). *Light Scattering by Systems of Particles: Null-Field Method with Discrete Sources – Theory and Programs* (Springer, Berlin).

Dolginov, A. Z., Gnedin, Yu. N., and Silant'ev, N. A. (1970). Photon polarization and frequency change in multiple scattering. *J. Quant. Spectrosc. Radiat. Transfer* **10**, 707–754.

Dolginov, A. Z., Gnedin, Yu. N., and Silant'ev, N. A. (1995). *Propagation and Polarization of Radiation in Cosmic Media* (Gordon and Breach, Basel).

Draine, B. T. and Flatau, P. J. (1994). Discrete dipole approximation for scattering calculations. *J. Opt. Soc. Am. A* **11**, 1491–1499.

Draine, B. T. and Flatau, P. J. (2012). User guide to the discrete dipole approximation code DDSCAT 7.2, http://arxiv.org/abs/1202.3424 (assessed November 2013).

Drew, T. B. (1961). *Handbook of Vector and Polyadic Analysis* (Reinhold, New York).

Dubovik, O., Sinyuk, A., Lapyonok, T., *et al.* (2006). Application of spheroid models to account for aerosol particle nonsphericity in remote sensing of desert dust. *J. Geophys. Res.* **111**, D11208.

Edmonds, A. R. (1996). *Angular Momentum in Quantum Mechanics* (Princeton University Press, Princeton, NJ).

Eppeldauer, G. P., Brown, S. W., and Lykke, K. R. (2005). Transfer standard filter radiometers: applications to fundamental scales. In *Optical Radiometry*, eds. A. C. Parr, R. U. Datla, and J. L. Gardner, pp. 155–211 (Elsevier, Amsterdam).

Fabelinskii, I. L. (1968). *Molecular Scattering of Light* (Plenum Press, New York).

Farafonov, V. G., Voshchinnikov, N. V., and Somsikov, V. V. (1996). Light scattering by a core-mantle spheroidal particle. *Appl. Opt.* **35**, 5412–5426.

Farquhar, I. E. (1964). *Ergodic Theory in Statistical Mechanics* (Wiley, London).

Fikioris, J. G. and Waterman, P. C. (1963). Multiple scattering of electromagnetic waves. Technical Memorandum RAD-TM-63-81, Avco Corporation, Wilmington, MA.

Fikioris, J. G. and Waterman, P. C. (2013). Multiple scattering of waves. III. The electromagnetic case. *J. Quant. Spectrosc. Radiat. Transfer* **123**, 8–16.

Foldy, L. L. (1945). The multiple scattering of waves. *Phys. Rev.* **67**, 107–119.

Freudenthaler, V., Homburg, F., and Jäger, H. (1996). Optical parameters of contrails from lidar measurements: linear depolarization. *Geophys. Res. Lett.* **23**, 3715–3718.

Fuller, K. A. (1995). Scattering and absorption cross sections of compounded spheres. III. Spheres containing arbitrarily located spherical inhomogeneities. *J. Opt. Soc. Am. A* **12**, 893–904.

Fuller, K. A. and Mackowski, D. W. (2000). Electromagnetic scattering by compounded spherical particles. In *Light Scattering by Nonspherical Particles: Theory, Measurements, and Applications*, ed. M. I. Mishchenko, J. W. Hovenier, and L. D. Travis, pp. 225–272 (Academic Press, San Diego).

Gans, R. (1924). Die Farbe des Meeres. *Ann. Phys.* **75**, 1–22.

Gehrels, T., ed. (1974). *Planets, Stars and Nebulae Studied with Photopolarimetry* (University of Arizona Press, Tucson, AZ).

Gelfand, I. M., Minlos, R. A., and Shapiro, Z. Ya. (1963). *Representations of the Rotation and Lorentz Groups and their Applications* (Pergamon Press, New York). (Original Russian edition: Gosudarstvennoe Izdatel'stvo Fiziko-Matematicheskoy Literatury, Moscow, 1958.)

Gershun, A. A. (1936). *The Light Field* (ONTI, Leningrad and Moscow) (in Russian). English translation by P. Moon and G. Timoshenko: *J. Phys. & Math.* **18**, 51–151 (1939).

Gibbs, J. W. and Wilson, E. B. (1909). *Vector Analysis* (Charles Scribner's Sons, New York).

Goldberger, M. L. and Watson, K. M. (1964). *Collision Theory* (Wiley, New York).

Goodman, J. W. (2005). *Introduction to Fourier Optics* (Roberts & Company, Englewood, CO).

Goodman, J. W. (2007). *Speckle Phenomena in Optics: Theory and Applications* (Roberts & Company, Englewood, CO).

Goody, R. M. and Yung, Y. L. (1989). *Atmospheric Radiation: Theoretical Basis* (Oxford University Press, New York).

Gouesbet, G. and Gréhan, G. (2011). *Generalized Lorenz–Mie Theories* (Springer, Berlin).

Grandy, W. T., Jr. (2000). *Scattering of Waves from Large Spheres* (Cambridge University Press, Cambridge, UK).

Gray, J. (2013). *Henri Poincaré – A Scientific Biography* (Princeton University Press, Princeton).

Green, G. (1828). *An Essay on the Application of Mathematical Analysis to the Theories of Electricity and Magnetism* (T. Wheelhouse, Nottingham).

Gross, P., Störzer, M., Fiebig, S., *et al.* (2007). A precise method to determine the angular distribution of backscattered light to high angles. *Rev. Sci. Instr.* **78**, 033105.

Gustafson, B. Å. S. (2000). Microwave analog to light-scattering measurements. In *Light Scattering by Nonspherical Particles: Theory, Measurements, and Applications*, ed. M. I. Mishchenko, J. W. Hovenier, and L. D. Travis, pp. 367–390 (Academic Press, San Diego).

Gustafson, B. Å. S. (2009). Scaled analogue experiments in electromagnetic scattering. *Light Scattering Rev.* **4**, 3–30.

Hanel, R. A., Conrath, B. J., Jennings, D. E., and Samuelson, R. E. (2003). *Exploration of the Solar System by Infrared Remote Sensing* (Cambridge University Press, Cambridge, UK).

Hansen, W. W. (1935). A new type of expansion in radiation problems. *Phys. Rev.* **47**, 139–143.

Hansen, J. E. and Hovenier, J. W. (1974). Interpretation of the polarization of Venus. *J. Atmos. Sci.* **31**, 1137–1160.

Hansen, J. E. and Travis, L. D. (1974). Light scattering in planetary atmospheres. *Space Sci. Rev.* **16**, 527–610.

Hansen, J. E., Sato, M., Kharecha, P., and von Schuckmann, K. (2011). Earth's energy imbalance and implications. *Atmos. Chem. Phys.* **11**, 13 421–13 449.

Hapke, B. (1990). Coherent backscatter and the radar characteristics of outer planet satellites. *Icarus* **88**, 407–417.

Hapke B. (2012). *Theory of Reflectance and Emittance Spectroscopy* (Cambridge University Press, Cambridge, UK).

Harmon, J. K., Slade, M. A., Vélez, R. A., *et al.* (1994). Radar mapping of Mercury's polar anomalies. *Nature* **369**, 213–215.

Healy, W. P. (1982). *Non-Relativistic Quantum Electrodynamics* (Academic Press, London).

Heaviside, O. (1885). Electromagnetic induction and its propagation. *The Electrician* **14**, 178–180; 306–307.

Heaviside, O. (1950). *Electromagnetic Theory* (Dover, New York).

Hergert, W. (2012). Gustav Mie: from electromagnetic scattering to an electromagnetic view of matter. In *The Mie Theory*, ed. W. Hergert and T. Wriedt, pp. 1–51 (Springer, Berlin).

Hertz, H. (1887). Ueber einen Einfluss des ultravioletten Lichtes auf die electrische Entladung. *Ann. Phys.* **267**, 983–1000.

Hill, S. C. and Benner, R. E. (1988). Morphology-dependent resonances. In *Optical Effects Associated with Small Particles*, eds. P. W. Barber and R. K. Chang, pp. 3–61 (World Scientific, Singapore).

Hill, S. C., Hill, A. C., and Barber, P. W. (1984). Light scattering by size/shape distributions of soil particles and spheroids. *Appl. Opt.* **23**, 1025–1031.

Ho, S.-T. and Kumar, P. (1993). Quantum optics in a dielectric: macroscopic electromagnetic-field and medium operators for a linear dispersive lossy medium – microscopic derivation of the operators and their commutation relations. *J. Opt. Soc. Am. B* **10**, 1620–1636.

Holt, A. R. (1982). The scattering of electromagnetic waves by single hydrometeors. *Radio Sci.* **17**, 929–945.

Holt, A. R., Uzunoglu, N. K., and Evans, B. G. (1978). An integral equation solution to the scattering of electromagnetic radiation by dielectric spheroids and ellipsoids. *IEEE Trans. Antennas Propag.* **26**, 706–712.

Hovenier, J. W. (1969). Symmetry relationships for scattering of polarized light in a slab of randomly oriented particles. *J. Atmos. Sci.* **26**, 488–499.

Hovenier, J. W. (2000). Measuring scattering matrices of small particles at optical wavelengths. In *Light Scattering by Nonspherical Particles: Theory, Measurements, and Applications*, ed. M. I. Mishchenko, J. W. Hovenier, and L. D. Travis, pp. 355–365 (Academic Press, San Diego).

Hovenier, J. W. and van der Mee, C. V. M. (2000). Basic relationships for matrices describing scattering by small particles. In *Light Scattering by Nonspherical Particles: Theory, Measurements, and Applications*, ed. M. I. Mishchenko, J. W. Hovenier, and L. D. Travis, pp. 61–85 (Academic Press, San Diego).

Hovenier, J. W., van de Hulst, H. C., and van der Mee, C. V. M. (1986). Conditions for the elements of the scattering matrix. *Astron. Astrophys.* **157**, 301–310.

Hovenier, J. W., van der Mee, C., and Domke, H. (2004). *Transfer of Polarized Light in Planetary Atmospheres—Basic Concepts and Practical Methods* (Kluwer, Dordrecht, The Netherlands).

Howell, J. R., Siegel, R., and Mengüç, M. P. (2011). *Thermal Radiation Heat Transfer* (CRC Press, Boca Raton, FL).

Huang, K.-N. (1980). Theory of angular distribution and spin polarization of photoelectrons. *Phys. Rev. A* **22**, 223–239.

Huckaby, J. L., Ray, A. K., and Das, B. (1994). Determination of size, refractive index, and dispersion of single droplets from wavelength-dependent scattering spectra. *Appl. Opt.* **33**, 7112–7125.

Huffman, D. R. (1988). The applicability of bulk optical constants to small particles. In *Optical Effects Associated with Small Particles*, ed. P. W. Barber and R. K. Chang, pp. 279–324 (World Scientific, Singapore).

Hunt, B. J. (1991). *The Maxwellians* (Cornell University Press, Ithaca, NY).

Hunt, A. J. and Huffman, D. R. (1973). A new polarization-modulated light scattering instrument. *Rev. Sci. Instrum.* **44**, 1753–1762.

Huttner, B. and Barnett, S. M. (1992). Quantization of the electromagnetic field in dielectrics. *Phys. Rev. A* **46**, 4306–4322.

Inan, U. S. and Marshall, R. A. (2011). *Numerical Electromagnetics: The FDTD Method* (Cambridge University Press, Cambridge, UK).

Ishimaru, A. (1978). *Wave Propagation and Scattering in Random Media* (Academic Press, New York). (Also: IEEE Press, New York, 1997.)

Ito, S., Kobayashi, S., and Oguchi, T. (2007). Multiple-scattering formulation of pulsed beam waves in hydrometeors and its application to millimeter-wave weather radar. *IEEE Geosci. Remote Sens. Lett.* **4**, 13–17.

Ivanov, V. V. (1994). Making of radiative transfer theory. *Trudy (Proc.) Astron. Observ. St. Petersburg Univ.* **44**, 6–29 (in Russian).

Jackson, J. D. (1998). *Classical Electrodynamics* (Wiley, New York).

Jaggard, D. L., Hill, C., Shorthill, R. W., *et al*. (1981). Light scattering from particles of regular and irregular shape. *Atmos. Environ.* **15**, 2511–2519.

James, G. L. (2007). *Geometrical Theory of Diffraction for Electromagnetic Waves* (IET Press, Herts, UK).

Jin, J. (2002). *The Finite Element Method in Electromagnetics* (Wiley, New York).

Joosten, J. G. H., Geladé, E. T. F., and Pusey, P. N. (1990). Dynamic light scattering by nonergodic media: Brownian particles trapped in polyacrylamide gels. *Phys. Rev. A* **42**, 2161–2175.

Kahnert, F. M. (2003). Numerical methods in electromagnetic scattering theory. *J. Quant. Spectrosc. Radiat. Transfer* **79–80**, 775–824.

Kahnert, M. (2013a). The T-matrix code *Tsym* for homogeneous dielectric particles with finite symmetries. *J. Quant. Spectrosc. Radiat. Transfer* **123**, 62–78.

Kahnert, M. (2013b). *T*-matrix computations for particles with high-order finite symmetries. *J. Quant. Spectrosc. Radiat. Transfer* **123**, 79–91.

Kahnert, M., Nousiainen, T., and Lindqvist, H. (2014). Model particles in atmospheric optics. *J. Quant. Spectrosc. Radiat. Transfer*, in press.

Kaye, P. H., Aptowicz, K., Chang, R. K., *et al.* (2007). Angularly resolved elastic scattering from airborne particles. In *Optics of Biological Particles*, ed. A. Hoekstra, V. Maltsev, and G. Videen, pp. 31–61 (Springer, Dordrecht, The Netherlands).

Kepler, J. (1604). *Ad Vitellionem Paralipomena, Quibus Astronomiæ pars Optica Traditur* (Frankfurt).

Kerker, M. (1969). *The Scattering of Light and Other Electromagnetic Radiation* (Academic Press, New York).

Khinchin, A. I. (1949). *Mathematical Foundations of Statistical Mechanics* (Dover, New York).

Khlebtsov, N. G. (1992). Orientational averaging of light-scattering observables in the *T*-matrix approach. *Appl. Opt.* **31**, 5359–5365.

Khlebtsov, N. G. (2013). T-matrix method in plasmonics: an overview. *J. Quant. Spectrosc. Radiat. Transfer* **123**, 184–217.

Khlebtsov, N. G., Bogatyrev, V. A., Dykman, L. A., and Melnikov, A. G. (1996). Spectral extinction of colloidal gold and its biospecific conjugates. *J. Colloid Interface Sci.* **180**, 436–445.

Kidd, R., Ardini, J., and Anton, A. (1989). Evolution of the modern photon. *Am. J. Phys*. **57**, 27–35.

Kimble, H. J. and Mandel, L. (1984). Photoelectric detection of polychromatic light. *Phys. Rev. A* **30**, 844–850.

Kittel, C. (1963). Q*uantum Theory of Solids* (Wiley, New York).

Kliger, D. S., Lewis, J. W., and Randall, C. E. (1990). *Polarized Light in Optics and Spectroscopy* (Academic Press, San Diego).

Kline, M. (1972). *Mathematical Thought from Ancient to Modern Times* (Oxford University Press, New York).

Knyazikhin, Y., Marshak, A., Larsen, M. L., *et al.* (2005). Small-scale drop size variability: impact on estimation of cloud optical properties. *J. Atmos. Sci.* **62**, 2555–2567.

Kobayashi, S., Oguchi, T., Tanelli, S., and Im, E. (2007). Backscattering enhancement on spheroid-shaped hydrometeors: considerations in water and ice particles of uniform size and Marshall–Palmer distributed rains. *Radio Sci.* **42**, RS2001.

Kokhanovsky, A. A. (2003). *Polarization Optics of Random Media* (Praxis Publishing, Chichester, UK).

Kramers, H. A. (1957). *Quantum Mechanics* (North-Holland, Amsterdam).

Krylov, V. I. (1962). *Approximate Calculation of Integrals* (MacMillan, New York).

Kuga, Y. and Ishimaru, A. (1984). Retroreflectance from a dense distribution of spherical particles. *J. Opt. Soc. Am. A* **1**, 831–835.

Kunz, K. S. and Luebbers, R. J. (1993). *Finite Difference Time Domain Method for Electromagnetics* (CRC Press, Boca Raton, FL).

Kuščer, I. and Ribarič, M. (1959). Matrix formalism in the theory of diffusion of light. *Opt. Acta* **6**, 42–51.

Kuz'min, V. L., Romanov, V. P., and Zubkov, L. A. (1994). Propagation and scattering of light in fluctuating media. *Phys. Rep.* **248**, 71–368.

Lakhtakia, A. and Mulholland, G. W. (1993). On two numerical techniques for light scattering by dielectric agglomerated structures. *J. Res. Natl. Inst. Stand. Technol.* **98**, 699–716.

Lamb, W. E., Jr. (1995). Anti-photon. *Appl. Phys. B* **60**, 77–84.

Lambert, J. H. (1760). *Photometria, sive de Mensura et Gradibus Luminis, Colorum et Umbrae* (Detlefsen, Augsburg).

Lambert, J. H. (2001). *Photometry, or on the Measure and Gradations of Light, Colors and Shade* (Illuminating Engineering Society of North America, New York). Translation from the Latin original by D. L. DiLaura.

Laven, P. (2003). Simulation of rainbows, coronas, and glories by use of Mie theory. *Appl. Opt.* **42**, 436–444.

Lax, M. (1951). Multiple scattering of waves. *Rev. Mod. Phys*. **23**, 287–310.

Lee, C. M. (1974). Spin polarization and angular distribution of photoelectrons in the Jacob–Wick helicity formalism. Application to autoionization resonances. *Phys. Rev. A* **10**, 1598–1604.

Lenoble, J., ed. (1985). *Radiative Transfer in Scattering and Absorbing Atmospheres: Standard Computational Procedures* (A. Deepak Publishing, Hampton, VA).

Lenoble, J. (1993). *Atmospheric Radiative Transfer* (A. Deepak Publishing, Hampton, VA).

Levine, H. and Schwinger, J. (1950). On the theory of electromagnetic wave diffraction by an aperture in an infinite plane conducting screen. *Commun. Pure Appl. Math.* **3**, 355–391.

Li, L.-W., Kang, X.-K., and Leong, M.-S. (2002). *Spheroidal Wave Functions in Electromagnetic Theory* (Wiley, New York).

Liou, K. N. (1992). *Radiation and Cloud Processes in the Atmosphere: Theory, Observation, and Modeling* (Oxford University Press, New York).

Liou, K. N. (2002). *An Introduction to Atmospheric Radiation* (Academic Press, San Diego).

Liou, K. N., Takano, Y., and Yang, P. (2000). Light scattering and radiative transfer in ice crystal clouds: applications to climate research. In *Light Scattering by Nonspherical Particles: Theory, Measurements, and Applications*, ed. M. I. Mishchenko, J. W. Hovenier, and L. D. Travis, pp. 417–449 (Academic Press, San Diego).

Litvinov, P. and Ziegler, K. (2008). Rigorous derivation of superposition *T*-matrix approach from solution of inhomogeneous wave equation. *J. Quant. Spectrosc. Radiat. Transfer* **109**, 74–88.

Liu, L. and Mishchenko, M. I. (2007). Scattering and radiative properties of complex soot and soot-containing aggregate particles. *J. Quant. Spectrosc. Radiat. Transfer* **106**, 262–273.

Liu, L., Mishchenko, M. I., and Arnott, W. P. (2008). A study of radiative properties of fractal soot aggregates using the superposition *T*-matrix method. *J. Quant. Spectrosc. Radiat. Transfer* **109**, 2656–2663.

Logan, N. A. (1965). Survey of some early studies of the scattering of plane waves by a sphere. *Proc. IEEE* **53**, 773–785.

Lommel, E. (1887). Die Photometrie der diffusen Zurückwerfung. *Sitzber. Acad. Wissensch. München* **17**, 95–124. (Reprinted in *Ann Phys. und Chem. (N.F.)* **36**, 473–502, 1889.)

Lorentz, H. A. (1916). *The Theory of Electrons* (B. G. Teubner, Leipzig).

Lorenz, L. (1890). Lysbevægelsen i og uden for en af plane Lysbølger belyst Kugle. *K. Dan. Vidensk. Selsk. Skr.* **6**, 1–62.

Lukš, A. and Peřinová, V. (2009). *Quantum Aspects of Light Propagation* (Springer, Berlin).

Lynch, D. K. and Livingston, W. (2001). *Color and Light in Nature* (Cambridge University Press, Cambridge, UK).

Lynch, D. K., Sassen, K., Starr, D. O'C., and Stephens, G., eds. (2002). *Cirrus* (Oxford University Press, Oxford).

Lyot, B. (1929). Recherches sur la polarisation de la lumière des planetes et de quelques substances terrestres. *Ann. Observ. Paris, Sect. Meudon* **8**, No. 1. (English translation: Research on the polarization of light from planets and from some terrestrial substances, NASA Tech. Transl. NASA TT F-187, Washington, DC, 1964.)

Macke, A. (2000). Monte Carlo calculations of light scattering by large particles with multiple internal inclusions. In *Light Scattering by Nonspherical Particles: Theory, Measurements, and Applications*, ed. M. I. Mishchenko, J. W. Hovenier, and L. D. Travis, pp. 309–322 (Academic Press, San Diego).

Macke, A. and Mishchenko, M. I. (1996). Applicability of regular particle shapes in light scattering calculations for atmospheric ice particles. *Appl. Opt.* **35**, 4291–4296.

Mackowski, D. W. (1994). Calculation of total cross sections of multiple-sphere clusters. *J. Opt. Soc. Am. A* **11**, 2851–2861.

Mackowski, D. (2012). The extension of Mie theory to multiple spheres. In *The Mie Theory*, eds. W. Hergert and T. Wriedt, pp. 223–256 (Springer, Berlin).

Mackowski, D. W. (2014). A general superposition solution for electromagnetic scattering by multiple scattering domains of optically active media. *J. Quant. Spectrosc. Radiat. Transfer* **133**, 264–270.

Mackowski, D. W. and Mishchenko, M. I. (1996). Calculation of the *T* matrix and the scattering matrix for ensembles of spheres. *J. Opt. Soc. Am. A* **13**, 2266–2278.

Mackowski, D. W. and Mishchenko, M. I. (2011). A multiple sphere *T*-matrix Fortran code for use on parallel computer clusters. *J. Quant. Spectrosc. Radiat. Transfer* **112**, 2182–2192.

Mackowski, D. W. and Mishchenko, M. I. (2013). Direct simulation of extinction in a slab of spherical particles. *J. Quant. Spectrosc. Radiat. Transfer* **123**, 103–112.

Mackowski, D., Kolokolova, L., and Sparks, W. (2011). *T*-matrix approach to calculating circular polarization of aggregates made of optically active materials. *J. Quant. Spectrosc. Radiat. Transfer* **112**, 1726–1732.

Mahon, B. (2003). *The Man Who Changed Everything: The Life of James Clerk Maxwell* (Wiley, Hoboken, NJ).

Mahon, B. (2009). *Oliver Heaviside: Maverick Mastermind of Electricity* (IET Press, Herts, UK).

Mandel, L. and Wolf, E. (1995). *Optical Coherence and Quantum Optics* (Cambridge University Press, Cambridge, UK).

Marchuk, G. I., Mikhailov, G. A., Nazaraliev, M. A., *et al.* (1980). *The Monte Carlo Methods in Atmospheric Optics* (Springer, Berlin). (Original Russian edition: Nauka, Novosibirsk, 1976.)

Marshak, A. and Davis, A. B., eds. (2005). *3D Radiative Transfer in Cloudy Atmospheres* (Springer, Berlin).

Marshak, A., Knyazikhin, Yu., Larsen, M. L., and Wiscombe, W. J. (2005). Small-scale drop size variability: empirical models of drop-size-dependent clustering in clouds // *J. Atmos. Sci.* **62**, 551–558.

Mätzler, C., ed. (2006). *Thermal Microwave Radiation: Applications for Remote Sensing* (IET Press, London).

Maxwell, J. C. (1873). *A Treatise on Electricity and Magnetism* (Clarendon Press, Oxford) (also Dover, New York, 1954).

Mazeron, P. and Muller, S. (1996). Light scattering by ellipsoids in a physical optics approximation. *Appl. Opt*. **35**, 3726–3735.

McCluney, W. R. (1994). *Introduction to Radiometry and Photometry* (Artech House, Boston, MA).

Meland, B., Alexander, J. M., Wong, C.-S., *et al.* (2012). Evidence for particle size–shape correlations in the optical properties of silicate clay aerosols. *J. Quant. Spectrosc. Radiat. Transfer* **113**, 549–558.

Meystre, P. and Sargent, M., III (1999). *Elements of Quantum Optics* (Springer, Berlin).

Mie, G. (1908). Beiträge zur Optik trüber Medien, speziell kolloidaler Metallösungen. *Ann. Physik* **25**, 377–445.

Miller, E. K., Medgyesi-Mitschang, L. N., and Newman, E. H. (1991). *Computational Electromagnetics: Frequency Domain Method of Moments* (IEEE Press, New York).

Mishchenko, M. I. (1991a). Light scattering by randomly oriented axially symmetric particles. *J. Opt. Soc. Am. A* **8**, 871–882. Errata: **9**, 497 (1992).

Mishchenko, M. I. (1991b). Reflection of polarized light by plane-parallel slabs containing randomly-oriented, nonspherical particles. *J. Quant. Spectrosc. Radiat. Transfer* **46**, 171–181.

Mishchenko, M. I. (1992a). Polarization characteristics of the coherent backscatter opposition effect. *Earth Moon Planets* **58**, 127–144.

Mishchenko, M. I. (1992b). Enhanced backscattering of polarized light from discrete random media: calculations in exactly the backscattering direction. *J. Opt. Soc. Am. A* **9**, 978–982.

Mishchenko, M. I. (1993). On the nature of the polarization opposition effect exhibited by Saturn's rings. *Astrophys. J.* **411**, 351–361.

Mishchenko, M. I. (2006). Radiative transfer in clouds with small-scale inhomogeneities: the microphysical approach. *Geophys. Res. Lett.* **33**, L14820.

Mishchenko, M. I. (2007). Electromagnetic scattering by a fixed finite object embedded in an absorbing medium. *Opt. Express* **15**, 13 188–13 202.

Mishchenko, M. I. (2008a). Multiple scattering by particles embedded in an absorbing medium. 1. Foldy–Lax equations, order-of-scattering expansion, and coherent field. *Opt. Express* **16**, 2288–2301.

Mishchenko, M. I. (2008b). Multiple scattering by particles embedded in an absorbing medium. 2. Radiative transfer equation. *J. Quant. Spectrosc. Radiat. Transfer* **109**, 2386–2390.

Mishchenko, M. I. (2009). Gustav Mie and the fundamental concept of electromagnetic scattering by particles: a perspective. *J. Quant. Spectrosc. Radiat. Transfer* **110**, 1210–1222.

Mishchenko, M. I. (2010). The Poynting–Stokes tensor and radiative transfer in discrete random media: the microphysical paradigm. *Opt. Express* **18**, 19 770–19 791.

Mishchenko, M. I. (2011). Directional radiometry and radiative transfer: a new paradigm. *J. Quant. Spectrosc. Radiat. Transfer* **112**, 2079–2094.

Mishchenko, M. I. (2013). Measurement of electromagnetic energy flow through a sparse particulate medium: a perspective. *J. Quant. Spectrosc. Radiat. Transfer* **123**, 122–134.

Mishchenko, M. I. and Dlugach, J. M. (2008). Accuracy of the scalar approximation in computations of diffuse and coherent backscattering by discrete random media. *Phys. Rev. A* **78**, 063822.

Mishchenko, M. I. and Hovenier, J. W. (1995). Depolarization of light backscattered by randomly oriented nonspherical particles. *Opt. Lett.* **20**, 1356–1358.

Mishchenko, M. I. and Lacis, A. A. (2003). Morphology-dependent resonances of nearly spherical particles in random orientation. *Appl. Opt.* **42**, 5551–5556.

Mishchenko, M. I. and Martin, P. A. (2013). Peter Waterman and *T*-matrix methods. *J. Quant. Spectrosc. Radiat. Transfer* **123**, 2–7.

Mishchenko, M. I. and Sassen, K. (1998). Depolarization of lidar returns by small ice crystals: an application to contrails. *Geophys. Res. Lett.* **25**, 309–312.

Mishchenko, M. I. and Travis, D. L. (1997). Satellite retrieval of aerosol properties over the ocean using polarization as well as intensity of reflected sunlight. *J. Geophys. Res.* **102**, 16 989–17 013.

Mishchenko, M. I. and Travis, L. D. (2008). Gustav Mie and the evolving discipline of electromagnetic scattering by particles. *Bull. Am. Meteorol. Soc.* **89**, 1853–1861.

Mishchenko, M. I., Rossow, W. B., Macke, A., and Lacis, A. A. (1996). Sensitivity of cirrus cloud albedo, bidirectional reflectance and optical thickness retrieval accuracy to ice particle shape. *J. Geophys. Res.* **101**, 16 973–16 985.

Mishchenko, M. I., Travis, L. D., Kahn, R. A., and West, R. A. (1997). Modeling phase functions for dustlike tropospheric aerosols using a shape mixture of randomly oriented polydisperse spheroids. *J. Geophys. Res.* **102**, 16 831–16 847.

Mishchenko, M. I., Hovenier, J. W., and Travis, L. D., eds. (2000). *Light Scattering by Nonspherical Particles: Theory, Measurements, and Applications* (Academic Press, San Diego).

Mishchenko, M. I., Travis, L. D., and Lacis, A. A. (2002). *Scattering, Absorption, and Emission of Light by Small Particles* (Cambridge University Press, Cambridge, UK; available in the .pdf format at http://www.giss.nasa.gov/staff/mmishchenko/books.html, assessed November 2013). Chinese edition: National Defense Industry Press, Beijing, 2013.

Mishchenko, M. I., Travis, L. D., and Lacis, A. A. (2006). *Multiple Scattering of Light by Particles: Radiative Transfer and Coherent Backscattering* (Cambridge University Press, Cambridge, UK; available in the .pdf format at http://www.giss.nasa.gov/staff/mmishchenko/books.html, assessed November 2013).

Mishchenko, M. I., Berg, M. J., Sorensen, C. M., and van der Mee, C. V. M. (2009a). On definition and measurement of extinction cross section. *J. Quant. Spectrosc. Radiat. Transfer* **110**, 323–327.

Mishchenko, M. I., Dlugach, J. M., Liu, L., *et al.* (2009b). Direct solutions of the Maxwell equations explain opposition phenomena observed for high-albedo solar system objects. *Astrophys. J.* **705**, L118–L122.

Mishchenko, M. I., Rosenbush, V. K., Kiselev, N. N., *et al.* (2010). *Polarimetric Remote Sensing of Solar System Objects* (Akademperiodyka, Kyiv; available in the .pdf format at http://arxiv.org/abs/1010.1171, assessed November 2013).

Mishchenko M. I., Ya. S. Yatskiv, V. K. Rosenbush, and G. Videen, eds. (2011a). *Polarimetric Detection, Characterization, and Remote Sensing* (Springer, Dordrecht, The Netherlands).

Mishchenko, M. I., V. P. Tishkovets, L. D. Travis, *et al.* (2011b). Electromagnetic scattering by a morphologically complex object: fundamental concepts and common misconceptions. *J. Quant. Spectrosc. Radiat. Transfer* **11**2, 671–692.

Mishchenko, M. I., Videen, G., Khlebtsov, N. G., and Wriedt, T. (2013a). Comprehensive *T*-matrix reference database: a 2012–2013 update. *J. Quant. Spectrosc. Radiat. Transfer* **123**, 145–152.

Mishchenko, M. I., Li, L., and Mackowski, D. W. (2013b). *T*-matrix modeling of linear depolarization by morphologically complex soot and soot-containing aerosols. *J. Quant. Spectrosc. Radiat. Transfer* **123**, 135–144.

Mishchenko, M. I., Goldstein, D., Chowdhary, J., and Lompado, A. (2013c). Radiative transfer theory verified by controlled laboratory experiments. *Opt. Lett.* **38**, 3522–3525.

Mobley, C. D. (1994). *Light and Water: Radiative Transfer in Natural Waters* (Academic Press, San Diego).

Modest, M. (2013). *Radiative Heat Transfer* (Academic Press, San Diego).
Morrison, J. A. and Cross, M.-J. (1974). Scattering of a plane electromagnetic wave by axisymmetric raindrops. *Bell Syst. Tech. J.* **53**, 955–1019.
Mudaliar, S. (2013). Multiple scattering volume-surface interactions. *IEEE Trans. Antennas Propag.* **61**, 3225–3236.
Muinonen, K. (1989). Scattering of light by crystals: a modified Kirchhoff approximation. *Appl. Opt.* **28**, 3044–3050.
Muinonen, K. (2004). Coherent backscattering of light by complex random media of spherical scatterers: numerical solution. *Waves Random Media* **14**, 365–388.
Muinonen, K., Mishchenko, M. I., Dlugach, J. M., *et al.* (2012). Coherent backscattering verified numerically for a finite volume of spherical particles. *Astrophys. J.* **760**, 118.
Müller, C. (1969). *Foundations of the Mathematical Theory of Electromagnetic Waves* (Springer, Berlin).
Muñoz, O. and Hovenier, J. W. (2011). Laboratory measurements of single light scattering by ensembles of randomly oriented small irregular particles in air. A review. *J. Quant. Spectrosc. Radiat. Transfer* **112**, 1646–1657.
Muñoz, O., Moreno, F., Guirado, D., *et al.* (2010). Experimental determination of scattering matrices of dust particles at visible wavelengths: the IAA light scattering apparatus. *J. Quant. Spectrosc. Radiat. Transfer* **111**, 187–196.
Muñoz, O., Moreno, F., Guirado, D., *et al.* (2012). The Amsterdam–Granada Light Scattering Database. *J. Quant. Spectrosc. Radiat. Transfer* **113**, 565–574.
Munz, P. (1975). Angular dependence and vectorial effect of the photoemission from EuO. *Solid State Commun*. **17**, 627–630.
Nahin, P. J. (2002). *Oliver Heaviside: The Life, Work, and Times of an Electrical Genius of the Victorian Age* (Johns Hopkins University Press, Baltimore).
Newton, R. G. (1982). *Scattering Theory of Waves and Particles* (Springer, New York). (Also: Dover, Mineola, NY, 2002.)
Nisato, G., Hébraud, P., Munch, J.-P., and Candau, S. J. (2000). Diffusing-wave-spectroscopy investigation of latex particle motion in polymer gels. *Phys. Rev. E* **61**, 2879–2887.
Nousiainen, T. (2009). Optical modeling of mineral dust particles: a review. *J. Quant. Spectrosc. Radiat. Transfer* **110**, 1261–1279.
Novotny, L. and Hecht, B. (2012). *Principles of Nano-Optics* (Cambridge University Press, Cambridge, UK).
Nussenzveig, H. M. (1992). *Diffraction Effects in Semiclassical Scattering* (Cambridge University Press, Cambridge, UK).
Oetking, P. (1966). Photometric studies of diffusely reflecting surfaces with applications to the brightness of the Moon. *J. Geophys. Res*. **71**, 2505–2513.
Oguchi, T. (1973). Scattering properties of oblate raindrops and cross polarization of radio waves due to rain: calculations at 19.3 and 34.8 GHz. *J. Radio Res. Lab. Japan* **20**, 79–118.
Onaka, T. (1980). Light scattering by spheroidal grains. *Ann. Tokyo Astron. Observ.* **18**, 1–54.
Ostro, S. J. (1993). Planetary radar astronomy. *Rev. Mod. Phys*. **65**, 1235–1279.
Oxenius, J. (1986). *Kinetic Theory of Particles and Photons* (Springer, Berlin).
Panetta, R. L., Liu, C., and Yang, P. (2013). A pseudo-spectral time domain method for light scattering computation. *Light Scattering Rev.* **8**, 139–188.

Peltoniemi, J., Hakala, T., Suomalainen, J., and Puttonen, E. (2009). Polarised bidirectional reflectance factor measurements from soil, stones, and snow. *J. Quant. Spectrosc. Radiat. Transfer* **110**, 1940–1953.

Penttilä, A. and Lumme, K. (2004). The effect of particle shape on scattering—a study with a collection of axisymmetric particles and sphere clusters. *J. Quant. Spectrosc. Radiat. Transfer* **89**, 303–310.

Perrin, F. (1942). Polarization of light scattered by isotropic opalescent media. *J. Chem. Phys*. **10**, 415–427.

Perry, R. J., Hunt, A. J., and Huffman, D. R. (1978). Experimental determination of Mueller scattering matrices for nonspherical particles. *Appl. Opt.* **17**, 2700–2710.

Peterson, B. and Ström, S. (1973). *T* matrix for electromagnetic scattering from an arbitrary number of scatterers and representations of E(3)*. *Phys. Rev. D* **8**, 3661–3678.

Peterson, B. and Ström, S. (1974). *T*-matrix formulation of electromagnetic scattering from multilayered scatterers. *Phys. Rev. D* **10**, 2670–2684.

Peterson, A. F., Ray, S. L., and Mittra, R. (1998). *Computational Methods for Electromagnetics* (IEEE Press, New York).

Petty, G. W. (2006). *A First Course in Atmospheric Radiation* (Sundog Publishing, Madison, WI).

Planck, M. (1906). *Theorie der Wärmestrahlung* (Verlag Von Johann Ambrosius Barth, Leipzig). (English translation: *The Theory of Heat Radiation*, Blakiston's Son & Co., Philadelphia, 1914).

Poincaré, H. (1890). Sur le problème des trois corps et les équations de la Dynamique. *Acta Math.* **13**, 1–270.

Poincaré, H. (1892). *Théorie Mathématique de la Lumière*, Vol. 2 (Georges Carré, Paris).

Poincaré, H. (1904). L'état actuel et l'avenir de la Physique mathématique. *Bull. Sci. Math.* **28**, 302–324. English translations: The principles of mathematical physics. In *Congress of Arts and Science, St. Louis, 1904*, Vol. I., ed. H. J. Rogers, pp. 604–622 (Riverside Press, Cambridge, MA, 1905); The present and the future of mathematical physics. *Bull Am. Math. Soc*. **37**, 25–38 (2000).

Poincaré, H. (1905). Sur la dynamique de l'électron. *Compt. Rend. Acad. Sci.* **140**, 1504–1508.

Poincaré, H. (1906). Sur la dynamique de l'électron. *Rend. Circ. Matem. Palermo* **21**, 129–175.

Pomraning, G. C. (1991). *Linear Kinetic Theory and Particle Transport in Stochastic Mixtures* (World Scientific, Singapore).

Power, E. A. (1964). *Introductory Quantum Electrodynamics* (Longmans, London).

Poynting, J. H. (1884). On the transfer of energy in the electromagnetic field. *Phil. Trans. R. Soc. London* **175**, 343–361.

Preisendorfer, R. W. (1965). *Radiative Transfer on Discrete Spaces* (Pergamon Press, Oxford).

Press, W. H., Teukolsky, S. A., Vetterling, W. T., and Flannery, B. P. (1992). *Numerical Recipes in FORTRAN* (Cambridge University Press, Cambridge, UK).

Priestley, M. B. (1992). *Spectral Analysis and Time Series* (Academic Press, London).

Prishivalko, A. P., Babenko, V. A., and Kuzmin, V. N. (1984). *Scattering and Absorption of Light by Inhomogeneous and Anisotropic Spherical Particles* (Nauka i Tekhnika, Minsk, USSR) (in Russian).

Psarev, V., Ovcharenko, A., Shkuratov, Yu., *et al.* (2007). Photometry of particulate surfaces at extremely small phase angles. *J. Quant. Spectrosc. Radiat. Transfer* **106**, 455–463.

Purcell, E. M. and Pennypacker, C. R. (1973). Scattering and absorption of light by nonspherical dielectric grains. *Astrophys. J.* **186**, 705–714.

Pusey, P. N. and van Megen, W. (1989). Dynamic light scattering by non-ergodic media. *Physica A* **157**, 705–741.

Pye, D. (2001). *Polarised Light in Science and Nature* (Institute of Physics, Bristol, UK).

Quinten, M. (2011). *Optical Properties of Nanoparticle Systems* (Wiley-VCH, Weinheim, Germany).

Ray, A. K. and Nandakumar, R. (1995). Simultaneous determination of size and wavelength-dependent refractive indices of thin-layered droplets from optical resonances. *Appl. Opt.* **34**, 7759–7770.

Rayleigh, Lord (1871a). On the light from the sky, its polarization and colour. *Phil. Mag.* **41**, 107–120, 274–279.

Rayleigh, Lord (1871b). On the scattering of light by small particles. *Phil. Mag.* **41**, 447–454.

Rayleigh, Lord (1881). On the electromagnetic theory of light. *Phil. Mag.* **12**, 81–101.

Rayleigh, Lord (1897). On the incidence of aerial and electric waves upon small obstacles in the form of ellipsoids or elliptic cylinders, and on the passage of electric waves through a circular aperture in a conducting screen. *Phil. Mag.* **44**, 28–52.

Rayleigh, Lord (1907). On the dynamical theory of gratings. *Proc. Roy. Soc. A* **79**, 399–416.

Robinson, F. N. H. (1973). *Macroscopic Electromagnetism* (Pergamon Press, Oxford).

Rose, M. E. (1957). *Elementary Theory of Angular Momentum* (Wiley, New York). (Also: Dover Publications, New York, 1995.)

Rosenbush, V. K. and Mishchenko, M. I. (2011). Opposition planetary phenomena in planetary astrophysics: observational results. In *Polarimetric Detection, Characterization, and Remote Sensing*, ed. M. I. Mishchenko, Ya. S. Yatskiv, V. K. Rosenbush, and G. Videen, pp. 409–436 (Springer, Dordrecht, The Netherlands).

Rother, T. and Kahnert, M. (2014). *Electromagnetic Wave Scattering on Nonspherical Particles: Basic Methodology and Simulations* (Springer, Berlin).

Rothwell, E. J. and Cloud, M. J. (2009). *Electromagnetics* (CRC Press, Boca Raton, FL).

Roychoudhuri, C., Kracklauer, A. F., and Creath, K., eds. (2008). *The Nature of Light: What is a Photon* (CRC Press, Boca Raton, FL).

Rozenberg, G. V. (1955). Stokes vector-parameter. *Uspekhi Fiz. Nauk* **56**(1), 77–110 (in Russian).

Sassen, K. (2000). Lidar backscatter depolarization technique for cloud and aerosol research. In *Light Scattering by Nonspherical Particles: Theory, Measurements, and Applications*, ed. M. I. Mishchenko, J. W. Hovenier, and L. D. Travis, pp. 393–416 (Academic Press, San Diego).

Saxon, D. S. (1955a). Tensor scattering matrix for the electromagnetic field. *Phys. Rev.* **100**, 1771–1775.

Saxon, D. S. (1955b). Lectures on the scattering of light (Scientific Report No. 9, Department of Meteorology, University of California at Los Angeles).

Scheffold, F., Skipetrov, S. E., Romer, S., and Schurtenberger, P. (2001). Diffusing-wave spectroscopy of nonergodic media. *Phys. Rev. E* **63**, 061404.

Schelkunoff, S. A. (1972). On teaching the undergraduate electromagnetic theory. *IEEE Trans. Education* **15**, 15–25.

Schnaiter, M., Büttner, S., Möhler, O., *et al.* (2012). Influence of particle size and shape on the backscattering linear depolarisation ratio of small ice crystals—cloud chamber measurements in the context of contrail and cirrus microphysics. *Atmos. Chem. Phys.* **12**, 10 465–10 484.

Schot, S. H. (1992). Eighty years of Sommerfeld's radiation condition. *Hist. Math.* **19**, 385–401.

Schuster, A. (1905). Radiation through a foggy atmosphere. *Astrophys. J.* **21**, 1–22.

Scully, M. O. and Zubairy, M. S. (1997). *Quantum Optics* (Cambridge University Press, Cambridge, UK).

Shchegrov, A. V., Maradudin, A. A., and Méndez, E. R. (2004). Multiple scattering of light from randomly rough surfaces. *Prog. Opt.* **46**, 117–241.

Sheng, P. (2006). *Introduction to Wave Scattering, Localization, and Mesoscopic Phenomena* (Springer, Berlin).

Shifrin, K. S. (1988). *Physical Optics of Ocean Water* (AIP Press, New York). (Original Russian edition: Gidrometeoizdat, Leningrad, 1983.)

Shkuratov, Yu. G., Muinonen, K., Bowell, E., *et al.* (1994). A critical review of theoretical models of negatively polarized light scattered by atmosphereless solar system bodies. *Earth Moon Planets* **65**, 201–246.

Shkuratov, Yu., Bondarenko, S., Ovcharenko, A., *et al.* (2006). Comparative studies of the reflectance and degree of linear polarization of particulate surfaces and independently scattering particles. *J. Quant. Spectrosc. Radiat. Transfer* **100**, 340–358.

Shkuratov, Yu., Bondarenko, S., Kaydash, V., *et al.* (2007). Photometry and polarimetry of particulate surfaces and aerosol particles over a wide range of phase angles. *J. Quant. Spectrosc. Radiat. Transfer* **106**, 487–508.

Shurcliff, W. A. (1962). *Polarized Light: Production and Use* (Harvard University Press, Cambridge, MA).

Silver, S., ed. (1949). *Microwave Antenna Theory and Design* (McGraw-Hill, New York).

Silvester, P. P. and Ferrari, R. L. (1996). *Finite Elements for Electrical Engineers* (Cambridge University Press, New York).

Smoluchowski, von M. (1908). Molekular-kinetische Theorie der Opaleszenz von Gasen im kritischen Zustande, sowie einiger verwandter Erscheinungen. *Ann. Phys.* **25**, 205–226.

Snabre, P. and Pouligny, B. (2008). Size segregation in a fluid-like or gel-like suspension settling under gravity or in a centrifuge. *Langmuir* **24**, 13 338–13 347.

Sobolev, V. V. (1975). *Light Scattering in Planetary Atmospheres* (Pergamon Press, Oxford). (Original Russian edition: Nauka, Moscow, 1972.)

Somerville, W. R. C., Auguié, B., and Le Ru, E. C. (2013). A new numerically stable implementation of the *T*-matrix method for electromagnetic scattering by spheroidal particles. *J. Quant. Spectrosc. Radiat. Transfer* **123**, 153–168.

Sommerfeld, A. (1912). Die Greensche Funktion der Schwingungsgleichung. *Jahresber. Deutsch. Math.-Verein.* **21**, 309–353.

Sorensen, C. M. (2001). Light scattering by fractal aggregates: a review. *Aerosol. Sci. Technol.* **35**, 648–687.

Spinrad, R. W., Carder, K. L., and Perry, M. J., eds. (1994). *Ocean Optics* (Oxford University Press, New York).

Stephens, G. L. (1994). *Remote Sensing of the Lower Atmosphere* (Oxford University Press, New York).

Stokes, G. G. (1852). On the composition and resolution of streams of polarized light from different sources. *Trans. Cambridge Philos. Soc.* **9**, 399–416.

Stoletov, A. G. (1889). *Actinoelectric Investigations* (*Актино-Электрические Исследования*) (V. Demakov Publishing House, St. Petersburg; available in the .pdf format at http://e-heritage.ru/ras/view/publication/general.html?id=42070560).

Stratton, J. A. (1941). *Electromagnetic Theory* (McGraw Hill, New York). (Also: Wiley, Hoboken, NJ, 2007.)

Suttorp, L. G. (1989). Statistical foundations of electrodynamic theory. In *Physics in the Making*, ed. A. Sarlemijn and M. J. Sparnaay, pp. 167–194 (Elsevier, Amsterdam).

Suttorp, L. G. and Wubs, M. (2004). Field quantization in inhomogeneous absorptive dielectrics. *Phys. Rev. A* **70**, 013816.

Szegő, G. (1959). *Orthogonal Polynomials* (American Mathematical Society, New York).

Taflove, A. and Hagness, S. C. (2005). *Computational Electrodynamics: The Finite-Difference Time-Domain Method* (Artech House, Boston).

Tai, C.-T. (1994). *Dyadic Green Functions in Electromagnetic Theory* (IEEE Press, New York).

Taylor, J. R., Zafiratos, C. D., and Dubson, M. A. (2004). *Modern Physics for Scientists and Engineers* (Prentice Hall, Upper Saddle River, NJ).

Thomas, G. E. and Stamnes, K. (1999). *Radiative Transfer in the Atmosphere and Ocean* (Cambridge University Press, Cambridge, UK).

Tinbergen, J. (1996). *Astronomical Polarimetry* (Cambridge University Press, Cambridge, UK).

Tishchenko, A. V. (2010). Rayleigh was right: electromagnetic fields and corrugated interfaces. *Opt. Photon. News* **21**(7), 50–54.

Tishkovets, V. P., Petrova, E. V., and Mishchenko, M. I. (2011). Scattering of electromagnetic waves by ensembles of particles and discrete random media. *J. Quant. Spectrosc. Radiat. Transfer* **112**, 2095–2127.

Tolstoy, I. (1981). *James Clerk Maxwell: A Biography* (Canongate, Edinburgh).

Tsang, L. and Ishimaru, A. (1984). Backscattering enhancement of random discrete scatterers. *J. Opt. Soc. Am. A* **1**, 836–839.

Tsang, L., Kong, J. A., and Shin, R. T. (1985). *Theory of Microwave Remote Sensing* (Wiley, New York).

Tsang, L., Kong, J. A., and Ding, K.-H. (2000). *Scattering of Electromagnetic Waves: Theories and Applications* (Wiley, New York).

Tu, H. and Ray, A. K. (2001). Analysis of time-dependent scattering spectra for studying processes associated with microdroplets. *Appl. Opt.* **40**, 2522–2534.

Tuchin, V. V., ed. (2002). *Handbook of Optical Biomedical Diagnostics* (SPIE Press, Bellingham, WA).

Tuchin, V. V. (2007). *Tissue Optics. Light Scattering Methods and Instruments for Medical Diagnostics* (SPIE Press, Bellingham, WA).

Tuchin, V. V., Wang, L. V., and Zimnyakov, D. A. (2006). *Optical Polarization in Biomedical Applications* (Springer, Berlin).

Twersky, V. (1964). On propagation in random media of discrete scatterers. *Proc. Symp. Appl. Math.* **16**, 84–116.

Uhlenbeck, G. E. and Ford, G. W. (1963). *Lectures in Statistical Mechanics* (American Mathematical Society, Providence, RI).

Ulaby, F. T. and Elachi, C., eds. (1990). *Radar Polarimetry for Geoscience Applications* (Artech House, Norwood, MA).

Vaillon, R., Geffrin, J.-M., Eyraud, C., *et al.* (2011). A new implementation of a microwave analog to light scattering measurement device. *J. Quant. Spectrosc. Radiat. Transfer* **112**, 1753–1760.

Van Albada, M. P. and Lagendijk, A. (1985). Observation of weak localization of light in a random medium. *Phys. Rev. Lett*. **55**, 2692–2695.

Van Bladel, J. (1961). Some remarks on Green's dyadic for infinite space. *IRE Trans. Antennas Propag.* **9**, 563–566.

Van Bladel, J. G. (2007). *Electromagnetic Fields* (Wiley, Hoboken, NJ).

van de Hulst, H. C. (1957). *Light Scattering by Small Particles* (Wiley, New York). (Also: Dover, New York, 1981.)

van de Hulst, H. C. (1980). *Multiple Light Scattering. Tables, Formulas, and Applications*, Vols. 1 and 2 (Academic Press, San Diego).

van der Mee, C. V. M. and Hovenier, J. W. (1990). Expansion coefficients in polarized light transfer. *Astron. Astrophys.* **228**, 559–568.

Varshalovich, D. A., Moskalev, A. N., and Khersonskii, V. K. (1988). *Quantum Theory of Angular Momentum* (World Scientific, Singapore). (Original Russian edition: Nauka, Leningrad, 1975.)

Verhulst, F. (2012). *Henri Poincaré—Impatient Genius* (Springer, New York).

Videen, G., Ngo, D., Chýlek, P., and Pinnick, R. G. (1995). Light scattering from a sphere with an irregular inclusion. *J. Opt. Soc. Am. A* **12**, 922–928.

Videen, G., Yatskiv, Ya., and Mishchenko, M., eds. (2004). *Photopolarimetry in Remote Sensing* (Kluwer Academic Publishers, Dordrecht, The Netherlands).

Vladimirov, V. S. (1971). *Equations of Mathematical Physics* (Marcel Dekker, New York).

Voit, F., Schäfer, J., and Kienle, A. (2009) Light scattering by multiple spheres: comparison between Maxwell theory and radiative-transfer-theory calculations. *Opt. Lett.* **34**, 2593–2595.

Volakis, J. L., Chatterjee, A., and Kempel, L. C. (1998). *Finite Element Method for Electromagnetics* (IEEE Press, New York).

Volkov, S. N., Samokhvalov, I. V., and Kim, D. (2013). Assessing and improving the accuracy of *T*-matrix calculation of homogeneous particles with point-group symmetries. *J. Quant. Spectrosc. Radiat. Transfer* **123**, 169–175.

Volten, H., Muñoz, O., Rol, E., *et al*. (2001). Scattering matrices of mineral aerosol particles at 441.6 nm and 632.8 nm. *J. Geophys. Res.* **106**, 17 375–17 402.

Voshchinnikov, N. V. and Farafonov, V. G. (1993). Optical properties of spheroidal particles. *Astrophys. Space Sci.* **204**, 19–86.

Wagner, R., Linke, C., Naumann, K.-H., *et al.* (2009). A review of optical measurements at the aerosol and cloud chamber AIDA. *J. Quant. Spectrosc. Radiat. Transfer* **110**, 930–949.

Waterman, P. C. (1971). Symmetry, unitarity, and geometry in electromagnetic scattering. *Phys. Rev. D* **3**, 825–839.

Watson, K. M. (1953). Multiple scattering and the many-body problem – applications to photomeson production in complex nuclei. *Phys. Rev*. **89**, 575–587.

Watson, K. M. (1969). Multiple scattering of electromagnetic waves in an underdense plasma. *J. Math. Phys*. **10**, 688–702.

Wehrse, R. and Kalkofen, W. (2006). Advances in radiative transfer. *Astron. Astrophys. Rev.* **13**, 3–29.

Weinzierl, B., Petzold, A., Esselborn, M., *et al.* (2009). Airborne measurements of dust layer properties, particle size distribution and mixing state of Saharan dust during SAMUM 2006. *Tellus B* **61**, 96–117.

Welch, A. J. and van Gemert, M. J. C., eds. (2011). *Optical-Thermal Response of Laser-Irradiated Tissue* (Springer, Berlin).

Wendisch, M. and Yang, P. (2012). *Theory of Atmospheric Radiative Transfer* (Wiley-VCH, Weinheim, Germany).

West, R. A. (1991). Optical properties of aggregate particles whose outer diameter is comparable to the wavelength. *Appl. Opt.* **30**, 5316–5324.

Whittaker, E. (1987). *A History of the Theories of Aether and Electricity*, Vols. I and II (American Institute of Physics, New York).

Wiscombe, W. J. (2005). Scales, tools and reminiscences. In *3D Radiative Transfer in Cloudy Atmospheres*, eds. A. Marshak and A. B. Davis, pp. 3–92 (Springer, Berlin).

Wolf, E. (1978). Coherence and radiometry. *J. Opt. Soc. Am.* **68**, 6–17.

Wolf, P.-E. and Maret, G. (1985). Weak localization and coherent backscattering of photons in disordered media. *Phys. Rev. Lett*. **55**, 2696–2699.

Wriedt, T., ed. (1999). *Generalized Multipole Techniques for Electromagnetic and Light Scattering* (Elsevier, Amsterdam).

Wriedt, T. (2002). Using the T-matrix method for light scattering computations by non-axisymmetric particles: superellipsoids and realistically shaped particles. *Part. Part. Syst. Charact.* **19**, 256–268.

Xue, J.-Z., Pine, D. J., Milner, S. T., *et al.* (1992). Nonergodicity and light scattering from polymer gels. *Phys. Rev. A* **46**, 6550–6563.

Yang, P. and Liou, K. N. (1996). Geometric-optics–integral-equation method for light scattering by nonspherical ice crystals. *Appl. Opt.* **35**, 6568–6584.

Yang, P. and Liou, K. N. (2000). Finite difference time domain method for light scattering by nonspherical and inhomogeneous particles. In *Light Scattering by Nonspherical Particles: Theory, Measurements, and Applications*, ed. M. I. Mishchenko, J. W. 1Hovenier, and L. D. Travis, pp. 173–221 (Academic Press, San Diego).

Yang, P. and Liou, K. N. (2006). Light scattering and absorption by nonspherical ice crystals. *Light Scattering Rev*. **1**, 31–71.

Yanovitskij, E. G. (1997). *Light Scattering in Inhomogeneous Atmospheres* (Springer, Berlin).

Yee, K. S. (1966). Numerical solution of initial boundary value problems involving Maxwell's equations in isotropic media. *IEEE Trans. Antennas Propag.* **14**, 302–307.

Yosida, K. (1960). *Lectures on Differential and Integral Equations* (Interscience, New York).

Yurkin, M. A. and Hoekstra, A. G. (2007). The discrete dipole approximation: an overview and recent developments. *J. Quant. Spectrosc. Radiat. Transfer* **106**, 558–589.

Yurkin, M. A. and Hoekstra, A. G. (2011). The discrete-dipole-approximation code ADDA: capabilities and known limitations. *J. Quant. Spectrosc. Radiat. Transfer* **112**, 2234–2247.

Zangwill, A. (2013). *Modern Electrodynamics* (Cambridge University Press, Cambridge, UK).

Zdunkowski, W., Trautmann, T., and Bott, A. (2007). *Radiation in the Atmosphere* (Cambridge University Press, Cambridge, UK).

Zender, C. S. and Talamantes, J. (2006). Solar absorption by Mie resonances in cloud droplets. *J. Quant. Spectrosc. Radiat. Transfer* **98**, 122–129.

Index

A

A-Train, 11
absorption coefficient, 34
absorption cross section, *see* cross section, absorption
Alexander's dark band, 251
amplitude scattering matrix, 57, 58
  backscattering, 197
  backscattering theorem for, 58, 59
  forward-scattering, 194, 195
  reciprocity relation for, 58, 59
  symmetry properties of, 186–188
angle
  azimuth, 36, 73
  phase, 363
  polar, 36, 73
  scattering, 186, 189
  zenith, *see* angle, polar
angular frequency, 5, 19
approximation
  first-order-scattering, *see* first-order-scattering approximation
  geometrical optics, 225–231
  physical optics, 231
  ray-tracing, *see* approximation, geometrical optics
  scalar, *see* scalar approximation
  single-scattering, *see* single-scattering approximation
associated Legendre functions, 380, 387
asymmetry parameter, 156, 199, 239, 243
attenuation coefficient, *see* extinction coefficient
averaging
  ensemble, 108, 109, 160–165
  orientation, 161, 164, 165
    analytical, 222
    effects of, 252
  over time, 107–109
  shape, 164, 165
    effects of, 253
  size, 164, 165
    effects of, 248, 252
azimuth angle, *see* angle, azimuth

B

backscattering depolarization ratio
  circular, 201, 209
  linear, 201, 209, 256, 257, 267–269
backscattering theorem, 58, 59, 149
Bessel functions, spherical, 214, 380
Bouguer–Beer law, *see* Bouguer law
Bouguer law, 318, 334
boundary conditions, 5, 17, 18, 43
  absorbing, 216, 217

C

charge density
  macroscopic, 16
  surface, 18
charge-coupled device, 112, 113, 128
circular-polarization column vector, 83
  rotation transformation rule for, 84, 394

coherency column vector, 83
of the coherent field, 298
transfer equation for, 299
coherent backscattering, xiii, 279, *also see* weak localization
coherent field, 291, 293–298
transfer equation for, 298, 299
Twersky expansion of, 291–293
coherent Stokes column vector, 299, 316
Stokes identity for, 330
Stokes–Verdet inequality for, 330
coherent transmission amplitude matrix, 298
reciprocity relation for, 333, 402
coherent transmission dyadic, 296
reciprocity relation for, 333, 402
coherent transmission Stokes matrix, 299
reciprocity relation for, 333, 402
complex permittivity, 20
conductivity, 16
constitutive parameters
frequency dependent, 20
frequency independent, 20
constitutive relations, 16, 17, 19, 20
continuity equation, 16
controlled laboratory measurements, 213
coordinate system
Cartesian, 73
laboratory, 161, 221
particle, 161, 221
right-handed, 36, 73
spherical, 36, 73
cosine integral, 307
cross section
absorption, 154, 199
differential scattering, 155
extinction, 142, 154, 195
geometrical, 155
scattering, 154, 199
current density, 16
surface, 18
cyclical diagrams, 359

D

delta function
solid-angle, 140
three-dimensional, 375
dichroism, 151
differential equation methods, 213
diffraction, 226, 227, 250
diffuse specific coherency dyadic, *see* specific coherency dyadic, diffuse
diffuse specific coherency matrix, *see* specific coherency matrix, diffuse
diffuse specific intensity column vector, *see* specific intensity column vector, diffuse
direct problem, 13
discrete dipole approximation, 219, 224
discrete random medium, 270, 369
Doppler shift, 4
dyad, 372
dyadic, 372
Hermitian, 373
identity, *see* identity dyadic
symmetric, 373
transpose of, 373
dyadic correlation function, 88, 299, 359
cyclical, 357, 359
ladder approximation for, 299–310
Twersky expansion of, 300
dyadic exponential, 295
dyadic propagation constant, 296
dyadic transition operator, 48, 49, 56, 57, 63
integral equation for, 48
dynamic light scattering, *see* scattering, dynamic

E

effective radius, 208
effective size parameter, *see* size parameter, effective
effective variance, 206
efficiency factor
for absorption, 155, 199
for extinction, 155, 199, 238–244
for scattering, 155, 199

electric displacement, 16
electric field, 5, 16
electric permittivity, 16
  complex, 20
  frequency-dependent, 20
  of a vacuum, 16
electric polarization, 16
electric susceptibility, 16
electromagnetic energy density, 23
  time-averaged, 39, 40
electromagnetic field
  monochromatic, 9, 19, 41
  polychromatic, 89–98
  quasi-monochromatic, 9, 93
electromagnetic scattering, 6, 7, 41–49
  monochromatic
    by a fixed object, 99–101
    by a stochastic object, 105, 106
  polychromatic
    by a fixed object, 101, 102
    by a stochastic object, 106, 107
electromagnetic scattering problem, standard, 43
      existence of solution, 43, 44, 47
      uniqueness of solution, 43, 44
electromagnetic scattering problems, classification of, 369
electromagnetic spectrum, *see* spectrum, electromagnetic
electromagnetic wave
  plane, 7, 30–35, 56, 74
    circularly polarized, 79, 81, 82, 84
    homogeneous, 32
    inhomogeneous, 32
    linearly polarized, 79, 80, 84
    quasi-monochromatic, *see* quasi-monochromatic plane wave
  spherical, 35–39, 52
    incoming, 38, 39
    outgoing, 35–38
  transverse, 32, 37, 39, 51, 52, 73
emission, thermal, 4
energy-budget problem, 10, 12, 13, 21–24, 151–153, 175, 176, 318, 319, 322
energy conservation, 22, 24
enhancement factor, 364
  scalar, 365
entrance pupil of a WCR, 124, 125, 141, 142
ergodic hypothesis, 109, 110
ergodicity, 108, 109, 110, 291, 325, 326
Euler angles, 161, 221, 378, 379
extended boundary condition method, 222
  iterative, 224
extinction coefficient, 318
extinction cross section, *see* cross section, extinction
extinction matrix
  coherency, 149, 150
  Stokes, 150, 195
    reciprocity relation for, 151
    symmetry property of, 151

F

far-field limit, 52
  theoretical criteria of, 53–56
far-field scattering, 50–61, 137–167
  by a stochastic object, 157–159
  by an ergodic random object, 159, 160
  polychromatic, 156–160
far zone, 51–56, 393
finite-difference time-domain method, 217, 224
finite element method, 216, 217, 224
first-order-scattering approximation, 177–179
  conditions of applicability of, 179–182
  effects of forward-scattering interference on, 181, 182
fluorescence, 4
Foldy approximation, 297
Foldy equations, 62–71
  far-field version of, 66–70
    conditions of applicability, 71, 393, 394
forward-scattering localization, 279, 328
Fredholm integral equation method, 219
frequency-domain formalism, 21

Fresnel's formulas, 225

G

Gauss theorem, 22
generalized spherical functions, 203
geometrical optics approximation, *see* approximation, geometrical optics
Gershun tube, 129
glory, 251
Green's function
  dyadic, free space, 45, 46
    differential equation for, 376
    radiation condition for, 377
    singularity of, 49
    symmetries of, 376
  scalar, 375
    differential equation for, 375
Green's matrices, 342
Green's theorem, dyadic, 45

H

halo, 256
Hankel functions, spherical, 214
Henyey–Greenstein phase function, 210, 211, 350

I

identity dyadic, 373
incident field, 6, 7, 9, 41, 45, 47
independent scattering, 331, 332, 370
integral equation methods, 213
intensity, 34, 37, 39, 75
interference structure, 240
inverse problem, 13

J

Jones' lemma, 381

K

Kronecker delta, 385

L

ladder diagrams, 309
ladder specific coherency dyadic, 311, 312
  integral equation for, 312
Legendre functions, associated, *see* associated Legendre functions
Legendre polynomials, 380, 387
Leibniz rule, 402
light scattering, 14, *also see* electromagnetic scattering
Lippmann–Schwinger equation, 48, 63
Lorentz force, 22
Lorenz–Mie
  coefficients, 214
    resonance behavior of, 241–243
  computer code, 214
  resonances, 241–245, 251, 266, 267
  scattering matrix, 200, 203, 214
  theory, 213–215, 236

M

magnetic field, 5, 16
magnetic induction, 16
magnetic permeability, 16
  of a vacuum, 16
magnetization, 16
matrix exponential, 298, 299
matrix propagation constant, 298
maximally crossed diagrams, *see* cyclical diagrams
Maxwell equations, macroscopic, 1, 15, 16
  curl, 5, 42
  frequency domain, 5, 19
measurement techniques for scattering, 231–235
  using microwaves, 233–235
  using visible and infrared light, 232, 233
medium
  absorbing, 25, 33
  active, 25
  discrete random, *see* discrete random medium
  gaseous, 332, 333
  lossless, 25, 39
  lossy, 25, 34
  nonabsorbing, 25, 33, 34, 37
  nondispersive, 19
  passive, 25
  time-dispersive, 17, 19
meridional plane, 73, 74
mesoscopic optical effects, 368
mesoscopic physics, 368

method of moments, 219, 224
microwave analog technique, 231, 233
modified Stokes column vector, 83
  rotation transformation rule for, 84, 394
modulator, electro-optic, 232
Monte Carlo method, 356
Mueller matrix, 132, 134, 232
multi-sphere method, 215, 224, 236

N

natural light, *see* polychromatic beam, unpolarized
near-field scattering, 61
Neumann expansion, 65, 71, 344
  convergence of, 66
  far-field, 70, 71
numerically exact computer solution, 3

O

observable, optical, 72, 99
optical-characterization problem, 13, 266–269
optical depth, 341
optical equivalence principle, 75, 95
optical theorem, 141, 151, 152
optical thickness, 341
orientation averaging, *see* averaging, orientation
orientation distribution function, 164
  uniform, 165, 185
outgoing wave, 35

P

parallel beam of light, 91
particle
  deterministic, 238
    scattering properties of, 238–246
  random morphologically complex, scattering properties of, 251–265
  random spherical, scattering properties of, 247–251
particle number density, 293
particles
  feldspar, 254
  fractal soot, 260–264
  irregular, 253
  macroscopic, 9
  spherically symmetric, 200
  statistically isotropic and mirror-symmetric random, 184, 185, 189
phase angle, *see* angle, phase
phase function, 156, 202
  expansion in Legendre polynomials, 206
  Henyey–Greenstein, *see* Henyey–Greenstein phase function
  normalization condition for, 202
phase matrix
  coherency, 147
    reciprocity relation for, 166, 397, 398
  normalized Stokes, 202, 203
    symmetry properties of, 203
  Stokes, 147, 148
    backscattering, 149
    for a statistically isotropic and mirror-symmetric random particle, 190–192
    inequalities for, 148
    reciprocity relation for, 148
    symmetry relations for, 192, 193
phase velocity, 31, 33, 37
phenomenological radiative transfer theory, *see* radiative transfer theory, phenomenological
photodiode, 112, 113
photoelectric detector, 112–114
  angular sensitivity of, 113, 114
  direction insensitive, 117
  polarization sensitivity of, 113, 114
photoelectric effect, 112, 113, 129
  QED theory of, 112, 113, 130
photometry
  directional, xiii
  phenomenological, 334–337
photomultiplier, 112, 113
photon, 129, 130, 285, 336, 337, 356
plane albedo, 351
plane wave, decomposition in spherical waves, 380, 381
Poincaré recurrence theorem, 109

point matching method, 217
generalized, 218
multiple-expansion, 218, 224
polar angle, *see* angle, polar
polarization
circular, 79, 81, 82, 84
degree of, 96
elliptical, 79, 82
degree of, 96
left-handed, 78, 80, 96
linear, 79, 80, 84
degree of, 96
signed, 98
right-handed, 78, 80, 81, 96
polarization analyzer, 232
polarization ellipse, 78–82
ellipticity of, 78
orientation of, 78
preferential, 96
polarization modulation technique, 233
polarization opposition effect, 281, 285, 367
polarization ratio
linear, 209, 210, 264, 265, 280, 398, 400
circular, 280, 284, 285, 402
polarizer, 131–134, 232, 234
polychromatic beam, 91, 92, 94
circularly polarized, 92
fully polarized, 92, 96
linearly polarized, 92
partially polarized, 92, 96
unpolarized, 92, 96
Poynting-meter, 111, 114–117
Poynting–Stokes tensor, 73, 87, 88
complex, 88
time-averaged
for a monochromatic field, 88
for a polychromatic field, 90, 91, 94
Poynting theorem, 10, 12, 22, 28
Poynting vector, 10, 22, 23, 28, 34, 37, 72, 73, 87
complex, 24
measurement of, 114–125
time-averaged, 10, 24
for a polychromatic field, 91, 94
probability density function, 108, 160, 161, 164, 165, 184, 185
normalization condition for, 109, 161, 164, 165, 184
pseudo-spectral time domain method, 217

Q

quadrature division points, *see* quadrature formula
quadrature formula, 161, 382–384
Gauss, 383
Lobatto, 384
Markov, 384
Radau, 384
quadrature weights, *see* quadrature formula
quantum electrodynamics, 2, 26, 28, 129, 285, 336, 337
quarter-wave plate, 232
quasi-monochromatic plane wave, 9, 94
unpolarized, 95

R

radiance, *see* specific intensity
radiation condition, 6, 43, 47, 220, 235
radiative transfer, xiii
in plane-parallel particulate media, 338–355
radiative transfer equation
boundary conditions for, 317
for a plane-parallel medium, 341
boundary conditions for, 341
for statistically isotropic and mirror-symmetric random particles, 318
integral, 316, 317
integro-differential, 316, 317, 329
scalar, 336, 343
radiative transfer theory, 3, 61
microphysical, 286–337
phenomenological, 334–337, 368, 370
radiometer
panoramic, 128
well-collimated, *see* well-collimated radiometer

rainbows, 250, 251
ray-tracing approximation, *see* approximation, geometrical optics
Rayleigh hypothesis, 217, 235
Rayleigh scattering, 210, 235, 239, 265, 366, 367, 399, 400
reflection matrix
  cyclical, 362, 363
  diffuse multiple-scattering, 363
  first-order, 404
  for the exact backscattering direction, 363, 364
  ladder, 342, 362
refractive index, 33, 35, 39
  relative, 45
relativity theory, 28
retarder, 134
ripple, high-frequency, 240
rotation matrix
  for circular-polarization representation, 84, 394
  for modified Stokes column vector, 84, 394
  Stokes, 77, 84

S

scalar approximation, 330, 343, 365, 366
scale invariance rule, 59, 60, 148, 150, 151, 155, 233
scattered field, 6, 7, 41, 45, 47
scattering
  Brillouin, 4
  by a multi-particle object, 1, 7
  dynamic, 277
  elastic, 4
  electromagnetic, *see* electromagnetic scattering
  far-field, *see* far-field scattering
  gaseous, 332, 333
  independent, *see* independent scattering
  microphysical approach to, 3
  monochromatic, xiii, 41
  multiple, 65, 66, 271–274, 285
  near-field, *see* near-field scattering
  polychromatic, xiii, 99
  Raman, 4
  static, 277
scattering angle, *see* angle, scattering
scattering cross section, *see* cross section, scattering
scattering dyadic, 56–58
  backscattering, 60
  reciprocity relation for, 58, 59
scattering matrix, Stokes, 185
  effects of morphology and orientation on, 200, 201
  for backward scattering, 198
  for forward scattering, 196
  for a spherically symmetric particle, 200
  for a statistically isotropic and mirror-symmetric random particle, 189
  inequalities for, 190
  normalized, 201–203
    expansion in generalized spherical functions, 203–209
    Rayleigh, 210
  symmetries of, 188, 189
scattering object, stochastic, 103–109
scattering plane, 185
separation of variables method for spheroids, 215, 224
shape averaging, *see* averaging, shape
sine integral, 307
single-scattering albedo, 154, 199
single-scattering approximation, 169
  conditions of validity of, 180, 181, 283, 284
size averaging, *see* averaging, size
size distribution, 165
  gamma, 206, 248, 400
  log normal, 267
  modified power law, 252
size parameter, 59
  effective, 208
Snell's law, 225, 251
solid angle element, differential, 38
specific coherency column vector
  diffuse, 315
    integral equation for, 316
    integro-differential equation for, 316

specific coherency dyadic
coherent, 313
diffuse, 313
integral equation for, 313
integro-differential equation for, 313, 314
ladder, 311
integral equation for, 312
specific coherency matrix, diffuse, 314, 315
integral equation for, 315
integro-differential equation for, 315
specific intensity, 319, 331, 343
nonnegativity of, 330, 334, 403
phenomenological, 336, 337
specific intensity column vector, 317, 362
cyclical, 362
diffuse, 316
integral equation for, 316
integro-differential equation for, 316, 329
Stokes–Verdet inequality for, 330
full, 317
integral equation for, 317,
integro-differential equation for, 317, 329
speckle pattern, 272–277
spectrum, electromagnetic, 14
speed of light
in a nonabsorbing material medium, 39
in a vacuum, 33
spherical albedo, 347
spherical harmonics, scalar, 380
completeness relation for, 381
symmetry relation for, 381
standard problem in radiative transfer, 339
static light scattering, *see* scattering, static
stationary phase method, 306, 390, 391
Stokes column vector, 75
modified, *see* modified Stokes column vector
of the coherent field, 299, *also see* coherent Stokes column vector
transfer equation for, 299
Stokes identity, 75, 76, 330
Stokes parameters, 73–85
ellipsometric content of, 77–82
for a polychromatic beam, 92, 94, 95
additivity of, 92
polarization analysis of, 96–98
for a quasi-monochromatic plane wave, 95
measurement of, 131–136
rotation transformation rule for, 76, 77
Stokes–Verdet inequality, 92, 95, 330

T

T matrix, 220, 221
for a cluster, 216, 221
rotation transformation rule for, 221
translation transformation rule for, 222
T-matrix computer programs, 223
T-matrix method, 219–224
invariant-imbedding, 224
superposition, 65, 216, 223, 224
thermal emission, *see* emission, thermal
total field, 7, 47
transformation dyadic, 100
transmission matrix
first-order, 404
ladder, 342
transport mean free path, 360
Twersky approximation, 288

V

vector, complex, 19
vector spherical wave functions, 213, 215, 217, 220, 236
translation addition theorem for, 215
volume integral equation, 44–47, 49, 62
existence of solution, 47
uniqueness of solution, 47
volume integral equation method, 218, 219

W

wave equation, vector, 44

wave number, 32, 37, 43
wave vector, 7, 31
wavelength
  free-space, 34
  in a nonabsorbing medium, 34
weak localization, xiii, 279, 328, 357–367
  angular profile of, 366, 367
    half-width at half-maximum, 366, 367
  by a plane-parallel discrete random medium, 361–367
  by Rayleigh particles, 366, 367
  by solar-system bodies, 367
  scalar theory of, 365
well-collimated radiometer, 111, 120–125, 129, 137–145, 176, 177, 319–321, 325, 326
  response to polychromatic light, 125–127
Wigner *d*-functions, 203, 385–389
  completeness of, 386
  orthogonality of, 386
  recurrence relation for, 386
  symmetry properties of, 385
Wigner *D*-functions, 221

Z

zenith angle, *see* angle, polar

Electromagnetic Scattering by Particles and Particle Groups

The scattering and absorption of light and other electromagnetic radiation by particles and particle groups are central to many science and engineering fields. Unfortunately, this discipline has gained the reputation of being very technically complex and incomprehensible. Now, this self-contained and accessible book provides a thorough introduction to the basic physical and mathematical principles of the subject.

For the first time, the theories of electromagnetic scattering, radiative transfer, and weak localization are combined into a unified, consistent branch of physical optics, directly based on the Maxwell equations. A particular focus is given to key aspects such as time and ensemble averaging at different scales, ergodicity, and the physical nature of measurements afforded by actual photopolarimeters.

Featuring over 100 end-of-chapter exercises, with hints and solutions provided, this clear, one-stop resource is ideal for self-study or classroom use, and will be invaluable to both graduate students and researchers in remote sensing, physical and biomedical optics, optical communications, optical particle characterization, atmospheric physics, and astrophysics.

Cover illustration:
image © Amy Johansson/Shutterstock.com.

Cover designed by Hart McLeod Ltd

CAMBRIDGE
UNIVERSITY PRESS
www.cambridge.org

ISBN 978-0-521-51992-2